

# R-spondin1 Regulates Cell Proliferation of Corneal Endothelial Cells via the Wnt3a/ $\beta$ -Catenin Pathway

Naoki Okumura,<sup>1,2</sup> Takahiro Nakamura,<sup>3</sup> EunDuck P. Kay,<sup>1</sup> Makiko Nakahara,<sup>1</sup> Shigeru Kinoshita,<sup>2</sup> and Noriko Koizumi<sup>1,2</sup>

<sup>1</sup>Department of Biomedical Engineering, Faculty of Life and Medical Sciences, Doshisha University, Kyotanabe, Japan

<sup>2</sup>Department of Ophthalmology, Kyoto Prefectural University of Medicine, Kyoto, Japan

<sup>3</sup>Research Center for Tissue Engineering and Inflammation, Faculty of Life and Medical Sciences, Doshisha University, Kyotanabe, Japan

Correspondence: Noriko Koizumi, Department of Biomedical Engineering, Faculty of Life and Medical Sciences, Doshisha University, Kyotanabe 610-0321, Japan; nkoizumi@mail.doshisha.ac.jp.

Submitted: February 4, 2014

Accepted: September 17, 2014

Citation: Okumura N, Nakamura T, Kay EP, Nakahara M, Kinoshita S, Koizumi N. R-spondin1 regulates cell proliferation of corneal endothelial cells via the Wnt3a/ $\beta$ -catenin pathway. *Invest Ophthalmol Vis Sci*. 2014;55:6861–6869. DOI:10.1167/iops.14-14091

**PURPOSE.** To evaluate the effect of Roof plate-specific spondin 1 (R-spondin1) on the proliferation of corneal endothelial cells (CECs) and to determine whether the Wnt/ $\beta$ -catenin pathway is involved in the activities of R-spondin1.

**METHODS.** The proliferation of rabbit CECs (RCECs) and human CECs (HCECs) was measured by 5-bromo-2'-deoxyuridine (BrdU) incorporation into DNA. The effect of R-spondin1 on CEC density was evaluated in ex vivo organ-cultured rabbit and human corneal tissues. The cell density of HCECs cultured with R-spondin1 was also evaluated in vitro. The subcellular localization of function-associated markers of CECs (zona occludens 1 [ZO-1] and Na<sup>+</sup>/K<sup>+</sup>-ATPase) was determined by immunohistochemistry. The expression of cell cycle proteins and localization of  $\beta$ -catenin were determined by immunoblotting.

**RESULTS.** The in vitro proliferation of RCECs and HCECs increased by 1.2- to 1.3-fold in response to R-spondin1. The CEC densities of rabbit and human corneal tissues were increased significantly by R-spondin1 treatment. Na<sup>+</sup>/K<sup>+</sup>-ATPase and ZO-1 were well preserved on the plasma membranes. When HCECs were maintained in the presence of R-spondin1 for up to 90 days, the maximum cell density was observed at approximately 50 days, and the cell density was maintained for up to 90 days. R-spondin1 facilitated the nuclear import of  $\beta$ -catenin in RCECs within 30 minutes, which subsequently upregulated cyclin D and downregulated p27, leading to G<sub>1</sub>/S progression by hyperphosphorylation of the retinoblastoma protein.

**CONCLUSIONS.** The unique effects of R-spondin1 on the proliferation of CECs, regardless of species, indicate that R-spondin1 may play a key role in maintaining corneal endothelium homeostasis through the Wnt/ $\beta$ -catenin pathway.

**Keywords:** R-spondin, corneal endothelial cells, homeostasis

Roof plate-specific spondin (R-spondin) proteins were recently identified as consisting of four members, with conserved cysteine-rich furin-like and thrombospondin domains.<sup>1–3</sup> R-spondin1 was identified as a gene expressed in the developing spinal cord. The proteins are also expressed in mouse ovary during development, as well as in the developing dermis and kidney.<sup>1–3</sup> Injection of human R-spondin1 into mice demonstrated a specific proliferative effect of R-spondin1 on intestinal epithelial crypt cells.<sup>4</sup> R-spondin1 has also been reported to prevent chemotherapy- or radiotherapy-induced oral mucositis in mouse models.<sup>4</sup>

In terms of downstream signaling, R-spondins activate the canonical Wnt/ $\beta$ -catenin-dependent signaling pathway,<sup>1–3,5–8</sup> which is one of the key signaling pathways involved in cell proliferation, differentiation, and morphogenesis during embryogenesis and adulthood.<sup>9–12</sup> The mechanism by which the R-spondin family activates the Wnt/ $\beta$ -catenin signaling pathway is not fully understood. R-spondins interact with membrane receptors, such as lipoprotein receptor-related protein 5 (LRP5) and LRP6,<sup>6</sup> Frizzled,<sup>5</sup> RNF43/ZNRF3,<sup>13,14</sup> and Syndecan-4.<sup>15</sup> R-spondins were also recently reported to bind to leucine-rich repeat-containing G-protein-coupled receptors 4 to 6 (LGR4–6)

and to mediate R-spondin-induced  $\beta$ -catenin signaling pathways.<sup>16–20</sup> Crystal structures showed that R-spondin1 binds to LGR5 and forms 2:2 LGR5-R-spondin1 complexes.<sup>20</sup> One interesting observation relevant to the present study is that LGR5 serves as a marker of resident stem cells in multiple adult tissues, including stomach, small intestine, colon, and hair follicles.<sup>21–23</sup> In addition, we recently reported that LGR5 is uniquely expressed in the peripheral region of human corneal endothelial cells (HCECs) and that LGR5-positive cells have some stem/progenitor cell-like characteristics.<sup>24</sup> These recent findings motivated us to study the effect of R-spondin1 on corneal endothelial cells (CECs).

The corneal endothelium (CE) is critical in maintaining homeostatic corneal transparency and clear vision. Restoration of clear vision lost because of endothelial disorders requires full-thickness corneal transplantation or endothelial keratoplasty. In addition to these surgical procedures, approaches employing regenerative medicine<sup>25–30</sup> and pharmaceutical therapy<sup>31–34</sup> have been extensively investigated as alternative procedures for treating CE dysfunction. Ironically, regenerative medicine and pharmaceutical therapy share a common obstacle: the poor proliferative capacity of HCECs. We

previously explored the usefulness of drug therapy for treating early-stage CE dysfunction and reported that the Rho kinase inhibitor increased the proliferative potency of the CE.<sup>31,32</sup> In addition, we recently demonstrated that corneal clarity and thickness were recovered following the administration of Rho-associated kinase inhibitor eye drops, especially in patients with the focal edema type of Fuchs' corneal dystrophy.<sup>33,34</sup> Full exploitation of the current developments in CE dysfunction therapy, however, will first require a better understanding of the mechanisms underlying the regulation of CE homeostasis and tissue regeneration.

The recent finding that LGR5-positive cells are stem/progenitor-like cells of CE<sup>24</sup> led us to investigate the effect of the LGR5 ligand, R-spondin1. In the present study, we evaluated the effect of R-spondin1 on cell proliferation and the functional phenotypes of CE. The effect of R-spondin1 on Wnt/ $\beta$ -catenin pathway was also evaluated.

## MATERIALS AND METHODS

### Ethics Statement

The human tissue used in this study was handled in accordance with the tenets set forth in the Declaration of Helsinki. Written consent was acquired from the next of kin of all deceased donors regarding the donation of eyes for this research. All tissue was recovered under the Uniform Anatomical Gift Act (UAGA) of the particular state where consent for the eye donation was obtained and the eyes were recovered.

### Cell Culture of Rabbit CECs

Rabbit eyes were purchased from the Funakoshi Corporation (Tokyo, Japan). Twenty rabbit eyes were used to culture rabbit CECs (RCECs). The RCECs were cultivated as described previously.<sup>29,31</sup> Briefly, Descemet's membrane with CECs was stripped and incubated in 0.6 U/mL Dispase II (Roche Applied Science, Penzberg, Germany) to release the CECs. After incubation for 60 minutes at 37°C, the CECs obtained from individual corneas were resuspended in culture medium and plated in one well of a six-well plate coated with FNC Coating Mix (Athena Environmental Sciences, Inc., Baltimore, MD, USA). All primary cell cultures and serial passages of CECs were performed in growth medium composed of Dulbecco's modified Eagle's medium (Life Technologies Corp., Carlsbad, CA, USA) supplemented with 10% fetal bovine serum, 50 U/mL penicillin, 50  $\mu$ g/mL streptomycin, and 2 ng/mL FGF-2 (Life Technologies Corp.). The RCECs were cultured in a humidified atmosphere at 37°C in 5% CO<sub>2</sub>. The culture medium was changed every 2 days. When the cells reached confluency in 10 to 14 days, they were rinsed in Ca<sup>2+</sup>- and Mg<sup>2+</sup>-free Dulbecco's phosphate-buffered saline (PBS), trypsinized with 0.05% Trypsin-EDTA (Life Technologies Corp.) for 5 minutes at 37°C, and then passaged at ratios of 1:2-4. Cultivated CECs at passages 1 through 3 were used for all experiments. The proliferation effects of R-spondin1 (1, 10, and 100 ng/mL) (R&D Systems, Inc., Minneapolis, MN, USA), Wnt3a (10, 50, and 100 ng/mL) (R&D Systems, Inc.), and LiCl (3 mM) (Sigma-Aldrich Corp., St. Louis, MO, USA) were tested.

### Cell Culture of HCECs

Six human donor corneas were obtained from SightLife (<http://www.sightlife.org/>, Seattle, WA, USA) for HCEC cultivation (Table). The HCECs were cultivated in a modified version of the protocol used for the RCECs, as described previously.<sup>30</sup> Briefly, the Descemet's membrane, including the CECs, was stripped and digested at 37°C for 2 hours with 1 mg/mL collagenase A (Roche Applied Science). After digestion at 37°C,

TABLE. Numbers of Human Donor Corneas Used for the Study

Purpose of Experiments	Number of Donor Corneas
Cell culture of HCECs	6
Organ culture	4

the HCECs obtained from individual corneas were resuspended in culture medium and plated in one well of a 12-well plate coated with FNC Coating Mix (Athena Environmental Sciences, Inc.). The culture medium was prepared according to published protocols,<sup>35</sup> but with some modifications. Briefly, a basal medium was prepared containing OptiMEM-I (Life Technologies Corp.), 8% fetal bovine serum (FBS), 5 ng/mL epidermal growth factor (Sigma-Aldrich Corp.), 20  $\mu$ g/mL ascorbic acid (Sigma-Aldrich Corp.), 200 mg/L calcium chloride (Sigma-Aldrich Corp.), 0.08% chondroitin sulfate (Wako Pure Chemical Industries, Ltd., Osaka, Japan), and 50  $\mu$ g/mL gentamicin. The basal medium was conditioned by the cultivation of inactivated 3T3 fibroblasts, and then recovered as the culture medium for HCECs. Inactivation of the 3T3 fibroblasts was performed as described previously.<sup>36,37</sup> Briefly, confluent 3T3 fibroblasts were incubated with 4  $\mu$ g/mL mitomycin C (Kyowa Hakko Kirin Co., Ltd., Tokyo, Japan) for 2 hours at 37°C under 5% CO<sub>2</sub>, and then trypsinized and plated onto plastic dishes at a density of  $2 \times 10^4$  cells/cm<sup>2</sup>. The HCECs were cultured in a humidified atmosphere at 37°C in 5% CO<sub>2</sub>, and the culture medium was changed every 2 days. When the HCECs reached confluency in 14 to 28 days, they were rinsed in Ca<sup>2+</sup>- and Mg<sup>2+</sup>-free PBS, trypsinized with 0.05% Trypsin-EDTA for 5 minutes at 37°C, and then passaged at a 1:2 ratio. Cultivated HCECs at passages 2 through 5 were used for all experiments. The proliferative effect of R-spondin1 was tested by supplementing the HCEC culture medium with R-spondin1 (1, 10, and 100 ng/mL) and then culturing the HCECs. The cell density was evaluated using KSS-400EB software (Konan Medical, Inc., Hyogo, Japan).

### BrdU ELISA

The RCECs or HCECs were cultured at a density of 5000 cells/well in a 96-well plate for 24 hours, and then incubated in the absence of serum for an additional 24 hours in the presence or absence of R-spondin1. DNA synthesis was detected as the incorporation of 5-bromo-2'-deoxyuridine (BrdU) into the Cell Proliferation Biotrak ELISA system, version 2 (GE Healthcare Life Sciences, Buckinghamshire, England), according to the manufacturer's instructions. Briefly, the RCECs or HCECs were incubated with 10  $\mu$ M BrdU for 24 hours at 37°C and 5% CO<sub>2</sub> in a humidified atmosphere. The cultured cells were incubated with 10  $\mu$ M BrdU labeling solution (Amersham Biosciences, Freiburg, Germany) for 2 hours and then incubated with 100  $\mu$ L monoclonal antibody against BrdU for 30 minutes. The BrdU absorbance was measured directly using a spectrophotometric microplate reader at a test wavelength of 450 nm with a Veritas microplate luminometer (Promega Corporation, Madison, WI, USA).

### Organ Culture

For rabbit organ culture experiments, 16 rabbit eyes were purchased from the Funakoshi Corporation. Cornea tissues were divided into four pieces and cultured with Dulbecco's modified Eagle's medium supplemented with R-spondin1 (1, 10, and 100 ng/mL) at 37°C. For human organ culture experiments, four independent human donor corneas were obtained from SightLife (Table). Cornea tissues were divided into two pieces and cultured with Minimum Essential Medium,

GlutaMAX Supplement (Life Technologies Corp.) supplemented with 100 ng/mL R-spondin1 at 37°C. The cell densities were quantified using KSS-400EB software following phalloidin staining.

### Histological Examination

Rabbit or human CECs cultured on Lab-Tek chamber slides (NUNC A/S, Roskilde, Denmark) or whole corneal specimens were fixed in 4% formaldehyde for 10 minutes at room temperature and incubated for 30 minutes with 1% bovine serum albumin (BSA). The proliferation of the CECs was investigated by conducting immunohistochemical analyses of Ki67 staining when the cells reached 60% to 80% confluency, using a 1:400 dilution of anti-mouse Ki67 antibody (Sigma-Aldrich Corp.). The function-related proteins of the CECs were investigated using antibodies for Na<sup>+</sup>/K<sup>+</sup>-ATPase (Upstate Biotechnology, Inc., Lake Placid, NY, USA), the protein associated with pump function and zona occludens 1 (ZO-1) (Zymed Laboratories, Inc., South San Francisco, CA, USA), and tight junction-associated protein. The secondary antibody consisted of a 1:2000 dilution of Alexa Fluor 488-conjugated goat anti-mouse IgG (Life Technologies Corp.). The cellular morphology was evaluated by actin staining with a 1:400 dilution of Alexa Fluor 488-conjugated phalloidin (Life Technologies Corp.). Cell nuclei were stained with 4',6-diamidino-2-phenylindole (DAPI; Vector Laboratories, Inc., Burlingame, CA, USA). The slides were then inspected by fluorescence microscopy (TCS SP2 AOBIS; Leica Microsystems, Wetzlar, Germany).

### Cytoplasmic and Nuclear Protein Extractions

Rabbit CECs cultured in each culture condition on 60-mm culture dishes were washed twice with PBS, and cells were detached by scraping. Cells were transferred to a 1.5-mL tube and pelleted by centrifugation at 500g for 3 minutes. Cytoplasmic and nuclear proteins were extracted using a NE-PER Nuclear and Cytoplasmic Extraction Kit (Thermo Fisher Scientific, Waltham, MA, USA), according to the manufacturer's instructions. Briefly, supernatant was removed, 100  $\mu$ L Cytoplasmic Extraction Reagent I (Thermo Fisher Scientific) was added, and the sample was incubated for 10 minutes on ice. Then, 5.5  $\mu$ L Cytoplasmic Extraction Reagent I was added, and the sample was centrifuged at 16,000g for 5 minutes. The supernatant containing the cytosolic portion was transferred to a fresh tube and stored at -80°C until further use. The remaining pellet containing the nuclear portion was suspended Nuclear Extraction Reagent (Thermo Fisher Scientific). The samples were placed on ice and vortexed for 15 seconds every 10 minutes, for a total of 40 minutes, followed by centrifugation at 16,000g for 10 minutes. The supernatant containing the nuclear portion was transferred to a fresh tube and stored at -80°C until further use. The purity of the fractions was verified by immunoblotting the cytoplasmic or nuclear proteins with  $\alpha$ -tubulin and lamin B antibodies. The cytoplasmic and nuclear proteins were used for further immunoblotting studies.

### Protein Preparation and Immunoblotting

The RCECs were washed with ice-cold PBS and lysed with an ice-cold RIPA buffer (Bio-Rad Laboratories, Hercules, CA, USA) containing Phosphatase Inhibitor Cocktail 2 (Sigma-Aldrich Corp.) and Protease Inhibitor Cocktail (Nacalai Tesque, Kyoto, Japan). The lysates were centrifuged at 15,000g for 10 minutes at 4°C to sediment the cell debris. The supernatant representing the total proteins was collected, and the protein concentration of the sample was determined with a BCA Protein Assay Kit (Takara Bio, Otsu, Japan). An equal amount of protein was fractionated by SDS-PAGE, and the proteins were

transferred to polyvinylidene fluoride membranes. The membranes were then blocked by 3% nonfat dry milk (Cell Signaling Technology, Inc., Danvers, MA, USA) in TBS-T buffer (50 mM Tris, pH 7.5, 150 mM NaCl<sub>2</sub>, and 0.1% Tween 20) for 1 hour at room temperature, followed by overnight incubation at 4°C with the following primary antibodies:  $\beta$ -catenin (1:3000; BD, Franklin Lakes, NJ, USA),  $\alpha$ -tubulin (1:3000; MBL, Nagoya, Japan), lamin B (1:1000; Cell Signaling Technology), cyclin D1 (1:1000; Cell Signaling Technology), p27 (1:1000; Santa Cruz Biotechnology, Santa Cruz, CA, USA), phosphorylated p27 at threonine 187 (1:1000; Life Technologies Corp.), phosphorylated Rb protein at serine 807/811 (1:1000; Cell Signaling Technology), and Glyceraldehyde 3-phosphate dehydrogenase (GAPDH, 1:3000; Abcam, Cambridge, UK). The blots were washed and then incubated with horseradish peroxidase-conjugated secondary antibodies (1:5000: anti-rabbit IgG, anti-mouse IgG; Cell Signaling Technology). The blots were developed with luminal-enhanced chemiluminescence (ECL) using the ECL Advance Western Blotting Detection Kit (GE Healthcare, Piscataway, NJ, USA), documented by LAS4000S (Fuji Film, Tokyo, Japan), and analyzed with ImageJ (National Institutes of Health, Bethesda, MD, USA) software.

### Statistical Analysis

Student's *t*-test was used to determine the statistical significance (*P* value) of the mean values of the two-sample comparison. The statistical significance determined by the comparison of multiple sample sets was analyzed using Dunnett's multiple-comparisons test. The values shown on the graphs represent the mean  $\pm$  SEM.

## RESULTS

### Effects of R-spondin1 on Cell Proliferation of CECs

The percentages of Ki67-positive cells were increased in a dose-dependent manner when the RCECs were treated with R-spondin1 (Fig. 1A). When the RCECs were treated with 100 ng/mL R-spondin1 for 24 hours, BrdU incorporation into DNA increased 1.3-fold (Fig. 1B). Human CECs treated with 100 ng/mL R-spondin1 also significantly increased BrdU incorporation by 1.2-fold (Fig. 1C). We then evaluated the effect of R-spondin1 on CEC proliferation in rabbit corneal tissue. After treating the cornea with R-spondin1 for 1 week, the tissue was stained with anti-Ki67 antibody. Because the peripheral area of the CE retains higher replication ability,<sup>38</sup> the proliferative response of peripheral CECs to R-spondin1 was compared to that of central CECs. A negligible increase was noted in the Ki67<sup>+</sup> cells in the central cornea, but a 4-fold increase in these cells occurred in the peripheral area of the CE (Fig. 2A). The cell densities of the central (0–2 mm from the center of the cornea) and peripheral (4–6 mm from the center of the cornea) areas of the CE were 2900 and 3600 cells/mm<sup>2</sup>, respectively, when maintained in R-spondin1-free medium for 1 week. On the other hand, the cell densities of the central and peripheral areas after organ culture in the presence of 100 ng/mL R-spondin1 for 1 week were 3800 and 4300 cells/mm<sup>2</sup>, respectively (Fig. 2B). When the corneas were cultured for 2 weeks, the cell densities of the central and peripheral areas increased to 4200 and 4600 cells/mm<sup>2</sup>, respectively (Fig. 2C).

The effect of R-spondin1 on the morphology of the CECs was also determined using ZO-1 and observing the organization of F-actin at the cortex. The subcellular localization of actin fibers and monolayer sheet morphology were maintained in both the central and peripheral regions after treatment with R-spondin1 (Fig. 2D). Zona occludens 1 was expressed at the



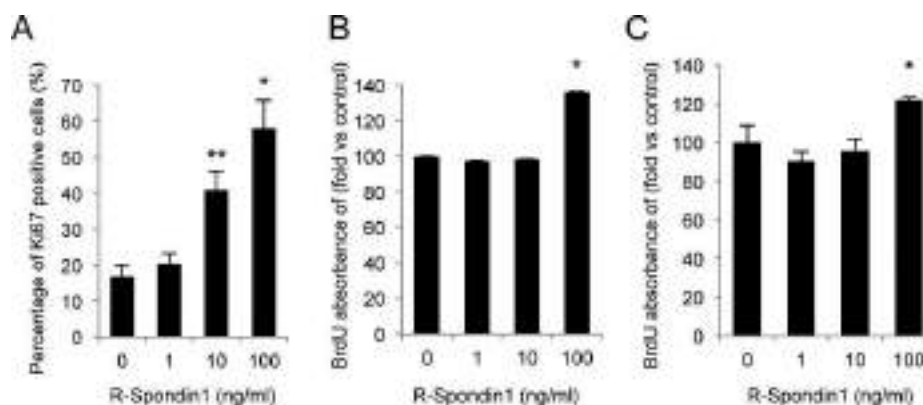


**FIGURE 1.** Effect of R-spondin1 on proliferation of cultured CECs. (A) Effect of R-spondin1 on the proliferation of cultured RCECs. The percentages of Ki67<sup>+</sup> cells cultured with 1, 10, or 100 ng/mL R-spondin1 for 24 hours were evaluated by fluorescence microscopy, and the data were then averaged and plotted ( $n = 6$ ). (B) RCECs were cultured at a density of 5000 cells/well in a 96-well plate in the presence of 1, 10, or 100 ng/mL R-spondin1. The effect of R-spondin1 on the proliferation of the RCECs was evaluated by a 5-bromo-2'-deoxyuridine (BrdU) incorporation assay after 24 hours. (C) HCECs were cultured at a density of 5000 cells/well in a 96-well plate in the presence of 1, 10, or 100 ng/mL R-spondin1. The effect of R-spondin1 on the proliferation of the HCECs was evaluated by a BrdU incorporation assay after 24 hours. \* $P < 0.01$ , \*\* $P < 0.05$ . All experiments were performed in triplicate.

intercellular junction and maintained a hexagonal cell morphology after treatment with R-spondin1 (Fig. 2E).

### Effect of R-spondin1 on Cell Proliferation and Phenotype of Human Corneal Endothelium

Because the replicative capacity of rabbit cornea differs from that of human CE, we also tested the effect of R-spondin1 on the proliferative capacity in HCECs. When we recovered HCECs from the donor corneas and cultured them in the presence of R-spondin1, we observed that the cell sizes were smaller than those of the control HCECs cultured without R-spondin1. The phase-contrast micrograph showed that HCECs maintained a monolayer cell sheet regardless of the presence or absence of R-spondin1 (Fig. 3A). The two functional marker proteins (Na<sup>+</sup>/K<sup>+</sup>-ATPase and ZO-1) were localized in the intercellular junctions of the monolayer of the hexagonal cells (Fig. 3B). We further determined the effect of R-spondin1 by maintaining serially passaged HCECs (passages 5–8) in the presence of R-spondin1. Interestingly, the cell density of HCECs was increased up to 49 days, after which the cell density was maintained in all conditions tested (Fig. 3C). We also evaluated the effect of R-spondin1 on cell proliferation in human corneal tissue. Similar to observations in rabbit cornea, the cell density of human CE was increased by R-spondin1: The cell density increased significantly from 2500 to 2700 cells/mm<sup>2</sup> in the central area and from 2800 to 3100 cells/mm<sup>2</sup> in the peripheral area after 2 weeks (Fig. 3D). The two functional proteins of the CE, Na<sup>+</sup>/K<sup>+</sup>-ATPase and ZO-1, were expressed and localized in the intracellular junctions of the HCECs, in both the central and peripheral regions (Figs. 3E, 3F). R-spondin1 stimulation had no effect on their subcellular localization. Similar to the findings observed in rabbit CE, the characteristic monolayer mosaic pattern of the cells was well preserved in the cells treated with R-spondin1. These findings indicate that HCECs and nonhuman CECs respond similarly to R-spondin1.

### R-spondin1 Facilitates G<sub>1</sub>/S Progression via Wnt3a/β-Catenin Signaling

R-spondins are known to activate the canonical Wnt/β-catenin-dependent signaling pathway.<sup>1–3,5–8</sup> We determined whether R-spondin1 stimulated cell proliferation of CECs through the Wnt/β-catenin-dependent pathway and whether a synergism

existed between R-spondin1 and Wnt3a. The characteristic monolayer hexagonal pattern of RCECs was well preserved in all culture conditions: Wnt3a (10, 50, or 100 ng/mL), R-spondin1 (100 ng/mL), or a combination of Wnt3a (100 ng/mL) and R-spondin1 (100 ng/mL) (Fig. 4A). The results of the BrdU assay showed that an increase in the incorporation of BrdU into the DNA of the cells was stimulated with Wnt3a in a dose-dependent manner. The RCECs treated with 100 ng/mL Wnt3a demonstrated a 40% increase in BrdU incorporation, and the RCECs treated with 100 ng/mL R-spondin1 showed a 50% increase (Fig. 4B). Interestingly, simultaneous treatment of the RCECs with R-spondin1 and Wnt3a resulted in a 50% increase in BrdU incorporation into DNA, suggesting that R-spondin1 may exert its activity through the Wnt signaling pathway.

We then conducted tests to determine whether the action of R-spondin1 depended on the canonical Wnt/β-catenin pathway. In the absence of Wnt3a, β-catenin is present in the cytoplasm. Wnt activation inhibits glycogen synthase kinase 3β (GSK-3β) activity, preventing β-catenin degradation and facilitating its translocation from the cytoplasm to the nucleus. When the cells were treated with R-spondin1 for 30 or 60 minutes, R-spondin1 facilitated the nuclear import of β-catenin within 30 minutes (Fig. 4C). On the other hand, the cytoplasmic fraction of β-catenin was not altered with or without treatment with R-spondin1. Rabbit CECs treated with LiCl (an inhibitor of GSK-3β) served as a positive control, showing a degree of nuclear import of β-catenin similar to that observed in the R-spondin1-treated cells.

### R-spondin1 Facilitates G<sub>1</sub>/S Progression via Downregulation of p27 and Upregulation of Cyclin D

Phosphorylation, ubiquitination, and the subsequent degradation of p27 are the major mechanism of G<sub>1</sub>/S progression in CECs.<sup>39,40</sup> A gradual, time-dependent decrease in p27 was seen in response to R-spondin1 stimulation (Fig. 4D). Phosphorylation of p27 at the Thr187 site was increased in the RCECs treated with R-spondin1 for 24 hours (Fig. 4D). This finding is similar to that of a previous report,<sup>40</sup> which clearly showed that the phosphorylation of p27 at Thr187 is a late G<sub>1</sub> event in the cell cycle. The hyperphosphorylation of Rb protein was observed in the RCECs treated with R-spondin1 for 24 hours. Note that the phosphorylation of Rb protein in the control

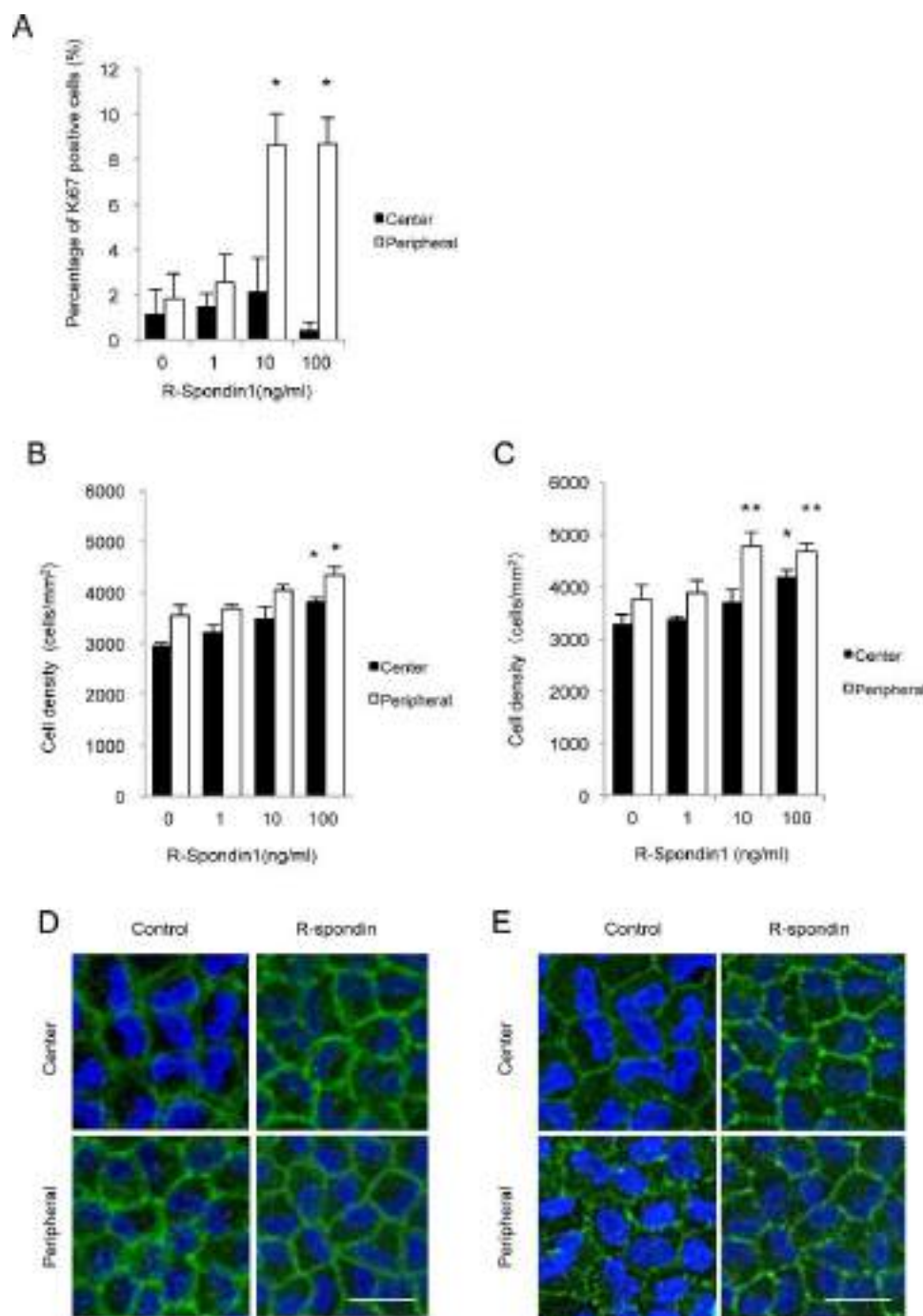


**FIGURE 2.** Effect of R-spondin1 on proliferation and cell density of rabbit CEC. (A) A rabbit cornea was divided into four pieces and organ-cultured with DMEM supplemented with 1, 10, or 100 ng/mL R-spondin1. The percentages of Ki67<sup>+</sup> cells were evaluated after 1 week in culture, and the data were averaged and plotted ( $n = 4$ ). (B, C) The cell density of the central (0–2 mm from the center of the cornea) and peripheral (4–6 mm from the center of the cornea) areas after organ culture with R-spondin1 for 1 week (B) and 2 weeks (C) was quantified by KSS-400EB software following phalloidin staining ( $n = 4$ ). The cell densities were evaluated in an area > 1 mm away from the cut edges of the cornea. (D, E) The effect of R-spondin1 on the morphology of the CECs was determined by F-actin (D) and ZO-1 (E). All experiments were performed in triplicate. Scale bars: 25  $\mu$ m.

cells was mediated by the growth medium, even in the absence of R-spondin1. In addition, the expression of cyclin D was enhanced for up to 24 hours in the presence of R-spondin1.

## DISCUSSION

Human CEC is a physiologically important monolayer of the cornea. The simple but crucial role of the endothelium is to

maintain cornea clarity.<sup>41</sup> The retention of the unique, contact-inhibited monolayer of the CEC, through which the active pump and barrier functions of the tissue operate, is essential for maintaining the transparency of the entire cornea. The human CEC has a limited wound healing capacity, in which residual CECs migrate and expand to cover the wound area. This unique wound repair process is explained in part by the fact that HCECs remain arrested at the G<sub>1</sub> phase of the cell cycle.<sup>42</sup>

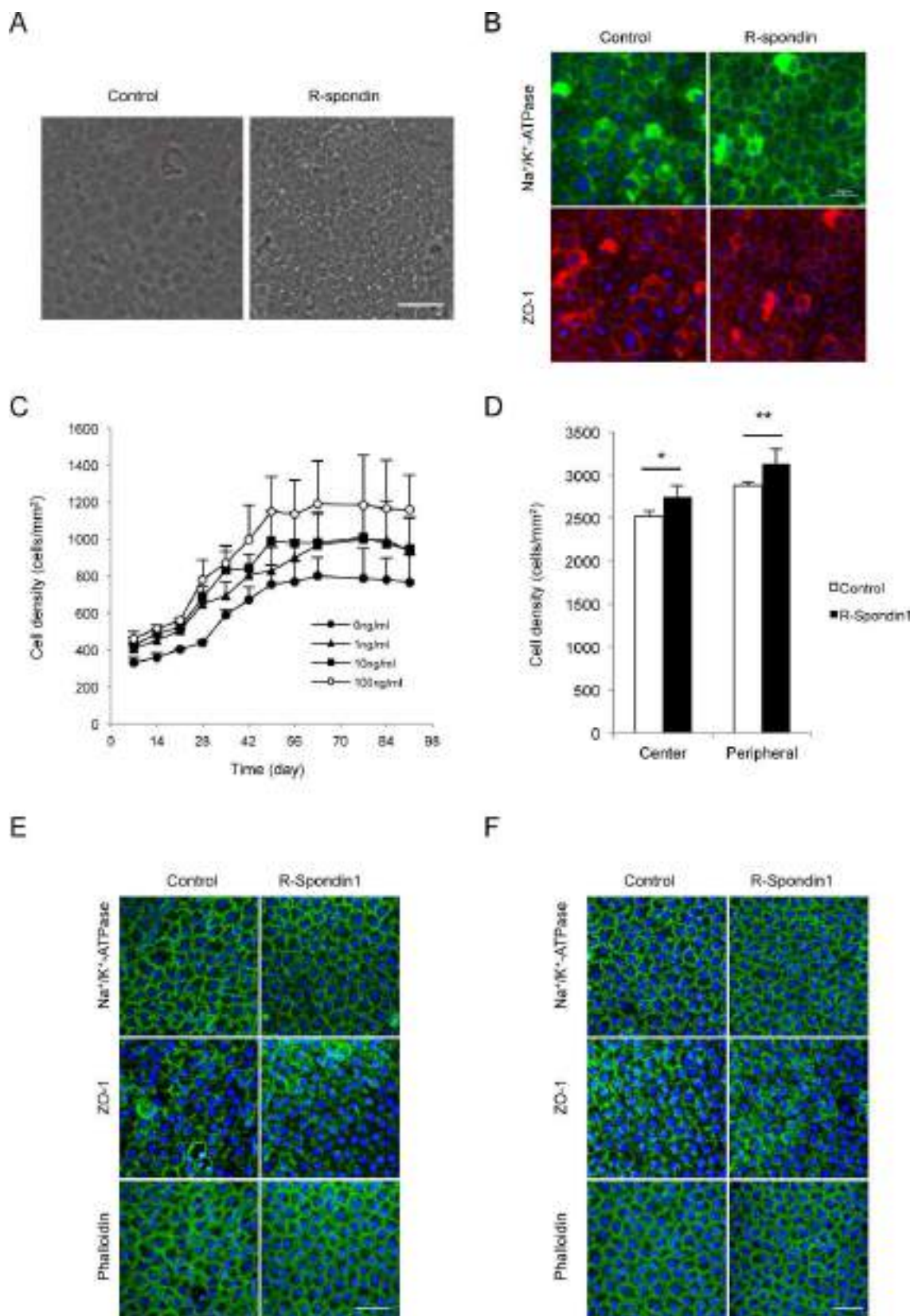


**FIGURE 3.** Effect of R-spondin1 on cell proliferation and phenotype of human CE. (A) HCECs were recovered from donor cornea and cultivated with culture medium supplemented with or without R-spondin1 (100 ng/mL). Representative phase-contrast images of the experiments performed in three independent donor corneas are shown. *Scale bar:* 200  $\mu$ m. (B) The two functional proteins of the CE, Na<sup>+</sup>/K<sup>+</sup>-ATPase and ZO-1, were immunostained in primary cultured HCECs treated with or without R-spondin1. *Scale bar:* 50  $\mu$ m. (C) Serial passaged HCECs (passages 5–8) were maintained in the presence of R-spondin1 at 1, 10, or 100 ng/mL for up to 91 days. The cell density was evaluated by KSS-400EB software ( $n = 6$ ). The experiments were performed in three independent lots. (D) Four human donor corneas were each divided into two pieces and cultured with or



without R-spondin1 (100 ng/mL), respectively. The cell density was evaluated by KSS-400EB software after 2 weeks following phalloidin staining ( $n = 4$ );  $*P < 0.01$ ,  $**P < 0.05$ . (E, F) The expression and localization of Na<sup>+</sup>/K<sup>+</sup>-ATPase, ZO-1, and F-actin were examined in ex vivo human corneal tissues ([E] center, [F] peripheral). Scale bar: 50  $\mu$ m.

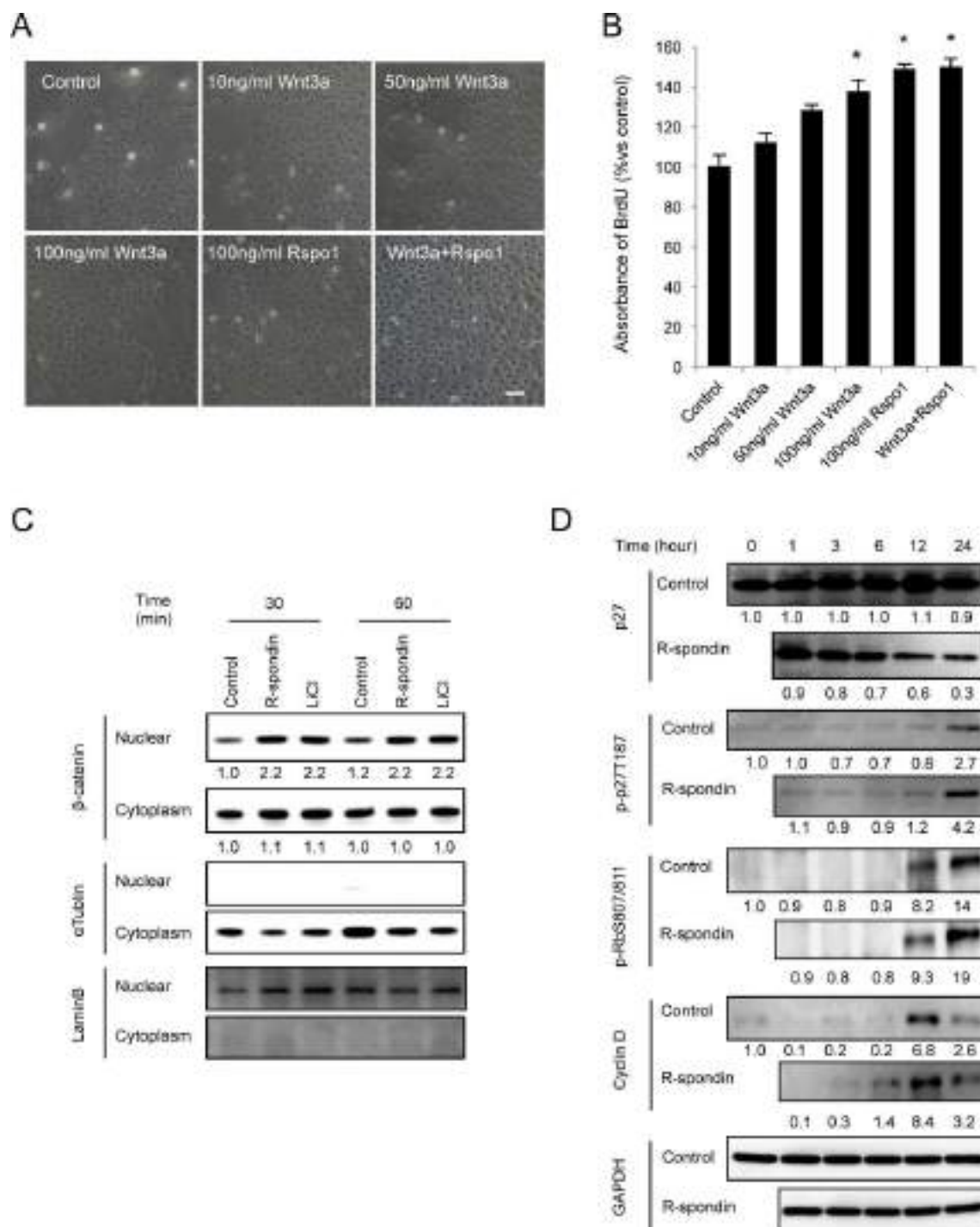


**FIGURE 4.** Involvement of Wnt3a/β-catenin signaling in the facilitation of G<sub>1</sub>/S progression, mediated by R-spondin1. (A) Phase-contrast images of RCECs treated with Wnt3a (10, 50, or 100 ng/mL), R-spondin1 (100 ng/mL), or a combination of Wnt3a (100 ng/mL) and R-spondin1 (100 ng/mL) for 48 hours. Scale bar: 200  $\mu$ m. (B) The effect of R-spondin1 on the proliferation of the RCECs was evaluated by a BrdU incorporation assay after 48 hours.  $*P < 0.01$ . The experiments were performed in triplicate. (C) After activation of the cells with R-spondin1, the nuclear fraction and the cytosolic fraction were prepared, and the nuclear translocation of β-catenin was evaluated by Western blotting. Lamin B was used as a marker for the nuclear fraction, and α-tubulin was used as a marker for the cytosolic fraction. (D) Serum-starved RCECs were treated with or without R-spondin1 (100 ng/mL) for 1, 3, 6, 12, or 24 hours. Then p27, phosphorylation of p27, phosphorylation of Rb, and cyclin D were evaluated by Western blotting. The relative density of immunoblotted bands was determined using ImageJ software. The averages of relative fold differences from independent duplicate experiments were then compared with the values from the control.

Although the existence of CE stem cells is still controversial, a recent study suggested that CE at the extreme periphery<sup>43</sup> or in the transition zone between the endothelial edge and the trabecular meshwork might include stem cells and thereby have proliferative potency.<sup>44,45</sup> We recently reported that LGR5-positive cells of the human CE exhibit stem/progenitor-like cell characteristics<sup>24</sup>; LGR 5 has recently been demonstrated to function as a high-affinity receptor of R-spondins to activate Wnt/ $\beta$ -catenin signaling.<sup>16,17,46</sup> R-spondins are known agonists of Wnt signaling and are involved in stem cell regulation, such as survival and differentiation.<sup>3,7,19</sup> These findings indicate that HCECs in the peripheral region may retain proliferative potential and that a continuous supply of new cells may be available to maintain the CE. Therefore, our aim was to determine whether R-spondin1 plays a key role in tissue homeostasis and tissue regeneration.

We demonstrated that R-spondin1 stimulated proliferation of both RCECs and HCECs in vitro and ex vivo. When the proliferative potential was compared following R-spondin1 stimulation, RCECs showed greater cell proliferative activity in the peripheral CE than in the central CE. Our results showed that approximately 8% of the Ki67-positive cells were observed in peripheral rabbit cornea, and these mitotic cells may increase peripheral cell density. However, despite the fact that limited numbers of Ki67-positive cells were observed in the central area, R-spondin1 increased the cell density in the center as well as in the peripheral area. One possible explanation may be that R-spondin1 predominantly enhances cell proliferation in the peripheral area, and the peripheral cells then proliferate and migrate toward the center where cells are not proliferating, resulting in a cell density increase in the central area. This cell migration from the periphery to the center is proposed as a CE homeostasis model in which cell clusters form niches in the extreme peripheral area and the peripheral CECs divide slowly and migrate toward the center.<sup>45</sup> Higher replication competence of the peripheral area during the wound healing process was also previously reported in an ex vivo system.<sup>40</sup> Further investigation is needed to clarify whether the response to R-spondin1 differs between LGR5-positive and -negative CECs,<sup>24</sup> but the greater potency of the proliferative activity of the peripheral CECs suggests that the response to R-spondin1 may be higher in peripheral LGR5-positive CECs.

We next evaluated the effect of R-spondin1 using human corneas, as the limitation of rabbit tissue for experiments on CE is that rabbit CE possesses an active proliferative ability that is not found in human corneas. For instance, rabbit CEC density was regenerated to its original level after cryoinjury in vivo.<sup>47</sup> Our findings that R-spondin1 promotes HCEC proliferation in human corneas agree with previous reports indicating that mechanical wounding or a combination of growth factors and release from contact inhibition promoted cell proliferation using ex vivo human cornea tissues.<sup>48,49</sup> However, the underlying mechanisms that explain how R-spondin1 enhances cell proliferation without mechanical wounding or contact inhibition release should be further studied.

We further demonstrated that R-spondin1 facilitated the nuclear import of  $\beta$ -catenin, which was subsequently involved in the transcription of cyclin D, one of the target genes of the  $\beta$ -catenin-involved LEF/TCF family of transcription factors.<sup>9</sup> Stimulation of the cells with R-spondin1 sequestered p27 from the cyclin D/Cdk4/Cdk6 complex to the cyclin E/Cdk2 complex, which subsequently phosphorylated p27, leading to the ubiquitination and degradation of p27. In this study, the phosphorylation of p27 by R-spondin1 aligns with previous reports showing that p27 plays a major role in G<sub>1</sub>/S progression in the CE.<sup>39,50,51</sup> The present study suggested that R-spondin1 facilitates G<sub>1</sub>/S progression through two G<sub>1</sub>

regulators—cyclin D (a positive regulator) and p27 (a negative regulator)—via the canonical Wnt/ $\beta$ -catenin pathway.

Our findings are the first to provide evidence that the Wnt/ $\beta$ -catenin pathway is involved in cell proliferation and maintenance of the functional phenotype in CE cells. The progenitor cells of CECs (LGR5<sup>+</sup>) in the peripheral region of the cornea may possibly proliferate in response to microenvironmental cues (in this case, R-spondin1). The unique tissue regenerative capacity of R-spondin1 may therefore be useful in the treatment of endothelial dysfunction.

## Acknowledgments

The authors thank Eri Mizuhara, Shinichiro Nakano, Kazuya Kakutani, and Yuki Tsujimoto for their technical assistance and Kana Hirata-Tominaga for her kind assistance and invaluable advice about R-spondin.

Supported by the Funding Program for Next Generation World-Leading Researchers from the Cabinet Office in Japan (NK, LS117).

Disclosure: N. Okumura, P; T. Nakamura, P; E.P. Kay, None; M. Nakahara, None; S. Kinoshita, P; N. Koizumi, P

## References

1. Kamata T, Katsube K, Michikawa M, Yamada M, Takada S, Mizusawa H. R-spondin, a novel gene with thrombospondin type 1 domain, was expressed in the dorsal neural tube and affected in Wnts mutants. *Biochim Biophys Acta*. 2004;1676:51–62.
2. Kazanskaya O, Glinka A, del Barco Barrantes I, Stannek P, Niehrs C, Wu W. R-Spondin2 is a secreted activator of Wnt/ $\beta$ -catenin signaling and is required for *Xenopus* myogenesis. *Dev Cell*. 2004;7:525–534.
3. Yoon JK, Lee JS. Cellular signaling and biological functions of R-spondins. *Cell Signal*. 2012;24:369–377.
4. Zhao J, Kim KA, De Vera J, Palencia S, Wagle M, Abo A. R-Spondin1 protects mice from chemotherapy or radiation-induced oral mucositis through the canonical Wnt/ $\beta$ -catenin pathway. *Proc Natl Acad Sci U S A*. 2009;106:2331–2336.
5. Nam JS, Turcotte TJ, Smith PF, Choi S, Yoon JK. Mouse cristin/R-spondin family proteins are novel ligands for the Frizzled 8 and LRP6 receptors and activate  $\beta$ -catenin-dependent gene expression. *J Biol Chem*. 2006;281:13247–13257.
6. Wei Q, Yokota C, Semenov MV, Doble B, Woodgett J, He X. R-spondin1 is a high affinity ligand for LRP6 and induces LRP6 phosphorylation and  $\beta$ -catenin signaling. *J Biol Chem*. 2007;282:15903–15911.
7. Kim KA, Wagle M, Tran K, et al. R-Spondin family members regulate the Wnt pathway by a common mechanism. *Mol Biol Cell*. 2008;19:2588–2596.
8. Han XH, Jin YR, Seto M, Yoon JKA. WNT/ $\beta$ -catenin signaling activator, R-spondin, plays positive regulatory roles during skeletal myogenesis. *J Biol Chem*. 2011;286:10649–10659.
9. Gordon MD, Nusse R. Wnt signaling: multiple pathways, multiple receptors, and multiple transcription factors. *J Biol Chem*. 2006;281:22429–22433.
10. Kikuchi A, Yamamoto H, Sato A. Selective activation mechanisms of Wnt signaling pathways. *Trends Cell Biol*. 2009;19:119–129.
11. Clevers H. Wnt/ $\beta$ -catenin signaling in development and disease. *Cell*. 2006;127:469–480.
12. Holland JD, Klaus A, Garratt AN, Birchmeier W. Wnt signaling in stem and cancer stem cells. *Curr Opin Cell Biol*. 2013;25:254–264.



13. Hao HX, Xie Y, Zhang Y, et al. ZNRF3 promotes Wnt receptor turnover in an R-spondin-sensitive manner. *Nature*. 2012;485:195–200.
14. Peng WC, de Lau W, Madoori PK, et al. Structures of Wnt-antagonist ZNRF3 and its complex with R-spondin 1 and implications for signaling. *PLoS One*. 2013;8:e83110.
15. Ohkawara B, Glinka A, Niehrs C. Rspo3 binds syndecan 4 and induces Wnt/PCP signaling via clathrin-mediated endocytosis to promote morphogenesis. *Dev Cell*. 2011;20:303–314.
16. Carmon KS, Gong X, Lin Q, Thomas A, Liu Q. R-spondins function as ligands of the orphan receptors LGR4 and LGR5 to regulate Wnt/beta-catenin signaling. *Proc Natl Acad Sci U S A*. 2011;108:11452–11457.
17. Glinka A, Dolde C, Kirsch N, et al. LGR4 and LGR5 are R-spondin receptors mediating Wnt/beta-catenin and Wnt/PCP signalling. *EMBO Rep*. 2011;12:1055–1061.
18. Xu K, Xu Y, Rajashankar KR, Robev D, Nikolov DB. Crystal structures of Lgr4 and its complex with R-spondin1. *Structure*. 2013;21:1683–1689.
19. Huch M, Dorrell C, Boj SF, et al. In vitro expansion of single Lgr5+ liver stem cells induced by Wnt-driven regeneration. *Nature*. 2013;494:247–250.
20. Peng WC, de Lau W, Forneris F, et al. Structure of stem cell growth factor R-spondin 1 in complex with the ectodomain of its receptor LGR5. *Cell Rep*. 2013;3:1885–1892.
21. Barker N, van Es JH, Kuipers J, et al. Identification of stem cells in small intestine and colon by marker gene Lgr5. *Nature*. 2007;449:1003–1007.
22. Barker N, Huch M, Kujala P, et al. Lgr5(+ve) stem cells drive self-renewal in the stomach and build long-lived gastric units in vitro. *Cell Stem Cell*. 2010;6:25–36.
23. Jaks V, Barker N, Kasper M, et al. Lgr5 marks cycling, yet long-lived, hair follicle stem cells. *Nat Genet*. 2008;40:1291–1299.
24. Hirata-Tominaga K, Nakamura T, Okumura N, et al. Corneal endothelial cell fate is maintained by LGR5 through the regulation of hedgehog and Wnt pathway. *Stem Cells*. 2013;31:1396–1407.
25. Mimura T, Yamagami S, Yokoo S, et al. Cultured human corneal endothelial cell transplantation with a collagen sheet in a rabbit model. *Invest Ophthalmol Vis Sci*. 2004;45:2992–2997.
26. Ishino Y, Sano Y, Nakamura T, et al. Amniotic membrane as a carrier for cultivated human corneal endothelial cell transplantation. *Invest Ophthalmol Vis Sci*. 2004;45:800–806.
27. Sumide T, Nishida K, Yamato M, et al. Functional human corneal endothelial cell sheets harvested from temperature-responsive culture surfaces. *FASEB J*. 2006;20:392–394.
28. Mimura T, Yamagami S, Yokoo S, et al. Sphere therapy for corneal endothelium deficiency in a rabbit model. *Invest Ophthalmol Vis Sci*. 2005;46:3128–3135.
29. Koizumi N, Sakamoto Y, Okumura N, et al. Cultivated corneal endothelial cell sheet transplantation in a primate model. *Invest Ophthalmol Vis Sci*. 2007;48:4519–4526.
30. Okumura N, Koizumi N, Ueno M, et al. ROCK inhibitor converts corneal endothelial cells into a phenotype capable of regenerating in vivo endothelial tissue. *Am J Pathol*. 2012;181:268–277.
31. Okumura N, Ueno M, Koizumi N, et al. Enhancement on primate corneal endothelial cell survival in vitro by a ROCK inhibitor. *Invest Ophthalmol Vis Sci*. 2009;50:3680–3687.
32. Okumura N, Koizumi N, Ueno M, et al. Enhancement of corneal endothelium wound healing by Rho-associated kinase (ROCK) inhibitor eye drops. *Br J Ophthalmol*. 2011;95:1006–1009.
33. Okumura N, Koizumi N, Kay EP, et al. The ROCK inhibitor eye drop accelerates corneal endothelium wound healing. *Invest Ophthalmol Vis Sci*. 2013;54:2493–2502.
34. Koizumi N, Okumura N, Ueno M, Nakagawa H, Hamuro J, Kinoshita S. Rho-associated kinase inhibitor eye drop treatment as a possible medical treatment for Fuchs corneal dystrophy. *Cornea*. 2013;32:1167–1170.
35. Nakahara M, Okumura N, Kay EP, et al. Corneal endothelial expansion promoted by human bone marrow mesenchymal stem cell-derived conditioned medium. *PLoS One*. 2013;8:e69009.
36. Koizumi N, Fullwood NJ, Bairaktaris G, Inatomi T, Kinoshita S, Quantock AJ. Cultivation of corneal epithelial cells on intact and denuded human amniotic membrane. *Invest Ophthalmol Vis Sci*. 2000;41:2506–2513.
37. Rheinwald JG, Green H. Serial cultivation of strains of human epidermal keratinocytes: the formation of keratinizing colonies from single cells. *Cell*. 1975;6:331–343.
38. Mimura T, Joyce NC. Replication competence and senescence in central and peripheral human corneal endothelium. *Invest Ophthalmol Vis Sci*. 2006;47:1387–1396.
39. Lee JG, Kay EP. Two populations of p27 use differential kinetics to phosphorylate Ser-10 and Thr-187 via phosphatidylinositol 3-Kinase in response to fibroblast growth factor-2 stimulation. *J Biol Chem*. 2007;282:6444–6454.
40. Lee JG, Song JS, Smith RE, Kay EP. Human corneal endothelial cells employ phosphorylation of p27(Kip1) at both Ser10 and Thr187 sites for FGF-2-mediated cell proliferation via PI 3-kinase. *Invest Ophthalmol Vis Sci*. 2011;52:8216–8223.
41. Bourne WM. Clinical estimation of corneal endothelial pump function. *Trans Am Ophthalmol Soc*. 1998;96:229–239.
42. Joyce NC, Navon SE, Roy S, Zieske JD. Expression of cell cycle-associated proteins in human and rabbit corneal endothelium in situ. *Invest Ophthalmol Vis Sci*. 1996;37:1566–1575.
43. He Z, Campolmi N, Gain P, et al. Revisited microanatomy of the corneal endothelial periphery: new evidence for continuous centripetal migration of endothelial cells in humans. *Stem Cells*. 2012;30:2523–2534.
44. Whikehart DR, Parikh CH, Vaughn AV, Mishler K, Edelhauser HE. Evidence suggesting the existence of stem cells for the human corneal endothelium. *Mol Vis*. 2005;11:816–824.
45. McGowan SL, Edelhauser HE, Pfister RR, Whikehart DR. Stem cell markers in the human posterior limbus and corneal endothelium of unwounded and wounded corneas. *Mol Vis*. 2007;13:1984–2000.
46. de Lau W, Barker N, Low TY, et al. Lgr5 homologues associate with Wnt receptors and mediate R-spondin signalling. *Nature*. 2011;476:293–297.
47. Minkowski JS, Bartels SP, Delori FC, Lee SR, Kenyon KR, Neufeld AH. Corneal endothelial function and structure following cryo-injury in the rabbit. *Invest Ophthalmol Vis Sci*. 1984;25:1416–1425.
48. Senoo T, Joyce NC. Cell cycle kinetics in corneal endothelium from old and young donors. *Invest Ophthalmol Vis Sci*. 2000;41:660–667.
49. Senoo T, Obara Y, Joyce NC. EDTA: a promoter of proliferation in human corneal endothelium. *Invest Ophthalmol Vis Sci*. 2000;41:2930–2935.
50. Joyce NC. Proliferative capacity of the corneal endothelium. *Prog Retin Eye Res*. 2003;22:359–389.
51. Kikuchi M, Zhu C, Senoo T, Obara Y, Joyce NC. p27kip1 siRNA induces proliferation in corneal endothelial cells from young but not older donors. *Invest Ophthalmol Vis Sci*. 2006;47:4803–4809.

# Cell Surface Markers of Functional Phenotypic Corneal Endothelial Cells

Naoki Okumura,<sup>1,2</sup> Hiroatsu Hirano,<sup>1</sup> Ryohei Numata,<sup>1</sup> Makiko Nakahara,<sup>1</sup> Morio Ueno,<sup>2</sup> Junji Hamuro,<sup>2</sup> Shigeru Kinoshita,<sup>2</sup> and Noriko Koizumi<sup>1</sup>

<sup>1</sup>Department of Biomedical Engineering, Faculty of Life and Medical Sciences, Doshisha University, Kyotanabe, Japan

<sup>2</sup>Department of Ophthalmology, Kyoto Prefectural University of Medicine, Kyoto, Japan

Correspondence: Noriko Koizumi, Department of Biomedical Engineering, Faculty of Life and Medical Sciences, Doshisha University, Kyotanabe 610-0321, Japan; nkoizumi@mail.doshisha.ac.jp.

Submitted: June 8, 2014

Accepted: October 24, 2014

Citation: Okumura N, Hirano H, Numata R, et al. Cell surface markers of functional phenotypic corneal endothelial cells. *Invest Ophthalmol Vis Sci*. 2014;55:7610-7618. DOI: 10.1167/iovs.14-14980

**PURPOSE.** Cultured human corneal endothelial cells (HCECs) are anticipated to serve as an alternative to donor corneas for the treatment of corneal endothelial dysfunction. However, corneal endothelial cells (CECs) tend to exhibit fibroblastic transformation, thereby losing their functional phenotype when cultured. The purpose of this study was to investigate the usefulness of surface markers of CECs displaying fibroblastic phenotypes as a means of cell characterization.

**METHODS.** The expression levels of 242 cell surface antigens were screened in cultured human and monkey CECs using flow cytometry. An expression intensity ratio of nonfibroblastic/fibroblastic CECs > 2 and of fibroblastic/nonfibroblastic CECs > 2 were selected as indicating nonfibroblastic and fibroblastic markers, respectively. Nonfibroblastic and fibroblastic CECs were mixed, and CD73-positive and -negative cells were sorted using flow cytometry and further cultured. The functional phenotype of the sorted cells was evaluated according to morphology and the expression of function-related (Na<sup>+</sup>/K<sup>+</sup>-ATPase and ZO-1) and fibroblastic (type I collagen and fibronectin) markers.

**RESULTS.** Flow cytometry analysis demonstrated that CD98, CD166, and CD340 are elevated in HCECs of nonfibroblastic phenotype, while CD9, CD49e, CD44, and CD73 are markers of fibroblastic phenotype HCECs. The CECs that sorted as CD73-negative exhibited normal hexagonal morphology and expressed functional markers, whereas CECs that sorted as CD73-positive exhibited the fibroblastic phenotype.

**CONCLUSIONS.** These markers will be useful for quality control to characterize the phenotype of cells destined for tissue engineering-based therapy. In addition, this selection protocol will provide a novel method for purification of functional cells.

**Keywords:** corneal endothelial cells, cell surface marker, tissue engineering, regenerative medicine

The corneal endothelium regulates the aqueous humor flow to the corneal stroma through a combination of pumps and a leaky barrier function, thereby maintaining corneal transparency.<sup>1</sup> Corneal endothelial cells (CECs) have severely limited proliferative ability,<sup>2,3</sup> so healing of wounds to the corneal endothelium is mainly performed by cell migration and spreading. Consequently, severe damage to the corneal endothelium resulting from pathologic conditions, such as Fuchs' corneal endothelial dystrophy, surgical stress, or endotheliitis, leads to corneal endothelial dysfunction, and ultimately to the loss of corneal transparency.<sup>4-6</sup> Corneal transplantation is the only therapeutic choice for treating corneal endothelial dysfunction, but this procedure is fraught with several associated problems, including a worldwide shortage of donor corneas and the technical difficulty of the surgical procedure itself, especially for patients with aphakia, postfiltration surgery, and post-tube surgery for glaucoma.<sup>5,7</sup>

Tissue engineering presently is viewed as a potential protocol that may overcome these problems and provide alternative treatments for corneal endothelial dysfunction.<sup>5,8</sup> Indeed, transplantation of cultured corneal endothelium as a form of sheet, with or without carrier, has enabled the recovery

of corneal transparency in animal models.<sup>9-12</sup> However, cultured corneal endothelial sheets, as cell monolayers, are highly fragile, making transplantation into the anterior chamber technically difficult. Consequently, researchers, including our group, are investigating the possibility of transplantation of cultured cells in the form of a cell suspension.<sup>13-16</sup> For instance, we reported that injection of cultured CECs, in combination with a Rho kinase (ROCK) inhibitor, enables regeneration of the corneal endothelium in rabbit and monkey models.<sup>16</sup>

Cultured human CECs (HCECs) have been anticipated as an alternative tissue source to donor corneas, but the in vitro expansion of HCECs is a bottleneck that currently limits therapy based on tissue engineering. The technical obstacles to cell cultivation arise from a number of features distinct to HCECs; namely, their limited proliferative ability and tendency to undergo spontaneous fibroblastic changes under culture conditions. These obstacles have persisted despite attempts to develop culture methods specifically for clinical use.<sup>17-21</sup>

We previously reported the usefulness of a ROCK inhibitor in enhancing cell proliferation through activation of the PI3 kinase/Akt signaling pathway.<sup>17,22</sup> The use of a conditioned

medium obtained from GMP-grade human bone marrow-derived mesenchymal stem cells (MSCs) also can potentiate HCEC proliferation.<sup>20</sup> We investigated methods to circumvent fibroblast formation by studying the fibrosis-related signaling pathways and found that activation of the TGF- $\beta$  signaling pathway has an important role in fibroblastic differentiation. This finding led to the development of a culture protocol for clinical application using SB431542 to inactivate TGF- $\beta$  signaling, which suppressed fibroblastic changes and maintained functional phenotypes.<sup>21</sup> This recent progress has reinvigorated the investigation of protocols for culturing of HCECs for clinical use.

In the present study, we screened the surface markers of HCECs showing normal (nonfibroblastic) and fibroblastic phenotypes as a quality control measure for the production of cultured HCECs for clinical use. We demonstrated that CD98, CD166, and CD340 are dominantly expressed in the normal CEC phenotype, while CD9, CD44, CD49e, and CD73 are markers for fibroblasts. In addition, CECs expressing a fibroblastic marker (e.g., CD73) showed increased expression of epithelial mesenchymal transformation (EMT) inducer genes, a fibroblastic phenotype based on morphological changes, and a greater production of extracellular matrix, in addition to the loss of the functional phenotype.

## MATERIALS AND METHODS

### Ethics Statement

The human tissue used in this study was handled in accordance with the tenets set forth in the Declaration of Helsinki. Human donor corneas were obtained from SightLife (Seattle, WA, USA). Informed written consent for eye donation for research was obtained from the next of kin of all deceased donors. All tissues were recovered under the tenets of the Uniform Anatomical Gift Act (UAGA) of the particular state in which the donor consent was obtained and the tissue was recovered. The monkey corneas used in this study were handled in accordance with the ARVO Statement for the Use of Animals in Ophthalmic and Vision Research. The protocols for the general welfare of the animals from which the corneas were harvested and the procedures for isolation of the corneas were approved by the institutional animal care and use committee of Nissei Bilis Co., Ltd. (Otsu, Japan). The animals were euthanized with an overdose of intravenous pentobarbital sodium for other research purposes, according to the guidelines on euthanasia of the American Veterinary Medical Association (AVMA); corneas were harvested after confirmation of cardiopulmonary arrest by veterinarians provided by Nissei Bilis Co., Ltd.

### Cell Cultures of HCECs

Human corneas were stored at 4°C in storage medium (Optisol-GS; Chiron Vision, Irvine, CA, USA). The HCECs were cultured according to published protocols, with some modifications.<sup>21</sup> A total of 10 human donor corneas (>60 years old) was used for the experiments. Briefly, the Descemet's membranes with the CECs were stripped from donor corneas and digested at 37°C with 1 mg/mL collagenase A (Roche Applied Science, Penzberg, Germany) for 12 hours. The HCECs obtained from a single donor cornea were seeded in one well of a 48-well plate coated with FNC Coating Mix (Athena Environmental Sciences, Inc., Baltimore, MD, USA). The culture medium was prepared according to published protocols. Briefly, basal medium was prepared with OptiMEM-I (Life Technologies Corp., Carlsbad, CA, USA), 8% fetal bovine serum (FBS), 5 ng/mL epidermal growth factor (EGF; Sigma-Aldrich Corp., St. Louis, MO, USA),

20  $\mu$ g/mL ascorbic acid (Sigma-Aldrich Corp.), 200 mg/L calcium chloride (Sigma-Aldrich Corp.), 0.08% chondroitin sulfate (Wako Pure Chemical Industries, Ltd., Osaka, Japan), and 50  $\mu$ g/mL of gentamicin. Inactivated 3T3 fibroblasts, prepared as previously described,<sup>20</sup> then were cultured with basal medium for 24 hours, and the conditioned basal medium was recovered as culture medium for the HCECs. The HCECs were cultured using culture medium prepared as above at 37°C in a humidified atmosphere containing 5% CO<sub>2</sub>, and the culture medium was changed every 2 days. The HCECs were passaged at ratios of 1:2 using 0.05% Trypsin-EDTA for 5 minutes at 37°C when they reached confluence. The HCECs at passages 2 through 5 were used for all experiments.

### Immortalization of HCECs Using Lentiviral Transduction of SV40 Large T Antigen and hTERT Genes

The HCECs exhibiting normal morphology and fibroblastic morphology were immortalized for cell sorting experiments using SV40 and hTERT to produce normal iHCEC and fibroblastic iHCECs cell lines, respectively. The coding sequences of the SV40 large T antigen and hTERT genes were amplified through PCR and were TA-cloned into a commercial lentiviral vector. The lentiviral vectors then were transfected to 293T cells (RCB2202; Riken Bioresource Center, Ibaraki, Japan), along with three helper plasmids (pLP1, pLP2, and pLP/VSVG; Life Technologies Corp.), using a commercial transfection reagent (Fugene HD; Promega Corp., Madison, WI, USA) for 48 hours. The supernatant of the culture medium was harvested, centrifuged briefly, and stored in a freezer at -80°C. For lentiviral transduction, the virus-containing supernatants of both genes were added to the cultures of HCECs in the presence of 5  $\mu$ g/mL of polybrene. The immortalized cells were cultured in Dulbecco's modified Eagle's medium (DMEM; Life Technologies Corp.) containing 10% FBS, and 1% penicillin and streptomycin; the medium was changed every two days. Once the immortalized cells were 80% confluent, the cells were trypsinized with 0.05% trypsin-EDTA and passaged.

### Cell Culture of Monkey CECs (MCECs)

The MCECs were cultured as described previously.<sup>12</sup> Briefly, the Descemet's membrane including the MCECs was stripped and digested at 37°C for 2 hours with 1 mg/mL collagenase A. The resulting cells were suspended in culture medium, then seeded in 1 well of a 6-well plate coated with FNC Coating Mix. The MCECs were cultured at 37°C in a medium composed of DMEM supplemented with 10% FBS, 50 U/mL penicillin, 50  $\mu$ g/mL streptomycin, and 2 ng/mL FGF-2 (Life Technologies Corp.) in a humidified atmosphere containing 5% CO<sub>2</sub>. The culture medium was changed every 2 days and MCECs were passaged at ratios of 1:2 to 4 using 0.05% Trypsin-EDTA (Life Technologies Corp.). Cultivated MCECs at passages 2 through 5 were used for all experiments.

### Flow Cytometry

Screening of cell surface markers was conducted by assessing the expression of markers through the Human Cell Surface Marker Screening Panel (BD Biosciences, San Jose, CA, USA) according to the manufacturer's protocol. Briefly, cultured HCECs (of normal morphology and fibroblastic morphology; not immortalized cells) and cultured MCECs (normal morphology and fibroblastic morphology) were detached with Accutase (BD Biosciences) at 37°C, washed twice with PBS, passed through a BD Falcon 70  $\mu$ m cell strainer (BD Biosciences), incubated in OptiMEM-I with the addition of 100 units/mL



DNase for 15 minutes at room temperature, and resuspended with BD Pharmingen Stain Buffer (BD Biosciences) containing 5 mM EDTA. The HCECs or MCECs ( $1.0 \times 10^4$  cells, respectively) were incubated with primary 242 antibodies and isotype IgGs (BD Biosciences) at the dilution indicated by the manufacturer's protocol for 30 minutes on ice. The cells were washed with BD Pharmingen Stain Buffer containing 5 mM EDTA and then incubated with AlexaFluor 647 conjugated IgGs (1:200 dilution, BD Biosciences) for 30 minutes. The cells were washed again with BD Pharmingen Stain Buffer containing 5 mM EDTA and analyzed by flow cytometry using a BD FACSCant II instrument (BD Biosciences) and CellQuest Pro software (BD Biosciences). For cell sorting experiments, MCECs or immortalized HCECs were washed twice with PBS and incubated with Accumax (Innovative Cell Technologies, San Diego, CA, USA) for 10 minutes at 37°C before cell sorting. Cells were recovered in FACS buffer composed of DMEM without Phenol Red (Nacalai Tesque, Kyoto, Japan) + 2% FBS, passed through a BD Falcon 70  $\mu$ m cell strainer (BD Biosciences), and resuspended in FACS buffer. The cells then were incubated with antibodies (CD73, 1:300; BD Pharmingen Stain Buffer), and mouse IgG (1:62.5; Dako, Glostrup, Denmark) for 30 minutes at 4°C, then incubated with AlexaFluor 488 conjugated IgG (1:1000 dilution; BD Biosciences) for 30 minutes at 4°C. After washing three times with PBS, the cells were resuspended in FACS buffer supplemented with 2  $\mu$ g/mL propidium iodide (Sigma-Aldrich Corp.) at a density of  $5 \times 10^6$  to  $1 \times 10^7$  cells/mL. The CD73-positive and -negative cells were sorted using a BD FACS Aria (BD Biosciences) and seeded at a density of  $2.5 \times 10^5$  cells on a 24-well cell culture plate for subsequent analysis.

### Immunofluorescent Staining

The MCECs and HCECs were cultured at a density of  $1 \times 10^5$  cells/well in a 24-well cell culture plate coated with FNC Coating Mix and were maintained for 3 to 4 weeks for immunofluorescence analysis. Cells were fixed in 95% ethanol supplemented with 5% acetic acid for 10 minutes at room temperature and incubated for 30 minutes with 1% BSA. Samples were incubated overnight at 4°C with antibodies against CD73 (1:300; BD Pharmingen Stain Buffer), CD166 (1:300; BD Pharmingen Stain Buffer), ZO-1 (1:300; Zymed Laboratories, South San Francisco, CA, USA), and  $\text{Na}^+/\text{K}^+$ -ATPase (1:300; Upstate Biotech, Lake Placid, NY, USA). After washing with PBS, either Alexa Fluor 488-conjugated goat anti-mouse (Life Technologies) or Alexa Fluor 594-conjugated goat anti-rabbit IgG (Life Technologies) was used as the secondary antibody at a 1:1000 dilution. Nuclei were stained with DAPI (Vector Laboratories, Burlingame, CA, USA). The cells, cultured

in a 48-well cell culture plate, were directly examined by fluorescence microscopy (BZ-9000; Keyence, Osaka, Japan).

### Semiquantitative RT-PCR

Total RNA was extracted from MCECs and HCECs using the RNeasy Mini kit (Qiagen, Hilden, Germany), after which the quality of the RNA preparations was measured with a NanoDrop spectrophotometer (Thermo Fisher Scientific, Inc., Waltham, MA, USA). The cDNA was synthesized using ReverTra Ace (Toyobo, Osaka, Japan) and subjected to PCR with the specific primers listed in Table 1. Glyceraldehyde 3-phosphate dehydrogenase (GAPDH) was used as an internal control for gene analysis. The PCR reactions were performed using Extaq DNA polymerase (Takara Bio, Inc., Otsu, Japan) under the following conditions: denaturation at 94°C for 30 seconds, 33 cycles of annealing at 54°C for 30 seconds, and elongation at 72°C for 30 seconds. The PCR products were separated by electrophoresis on 1.5% agarose gels, stained with ethidium bromide, and detected under ultraviolet illumination.

### Quantitative Real-Time PCR

Gene expression levels were analyzed using TaqMan real-time PCR (Applied Biosystems, Foster City, CA, USA). Total RNA was extracted with the RNeasy mini kit, and cDNA was synthesized using ReverTra Ace. Taqman primers for *ZO1*, Hs01551861\_ml; *ATP1A1*, Hs00167556\_ml; *FN1*, Hs01549976\_ml; and TaqMan predevelopment human GAPDH (Applied Biosystems) were used. The PCR was performed using the StepOne (Applied Biosystems) real-time PCR system. The GAPDH was used as an internal standard.

### Statistical Analysis

The statistical significance (*P* value) of mean values for 2-sample comparisons was determined by the Student's *t*-test. The statistical significance for the comparison of multiple sample sets was determined with the Dunnett's multiple-comparisons test. Values shown on the graphs represent the mean  $\pm$  SE.

## RESULTS

### Cell Surface Markers of Normal and Fibroblastic Morphological CECs

Primate CECs often exhibit morphological fibroblastic changes and lose their functional phenotypes,<sup>21,23</sup> although a cell culture maintaining the normal phenotype sometimes is

TABLE 1. Oligonucleotide Sequences

Gene	Sense Primer	Antisense Primer	Size, bp
<i>CD73</i>	5'-GTTCTCTGTAGTCCAGGCCTATG-3'	5'-ACATTTTCATCCGTGTGTCTCAG-3'	316
<i>CD166</i>	5'-CCCCAGAGGAATTTTGTGTTTAC-3'	5'-AGCCTGATGTTATCTTTTCATCCA-3'	289
<i>ZO1</i>	5'-CCAGCTTCTCGAAGAACAC-3'	5'-GAACGAGGCATCATCCCTAA-3'	218
<i>ATP1A1</i>	5'-ACGGCAGTGATCTAAAGGACAT-3'	5'-GAAGAATCATGTGAGCAGCTTG-3'	255
<i>CDH2</i>	5'-CCAGGTCTTGAGCAGTGACA-3'	5'-TTCCAACCTTCACCTTGACC-3'	185
<i>COL1A1</i>	5'-ATGGATTCCAGTTCGAGTATGG-3'	5'-GACAGTGACGCTGTAGGTGAAG-3'	242
<i>COL4A1</i>	5'-AGCAAGGTGTTACAGGATTGGT-3'	5'-AGAAGGACACTGTGGGTCATCT-3'	392
<i>COL8A1</i>	5'-AGAGGGGAGAAAGGACCAATAG-3'	5'-CCTACTTCACCAAGGAAACCTG-3'	221
<i>SNAIL</i>	5'-ACTGCAAATACTGCAACAAGGA-3'	5'-TCTTGACATCTGAGTGGGTCTG-3'	240
<i>SNAIL2</i>	5'-CCTGTCATACCACAACCAGAGA-3'	5'-CTTCATCACTAATGGGGCTTTC-3'	211
<i>ZEB1</i>	5'-TTAGTTGCTCCCTGTGCAGTTA-3'	5'-TGTGTGAGCTATAGGAGCCAGA-3'	261
<i>GAPDH</i>	5'-GAGTCAACGGATTTGGTCGT-3'	5'-TTGATTTTGGAGGGATCTCG-3'	238

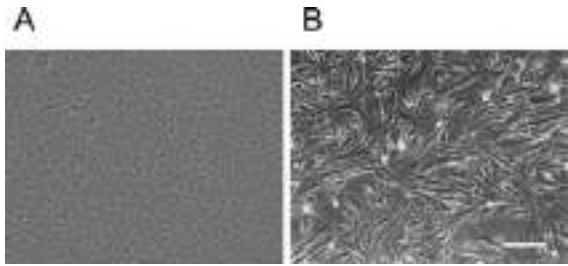


**FIGURE 1.** Nonfibroblastic and fibroblastic phenotypes exhibited during primary culture of HCECs. Primary cultivated HCECs demonstrated various phenotypes during cultivation using the same culture protocol. Representative phenotypes are presented. (A) Nonfibroblastic phenotype in which the cells maintained the characteristic polygonal contact-inhibited shape and monolayer. (B) Fibroblastic phenotype in which the cells were stratified and fibroblastic. Scale bar: 100  $\mu$ m.

observed. Representative phenotypes of primary cultured nonfibroblastic (normal) and fibroblastic cultured HCECs are shown (Figs. 1A, 1B). Cell surface markers for normal morphological CECs and fibroblastic CECs were evaluated by screening for the expression of 242 cell surface antigens by flow cytometry. The ratio of the mean fluorescence intensity of normal CECs and fibroblastic CECs was calculated. The markers that showed ratios of primary cultured nonfibroblastic/fibroblastic HCECs  $> 2$  (Supplemental Table S1) and primary cultured fibroblastic/nonfibroblastic HCECs  $> 2$  (Supplemental Table S2) are listed. The markers conserved in humans and monkeys are more reliable, so we further screened cell surface markers for normal morphological MCECs and fibroblastic MCECs (Fig. 2A), selecting markers that showed nonfibroblastic/fibroblastic or fibroblastic/nonfibroblastic ratios that were confirmed in MCECs as well as in HCECs (Table 2). The protein expression of CD73, which was used as a representative marker of fibroblastic cells, was not observed in normal phenotype MCECs, while it was observed at the cell membrane in fibroblastic MCECs (Fig. 2B). On the

**TABLE 2.** Selected Markers of Nonfibroblastic and Fibroblastic CECs

Nonfibroblastic Phenotype	Fibroblastic Phenotype
CD98	CD9
CD166	CD44
CD340	CD49e
	CD73

other hand, CD166, which was used as a representative marker of normal cells, was observed at the cell membrane of nonfibroblastic MCECs, but not in fibroblastic MCECs. The PCR data also indicated that *CD73* was strongly expressed at the mRNA level in fibroblastic cells, but not in normal cells, while *CD166* was expressed in normal cells, but to a lesser extent in fibroblastic cells (Fig. 2C).

**CD73 Marks Fibroblastic MCECs With the Loss of Functional Phenotype via Epithelial Mesenchymal Transformation**

Our goal was to detect possible contamination with vulnerable fibroblastic transformed cells, so we further investigated the reliability of using CD73 as a potential fibroblastic marker, since CD73 reportedly is involved in lung and liver fibrosis.<sup>24,25</sup> Experiments were conducted to determine whether fibroblastic cells could be detected by CD73 in a mixture of normal and fibroblastic cells by mixing nonfibroblastic MCECs and fibroblastic MCECs at 1:1 ratio (Fig. 3A) and then sorting out the CD73-negative and -positive cells (Fig. 3B). After culturing, the CD73-negative sorted MCECs exhibited a normal hexagonal morphology, whereas the CD73-positive MCECs exhibited fibroblastic morphology (Fig. 3C). The PCR analysis showed that CD73-negative MCECs did not express *CD73*, while CD73-positive MCECs expressed *CD73* at the mRNA level (Fig. 3D). A nonfibroblastic marker, *CD166*, was expressed in the CD73-negative MCECs, but *CD166* was expressed at a lower rate in the CD73-positive cells (Fig. 3D). The CD73-positive cells also expressed higher levels of *COL1A1*, an extracellular matrix

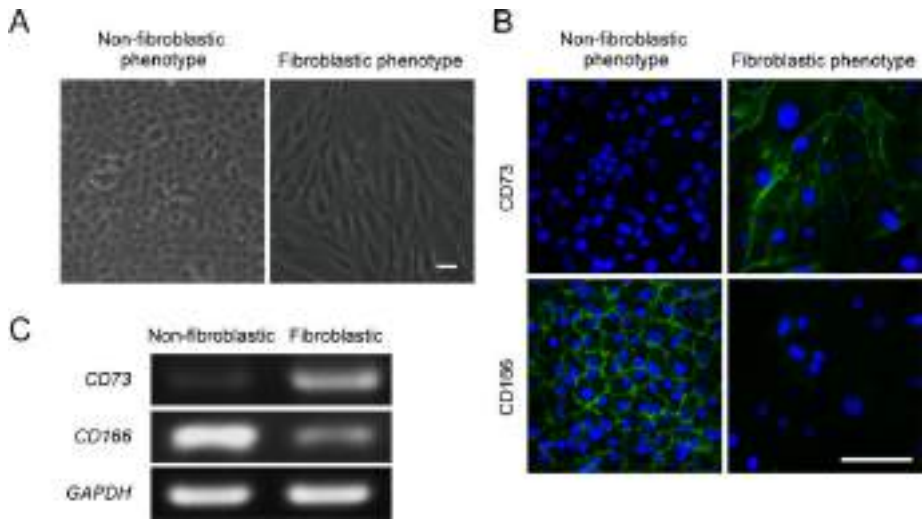


**FIGURE 2.** Expression of CD73 and CD166 in nonfibroblastic and fibroblastic MCECs. (A) The image on the left shows the MCECs of normal phenotype, while the image on the right shows MCECs of fibroblastic phenotype. Scale bar: 100  $\mu$ m. (B) The MCECs of nonfibroblastic and fibroblastic phenotypes were immunostained with the antibodies against CD73 and CD166. The fibroblastic phenotype cells expressed CD73 at the cell membrane, while no expression was observed in cells of normal phenotype. The CD166 was expressed at the cell membrane of normal phenotype cells, while it was very weakly stained in fibroblastic phenotype cells. Scale bar: 100  $\mu$ m. (C) The mRNA levels of *CD73* and *CD166* were evaluated using PCR. Gene *CD73* was expressed at higher levels in fibroblastic MCECs than in normal MCECs. On the other hand, *CD166* was expressed at higher levels in normal MCECs than in fibroblastic MCECs.

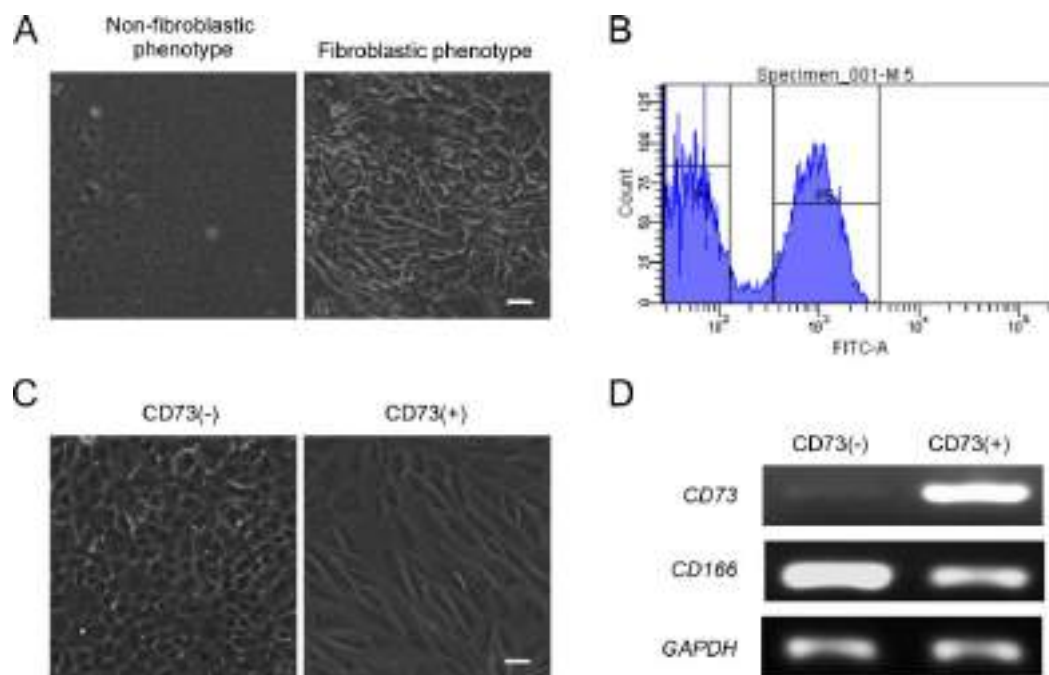


**FIGURE 3.** Cell sorting of MCECs by CD73. (A, B) Cultured MCECs exhibiting nonfibroblastic and fibroblastic phenotypes were harvested from the culture plate and mixed at 1:1 ratio. Mixed cells were stained for CD73 and were sorted by flow cytometry. Two peaks, CD73-positive and -negative, were observed. *Scale bar:* 100  $\mu$ m. (C) The MCECs were sorted according to the expression level of CD73 and were cultured to reach confluence. The CD73-negative cells had a hexagonal normal morphology, while CD73-positive cells had a fibroblastic morphology. *Scale bar:* 100  $\mu$ m. (D) The mRNA expression levels of *CD73* and *CD166* in sorted CD73-negative and -positive cells evaluated by PCR. The CD73-positive sorted cells expressed *CD73* at the mRNA level, while CD73-negative sorted cells expressed almost no *CD73*. On the other hand, *CD166* mRNA was expressed at a higher level in CD73-negative sorted cells than in CD73-positive sorted cells. These experiments were performed in triplicate.

protein produced under pathologic conditions by the corneal endothelium (Fig. 4A).<sup>26,27</sup> On the other hand, the CD73-positive cells showed a much lower expression of *COL4A1* and *COL8A1*, which normally are produced by the corneal endothelium (Fig. 4A). The CD73-positive cells also expressed higher levels of genes associated with induction of the epithelial mesenchymal transformation (EMT), such as *SNAIL*, *SNAIL2*, and *ZEB1* (Fig. 4B). Staining for endothelial characteristics revealed that the staining pattern of ZO-1 and Na<sup>+</sup>/K<sup>+</sup>-ATPase at the plasma membrane was well preserved in CD73-negative MCECs, whereas the CD73-positive MCECs lost the characteristic staining profile of ZO-1 and Na<sup>+</sup>/K<sup>+</sup>-ATPase at the plasma membrane (Fig. 4C). The data for immunofluorescence staining were supported by mRNA expression data for *ZO1*, *ATP1A1*, and *CDH2*, which were expressed in CD73-negative MCECs, but showed low expression in CD73-positive MCECs (Fig. 4D).

### CD73 as a Cell Surface Marker for Fibroblastic HCECs

We also investigated whether CD73 could be used to detect the fibroblastic forms of human as well as monkey CECs. The primary cultured HCECs tended to undergo fibroblastic changes when passed through a cell strainer for flow cytometry, so we established immortalized nonfibroblastic and fibroblastic HCECs cell lines (Fig. 5A). The same types of experiments performed with MCECs were repeated with immortalized HCECs and cells expressing or not expressing CD73 were cultured (Fig. 5B). Flow cytometry analysis demonstrated that the purity of CD73-negative sorted immortalized HCECs was 97.6% (Fig. 5C). The CD73-negative immortalized HCECs again exhibited a normal hexagonal, contact-inhibited morphology, while CD73-positive immortal-

ized HCECs exhibited a fibroblastic, stratified morphology (Fig. 5D).

Immunostaining showed that CD73 was expressed in the CD73-positive sorted immortalized HCECs, but not in CD73-negative sorted immortalized HCECs (even after further cultivation, Fig. 5E). The ZO-1 and Na<sup>+</sup>/K<sup>+</sup>-ATPase were functionally expressed at the plasma membrane in CD73-negative immortalized HCECs, while CD73-positive immortalized HCECs lost this normal expression of ZO-1 and Na<sup>+</sup>/K<sup>+</sup>-ATPase (Fig. 5E). The CD73-positive sorted immortalized HCECs expressed higher CD73 at the mRNA level than CD73-negative sorted immortalized HCECs (Fig. 5F).

Quantitative PCR analysis showed that expression of *ZO1* and *ATP1A1* was significantly reduced in CD73-positive cells compared to CD73-negative cells (Fig. 5G). On the other hand, expression of *FN1* was higher in CD73-positive cells than in CD73-negative cells (Fig. 5G).

### DISCUSSION

Extensive progress recently has raised the possibility of new therapeutic modalities based on tissue engineering techniques for various diseases.<sup>28,29</sup> However, although the FDA regulates interstate commerce in human cells and tissue-based products (HCT/Ps),<sup>30</sup> and although other countries also have similar systems,<sup>31</sup> the current regulatory frameworks are not presently viewed as providing sufficient coverage of innovative tissue engineering therapies.<sup>32</sup> In the present study, we investigated biological markers of HCECs for quality control with a view to clinical settings where cell characterization could be ensured. The Na<sup>+</sup>/K<sup>+</sup>-ATPase and ZO-1 investigated here are used frequently for research purposes, as coexpression of these proteins is recognized as identifying cells that possess pump



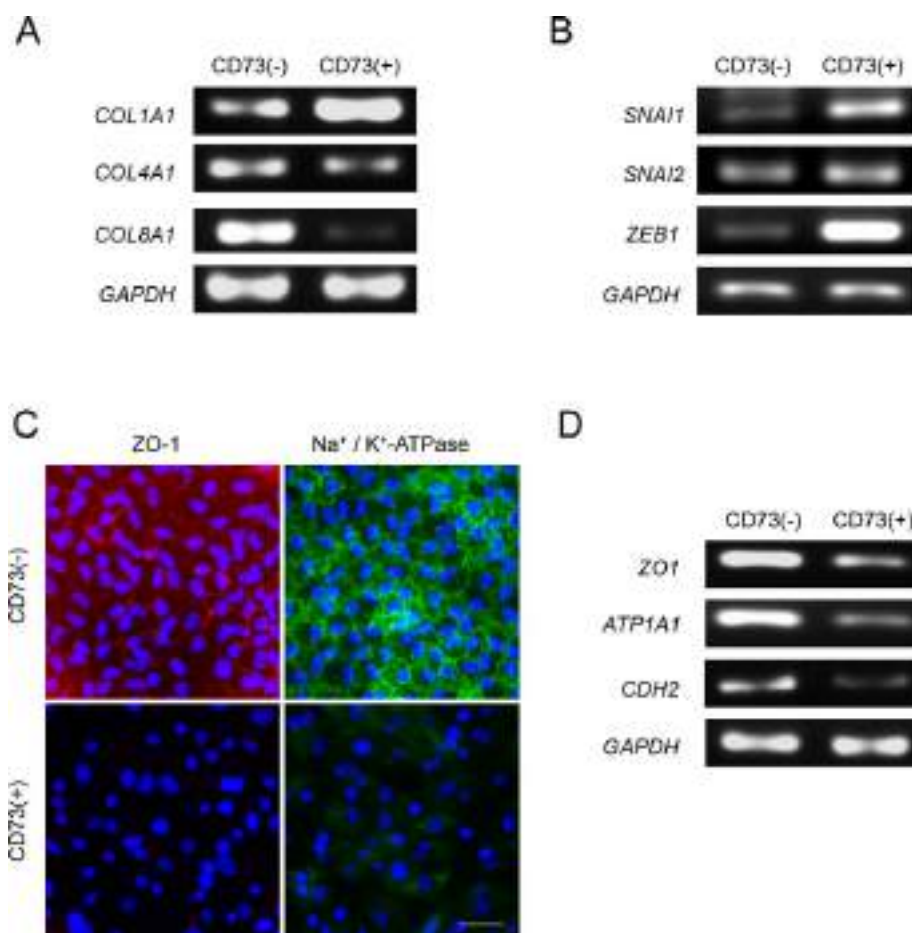


**FIGURE 4.** Functional analysis of CD73-positive MCECs. (A) Expressions of *COL1A1* (pathologic collagen of corneal endothelium), *COL4A1* (normal collagen), and *COL8A1* (normal collagen) in CD73-negative and -positive sorted cells were evaluated using PCR. Greater expression of *COL1A1* was seen in CD73-positive cells than in CD73-negative cells. Greater expression of *COL4A1* and *COL8A1* was found in CD73-negative sorted cells than in CD73-positive cells. (B) Expression of EMT inducer genes (*SNAI1*, *SNAI2*, and *ZEB1*) was evaluated by PCR. The CD73-positive sorted cells showed greater expression of *SNAI1*, *SNAI2*, and *ZEB1* when compared to CD73-negative cells. (C) Immunofluorescence staining of CD73-negative or -positive sorted cells by ZO-1 and Na<sup>+</sup>/K<sup>+</sup>-ATPase. Both ZO-1 and Na<sup>+</sup>/K<sup>+</sup>-ATPase were stained at the plasma membrane of CD73-negative cells. However, their expression was disrupted and decreased in CD73-positive cells. Scale bar: 50  $\mu$ m. (D) Expression levels of *ZO1*, *ATP1A1*, and *CDH2* were evaluated using PCR. The CD73-negative cells expressed *ZO1*, *ATP1A1*, and *CDH2* at the mRNA level, while their expression was decreased in CD73-positive cells. These experiments were performed in triplicate.

and barrier functional activity.<sup>33,34</sup> However, these proteins are not specific to corneal endothelium and are expressed in other organs, such as the heart, kidneys, and brain.<sup>35-38</sup> The genes that are known to have a role in corneal endothelium, such as *SLC4A* (Na, HCO<sub>3</sub> co-transporter), *COL4A2* (type IV collagen), *COL8A2* (type VIII collagen), and *CDH2* (N-cadherin), also have been used as markers.<sup>39</sup> However, no single specific gene was identified as an HCEC marker,<sup>40</sup> even though gene expression profiles were reported in donor corneal endothelium.<sup>41,42</sup>

Recently, Glypican-4 and CD200 were proposed as HCEC markers to distinguish HCECs from corneal stromal fibroblasts, based on RNA sequencing and immunofluorescence staining.<sup>43</sup> However, the practical problem of HCEC culture is the potential contamination with vulnerable transformed HCECs,<sup>21</sup> so the purity of the cultured HCECs destined for clinical use must first be ensured. The lack of a specific marker led us to screen surface antigens that could be used to identify whether cultured cells retain their functional phenotype or have undergone fibroblastic changes. Further studies are required to determine which marker or combination of markers will be

most appropriate for quality control, but assessment of markers using flow cytometry will provide us with a quantitative threshold by which to ensure the functional characteristics for clinical application.

The results of the current study also pointed to the novel possibility of an in vitro cell expansion protocol, whereby purified HCECs can be separated from a general culture cell population possibly contaminated with transformed HCECs simply by using the positive and negative cell selection that is readily accomplished by FACS. Recent developments have enabled the inhibition of fibroblastic changes and greater success rates for cell culture,<sup>21</sup> but a cell selection technique still would be anticipated to ultimately circumvent potential contamination by fibroblastic cells.<sup>43</sup> Peh GS et al.<sup>44</sup> reported the separation of prefluorescein-labeled corneal stromal fibroblasts from a mixture of fibroblasts and HCECs by magnetic affinity cell separation (MACS) and suggested that this type of selection strategy would be useful for depleting the cultures of contaminating cells. To the best of our knowledge, ours is the first report showing this depletion of fibroblastic cells and purification of normal phenotype CECs from a mixed

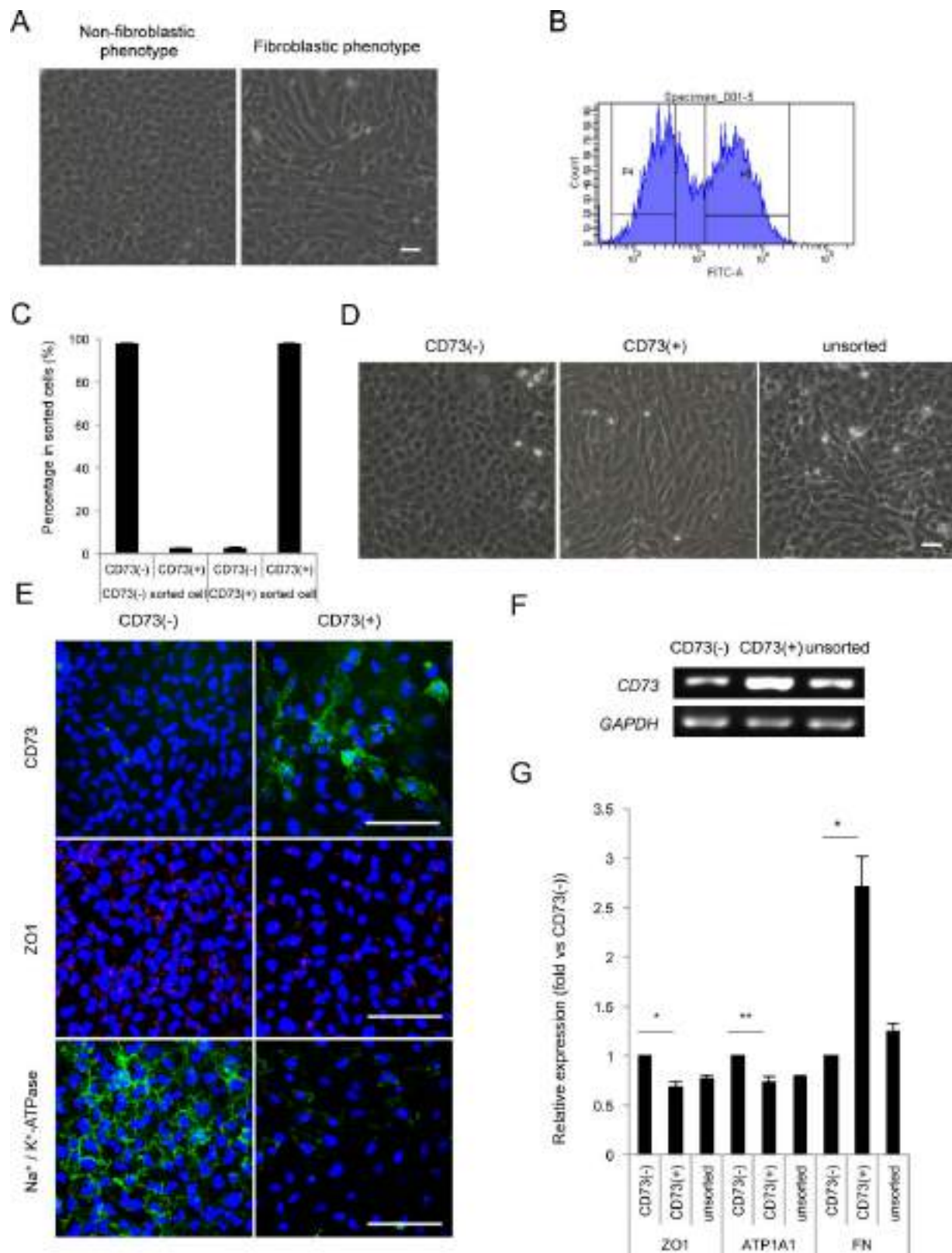


**FIGURE 5.** Cell sorting of immortalized HCECs and functional analysis of CD73-positive immortalized HCECs. (A) Normal hexagonal contact-inhibited phenotype HCECs and fibroblastic HCECs were immortalized using SV40 and hTERT to establish cell lines. (B) Immortalized normal HCECs and fibroblastic HCECs were harvested from culture plates and mixed. The CD73-negative and -positive cells then were sorted by flow cytometry. (C) The CD73-negative and -positive immortalized HCECs were sorted and CD73 expression was analyzed using flow cytometry. A total of 96.7% of CD73-negative sorted cells expressed CD73, while 97.6% of CD73-positive sorted cells did not express CD73. (D) The CD73-negative and -positive sorted immortalized HCECs were seeded and cultured until confluent. The CD73-negative cells showed hexagonal morphology, while CD73 (+) and unsorted control cells showed fibroblastic morphology. (E) Immunofluorescence staining of CD73, ZO-1, and Na<sup>+</sup>/K<sup>+</sup>-ATPase. The

CD73 staining was confirmed in CD73-positive sorted cells, while it was not stained in CD73-negative sorted cells. The CD73-negative cells expressed ZO-1 and Na<sup>+</sup>/K<sup>+</sup>-ATPase at the plasma membrane, while their expression was disrupted in CD73-positive cells. *Scale bar*: 100  $\mu$ m. (F) Expression of *CD73* was assessed using PCR. The CD73-positive cells expressed higher levels of *CD73* mRNA than did the CD73-negative cells. (G) Expression of *ZO1*, *ATP1A1*, and *FN1* was assessed by quantitative PCR. The CD73-positive cells expressed less *ZO1* and *ATP1A1*, while expression of *FN1* was higher than in CD73-negative cells. \**P* < 0.01, \*\**P* < 0.05.

cell population using FACS. Although we successfully separated fibroblastic cells from the immortalized HCEC-population by FACS, primary cultured HCECs tended to exhibit fibroblastic changes after cell sorting by our current protocol, due to complete cell dissociation for FACS (data not shown). Thus, the details of this selection procedure, especially for human cells, should be optimized; for example, through the use of antifibroblastic molecule during cell dissociation<sup>21</sup> and the separation by MACS rather than FACS.<sup>44</sup> These results suggest that the depletion of fibroblastic cells based on cell surface antigens should be explored further to isolate a purified cell population for clinical use.

We considered that detection of fibroblastic cell contamination would be possible if we could discover a marker for fibroblastic HCECs. Indeed, CD73 enabled the detection of fibroblastic cells, and further separation of normal and fibroblastic cells. The CD73 (ecto-5'-nucleotidase) is membrane-bound glycoprotein that metabolizes adenosine 5'-monophosphate (AMP) to adenosine.<sup>45</sup> Expression of CD73 is observed in a variety of cell types and regulates various physiological phenomena, such as ion and fluid transport, barrier function, adaptation to hypoxia, and inflammation.<sup>45</sup> Little is known regarding the involvement of CD73 in fibroblastic transformation, but this glycoprotein has an important role in bleomycin-induced lung injury<sup>24</sup> and hepatic fibrosis<sup>25</sup> through the conversion of AMP to adenosine. In the corneal endothelium, we showed that EMT inducer genes, such as *SNAIL1*, *SNAIL2*, and *ZEB1*, were activated in CD73-positive cells,<sup>21</sup> which suggests that the EMT might be involved in the elevated expression of CD73.

In conclusion, we demonstrated that CD98, CD166, and CD340 could serve as markers of the nonfibroblastic phenotype of HCECs, and that CD9, CD44, CD49e, and CD73 could serve as markers of the fibroblastic phenotype of these cells. These markers could be used for quality control to characterize the cellular phenotype used in therapies based on tissue engineering, though the threshold for clinical use should be explored further. Further, if positive and negative cell selection proves applicable to clinical settings, cell sorting based on these cell surface markers will provide a novel strategy for purifying functional cells.

### Acknowledgments

The authors thank Satoshi Kawasaki, Kenta Yamasaki, Kazuko Asada, Munetoyo Toda, and Yuji Sakamoto for their valuable assistance with the experiments.

Disclosure: N. Okumura, P; H. Hirano, P; R. Numata, None; M. Nakahara, None; M. Ueno, P; J. Hamuro, None; S. Kinoshita, P; N. Koizumi, P

### References

- Bourne WM. Clinical estimation of corneal endothelial pump function. *Trans Am Ophthalmol Soc*. 1998;96:229-239, discussion 239-242.
- Joyce NC. Proliferative capacity of the corneal endothelium. *Prog Retin Eye Res*. 2003;22:359-389.
- Joyce NC. Cell cycle status in human corneal endothelium. *Exp Eye Res*. 2005;81:629-638.
- Koizumi N, Suzuki T, Uno T, et al. Cytomegalovirus as an etiologic factor in corneal endotheliitis. *Ophthalmology*. 2008;115:292-297.
- Tan DT, Dart JK, Holland EJ, Kinoshita S. Corneal transplantation. *Lancet*. 2012;379:1749-1761.
- Eye Bank Association of America. *Eye Banking Statistical Report*. Washington, DC: Eye Bank Association of America; 2012.
- Lee JA, Djalilian AR, Riaz KM, et al. Clinical and histopathologic features of failed Descemet stripping automated endothelial keratoplasty grafts. *Cornea*. 2009;28:530-535.
- Koizumi N, Okumura N, Kinoshita S. Development of new therapeutic modalities for corneal endothelial disease focused on the proliferation of corneal endothelial cells using animal models. *Exp Eye Res*. 2012;95:60-67.
- Mimura T, Yamagami S, Yokoo S, et al. Cultured human corneal endothelial cell transplantation with a collagen sheet in a rabbit model. *Invest Ophthalmol Vis Sci*. 2004;45:2992-2997.
- Ishino Y, Sano Y, Nakamura T, et al. Amniotic membrane as a carrier for cultivated human corneal endothelial cell transplantation. *Invest Ophthalmol Vis Sci*. 2004;45:800-806.
- Sumide T, Nishida K, Yamato M, et al. Functional human corneal endothelial cell sheets harvested from temperature-responsive culture surfaces. *FASEB J*. 2006;20:392-394.
- Koizumi N, Sakamoto Y, Okumura N, et al. Cultivated corneal endothelial cell sheet transplantation in a primate model. *Invest Ophthalmol Vis Sci*. 2007;48:4519-4526.
- Mimura T, Shimomura N, Usui T, et al. Magnetic attraction of iron-endocytosed corneal endothelial cells to Descemet's membrane. *Exp Eye Res*. 2003;76:745-751.
- Mimura T, Yokoo S, Araie M, Amano S, Yamagami S. Treatment of rabbit bullous keratopathy with precursors derived from cultured human corneal endothelium. *Invest Ophthalmol Vis Sci*. 2005;46:3637-3644.
- Patel SV, Bachman LA, Hann CR, Bahler CK, Fautsch MP. Human corneal endothelial cell transplantation in a human ex vivo model. *Invest Ophthalmol Vis Sci*. 2009;50:2123-2131.
- Okumura N, Koizumi N, Ueno M, et al. ROCK inhibitor converts corneal endothelial cells into a phenotype capable of regenerating in vivo endothelial tissue. *Am J Pathol*. 2012;181:268-277.
- Okumura N, Ueno M, Koizumi N, et al. Enhancement on primate corneal endothelial cell survival in vitro by a ROCK inhibitor. *Invest Ophthalmol Vis Sci*. 2009;50:3680-3687.
- Peh GS, Toh KP, Wu FY, Tan DT, Mehta JS. Cultivation of human corneal endothelial cells isolated from paired donor corneas. *PLoS One*. 2011;6:e28310.
- Shima N, Kimoto M, Yamaguchi M, Yamagami S. Increased proliferation and replicative lifespan of isolated human corneal endothelial cells with L-ascorbic acid 2-phosphate. *Invest Ophthalmol Vis Sci*. 2011;52:8711-8717.
- Nakahara M, Okumura N, Kay EP, et al. Corneal endothelial expansion promoted by human bone marrow mesenchymal stem cell-derived conditioned medium. *PLoS One*. 2013;8:e69009.
- Okumura N, Kay EP, Nakahara M, Hamuro J, Kinoshita S, Koizumi N. Inhibition of TGF-beta signaling enables human corneal endothelial cell expansion in vitro for use in regenerative medicine. *PLoS One*. 2013;8:e58000.



22. Okumura N, Koizumi N, Kay EP, et al. The ROCK inhibitor eye drop accelerates corneal endothelium wound healing. *Invest Ophthalmol Vis Sci.* 2013;54:2493-2502.
23. Peh GS, Beuerman RW, Colman A, Tan DT, Mehta JS. Human corneal endothelial cell expansion for corneal endothelium transplantation: an overview. *Transplantation.* 2011;91:811-819.
24. Volmer JB, Thompson LF, Blackburn MR. Ecto-5'-nucleotidase (CD73)-mediated adenosine production is tissue protective in a model of bleomycin-induced lung injury. *J Immunol.* 2006;176:4449-4458.
25. Fausther M, Sheung N, Saiman Y, Bansal MB, Dranoff JA. Activated hepatic stellate cells upregulate transcription of ecto-5'-nucleotidase/CD73 via specific SP1 and SMAD promoter elements. *Am J Physiol Gastrointest Liver Physiol.* 2012;303:G904-G914.
26. Kawaguchi R, Saika S, Wakayama M, Ooshima A, Ohnishi Y, Yabe H. Extracellular matrix components in a case of retrocorneal membrane associated with syphilitic interstitial keratitis. *Cornea.* 2001;20:100-103.
27. Weller JM, Zenkel M, Schlotzer-Schrehardt U, Bachmann BO, Tourtas T, Kruse FE. Extracellular matrix alterations in late-onset Fuchs' corneal dystrophy. *Invest Ophthalmol Vis Sci.* 2014;55:3700-3708.
28. Okano H, Nakamura M, Yoshida K, et al. Steps toward safe cell therapy using induced pluripotent stem cells. *Circ Res.* 2013;112:523-533.
29. Tabar V, Studer L. Pluripotent stem cells in regenerative medicine: challenges and recent progress. *Nat Rev Genet.* 2014;15:82-92.
30. Lysaght T, Campbell AV. Regulating autologous adult stem cells: the FDA steps up. *Cell Stem Cell.* 2011;9:393-396.
31. Sipp D. Hope alone is not an outcome: why regulations makes sense for the global stem cell industry. *Am J Bioeth.* 2010;10:33-34.
32. Hyun I. Allowing innovative stem cell-based therapies outside of clinical trials: ethical and policy challenges. *J Law Med Ethics.* 2010;38:277-285.
33. Barry PA, Petroll WM, Andrews PM, Cavanagh HD, Jester JV. The spatial organization of corneal endothelial cytoskeletal proteins and their relationship to the apical junctional complex. *Invest Ophthalmol Vis Sci.* 1995;36:1115-1124.
34. Sugrue SP, Zieske JD. ZO1 in corneal epithelium: association to the zonula occludens and adherens junctions. *Exp Eye Res.* 1997;64:11-20.
35. Fanning AS, Anderson JM. Zonula occludens-1 and -2 are cytosolic scaffolds that regulate the assembly of cellular junctions. *Ann N Y Acad Sci.* 2009;1165:113-120.
36. Sune G, Sarro E, Puigmule M, et al. Cyclophilin B interacts with sodium-potassium ATPase and is required for pump activity in proximal tubule cells of the kidney. *PLoS One.* 2010;5:e13930.
37. Corti C, Xuereb JH, Crepaldi L, Corsi M, Michielin F, Ferraguti F. Altered levels of glutamatergic receptors and Na<sup>+</sup>/K<sup>+</sup> ATPase- $\alpha$ 1 in the prefrontal cortex of subjects with schizophrenia. *Schizophr Res.* 2011;128:7-14.
38. Sanchez C, Corrias A, Bueno-Orovio A, et al. The Na<sup>+</sup>/K<sup>+</sup> pump is an important modulator of refractoriness and rotor dynamics in human atrial tissue. *Am J Physiol Heart Circ Physiol.* 2012;302:H1146-1159.
39. Hatou S, Yoshida S, Higa K, et al. Functional corneal endothelium derived from corneal stroma stem cells of neural crest origin by retinoic acid and Wnt/beta-catenin signaling. *Stem Cells Dev.* 2013;22:828-839.
40. Chng Z, Peh GS, Herath WB, et al. High throughput gene expression analysis identifies reliable expression markers of human corneal endothelial cells. *PLoS One.* 2013;8:e67546.
41. Sakai R, Kinouchi T, Kawamoto S, et al. Construction of human corneal endothelial cDNA library and identification of novel active genes. *Invest Ophthalmol Vis Sci.* 2002;43:1749-1756.
42. Gottsch JD, Seitzman GD, Margulies EH, et al. Gene expression in donor corneal endothelium. *Arch Ophthalmol.* 2003;121:252-258.
43. Cheong YK, Ngho ZX, Peh GS, et al. Identification of cell surface markers glypican-4 and CD200 that differentiate human corneal endothelium from stromal fibroblasts. *Invest Ophthalmol Vis Sci.* 2013;54:4538-4547.
44. Peh GS, Lee MX, Wu FY, Toh KP, Balchousur D, Mehta JS. Optimization of human corneal endothelial cells for culture: the removal of corneal stromal fibroblast contamination using magnetic cell separation. *Int J Biomater.* 2012;2012:601302.
45. Colgan SP, Eltzschig HK, Eckle T, Thompson LF. Physiological roles for ecto-5'-nucleotidase (CD73). *Purinergic Signal.* 2006;2:351-360.

# New Therapeutic Modality for Corneal Endothelial Disease Using Rho-Associated Kinase Inhibitor Eye Drops

Noriko Koizumi, MD, PhD,\*† Naoki Okumura, MD, PhD,\*† Morio Ueno, MD, PhD,†  
and Shigeru Kinoshita, MD, PhD†

**Abstract:** Corneal endothelial dysfunction accompanied by visual disturbance is a primary indication for corneal endothelial transplantation. However, despite the value and potential of endothelial graft surgery, a strictly pharmacological approach for treating corneal endothelial dysfunction remains an attractive proposition. Previously, we reported that the selective Rho-associated kinase (ROCK) inhibitor Y-27632 promotes cell adhesion and proliferation, and inhibits the apoptosis of primate corneal endothelial cells in culture. These findings have led us to develop a novel medical treatment for the early phase of corneal endothelial disease using ROCK inhibitor eye drops. In rabbit and monkey models of partial endothelial dysfunction, we showed that corneal endothelial wound healing was accelerated via the topical application of ROCK inhibitor to the ocular surface, resulting in the regeneration of a corneal endothelial monolayer with a high endothelial cell density. Based on these animal studies, we are now attempting to advance the clinical application of ROCK inhibitor eye drops for patients with corneal endothelial dysfunction. A pilot clinical study was performed at the Kyoto Prefectural University of Medicine, and the effects of Y-27632 eye drops after transcorneal freezing were evaluated in 8 patients with corneal endothelial dysfunction. We observed a positive effect of ROCK inhibitor eye drops in treating patients with central edema caused by Fuchs corneal endothelial dystrophy. We believe that our new findings will contribute to the establishment of a new approach for the treatment of corneal endothelial dysfunction.

**Key Words:** corneal endothelial cells, proliferation, Rho kinase (ROCK) inhibitor, corneal endothelial dysfunction, Fuchs corneal dystrophy

(*Cornea* 2014;33(Suppl):S25–S31)

From the \*Department of Biomedical Engineering, Faculty of Life and Medical Sciences, Doshisha University, Kyotanabe, Japan; and †Department of Ophthalmology, Kyoto Prefectural University of Medicine, Kyoto, Japan. Supported in part by the Adaptable and Seamless Technology Transfer Program through Target-Driven R&D (S. Kinoshita, N. Okumura, M. Ueno, and N. Koizumi: AS2314212G) from the Japan Science and Technology Agency, and the Funding Program for Next Generation World-Leading Researchers from the Cabinet Office in Japan (N. Koizumi: LS117).

The authors have applied for patents from Senju Pharmaceutical Co, Doshisha University, and Kyoto Prefectural University of Medicine.

Reprints: Noriko Koizumi, MD, PhD, Department of Biomedical Engineering, Faculty of Life and Medical Sciences, Doshisha University, Kyotanabe 610-0321, Japan (e-mail: nkoizumi@mail.doshisha.ac.jp).

Copyright © 2014 by Lippincott Williams & Wilkins

The corneal endothelium is the innermost layer of the cornea and plays an essential role in the maintenance of corneal transparency via its barrier and pump functions. Primate corneal endothelium is nonregenerative in vivo. Because endothelial cell loss caused by dystrophy, trauma, or surgical intervention is followed by a compensatory enlargement of the remaining endothelial cells, the outcome is often irreversible corneal endothelial dysfunction. As a treatment for corneal endothelial dysfunction, corneal endothelial transplants using a donor graft, such as Descemet stripping automated endothelial keratoplasty<sup>1,2</sup> or more recently Descemet membrane endothelial keratoplasty,<sup>3</sup> have been performed. However, several severe problems can arise in association with corneal endothelial transplantation, including allograft rejection, primary graft failure, and severe loss of cell density.<sup>4,5</sup> Further, the age and health of endothelial graft tissue might affect the efficacy of transplantation, especially because donor tissue tends to come from cadavers. Because long-term efficacy from surgical techniques is not satisfactory, there is a need for better, less invasive treatment options. To the best of our knowledge, no clinically useful pharmacological treatment has been developed to date to treat corneal endothelial dysfunction effectively.

The purpose of our current research is to develop new surgical and medical treatments for corneal endothelial diseases that provide a healthy corneal endothelium with high cell density. To achieve this, we are currently focusing on the proliferation of corneal endothelial cells (CECs) both in vivo and in vitro. We developed several techniques for the efficient cell culture of human CECs<sup>6–8</sup> and examined the feasibility of cultivated corneal endothelial transplantation using either cultivated corneal endothelial sheet transplantation<sup>9–11</sup> or a cell-injection procedure.<sup>12</sup> Currently, our efforts are aimed at developing feasible medical treatments for the early stages of corneal endothelial dysfunction, such as those that involve the use of rho-associated kinase (ROCK) inhibitor eye drops. In this review, we report our recent progress toward the development of new therapeutic modalities for corneal endothelial disease with a focus on the proliferation of CECs and the results of our clinical study.

## EFFECT OF RHO KINASE INHIBITOR ON PRIMATE CECs IN CULTURE

Although human CECs are arrested at the G1 phase of the cell cycle,<sup>13</sup> they retain the capacity to proliferate in vitro.<sup>14–17</sup> Medical treatment for corneal endothelial disease

has been sought for a long time by clinicians and patients. However, to the best of our knowledge, no clinically practical medical therapy has been developed to treat corneal endothelial dysfunction.

The Rho/Rho-kinase (ROCK) pathway is reportedly involved in regulating the cytoskeleton, cell migration, cell proliferation, and apoptosis.<sup>18–21</sup> It has also been reported by our collaborators that a selective ROCK inhibitor, Y-27632, diminished the dissociation-induced apoptosis of human embryonic stem cells.<sup>22</sup> We screened several low-molecular chemical compounds and found that the modulation of Rho/ROCK signaling was important for numerous cellular functions, and that the ROCK pathway might be a potential therapeutic target for the treatment of corneal endothelial disease.

We examined the effect of Y-27632 on primate CECs in vitro and found that inhibition of Rho/ROCK signaling by Y-27632 inhibited dissociation-induced apoptosis and promoted the adhesion and proliferation of monkey CECs.<sup>6</sup>

### MOLECULAR MECHANISM OF ACTION OF ROCK INHIBITORS ON CEC PROLIFERATION

Recently, we investigated the molecular mechanism by which Y-27632 stimulates the proliferation of monkey and human CECs. We first examined the expression of G<sub>1</sub> proteins of the cell cycle and the expression of phosphorylated Akt in monkey CECs treated with Y-27632, and found that Y-27632 facilitated the degradation of p27Kip1 (p27), and promoted the expression of cyclin D via PI 3-kinase signaling (Figs. 1, 2).<sup>23</sup> In addition, we investigated a novel, selective ROCK inhibitor, Y-39983, and found that a lower concentration of Y-39983 (0.3 or 3.0  $\mu$ M) stimulated the proliferation

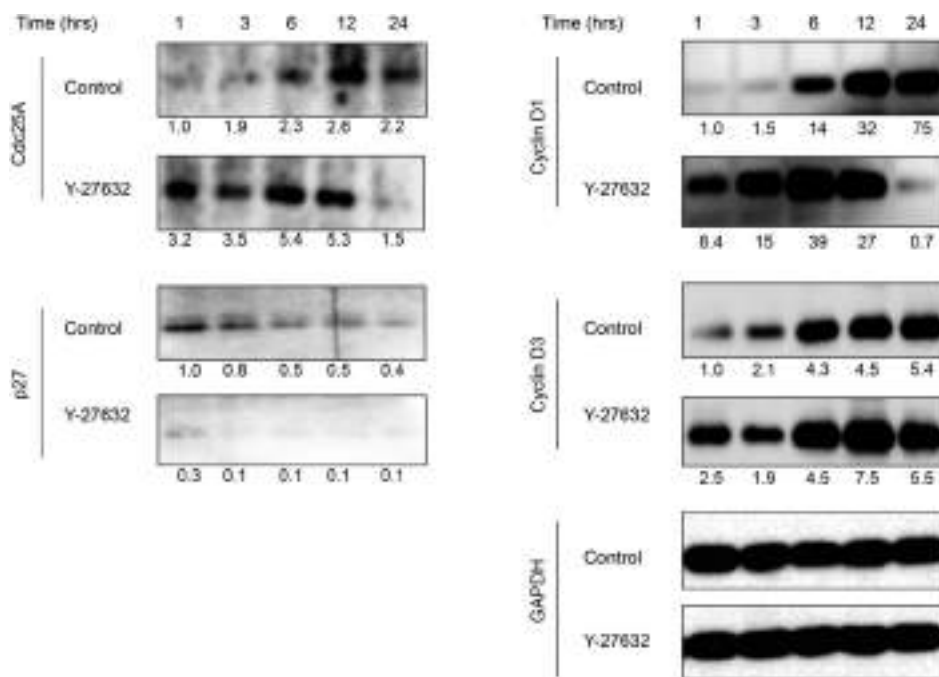
of CECs to the same level as stimulation with 10  $\mu$ M Y-27632. Although contradictory findings have been reported by other groups,<sup>24</sup> our results showed that Y-39983 produced a 1.6- to 1.8-fold increase of 5-bromo-2-deoxyuridine incorporation and increased the percentage of Ki67-positive human CECs in a dose-dependent manner.<sup>23</sup>

### ROCK INHIBITOR EYE DROPS IN ANIMAL MODELS

The concept of eye-drop treatment is to recover corneal endothelial function by stimulating the in vivo proliferation of residual CECs in patients. Toward this goal, we examined the effect of Y-27632 ROCK inhibitor eye drops on CECs using an animal partial corneal endothelial defect model. The target of pharmacological treatment is the early phase of corneal endothelial disease in patients who retain some healthy CECs. First, we reported the effect of ROCK inhibitor eye drops using a partial endothelial injury rabbit model. After creating a 7-mm-diameter corneal endothelial wound by transcorneal freezing, we applied 10 mM of Y-27632 6 times daily for 2 days as an eye drop. The Y-27632-treated eyes showed less corneal edema, and the mean wound area was significantly smaller than that of control eyes.<sup>25</sup> We also confirmed that the proliferation of rabbit CECs was enhanced by Y-27632 in a dose-dependent manner (Fig. 3). These results demonstrated that the topical administration of a selective ROCK inhibitor, Y-27632, promoted corneal endothelial wound healing by stimulating the proliferation of CECs.

Based on these findings, we investigated the application of ROCK inhibitor eye drops in a clinical setting, and conducted a similar experiment using a partial corneal

**FIGURE 1.** Effect of the ROCK inhibitor Y-27632 on G<sub>1</sub>/S progression. Monkey CECs were serum starved for 24 hours before treatment with growth-medium containing 10  $\mu$ M of Y-27632. After 1, 3, 6, 12, or 24 hours, Cdc25A, p27, cyclin D1, and cyclin D3 protein levels were measured. Y-27632 produced a 3.2-fold increase in the expression of Cdc25A within 1 hour and maintained expression up to 12 hours. Y-27632 stimulation produced a 0.3-fold reduction of p27, and 8.4-fold and 2.5-fold increases in cyclin D1 and D3 expression, respectively, at 1 hour. The relative density of the immunoblot bands was determined by Image J (NIH) software. Relative fold differences were compared with control (glyceraldehyde 3-phosphate dehydrogenase) values at 1 hour. Reprinted from Okumura et al<sup>23</sup> with permission from the Association for Research in Vision and Ophthalmology.





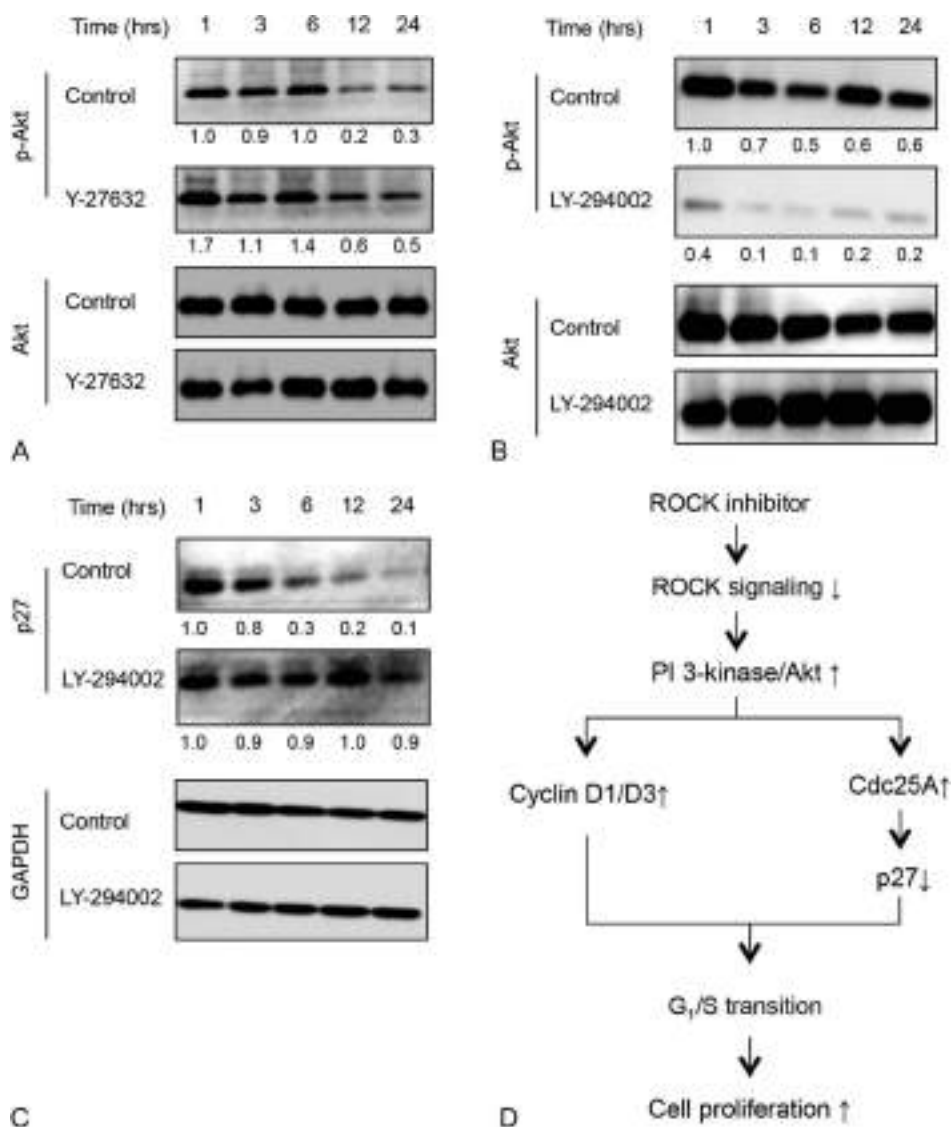


**FIGURE 2.** Involvement of PI 3-kinase signaling in Y-27632-mediated p27 degradation and upregulation of cyclin D. A–C, Serum-starved CECs were treated with or without Y-27632 for 1, 3, 6, 12, or 24 hours. Phosphorylation of Akt, total Akt, and p27 were evaluated by Western blotting. The phosphorylation of Akt was sustained 1.7-fold higher in Y-27632-treated cells compared with that in control cells at 1 hour. LY294002 abolished the phosphorylation of Akt and maintained the p27 levels. The relative density of immunoblot bands was determined by Image J software. Relative fold differences were compared with control (glyceraldehyde 3-phosphate dehydrogenase) values at 1 hour. D, Schematic diagram of the ROCK inhibitor pathway for control of the cell cycle. Reprinted from Okumura et al<sup>23</sup> with permission from the Association for Research in Vision and Ophthalmology.

endothelial dysfunction model in monkeys whose CECs do not proliferate well in vivo. The topical application of Y-27632 eye drops greatly enhanced wound healing of the corneal endothelium and enabled the corneal endothelium to retain a high cell density 1 month after treatment (Fig. 4).<sup>26</sup> Further, the regenerated corneal endothelium of the central damaged area demonstrated physiological hexagonal cell morphology with the expression of function-related proteins, such as ZO-1 and Na<sup>+</sup>/K<sup>+</sup>-ATPase.<sup>26</sup> These findings suggest that the ROCK inhibitor Y-27632 eye drops enhance both the functional and morphological recoveries of a primate's CECs in vivo.

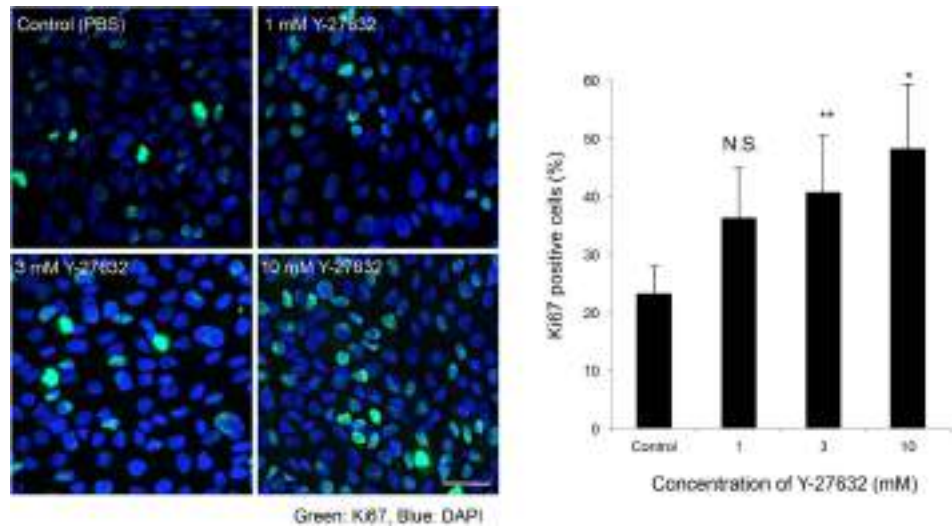
### PILOT CLINICAL STUDY OF ROCK INHIBITOR EYE DROPS FOR PATIENTS WITH CORNEAL ENDOTHELIAL DYSFUNCTION

Based on results obtained from previous animal studies, we obtained approval from the Institutional Review Board of Kyoto Prefectural University of Medicine and began a clinical

pilot study of ROCK inhibitor eye-drop treatment for bullous keratopathy in 2010. Because visual acuity is severely influenced by other ocular diseases, such as retinal degeneration, glaucoma, or cataract, central corneal thickness was chosen as the primary endpoint for evaluation of corneal endothelial function.

Eight eyes from 8 patients scheduled for Descemet stripping automated endothelial keratoplasty were included in this study. Four eyes presented with diffuse corneal edema caused by argon laser iridotomy-induced bullous keratopathy, or keratopathy in pseudexfoliation syndrome. The other 4 eyes had central corneal edema caused by the late onset of Fuchs corneal dystrophy. All eyes underwent trans-corneal freezing using a 2-mm-diameter stainless steel rod, followed by Y-27632 eye-drop application 6 times a day for 1 week. The 4 patients with diffuse corneal edema showed no reduction in corneal thickness and no improvement in visual acuity. In contrast, 3 of the 4 eyes with central corneal edema caused by Fuchs corneal dystrophy showed a decrease in

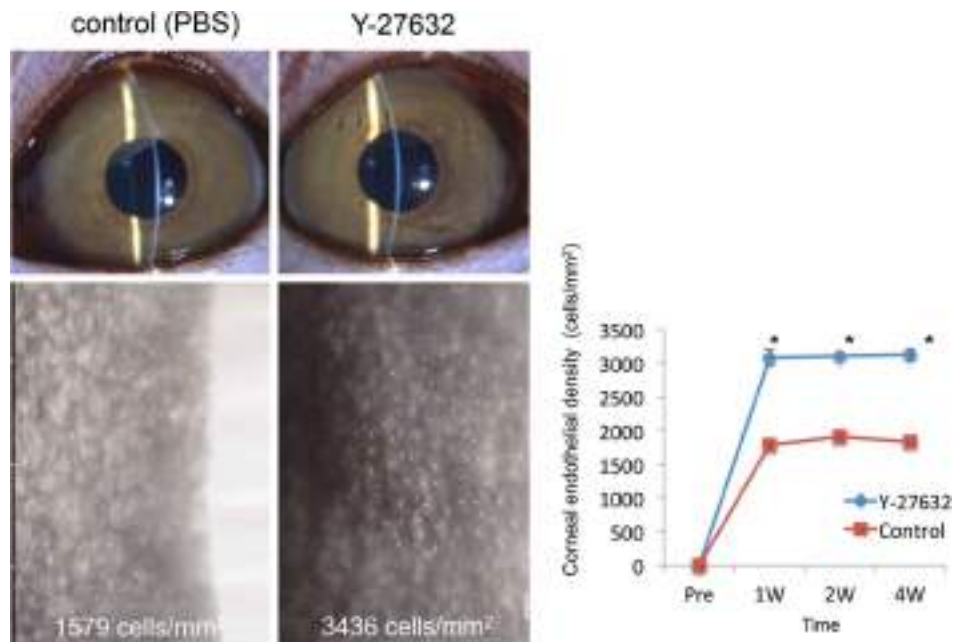
**FIGURE 3.** The effect of Y-27632 eye-drop instillation on *in vivo* cell proliferation in a rabbit model. The number of Ki67-positive cells (green) among the undamaged peripheral corneal endothelium was evaluated. Cell nuclei were stained blue with 4'-6-diamidino-2-phenylindole. The percentages of Ki67-positive cells at the edge of the original wounded area were evaluated by fluorescence microscopy, and the mean value was plotted as a bar chart ( $n = 6$ ). The percentage of Ki67-positive cells was significantly increased in corneal endothelium treated with 3 or 10 mM of Y-27632. Scale bar = 100  $\mu\text{m}$ . \* $P < 0.01$ , \*\* $P < 0.05$ . Reprinted from Okumura et al<sup>23</sup> with permission from the Association for Research in Vision and Ophthalmology.



central corneal thickness, which was maintained with time.<sup>26</sup> In one of these patients, corneal clarity recovered, and vision improved to 20/20 at 2 weeks after treatment, and endothelial function and vision have been well maintained for up to 24 months posttreatment (Figs. 5, 6).<sup>27</sup> A previous case report described the clinical observation of this patient using a wide-field contact specular microscope. We observed a high density of smaller endothelial cells in the central cornea from

which endothelial cells had been removed by transcorneal freezing compared with those in the peripheral area.<sup>27</sup> Although corneal endothelial stem cells have not been specifically identified and their exact location has not been determined, several groups reported that CECs in the peripheral area of the cornea retained a high proliferative ability.<sup>28</sup> We recently reported that LGR5 is uniquely expressed in the peripheral lesion of human CECs and that LGR5-positive

**FIGURE 4.** ROCK inhibitor Y-27632 eye drops promote the recovery of cell density in a corneal endothelial partial damage primate model. Slit-lamp microscopy examination revealed both Y-27632-treated and nontreated corneas recovered their transparency 1 month after transcorneal freezing. In the control group, noncontact specular microscopy showed enlarged corneal endothelium migrating into the damaged area at a density of approximately 1500 cells per square millimeter, 1 week after injury. However, the corneal endothelium of the Y-27632-treated group was reconstructed with a normal cell density of approximately 3000 cells per square millimeter. Noncontact specular microscopy analysis revealed that CEC density was significantly higher in the Y-27632-treated group than in the control group throughout the 4-week observation period ( $n = 6$ , \* $P < 0.01$ ). Modified and reprinted from Okumura et al<sup>26</sup> with permission from the Association for Research in Vision and Ophthalmology.



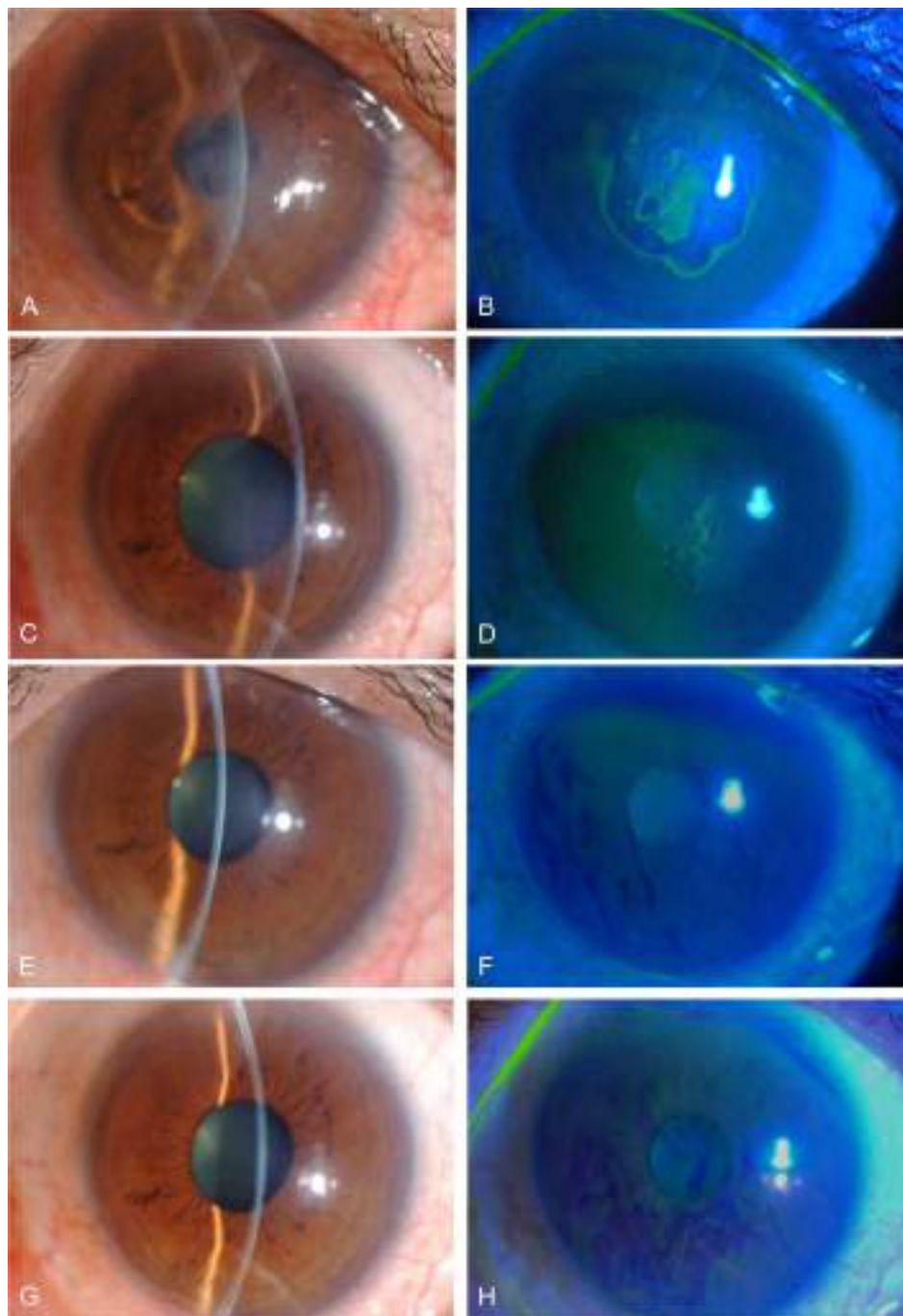


**FIGURE 5.** Slit-lamp photographs of a patient with Fuchs corneal dystrophy before and after transcorneal freezing and ROCK inhibitor treatment. Before treatment, a central corneal edema (A) accompanied by a lesion of epithelial bullae (B) was detected. Three days after treatment, the corneal erosion created by the transcorneal freezing had already healed, and mild bullae were detected (C, D). It should be noted that less corneal edema was observed at 2 days than in the pre-treatment image. Six months after treatment, the corneal edema was significantly reduced, and the cornea had recovered its clarity (E). No epithelial damage was observed by fluorescein staining (F). Two years after treatment, the patient's cornea remains clear with good (20/16) vision (G, H). Reprinted from Koizumi et al<sup>27</sup> with permission from Lippincott Williams & Wilkins.

cells have some stem/progenitor cell characteristics.<sup>29</sup> Although our clinical finding provides indirect evidence, it strongly suggests that the *in vivo* proliferation of CECs was stimulated by the ROCK inhibitor. However, the possibility that the reestablishment of each patient's endothelium was not solely a direct result of the ROCK inhibitor administration,<sup>30</sup> but could have been the result of denudation of pathologic endothelial cells, should be noted. These cases demonstrate the possibility of successful medical treatment involving the use of ROCK inhibitor eye drops or other

pharmacological agents as an alternative to graft surgery for early phases of corneal endothelial dysfunction.

## CONCLUSIONS

Here, we reviewed our recent studies that focused on developing new pharmacological treatments for corneal endothelial dysfunction using ROCK inhibitors. We showed that inhibition of Rho/ROCK signaling using a specific ROCK inhibitor Y-27632 promoted cell proliferation and



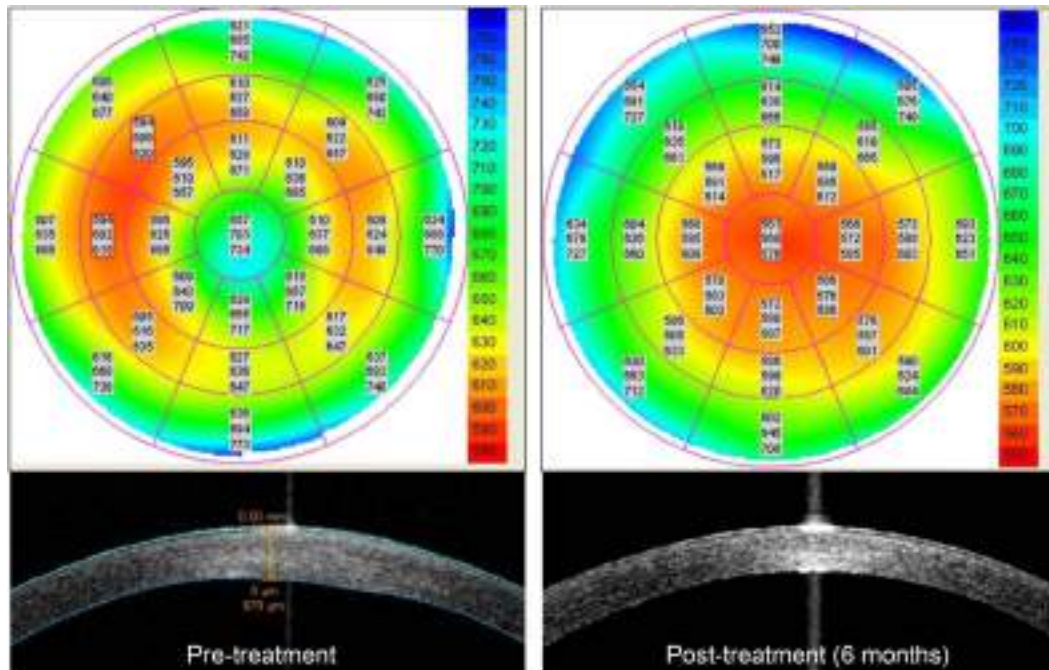


**FIGURE 6.** Examination using anterior segment optical coherence tomography shows remarkable improvement of corneal edema in a patient with Fuchs corneal dystrophy treated with ROCK inhibitor eye drops 6 months after initiation of treatment.

wound healing in both in vitro and in vivo animal models. In addition, the effect of Y-27632 eye drops after transcorneal freezing was evaluated in 8 patients with corneal endothelial dysfunction. The Y-27632 eye drops demonstrated efficacy in treating patients with central corneal edema caused by Fuchs corneal dystrophy. Further, ROCK inhibitor eye drops promoted corneal endothelial wound healing and were effective for treating corneal endothelial dysfunction.

There were some limitations in these studies. For example, the period of ROCK inhibitor treatment was very short (1 week) because of its high cost. However, we expect that the continuous use of ROCK inhibitors might be effective for preventing endothelial cell loss over a long period. The discovery and introduction into clinical practice of new pharmacological agents that are safe and effective are highly desirable. If we can develop a successful medical treatment for corneal endothelial dysfunctions such as Fuchs corneal dystrophy, many patients will be able to avoid corneal transplantation throughout their lifetimes. We hope to elucidate the mechanism(s) underlying endothelial disease and develop novel medical treatments in the future.

#### ACKNOWLEDGMENTS

The authors thank Dr Yoshiki Sasai, Dr Junji Hamuro, and Dr Hiroko Nakagawa for their assistance and invaluable advice and technical assistance during this project, and thank Dr Shinichiro Nakamura and Dr Yuji Sakamoto for their support in monkey experiments. The authors also thank laboratory members in Doshisha University for their dedicated research work in corneal endothelial tissue engineering.

#### REFERENCES

- Price FW Jr, Price MO. Descemet's stripping with endothelial keratoplasty in 50 eyes: a refractive neutral corneal transplant. *J Refract Surg.* 2005;21:339–345.
- Gorovoy MS. Descemet-stripping automated endothelial keratoplasty. *Cornea.* 2006;25:886–889.
- Melles GR, Ong TS, Ververs B, et al. Descemet membrane endothelial keratoplasty (DMEK). *Cornea.* 2006;25:987–990.
- Terry MA, Chen ES, Shamie N, et al. Endothelial cell loss after Descemet's stripping endothelial keratoplasty in a large prospective series. *Ophthalmology.* 2008;115:488–496.e483.
- Price MO, Fairchild KM, Price DA, et al. Descemet's stripping endothelial keratoplasty five-year graft survival and endothelial cell loss. *Ophthalmology.* 2011;118:725–729.
- Okumura N, Ueno M, Koizumi N, et al. Enhancement on primate corneal endothelial cell survival in vitro by a ROCK inhibitor. *Invest Ophthalmol Vis Sci.* 2009;50:3680–3687.
- Nakahara M, Okumura N, Kay EP, et al. Corneal endothelial expansion promoted by human bone marrow mesenchymal stem cell-derived conditioned medium. *PLoS One.* 2013;8:e69009.
- Okumura N, Kay EP, Nakahara M, et al. Inhibition of TGF-beta signaling enables human corneal endothelial cell expansion in vitro for use in regenerative medicine. *PLoS One.* 2013;8:e58000.
- Koizumi N, Sakamoto Y, Okumura N, et al. Cultivated corneal endothelial cell sheet transplantation in a primate model. *Invest Ophthalmol Vis Sci.* 2007;48:4519–4526.
- Koizumi N, Sakamoto Y, Okumura N, et al. Cultivated corneal endothelial transplantation in a primate: possible future clinical application in corneal endothelial regenerative medicine. *Cornea.* 2008;27:S48–S55.
- Koizumi N, Okumura N, Kinoshita S. Development of new therapeutic modalities for corneal endothelial disease focused on the proliferation of corneal endothelial cells using animal models. *Exp Eye Res.* 2012;95:60–67.
- Okumura N, Koizumi N, Ueno M, et al. ROCK inhibitor converts corneal endothelial cells into a phenotype capable of regenerating in vivo endothelial tissue. *Am J Pathol.* 2012;181:268–277.
- Joyce NC. Proliferative capacity of the corneal endothelium. *Prog Retin Eye Res.* 2003;22:359–389.

14. Engelmann K, Bohnke M, Friedl P. Isolation and long-term cultivation of human corneal endothelial cells. *Invest Ophthalmol Vis Sci.* 1988;29:1656–1662.
15. Senoo T, Joyce NC. Cell cycle kinetics in corneal endothelium from old and young donors. *Invest Ophthalmol Vis Sci.* 2000;41:660–667.
16. Miyata K, Drake J, Osakabe Y, et al. Effect of donor age on morphologic variation of cultured human corneal endothelial cells. *Cornea.* 2001;20:59–63.
17. Zhu C, Joyce NC. Proliferative response of corneal endothelial cells from young and older donors. *Invest Ophthalmol Vis Sci.* 2004;45:1743–1751.
18. Olson MF, Ashworth A, Hall A. An essential role for Rho, Rac, and Cdc42 GTPases in cell cycle progression through G1. *Science.* 1995;269:1270–1272.
19. Hall A. Rho GTPases and the actin cytoskeleton. *Science.* 1998;279:509–514.
20. Riento K, Ridley AJ. Rocks: multifunctional kinases in cell behaviour. *Nat Rev Mol Cell Biol.* 2003;4:446–456.
21. Coleman ML, Marshall CJ, Olson MF. RAS and RHO GTPases in G1-phase cell-cycle regulation. *Nat Rev Mol Cell Biol.* 2004;5:355–366.
22. Watanabe K, Ueno M, Kamiya D, et al. A ROCK inhibitor permits survival of dissociated human embryonic stem cells. *Nat Biotechnol.* 2007;25:681–686.
23. Okumura N, Nakano S, Kay EP, et al. Involvement of cyclin D and p27 in cell proliferation mediated by ROCK inhibitors Y-27632 and Y-39983 during corneal endothelium wound healing. *Invest Ophthalmol Vis Sci.* 2014;55:318–329.
24. Pipparelli A, Arsenijevic Y, Thuret G, et al. ROCK inhibitor enhances adhesion and wound healing of human corneal endothelial cells. *PLoS One.* 2013;8:e62095.
25. Okumura N, Koizumi N, Ueno M, et al. Enhancement of corneal endothelium wound healing by Rho-associated kinase (ROCK) inhibitor eye drops. *Br J Ophthalmol.* 2011;95:1006–1009.
26. Okumura N, Koizumi N, Kay EP, et al. The ROCK inhibitor eye drop accelerates corneal endothelium wound healing. *Invest Ophthalmol Vis Sci.* 2013;54:2493–2502.
27. Koizumi N, Okumura N, Ueno M, et al. Rho-associated kinase inhibitor eye drop treatment as a possible medical treatment for Fuchs corneal dystrophy. *Cornea.* 2013;32:1167–1170.
28. Mimura T, Joyce NC. Replication competence and senescence in central and peripheral human corneal endothelium. *Invest Ophthalmol Vis Sci.* 2006;47:1387–1396.
29. Hirata-Tominaga K, Nakamura T, Okumura N, et al. Corneal endothelial cell fate is maintained by LGR5 through the regulation of hedgehog and Wnt pathway. *Stem Cells.* 2013;31:1396–1407.
30. Koizumi N, Okumura N, Kinoshita S. Author response: human corneal endothelium regeneration: effect of ROCK Inhibitor. *Invest Ophthalmol Vis Sci.* 2013;54:5594–5595.



# Cell-Based Approach for Treatment of Corneal Endothelial Dysfunction

Naoki Okumura, MD, PhD,\*† Shigeru Kinoshita, MD, PhD,† and Noriko Koizumi, MD, PhD\*

**Abstract:** Decompensation of the corneal endothelium causes severe visual impairments that lead to blindness. Although corneal transplantation is a well-known effective therapy for corneal endothelial dysfunction, many patients are not afforded that therapeutic opportunity owing to the worldwide shortage of donor corneas. Thus, a tissue engineering-based therapy for treating corneal endothelial dysfunction is highly anticipated. Obstacles associated with the development of tissue engineering therapy include *in vitro* culture of corneal endothelial cells (CECs) and the techniques used to transplant those cells. Limited proliferation ability, cellular senescence, and fibroblastic transformation during culture are all problems associated with the cultivation of CECs. In addition, transplantation of cultured CECs is technically difficult because the corneal endothelium is composed of a fragile monolayer sheet of cells located at the posterior cornea. In this review article, we present our recent findings using a novel cell culture protocol and show that modulation of CEC adhesion properties through a Rho-kinase inhibitor enables transplantation of CECs in the form of a cell suspension without the use of a carrier. Finally, we provide an update on the clinical application status of a cell-based therapy for treating corneal endothelial dysfunction.

**Key Words:** corneal transplantation, corneal endothelial cells, Rho-kinase inhibitor, corneal endothelial dysfunction

(*Cornea* 2014;33(Suppl):S37–S41)

The corneal endothelium is known to maintain corneal transparency through its pump and barrier functions.<sup>1</sup> Because the proliferative potential of corneal endothelial cells (CECs) is extremely limited,<sup>2</sup> CEC damage due to various pathologic conditions prompts residual cells to migrate and spread to cover the damaged area. Meanwhile, the residual cells compensate for their loss and maintain corneal transparency. However, decompensation of the corneal endothelium causes severe visual impairment that leads to blindness. Although corneal transplantation is a well-known effective therapy for corneal

endothelial dysfunction, many patients are not afforded that therapeutic opportunity owing to the worldwide shortage of donor corneas.<sup>3</sup> Therefore, a tissue engineering-based therapy for treating corneal endothelial dysfunction is urgently required. This review article presents our recent findings aimed toward a tissue engineering-based therapy for corneal endothelial dysfunction and outlines our future perspectives.

## ESTABLISHMENT OF A CELL CULTIVATION PROTOCOL

One technical obstacle for the establishment of a tissue engineering-based therapy for corneal endothelial dysfunction is the development of a successful and reliable cell cultivation protocol for clinical application.<sup>4</sup> In that regard, the limited proliferation ability, cellular senescence, and fibroblastic transformation of CECs in culture are known to be major problems associated with their cultivation.<sup>4–6</sup> Although our research group and others continually strive toward the development of a successful culture method,<sup>4,7–11</sup> a protocol specifically designed for clinical application has yet to be established. Thus, we focused our investigations on establishing an *in vitro* expansion culture protocol that provides sufficient numbers of CECs, while simultaneously maintaining a functional phenotype.

In 2009, we reported that the selective Rho-associated kinase (ROCK) inhibitor, Y-27632, increased the proliferative potential of cultivated CECs, indicating that it is applicable for the cultivation of CECs.<sup>12</sup> Moreover, we recently demonstrated that ROCK inhibitors use both cyclin D and p27 through PI 3-kinase signaling to promote CEC proliferation.<sup>13</sup> The RhoA/ROCK pathway is involved in regulating various cell functions such as migration, apoptosis, differentiation, and proliferation; however, these regulations are cell-type dependent.<sup>14,15</sup> Because the ROCK pathway is involved in a variety of diseases, ROCK inhibitors have been developed as therapeutic drugs.<sup>16</sup> To culture CECs for clinical application, we currently use a ROCK inhibitor-supplemented medium after having assessed and confirmed its safety.

In an effort to establish a more efficient cell culture, we also demonstrated that conditioned medium obtained from good manufacturing practice-grade human bone marrow-derived mesenchymal stem cells (MSCs) enhanced CEC proliferation (Fig. 1).<sup>17</sup> Before using the conditioned medium, we observed that 3T3 cells functioned as feeder cells to support the cultivation of CECs. However, the use of 3T3 cells raises the possibility of contamination with xenogenic pathogens and immunogens. Nonetheless, because safety is essential for clinical applications, we tested the feeder potency of several kinds of cells and found that MSCs enable efficient cell proliferation. In addition, MSCs

From the \*Department of Biomedical Engineering, Faculty of Life and Medical Sciences, Doshisha University, Kyotamabe, Japan; and †Department of Ophthalmology, Kyoto Prefectural University of Medicine, Kyoto, Japan. Supported in part by the Highway Program for Realization of Regenerative Medicine (S.K. and N.O.) and the Funding Program for Next Generation World-Leading Researchers from the Cabinet Office in Japan (N.K.: LS117).

The authors have no conflicts of interest to disclose.

Reprints: Noriko Koizumi, MD, PhD, Department of Biomedical Engineering, Faculty of Life and Medical Sciences, Doshisha University, Kyotamabe 610-0321, Japan (e-mail: nkoizumi@mail.doshisha.ac.jp).

Copyright © 2014 by Lippincott Williams & Wilkins



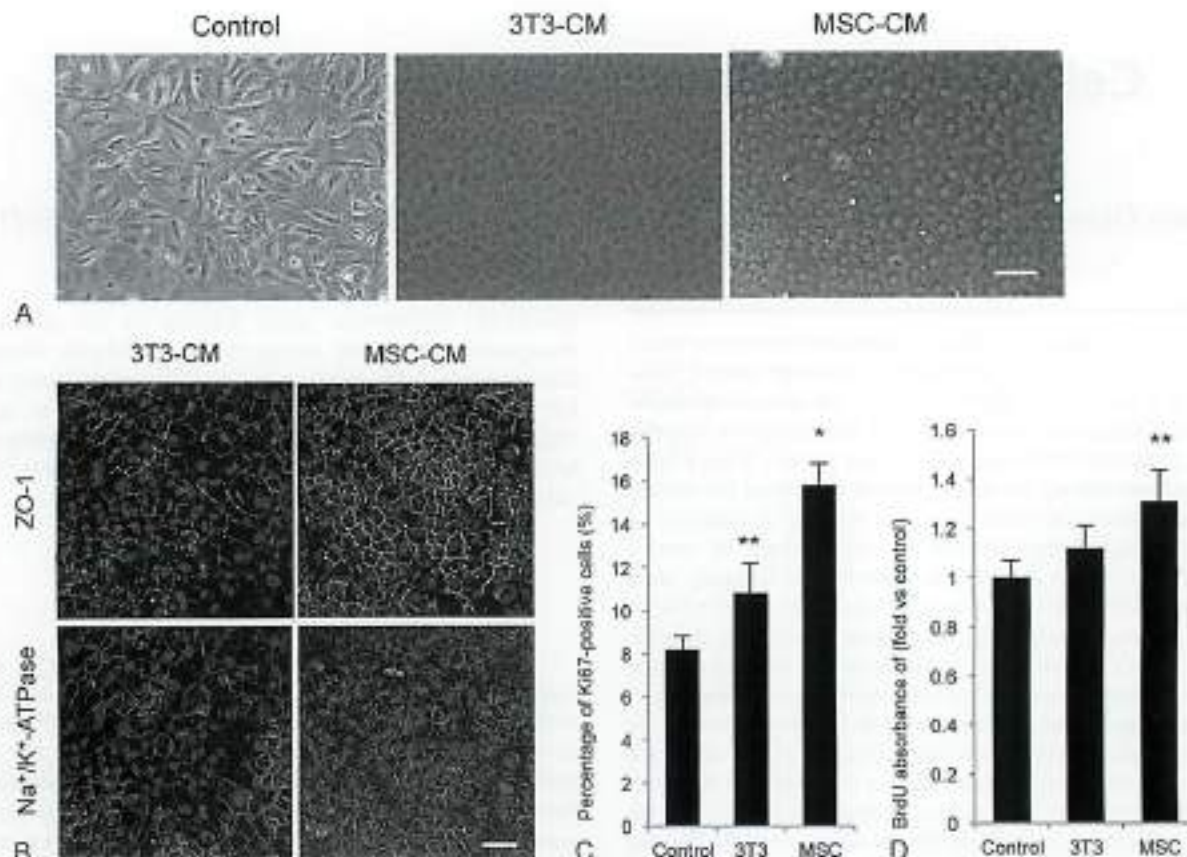


**FIGURE 1.** Conditioned medium from MSCs enhances the cell culture of CECs. **A**, Effect of MSC-conditioned media (CM) on the morphology of primary cultures of human corneal epithelial cells (HCECs). Representative phase-contrast images of primary cultures in different CM. Cultured HCECs were maintained in basal growth medium, MSC-CM, or NIH3T3-CM for 30 days. Scale bar: 200  $\mu$ m. **B**, HCECs cultured in either MSC-CM or NIH3T3-CM for 14 days expressed ZO-1 and Na<sup>+</sup>/K<sup>+</sup>-ATPase. The photographs are representative of 2 independent experiments. **C**, to test proliferative potential, HCECs maintained for 5 days under experimental conditions were immunostained with the cell cycle progression population marker Ki67, and the percentages of Ki67-positive cells were then evaluated. The experiment was performed in duplicate. Scale bar: 200  $\mu$ m. **D**, HCECs were cultured in basal growth medium (control), NIH3T3-CM, or MSC-CM. Proliferation of HCECs was evaluated using a BrdU incorporation assay after 5 days of incubation. Experiments were performed in triplicate. \* $P < 0.01$ , \*\* $P < 0.05$ . Reproduced with permission from Nakahara et al.<sup>6</sup>

counteract the decrease in cell density associated with cell migration that is thought to be caused by cellular senescence.<sup>6</sup>

Another major obstacle is the morphological fibroblastic change of human corneal endothelial cells while in culture. Although human corneal endothelial cells can be cultivated into a normal phenotype, they eventually exhibit massive fibroblastic transformation and lose pump and barrier function after long-term culture or subculture.<sup>4,5</sup> We investigated the activation of fibrosis-related pathways during fibroblastic transformation and found that transforming growth factor beta (TGF- $\beta$ ) signaling plays an important role.<sup>5</sup> In that study, we also discovered that inhibition of TGF- $\beta$  signaling enables CECs to counteract the fibroblastic change and to maintain the contact-inhibited phenotype with normal functions (Fig. 2).<sup>5</sup>

Based on these 3 recently established culture techniques, that is, the use of ROCK inhibitors, the use of conditioned medium obtained from MSCs, and inhibition of TGF- $\beta$  signaling, an *in vitro* expansion protocol for clinical application was developed. We are currently culturing CECs of good manufacturing practice-grade in the cell-processing center of

Kyoto Prefectural University of Medicine. Although there are currently no laws against the use of certified prion-free fetal bovine serum for tissue engineering,<sup>16</sup> we believe that it might become problematic in the future, highlighting the need for a serum-free culture protocol. In addition, safe and standardized methods for cell stocking and transportation need to be established for the delivery of cultivated CECs from the cell-processing center to the hospital for clinical applications.

## TRANSPLANTATION OF CULTIVATED CORNEAL ENDOTHELIAL CELLS

Modern corneal transplantation techniques such as Descemet stripping automated endothelial keratoplasty and Descemet membrane endothelial keratoplasty are widely performed for the treatment of corneal endothelial dysfunction.<sup>3</sup> The excellent clinical outcomes associated with Descemet stripping automated endothelial keratoplasty and Descemet membrane endothelial keratoplasty indicate that replacement of the corneal endothelium is sufficient for treating corneal endothelial



dysfunction, as opposed to full-thickness corneal replacement through penetrating keratoplasty. This has prompted researchers to posit that replacement of the damaged recipient cornea using cultured CECs using a tissue-engineering technique will become the future treatment of corneal endothelial dysfunction.

There are currently 2 known methods for the transplantation of cultured CECs. The first method involves transplantation of a cultured corneal endothelial sheet, and the second method involves injection of cultured CECs as a cell suspension. Several research groups, as well as our group, have reported successful transplantation of a cultured corneal endothelial sheet in an animal model.<sup>17–20</sup> However, the transplantation of a flexible monolayer cell sheet to the anterior chamber is technically

difficult. In addition, the development of an artificial carrier is also a current obstacle for cell-sheet transplantation. Thus, we focused our efforts on developing a method to regenerate corneal endothelium through cell injection to overcome the known difficulties associated with cultured corneal endothelial sheet transplantation (Table 1). The main disadvantage associated with CEC injection is that the injected cultured CECs are removed by the flow of aqueous humor, resulting in the poor adhesion of injected cells onto the corneal tissue.<sup>21</sup> Magnetic cell guidance using iron powder incorporated into cultivated CECs has been attempted<sup>22,23</sup>; however, this method has yet to be applied in humans. This idea led us to the hypothesis that modification of the adhesive property of CECs using ROCK inhibitors might enable the injected cultured CECs to attach to the cornea and regenerate the corneal endothelium. During the establishment of an efficient cell culture of CECs, we observed that ROCK inhibition promoted cell adhesion to the substrate.<sup>12</sup> Indeed, after injecting cultured CECs together with a ROCK inhibitor into the anterior chamber of a rabbit corneal endothelial dysfunction model, we discovered that corneal transparency recovered and the corneal endothelium was regenerated as a monolayer (Fig. 3).<sup>21</sup> To confirm this finding, we conducted the same experiment in a monkey model of corneal endothelial dysfunction, because monkey CECs are similar to human CECs, having limited proliferative ability. Injection of cultured CECs with a ROCK inhibitor regenerated healthy corneal endothelium and recovered corneal transparency in the monkey model, similar to the findings in the rabbit model.<sup>21</sup> In terms of safety, no severe local (such as secondary glaucoma and cell aggregation) or systemic (such as pulmonary embolus and tumor formation) adverse effects were observed.

We recently obtained approval from the Japanese Ministry of Health, Labour and Welfare to perform cultured cell injection to treat corneal endothelial dysfunction. A first-in-man clinical trial has now been initiated at Kyoto Prefectural University of Medicine after obtaining the necessary approval (clinical trial registration: UMIN000012534).

## CONCLUSIONS

A tissue engineering-based therapy for treating corneal endothelial dysfunction is urgently required. We hope that our new cell-based regenerative therapy will provide a less invasive and more effective method for the treatment of patients with corneal endothelial dysfunction.

**TABLE 1.** Characteristics of Endothelial Sheet Transplantation Versus Cell Injection Therapy

	Endothelial Sheet Transplantation	Cell Injection Therapy
Surgery	Difficult	Minimally invasive
Artificial material	Required	Not required
Visual acuity	Dependent on carrier	Transparent cornea without carrier
Complications	Multiple	Some
Preservation	Difficult	Master-cell banking
Transportation	Difficult	Easy

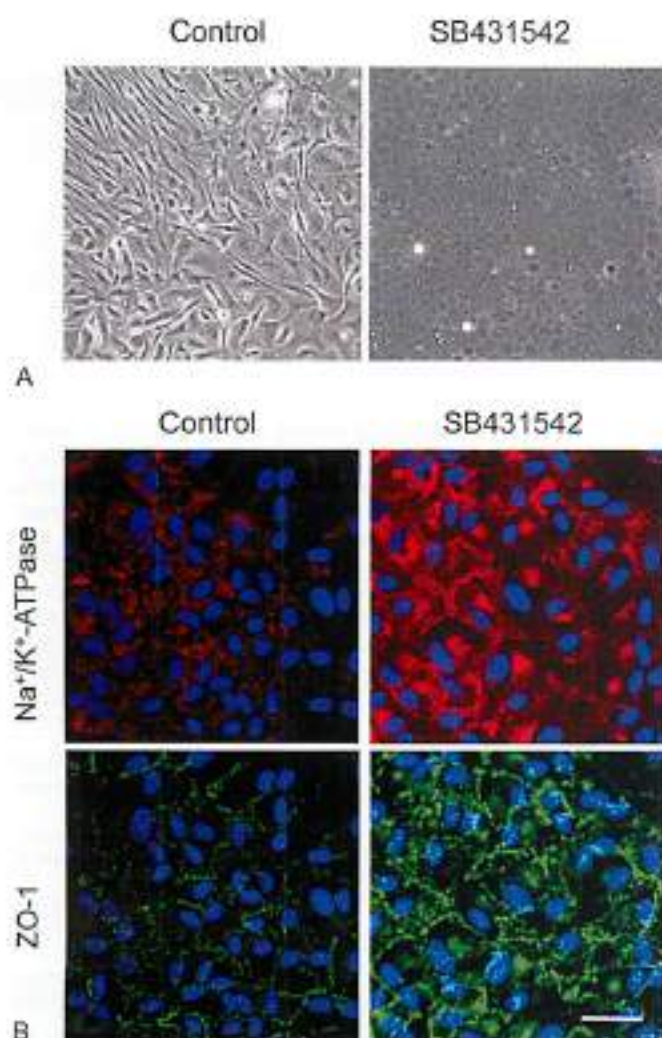


**FIGURE 2.** Inhibition of TGF- $\beta$  counteracts the fibroblastic change of CECs. **A**, Human corneal epithelial cells cultured with SB431542, an inhibitor of TGF- $\beta$  signaling, exhibited a hexagonal cell shape and formed a contact-inhibited monolayer, whereas control CECs developed fibroblastic morphology. **B**, Blocking TGF-receptor signaling by SB431542 enabled the subcellular localization of Na<sup>+</sup>/K<sup>+</sup>-ATPase and ZO-1 at the plasma membrane and protein expression to be maintained. Scale bar: 100  $\mu$ m. Reproduced with permission from *PLoS One* from Okumura et al.<sup>5</sup>



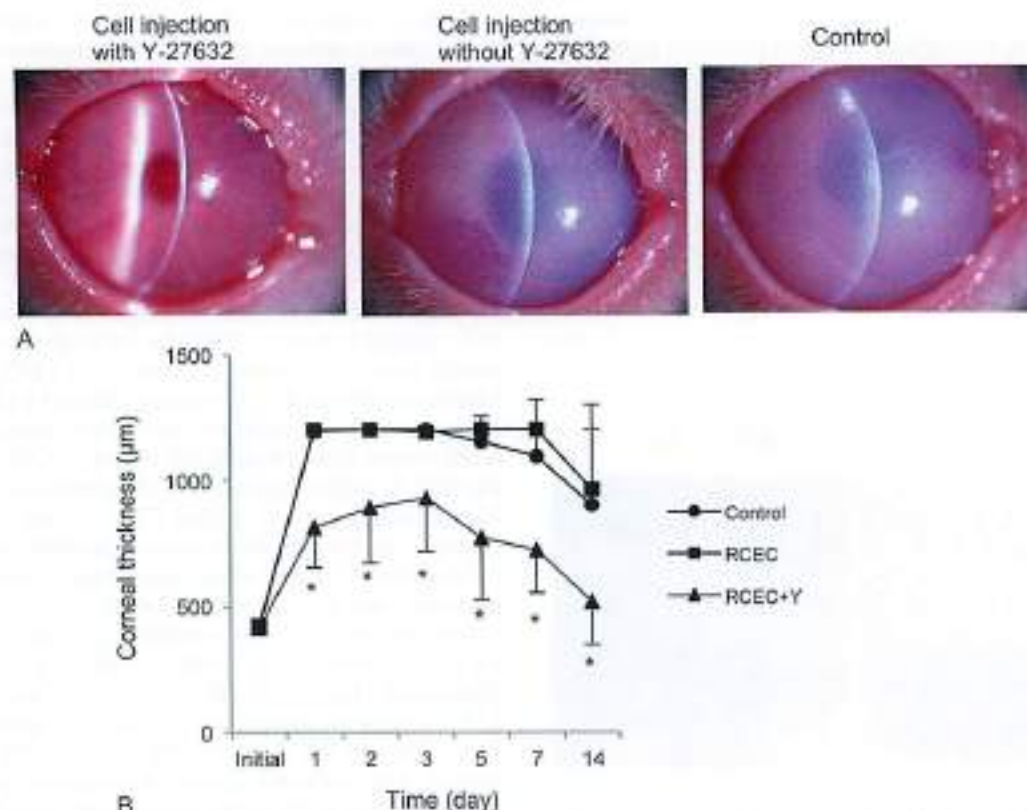


**FIGURE 3.** Coinjection of CECs with ROCK inhibitor recovers corneal transparency in a corneal endothelial dysfunction model. **A,** Slit-lamp photographs of rabbit eyes injected with cultivated rabbit corneal epithelial cells (RCECs) with the selective ROCK inhibitor Y-27632, cultivated RCECs without Y-27632, and the control corneal endothelial dysfunction model after 48 hours. Rabbit eyes injected with cultivated RCECs combined with Y-27632 recovered complete transparency of the cornea. In contrast, eyes injected with cultivated RCECs without Y-27632 and control eyes exhibited a hazy cornea with severe edema. The iris and pupil were clearly observable through the transparent cornea in the eyes injected with cultivated RCECs together with Y-27632; however, they were not observable in eyes injected with cultivated RCECs without Y-27632 or in control eyes because of corneal haziness caused by the corneal endothelial dysfunction. **B,** In control eyes and in eyes injected with RCECs without Y-27632, corneal edema was prominent (over 1200  $\mu\text{m}$ ) at day 1 and persisted throughout the observation period. In contrast, in eyes injected with RCECs together with Y-27632, corneal edema was moderate (<800  $\mu\text{m}$ ) at day 1 and gradually recovered to normal levels. Reproduced with permission from Elsevier from Okumura et al.<sup>21</sup>

## ACKNOWLEDGMENTS

The authors thank Drs Morio Ueno, Junji Hamuro, Chie Sotozono, Takahiro Nakamura, Hiroko Nakagawa, Michio Hagiya, Eun Duck P. Kay, Makiko Nakahara, Ryohei Numata, Junji Kitano, Yuji Sakamoto, Hiroaki Takahashi, and Yoshiki Sasai for their invaluable advice and contribution; Mr Monty Montoya and Mr Bernie Iliakis (SightLife) for providing the donor corneas; and Mr John Bush for reviewing the article. The authors are also grateful to Ludovic Craxford, PhD, for providing editorial support in the preparation of this article.

## REFERENCES

- Boome WM. Clinical estimation of corneal endothelial pump function. *Trans Am Ophthalmol Soc.* 1998;96:229-239; discussion 239-242.
- Joyce NC. Proliferative capacity of corneal endothelial cells. *Exp Eye Res.* 2012;95:16-23.
- Tan DT, Dart JK, Holland EJ, et al. Corneal transplantation. *Lancet.* 2012;379:1749-1761.
- Peh GS, Beuerman RW, Colman A, et al. Human corneal endothelial cell expansion for corneal endothelium transplantation: an overview. *Transplantation.* 2011;91:811-819.
- Okumura N, Kay EP, Nakahara M, et al. Inhibition of TGF-beta signaling enables human corneal endothelial cell expansion in vitro for use in regenerative medicine. *PLoS One.* 2013;8:e58000.
- Nakahara M, Okumura N, Kay EP, et al. Corneal endothelial expansion promoted by human bone marrow mesenchymal stem cell-derived conditioned medium. *PLoS One.* 2013;8:e69009.
- Miyata K, Drake J, Osakabe Y, et al. Effect of donor age on morphologic variation of cultured human corneal endothelial cells. *Cornea.* 2001;20:59-63.
- Peh GS, Toh KP, Wu FY, et al. Cultivation of human corneal endothelial cells isolated from paired donor corneas. *PLoS One.* 2011;6:e28310.
- Yamaguchi M, Yokoo S, Mizawa T, et al. Effects of TGF-beta2 on immune response-related gene expression profiles in the human corneal endothelium. *Invest Ophthalmol Vis Sci.* 2004;45:515-521.
- Yamaguchi M, Ebihara N, Shima N, et al. Adhesion, migration, and proliferation of cultured human corneal endothelial cells by laminin-5. *Invest Ophthalmol Vis Sci.* 2011;52:679-684.
- Shima N, Kimoto M, Yamaguchi M, et al. Increased proliferation and replicative lifespan of isolated human corneal endothelial cells with L-ascorbic acid 2-phosphate. *Invest Ophthalmol Vis Sci.* 2011;52:8711-8717.



12. Okumura N, Ueno M, Koizumi N, et al. Enhancement on primate corneal endothelial cell survival in vitro by a ROCK inhibitor. *Invest Ophthalmol Vis Sci.* 2009;50:3680–3687.
13. Okumura N, Nakano S, Kay EP, et al. Involvement of cyclin D and p27 in cell proliferation mediated by ROCK inhibitors Y-27632 and Y-39983 during corneal endothelium wound healing. *Invest Ophthalmol Vis Sci.* 2014;55:318–329.
14. Yoshizaki H, Ohba Y, Parrini MC, et al. Cell type-specific regulation of RhoA activity during cytokinesis. *J Biol Chem.* 2004;279:44756–44762.
15. Liao JK, Seto M, Noma K. Rho kinase (ROCK) inhibitors. *J Cardiovasc Pharmacol.* 2007;50:17–24.
16. Nishida R, Okumura N, Nakamura M, et al. Cultivation of corneal endothelial cells on a pericellular matrix prepared from human decidua-derived mesenchymal cells. *PLoS One.* 2014;9:e88169.
17. Ishino Y, Sano Y, Nakamura T, et al. Amniotic membrane as a carrier for cultivated human corneal endothelial cell transplantation. *Invest Ophthalmol Vis Sci.* 2004;45:800–806.
18. Minura T, Yamagami S, Yokoo S, et al. Cultured human corneal endothelial cell transplantation with a collagen sheet in a rabbit model. *Invest Ophthalmol Vis Sci.* 2004;45:2992–2997.
19. Sumida T, Nishida K, Yamato M, et al. Functional human corneal endothelial cell sheets harvested from temperature-responsive culture surfaces. *FASEB J.* 2006;20:392–394.
20. Koizumi N, Sakamoto Y, Okumura N, et al. Cultivated corneal endothelial cell sheet transplantation in a primate model. *Invest Ophthalmol Vis Sci.* 2007;48:4519–4526.
21. Okumura N, Koizumi N, Ueno M, et al. ROCK inhibitor converts corneal endothelial cells into a phenotype capable of regenerating in vivo endothelial tissue. *Am J Pathol.* 2012;181:268–277.
22. Minura T, Shimomura N, Usui T, et al. Magnetic attraction of iron-endocytosed corneal endothelial cells to Descemet's membrane. *Exp Eye Res.* 2003;76:745–751.
23. Patel SV, Bruchman LA, Hann CR, et al. Human corneal endothelial cell transplantation in a human ex vivo model. *Invest Ophthalmol Vis Sci.* 2009;50:2123–2131.

# Cultivated oral mucosal epithelial transplantation for persistent epithelial defect in severe ocular surface diseases with acute inflammatory activity

Chie Sotozono,<sup>1</sup> Tsutomu Inatomi,<sup>1</sup> Takahiro Nakamura,<sup>1,2</sup> Noriko Koizumi,<sup>1,3</sup> Norihiko Yokoi,<sup>1</sup> Mayumi Ueta,<sup>1,2</sup> Kotone Matsuyama,<sup>4</sup> Hideaki Kaneda,<sup>4</sup> Masanori Fukushima<sup>4</sup> and Shigeru Kinoshita<sup>1</sup>

<sup>1</sup>Department of Ophthalmology, Kyoto Prefectural University of Medicine, Kyoto, Japan

<sup>2</sup>Research Center for Inflammation and Regenerative Medicine, Faculty of Life and Medical Sciences, Doshisha University, Kyoto, Japan

<sup>3</sup>Department of Biomedical Engineering, Faculty of Life and Medical Sciences, Doshisha University, Kyoto, Japan

<sup>4</sup>Translational Research Informatics Center, Foundation for Biomedical Research and Innovation, Kobe, Japan

## ABSTRACT.

**Purpose:** To assess the clinical efficacy of cultivated oral mucosal epithelial transplantation (COMET) for the treatment of persistent epithelial defect (PED).

**Methods:** We treated 10 eyes of nine patients with PED (Stevens–Johnson syndrome: three eyes; thermal/chemical injury: five eyes; ocular cicatricial pemphigoid: two eyes) with COMET at Kyoto Prefectural University of Medicine, Kyoto, Japan from 2002 to 2008.

**Results:** Preoperatively, PED existed on over more than 50% of the corneal surface in seven eyes. Severe ocular surface inflammation with fibrovascular tissue surrounded the PED in all 10 eyes. At 24-weeks postoperative, PED had improved in all cases except 1 in which the patient was unable to return to the hospital (95% CI, 55.5–99.7; Wilcoxon signed-rank test,  $p = 0.0078$ ). The preoperative median of logarithmic minimum angle of resolution was 1.85 (range 0.15–2.70), and 1.85, 1.85, and 1.52 at the 4th, 12th, and 24th postoperative week, respectively. The mean total preoperative ocular surface grading score was 7.0 (range 4–17). At 4 and 12 weeks postoperative, the total ocular surface grading score had improved significantly ( $p = 0.0020$ ,  $p = 0.0078$ ), and at 24 weeks postoperative, it was 3.0 (range 2–12,  $p = 0.0234$ ). During the follow-up period (median 23.3 months, range 5.6–39.7 months), no recurrence of PED was observed in any eye, and long-term ocular surface stability was obtained.

**Conclusion:** COMET enabled complete epithelialization of PED and stabilization of the ocular surface in patients with severe ocular surface disease, thus preventing end-stage cicatrization and vision loss at a later stage.

**Key words:** acute inflammatory activity – cultivated oral mucosal epithelial transplantation (COMET) – limbal stem cell deficiency (LSCD) – persistent epithelial defect (PED)

## Introduction

Corneal renewal and repair are mediated by corneal epithelial stem cells located mainly in the limbus, the narrow region between the cornea and the bulbar conjunctiva (Kinoshita et al. 2001). Damage or depletion of the corneal epithelial stem cells, known as limbal stem cell deficiency (LSCD), leads to conjunctival invasion that results in vascularization of the cornea with an associated profound loss of vision (Kinoshita et al. 2001). LSCD can be caused by Stevens–Johnson syndrome (SJS), ocular cicatricial pemphigoid (OCP) and thermal or chemical injury, which are all characterized by the loss of corneal epithelial stem cells. Such LSCD may cause severe ocular surface diseases (OSDs) in which cicatrization resulting from conjunctival fibrosis, symblepharon and severe dry eye greatly disrupt visual function.

Limbal stem cell deficiency can be classified into two categories, acute and chronic, based on the onset and progression pattern of the disease. In cases such as SJS and thermal/chemical injury, epithelial defect occurs suddenly and is accompanied by massive inflammation on the ocular surface. During the several weeks that follow, epithelialization progresses with subsequent scar tissue formation, such as that associated with conjunctival shrinkage. In contrast, the onset of OCP is difficult to determine. In OCP cases, cicatrization progresses gradually with-

Acta Ophthalmol. 2014; 92: e447–e453

© 2014 The Authors. Acta Ophthalmologica published by John Wiley & Sons Ltd on behalf of Acta Ophthalmologica Scandinavica Foundation

This is an open access article under the terms of the Creative Commons Attribution-NonCommercial-NoDerivs License, which permits use and distribution in any medium, provided the original work is properly cited, the use is non-commercial and no modifications or adaptations are made.

doi: 10.1111/aos.12397

Support in part by grant-in-aid for Scientific Research from Japanese Ministry of Health a grant-in-aid for Scientific Research, and a Research Grant of the Coordination, Support and Training program for translational research both from Japanese Ministry of Education.

The author(s) have no proprietary or commercial interest in any materials discussed in this article.

out an acute episode. However, those patients are sometimes observed with acute manifestations consisting of intense conjunctival hyperaemia and localized epithelial defects. Acute OCP causes rapid shrinkage of the conjunctiva (Mondino et al. 1979), similar to that which occurs in a thermal/chemical injury or in the acute phase of SJS.

Regardless of the causes, such LSCD in severe OSDs may sometimes cause persistent epithelial defects (PED) with prolonged inflammation on the ocular surface. A PED occurring in the sub-acute phase of LSCD is very difficult to treat. Massive inflammation on the ocular surface is often uncontrollable, even with the use of systemic and/or local steroids. The effects of local treatment with eye ointment or a medical-use soft contact lens are limited. Exposure of the corneal stroma can induce infectious or non-infectious corneal stromal thinning and perforation. Even if epithelialization can be achieved, long-standing inflamed PED eventually results in symblepharon, conjunctivalization and neovascularization of the cornea, leading to blindness in the long term. Although early reports demonstrated the effectiveness of amniotic membrane transplantation for PED (Shimazaki et al. 1997; Gomes et al. 2003), further research by our group and others showed that the effects of this technique on PED are limited (Azura-Blanco et al. 1999; Meller et al. 2000; Tamhane et al. 2005; Saw et al. 2007; Rahman et al. 2009; Tandon et al. 2011; Hino et al. 2012).

Ophthalmologists are continually challenged with the task of developing treatments for severe OSDs in which no medical or surgical treatments exist. To that end, beginning in 2002, our group was the first in the world to perform ocular surface reconstruction using tissue-engineered autologous oral mucosal epithelial sheets (Nakamura et al. 2004), and since that time we have continued to perform autologous cultivated oral mucosal epithelial transplantation (COMET) after careful determination of the surgical indication (Ang et al. 2006; Inatomi et al. 2006a; Inatomi et al. 2006b; Nakamura et al. 2011). In the clinical setting, deciding the indication and postoperative management are extremely important.

To clarify the effectiveness, disease-specific outcomes and safety of

COMET, we analysed the clinical data for all 72 patients treated with COMET at our facility since 2002. We reported that for 46 eyes of 40 LSCD patients, COMET resulted in favourable long-term visual acuity (VA) outcomes (Sotozono et al. 2013). The purpose of this present study was to summarize the long-term clinical outcomes of 10 eyes of nine of those 72 patients who underwent COMET with the primary objective of treating PED with acute inflammatory activity.

## Methods

### Study design

The medical records of all patients who underwent COMET at the Department of Ophthalmology, Kyoto Prefectural University of Medicine, Kyoto, Japan, from June 2002 until December 2008 were retrospectively examined and recorded on case report forms. All of the data relating to the oral mucosal epithelial sheets, surgical outcomes and adverse events were evaluated, and statistical analyses were conducted using the data obtained. This retrospective outcome study protocol was approved by the Ethical Review Board of Kyoto Prefectural University of Medicine in 2009.

The study included 81 eyes of 72 patients, and those eyes were classified into one of the following four categories according to the purpose of treatment with COMET: (i) corneal reconstruction for visual improvement, (ii) corneal reconstruction for the treatment of PED with acute inflammatory activity, (iii) conjunctival fornix reconstruction and (iv) others (Fig. 1). In this present study, we report the results of COMET for the purpose of corneal reconstruction to treat PED with acute inflammatory activity.

### Patients

Cultivated oral mucosal epithelial transplantation was performed on nine consecutive patients (10 eyes) with LSCD who were diagnosed with PED accompanying acute inflammatory activity on the ocular surface. Inclusion criteria were as follows: (i) LSCD, (ii) a history of an acute episode of epithelial defect, (iii) a PED existing for more than 1 month, (iv) persistent ocular surface inflammation even in the use of systemic and/or local steroids, (v) resistance to conventional therapy such as eye ointments or a medical-use soft contact lens and (vi) fibrovascular tissue surrounding the PED.

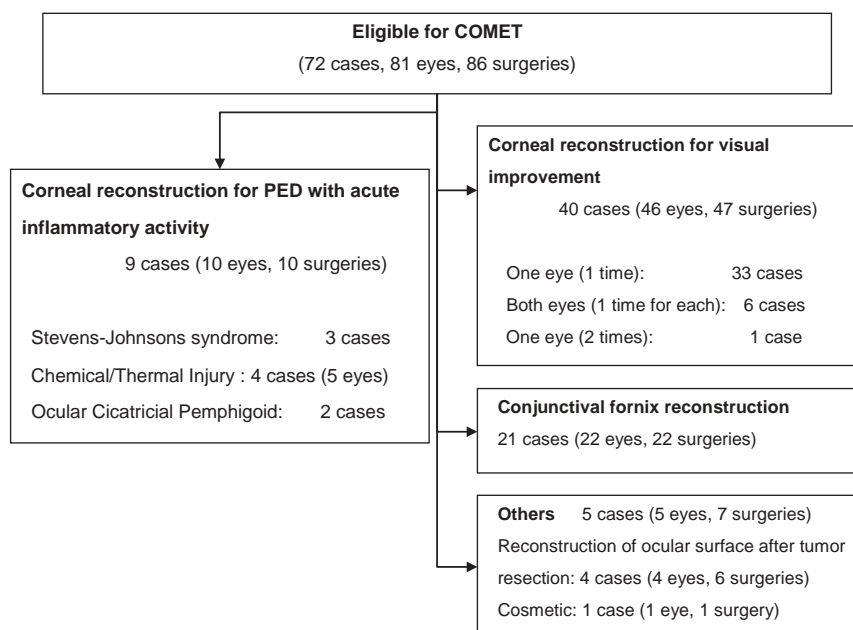


**Fig. 1.** Study flow diagram. Seventy-two patients (81 eyes) underwent cultivated oral mucosal epithelial transplantation (COMET) between June 2002 and December 2008, and nine patients (10 eyes) with persistent epithelial defect (PED) with accompanying acute inflammatory activity were included in this study.



For each patient, the final decision to perform COMET was made by the team of corneal specialists at our university hospital. As eyes with stem cell deficiency can be asymptomatic carriers of methicillin-resistant *Staphylococcus aureus* (MRSA) (Sotozono et al. 2002), a conjunctival swab was cultured preoperatively and antibiotics were used when deemed necessary.

#### Cell culture

All COMET sheets were prepared at the Good Manufacturing Practices (GMP)-graded Cell Processing Center at Kyoto Prefectural University of Medicine as described previously (Nakamura et al. 2004; Ang et al. 2006; Inatomi et al. 2006a,b). Autologous oral mucosal epithelial cells were obtained from a 6-mm-diameter biopsy specimen taken from the patient's buccal mucosa and were then co-cultured with mitomycin C-inactivated 3T3 fibroblasts (NIH-3T3-4; RIKEN Cell Bank, Tsukuba, Japan) on an amniotic membrane spread on the bottom of a culture insert. The cultured cells were submerged in medium for approximately 1 week and then exposed to air by lowering the level of the medium (airlifting) for 1–2 days. All amniotic membrane was obtained from caesarean sections, and the preparation method was performed as described previously (Nakamura et al. 2004). Although foetal bovine serum was initially used as the culture medium, autologous serum was subsequently selected as the serum of choice to reduce the risk of transmitting non-human pathogens (Ang et al. 2006).

#### Transplantation and postoperative management

For each patient, the surgical procedure and postoperative management were performed as previously described (Ang et al. 2006; Inatomi et al. 2006a, b; Nakamura et al. 2011). In patients with symblepharon or a large area of bare sclera exposed during surgery, amniotic membrane was transplanted onto the bare sclera in order to reconstruct the conjunctival fornices (Solomon et al. 2003). In patients with a cataract, phaco-emulsification/aspiration plus intraocular lens implantation was carried out simultaneously with COMET. In patients with an eyelid

abnormality, eyelid surgery was combined with COMET (Takeda et al. 2011).

Systemic corticosteroid (betamethasone, 1 mg/day) and cyclosporine (2–3 mg/kg/day) were administered to prevent postoperative inflammation and an immunological response and then tapered depending on the clinical findings. Dexamethasone (0.1%) and antibiotic eye drops were instilled four times per day. Dry eye patients received a topical administration of artificial tears. A therapeutic soft contact lens was used for at least 1 month to protect the transplanted epithelium from mechanical ablation.

#### Clinical outcomes

The primary outcome was defined as epithelialization of the PED. Secondary outcomes included a change in best-corrected VA (BCVA) and changes in the ocular surface grading score.

The ocular surface conditions including corneal appearance (epithelial defects, clinical conjunctivalization, neovascularization, opacification, keratinization and symblepharon) were alternately graded by 2 of 3 ophthalmologists (C.S., T.I. and T.N.) on a scale from 0 to 3 according to their severity, in accordance with our previously reported grading system (Sotozono et al. 2007). Furthermore, findings on upper and lower fornix shortening were included when grading the conjunctival cicatrization. The sum of each grading score was defined as the ocular surface grading score (maximum score 24) (Table 2).

Each patient's epithelial defect, logarithmic minimum angle of resolution (logMAR), ocular surface grading score and data on adverse events related to COMET or postoperative management were recorded before surgery, at the 4th, 12th and 24th postoperative week and at the final follow-up examination.

#### Statistical analysis

The change in epithelial defect, BCVA and ocular surface grading score from baseline at each visit, except for the final visit, was analysed using the Wilcoxon signed-rank test. All statistical analyses were conducted at the Translational Research Informatics Center (Kobe, Japan) using SAS soft-

ware, version 9.1 (SAS Institute Inc., Cary, NC, USA) or JMP software, version 8.2 (SAS Institute Inc.).

## Results

#### Patient characteristics

A total of 10 surgeries (10 eyes in nine patients) were performed on three eyes with SJS, five eyes with thermal or chemical injury and two eyes with OCP (Fig. 1, Table 1). Epithelial defects persisted, with extensive ocular surface inflammation accompanying the progress of cicatrization of the ocular surface (Fig. 2). The duration of the PED ranged from 1 to 15 months (median 3 months). In all patients, the condition was intractable and unresponsive to medical treatments including systemic and local steroids. Amniotic membrane transplantation carried out at previous hospital was failed in both eyes with severe chemical injury (Case 1). In all three patients with SJS, MRSA was detected in both eyes, necessitating both preoperative and postoperative anti-MRSA therapy.

#### Contralateral eyes of unilateral treatment with COMET

All three cases with Stevens–Johnson syndrome (Cases 5, 6, and 7) and both cases with ocular cicatricial pemphigoid (Cases 8 and 9) were damaged bilaterally and had PED in both eyes except 1 case with OCP (Case 9). Case 5 with SJS presented at our hospital at 1 month after disease onset. In that case, the PED in the contralateral eye healed 6 months later without undergoing COMET; however, severe conjunctivalization, neovascularization and opacification of the cornea had progressed. Two patients with SJS presented at our hospital following PED and subsequent corneal infection or perforation in the contralateral eye (Fig. 3, Cases 6 and 7). In the contralateral eye of 1 patient with OCP, rapid progression of the cicatrization had previously occurred following PED (Fig. 3, Case 8). In another case with OCP (Case 9), the contralateral eye was already severely cicatrized. In all five cases, the contralateral eye had lost vision prior to undergoing treatment with COMET.

**Table 1.** Summary of the clinical outcomes of COMET.

Case No.	Disease	Age/sex	Duration of the disorder (months)	Duration of PED (months)	Eye (L/R)	Prior surgery (Y/N)	Combination surgery	Visual acuity			Total ocular surface score			Follow-up month
								Pre	24W	Last	Pre	24W	Last	
1	Chemical injury	33/M	3	3	R	Y	No	0.002	0.002	0.002	8	5	7	27.2
					L	Y	No	0.03	0.1	0.4	6	3	4	27.2
2	Thermal injury	27/M	3	3	L	N	AMT+Eyelid surgery	0.002	0.03	0.04	6	5	7	31.4
3	Thermal injury	29/M	1	1	R	N	Eyelid surgery	0.7	0.15	0.03	4	6	9	16.5
4	Thermal injury	61/M	3	3	R	N	AMT	0.01	—	0.01	6	3	3	33
5	SJS	8/F	8	8	R	N	No	0.7	0.1	0.002	8	2	5	39.7
6	SJS	30/M	14	14	R	N	AMT	0.02	0.004	0.01	12	12	17	18.4
7	SJS	62/M	15	15	L	N	AMT+CS+Other	0.01	0.01	0.01	6	3	4	19.4
8	OCP	73/M	42	3	R	N	AMT	0.002	0.06	0.09	17	3	3	9.5
9	OCP	83/M	18	7	L	Y	No	0.02	—	0.03	17	—	2	5.6

COMET, autologous cultivated oral mucosal epithelial transplantation; SJS, Stevens–Johnson syndrome; OCP, ocular cicatricial pemphigoid; AMT, amniotic membrane transplantation; CS, cataract surgery; F, female; M, male; Y, yes; N, no.

Visual acuity below 0.01 is shown in italics. Counting fingers, hand motion and light perception were determined to be 0.004, 0.002 and 0.001, respectively.

Asterisks (\*) indicates cases in which foetal bovine serum (FBS) was used as a culture medium for the epithelial sheet. We used autologous serum (AS) in other cases.

### Epithelial sheet cultivation and transplantation

Cultivated autologous oral mucosal epithelial sheets were successfully generated from all patients. In each case, COMET was successfully performed and no epithelial damage was observed during surgery. Amniotic membrane transplantation (AMT) was combined with COMET in five of the 10 surgeries, and cataract surgery was combined with COMET in 1 eye. In two cases with thermal injury, eyelid surgery to correct entropion was combined with COMET (Table 1).

### Epithelialization outcomes

Preoperatively, epithelial defects were present on over 50% of the corneal surface (score 3) in seven eyes, on 25–50% of the corneal surface (score 2) in one eye and on <25% of the corneal surface (score 1) in two eyes. Severe ocular surface inflammation with fibrovascular tissue surrounding the PED was observed in all 10 eyes. In all eyes, the transplanted epithelium completely covered the corneal surface during COMET surgery, and ocular surface inflammation decreased during the first few weeks following surgery. At the 4th postoperative week, seven eyes (70%) had achieved complete epithelialization and three eyes showed a small epithelial defect (two cases with

severe thermal burn and one case of SJS with severe dry eye). At the 24th postoperative week, PED had improved in all patients except one patient who did not undergo the 24th postoperative week follow-up (95% CI, 55.5–99.7%; Wilcoxon signed-rank test,  $p = 0.0078$ ) (Figs. 2, 4). The mean follow-up period was 21.5 months (range 5.6–39.7 months; median 23.3 months), and complete epithelialization was maintained in all eyes (Table 1, Figs. 2, 4A).

### VA outcomes

In all patients, no significant difference was found between preoperative and postoperative VA. The median logMAR was 1.85 before COMET (range 0.15–2.70) and 1.85, 1.85 and 1.52 at 4, 12 and 24 weeks (Wilcoxon signed-rank test,  $p = 0.8$ , 0.6, 0.8), respectively, postoperative; that is, VA was maintained in all cases.

### Ocular surface grading score outcomes:

Preoperatively, the median ocular surface grading score was 7.0 (range 4–17). While the epithelial defect score was high, other grading scores of cicatricial changes were low. At 4, 12 and 24 weeks postoperative, the ocular surface grading score improved significantly ( $p = 0.0020$ ,  $p = 0.0078$ , and  $p = 0.0234$ , respectively). The median

ocular surface grading score at 4, 12, and 24 weeks postoperative and at the final follow-up was 3.0, 4.0, 3.0 and 5.0, respectively.

### Adverse events

Adverse events included slight elevation of intraocular pressure (IOP) due to steroid use in two patients, although in both cases the IOP returned to the normal range after steroid use was reduced. Moderate MRSA-related corneal infection occurred in one patient; however, the infection healed without perforation. No systemic adverse events occurred in any of the patients.

## Discussion

Persistent epithelial defect with LSCD at an acute inflammatory stage has been a major problem for ophthalmologists. The clinical course is progressive with subsequent conjunctivalization and neovascularization of the cornea, as well as fornix shortening and subconjunctival fibrosis. Limbal transplantation and AMT do not guarantee epithelialization in such severely inflamed eyes (Azura-Blanco et al. 1999; Rao et al. 1999; Meller et al. 2000; Tamhane et al. 2005; Saw et al. 2007; Rahman et al. 2009; Tandon et al. 2011; Hino et al. 2012). In fact, in two eyes in this study, AMT had previously been performed unsuccessfully at another hospital. To date, there is no

**Table 2.** Ocular surface grading system for COMET.

Variable		Variable scores			
Category	Variable name	0	1	2	3
Corneal appearance	Symblepharon	No symblepharon	Involving only the conjunctiva	Less than 1/2 of the corneal surface	More than 1/2 of the corneal surface
	Epithelial defect	No defect	Less than 1/4 of the corneal surface	1/4–1/2 of the corneal surface	More than 1/2 of the corneal surface
	Conjunctivalization	Absence of conjunctivalization	Less than 1/4 of the corneal surface	1/4–1/2 of the corneal surface	More than 1/2 of the corneal surface
	Neovascularization	No neovascularization	Confined to the corneal periphery	Extending up to the pupil margin	Extending beyond the pupil margin into the central cornea
	Opacification	Iris details clearly visualized	Partial obscuration of the iris details	Iris details poorly seen with pupil margin visible	Complete obscuration of iris and pupil details
	Keratinization	No corneal keratinization	Less than 1/4 of the corneal surface	1/4–1/2 of the corneal surface	More than 1/2 of the corneal surface
Conjunctival appearance	Fornix shortening (Upper)	Normal depth	Shortened by less than 1/4	Shortened by 1/4–1/2	Shortened by more than 1/2
	(Lower)	Normal depth	Shortened by less than 1/4	Shortened by 1/4–1/2	Shortened by more than 1/2

This scoring system as previously reported has been refined by the findings on the prognostic significance of the degree or severity of ocular surface disorders obtained in this work. The scoring system could be classified broadly as corneal complications and conjunctival complications, respectively.

reliable therapy to achieve epithelialization in such cases, and inhibition of the progression of cicatrization is very difficult to achieve.

This study demonstrated the successful use of COMET to treat PED. The

disease status was characterized by a history of an acute episode of PED and prolonged inflammation on the ocular surface. We defined this condition as PED with acute inflammatory activity. In all eyes, the cornea was epithelialized

immediately after undergoing COMET, and the inflamed ocular surface stabilized during the first few weeks following surgery. In all patients, sustained clinical remission was achieved within 1 or 2 months postoperative. Long-term

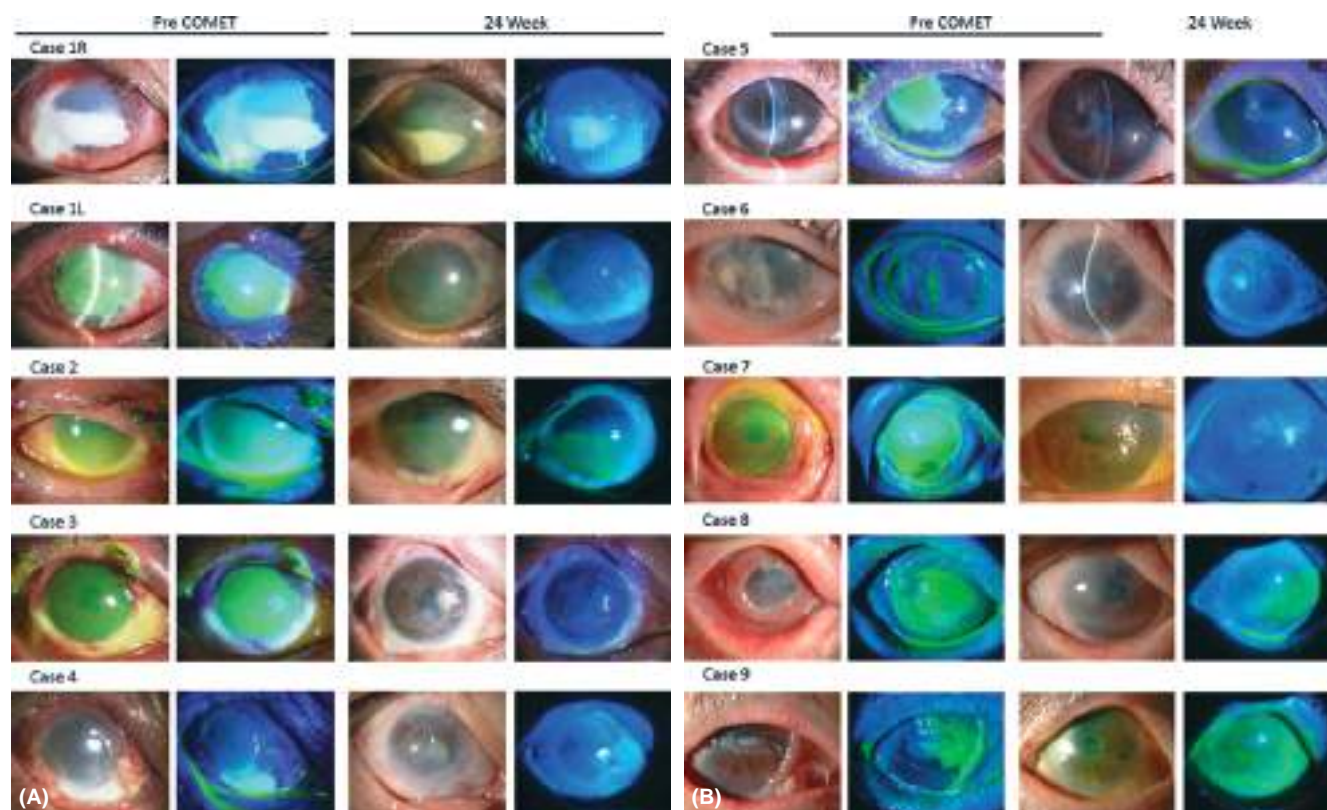


**Fig. 2.** Slit-lamp appearances of all eyes with PED treated by cultivated oral mucosal epithelial transplantation (COMET). (Left two columns) Preoperatively, epithelial defect persisted in all eyes, with massive inflammation on the ocular surface. Note the subconjunctival fibrosis around the PED. (Right two columns) Ocular surface appearance at the 24th postoperative week. Ocular surface stabilization and complete epithelialization were achieved in all eyes.





**Fig. 3.** Clinical courses of the contralateral eyes not treated with COMET. Note the non-infectious corneal stromal melting and perforation in Case 6 (left), the MRSA infection in Case 7 (middle) and the cicatrization in Case 8 after PED with acute inflammatory activity (right).

follow-up revealed that epithelialization and stabilization of the ocular surface were maintained over a long period.

In eyes with early-stage PED without stromal damage, VA is usually undisturbed. Therefore, the severity and prognosis of the disease are often underestimated. However, prolonged PED induces conjunctivalization of the cornea and/or stromal melting. In fact, in some of the cases, conjunctivalization progressed during the period from the oral mucosal biopsy to transplantation of the prepared epithelial sheet. It should be emphasized that in the bilateral cases, the similarly afflicted contralateral eyes lost vision because of corneal perforation, infection or severe cicatrization. We consider that epithelialization resulting from COMET prevented complications such as corneal ulceration and perforation. The fact that no significant difference was found between preoperative and postoperative VA means that COMET effectively worked to maintain the patient's preoperative VA, thus preventing loss of

VA, or in cases of prolonged PED, any further loss of VA. The ocular surface grading score indicates the degree of cicatrization of the ocular surface and is known to correlate well with VA (Sotozono et al. 2007). In this study, it is remarkable that the ocular surface grading score was improved both at the 24th postoperative week and at the final follow-up. Only in one patient with moderate MRSA infection (Case 6) had fornix shortening and conjunctivalization progressed after the remission of infection. We theorize that epithelialization resulting from COMET may have prevented the progression of cicatrization of the ocular surface at a later stage.

We hypothesize that one of the mechanisms by which COMET has a positive treatment effect on subacute PED is the decrease in massive inflammation on the ocular surface. A similar effect can be obtained by cultivated corneal limbal epithelial transplantation (CLET) (Koizumi et al. 2001). Conventional stem cell transplantation

such as limbal transplantation (LT) requires several weeks for the corneal epithelium from the donor cornea to migrate and cover the corneal surface. In contrast, transplantation of cultivated epithelium covers the entire cornea during surgery and works to resolve the ocular surface inflammation. Previously, we compared the resolution of inflammation on the ocular surface in the eyes of an SJS patient who underwent CLET for one eye and conventional LT for the fellow eye. Our findings showed that ocular inflammation and IL-8 levels in tears decreased more rapidly in the eye that underwent CLET and that ocular cicatrization was higher in the eye that underwent conventional LT (Ang et al. 2007). Whereas long-term postoperative immunosuppressive therapy to prevent epithelial rejection is needed after allo CLET, it is not necessary after COMET. Thus, we select either CLET or COMET depending on the disease and how severely the eye is affected.

In this present study, we found differences among the three disease categories. In the patients with thermal or chemical injury, the reconstructed ocular surface has been maintained for a long period of time, up until the present date. All three SJS patients required both preoperative and postoperative anti-MRSA therapies. Due to the fact that OCP is a progressive

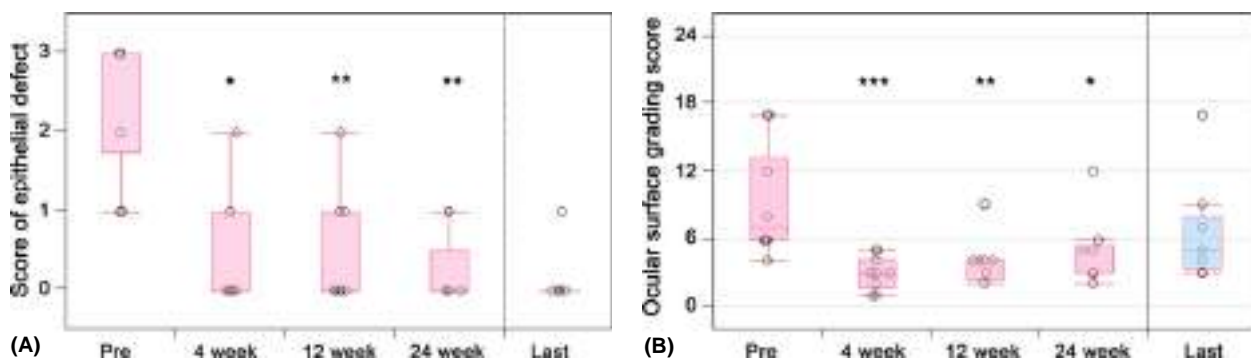


**Fig. 4.** Preoperative and postoperative scores of ocular surface. (A) Preoperative and postoperative scores of the corneal epithelial defects. The epithelial defect scores for each patient were calculated using the previously reported grading system (Sotozono et al. 2007). The scores before surgery and at the 4th, 12th and 24th postoperative weeks and at the final follow-up examination were calculated. The change from baseline at each visit, except for the final visit, was analysed using the Wilcoxon signed-rank test. The bottom and top lines of the box represent the 25th and 75th percentiles, respectively. The circles represent the individual scores of the patients. The horizontal lines below and above the box represent the lowest and highest values, respectively (or are located 1.5 times the interquartile range away from the box). \* $p = 0.0156$ ; \*\* $p = 0.0078$  (Wilcoxon signed-rank test). (B) Preoperative and postoperative ocular surface grading score. Ocular surface grading scores for each patient were calculated using the previously reported grading system (Sotozono et al. 2007). Scores for 8 components of the ocular surface were calculated by the grading system. The total scores before surgery and at the 4th, 12th and 24th postoperative weeks and last follow-up examination were calculated. The change in ocular surface grading score from baseline at each visit, except for the last visit, was analysed using the Wilcoxon signed-rank test. The circles represent the individual scores of the patients. The horizontal line within each box represents the median value, the bottom and top lines of the box represent the 25th and 75th percentiles, respectively, and the horizontal lines below and above the box represent the lowest and highest values, respectively (or are located 1.5 times the interquartile range away from the box). \* $p = 0.0234$ ; \*\* $p = 0.0078$ ; \*\*\* $p = 0.0020$  (Wilcoxon signed-rank test).

autoimmune disease, conjunctival cicatrization gradually progressed after COMET in the two OCP cases in this study.

Persistent epithelial defect also occurs in the chronic stage of LSCD. Eyes with chronic PED are accompanied by severe dryness of the ocular surface and sometimes blink-related mechanical trauma. Chronic PED is not usually inflamed, and anti-inflammatory medication is ineffective. Surgical treatments such as LT or AMT are also ineffective. Transplanted epithelium easily detaches in eyes with chronic PED due to severe dryness of the eye. Thus, we consider chronic PED to be a contraindication for COMET, so it is important to distinguish chronic PED from subacute PED with inflammatory activity. It should be noted that the management of chronic PED is extremely difficult. Eye ointments, artificial tears and bandaging of the eye are all necessary. Moreover, attention should be paid to infectious or non-infectious stromal melting. However, such intensive care does not guarantee re-epithelialization, and PED with acute inflammatory activity can shift to chronic PED when the condition persists.

Limitations of this study included the small number of the patients, varying aetiology of PED, and that this was a non-randomized study with no control group. Prospective studies are necessary to evaluate and confirm the efficacy of COMET.

In conclusion, the findings of this present study show that in all treated eyes, COMET resulted in complete re-epithelialization as well as ocular surface stabilization, thus preventing end-stage cicatrization and vision loss. COMET provides a new therapeutic modality for the treatment of PED and greatly contributes to the improvement of the visual prognosis in cases of severe OSDs.

## References

- Ang LP, Nakamura T, Inatomi T et al. (2006): Autologous serum-derived cultivated oral epithelial transplants for severe ocular surface disease. *Arch Ophthalmol* **124**: 1543–1551.
- Ang LP, Sotozono C, Koizumi N, Suzuki T, Inatomi T & Kinoshita S (2007): A comparison between cultivated and conventional limbal stem cell transplantation for Stevens-Johnson syndrome. *Am J Ophthalmol* **143**: 178–180.
- Azuara-Blanco A, Pillai CT & Dua HS (1999): Amniotic membrane transplantation for ocular surface reconstruction. *Br J Ophthalmol* **83**: 399–402.
- Gomes JA, dos SM, Cunha MC, Mascaro VL, Barros JN & de SL (2003): Amniotic membrane transplantation for partial and total limbal stem cell deficiency secondary to chemical burn. *Ophthalmology* **110**: 466–473.
- Hino T, Sotozono C, Inatomi T et al. (2012): Indications and surgical outcomes of amniotic membrane transplantation. *Nihon Ganka Gakkai Zasshi* **116**: 374–378.
- Inatomi T, Nakamura T, Koizumi N, Sotozono C, Yokoi N & Kinoshita S (2006a): Midterm results on ocular surface reconstruction using cultivated autologous oral mucosal epithelial transplantation. *Am J Ophthalmol* **141**: 267–275.
- Inatomi T, Nakamura T, Kojyo M, Koizumi N, Sotozono C & Kinoshita S (2006b): Ocular surface reconstruction with combination of cultivated autologous oral mucosal epithelial transplantation and penetrating keratoplasty. *Am J Ophthalmol* **142**: 757–764.
- Kinoshita S, Adachi W, Sotozono C et al. (2001): Characteristics of the human ocular surface epithelium. *Prog Retin Eye Res* **20**: 639–673.
- Koizumi N, Inatomi T, Suzuki T, Sotozono C & Kinoshita S (2001): Cultivated corneal epithelial transplantation for ocular surface reconstruction in acute phase of Stevens-Johnson syndrome. *Arch Ophthalmol* **119**: 298–300.
- Meller D, Pires RT, Mack RJ et al. (2000): Amniotic membrane transplantation for acute chemical or thermal burns. *Ophthalmology* **107**: 980–989.
- Mondino BJ, Brown SI, Lempert S & Jenkins MS (1979): The acute manifestations of ocular cicatricial pemphigoid: diagnosis and treatment. *Ophthalmology* **86**: 543–555.
- Nakamura T, Inatomi T, Sotozono C, Amemiya T, Kanamura N & Kinoshita S (2004): Transplantation of cultivated autologous oral mucosal epithelial cells in patients with severe ocular surface disorders. *Br J Ophthalmol* **88**: 1280–1284.
- Nakamura T, Takeda K, Inatomi T, Sotozono C & Kinoshita S (2011): Long-term results of autologous cultivated oral mucosal epithelial transplantation in the scar phase of severe ocular surface disorders. *Br J Ophthalmol* **95**: 942–946.
- Rahman I, Said DG, Maharajan VS & Dua HS (2009): Amniotic membrane in ophthalmology: indications and limitations. *Eye (Lond)* **23**: 1954–1961.
- Rao SK, Rajagopal R, Sitalakshmi G & Padmanabhan P (1999): Limbal autografting: comparison of results in the acute and chronic phases of ocular surface burns. *Cornea* **18**: 164–171.
- Saw VP, Minassian D, Dart JK et al. (2007): Amniotic membrane transplantation for ocular disease: a review of the first 233 cases from the UK user group. *Br J Ophthalmol* **91**: 1042–1047.
- Shimazaki J, Yang HY & Tsubota K (1997): Amniotic membrane transplantation for ocular surface reconstruction in patients with chemical and thermal burns. *Ophthalmology* **104**: 2068–2076.
- Solomon A, Espana EM & Tseng SC (2003): Amniotic membrane transplantation for reconstruction of the conjunctival fornices. *Ophthalmology* **110**: 93–100.
- Sotozono C, Inagaki K, Fujita A et al. (2002): Methicillin-resistant *Staphylococcus aureus* and methicillin-resistant *Staphylococcus epidermidis* infections in the cornea. *Cornea* **21**(Suppl): S94–S101.
- Sotozono C, Ang LP, Koizumi N et al. (2007): New grading system for the evaluation of chronic ocular manifestations in patients with Stevens-Johnson syndrome. *Ophthalmology* **114**: 1294–1302.
- Sotozono C, Inatomi T, Nakamura T et al. (2013): Visual improvement after cultivated oral mucosal epithelial transplantation. *Ophthalmology* **120**: 193–200.
- Takeda K, Nakamura T, Inatomi T, Sotozono C, Watanabe A & Kinoshita S (2011): Ocular surface reconstruction using the combination of autologous cultivated oral mucosal epithelial transplantation and eyelid surgery for severe ocular surface disease. *Am J Ophthalmol* **152**: 195–201.
- Tamhane A, Vajpayee RB, Biswas NR et al. (2005): Evaluation of amniotic membrane transplantation as an adjunct to medical therapy as compared with medical therapy alone in acute ocular burns. *Ophthalmology* **112**: 1963–1969.
- Tandon R, Gupta N, Kalaivani M, Sharma N, Titiyal JS & Vajpayee RB (2011): Amniotic membrane transplantation as an adjunct to medical therapy in acute ocular burns. *Br J Ophthalmol* **95**: 199–204.

Received on September 4th, 2013.

Accepted on February 22nd, 2014.

### Correspondence:

Chie Sotozono, MD, PhD  
Department of Ophthalmology  
Kyoto Prefectural University of Medicine  
465 Kajii-cho, Hirokoji-agaru  
Kawaramachi-dori, Kamigyo-ku  
Kyoto 602-0841, Japan  
Tel: +81 75 251 5578  
Fax: +81 75 251 5663  
Email: csotozon@koto.kpu-m.ac.jp.

The authors wish to thank Dr. Shin Kawamata of the Foundation for Biological Research and Innovation, Dr. Kazunori Takeda, Dr. Hiroaki Kato, Dr. Hiroshi Tanaka, Dr. Yuji Yamamoto and Dr. Takahiro Yamawaki of Kyoto Prefectural University of Medicine for data collection, Keiko Miyakoda for data analysis and interpretation and Mr. John Bush for reviewing the manuscript.

# Synthetic Molecules that Protect Cells from Anoikis and Their Use in Cell Transplantation\*\*

Heidie L. Frisco-Cabanas, Mizuki Watanabe, Naoki Okumura, Kosuke Kusamori, Naohiro Takemoto, Junichiro Takaya, Shin-ichi Sato, Sayumi Yamazoe, Yoshinobu Takakura, Shigeru Kinoshita, Makiya Nishikawa,\* Noriko Koizumi,\* and Motonari Uesugi\*

**Abstract:** One of the major problems encountered in cell transplantation is the low level of survival of transplanted cells due to detachment-induced apoptosis, called anoikis. The present study reports on the chemical synthesis and biological evaluation of water-soluble molecules that protect suspended cells from anoikis. The synthetic molecules bind to and induce clusters of integrins and heparan-sulfate-bound syndecans, two classes of receptors that are important for extracellular matrix-mediated cell survival. Molecular biological analysis indicates that such molecules prolong the survival of suspended NIH3T3 cells, at least in part, by promoting clustering of syndecan-4 and integrin  $\beta 1$  on the cell surface, leading to the activation of small GTPase Rac-1 and Akt. In vivo experiments using animal disease models demonstrated the ability of the molecules to improve cell engraftment. The cluster-inducing molecules may provide a starting point for the design of new synthetic tools for cell-based therapy.

Cell-based therapy is an exciting new field that has shown great potential in the treatment of diseases, such as diabetes, neurodegenerative diseases, and cardiovascular diseases.<sup>[1]</sup> Cell transplantation restores lost function in damaged tissues or compromised organs by replacing damaged cells with viable, functional cells. However, despite its potential benefits, the clinical application of cell transplantation remains limited. One of the major problems encountered in cell transplantation is the low level of survival of transplanted cells, which reduces both the cell number and engraftment to the recipient tissue.<sup>[2]</sup> Various strategies have been used to

increase the survival of transplanted cells: pretreatment of cells with growth factors or cytokines, genetic modifications to induce overexpression of prosurvival molecules, and transplantation together with artificial or animal-derived extracellular matrixes.<sup>[3]</sup> Each approach has limitations and potential side effects, e.g., unwanted cell proliferation or differentiation, immune attack, or mechanical stress.<sup>[4]</sup> New strategies are needed to improve the survival of transplanted cells for cell-based therapies.

Transplanted cells are particularly susceptible to anoikis, a form of detachment-induced apoptosis.<sup>[5]</sup> During injection, the cells are detached from the host matrix or cell culture substrate, resulting in loss of cell-matrix signaling and, ultimately, cell death. The association of transplanted cells with the extracellular matrix, which is primarily maintained by integrins, activates survival signaling pathways.<sup>[6]</sup> Although the signals transduced by integrins play a major role in cell survival, they alone are not sufficient for survival. It is increasingly clear that two cell membrane receptors, integrins and heparan-sulfate-containing syndecans, play a synergistic role in the generation of intracellular survival signals.<sup>[7]</sup> For example, both the integrin-binding and heparin-binding domains of fibronectin, a major extracellular matrix protein, are needed to regulate and stabilize its survival activity.<sup>[8]</sup> Syndecans act as receptors for extracellular matrix proteins and soluble ligands, and can recruit integrins at the cell surface and promote their clustering and co-localization.<sup>[9]</sup> On the other hand, binding of integrins to the extracellular matrix, independently of syndecans, is required to potentiate

[\*] H. L. Frisco-Cabanas, Dr. M. Watanabe,<sup>[†]</sup> N. Takemoto, J. Takaya, Dr. S. Sato, Dr. S. Yamazoe, Prof. M. Uesugi  
Institute for Integrated Cell-Material Sciences (WPI-iCeMS) and  
Institute for Chemical Research, Kyoto University  
Uji, Kyoto 611-0011 (Japan)  
E-mail: uesugi@scl.kyoto-u.ac.jp  
Dr. N. Okumura,<sup>[‡]</sup> Prof. N. Koizumi  
Faculty of Life and Medical Sciences, Doshisha University  
Kyotanabe, Kyoto 610-0394 (Japan)  
E-mail: nkoizumi@mail.doshisha.ac.jp  
Dr. K. Kusamori,<sup>[‡]</sup> Prof. Y. Takakura, Dr. M. Nishikawa  
Graduate School of Pharmaceutical Sciences, Kyoto University  
Kyoto, Kyoto 606-8501 (Japan)  
E-mail: makiya@pharm.kyoto-u.ac.jp  
Prof. S. Kinoshita  
Department of Ophthalmology, Kyoto Prefectural University of  
Medicine (Japan)

H. L. Frisco-Cabanas, J. Takaya  
Graduate School of Medicine Kyoto University (Japan)

[†] These authors contributed equally to the work.

[\*\*] We thank Nagase & Co., Ltd. for sharing chemical samples. This work was supported in part by JSPS (LR018 to M.U. and LS117 to N.K.) and the Collaborative Research Program of the Institute for Chemical Research, Kyoto University (2013-51, 2012-10, 2011-26, and 2010-24). The Uesugi research group participates in the Global COE program "Integrated Materials Science" (no B-09). iCeMS is supported by World Premier International Research Center Initiative (WPI), MEXT (Japan). This work was inspired by the international and interdisciplinary environments of the iCeMS and JSPS Asian CORE Program, "Asian Chemical Biology Initiative". The upgrade of the confocal microscope was supported by the New Energy and Industrial Technology Development Organization (NEDO) of Japan and Yokogawa Electric Corporation.



Supporting information for this article is available on the WWW under <http://dx.doi.org/10.1002/anie.201405829>.

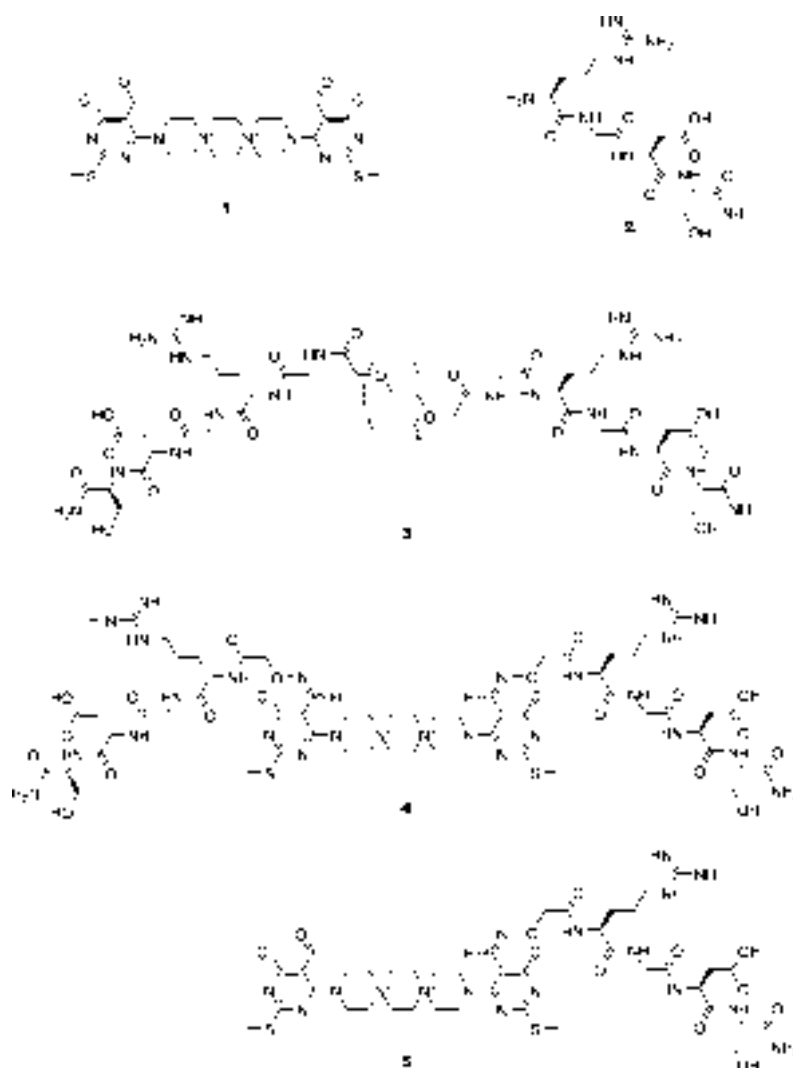


the syndecan-mediated signals.<sup>[10]</sup> Binding of the two fibronectin domains to integrin and syndecan synergistically promotes cell survival.

We took advantage of the synergistic effect of the two receptors to design a hybrid molecule that contains both integrin- and heparan-sulfate-binding/assembling modules. We introduced an RGDS peptide<sup>[11]</sup> as the integrin-binding module and adhesamine,<sup>[12]</sup> a synthetic molecule that selectively binds to and clusters the heparan sulfate of syndecans, as the heparan-sulfate-binding/assembling module. We predicted that the covalent conjugation of the highly water-soluble RGDS peptide with adhesamine would generate a synthetic soluble factor that binds simultaneously to and causes clustering of integrin and heparan-sulfate-containing syndecans, allowing suspended cells to evade anoikis. Ultimately, the higher cell viability should result in a higher engraftment efficiency and improve transplantation success. Such a synthetic molecule would also provide a relatively safe alternative for xeno-free and chemically-defined cell transplantation, which appears to be essential for the success of cell-based therapy.

Adhesamine (molecule **1**, Scheme 1) was covalently conjugated with one or two amino-oxyacetic acid-functionalized RGDS peptides **2** through oxime ligation with the aldehyde groups of adhesamine, whose modifications have been shown to be well tolerated. To check if these modifications affect the ability of adhesamine to bind to heparan sulfate, we examined the affinity of molecules **4** and **5** (Scheme 1) for the heparin polymer, a model of heparan sulfate, using isothermal titration calorimetry. Molecule **5** exhibited an affinity to heparin comparable to that of adhesamine, whereas molecule **4** displayed only half of the affinity of adhesamine (Table S1 and Figure S1). Previous results suggested that the pyrimidine moieties of adhesamine stack with each other upon binding to heparin or heparan sulfate.<sup>[13]</sup> Presumably, the coupling of the bulky peptides with both of the pyrimidine moieties prevents the stacking interaction due to steric hindrance. Despite their reduced affinity, the attachment of the RGDS peptide rendered the conjugates highly water-soluble. Their solubility, in addition to their role as integrin-binding modules, makes molecules **4** and **5** suitable for inhibiting anoikis of suspended cells. The solubility in water allows the molecules to be injected together with the suspended cells, without adhering to the tubes or syringes used during cell culture and transplantation.

We first examined the ability of the synthetic molecules to inhibit anoikis of NIH3T3 cells, an anchorage-dependent mouse embryo fibroblast cell line often used in anoikis studies. A round-bottom, noncoated plate was used in order to reduce or remove cell-substrate interactions, cells were strained twice prior to the assay to ensure single cell suspension, and serum-free media were used throughout the



**Scheme 1.** Chemical structures of molecules **1**–**5**. Counteranions (TFA or acetic acid) are omitted for clarity.

assay; these are conditions which promote anoikis. After 72 hours of incubation under anoikis conditions, the viability of suspended cells was quantified by measuring NADPH dehydrogenase activity.

No detectable live cells were found in DMSO-treated (control) samples (Figure 1). As expected, detachment from the extracellular matrix and loss of signals from cell–cell interaction or soluble factors in serum resulted in cell death. In contrast, the addition of the adhesamine–RGDS conjugates (molecules **4** and **5**) significantly reduced anoikis of floating cells (Figure 1). Molecule **5** exhibited the greatest activity, rescuing approximately 100% of the cells from anoikis. Adhesamine (molecule **1**) alone displayed no significant inhibition of anoikis. Instead, this lipophilic molecule induced cell attachment to the plastic plates, as previously reported.<sup>[12]</sup> Both the RGDS peptide (molecule **2**, Scheme 1) and RGDS dimer (molecule **3**, Scheme 1) failed to inhibit anoikis or induce cell attachment (Figure 1), which is not surprising, because soluble integrin ligands usually block the receptor function rather than activate it. Even the combina-

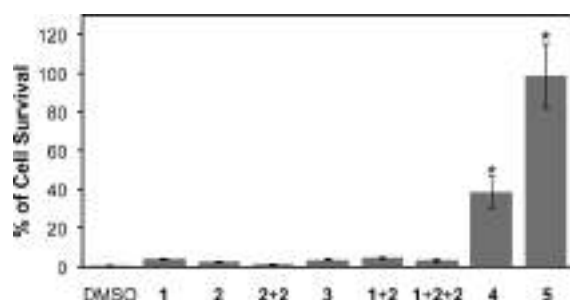


**Figure 1.** Effects of adhesamine-RGDS derivatives on cell viability. Cell viability of suspended cells after incubation with molecules **1**–**5** (60  $\mu$ M) for 72 h was determined using WST-8 assay, normalized to cells immediately after plating (100%). **2** + **2**, **1** + **2**, and **1** + **2** + **2** indicate molecule **2** (120  $\mu$ M), molecules **1** and **2** (60  $\mu$ M each), and molecules **1** and **2** (60  $\mu$ M and 120  $\mu$ M, respectively), respectively. Results from three independent experiments are shown (mean value  $\pm$  standard deviation,  $n = 3$  for each experiment). \* indicates a significant difference compared to the DMSO control ( $p < 0.001$ ).

tion of adhesamine (molecule **1**) and an RGDS peptide (molecule **2**) exhibited no significant inhibition of anoikis (Figure 1). Moreover, the addition of excess amounts of either molecule **1** or **2** impaired the activities of molecules **4** and **5** (Figure S2), suggesting that both modules of molecules **4** and **5** interact simultaneously with their receptors. These results indicate that the covalent conjugation of adhesamine with RGDS peptides is essential for preventing anoikis of suspended cells.

Time-course experiments showed that essentially all of the suspended cells in the control (DMSO) treatment underwent cell death after 48 h, while cells treated with molecules **4** and **5** had about 50 and 100% survival, respectively, after 72 h (Figure S3A). The inhibition of anoikis by molecules **4** and **5**, even at a relatively low concentration (6  $\mu$ M) was greater than the inhibition by fibronectin or Y-27632, a ROCK (Rho-associated coiled-coil forming kinase) inhibitor that is often used to block anoikis (Figure S3B).<sup>[14]</sup>

We next evaluated the effect of molecules **4** and **5** on the apoptotic response of cells under anoikis conditions. The time course of annexin-V expression showed that cells alone (control) readily underwent apoptosis after 72 h (Figure S4). Treatment with molecule **4** or **5** lowered the percentages of apoptotic cells (Figure S4), consistent with the results of the cell viability assays.

The activation of caspases, in particular caspase-8, is a major initiating event in anoikis.<sup>[15]</sup> Therefore, we investigated the effect of molecules **4** and **5** on the caspase activity. Incubation of NIH3T3 cells under anoikis conditions increased the caspase activity, measured as the luminescence of caspase-8 substrate after 12 h (Figure S5A). The treatment of cells with molecule **4** or **5** inhibited the anoikis-induced activation of caspase-8. The level of inhibition was similar to the level of caspase-3 activation in cells treated with molecule **4** or **5** (Figure S5B). Caspase-3 is an effector caspase involved in the execution of apoptotic pathways, and has been reported to be upregulated in fibroblast cells undergoing anoikis.<sup>[16]</sup> These results collectively suggest that molecules **4** and **5** are directly involved in the protection of cells from anoikis.

To determine the signaling mechanism by which molecules **4** and **5** inhibit anoikis of NIH3T3 cells, we initially examined the status of the Akt- and the ERK-dependent pathways, which are signaling cascades that have established roles in anchorage-mediated survival.<sup>[17]</sup> Western blot analysis revealed that the addition of molecule **4** or **5** resulted in a clear increase in Akt phosphorylation (Figure 2A and S6A),

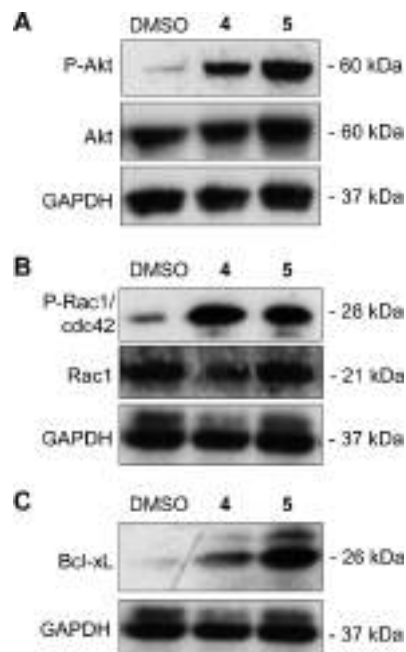


**Figure 2.** Effects of molecules **4** and **5** on phosphorylation and expression of proteins of cells under anoikis conditions. A) Akt, B) Rac-1/cdc42, a homolog of cell division control protein 42 in the Rho family of GTPases, and C) Bcl-xL, B-cell lymphoma-extra-large. Expression of proteins after a 12 h incubation with molecule **4** or **5** was evaluated using Western blot analysis. The upper panel shows the phosphorylated form of the protein (A and B); the middle panel shows total protein (A, B, and C); and the bottom panel shows glyceraldehyde 3-phosphate dehydrogenase (GAPDH) as a loading control (A, B, and C). Representative images from three independent experiments are shown for each protein.

but not in ERK1/2 phosphorylation (Figure S7A). Akt, serine/threonine-specific protein kinase B (PKB), plays a central role in cell survival signaling: integrin-, growth-factor- and cell-cell-mediated signal transductions converge at the activation of this kinase. Anoikis inhibition by Akt activators has been previously reported, demonstrating that Akt can suppress anoikis.<sup>[18]</sup> Our results suggest that the inhibition of anoikis by molecules **4** and **5** occurs at least partly through Akt activation.

The FAK-PI3K cascade is an upstream pathway of Akt in anchorage-mediated survival.<sup>[19]</sup> Interestingly, the addition of molecule **4** or **5** failed to increase the phosphorylation of PI3K, but upregulated the expression of total PI3K (Figure S7B). Addition of molecule **4** or **5** also failed to increase the phosphorylation of focal adhesion kinase (FAK), an even more upstream kinase,<sup>[20]</sup> but total FAK expression increased compared to the control (Figure S7C). Although the reasons

for the increased expression of PI3K and FAK by molecule **4** or **5** remain unknown, the FAK-PI3K pathway does not appear to be involved in the induced phosphorylation of Akt by molecules **4** and **5**.

The Rho family of small GTPase Rac-1 is another upstream stimulator of Akt activity.<sup>[21]</sup> Phosphorylation of Rac-1 is strongly involved in attachment-dependent cell survival, especially through syndecans.<sup>[22]</sup> The phosphorylation of Rac-1 increased in cells treated with molecule **4** or **5** (Figure 2B and S6B). The induced phosphorylation of Akt and Rac-1 supports a model in which the binding of molecules **4** and **5** to both integrin and heparan sulfate leads to the activation of small GTPase Rac-1, in turn stimulating Akt phosphorylation.

We next examined the expression levels of Bcl-xL, a key anti-apoptotic protein that is upregulated by Akt.<sup>[23]</sup> The overexpression of Bcl-xL has previously been shown to abolish anoikis. Western blot analysis showed, as previously reported,<sup>[24]</sup> that incubation under anoikis conditions down-regulated the expression of Bcl-xL in untreated cells (Figure 2C and S6C). The addition of molecule **4** or **5** resulted in a marked increase in Bcl-xL expression (Figure 2C and S6C), consistent with the stimulation of Akt phosphorylation by molecules **4** and **5**.

Previous studies demonstrated that adhesamine (molecule **1**) induces a clustering of heparan-sulfate-bound syndecans, most significantly syndecan-4, on the cell surface.<sup>[13]</sup> We used immunostaining to determine if molecules **4** and **5** promote similar clustering of syndecan-4. Suspended NIH3T3 cells incubated with molecule **4** or **5** (60  $\mu$ M) for 24 h in a serum-free medium were collected and fixed immediately after re-attachment to glass plates. Microscopic observation showed that molecule **4** or **5** did promote clustering of syndecan-4 at the cell surface (Figure 3).

The addition of an RGDS moiety was expected to allow molecules **4** and **5** bind to integrins and promote their co-clustering with syndecans. Among a number of clustering combinations of syndecans and integrins, we examined that of syndecan-4 and integrin  $\beta$ 1, which is considered to be the most important combination for the cell survival mediated by the extracellular matrix.<sup>[7]</sup> Immunostaining images of cells treated with molecule **4** or **5** did indeed show co-localization of syndecan-4 and integrin  $\beta$ 1 at the cell surface (Figure 3). The extent of co-localization at the cell surface was quantified using Pearson's correlation coefficient (Figure S8). These results suggest that adhesamine-RGDS derivatives act as soluble ligands, whose activity promote syndecan-4 and integrin  $\beta$ 1 recruitment to the cell surface, and induce their clustering and co-localization. Presumably, this clustering leads to an activation of the downstream signaling survival pathway that involves Rac-1 activation, leading to Akt activation and Bcl-xL upregulation.

Finally, we examined the ability of molecule **4** to enhance cell engraftment in cell transplantation procedures. Due to the potential degradation of the peptide segments in vivo, we selected molecule **4**, which is equipped with two peptides and is more readily synthesized than molecule **5**.

Molecule **4** was first tested for its ability to promote the engraftment of bone-marrow-derived cells (BMDCs) in

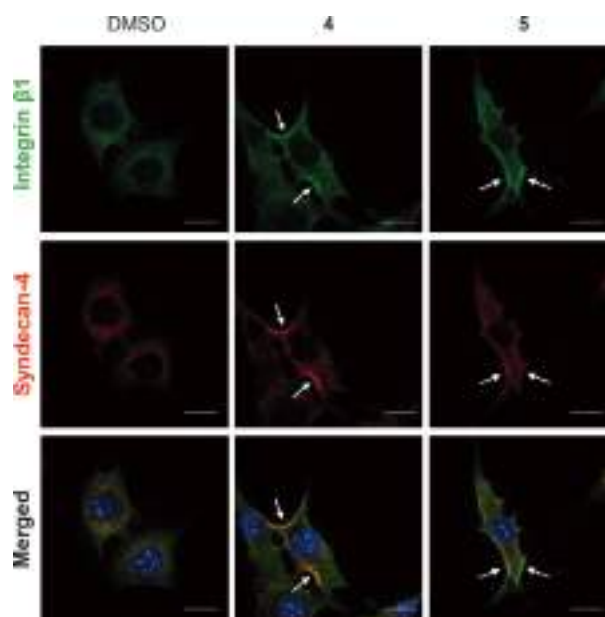


**Figure 3.** Effects of molecules **4** and **5** on syndecan-4 and integrin  $\beta$ 1 co-localization. Suspended cells incubated with each molecule **4** and **5** (60  $\mu$ M) for 24 h in serum-free medium were collected and re-attached to glass-bottom plates for 2 h. Cells were stained with anti-integrin  $\beta$ 1 and syndecan-4 antibodies, counterstained with DAPI, and visualized by fluorescence microscopy. The representative images for each treatment from three independent experiments are shown. (Scale bar = 10  $\mu$ m)

a type 2 diabetic (db/db) mouse model, which displays delayed and poor wound healing.<sup>[25]</sup> Wound healing required 28 days or more in the control group, and was accelerated by injection of BMDCs (Figure 4). Co-injection of cells with 6  $\mu$ M of molecule **4** further improved the BMDC-mediated wound healing (Figure 4 and S9). Note that the administration of

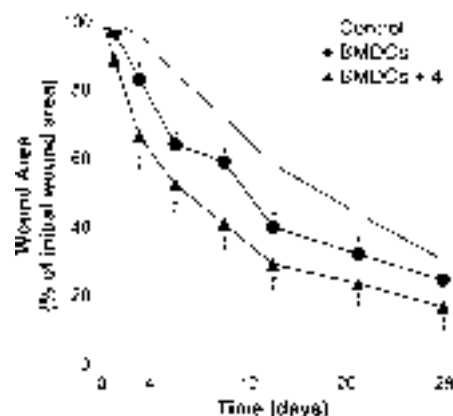


**Figure 4.** Effects of molecule **4** on wound healing in diabetic mice. Mice received intradermal injections of BMDCs near the injury site, with or without pretreatment with molecule **4** (6  $\mu$ M). Hank's balanced salt solution without cells was injected as a control. Wound size was measured from Day 0. Experiments were carried out in duplicate, and results of a representative experiment are shown, expressed as mean value  $\pm$  standard deviation of 4–6 mice. \* $p$  < 0.05 compared to the control group; and # $p$  < 0.05 compared to the BMDCs only group.



molecule **4** alone has no significant effect on wound healing (data not shown).

The *in vivo* effect of molecule **4** was further investigated using a rabbit model of bullous keratopathy. The corneal endothelium maintains transparency through barrier and  $\text{Na}^+/\text{K}^+$  transport systems. In bullous keratopathy, the dysfunction of the endothelium causes corneal cloudiness and severe visual impairment, and is usually treated by corneal transplantation. However, recent research showed that a co-injection of suspended corneal endothelial cells (CECs) with a Rho kinase inhibitor directly into the anterior chambers successfully recovered corneal transparency in rabbit and monkey models of corneal endothelial dysfunction.<sup>[26]</sup> Similarly, the co-injection of molecule **4** (10  $\mu\text{M}$ ) with suspended CECs in the rabbit model recovered the corneal transparency after 7 days, whereas the treatment with CECs alone exhibited hazy cornea (Figure 5). Complications related

CECs, but without molecule **4**, exhibited a stratified fibroblastic phenotype after 14 days (Figure S11C). In contrast, CECs injection with molecule **4** regenerated the hexagonal, contact-inhibited phenotype (Figure S11C). Thus, the transplantation of cultured rabbit CECs together with molecule **4** enhanced the cell engraftment and recovery of corneal transparency without the usual complications associated with corneal transplantation. Together, the positive effects of molecule **4** on the treatment of these two disease models suggest that the synthetic molecule serves as an adjuvant for cell therapy. It would be interesting to see whether molecule **4** or its derivatives can be applied to more complex cell transplantation systems.

The present study describes the chemical synthesis and biological evaluation of soluble, hybrid molecules that target two receptors essential for transmitting survival signals—syndecans and integrins. Integrin has long been recognized as a promising drug target, particularly for cancer therapy.<sup>[27]</sup> The drug, Cilengitide, is the first clinically applied integrin antagonist that uses the RGD sequence.<sup>[28]</sup> Despite progress in the development of integrin antagonists, the only soluble small-molecule integrin agonists that have been explored to date are an allosteric inhibitor-derived agonists, which stimulates ligand binding but blocks the functions of integrins, and short peptides from tenascin-C.<sup>[29]</sup> The self-assembling hybrid molecules described herein are the first soluble, synthetic dual agonists of syndecan and integrin that are useful for anoikis inhibition and, therefore, have potential applications in cell transplant therapy.

Integrins are known to be activated by both extracellular ligand binding and intracellular signaling.<sup>[30]</sup> The extracellular ligand binding alone is not sufficient to induce the integrin clustering necessary to generate significant survival signals. It has been suggested that intracellular signals induce a conformational change in integrin, to a high-affinity state that increases ligand binding. The integrin clustering caused by molecules **4** and **5** through their RGD moieties might be potentiated by intracellular signals that are generated by syndecan-4 clustering induced by the molecules' adhesamine moieties. Consistent with our results, a recent investigation showed that Rac-1 activation, a direct consequence of syndecan-4 clustering, promotes integrin clustering, which in turn activates Rac-1, establishing a positive feedback loop.<sup>[31]</sup> Because detailed three-dimensional structures of molecules **4** and **5** are not available, it is difficult to determine the contribution of each module in eliciting the biological activity. Nevertheless, molecules **4** and **5** provide a starting point for designing synthetic tools for cell-based therapy. Spatially regulated ligation of adhesamine and RGD peptides could potentially lead to the design of synthetic molecules with even more potent activities.

Received: June 2, 2014

Published online: September 2, 2014

**Keywords:** adhesamine · anoikis · cell engraftment · peptides · self-assembly

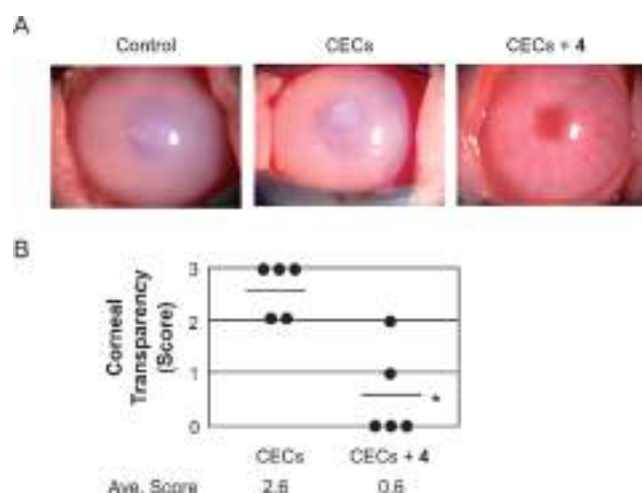


**Figure 5.** Effects of molecule **4** on a rabbit model of bullous keratopathy. Eyes were injected with cultivated rabbit corneal endothelial cells (CECs), with or without molecule **4** (10  $\mu\text{M}$ ). No treatment group served as control. A) Photographs showing corneal transparency, and B) quantitative assessment of corneal transparency, one week after injection. Corneal transparency scores: 0 = clear cornea with iris details clearly visualized; 1 = partial obscuration of the iris details; 2 = iris details poorly seen with pupil margin just visible; 3 = complete obscuration of iris and pupil details. \* indicates significant difference ( $p < 0.01$ ) between mean scores of rabbits treated with molecule **4** and CECs versus CECs only ( $n = 5$  for each group).

to cell injection therapy, such as the abnormal deposition of injected cells and elevation of intraocular pressure, were not observed during the experiments (Figure S10). CECs co-injected with molecule **4** covered denuded Descemet's membrane and exhibited hexagonal morphology, whereas CECs injected without molecule **4** failed to cover the Descemet's membrane 3 h past injection (Figure S11A). After 7 days, CECs injected with molecule **4** displayed characteristic staining patterns for ZO-1 (gap junction marker) and  $\text{Na}/\text{K}$ -ATPase at the plasma membranes (Figure S11B). In addition, corneal endothelial cells expressed Dil, suggesting that the corneal endothelium was regenerated by injected CECs (Figure S11B). Endothelium treated with

- [1] M. A. Fischbach, J. A. Bluestone, W. A. Lim, *Sci. Transl. Med.* **2013**, *5*, 179ps7.
- [2] I. Zvibel, F. Smets, H. Soriano, *Cell Transplant.* **2002**, *11*, 621–630.
- [3] M. L. Taddei, E. Giannoni, T. Fiaschi, P. Chiarugi, *J. Pathol.* **2012**, *226*, 380–393.
- [4] a) I. Pusic, J. F. DiPersio, *Curr. Pharm. Des.* **2008**, *14*, 1950–1961; b) S. F. Badylak, *Biomaterials* **2007**, *28*, 3587–3593.
- [5] S. M. Frisch, H. Francis, *J. Cell Biol.* **1994**, *124*, 619–626.
- [6] F. G. Giancotti, E. Ruoslahti, *Science* **1999**, *285*, 1028–1033.
- [7] M. R. Morgan, M. J. Humphries, M. D. Bass, *Nat. Rev. Mol. Cell Biol.* **2007**, *8*, 957–969.
- [8] J. Jeong, I. Han, Y. Lim, J. Kim, I. Park, A. Woods, J. R. Couchman, E. Oh, *Biochem. J.* **2001**, *357*, 531–537.
- [9] J. R. Couchman, *Nat. Rev. Mol. Cell Biol.* **2003**, *4*, 926–937.
- [10] R. O. Hynes, *Cell* **1992**, *69*, 11–25.
- [11] M. D. Pierschbacher, E. Ruoslahti, *Nature* **1984**, *309*, 30–33.
- [12] S. Yamazoe, H. Shimogawa, S. Sato, J. D. Esko, M. Uesugi, *Chem. Biol.* **2009**, *16*, 773–782.
- [13] N. Takemoto, T. Suehara, H. L. Frisco, S. Sato, T. Sezaki, K. Kusamori, Y. Kawazoe, S. M. Park, S. Yamazoe, Y. Mizuhata, et al., *J. Am. Chem. Soc.* **2013**, *135*, 11032–11039.
- [14] K. Watanabe, M. Ueno, D. Kamiya, A. Nishiyama, M. Matsumura, T. Wataya, J. B. Takahashi, S. Nishikawa, S. Nishikawa, K. Muguruma, Y. Sasai, *Nat. Biotechnol.* **2007**, *25*, 681–686.
- [15] D. G. Stupack, X. S. Puente, S. Boutsaboualoy, C. M. Storgard, D. A. Cheresch, *J. Cell Biol.* **2001**, *155*, 459–470.
- [16] M. C. Guadamillas, A. Cerezo, M. A. del Pozo, *J. Cell Sci.* **2011**, *124*, 3189–3197.
- [17] S. R. Datta, A. Brunet, M. E. Greenberg, *Genes Dev.* **1999**, *13*, 2905–2927.
- [18] M. Schmidt, S. Hövelmann, T. L. Beckers, *Br. J. Cancer* **2002**, *87*, 924–932.
- [19] H. Xia, R. S. Nho, J. Kahm, J. Kleidon, C. A. Henke, *J. Biol. Chem.* **2004**, *279*, 33024–33034.
- [20] N. K. Zouq, J. A. Keeble, J. Lindsay, A. J. Valentijn, L. Zhang, D. Mills, C. E. Turner, C. H. Streuli, A. P. Gilmore, *J. Cell Sci.* **2009**, *122*, 357–367.
- [21] S. J. Coniglio, T. S. Jou, M. Symons, *J. Biol. Chem.* **2001**, *276*, 28113–28120.
- [22] M. D. Bass, K. A. Roach, M. R. Morgan, Z. Mostafavi-Pour, T. Schoen, T. Muramatsu, U. Mayer, C. Ballestrem, J. P. Spatz, M. J. Humphries, *J. Cell Biol.* **2007**, *177*, 527–538.
- [23] J. Grossmann, *Apoptosis* **2002**, *7*, 247–260.
- [24] U. Rodeck, M. Jost, J. DuHadaway, C. Kari, P. J. Jensen, B. Risse, D. L. Ewert, *Proc. Natl. Acad. Sci. USA* **1997**, *94*, 5067–5072.
- [25] J. Wan, L. Xia, W. Liang, Y. Liu, Q. Cai, *J. Diabetes Res.* **2013**, 647107.
- [26] a) N. Okumura, N. Koizumi, M. Ueno, Y. Sakamoto, H. Takahashi, H. Tsuchiya, J. Hamuro, S. Kinoshita, *Am. J. Pathol.* **2012**, *181*, 268–277; b) N. Okumura, M. Ueno, N. Koizumi, Y. Sakamoto, K. Hirata, J. Hamuro, S. Kinoshita, *Invest. Ophthalmol. Visual Sci.* **2009**, *50*, 3680–3687.
- [27] D. Cox, M. Brennan, N. Moran, *Nat. Rev. Drug Discovery* **2010**, *9*, 804–820.
- [28] C. Mas-Moruno, F. Rechenmacher, H. Kessler, *Anti-Cancer Agents Med. Chem.* **2010**, *10*, 753–768.
- [29] a) J. W. Yang, C. V. Carman, M. Kim, A. Salas, M. Shimaoka, T. A. Springer, *J. Biol. Chem.* **2006**, *281*, 37904–37912; b) Y. Saito, H. Imazeki, S. Miura, T. Yoshimura, H. Okutsu, Y. Harada, T. Ohwaki, O. Nagao, S. Kamiya, R. Hayashi, et al., *J. Biol. Chem.* **2007**, *282*, 34929–34937.
- [30] R. O. Hynes, *Cell* **2002**, *110*, 673–687.
- [31] a) M. D. Bass, K. A. Roach, M. R. Morgan, Z. Mostafavi-Pour, T. Schoen, T. Muramatsu, U. Mayer, C. Ballestrem, J. P. Spatz, M. J. Humphries, *J. Cell Biol.* **2007**, *177*, 527–538; b) E. Hirsch, L. Barberis, M. Brancaccio, O. Azzolino, D. Xu, J. M. Kyriakis, L. Silengo, F. G. Giancotti, G. Tarone, R. Fässler, F. Altruda, *J. Cell Biol.* **2002**, *157*, 481–492.

RESEARCH ARTICLE

# Derivation of Mesenchymal Stromal Cells from Pluripotent Stem Cells through a Neural Crest Lineage using Small Molecule Compounds with Defined Media

Makoto Fukuta<sup>1,2,3\*</sup>, Yoshinori Nakai<sup>4\*</sup>, Kosuke Kirino<sup>5\*</sup>, Masato Nakagawa<sup>6</sup>, Kazuya Sekiguchi<sup>1,2,7</sup>, Sanae Nagata<sup>2</sup>, Yoshihisa Matsumoto<sup>1,2,3</sup>, Takuya Yamamoto<sup>6,8</sup>, Katsutsugu Umeda<sup>9</sup>, Toshio Heike<sup>9</sup>, Naoki Okumura<sup>10</sup>, Noriko Koizumi<sup>10</sup>, Takahiko Sato<sup>4</sup>, Tatsutoshi Nakahata<sup>5</sup>, Megumu Saito<sup>5</sup>, Takanobu Otsuka<sup>3</sup>, Shigeru Kinoshita<sup>4</sup>, Morio Ueno<sup>4\*</sup>, Makoto Ikeya<sup>2\*</sup>, Junya Toguchida<sup>1,2,7\*</sup>



OPEN ACCESS

**Citation:** Fukuta M, Nakai Y, Kirino K, Nakagawa M, Sekiguchi K, et al. (2014) Derivation of Mesenchymal Stromal Cells from Pluripotent Stem Cells through a Neural Crest Lineage using Small Molecule Compounds with Defined Media. PLoS ONE 9(12): e112291. doi:10.1371/journal.pone.0112291

**Editor:** Maurilio Sampaoli, Stem Cell Research Institute, Belgium

**Received:** March 24, 2014

**Accepted:** October 6, 2014

**Published:** December 2, 2014

**Copyright:** © 2014 Fukuta et al. This is an open-access article distributed under the terms of the [Creative Commons Attribution License](https://creativecommons.org/licenses/by/4.0/), which permits unrestricted use, distribution, and reproduction in any medium, provided the original author and source are credited.

**Funding:** This work was supported in part by Grants-in-Aid for Scientific Research from JSPS (#25293320), a grant from Core Center for iPS Cell Research, Research Center Network for Realization of Regenerative Medicine from JST, and the Leading Project for Realization of Regenerative Medicine from MEXT to MI and JT. MI was also supported by the Adaptable and Seamless Technology Transfer Program through target-driven R&D, Exploratory Research from JST (AS242Z00931P). JT was also supported by the Center for Clinical Application Research on Specific Disease/Organ from JST. MU was also supported by Grants-in-Aid for Scientific Research from JSPS (#20791288). The funders had no role in the study design, data collection and analysis, decision to publish, or preparation of the manuscript.

**Competing Interests:** The authors have declared that no competing interests exist.

1. Department of Tissue Regeneration, Institute for Frontier Medical Sciences, Kyoto University, Kyoto, Japan, 2. Department of Cell Growth and Differentiation, Center for iPS Cell Research and Application, Kyoto University, Kyoto, Japan, 3. Department of Orthopaedic Surgery, Graduate School of Medical Sciences, Nagoya City University, Nagoya, Japan, 4. Department of Ophthalmology, Kyoto Prefectural University of Medicine, Kyoto, Japan, 5. Department of Clinical Application, Center for iPS Cell Research and Application, Kyoto University, Kyoto, Japan, 6. Department of Reprogramming Science, Center for iPS Cell Research and Application, Kyoto University, Kyoto, Japan, 7. Department of Orthopaedic Surgery, Graduate School of Medicine, Kyoto University, Kyoto, Japan, 8. Institute for Integrated Cell-Material Sciences (WPI-iCeMS), Kyoto University, Kyoto, Japan, 9. Department of Pediatrics, Graduate School of Medicine, Kyoto University, Kyoto, Japan, 10. Department of Biomedical Engineering, Faculty of Life and Medical Sciences, Doshisha University, Kyotanabe, Japan

\*[mueno@koto.kpu-m.ac.jp](mailto:mueno@koto.kpu-m.ac.jp) (MU); [mikeya@cira.kyoto-u.ac.jp](mailto:mikeya@cira.kyoto-u.ac.jp) (MI); [togjun@frontier.kyoto-u.ac.jp](mailto:togjun@frontier.kyoto-u.ac.jp) (JT)

These authors contributed equally to this work.

## Abstract

Neural crest cells (NCCs) are an embryonic migratory cell population with the ability to differentiate into a wide variety of cell types that contribute to the craniofacial skeleton, cornea, peripheral nervous system, and skin pigmentation. This ability suggests the promising role of NCCs as a source for cell-based therapy. Although several methods have been used to induce human NCCs (hNCCs) from human pluripotent stem cells (hPSCs), such as embryonic stem cells (ESCs) and induced pluripotent stem cells (iPSCs), further modifications are required to improve the robustness, efficacy, and simplicity of these methods. Chemically defined medium (CDM) was used as the basal medium in the induction and maintenance steps. By optimizing the culture conditions, the combination of the GSK3 $\beta$  inhibitor and TGF $\beta$  inhibitor with a minimum growth factor (insulin) very efficiently induced hNCCs (70–80%) from hPSCs. The induced hNCCs expressed cranial NCC-related genes and stably proliferated in CDM supplemented with EGF and FGF2 up to at least 10



passages without changes being observed in the major gene expression profiles. Differentiation properties were confirmed for peripheral neurons, glia, melanocytes, and corneal endothelial cells. In addition, cells with differentiation characteristics similar to multipotent mesenchymal stromal cells (MSCs) were induced from hNCCs using CDM specific for human MSCs. Our simple and robust induction protocol using small molecule compounds with defined media enabled the generation of hNCCs as an intermediate material producing terminally differentiated cells for cell-based innovative medicine.

## Introduction

In order to apply human pluripotent stem cells (hPSCs) to innovative medicine, such as cell therapy, disease modeling, and drug discovery, robust and efficient methods to produce the desired cell types without contaminating undesired cells are indispensable [1]. Since the contamination of hPSCs, in particular, may cause serious adverse effects, careful monitoring, which requires a considerable amount of time and cost, has to be conducted. Therefore, it would be beneficial to have intermediate cells between hPSCs and terminally differentiated cells, which are proved to have no contaminated hPSCs, contain limited but multiple differentiation properties, and stably proliferate without phenotypic changes. One of the promising candidates with such features is the neural crest cell (NCC) [2].

The neural crest emerges at the border of the neural and non-neural ectoderm in gastrula embryos during vertebrate development [3]. Cells in the neural crest, and later in the dorsal part of the neural tube, eventually delaminate and migrate throughout the body while retaining their characteristic phenotype [4]. When they reach their target tissues, NCCs differentiate into specific cell types depending on the location [5]. NCCs give rise to the majority of cranial bone, cartilage, smooth muscle, and pigmented cells in the cranial region, as well as neurons and glia in the peripheral nervous system [3–5]. Cardiac NCCs are known to contribute to valves in the heart, while vagal NCCs differentiate into enteric ganglia in the gut [6]. NCCs give rise to neurons and glia in the peripheral nervous system in the trunk region, secretory cells in the endocrine system, and pigmented cells in the skin.

Using a lineage-tracing system, rodent neural crest-derived cells were detected in adult tissues such as bone marrow, and still retained multipotent differentiation properties, which indicated that these cells are one of the cell-of-origin of multipotent mesenchymal stromal cells (MSCs) [7, 8]. Therefore, the production of human MSCs (hMSCs) from hPSCs via NCC lineage is a promising approach for the use of hPSCs in innovative medicine [9, 10]. A considerable number of studies have been dedicated to establishing robust and efficient induction methods from hPSCs to hNCCs in the past decade [11–13]. However, most of these studies used non-human stromal feeder cells or only achieved low induction

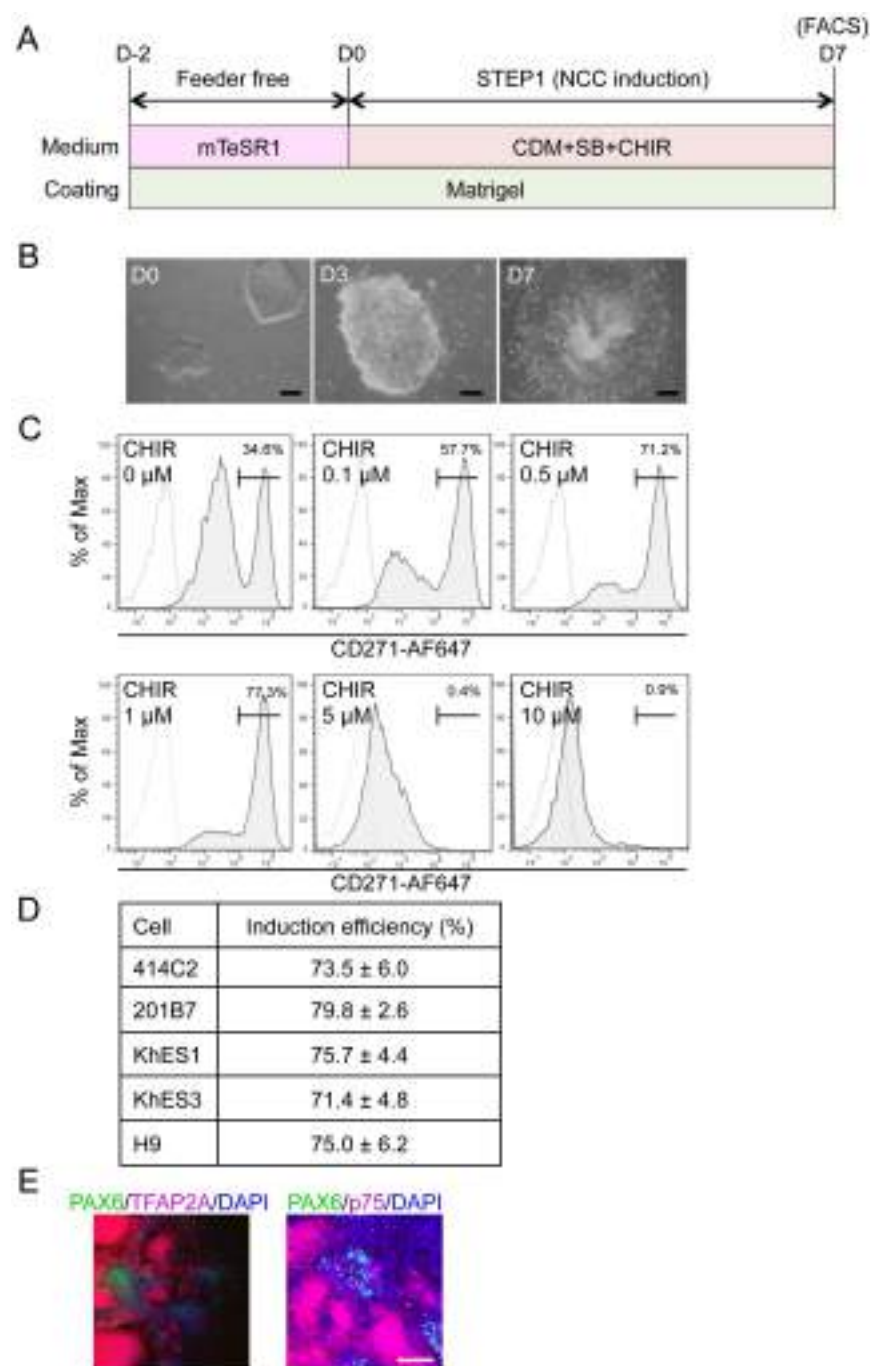


**Figure 1. Induction of p75<sup>high</sup> cells from hPSCs.** A) Schematic representation of the protocol. B) Morphology of colonies during the induction. Phase contrast images were taken on days 0, 3, and 7. Scale bar, 200  $\mu$ m. C) The fraction of p75-positive cells in 201B7 cells was treated with SB431542 (SB) (10  $\mu$ M) and CHIR99021 (CHIR) (indicated concentration) for seven days, stained with an anti-p75 antibody, and analyzed by FACS. D) Fraction of the p75<sup>high</sup> population induced by SB (10  $\mu$ M) and CHIR (1  $\mu$ M) from hESCs (KhES1, KhES3, H9) and hiPSCs (414C2, 201B7). Average  $\pm$  SD. N=3, biological triplicate. E) Immunocytochemical analyses of colonies on day 7 (201B7). Cells were stained with antibodies against PAX6, TFAP2A, and p75. Scale bar, 100  $\mu$ m.

doi:10.1371/journal.pone.0112291.g001

efficiencies. An ideal method from the standpoint of clinical applications is free from xeno-materials, such as feeder cells or serum, and can be performed using a chemically defined medium (CDM). Two groups have published protocols that are compatible with these requirements [14, 15]. The first group employed a two-step approach, in which hPSCs were firstly dissociated into single cells and cultured with CDM for two weeks for the adaptation. Cells were then cultured with CDM that was supplemented with an activator of Wnt signaling and inhibitor of Activin/Nodal/TGF $\beta$  signaling, but was free from BMP signaling modulation [14]. The other group used MEF-conditioned hESC media for the initial step, and replaced it with knockout serum replacement (KSR)-based medium, which thereafter was gradually replaced with an increasing amount of N2 media. They employed an inhibitor for BMP signaling in addition to an inhibitor for Activin/Nodal/TGF $\beta$  signaling during the initial 3 days, and then replaced them with an activator of Wnt signaling [15]. Therefore, the requirement for signal modulators, particularly BMP signaling inhibitors, remains controversial. Further modifications are still needed to improve the robustness, efficacy, and simplicity of these methods.

We here developed a robust and efficient induction protocol using CDM containing inhibitors for TGF $\beta$  signaling and GSK3 $\beta$ , but not for BMP signaling with minimal growth factors. The protocol very efficiently induced hNCCs (70–80%) from hPSCs irrespective of the type (hESCs vs hiPSCs) or generating method (viral-integrated vs plasmid-episomal). Genome-wide analyses revealed that induced hNCCs retained their gene expression profile as NCCs even after 10 passages. As for differentiation properties, induced hNCCs successfully differentiated into peripheral neurons, glia, melanocytes and corneal endothelial cells. In addition, induced hNCCs were able to produce cells comparable to hMSCs, which were free from contaminated hPSCs and could differentiate into osteo-, chondro-, and adipogenic cells. Furthermore, using iPSCs generated and maintained under feeder-free and xeno-free culture systems, we successfully induced hNCCs, hMSCs, and osteogenic cells using chemically defined media.

## Materials and Methods

### Ethics statement

The experimental protocols dealing human subjects were approved by the Ethics Committee of the Department of Medicine and Graduate School of Medicine, Kyoto University. Written informed consent was provided by each donor.

### Cell lines

hESCs (H9, KhES1, and KhES3) and hiPSCs (414C2 and 201B7) were used in this study [16–19]. They were maintained on SNL feeder cells [20] in Primate ES cell medium (ReproCELL, Tokyo, Japan) supplemented with 4 ng/ml recombinant human FGF2 (WAKO, Osaka, Japan). 987A3, hiPSCs generated and maintained



under feeder-free and xeno-free culture systems from human primary fibroblasts, were maintained on iMatrix-551 (rLN511E) (Nippi, Tokyo, Japan)-coated cell culture plates with StemFit (Ajinomoto, Tokyo, Japan) as described previously [21]. Bone marrow derived hMSCs were obtained from donors and used in our previous study [22]. Human corneal endothelial cells were isolated from human corneal tissues obtained for research purpose from SightLife (Seattle, WA, USA).

### Culture media and reagents

mTeSR1 medium (STEMCELL Technology, Vancouver, Canada) was used for the feeder-free culture of PSCs. The induction and maintenance of hNCCs were performed using previously reported CDM [23], which contains Iscove's modified Dulbecco's medium/Ham's F-12 1:1, 1x chemically defined lipid concentrate (GIBCO, Grand Island, NY, USA), 15 µg/ml apo-transferrin (Sigma, St. Louis, MO, USA), 450 µM monothioglycerol (Sigma), 5 mg/ml purified BSA (99% purified by crystallization; Sigma), 7 µg/ml Insulin (WAKO), and penicillin/streptomycin (Invitrogen, Carlsbad, CA, USA). Culture dishes were coated with growth factor-reduced Matrigel (BD, Bedford, MA, USA) or fibronectin (Millipore, Bedford, CA, USA). EGF (R&D, Minneapolis, USA) and FGF2 were used to maintain hNCCs [24]. SB431542 (SB) (Sigma), CHIR99021 (CHIR) (WAKO), BMP4 (R&D), DMH1 (Tocris, Bristol, UK), LDN193189 (Stemgent, Cambridge, MA, USA), and recombinant human Noggin (R&D) were used to modulate growth factor signals. Retinoic acid (RA) (Sigma) was used to modulate hNCCs.

### Fluorescence-Activated Cell Sorting (FACS)

FACS was performed by AriaII (BD) according to the manufacturer's protocol. The antibodies used in FACS were listed in Table S1. In all experiments, FACS histograms of isotype controls were similar to those without antibodies; therefore, histograms without antibodies were used as control populations.

### Immunocyto- and immunohistochemistry

Prior to performing immunostaining with antibodies, cells on plates were fixed with 4% paraformaldehyde at 4°C for 15 minutes, washed two times with PBS, and incubated with 0.3% TritonX100 at 4°C for 30 minutes as the surface-active agent for penetration processing, and any nonspecific binding was blocked with 2% skim milk/PBS at 4°C for 1 hour. Cornea samples obtained from rabbits euthanized three days after the injection of cells were fixed with 4% paraformaldehyde and incubated in 1% bovine serum albumin (BSA) (Sigma) to block other bindings. DAPI (1:5000; Sigma) was used to counterstain nuclei. The primary antibodies used in this study were summarized in Table S1. The observation and assessment of samples were performed with BZ-9000E (Keyence, Osaka, Japan).

## RT-PCR and qPCR

Total RNA was purified with the RNeasy Mini kit (Qiagen, Valencia, CA, USA) and treated with the DNase-one kit (Qiagen) to remove genomic DNA. One microgram of total RNA was reverse transcribed for single-stranded cDNA using a random primer and Superscript III reverse transcriptase (Invitrogen), according to the manufacturer's instructions. PCR was performed with ExTaq (Takara, Shiga, Japan). Quantitative PCR with the Thunderbird SYBR qPCR Mix (TOYOBO, Osaka, Japan) was performed using the StepOne real-time PCR system (Applied Biosystems, Forester City, CA, USA) in duplicate or triplicate. Primer sequences were listed in Table S2.

## cDNA microarray

Total RNA was prepared using the RNeasy Mini Kit (Qiagen). cDNA was synthesized using the GeneChip WT (Whole Transcript) Sense Target Labeling and Control Reagents kit as described by the manufacturer (Affymetrix, Santa Clara, CA, USA). Hybridization to the GeneChip Human Gene 1.0 ST expression arrays, washing, and scanning were performed according to the manufacturer's protocol (Affymetrix). Expression values were calculated using the RMA summarization method and the data obtained were analyzed by GeneSpring GX 11.5.6 (Agilent Technologies, Santa Clara, CA, USA) for correlation coefficients, scatter plots, a volcano plot, heat maps, and hierarchical clustering (Distance metrics: Pearson's Centered, Linkage rule: Average). Differentially expressed genes were identified by statistical analyses and fold changes. Statistical analyses were performed using a one-way ANOVA with a Benjamini and Hochberg False Discovery Rate (BH-FDR = 0.01) multiple testing correction followed by Tukey HSD post hoc tests (GeneSpring GX). Microarray data have been submitted to the Gene Expression Omnibus (GEO) public database at NCBI, and the accession number is GSE 60313. Data for hBM90, 91, and 94 have already been described [22]. Data from GSE44727 and GSE45223 were used for a comparison analysis in Figure S3.

## Differentiation of hPSC-derived hNCCs

### Peripheral neuronal differentiation

Sorted hNCCs were cultured in CDM supplemented with 10  $\mu$ M SB and 1  $\mu$ M CHIR as a sphere using the hanging drop technique ( $1 \times 10^4$  cells per sphere) as previously described [25]. Twenty-four hours after the hanging drop culture, spheres were plated onto Polyornithine/laminin/fibronectin (PO/Lam/FN)-coated plates in DMEM/F12 (Invitrogen) supplemented with 1 x N2 supplement (GIBCO), 1 x GlutaMAX (Invitrogen), 20 ng/ml FGF2, and 20 ng/ml EGF. These cells were cultured for two days under these conditions and the medium was then replaced with DMEM/F12 supplemented with 1 x N2 supplement, 1 x GlutaMAX, and 10 ng/ml BDNF (R&D), GDNF (R&D), NT-3 (R&D), and NGF (R&D). The medium was changed every 3 days and passages were performed every week [26].

Differentiation was confirmed by immunostaining for peripherin, Tuj-1, and GFAP 3 weeks after induction.

#### Melanocyte differentiation

Cells were plated onto fibronectin-coated dishes in CDM supplemented with 10  $\mu$ M SB and 1  $\mu$ M CHIR. Melanocyte induction was performed the next day with CDM supplemented with 1  $\mu$ M CHIR, 25 ng/ml BMP4, and 100 nM endothelin-3 (American Peptide Company, Sunnyvale, CA, USA) [15, 27, 28]. The medium was changed every other day. Differentiation was confirmed by induction of the *MITF* and *c-KIT* genes on day 7.

#### Corneal endothelial cell differentiation

Cells were induced to corneal endothelial cells with corneal endothelial cell-conditioned CDM. Conditioned CDM was derived by collecting medium from cultured human corneal endothelial cells [29]. The selective ROCK inhibitor Y-27632 (WAKO) was used on the first day of the induction. The medium was changed every two days, and cells were analyzed by immunocytochemistry after twelve days. RT-qPCR was performed 3, 5, and 8 days after the induction.

#### Induction of hMSCs from hNCCs

Cells were plated onto tissue culture dishes (BD) at a density of  $6.5 \times 10^4$  cell/cm<sup>2</sup> in CDM supplemented with 10  $\mu$ M SB and 1  $\mu$ M CHIR. The medium was replaced the next day with  $\alpha$ MEM (Nacalai Tesque, Tokyo, Japan) supplemented with 10% fetal bovine serum (FBS) (Nichirei Inc., Tokyo, Japan) [14, 26]. The morphology of cells started to change approximately 4 days after the induction. Passages were performed every week using 0.25% trypsin-EDTA (GIBCO) at a density of  $1 \times 10^4$  cells/cm<sup>2</sup>. hMSC markers (CD73, CD44, CD45 and CD105) were analyzed by FACS 14 days after the hMSC induction. We used STK2 (DS Pharma Biomedical, Osaka, Japan) as the MSC medium and tissue culture dishes coated with fibronectin for the hMSC induction under chemically defined media conditions.

#### Differentiation of hNCC-derived hMSCs

##### Osteogenic differentiation

A total of  $2.5 \times 10^5$  induced hMSCs/well were seeded on 6-well dishes (BD) and cultured in osteogenic induction medium,  $\alpha$ MEM, 10% FBS, 0.1  $\mu$ M dexamethasone, 50  $\mu$ g/ml ascorbic acid, and 10 mM  $\beta$ -glycerophosphate for 2 weeks for osteogenic differentiation [24]. STK3 (DS Pharma) was used as the osteogenic induction medium instead of the osteogenic induction medium to achieve osteogenic differentiation under chemically defined media conditions. The culture medium was changed every other day for 1 week. Differentiation properties were confirmed by the formation of calcified nodules, as detected with Alizarin Red staining. Briefly, culture wells were washed twice in phosphate-buffered saline (PBS) and fixed for 10 minutes at room temperature in 100% ethyl alcohol. The



Alizarin Red solution (40 mM, pH 4.2) was applied to the fixed wells for 10 min at room temperature. Non-specific staining was removed by several washes with water.

### Chondrogenic differentiation

Two-dimensional chondrogenic induction was performed as previously described [30]. Briefly, cells ( $1.5 \times 10^5$ ) that induced hMSCs were suspended in 5  $\mu$ l of chondrogenic medium (DMEM: F12 (Invitrogen), 1% (v/v) ITS1 mix (BD), 0.17 mM AA2P, 0.35 mM Proline (Sigma), 0.1 mM dexamethasone (Sigma), 0.15% (v/v) glucose (Sigma), 1 mM Na-pyruvate (Invitrogen), 2 mM GlutaMax, and 0.05 mM MTG supplemented with 40 ng/ml PDGF-BB and 1% (v/v) FBS (Nishirei)), and were subsequently transferred to fibronectin-coated 24-well plates (BD). A total of 1 ml of the chondrogenic medium was added after 1 hour. TGF $\beta$ 3 (R&D) was subsequently added at 10 ng/ml on days 3 to 6, and BMP4 was added to a concentration of 50 ng/ml on day 10. Micromass cultures were maintained at 37°C under 5% CO<sub>2</sub> and 5% O<sub>2</sub> for 16 days. Differentiation properties were confirmed by Alcian Blue staining. Briefly, induced cells were fixed for 30 minutes with 10% formalin (Sigma) and rinsed with PBS. These cells were then stained overnight with Alcian Blue solution (1% Alcian Blue (MUTO PURE CHEMICAL CO., LTD, Tokyo, Japan) in 3% glacial acetic and 1% HCl, pH 1) and destained with the acetic acid solution.

### Adipogenic differentiation

Cells were seeded onto 6-well tissue culture dishes at a density of  $5.0 \times 10^5$  cells/well for adipogenic differentiation, and were cultured in  $\alpha$ MEM containing 10% FBS, 1 mM dexamethasone, 10 mg/ml insulin, and 0.5 mM isobutylxanthine for 3 weeks [31]. Induced cells were fixed in 10% formalin for 1 hour at room temperature, followed by 20 minutes in 0.3% Oil Red O staining solution (Sigma).

## Results

### Derivation of p75<sup>high</sup> cells from hPSCs

To transfer hPSCs from feeder to feeder-free culture conditions, colonies were dissociated into small cell clumps (about 10 cells/clumps) by pipetting several times, seeded on matrigel-coated dishes (2–4 clumps/cm<sup>2</sup>), and cultured with mTeSR1 medium for two days. hNCC induction was then initiated by substituting CDM supplemented with chemicals (Figure 1A). Cells gradually migrated from colonies and proliferated during the induction (Figure 1B). Cells were harvested after 7 days of being induced, and were subsequently sorted according to the expression of p75 (Figure 1C). We detected two peaks in p75-positive populations, designated p75<sup>low</sup> and p75<sup>high</sup>, and the efficiency of hNCC induction was evaluated based on the fraction of p75<sup>high</sup> cells.

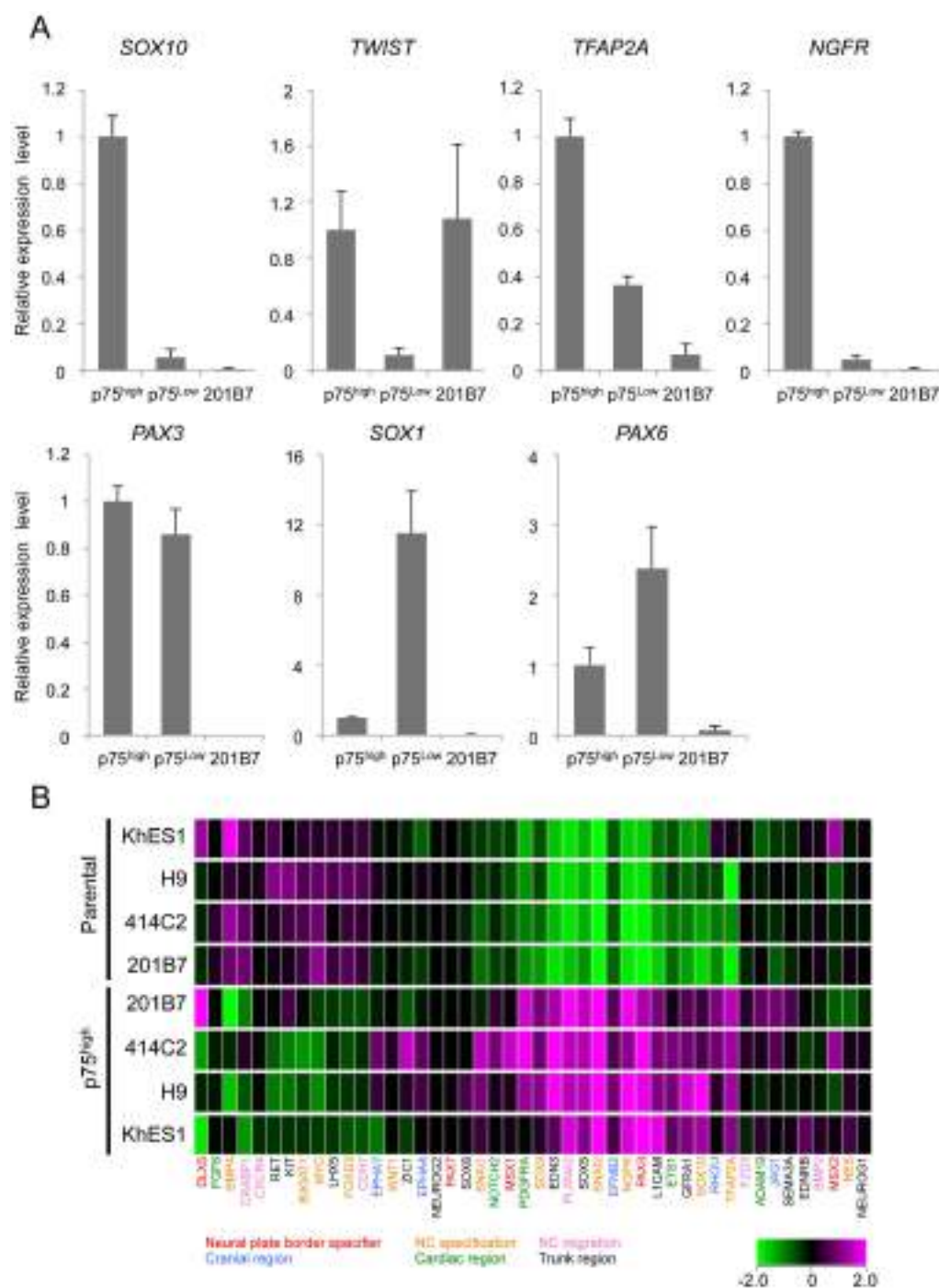


**Figure 2. Expression profiles of sorted p75<sup>high</sup> cells.** A) The expression of marker genes in sorted p75<sup>high</sup> and p75<sup>low</sup> cells. The mRNA expression of each gene was analyzed by RT-qPCR in undifferentiated 201B7 (hiPSCs) and sorted p75<sup>low</sup> and p75<sup>high</sup> cells, and was shown as a relative value using the level in sorted p75<sup>high</sup> cells as 1.0. Average  $\pm$  SD. N=3, biological triplicates. B) Clustering analyses of NCC markers in p75<sup>high</sup> populations from several hESC and hiPSC lines. Marker genes for each sub-population of NCCs were labeled using the indicated colors.

doi:10.1371/journal.pone.0112291.g002

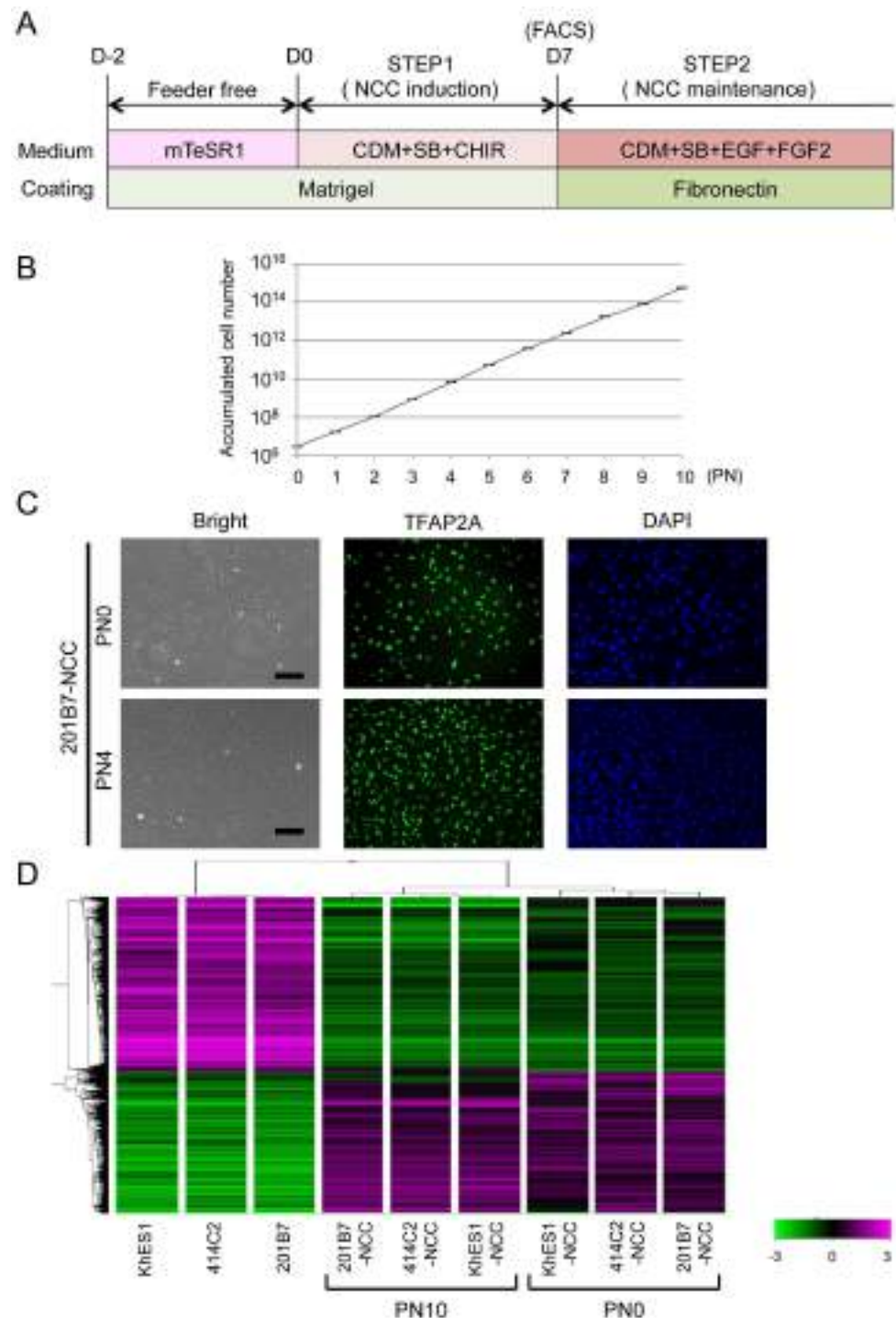


**Figure 3. Sustained expansion of hNCCs with original characteristics.** A) Schematic representation of the culture conditions. B) Growth profile of 201B7-derived hNCCs. Average  $\pm$  SD. N=3, biological triplicate. C) Phase contrast images and immunostaining of TFAP2A in 201B7-derived hNCCs at PN0 and PN4, Scale bar, 200  $\mu$ m. D) Hierarchical clustering analyses of hPSCs and hPSC-derived hNCCs at PN0 and PN10.

doi:10.1371/journal.pone.0112291.g003



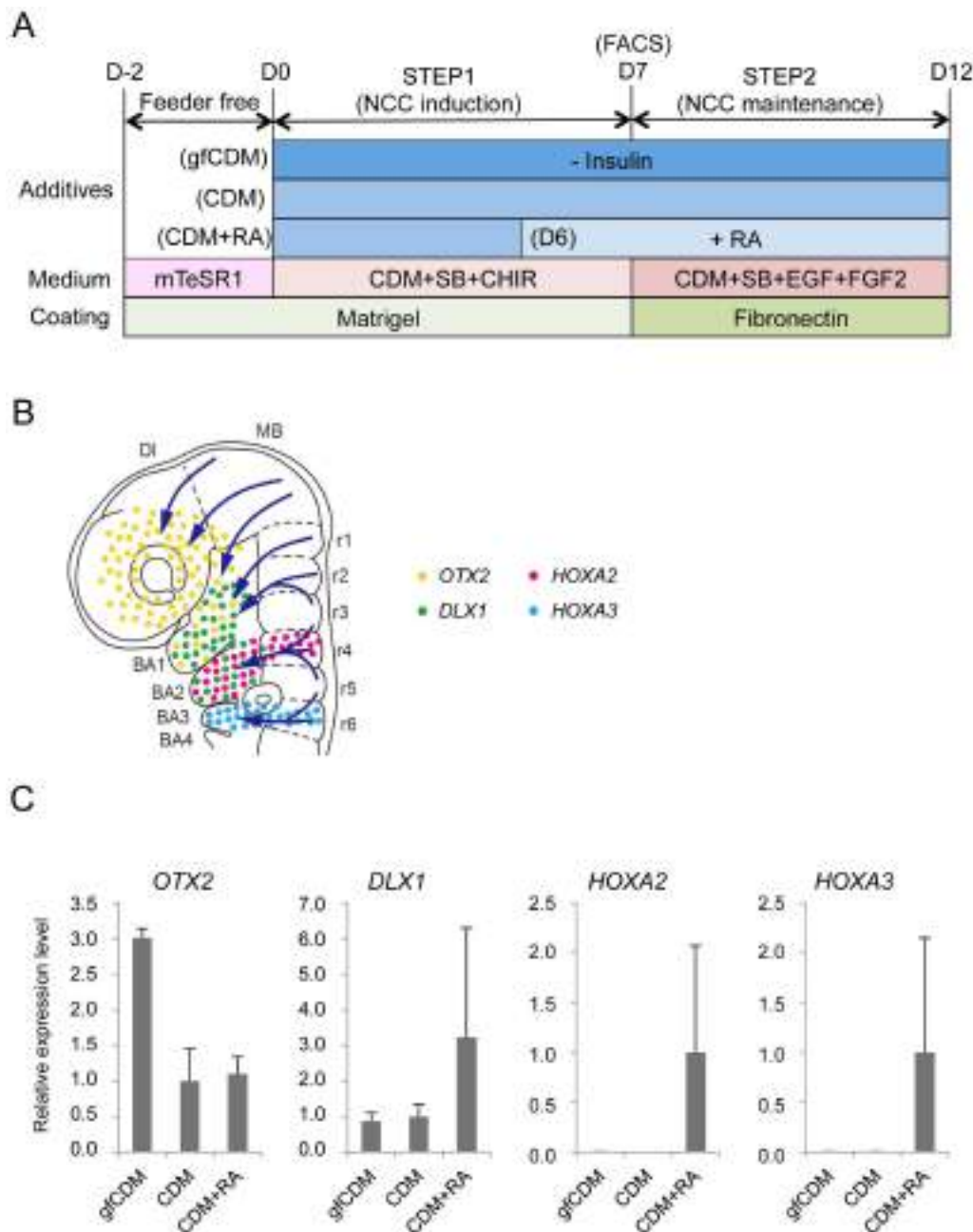


**Figure 4. Modulation of regional characteristics of hNCCs.** A) Schematic representation of culture conditions for the induction and maintenance of hNCCs. RA, retinoic acid (100 nM). B) Schematic distribution of marker-positive cells in the murine embryo. DI, diencephalon; MB, midbrain; BA1 to BA4, branchial arch 1 to branchial arch 4; r1 to r6; rhombomere 1 to rhombomere 6. C) The mRNA expression of regional specifier genes in hNCCs.  $p75^{\text{high}}$  cells were collected at the end of the hNCC induction by FACS and seeded onto fibronectin-coated dishes. RNAs were extracted when cells reached a semi-confluent state and used for RT-qPCR. The relative expression level of each gene was demonstrated using the value of cells cultured in CDM (OTX2 and DLX1) or CDM + RA (HOXA2 and HOXA3) as 1.0. Average  $\pm$  SD. N=3, biological triplicate.

doi:10.1371/journal.pone.0112291.g004

The effects of SB, which has been shown to inhibit Activin/Nodal/TGF $\beta$  signaling and induce neural cells and hNCCs from hPSCs without the help of other chemicals, were firstly evaluated [14]. In accordance with the reported data,

CDM supplemented with SB successfully delivered  $p75^{\text{high}}$  cells with a PAX6-positive neuroectoderm from 201B7 (date not shown), while the induction efficiency of  $p75^{\text{high}}$  cells was approximately 35% (0  $\mu\text{M}$  in [Figure 1C](#)). The activation of Wnt signaling was previously shown to play a key role in the induction of hNCCs [14, 15], and can be achieved using the GSK3 $\beta$  inhibitor BIO or CHIR. Therefore, we attempted to determine the most effective concentration of CHIR with a fixed concentration of SB (10  $\mu\text{M}$ ) to induce  $p75^{\text{high}}$  cells. The results obtained revealed that CHIR successfully induced  $p75^{\text{high}}$  cells in a dose-dependent manner up to 1  $\mu\text{M}$ , whereas higher concentrations of CHIR markedly inhibited the production of  $p75^{\text{high}}$  cells ([Figure 1C](#)). We finally examined the effects of BMP signaling on this induction. The addition of BMP4 markedly inhibited the production of  $p75^{\text{high}}$  cells, and these results were compatible with BMP signal inhibiting neural differentiation ([Figure S1A](#)). However, the treatment with DMH1 (10  $\mu\text{M}$ ), a specific inhibitor of SMAD1/5/8 phosphorylation, also reduced the  $p75^{\text{high}}$  fraction ([Figure S1B](#)). The inhibitory effect of DMH1 on the induction of  $p75$  was confirmed at different dosages, and other cytoplasmic (LDN193189) or extracellular (Noggin) inhibitors for BMP signaling also decreased the efficiency ([Figure S1C](#)). Therefore, the combination of SB (10  $\mu\text{M}$ ) and CHIR (1  $\mu\text{M}$ ) most effectively induced  $p75^{\text{high}}$  cells from 201B7 hiPSCs. This result was reproduced in other hPSCs such as hESCs (H9, KhES1, and KhES3) and episomal hiPSCs (414C2) ([Figure 1D](#)). Most cells outgrowing from colonies were stained with NCC markers,  $p75$  and TFAP2A, whereas the cells in colonies were positive for PAX6, a marker for the neuroectoderm ([Figure 1E](#)).

### $p75^{\text{high}}$ cells expressed early NCC markers

The expression of marker genes were compared between  $p75^{\text{high}}$  and  $p75^{\text{low}}$  cells ([Figure 2A](#)). Sorted  $p75^{\text{high}}$  cells expressed a number of genes in the early stage of NCCs, such as *SOX10*, *TWIST*, and *TFAP2A* genes. In contrast, the expression of these genes was significantly lower in the  $p75^{\text{low}}$  fraction than in  $p75^{\text{high}}$  fraction. The expression of *PAX3*, which is a marker both for NCCs and neurons, was high in both the  $p75^{\text{high}}$  and  $p75^{\text{low}}$  fractions. The expression of *PAX6* and *SOX1*, which are neural markers, was higher in the  $p75^{\text{low}}$  fraction, which is consistent with some populations of  $p75$ -negative or TFAP2A-negative cells expressing PAX6 ([Figure 1E](#)). These results indicated the relative enrichment of NCC cells in the  $p75^{\text{high}}$  cell population.

In an attempt to further characterize  $p75^{\text{high}}$  cells, genome-wide expression profiles were compared between sorted  $p75^{\text{high}}$  cells and their corresponding hPSCs using a cDNA microarray (Affymetrix Gene 1.0 ST), and we found that the overall profiles of  $p75^{\text{high}}$  cells derived from several PSCs were similar to each other ([Figure S2](#)). Based on the previous report [32], 46 genes were selected as markers for distinct NC-subpopulations and the expression level of these genes were compared between hNCCs and parental PSCs ([Figure 2B](#)). hNCCs in this study highly expressed early stage-related genes such as neural plate border specifier (*PAX3*) and NC specification (*SNAI2*, *NGFR*, *TFAP2A*, *SOX9*, and

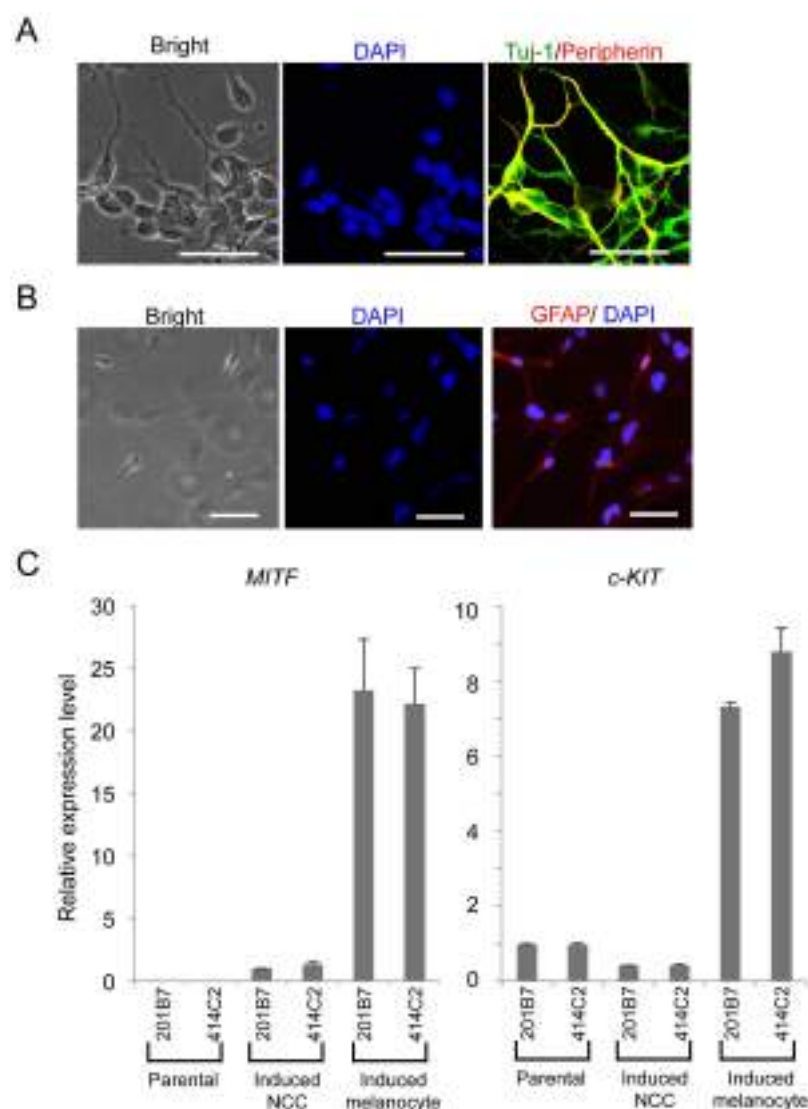


**Figure 5. Derivation of peripheral neural cells, glia, and melanocytes from hNCCs.** A) Neuronal differentiation of 201B7-derived hNCCs. Cells were stained with an antibody against peripherin (red) and Tuj-1 (green). B) The glial differentiation of 201B7-derived hNCCs. Cells were stained with an antibody against GFAP. Scale bar, 50  $\mu$ m. C) Melanocyte differentiation of 201B7-derived hNCCs. The mRNA expression levels of *MITF* and *c-KIT* genes were shown as a relative value using the value in 201B7-derived hNCCs and 201B7 as 1.0, respectively. Average  $\pm$  SD. N=3, biological triplicates.

doi:10.1371/journal.pone.0112291.g005

SOX10), but also some region-specifying genes (EFNB2 for cranial, PDGFRA for cardiac, and SOX5 for trunk region), suggesting the heterogeneous population of p75<sup>high</sup> cells, which were designated hNCCs hereafter. The profiles of the current hNCCs were compared with those of two PSC-derived NCCs, which were induced by different protocols in previous studies [15, 32] (Figure S3). Although the three types of PSC-derived NCCs all highly expressed some genes, such as SNAI2, their



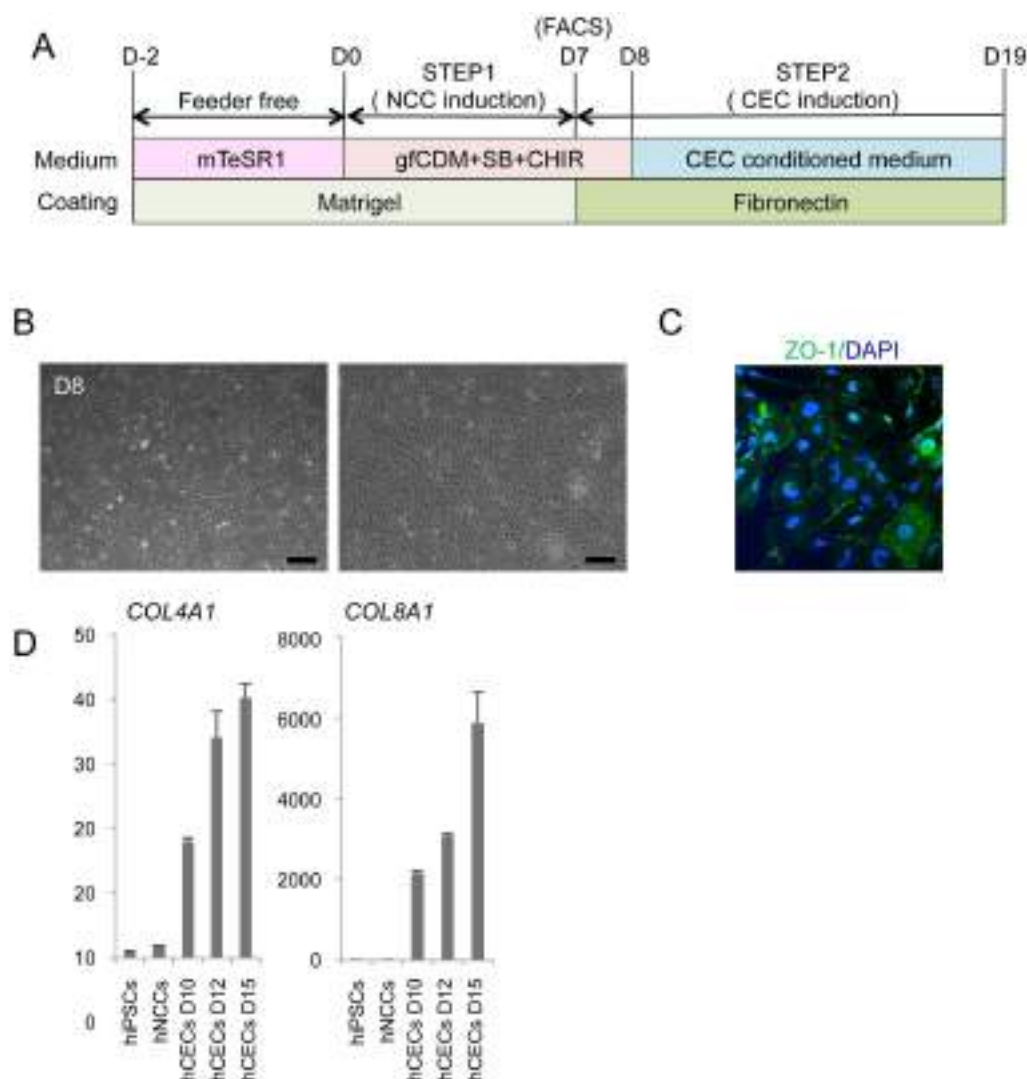


**Figure 6. Derivation of corneal endothelial cells from hNCCs.** A) Schematic protocol for the induction of corneal endothelial cells. B) Phase contrast images of cells before (D8) and after (D19) the induction. Scale bar, 200  $\mu$ m. C) The expression of ZO-1 in cells at D12. Cells were stained with an antibody against ZO-1. D) The mRNA expression of corneal endothelial cell marker genes. RNAs were extracted from cells at D10, D12, and D15. The expression level of each gene was demonstrated as a relative value using the value in human primary corneal endothelial cells as 1.0. Average  $\pm$  SD. N=3, technical triplicate. We performed this CEC induction twice and confirmed its reproducibility.

doi:10.1371/journal.pone.0112291.g006

expression profiles were considerably different, suggesting the protocol-dependent heterogeneity of PSC-derived NCCs.

### Sustained expansion of hNCCs with original characteristics

We investigated whether hNCCs could be stably expanded. The growth of hNCCs cultured in the hNCC induction medium (CDM with SB and CHIR) was very slow (data not shown). We employed a cultured condition using CDM supplemented with SB, EGF (20 ng/ml), and FGF2 (20 ng/ml) based on the

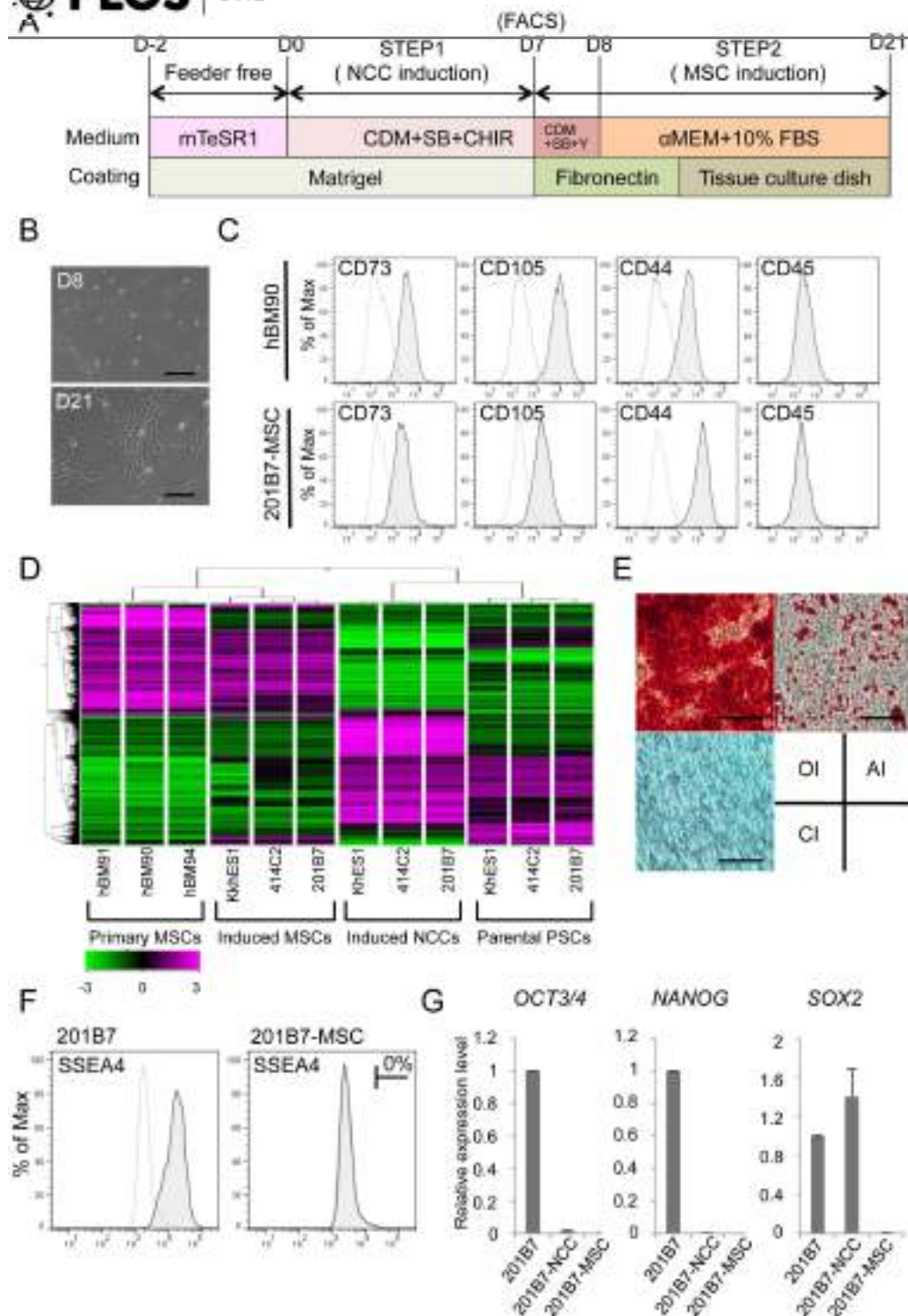


**Figure 7. Derivation of hMSCs from hNCCs.** A) Schematic protocol for the induction of hMSCs. B) Phase contrast images of cells before (D8) and after (D21) the induction. Scale bar, 200  $\mu$ m. C) Expression of surface markers in hBM-MSCs (hBM90) and 201B7-derived MSCs (201B7-MSC). D) Hierarchical clustering analyses by genome-wide gene expression profiles. RNAs were extracted from hBM-MSCs (BM90, BM91 and BM94), induced-MSCs, and the corresponding hNCCs and hPSCs. E) Differentiation properties of induced-MSCs. The induction for osteogenic (OI), chondrogenic (CI), and adipogenic (AI) lineages was performed as described in the Materials and Methods section and evaluated by Alizarin Red staining (OI), Alcian Blue staining (CI), and Oil Red O staining (AI), respectively. Scale bar, 100  $\mu$ m. F) Population of SSEA4-positive cells. G) The expression levels of pluripotent markers (OCT3/4, NANOG and SOX2) in hPSCs, hNCCs, and hMSCs. Average  $\pm$  SD. N=3, biological triplicates.

doi:10.1371/journal.pone.0112291.g007

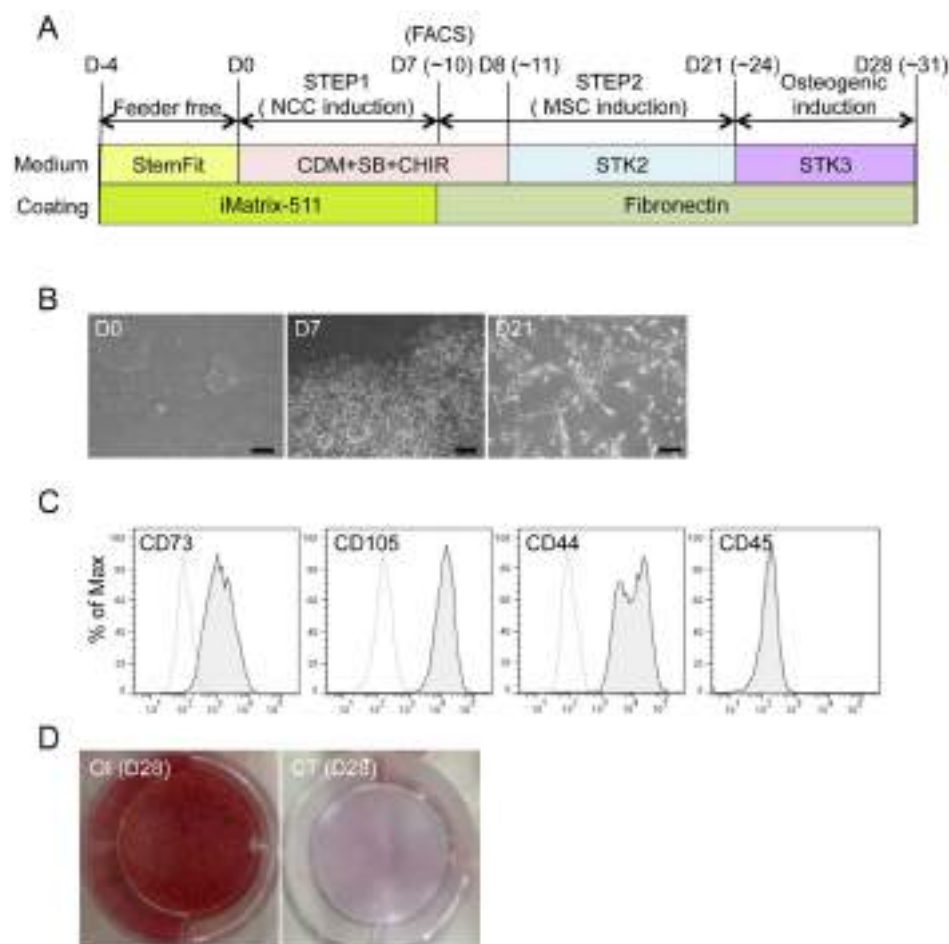


**Figure 8. Derivation of hMSCs from hNCCs under defined culture conditions.** A) Schematic protocol for the induction of hMSCs from hNCCs under defined culture conditions. B) Phase contrast images of cells 0, 7, and 21 days after the hNCC and hMSC induction, respectively. Scale bar, 200  $\mu$ m. C) Expression of hMSC-related surface markers in hMSCs induced under defined culture conditions. D) Osteogenic differentiation (OI) properties of hMSCs induced under defined culture conditions. hMSCs were cultured during the induction period in STK2 as a control.

doi:10.1371/journal.pone.0112291.g008

findings of previous studies [33], and consequently observed marked improvements in growth and the stable proliferation of hNCCs even after 10 passages (Figures 3A, B). The expanded hNCCs maintained their original cell morphology and all cells expressing NCC markers, such as TFAP2A (Figure 3C). The global gene expression profiles of hNCCs after prolonged expansion (PN10) were similar to those of early-passage cells (PN0) (Figure S4A and S4B, correlation coefficient = 0.96 to 0.98) and markedly different from those of original hPSCs (Figures 3D and S4C).



## Modulation of the characteristics of hNCCs by insulin and retinoic acid (RA)

The results of the microarray analyses revealed that induced hNCCs expressed some genes characteristic to cranial NCCs (high for *OTX2* and *DLX1*; low for *HOXA2* and *HOXA3*) (date not shown). A previous study demonstrated that the depletion of insulin from CDM (growth-factor free CDM; hereafter referred to as gfCDM) induced a more anterior neuroectoderm (rostral hypothalamic progenitor-like cells), while retinoic acid (RA) exhibited posteriorizing activity [15]. Therefore, we compared the expression of regional markers in hNCCs cultured with gfCDM, CDM, and CDM with RA (100 nM) (Figure 4A). As expected, the expression of *OTX2*, a marker for mesencephalic NCCs (Figure 4B) [34], was slightly higher under the gfCDM condition than under the CDM condition (Figure 4C). The *DLX1* gene, a marker for first and second branchial arch NCCs (Figure 4B) [35], was expressed in cells cultured under all conditions, and was the highest in CDM with the RA condition (Figure 4C). The expression of the *HOXA2* and *HOXA3* genes, which are markers of the second and third branchial arches, was negligible under the gfCDM and CDM conditions (Figures 4B, C) [36, 37]. Taken together, these results indicated that the regional identities of hNCCs could be modulated by exogenous signals including insulin and RA.

## Derivation of peripheral neurons, glia, and melanocytes from hNCCs

We next examined the differentiation potentials of induced hNCCs. Neuronal differentiation was initiated by sphere formation and promoted by culture media containing a mixture of factors (BDNF, GDNF, NGF, and NT-3). Cells expressed  $\beta$ -tubulin and peripherin after 14 days, which indicated differentiation into peripheral neurons (Figure 5A). Further cultivation under the same conditions (4 to 6 weeks) promoted the glial differentiation of hNCCs (Figure 5B).

Melanocytes are well-known derivatives of NCCs. Using a previously described method that included CHIR, EDN3, and BMP4 [15, 38], induced hNCCs expressed microphthalmia-associated transcription factor (*MITF*) and *c-KIT*, markers for melanocytes (Figure 5C). These differentiation properties were compatible with those of NCCs *in vivo*.

## Derivation of corneal endothelial cells from hNCCs

Cranial NCCs have been shown to exhibit the ability to differentiate into corneal endothelial cells *in vivo* [39, 40]. Therefore, we examined whether hNCCs grown in gfCDM, which preferentially expressed more anterior NCC markers (Figures 4B, C), could differentiate into cells harboring the characteristics of corneal endothelial cells. When 201B7-derived hNCCs were cultured in the conditioned medium of corneal endothelial cells for twelve days (Figure 6A), cells changed their morphology into that of polygonal corneal endothelial-like cells (

[Figure 6B](#)) and started to express the corneal endothelial marker, ZO-1 ([Figure 6C](#)). Descemet's membrane is known to consist of collagen type 4 and collagen type 8, which are derived from the corneal endothelium [41]. The mRNA expression of the *COL4A1* and *COL8A1* genes was confirmed in induced endothelial-like cells ([Figure 6D](#)). These results strongly suggested that the hNCCs induced in this study possessed the characteristics of cranial NCCs, which exhibit the potential to differentiate into cranial NCC-derived structures.

### Derivation of hMSCs from hNCCs

Cranial NCCs also have differentiation properties toward mesenchymal cells, which construct the cranio-facial skeleton, and may be referred as MSCs [3]. In order to derivate hMSCs from hNCCs, the culture medium was changed from that for hNCC to  $\alpha$ MEM with 10% FBS ([Figure 7A](#)), which we used previously for human bone marrow-derived MSCs (hBM-MSCs) [24]. Through the induction of hMSCs, the expression of *NGFR* and *SOX10* reduced rapidly within 48 hours (PN0) of the medium change, while that of *PAX3* and *TFAP2A* reduced gradually until passage 3 ([Figure S5A](#)). Conversely, the expression of MSC markers (*CD73*, *CD105*, and *CD44*) increased rapidly within 48 hours, reached a maximum by passage number 2, and maintained their expression at a level comparable to that in BMMSCs ([Figure S5B](#)). These results indicated that the transition from NCCs to MSCs was gradual during passage number three. Cells passaged three times in the medium showed a typical fibroblastic morphology similar to that of hMSCs ([Figure 7B](#)), and expressed surface markers for hMSCs (positive for *CD73*, *CD105*, and *CD44*, and negative for *CD45*) ([Figure 7C](#)). Microarray analyses revealed that hNCC-derived MSCs had a global expression pattern similar to that of primary hBM-MSCs ([Figure 7D](#)). Differentiation properties toward osteogenic, chondrogenic, and adipogenic lineages are one of the criteria required for MSCs [42], which were clearly confirmed in hNCC-derived MSCs ([Figure 7E](#)). FACS analysis showed that there was no SSEA4-positive cells ([Figure 7F](#)) and the expression of PSC marker genes was below detectable levels ([Figure 7G](#)).

### Derivation of osteogenic cells from hiPSCs under defined culture conditions

We determined the feasibility of inducing terminally differentiated cells from iPSCs under defined culture conditions ([Figure 8](#)). 987A3 hiPSCs were used as the initial material, which have been generated and maintained under feeder-free and xeno-free conditions [21]. Cells were dissociated into single cells, seeded on iMatrix-coated dishes ( $0.83\text{--}1.35\text{ cells/cm}^2$ ), and cultured with StemFit medium for five days. hNCCs were then induced for seven to ten days ([Figure 8A](#)). The efficiency of hNCC induction under these conditions was  $40.9 \pm 5.5\%$  ( $\pm$  SD,  $N=3$ , biological triplicate). The induction of hMSCs was performed using CDM for MSCs (STK2) instead of  $\alpha$ MEM/10% FBS ([Figure 8A](#)). After several passages of hNCCs in STK2, the morphology of cells changed from cuboidal to fibroblastic,

similar to that of hBM-MSCs (Figure 8B). The expression patterns of surface markers were compatible with those of hMSCs (positive for CD73, CD105, and CD44, and negative for CD45) (Figure 8C) and the differentiation properties for osteogenic, chondrogenic, and adipogenic lineages were confirmed when the standard FBS-containing induction medium was used (Figure S6). Osteogenic differentiation was also confirmed using the chemically-defined osteogenic medium (STK3) (Figure 8D). These results indicated that all steps from iPSC to osteogenic cells could be performed under defined culture conditions.

## Discussion

In the present study, we developed a simple and efficient induction method for hNCCs from hPSCs. The induction efficiency of this method was high (70–80%) irrespective with the type of hPSC. The induced hNCCs exhibited the cranial NCC characters under maintenance culture conditions, while further treatment with insulin and RA marginally posteriorized hNCCs. Consistent with the expression of cranial NCC markers, induced hNCCs could differentiate into corneal endothelial cells, which is a characteristic of cranial NCCs.

Our protocol was independent of the BMP signal. In our protocol, DMH1, a specific BMP inhibitor, clearly attenuated the induction efficiency of the p75<sup>high</sup> fraction (Figure S1). This result clearly contradicted the findings of previous studies (no effect [14] or increased efficiency [15]). The marked differences in the findings of these studies may be attributed to the seeding density used at the beginning of induction. The seeding density of our protocol was approximately 2–4 clumps/cm<sup>2</sup> (approximately 20 cells/cm<sup>2</sup>), while other studies used  $1 \times 10^4$  cells/cm<sup>2</sup> [26]. Both CNS and neural crest fates were previously observed when cells were seeded at a low density, while CNS cells primarily formed at a high density [43]. In accordance with these findings, the efficiency of the NCC induction was markedly decreased if clumps were seeded at a higher density (data not shown). The high density of hNCCs may have exaggerated local BMP signaling secreted from the hNCCs themselves. Therefore, we combined high density seeding with the BMP inhibitor treatment; however, the efficiency was still low (data not shown). Based on these results, we could not account for the differences between our protocol and those of previous studies.

In order to compare the hNCCs in this study with those in previous studies, we analyzed gene expression profiles of hNCCs published previously. The comparison of the relative induction levels of NCC specific genes revealed that hNCCs differentiated by our protocol and previous studies showed similarities in some aspects, but overall profiles were different from each other (Figure S3). These results indicated that induction protocols reported in this study and in the previous studies induced different subset of hNCCs.

Induced hNCCs exhibited differentiation properties for multiple cell lineages including peripheral neurons, glial cells, melanocytes, and corneal endothelial cells, and also delivered hMSCs that further differentiated into osteogenic,



chondrogenic, and adipogenic cells. These properties are compatible with NCCs being multipotent stem cells [3]. However, clonal analyses are indispensable for confirming the stemness of induced hNCCs. Previous clonal analyses revealed that 63–65% of the hNCC clones could differentiate into multi-lineage cells positive for markers of neurons, glial cells, and smooth muscle cells [43, 44], suggesting that hNCCs induced from hPSCs were multipotent on the clonal level. Although stemness has yet to be investigated in this study, induced hNCCs in this protocol will be a promising cell source for various types of research.

Human diseases that have been related to the development of hNCCs include Hirschsprung's disease, DiGeorge syndrome, Waardenburg syndrome, Charcot-Marie-tooth disease, Hermansky-Pudlak syndrome, familial dysautonomia, Chediak-Higashi syndrome, and CHARGE syndrome [45, 46]. hNCCs containing the mutations responsible for these diseases can be induced from hiPSCs established from the respective patients; therefore, this will be a powerful tool for creating *in vitro* disease models that can contribute to a more detailed understanding of the pathogenesis of NCC disorders and also to the development of novel therapeutic modalities [15]. In addition, hNCCs have been shown to be the cell-of-origin of some cancers such as neuroblastoma [47], which indicates that hNCCs can be used in *in vitro* transformation experiments. We have already confirmed that the survival rate of freeze-stocked hNCCs was satisfactory and the freeze and thaw process had no impact on the growth and differentiation properties of these cells (data not shown). These are favorable features for a material in research because it is important to use cells of the same quality in order to evaluate reproducibility.

Induced hNCCs-derivatives can also be used for cell therapy. In this regard, hNCC-derived hMSCs will be a very useful material. hMSCs have been used in a wide range of regenerative medicines, and promising results have been reported in some cases [48, 49]. In contrast with the advances reported in clinical applications, many issues related to the biology of hMSCs have yet to be investigated, one of which is the cell-of-origin of hMSCs. hNCCs may be the precursors of hMSCs based on the finding that craniofacial skeletal tissues are derived from NCCs [50]. This has also been supported in lineage tracing experiments using P0-cre mice [51, 52]. Current sources of hMSCs include bone marrow, fat tissue, synovium, and umbilical cord; however, it remains unclear whether NCC-derived cells exist in all of these adult tissues and serve as the source of hMSCs. A comparison between hNCC-derived MSCs and somatic tissue-derived hMSCs may provide more information related to this issue.

One of the limitations of current hMSCs is their limited proliferative activity, which may pose problems in their application to conditions requiring a large amount of cells. This can be overcome if hNCC-derived MSCs are used because hNCCs can be induced from hPSCs, which have unlimited proliferative activity. Two issues are important for this application. One is to be free from infectious substances that may be derived from animal materials. Using iPSCs generated and maintained under feeder-free and xeno-free conditions, we successfully induced hNCCs and hMSCs with minimum animal material (BSA in CDM) (Figure 8A).

Furthermore, we generated terminally differentiated cells (osteogenic cells) from these MSCs under chemically defined media. To the best of our knowledge, this is the first study to demonstrate the induction of osteogenic cells under feeder-free and serum-free conditions from PSCs. The other concern relates to the contamination of undifferentiated cells, particularly parental hPSCs, which may lead to serious conditions such as the formation of malignant tumors [53]. We confirmed that hNCC-derived hMSCs were free from SSEA4-expressing cells and the expression of PSC-marker genes was below detectable levels (Figures 7F, G). Although more precise and meticulous analyses are required to prove the safety of these cells, the results of the present study have provided evidence to promote the use of hNCC-derived hMSCs for cell therapy.

## Supporting Information

**Figure S1. Effect of the BMP signal on the induction of p75<sup>high</sup> cells.** hiPSCs (201B7) were treated in NCC induction media with BMP4 (10 ng/ml) (A) or DMH1 (10  $\mu$ M) (B), and the fraction of p75-positive cells was analyzed by FACS. C) Effects of BMP signal inhibitors on the induction of p75<sup>high</sup> cells. 201B7 cells were treated with each BMP inhibitor at the indicated dosage, and the fraction of p75-positive cells was analyzed by FACS.

[doi:10.1371/journal.pone.0112291.s001](https://doi.org/10.1371/journal.pone.0112291.s001) (TIFF)

**Figure S2. Global comparison of the expressions of genes between PSCs and p75<sup>high</sup> cells.** A) A volcano plot showing the P value for differences in the expression of each gene between the average of PSC lines (H9, KhES1, 414C2, and 201B7) and the average of corresponding p75<sup>high</sup> cells. A total of 562 entities downregulated and 447 entities upregulated in p75<sup>high</sup> cells were identified as a differentially expressed gene set. B) Heat map analyses revealed global similarities among hNCCs derived from each PSC line.

[doi:10.1371/journal.pone.0112291.s002](https://doi.org/10.1371/journal.pone.0112291.s002) (TIFF)

**Figure S3. Expression of NCC marker genes in induced NCCs from PSCs.** The induction ratio of NCC markers relative to a corresponding pluripotent baseline was demonstrated in each induced NCC. iPS NCCs, GSE44727.

WA09\_NC\_Day11, 45223. Marker genes for each sub-population of NCC were labeled using the indicated colors.

[doi:10.1371/journal.pone.0112291.s003](https://doi.org/10.1371/journal.pone.0112291.s003) (TIFF)

**Figure S4. Comparison of gene expression profiles between hNCCs at different passages by scatter plotting.** RNAs were extracted from hNCCs derived from 201B7 (A) and KhES1 (B) at different passages (PN0, PN4 and PN10), and analyzed using microarrays. C) Correlation coefficient analysis was performed using these data.

[doi:10.1371/journal.pone.0112291.s004](https://doi.org/10.1371/journal.pone.0112291.s004) (TIFF)

**Figure S5. The expression of markers for hNCCs and hMSCs in each passage.** A gradual transition from hNCCs to hMSCs was observed in hNCC markers (A)

and hMSC markers (B). Average  $\pm$  SD. N=3, biological triplicates. Regarding BMSCs, cDNA was prepared from the bone marrow stromal cells of four healthy donors (BM25, 26, 34, and 107), and the average was presented as BMSCs in each graph.

[doi:10.1371/journal.pone.0112291.s005](https://doi.org/10.1371/journal.pone.0112291.s005) (TIFF)

**Figure S6. Osteogenic-, chondrogenic-, adipogenic induction from feeder-free hiPSCs through hNCC-derived hMSCs.** Differentiation properties of hNCC-MSCs. The induction for osteogenic (OI), chondrogenic (CI), and adipogenic (AI) lineages was performed as described in the Materials and Methods section and evaluated by Alizarin Red staining (OI), Alcian Blue staining (CI), and Oil Red O staining (AI), respectively. Scale bar, 200  $\mu$ m.

[doi:10.1371/journal.pone.0112291.s006](https://doi.org/10.1371/journal.pone.0112291.s006) (TIFF)

**Table S1.** Information of primary antibodies used in this study.

[doi:10.1371/journal.pone.0112291.s007](https://doi.org/10.1371/journal.pone.0112291.s007) (TIF)

**Table S2.** Information of PCR primers used in this study.

[doi:10.1371/journal.pone.0112291.s008](https://doi.org/10.1371/journal.pone.0112291.s008) (TIF)

## Acknowledgments

We thank Dr. H. Tanaka for the kind advice and help in the corneal endothelium induction, M. Shibata, K.R. Komatsu, and J. Nakai for their technical assistance, and T. Kato, Y. Jin, S. Tamaki, and S. Hinenno for their support during this study.

## Author Contributions

Conceived and designed the experiments: MF NK TN MS TO SK MU MI JT. Performed the experiments: MF YN KK KS SN YM TY NO TS MI. Analyzed the data: MF YN KK NK MU TS MI. Contributed reagents/materials/analysis tools: MN TY KU TH. Wrote the paper: MF YN TY MU MI JT.

## References

1. Liu Z, Tang Y, Lu S, Zhou J, Du Z, et al. (2013) The tumorigenicity of iPS cells and their differentiated derivatives. *J Cell Mol Med* 17: 782–791.
2. Le Douarin NM, Dupin E (2003) Multipotentiality of the neural crest. *Curr Opin Genet Dev* 13: 529–536.
3. Sauka-Spengler T, Bronner-Fraser M (2008) A gene regulatory network orchestrates neural crest formation. *Nat Rev Mol Cell Biol* 9: 557–568.
4. Kalcheim C, Burstyn-Cohen T (2005) Early stages of neural crest ontogeny: formation and regulation of cell delamination. *Int J Dev Biol* 49: 105–116.
5. Kalcheim C (2000) Mechanisms of early neural crest development: from cell specification to migration. *Int Rev Cytol* 200: 143–196.
6. Vincent SD, Buckingham ME (2010) How to make a heart: the origin and regulation of cardiac progenitor cells. *Curr Top Dev Biol* 90: 1–41.



7. **Neirinckx V, Coste C, Rogister B, Wislet-Gendebien S** (2013) Concise review: adult mesenchymal stem cells, adult neural crest stem cells, and therapy of neurological pathologies: a state of play. *Stem Cells Transl Med* 2: 284–296.
8. **Neirinckx V, Marquet A, Coste C, Rogister B, Wislet-Gendebien S** (2013) Adult bone marrow neural crest stem cells and mesenchymal stem cells are not able to replace lost neurons in acute MPTP-lesioned mice. *PLoS One* 8: e64723.
9. **Giuliani M, Oudrhiri N, Noman ZM, Vernochet A, Chouaib S, et al.** (2011) Human mesenchymal stem cells derived from induced pluripotent stem cells down-regulate NK-cell cytolytic machinery. *Blood* 118: 3254–3262.
10. **Villa-Diaz LG, Brown SE, Liu Y, Ross AM, Lahann J, et al.** (2012) Derivation of mesenchymal stem cells from human induced pluripotent stem cells cultured on synthetic substrates. *Stem Cells* 30: 1174–1181.
11. **Liu Q, Spusta SC, Mi R, Lassiter RN, Stark MR, et al.** (2012) Human neural crest stem cells derived from human ESCs and induced pluripotent stem cells: induction, maintenance, and differentiation into functional schwann cells. *Stem Cells Transl Med* 1: 266–278.
12. **Chimge NO, Bayarsaihan D** (2010) Generation of neural crest progenitors from human embryonic stem cells. *J Exp Zool B Mol Dev Evol* 314: 95–103.
13. **Milet C, Monsoro-Burq AH** (2012) Embryonic stem cell strategies to explore neural crest development in human embryos. *Dev Biol* 366: 96–99.
14. **Menendez L, Yatskievych TA, Antin PB, Dalton S** (2011) Wnt signaling and a Smad pathway blockade direct the differentiation of human pluripotent stem cells to multipotent neural crest cells. *Proc Natl Acad Sci U S A* 108: 19240–19245.
15. **Mica Y, Lee G, Chambers SM, Tomishima MJ, Studer L** (2013) Modeling neural crest induction, melanocyte specification, and disease-related pigmentation defects in hESCs and patient-specific iPSCs. *Cell Rep* 3: 1140–1152.
16. **Suemori H, Yasuchika K, Hasegawa K, Fujioka T, Tsuneyoshi N, et al.** (2006) Efficient establishment of human embryonic stem cell lines and long-term maintenance with stable karyotype by enzymatic bulk passage. *Biochem Biophys Res Commun* 345: 926–932.
17. **Amit M, Carpenter MK, Inokuma MS, Chiu CP, Harris CP, et al.** (2000) Clonally derived human embryonic stem cell lines maintain pluripotency and proliferative potential for prolonged periods of culture. *Dev Biol* 227: 271–278.
18. **Okita K, Matsumura Y, Sato Y, Okada A, Morizane A, et al.** (2011) A more efficient method to generate integration-free human iPS cells. *Nat Methods* 8: 409–412.
19. **Takahashi K, Tanabe K, Ohnuki M, Narita M, Ichisaka T, et al.** (2007) Induction of pluripotent stem cells from adult human fibroblasts by defined factors. *Cell* 131: 861–872.
20. **McMahon AP, Bradley A** (1990) The Wnt-1 (int-1) proto-oncogene is required for development of a large region of the mouse brain. *Cell* 62: 1073–1085.
21. **Nakagawa M, Taniguchi Y, Senda S, Takizawa N, Ichisaka T, et al.** (2014) A novel efficient feeder-free culture system for the derivation of human induced pluripotent stem cells. *Sci Rep* 4: 3594.
22. **Nasu A, Ikeya M, Yamamoto T, Watanabe A, Jin Y, et al.** (2013) Genetically matched human iPS cells reveal that propensity for cartilage and bone differentiation differs with clones, not cell type of origin. *PLoS One* 8: e53771.
23. **Wataya T, Ando S, Muguruma K, Ikeda H, Watanabe K, et al.** (2008) Minimization of exogenous signals in ES cell culture induces rostral hypothalamic differentiation. *Proc Natl Acad Sci U S A* 105: 11796–11801.
24. **Colleoni S, Galli C, Giannelli SG, Armentero MT, Blandini F, et al.** (2010) Long-term culture and differentiation of CNS precursors derived from anterior human neural rosettes following exposure to ventralizing factors. *Exp Cell Res* 316: 1148–1158.
25. **James MJ, Jarvinen E, Wang XP, Thesleff I** (2006) Different roles of Runx2 during early neural crest-derived bone and tooth development. *J Bone Miner Res* 21: 1034–1044.
26. **Lee G, Chambers SM, Tomishima MJ, Studer L** (2010) Derivation of neural crest cells from human pluripotent stem cells. *Nat Protoc* 5: 688–701.

27. Ohta S, Imaizumi Y, Okada Y, Akamatsu W, Kuwahara R, et al. (2011) Generation of human melanocytes from induced pluripotent stem cells. *PLoS One* 6: e16182.
28. Fang D, Leishear K, Nguyen TK, Finko R, Cai K, et al. (2006) Defining the conditions for the generation of melanocytes from human embryonic stem cells. *Stem Cells* 24: 1668–1677.
29. Ju C, Zhang K, Wu X (2012) Derivation of corneal endothelial cell-like cells from rat neural crest cells in vitro. *PLoS One* 7: e42378.
30. Umeda K, Zhao J, Simmons P, Stanley E, Elefanty A, et al. (2012) Human chondrogenic paraxial mesoderm, directed specification and prospective isolation from pluripotent stem cells. *Sci Rep* 2: 455.
31. Okamoto T, Aoyama T, Nakayama T, Nakamata T, Hosaka T, et al. (2002) Clonal heterogeneity in differentiation potential of immortalized human mesenchymal stem cells. *Biochem Biophys Res Commun* 295: 354–361.
32. Kreitzer FR, Salomonis N, Sheehan A, Huang M, Park JS, et al. (2013) A robust method to derive functional neural crest cells from human pluripotent stem cells. *Am J Stem Cells* 2: 119–131.
33. Lee G, Ramirez CN, Kim H, Zeltner N, Liu B, et al. (2012) Large-scale screening using familial dysautonomia induced pluripotent stem cells identifies compounds that rescue IKBKAP expression. *Nat Biotechnol* 30: 1244–1248.
34. Kimura C, Takeda N, Suzuki M, Oshimura M, Aizawa S, et al. (1997) Cis-acting elements conserved between mouse and pufferfish *Otx2* genes govern the expression in mesencephalic neural crest cells. *Development* 124: 3929–3941.
35. Qiu M, Bulfone A, Ghattas I, Meneses JJ, Christensen L, et al. (1997) Role of the *Dlx* homeobox genes in proximodistal patterning of the branchial arches: mutations of *Dlx-1*, *Dlx-2*, and *Dlx-1* and *-2* alter morphogenesis of proximal skeletal and soft tissue structures derived from the first and second arches. *Dev Biol* 185: 165–184.
36. Manley NR, Capecchi MR (1995) The role of *Hoxa-3* in mouse thymus and thyroid development. *Development* 121: 1989–2003.
37. Liu Z, Yu S, Manley NR (2007) *Gcm2* is required for the differentiation and survival of parathyroid precursor cells in the parathyroid/thymus primordia. *Dev Biol* 305: 333–346.
38. Motohashi T, Aoki H, Yoshimura N, Kunisada T (2006) Induction of melanocytes from embryonic stem cells and their therapeutic potential. *Pigment Cell Res* 19: 284–289.
39. Johnston MC, Noden DM, Hazelton RD, Coulombre JL, Coulombre AJ (1979) Origins of avian ocular and periocular tissues. *Exp Eye Res* 29: 27–43.
40. Trainor PA, Tam PP (1995) Cranial paraxial mesoderm and neural crest cells of the mouse embryo: co-distribution in the craniofacial mesenchyme but distinct segregation in branchial arches. *Development* 121: 2569–2582.
41. Fitch JM, Birk DE, Linsenmayer C, Linsenmayer TF (1990) The spatial organization of Descemet's membrane-associated type IV collagen in the avian cornea. *J Cell Biol* 110: 1457–1468.
42. De Schauwer C, Meyer E, Van de Walle GR, Van Soom A (2011) Markers of stemness in equine mesenchymal stem cells: a plea for uniformity. *Theriogenology* 75: 1431–1443.
43. Lee G, Kim H, Elkabetz Y, Al Shamy G, Panagiotakos G, et al. (2007) Isolation and directed differentiation of neural crest stem cells derived from human embryonic stem cells. *Nat Biotechnol* 25: 1468–1475.
44. Curchoe CL, Maurer J, McKeown SJ, Cattarossi G, Cimadamore F, et al. (2010) Early acquisition of neural crest competence during hESCs neuralization. *PLoS One* 5: e13890.
45. Bajpai R, Chen DA, Rada-Iglesias A, Zhang J, Xiong Y, et al. (2010) *CHD7* cooperates with PBAF to control multipotent neural crest formation. *Nature* 463: 958–962.
46. Lee G, Papapetrou EP, Kim H, Chambers SM, Tomishima MJ, et al. (2009) Modelling pathogenesis and treatment of familial dysautonomia using patient-specific iPSCs. *Nature* 461: 402–406.
47. Jiang M, Stanke J, Lahti JM (2011) The connections between neural crest development and neuroblastoma. *Curr Top Dev Biol* 94: 77–127.
48. Caplan AI (2007) Adult mesenchymal stem cells for tissue engineering versus regenerative medicine. *J Cell Physiol* 213: 341–347.

49. **Silva NA, Sousa N, Reis RL, Salgado AJ** (2013) From basics to clinical: A comprehensive review on spinal cord injury. *Prog Neurobiol*.
50. **Helms JA, Schneider RA** (2003) Cranial skeletal biology. *Nature* 423: 326–331.
51. **Morikawa S, Mabuchi Y, Niibe K, Suzuki S, Nagoshi N, et al.** (2009) Development of mesenchymal stem cells partially originate from the neural crest. *Biochem Biophys Res Commun* 379: 1114–1119.
52. **Takashima Y, Era T, Nakao K, Kondo S, Kasuga M, et al.** (2007) Neuroepithelial cells supply an initial transient wave of MSC differentiation. *Cell* 129: 1377–1388.
53. **Cai J, Yang M, Poremsky E, Kidd S, Schneider JS, et al.** (2010) Dopaminergic neurons derived from human induced pluripotent stem cells survive and integrate into 6-OHDA-lesioned rats. *Stem Cells Dev* 19: 1017–1023.

# Ocular Surface Reconstruction With a Tissue-Engineered Nasal Mucosal Epithelial Cell Sheet for the Treatment of Severe Ocular Surface Diseases

MASAKAZU KOBAYASHI,<sup>a</sup> TAKAHIRO NAKAMURA,<sup>b,c</sup> MAKOTO YASUDA,<sup>d</sup> YUIKO HATA,<sup>c</sup> SHOKI OKURA,<sup>a</sup> MIYU IWAMOTO,<sup>a</sup> MAHO NAGATA,<sup>c</sup> NIGEL J. FULLWOOD,<sup>e</sup> NORIKO KOIZUMI,<sup>a,c</sup> YASUO HISA,<sup>d</sup> SHIGERU KINOSHITA<sup>c</sup>

**Key Words.** Nasal mucosa • Ocular surface • Dry eye • Goblet cell • Mucin

## ABSTRACT

Severe ocular surface diseases (OSDs) with severe dry eye can be devastating and are currently some of the most challenging eye disorders to treat. To investigate the feasibility of using an autologous tissue-engineered cultivated nasal mucosal epithelial cell sheet (CNMES) for ocular surface reconstruction, we developed a novel technique for the culture of nasal mucosal epithelial cells expanded *ex vivo* from biopsy-derived human nasal mucosal tissues. After the protocol, the CNMESs had 4–5 layers of stratified, well-differentiated cells, and we successfully generated cultured epithelial sheets, including numerous goblet cells. Immunohistochemistry confirmed the presence of keratins 3, 4, and 13; mucins 1, 16, and 5AC; cell junction and basement membrane assembly proteins; and stem/progenitor cell marker p75 in the CNMESs. We then transplanted the CNMESs onto the ocular surfaces of rabbits and confirmed the survival of this tissue, including the goblet cells, up to 2 weeks. The present report describes an attempt to overcome the problems of treating severe OSDs with the most severe dry eye by treating them using tissue-engineered CNMESs to supply functional goblet cells and to stabilize and reconstruct the ocular surface. The present study is a first step toward assessing the use of tissue-engineered goblet-cell transplantation of nonocular surface origin for ocular surface reconstruction. *STEM CELLS TRANSLATIONAL MEDICINE* 2015;4:99–109

## INTRODUCTION

In cases of severe ocular surface disease (OSD), such as Stevens-Johnson syndrome (SJS) and ocular cicatricial pemphigoid (OCP), corneal epithelial stem cells are destroyed and the neighboring conjunctival epithelial cells (ECs) invade onto the corneal surface, resulting in chronic inflammation, stromal scarring, and neovascularization that ultimately leads to pathologic keratinization [1, 2]. In most such cases, a definite observable loss occurs of mucin-producing goblet cells from the ocular surface, severely affecting ocular-surface homeostasis and leading to severe dry eye [1–4].

To date, many studies have focused on the establishment of a surgical treatment of severe OSDs [5–10]. For such patients, cultivated corneal, conjunctival, and oral epithelial stem cell transplantation has been developed to improve the postoperative outcomes of ocular surface reconstruction [11–15]. When these surgical modalities are used, a reasonable amount of tear film is required to maintain the transplanted graft; thus, the patients with the most severe form of dry eye do not meet the surgical indication, and no therapeutic methods are available

to reconstruct the ocular surface. To date, no reports have been published regarding the surgical procedures from the aspect of supplying tears or goblet cells to the ocular surface. Therefore, potential new treatments are needed for patients with severe OSDs (e.g., SJS and OCP) and the most severe form of dry eye.

Human nasal mucosal epithelium contains enriched goblet cells that secrete the necessary amount of mucin required for tear stabilization. Several groups have previously reported that whole nasal mucosal tissue transplantation (both epithelial and subepithelial tissues) is, in part, effective for treating severe conjunctival mucin deficiency syndrome and eyelid and ocular surface reconstruction [16, 17]. Because of the limited nasal donor site, we believe that the *ex vivo* expansion of goblet cells using a novel cell culture technique is a useful and promising procedure for developing the next generation of ocular-surface reconstruction surgeries. However, currently, no reports have been published regarding the development of tissue-engineered goblet cell transplantation using nasal mucosal epithelium.

The purpose of the present study was to investigate the use of a tissue-engineered cultivated

<sup>a</sup>Department of Biomedical Engineering, Faculty of Life and Medical Sciences, and <sup>b</sup>Research Center for Inflammation and Regenerative Medicine, Doshisha University, Kyoto, Japan; Departments of <sup>c</sup>Ophthalmology and <sup>d</sup>Otolaryngology-Head and Neck Surgery, Kyoto Prefectural University of Medicine, Kyoto, Japan; <sup>e</sup>Biomedical and Life Sciences, School of Health and Medicine, Lancaster University, Lancaster, United Kingdom

Correspondence: Takahiro Nakamura, M.D., Ph.D., Department of Ophthalmology, Kyoto Prefectural University of Medicine, 465 Kajii-cho, Hirokoji-agaru, Kawaramachi-dori, Kamigyo-ku, Kyoto 602-0841, Japan. Telephone: 81-75-251-5578; E-Mail: [tnakamur@koto.kpu-m.ac.jp](mailto:tnakamur@koto.kpu-m.ac.jp)

Received August 15, 2014; accepted for publication October 27, 2014; first published online in *SCTM EXPRESS* November 19, 2014.

©AlphaMed Press  
1066-5099/2014/\$20.00/0

<http://dx.doi.org/10.5966/sctm.2014-0169>



nasal mucosal epithelial cell sheet (CNMES) to supply functional goblet cells and stabilize and reconstruct the ocular surface in an attempt to ultimately overcome the difficulties associated with treating patients with severe OSDs with the most severe form of dry eye (supplemental online Fig. 1). In the present study, we cultured nasal cells on amniotic membrane (AM) expanded ex vivo from biopsy-derived human nasal mucosal tissues and successfully generated CNMESs that included a high density of goblet cells. The generated CNMESs were then transplanted onto the ocular surfaces of rabbits, and the survival of the cell sheets was subsequently evaluated. The present study is a first step toward assessing the use of tissue-engineered goblet cell transplantation of nonocular surface origin for ocular surface reconstruction.

## MATERIALS AND METHODS

### Nasal Mucosal Epithelial Cell Culture

The Institutional Review Board for Human Studies of Kyoto Prefectural University of Medicine, Kyoto, Japan approved all the surgical procedures performed in the present study (approval no. RBMR-C-978), and all patients and enrolled volunteer subjects had provided informed consent in accordance with the tenets set forth in the Declaration of Helsinki for research involving human subjects.

Human AM was obtained at elective cesarean section from volunteers who were seronegative for human immunodeficiency virus, human hepatitis B and C, and syphilis. The AM was then deprived of amniotic epithelial cells by incubation with 0.02% EDTA (Nacalai Tesque Inc., Kyoto, Japan, <http://www.nacalai.co.jp/en>) at 37°C for 2 hours.

The nasal mucosal tissues used in the present study were obtained during nasal disease surgery performed in the Department of Otolaryngology-Head and Neck Surgery, Kyoto Prefectural University of Medicine. Nasal mucosal epithelial cells were cultured via the use of our newly developed culture system and were cocultured with human mesenchymal stem cells (MSCs) (Lonza Co., Basel, Switzerland, <http://www.lonza.com>). To culture the cells, the MSCs were first plated onto 6-well, collagen-coated dishes (Iwaki Glass Co., Ltd., Chiba, Japan, <https://www.igc.co.jp/en/>) at a density of  $3 \times 10^4$  cells per  $\text{cm}^2$ . The denuded AM was then spread, epithelial basement membrane side up, on the bottom of a 0.4- $\mu\text{m}$  pore-size culture insert (Corning Inc., Corning, NY, <http://www.corning.com>), and these culture inserts were then placed in dishes containing MSCs. In addition, a previously reported air-lifting technique was used to promote goblet cell differentiation and epithelial barrier functions [13, 14, 18].

In brief, the blood and submucosal connective tissues were first removed to the extent possible using microscissors. The tissues were then cut into small pieces and incubated overnight at 4°C with 1% pronase (Roche Applied Science, Penzberg, Germany, <https://www.roche-applied-science.com>). Next, the tissues were carefully removed from the dishes and then put into a 0.05% trypsin-EDTA solution for 8 minutes at room temperature (RT) to separate the cells. Enzyme activity was stopped using culture medium containing Dulbecco's modified Eagle's medium/F12 (Life Technologies, Carlsbad, CA, <http://www.lifetechnologies.com>), defined keratinocyte-serum-free medium (Life Technologies) (1:5 mixture ratio) with 3% fetal bovine serum (HyClone Laboratories, Tauranga, New Zealand, <http://www.hyclone.com>), insulin (1  $\mu\text{l/ml}$ ), hydrocortisone (1  $\mu\text{l/ml}$ ), GA1000 (1  $\mu\text{l/ml}$ ), retinoic acid (1  $\mu\text{l/ml}$ ),

transferrin (1  $\mu\text{l/ml}$ ), triiodothyronine (1  $\mu\text{l/ml}$ ), and epinephrine (1  $\mu\text{l/ml}$ ) (all from Lonza Co.). The cell suspension was filtered through a cell strainer (BD Biosciences, Franklin Lakes, NJ, <http://www.bdbiosciences.com>) and then centrifuged 2 times for 5 minutes at 1,000 rpm. The resultant cell pellet was then resuspended in culture medium containing keratinocyte growth factor (KGF) (20 ng/ml) (Wako Pure Chemical Industries, Ltd., Osaka, Japan) and  $\rho$ -associated protein kinase (ROCK) inhibitor Y-27632 (1  $\mu\text{l/ml}$ ) (Abcam, Cambridge, MA, <http://www.abcam.com>). The nasal mucosal cells ( $3 \times 10^5$  cells per milliliter) were then seeded onto denuded AM spread on the bottom of culture inserts and cocultured with human MSCs. From 1 day after plating, culture medium without ROCK inhibitor Y-27632 was used. The cultured cells were then submerged in medium for 1 week at 37°C in 5% carbon dioxide and exposed to air by lowering the medium level (air lifting) for 1 additional week. The culture medium was changed every other day during the submerged condition and daily during the air-lifting process.

### Corneal, Conjunctival, and Oral Mucosal Epithelial Cell Culture

We cultured human corneal, conjunctival, and oral mucosal epithelial cells using a previously reported system [19]. In brief, for the corneal or conjunctival epithelial cell culture, the donor corneal rims (SightLife, Seattle, WA, <http://www.sightlife.org>) were first incubated at 37°C for 1 hour with 1.2 IU of dispase to separate the epithelial cells. Cells from the limbal and conjunctival regions were carefully separated from the underlying tissue. The resultant corneal or conjunctival epithelial cells were then seeded onto denuded AM spread on the bottom of culture inserts and cocultured with mitomycin C (MMC)-inactivated 3T3 fibroblasts.

For the oral mucosal epithelial cell culture, a small oral mucosal biopsy was performed with the patient under local anesthesia. The oral epithelium was then incubated at 4°C for 5 hours with 1.2 IU of dispase, followed by treatment with 0.05% trypsin-EDTA solution for 10 minutes to separate the cells. The resultant oral epithelial cells were then seeded onto denuded AM spread on the bottom of culture inserts and cocultured with MMC-inactivated 3T3 fibroblasts.

### Electron Microscopy

Native human nasal mucosal tissue and CNMESs were examined using scanning electron microscopy (SEM) and transmission electron microscopy (TEM) [19, 20]. The specimens were fixed in 2.5% glutaraldehyde in 0.1 M phosphate-buffered saline (PBS), washed 3 times for 15 minutes in PBS, and postfixed for 2 hours in 2% aqueous osmium tetroxide. They were then washed 3 more times in PBS before being passed through a graded ethanol series (i.e., 50%, 70%, 80%, 90%, 95%, and 100%). For SEM examination, the specimens were transferred to hexamethyldisilazane (TAAB Laboratories Equipment Ltd., Aldermaston, U.K., <http://www.taab.co.uk>) for 10 minutes and then allowed to air dry. Once dry, the specimens were mounted on aluminum stubs and sputter-coated with gold before undergoing examination using a digital SEM (JSM 5600; JEOL U.K., Ltd., Welwyn Garden City, U.K., <http://www.jeoluk.com>). For the TEM examination, the specimens were embedded in epoxy resin (Agar 100-epoxy resin; Agar Scientific Ltd., Stansted, U.K., <http://www.agarscientific.com>). Ultrathin (70-nm) sections were collected on copper grids

and stained for 30 minutes with 1% vanadyl sulfate and 1% phosphotungstic acid and then for 20 minutes with Reynold's lead citrate before examination using TEM (JEM 1010; Jeol U.K.).

### Antibodies and Reagents

The following antibodies were used in the present study: mouse monoclonal antibodies anti-keratin 1 (dilution  $\times 20$ ) / 4 ( $\times 200$ ) / 10 ( $\times 50$ ) / 13 ( $\times 200$ ) (Novocastra Ltd., Newcastle Upon Tyne, U.K., <http://www.leicabiosystems.com>), anti-keratin 3 ( $\times 50$ ) (Progen Biotechnik GmbH, Heidelberg, Germany, <http://www.progen.de>), anti-ZO1 ( $\times 25$ ) (Zymed Laboratories, South San Francisco, CA, <http://www.invitrogen.com>), anti-desmoplakin ( $\times 1$ ) (Progen Biotechnik), anti-laminin 5 ( $\times 100$ ) (Chemicon International, Inc., Temecula, CA, <http://www.chemicon.com>), anti-collagen 7 ( $\times 100$ ) (Chemicon), anti-MUC1 ( $\times 20$ ) (Progen Biotechnik), anti-MUC16 ( $\times 400$ ) (Abcam), anti-mucin 5AC (MUC5AC) ( $\times 100$ ) (Thermo Fisher Scientific, Inc., Waltham, MA, <http://www.thermofisher.com>), anti-p75 ( $\times 200$ ) (Abcam), and anti-Ki-67 ( $\times 200$ ) (BD Pharmingen, San Diego, CA, <http://www.bdbiosciences.com>). Rabbit polyclonal antibodies anti-ZO1 ( $\times 25$ ) (Zymed Laboratories) and anti-keratin 12 ( $\times 200$ ) (TransGenic Inc., Kumamoto, Japan, <http://www.transgenic.co.jp>). Goat polyclonal antibody anti-keratin 12 ( $\times 100$ ) (Santa Cruz Biotechnology, Inc., Santa Cruz, CA, <http://www.scbt.com>). Rat polyclonal antibody anti-galectin 3 ( $\times 100$ ) (Santa Cruz Biotechnology). Secondary antibodies included Alexa 488 goat anti-mouse or rabbit IgG ( $\times 1,500$ ) (Molecular Probes, Inc., Eugene, OR, <http://probes.invitrogen.com>), and fluorescein-conjugated donkey anti-mouse, -goat, or -rat IgG ( $\times 100$ ) (Jackson ImmunoResearch Laboratories, Inc., West Grove, PA, <http://www.jacksonimmuno.com>). The sections were coverslipped using antifading mounting medium containing propidium iodide (Vectorshield; Vector Laboratories, Inc., Burlingame, CA, <http://www.vectorlabs.com>).

### Immunohistochemistry

Immunohistochemical studies were performed according to our previously described method [19, 20]. In brief, 8- $\mu$ m-thin frozen sections were placed on silane-coated slides, air dried, and fixed in 100% acetone at 4°C for 15 minutes. After washing in PBS containing 0.15% Triton X-100 surfactant (Dow Chemical Co., Midland, MI, <http://www.dow.com>) at RT for 15 minutes, the sections were incubated with 1% bovine serum albumin (BSA) (Sigma-Aldrich, St. Louis, MO, <http://www.sigmaaldrich.com>) at RT for 30 minutes to block nonspecific binding. The sections were then incubated with primary antibody at RT for 1 hour and washed 3 times in PBS containing 0.15% Triton X-100 for 15 minutes. Control incubations were conducted with the appropriate normal mouse, rat, goat, and rabbit IgG at the same concentration as the primary antibody, and the primary antibody for the respective specimen was omitted. The sections were then incubated with the appropriate secondary antibodies at RT for 1 hour. After being washed 3 times with PBS, the sections were coverslipped using glycerol containing propidium iodide (Nacalai Tesque, Inc., Kyoto, Japan, <http://www.nacalai.co.jp>), and examined under a confocal microscope (FluoView; Olympus Corporation, Tokyo, Japan, <http://www.olympus-global.com>).

### Enzyme-Linked Immunosorbent Assay

Quantification of the mucin (MUC) 5AC (MUC5AC) expression level of the cultivated EC sheets (nasal, corneal, conjunctival, and

oral ECs) was performed using enzyme-linked immunosorbent assay (ELISA). Each sheet was incubated with Hanks' balanced salt solution (1 ml per well, 24-well plates) for 48 hours at 37°C. The resultant supernatant solution of each cultivated EC sheet was incubated overnight at 40°C. The wells were washed 3 times with 0.05% Tris-buffered saline with Tween-20 (TBST) and then incubated with 1% BSA for 1 hour at RT. Next, the wells were incubated with anti-MUC5AC antibody for 1 hour at RT. The wells were then washed 3 times with TBST and incubated with secondary antibody (sheep anti-mouse IgG-horseradish peroxidase; GE Healthcare, Little Chalfont, U.K., <http://www.gehealthcare.com>) for 1 hour at RT. Finally, the wells were incubated with tetramethylbenzidine (Sigma-Aldrich) for 30 minutes at RT. The reaction was stopped by adding 0.5 M sulfuric acid solution (Nacalai Tesque). The absorbance was read at 450 nm using a microplate reader.

### Human CNMES Transplantation

The human CNMESs were transplanted onto albino rabbits (2–2.5 kg) according to our previous protocol [21]. Anesthesia was induced in all rabbits by intramuscular injection of xylazine hydrochloride (5 mg/ml) and ketamine hydrochloride (50 mg/ml). All the rabbits were treated in accordance with the Association for Research in Vision and Ophthalmology Statement for the Use of Animals in Ophthalmic and Vision Research, and the experimental procedure was approved by the Committee for Animal Research at Kyoto Prefectural University of Medicine.

First, the rabbit conjunctival tissues (approximately 10 mm  $\times$  5 mm in size) were removed. Next, the CNMESs were placed over the excised area and secured in place with 10-0 nylon sutures. After surgery, the rabbits were given FK506 (300  $\mu$ m/day) (Astellas Pharma Inc., Tokyo, Japan, <http://www.astellas.com>) intramuscularly during the observation periods and treated with antibiotic ointment (Santen Pharmaceutical Co., Ltd, Osaka, Japan, <http://www.santen.com>) and steroid ointment (Shionogi Co., Ltd., Osaka, Japan, <http://www.shionogi.com>) every day [22].

## RESULTS

### Histological Examination of CNMESs

We first examined the histological characteristics of the CNMESs using hematoxylin and eosin staining (Fig. 1A). For comparison purposes, we also examined the cultivated corneal, conjunctival, and oral mucosa EC sheets using our previously reported technique (Fig. 1B–1D) [13, 14, 19]. Native nasal mucosal epithelium, the stratified ciliated columnar epithelium in the nasal mucosa, lies on the basement membrane, and ciliated cells and goblet cells were seen in the epithelial layer (Fig. 1A1). In contrast, the corneal, conjunctival, and oral mucosal epithelium all consisted of nonkeratinized, stratified squamous EC layers (Fig. 1B1, 1C1, 1D1).

After 2 weeks of culture, not only the cultivated corneal, conjunctival, and oral mucosal EC sheets, but also the CNMESs, showed 4–5 layers of stratified well-differentiated cells (Fig. 1A2, 1B2, 1C2, 1D2). Phase-contrast microscopy photographs indicated that a confluent primary culture of ECs had been established that covered the entire AM (Fig. 1A3, 1B3, 1C3, 1D3) and that goblet-like cells were only present in the CNMESs (Fig. 1A3). Thus, tissue-engineered CNMESs on AM were successfully generated.

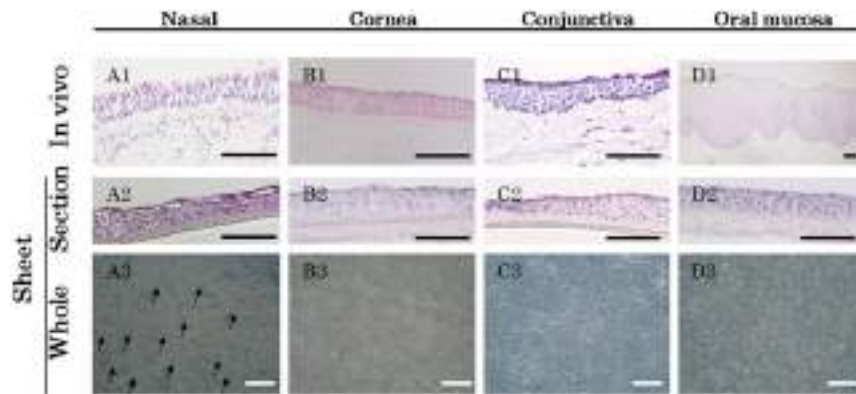


**Figure 1.** Histological examination of the cultivated nasal mucosal epithelial cell sheet. Light micrographs showing cross-sections of nasal (A1, A2), corneal (B1, B2), conjunctival (C1, C2), and oral (D1, D2) epithelial cells (ECs), both native tissue and in the cultured sheet stained with hematoxylin and eosin. Phase contrast images showing a confluent primary culture of nasal (A3), corneal (B3), conjunctival (C3), and oral (D3) ECs after 2 weeks in culture. Arrows indicate cells with a goblet-like appearance (A3). Scale bars = 100  $\mu$ m.

### Ultrastructural Examination of CNMESs

SEM examination of native nasal mucosa revealed ciliated and non-ciliated regions with numerous blobs of mucus (Fig. 2A). In contrast, SEM examination of the CNMESs revealed that the surface consisted of nonciliated cells with microvilli that were covered by strands and blobs of mucus (Fig. 2E). TEM examination of the native nasal mucosa revealed a region of goblet cells that contained numerous mucus-filled vesicles (Fig. 2B). TEM examination of the CNMESs revealed multiple layers of goblet cells containing numerous mucus-filled vesicles (Fig. 2F), with some mucus observed on the apical cell surface or trapped between the base of the cells and the AM. Both native nasal mucosa and CNMESs were found to have desmosomal junctions (Fig. 2C, 2G) and hemidesmosomes (Fig. 2D, 2H), respectively, indicating that tissue-engineered CNMESs with numerous goblet cells were successfully generated.

### Cell Biological Characteristics of CNMESs

#### Keratin Expression Patterns

The expression patterns of several tissue-specific keratins in the native tissue (supplemental online Fig. 2) and in the CNMESs (Fig. 3) were investigated by immunohistochemistry. In the normal nasal mucosa, expression of stratified keratin 4 was shown in the superficial layer and keratin 13 in all epithelial layers (supplemental online Fig. 2A1, 2A2). Cornea-specific keratin 3 was expressed in all epithelial layers (supplemental online Fig. 2A3). In contrast, expression of cornea-specific keratin 12 and keratinization-related keratins 1 and 10 were not observed (supplemental online Fig. 2A4–2A6). In addition, expression of keratins 4, 3, and 12 was confirmed in the corneal epithelium; however, no expression was found for keratins 1, 10, and 13 (supplemental online Fig. 2B1–2B6). The keratin expression patterns in the conjunctival and oral mucosal epithelium were nearly identical, except for the expression of keratin 3 (supplemental online Fig. 2C1–2C6, 2D1–2D6).

Immunohistochemical examination of the CNMESs revealed the expression of keratins 3, 4, and 13 (Fig. 3A1–3A3) but no expression of keratins 1, 10, and 12 (Fig. 3A4–3A6). Examination of the cultivated corneal epithelium revealed the expression of keratins 4, 3, 12, and 13 but no expression of keratins 1 and 10 (Fig. 3B1–3B6). The keratin expression patterns of the cultivated conjunctival and

oral mucosal epithelium were nearly identical (Fig. 3C1–3C6, 3D1–3D6). These findings show that using our newly developed culture conditions, the cell biological characteristics of the keratin expression patterns of native nasal mucosal epithelium in the CNMESs were maintained.

#### Cell Junction and Basement Membrane Assembly Protein Expression

The immunohistochemistry findings revealed cell-junction and basement membrane assembly protein expression (supplemental online Fig. 3). ZO-1, a tight-junction-related component, was expressed in apical cells in the normal nasal, corneal, conjunctival, and oral mucosal epithelium (supplemental online Fig. 3A1, 3B1, 3C1, 3D1). Desmoplakin, a cell-to-cell junction component, was expressed in the cell membrane of epithelial cells in all tissues (supplemental online Fig. 3A2, 3B2, 3C2, 3D2). The basement membrane assembly proteins laminin 5 and collagen 7 were expressed in the basement membrane in all tissues (supplemental online Fig. 3A3–3A4, 3B3–3B4, 3C3–3C4, 3D3–3D4). The CNMESs were found to express all the markers examined in the present study (supplemental online Fig. 3A5–3A8). These expression patterns were also observed in the other cultivated sheets (supplemental online Fig. 3B5–3B8, 3C5–3C8, 3D5–3D8). Thus, the CNMESs exhibited the proper cell junction and basement membrane assembly protein, which is thought to be essential for adaptation to clinical applications.

#### Membrane-Type Mucin Expression Patterns

MUC1 and MUC16, membrane-bound mucins [23], were expressed in the superficial layer of the normal nasal, corneal, and conjunctival mucosal epithelium (supplemental online Fig. 4A1, 4A2, 4B1, 4B2, 4C1, 4C2). In contrast, they were not expressed in the normal oral mucosal epithelium (supplemental online Fig. 4D1, 4D2). Galectin 3 was expressed in all epithelium (supplemental online Fig. 4A3, 4B3, 4C3, 4D3).

MUC1, MUC16, and galectin 3 were expressed mainly in the superficial layer of the CNMESs (supplemental online Fig. 4A4–4A6). These expression patterns were similar to those seen in the native nasal mucosa. The membrane-type mucin expression patterns of the other cultured sheets were nearly identical to those of native epithelium (supplemental online Fig. 4B4–4B6, 4C4–4C6, 4D4–4D6).

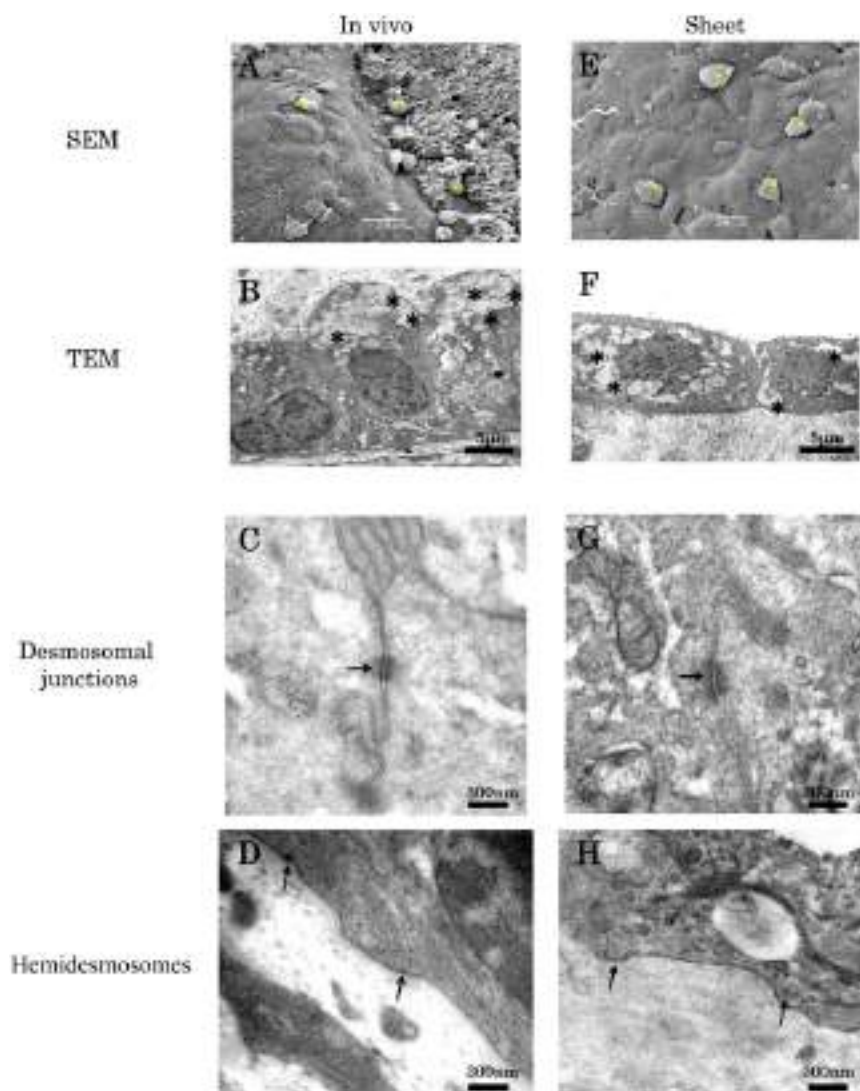


**Figure 2.** Ultrastructural examination of the cultivated nasal mucosal epithelial cell sheet (CNMES). Scanning electron microscopy examination of native nasal mucosa (A) and the CNMES (E). Yellow asterisks indicate blobs of mucus. Transmission electron microscopy examination of native nasal mucosa (B, C, D) and the CNMES (F, G, H). Asterisks indicate mucus-filled vesicles (B, F). Arrows indicate desmosomes (C, G) and hemidesmosomes (D, H). Abbreviations: SEM, scanning electron microscopy; TEM, transmission electron microscopy.

### Secretory-Type Mucin Expression (MUC5AC)

Immunohistochemical examination revealed the presence of MUC5AC, a marker of goblet cells, in the normal nasal mucosal and conjunctival epithelial cells (Fig. 4A1, 4C1). In contrast, no expression of MUC5AC was observed in the normal corneal and oral mucosal epithelium (Fig. 4B1, 4D1). MUC5AC was only expressed in the superficial cells of the CNMESs (Fig. 4A2, 4A3). The protein levels of MUC5AC in the cultured sheet were examined by ELISA (Fig. 4E). The expression level of MUC5AC in the CNMESs was higher than that in the other cultivated sheets ( $p < .02$ ). These findings illustrate that tissue-engineered CNMESs with numerous MUC5AC-positive goblet cells were successfully produced.

### Possible Epithelial Stem/Progenitor Cell Marker p75

A possible stem/progenitor cell marker [24], p75, was sporadically expressed in the basal cells of the human nasal, conjunctival, and oral mucosal epithelium; however, its expression was not

observed in the normal corneal epithelium (supplemental online Fig. 5A–5D). Expectedly, p75 expression was observed in the basal cell layer of the CNMESs and other cultivated sheets (supplemental online Figure 5E–5H), suggesting that stem/progenitor cells might be included in the CNMESs that were generated. However, no reliable markers exist for nasal mucosal epithelial stem cells, and our findings only showed the expression of p75 in the nasal mucosal epithelium. Therefore, much more information is needed to clearly demonstrate these subjects.

### Xenotransplantation of Human CNMESs

#### Clinical Findings

Human CNMESs were transplanted onto the conjunctival surface of the rabbit eyes and fixed with 10-0 nylon sutures (Fig. 5A). At both 7 days and 2 weeks after transplantation, the transplanted conjunctiva surfaces in all treated eyes were confirmed to be clear and smooth and without any extensive postoperative



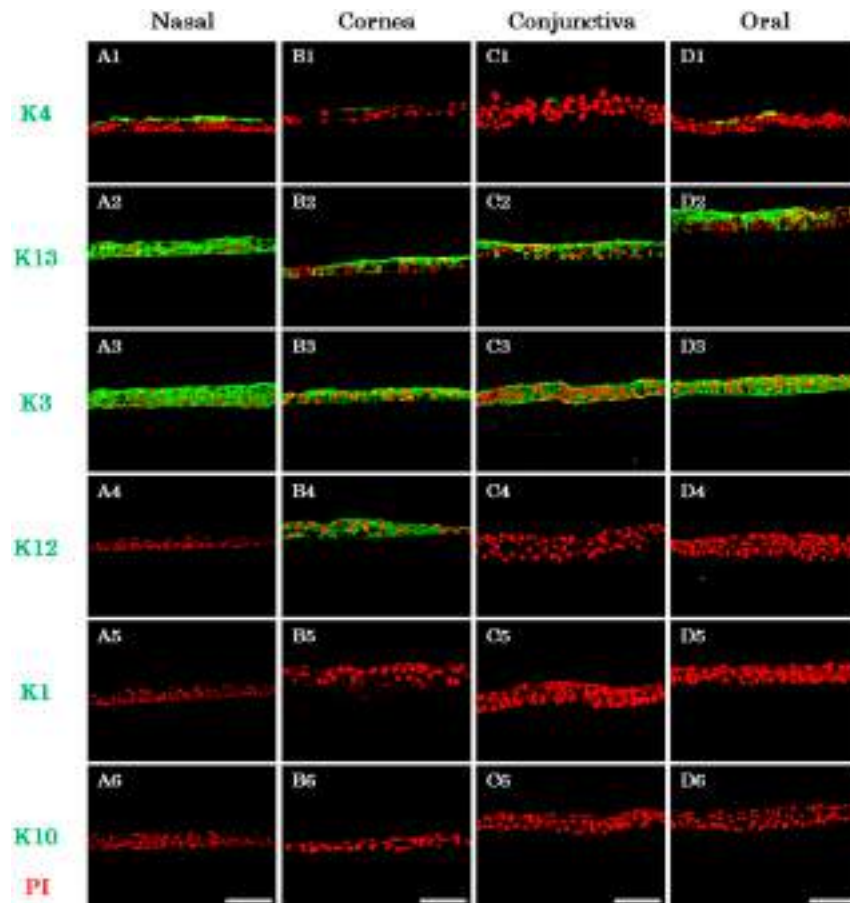


**Figure 3.** Keratin expression patterns in the cultivated nasal mucosal epithelial cell sheet. Images show the immunofluorescence of keratin 4 (A1, B1, C1, D1), 13 (A2, B2, C2, D2), 3 (A3, B3, C3, D3), 12 (A4, B4, C4, D4), 1 (A5, B5, C5, D5), and 10 (A6, B6, C6, D6) in the nasal (A1–A6), corneal (B1–B6), conjunctival (C1–C6), and oral (D1–D6) cultured sheets. Scale bars = 100  $\mu$ m. Abbreviations: K, keratin; PI, propidium iodide.

inflammation. In addition, fluorescein staining confirmed that the entire conjunctiva surface was covered by xeno-CNMEs (Fig. 5A). The slit-lamp examination findings were the same in all 3 rabbits.

#### Cell Biological Characteristics of Transplanted CNMEs

Histological examination of the transplanted CNMEs at 14 days postoperatively revealed that they were well adhered to the host tissues, with evidence of subepithelial cell infiltration (Fig. 5B). Hematoxylin-eosin staining showed that the transplanted CNMEs contained well-stratified differentiated cells (Fig. 5B). In order to confirm the presence of transplanted human CNME cells on the rabbit conjunctival surface, we examined their expression of anti-human nuclei and found positive expression of it in the transplanted areas (Fig. 5C).

Next, the expression pattern of several cell biological markers in the transplanted CNMEs was examined (Fig. 6). Keratins 4 and 13 were found to be expressed in the superficial and intermediate layers, with no discernible immunostaining in the basal cell layers (Fig. 6A, 6B). Keratins 1, 3, 10, and 12 were not expressed in any layer (Fig. 6C–6F). ZO-1 was expressed in the apical cells in the transplanted CNME, and desmoplakin was expressed in the cell membrane of the transplanted CNME cells (Fig. 6G, 6H). The basement membrane assembly proteins collagen 7 and laminin 5 were also expressed in the transplanted CNMEs (Fig. 6I, 6J). Sporadic expression of Ki67 and p75 was found in the basal layer

of the transplanted CNMEs (Fig. 6K, 6L). MUC1 and MUC16 were expressed in the superficial layer in the transplanted CNMEs, and galectin 3 was expressed in all CNME layers (Fig. 6M–6O). Immunohistochemistry confirmed the presence of MUC5AC in the transplanted CNMEs (Fig. 6P). These findings indicate that the generated CNMEs are well-adapted to native situations, with good postoperative function.

#### DISCUSSION

Severe OSDs are some of the most challenging clinical entities facing ophthalmologists worldwide. Although much attention is focused each year on the development of regenerative cell therapy using corneal, conjunctival, and oral mucosal epithelial stem cells, no reports have been published regarding a comparative examination of the cell biological characterization of the corneal, conjunctival, and oral epithelial sheets. Moreover, severe OSDs with severe dry eye remain some of the most difficult disorders to treat using the currently available treatment methods. The ocular surfaces of those patients exhibited a complete loss of conjunctival goblet cells, resulting in the clinical change of the mucosal epithelium from wet to pathologically keratinized. Subsequently, the ocular surfaces in those cases become severely compromised. However, these patients are presently considered to not meet the surgical indications. As a first step in the development of

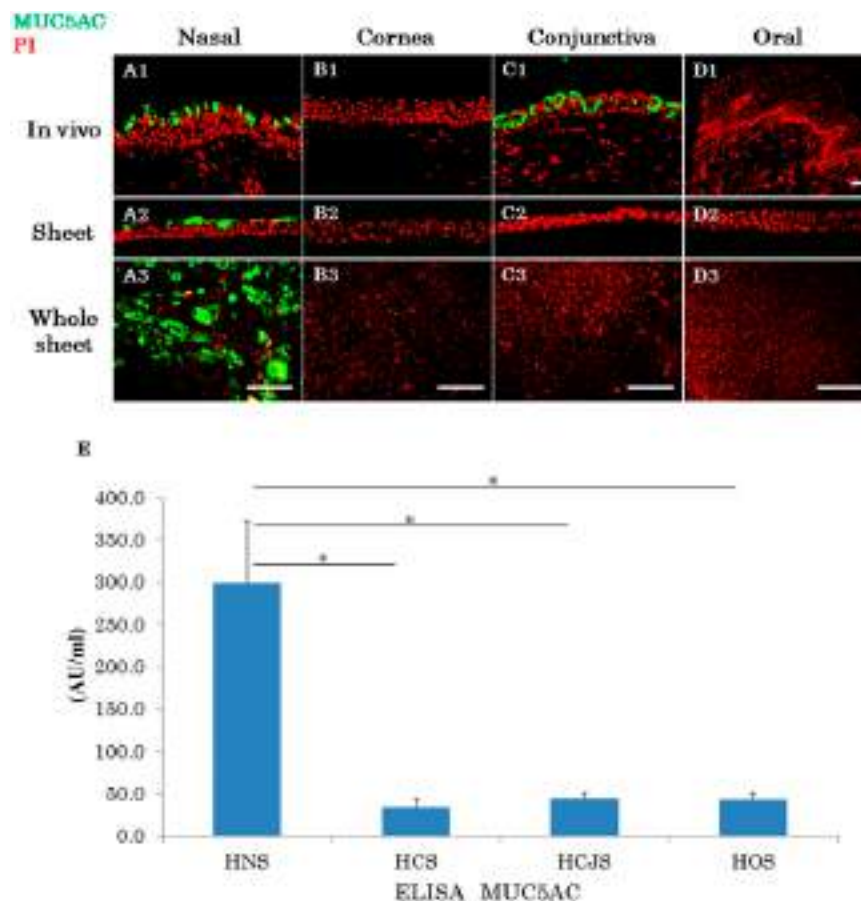


**Figure 4.** Expression patterns of mucin 5AC (MUC5AC). Immunofluorescence of MUC5AC in native nasal (A1), corneal (B1), conjunctival (C1), and oral (D1) mucosal epithelium. Immunofluorescence of MUC5AC in the cultured nasal (A2, A3), corneal (B2, B3), conjunctival (C2, C3), and oral (D2, D3) epithelial cell sheets. Scale bars = 100 μm. (E): The protein levels of MUC5AC in the cultured epithelial sheets were examined by ELISA. Mean ± SEM. \*,  $p < .02$ ;  $n = 8$ . Abbreviations: ELISA, enzyme-linked immunosorbent assay; HCS, human corneal epithelial sheet; HCJS, human conjunctival epithelial sheet; HNS, human nasal mucosal epithelial sheet; HOS, human oral mucosal epithelial sheet; PI, propidium iodide.

a novel treatment method for these patients, the transplantation of functional goblet cells onto the ocular surface might offer one possible approach, because goblet cells with secreted mucin are an essential component for maintaining ocular surface homeostasis. Although it is quite difficult to maintain goblet cells in *in vitro* culture conditions, we successfully generated confluent cultures of nasal mucosal ECs with numerous goblet cells expanded *ex vivo* from biopsy-derived nasal mucosal tissues and compared them with other types of cultured epithelial sheets. The present study is a first step toward assessing the efficacy of a novel tissue-engineered autologous transplantation of functional goblet cells of nonocular surface origin.

In 1990, Naumann et al. introduced autologous nasal mucosal tissue transplantation in severe mucus deficiency syndrome [16]. Most recently, Kim et al. reported that autologous nasal mucosal tissue transplantation is a feasible treatment of patients with cicatricial OSD [17]. The ocular surface is composed of two different types of ECs (i.e., corneal and conjunctival), and goblet cells are diffusely located throughout the entire conjunctival area. In these reports, the nasal graft size was around 2 cm<sup>2</sup>, and because of the limited nasal donor site, it is impossible to supply the goblet cells to the entire ocular surface using this procedure. Hence, the condition is far from the physiological ocular surface. To reconstruct the ocular surface as close as possible to its normal physiological

state, we believe that the *ex vivo* expansion of goblet cells using our newly discovered cell culture technique is a useful and promising procedure for developing the next generation of ocular surface reconstruction methods.

The culture of goblet cells has long been a challenging and difficult subject for scientists worldwide. In the present study, we successfully developed a novel culture system to generate CNMESs that include numerous goblet cells. Our new culture system is unique in several important aspects, because it includes the use of human MSCs to assist EC growth, the use of ROCK inhibitor Y-27632 to assist in the initial cell attachment, and the use of KGF to induce goblet cell differentiation.

Worldwide, the most popular cells used in the EC culture process are mouse-derived 3T3 feeder cells, because they are widely recognized for their effectiveness [25]. However, the use of those cells requires the use of xenobiotic materials in the culture system. Therefore, the use of human MSCs as an alternative to 3T3 feeder cells is significantly advantageous, because it eliminates the need for xenobiotic-free material in the culture process. Although we have not compared the effectiveness of 3T3 feeder cells with MSCs, the use of human MSCs is of clinical importance in the development of autologous tissue-engineered cell sheets for clinical transplantation.

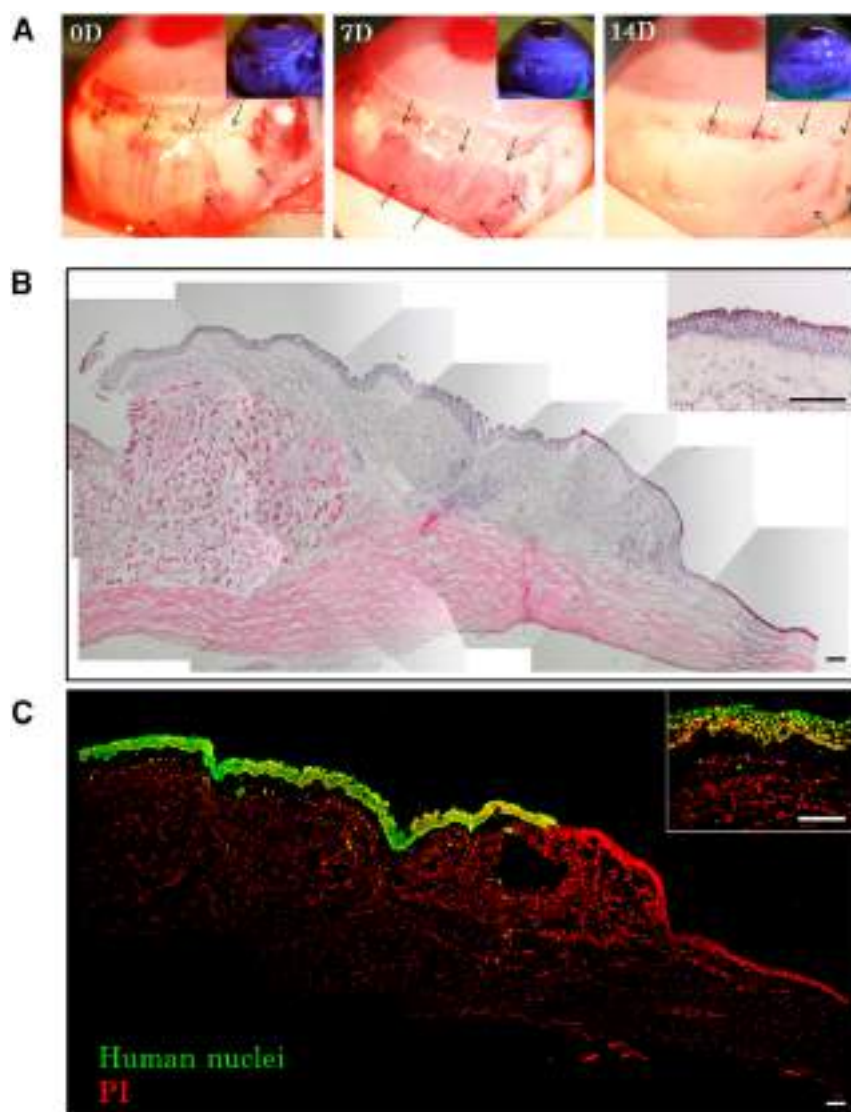


**Figure 5.** Xenotransplantation of a human cultivated nasal mucosal epithelial cell sheet. **(A):** Representative slit-lamp photographs of a rabbit taken immediately after transplantation, 7 days after transplantation, and 14 days after transplantation, with and without fluorescein. Arrows indicate the transplanted cell sheet. **(B, C):** Hematoxylin and eosin staining **(B)** and immunofluorescence **(C)** of anti-human nuclei at the transplanted conjunctival area. Scale bars = 100  $\mu\text{m}$ . Abbreviations: D, day(s); PI, propidium iodide.

Watanabe et al. reported that the application of ROCK inhibitor Y-27632 promotes the survival of dissociated human embryonic stem cells [26], and our group recently reported that Y-27632 enhances the adhesion of corneal endothelial cells to a substrate [27]. In our experimental observation under the phase-contrast microscope, we found that the application of Y-27632 to our culture system enhanced the initial attachment of human nasal ECs onto the AM. That finding encouraged us to explore the use of Y-27632 in our attempt to develop a better protocol of tissue-engineered nasal cell culture techniques.

Epidermal growth factor (EGF) is widely used for the culture of nasal ECs [18]. However, when using this method, we found it was difficult to generate cultured cell sheets that included a sufficient number of goblet cells, although the cell growth was comparatively fast. Thus, we developed our culture protocol and discovered that although the cell growth with KGF was slower than that with EGF, KGF effectively promotes sufficient goblet cell

differentiation in human nasal ECs. It has been reported that KGF and its receptor are expressed in the nasal mucosa [28] and that KGF stimulates the proliferation of ECs without impairing differentiation [29]. KGF also reportedly promotes goblet cell differentiation through the regulation of a goblet cell silencer inhibitor [30]. In view of these findings, KGF is one of the key factors to generate the goblet cell-rich cultured EC sheets.

Reportedly, cytokeratins play an important physiological and biological role in maintaining the integrity of ECs [31–34]. In those studies, defined subsets of individual cytokeratin pairs were characteristically expressed, depending on the EC type and level of differentiation. We have demonstrated that the keratin 1 and 10 pair, an epidermal keratinization marker, is not expressed in any layers in native nasal epithelium or in the CNMESs. We also confirmed that the keratin 4 and 13 pair, a nonkeratinized, mucosal epithelial marker, is expressed in both of them. These results led us to believe that, similar to other epithelial sheets, the







cell layers. These findings encouraged us to perform the transplantation of the CNMESs onto a native ocular surface.

The ocular surface is normally covered with tear film, which has a variety of components, including the mucus layer on the epithelial surface [36–39]. Mucin is a major component of tear film, which is essential for good vision. Thus, the mucin expression involvement in the CNMESs produced in the present study is of particular interest. Similar to that with the other cultured cell sheets, membrane-associated mucins (MUC1 and MUC16) were expressed in the CNMESs. However, unlike the other cell sheet, which did not express secretory mucin MUC5AC, the CNMESs we produced involved abundant MUC5AC expression and might be a main advantage for tear film stabilization and ocular surface reconstruction.

After the successful culture of human CNMESs, we transplanted it onto the ocular surfaces to investigate the viability of using the CNMESs as a substitute for functional ocular surface ECs. Two weeks after xenotransplantation of the human CNMESs, the transplanted sites were free of epithelial defects, indicating the complete survival of the transplanted CNMESs. Importantly, we confirmed the presence of junction-related proteins, the proliferation marker, and the stem/progenitor cell marker in the transplanted CNMESs. Most importantly, although we could not completely rule out the contamination of MUC5AC derived from rabbit conjunctiva, we observed that the secretory-type mucin marker MUC5AC was intensely expressed in the transplanted CNMESs, suggesting that the CNMESs have the potential ability to treat severe OSDs with goblet cell deficiency. In addition, we noted a decreased expression of keratin 3 in the transplanted CNMESs, suggesting that transplanted CNMESs might change their biological character in adjustment to the surrounding microenvironment.

## CONCLUSION

To the best of our knowledge, our study is the first to demonstrate the survival of tissue-engineered cultured epithelial cells derived

from nasal biopsies. In the present study, we successfully generated functional CNMESs with numerous goblet cells. In addition, we successfully performed xenotransplantation of these cells onto a rabbit ocular surface. We believe that this approach to treating severe OSD eyes with severe dry eye has great potential. However, it is important to note that this technique is still in its early stages and that many questions have yet to be addressed, including questions about the longevity and mobility of the autologously transplanted nasal ECs on the host eye. Thus, the long-term postoperative outcomes of CNMES transplantation remain unclear, and additional investigation is needed to elucidate the feasibility and efficacy of using CNMESs in the clinical setting.

## ACKNOWLEDGMENTS

We thank John Bush for reviewing our report. This study was supported in part by Grants-in-Aid for scientific research from the Japanese Ministry of Education, Culture, Sports, Science and Technology (Kiban C), Biotechnology and Biological Sciences Research Council, and Wellcome Trust, United Kingdom.

## AUTHOR CONTRIBUTIONS

M.K.: provision of study material or patients, collection and/or assembly of data, data analysis and interpretation, manuscript writing; T.N.: conception and design, financial support, collection and/or assembly of data, data analysis and interpretation, manuscript writing, final approval of manuscript; M.Y., Y. Hata, and Y. Hisa: provision of study material or patients; S.O., M.I., M.N., and N.J.F.: collection and/or assembly of data; N.K. and S.K.: financial support.

## DISCLOSURE OF POTENTIAL CONFLICTS OF INTEREST

The authors indicated no potential conflicts of interest.

## REFERENCES

- 1 Tseng SC. Concept and application of limbal stem cells. *Eye (Lond)* 1989;3:141–157.
- 2 Chiou AG, Florakis GJ, Kazim M. Management of conjunctival cicatrizing diseases and severe ocular surface dysfunction. *Surv Ophthalmol* 1998;43:19–46.
- 3 Kinoshita S, Adachi W, Sotozono C et al. Characteristics of the human ocular surface epithelium. *Prog Retin Eye Res* 2001;20:639–673.
- 4 Tseng SC, Hirst LW, Maumenee AE et al. Possible mechanisms for the loss of goblet cells in mucin-deficient disorders. *Ophthalmology* 1984;91:545–552.
- 5 Thoft RA. Conjunctival transplantation. *Arch Ophthalmol* 1977;95:1425–1427.
- 6 Thoft RA. Keratoepithelioplasty. *Am J Ophthalmol* 1984;97:1–6.
- 7 Kenyon KR, Tseng SC. Limbal autograft transplantation for ocular surface disorders. *Ophthalmology* 1989;96:709–722.
- 8 Tsai RJ, Tseng SC. Human allograft limbal transplantation for corneal surface reconstruction. *Cornea* 1994;13:389–400.
- 9 Tseng SC, Prabhasawat P, Barton K et al. Amniotic membrane transplantation with or without limbal allografts for corneal surface reconstruction in patients with limbal stem cell deficiency. *Arch Ophthalmol* 1998;116:431–441.
- 10 Tsubota K, Satake Y, Kaido M et al. Treatment of severe ocular-surface disorders with corneal epithelial stem-cell transplantation. *N Engl J Med* 1999;340:1697–1703.
- 11 Pellegrini G, Traverso CE, Franzi AT et al. Long-term restoration of damaged corneal surfaces with autologous cultivated corneal epithelium. *Lancet* 1997;349:990–993.
- 12 Tsai RJ, Li LM, Chen JK. Reconstruction of damaged corneas by transplantation of autologous limbal epithelial cells. *N Engl J Med* 2000;343:86–93.
- 13 Koizumi N, Inatomi T, Suzuki T et al. Cultivated corneal epithelial stem cell transplantation in ocular surface disorders. *Ophthalmology* 2001;108:1569–1574.
- 14 Nakamura T, Inatomi T, Sotozono C et al. Transplantation of cultivated autologous oral mucosal epithelial cells in patients with severe ocular surface disorders. *Br J Ophthalmol* 2004;88:1280–1284.
- 15 Nishida K, Yamato M, Hayashida Y et al. Corneal reconstruction with tissue-engineered cell sheets composed of autologous oral mucosal epithelium. *N Engl J Med* 2004;351:1187–1196.
- 16 Naumann GO, Lang GK, Rummelt V et al. Autologous nasal mucosa transplantation in severe bilateral conjunctival mucus deficiency syndrome. *Ophthalmology* 1990;97:1011–1017.
- 17 Kim JH, Chun YS, Lee SH et al. Ocular surface reconstruction with autologous nasal mucosa in cicatricial ocular surface disease. *Am J Ophthalmol* 2010;149:45–53.
- 18 Huang TW, Young YH, Cheng PW et al. Culture of nasal epithelial cells using chitosan-based membranes. *Laryngoscope* 2009;119:2066–2070.
- 19 Nakamura T, Endo K, Cooper LJ et al. The successful culture and autologous transplantation of rabbit oral mucosal epithelial cells on amniotic membrane. *Invest Ophthalmol Vis Sci* 2003;44:106–116.
- 20 Nakamura T, Hamuro J, Takaishi M et al. LRIG1 inhibits STAT3-dependent inflammation to maintain corneal homeostasis. *J Clin Invest* 2014;124:385–397.
- 21 Takaoka M, Nakamura T, Sugai H et al. Sutureless amniotic membrane transplantation

for ocular surface reconstruction with a chemically defined bioadhesive. *Biomaterials* 2008; 29:2923–2931.

**22** Tanioka H, Kawasaki S, Yamasaki K et al. Establishment of a cultivated human conjunctival epithelium as an alternative tissue source for autologous corneal epithelial transplantation. *Invest Ophthalmol Vis Sci* 2006;47:3820–3827.

**23** Argüeso P, Guzman-Aranguez A, Mantelli F et al. Association of cell surface mucins with galectin-3 contributes to the ocular surface epithelial barrier. *J Biol Chem* 2009;284: 23037–23045.

**24** Nakamura T, Endo K, Kinoshita S. Identification of human oral keratinocyte stem/progenitor cells by neurotrophin receptor p75 and the role of neurotrophin/p75 signaling. *STEM CELLS* 2007; 25:628–638.

**25** Rheinwald JG, Green H. Serial cultivation of strains of human epidermal keratinocytes: The formation of keratinizing colonies from single cells. *Cell* 1975;6:331–343.

**26** Watanabe K, Ueno M, Kamiya D et al. A ROCK inhibitor permits survival of dissociated human embryonic stem cells. *Nat Biotechnol* 2007;25:681–686.

**27** Okumura N, Ueno M, Koizumi N et al. Enhancement on primate corneal endothelial cell

survival in vitro by a ROCK inhibitor. *Invest Ophthalmol Vis Sci* 2009;50:3680–3687.

**28** Ishibashi T, Tanaka T, Nibu K et al. Keratinocyte growth factor and its receptor messenger RNA expression in nasal mucosa and nasal polyps. *Ann Otol Rhinol Laryngol* 1998;107: 885–890.

**29** Miyashita H, Yokoo S, Yoshida S et al. Long-term maintenance of limbal epithelial progenitor cells using rho kinase inhibitor and keratinocyte growth factor. *STEM CELLS TRANSLATIONAL MEDICINE* 2013;2:758–765.

**30** Iwakiri D, Podolsky DK. Keratinocyte growth factor promotes goblet cell differentiation through regulation of goblet cell silencer inhibitor. *Gastroenterology* 2001;120:1372–1380.

**31** Franke WW, Schiller DL, Moll R et al. Diversity of cytokeratins: Differentiation specific expression of cytokeratin polypeptides in epithelial cells and tissues. *J Mol Biol* 1981;153: 933–959.

**32** Tseng SC, Jarvinen MJ, Nelson WG et al. Correlation of specific keratins with different types of epithelial differentiation: Monoclonal antibody studies. *Cell* 1982;30:361–372.

**33** Sun TT, Eichner R, Nelson WG et al. Keratin classes: Molecular markers for different

types of epithelial differentiation. *J Invest Dermatol* 1983;81(suppl):109s–115s.

**34** Eichner R, Bonitz P, Sun TT. Classification of epidermal keratins according to their immunoreactivity, isoelectric point, and mode of expression. *J Cell Biol* 1984;98: 1388–1396.

**35** Schermer A, Galvin S, Sun TT. Differentiation-related expression of a major 64K corneal keratin in vivo and in culture suggests limbal location of corneal epithelial stem cells. *J Cell Biol* 1986;103: 49–62.

**36** Nichols BA, Chiappino ML, Dawson CR. Demonstration of the mucous layer of the tear film by electron microscopy. *Invest Ophthalmol Vis Sci* 1985;26:464–473.

**37** Inatomi T, Spurr-Michaud S, Tisdale AS et al. Expression of secretory mucin genes by human conjunctival epithelia. *Invest Ophthalmol Vis Sci* 1996;37:1684–1692.

**38** Govindarajan B, Gipson IK. Membrane-tethered mucins have multiple functions on the ocular surface. *Exp Eye Res* 2010;90:655–663.

**39** Guzman-Aranguez A, Argüeso P. Structure and biological roles of mucin-type O-glycans at the ocular surface. *Ocul Surf* 2010; 8:8–17.



See [www.StemCellsTM.com](http://www.StemCellsTM.com) for supporting information available online.



Published in final edited form as:

*Acta Biomater.* 2015 June ; 19: 1–9. doi:10.1016/j.actbio.2015.03.017.

## Synthetic bone mimetic matrix-mediated *in situ* bone tissue formation through host cell recruitment

Yu-Ru Shih<sup>a,1</sup>, Ameya Phadke<sup>a,1</sup>, Tomonori Yamaguchi<sup>b,c,1</sup>, Heemin Kang<sup>a</sup>, Nozomu Inoue<sup>c</sup>, Koichi Masuda<sup>b,\*</sup>, and Shyni Varghese<sup>a,\*</sup>

<sup>a</sup>Department of Bioengineering, Jacobs School of Engineering, University of California, San Diego, La Jolla, CA 92093, USA

<sup>b</sup>Department of Orthopaedic Surgery, School of Medicine, University of California, San Diego, La Jolla, CA 92093, USA

<sup>c</sup>Department of Biomedical Engineering, Graduate School of Life and Medical Sciences, Doshisha University, Kyoto, Japan

### Abstract

Advances in tissue engineering have offered new opportunities to restore anatomically and functionally compromised tissues. Although traditional tissue engineering approaches that utilize biomaterials and cells to create tissue constructs for implantation or biomaterials as a scaffold to deliver cells are promising, strategies that can activate endogenous cells to promote tissue repair are more clinically attractive. Here, we demonstrate that an engineered injectable matrix mimicking a calcium phosphate (CaP)-rich bone-specific microenvironment can recruit endogenous cells to form bone tissues *in vivo*. Comparison of matrix alone with that of bone marrow-soaked or bFGF-soaked matrix demonstrate similar extent of neo-bone formation and bridging of decorticated transverse processes in a posterolateral lumbar fusion rat model. Synthetic biomaterials that stimulate endogenous cells without the need for biologics to assist tissue repair could circumvent limitations associated with conventional tissue engineering approaches, including *ex vivo* cell processing and laborious efforts, thereby accelerating the translational aspects of regenerative medicine.

### Graphical Abstract

\*Corresponding author. Department of Bioengineering, University of California San Diego, 9500 Gilman Drive, MC 0412, La Jolla, CA 92093, United States. Phone: +1 858 822-7920, Fax: +1 858 534 5722, svarghese@ucsd.edu (S. Varghese), Department of Orthopaedic Surgery, University of California San Diego, komasuda@ucsd.edu (K. Masuda).

<sup>1</sup>Y.R.S., A.P. and T.Y contributed equally to this work

**Publisher's Disclaimer:** This is a PDF file of an unedited manuscript that has been accepted for publication. As a service to our customers we are providing this early version of the manuscript. The manuscript will undergo copyediting, typesetting, and review of the resulting proof before it is published in its final citable form. Please note that during the production process errors may be discovered which could affect the content, and all legal disclaimers that apply to the journal pertain.

#### Disclosures

Authors declare no conflict of interest.

#### Appendix A. Supplementary data

Supplementary Figure S1

Supplementary Movie S1–S3



## Keywords

Biomimetic materials; bone grafts; posterolateral fusion; spine; biomineralization; endogenous cell recruitment

## 1. Introduction

Bone grafting has become an increasingly prevalent procedure. Bone is the third most transplanted tissue after skin and blood with over 500,000 bone grafting procedures performed annually in the United States alone [1]. A variety of procedures necessitate the use of bone grafts: these include spinal fusion procedures and large bone defects arising from trauma or excision of large segments of bone due to infection or tumor invasion. Among these, spinal fusions are increasingly predominant and the frequency and healthcare costs associated with spinal fusion have increased at a higher rate than other common inpatient procedures [2]. Spinal fusion procedures are typically used to treat conditions arising from damage to the intervertebral disc, nerve compression, and spondylolistheses, among others.

Although autograft remains the gold standard, associated comorbidities and limited supply continue to motivate developments of alternative strategies for spinal fusion. Tissue engineering strategies involving biologics such as osteoprogenitors and recombinant proteins have been touted as powerful approaches to treat non-uniform defects. These approaches often utilize a cell-laden three-dimensional (3-D) scaffold, which provides structural support and instructive cues. One such strategy involves delivery of osteoinductive growth factors, such as recombinant bone morphogenetic proteins (BMPs), with recombinant human BMP-2 (rhBMP-2) and BMP-7 (rhBMP-7) currently approved for clinical use in various parts of the world [3, 4]. While BMPs are powerful inducers of bone tissue formation and delivery of BMPs leads to favorable clinical outcome through bone regeneration, the BMP-mediated bone tissue repair suffers from a number of shortcomings. These limitations include the high cost associated with the large dose of BMPs required as well as the accompanying side effects, such as respiratory effects, ectopic bone formation, local bone resorption at the implant site, and even an increase in the risk for cancer [5]. Other biologic additives such as exogenous cells [6], demineralized bone [7], bone marrow aspirate [8], platelet-rich plasma [9] or bFGF [10] have been used in combination with biomaterials or bone grafts to improve the therapeutic outcome in animal models. Recently, silicated calcium phosphates mixed with bone marrow aspirate have shown to promote posterolateral lumbar fusion in patients [11]. A report by Acharya *et al.* suggest that in the absence of biologic additives such as bone marrow, exogenous cells or demineralized bone matrix, synthetic calcium phosphates do not promote posterolateral fusion in patients [12]. Although such biomaterial-assisted inclusion of biologics to repair bone tissue is highly potent, new approaches that are cost-



effective and pose minimal side effects are warranted by developing biomaterials that can recruit endogenous cells and direct their differentiation into osteoblasts to form functional bone tissue.

We have recently shown that biomineralized matrices of poly(ethylene glycol) diacrylate-co-N-acryloyl 6-aminocaproic acid (PEGDA-co-A6ACA) promote osteogenic differentiation of human mesenchymal, embryonic stem cells, and induced pluripotent stem cells *in vitro* in growth medium devoid of any osteogenic-inducing factors [13–16]. We also showed that when subcutaneously implanted in rats, these materials contributed to ectopic bone formation by recruiting endogenous cells [17]. In this study, we examined the potential of these engineered matrices, emulating the calcium phosphate (CaP)-rich bone environment, (hereafter referred to as grafts) for their ability to induce bone formation and assist spinal fusion in rats. In addition to grafts alone, we also examined grafts supplemented with bone marrow flush or bFGF. Germane to our previous findings, the results described here show that the biomineralized material alone supported bone formation and assisted bridging of decorticated transverse process in a rodent.

## 2. Materials and Methods

### 2.1 Synthetic grafts

Formulation of the synthetic graft: Porous PEGDA-co-A6ACA hydrogels were prepared using a template-leaching method similar to that previously described [15, 16]. Briefly, 110 mg of polymethyl methacrylate (PMMA) microspheres (mean diameter: 165  $\mu\text{m}$ ) (Bangs Laboratories, MI) were poured into cylindrical polypropylene molds measuring 7 mm in diameter and tapped vigorously for 20–30 seconds to ensure optimal packing of microspheres. The microsphere-filled molds were sintered at 140°C for 26 hours and allowed to cool to room temperature for at least 4 hours. A precursor solution to create the polymer network was prepared by adding 20% poly(ethylene glycol)-diacrylate (PEGDA;  $M_n$ : 3.4 kDa; [w/v]) to a 0.5 M solution of N-acryloyl 6-aminocaproic acid (A6ACA) in 0.5 M NaOH and chilled on ice for 15 minutes. Polymerization was initiated by the addition of 0.5% ammonium persulfate and 0.07% N,N,N',N'-tetramethylethylenediamine. Approximately 0.110 ml of the precursor solution was poured into each PMMA mold and vacuum-infiltrated by cycling between ambient pressure and 28 in Hg vacuum every 5 minutes, with 3 cycles. The infiltrated samples were allowed to polymerize under humid conditions at 37°C for 2 hours. PMMA templates were removed by washing in acetone for 3 days (with two daily changes of solution), and subsequently immersing the hydrogels in decreasing concentrations of acetone in deionized (DI) water (90%, 70%, 30%, 0%) for 24, 12, 6 and 6 hours, respectively. The porous hydrogels were washed in deionized (DI) water for at least 3 days with three daily changes of water to remove traces of acetone, and then scraped to remove any thin non-porous layer at the surface and dried at 37°C for 24 hours.

The grafts were mineralized using a previously described procedure with some modifications [13, 17, 18]. Briefly, the macroporous hydrogels were re-swollen in simulated body fluid (m-SBF), prepared as detailed previously [19] for 12 hours, minced into pieces with a surgical scalpel, and then mineralized by immersion in 40 mM  $\text{Ca}^{2+}$ /24 mM  $\text{PO}_4^{3-}$  (pH = 5.2) under vacuum to ensure optimal infiltration of the solution into the scaffold

interior for 1 hour. Excess solution was removed from the graft pores by gently pressing on a paper towel, and the grafts were immersed in fresh m-SBF for an additional 48 hours. The mineralized grafts were washed briefly in sterile PBS for 6 hours to remove excess m-SBF from the pores, loaded into 1-ml syringes (Terumo Medical, Inc.) (0.3 ml/syringe), frozen at  $-80^{\circ}\text{C}$  and lyophilized for 48 hours.

## 2.2 Scanning electron microscopy (SEM) and energy dispersive spectra (EDS)

Mineralized matrices were imaged with SEM to investigate the morphology of the mineralized matrices. Samples were rinsed in DI water for 5 minutes to remove unbound ions, cut into thin slices, flash-frozen, and lyophilized. Samples were coated with Iridium for 7 seconds in the sputter (Emitech, K575X) and imaged with SEM (Philips XL30 ESEM). EDS analysis was performed to determine the composition of the minerals using an integrated EDS system and ICA software to quantify Ca/P atomic ratio from elemental spectra.

## 2.3 Surgical procedure

Twenty-three male athymic rats (*rmu/rnu*, Harlan) weighing 250–300 g used for the study were in compliance with the NIH Guide for Care and Use of Laboratory Animals with the approval of the Institutional Animal Care and Use Committee at the University of California, San Diego. Two of the 23 rats were used as bone marrow donors. After sacrifice, the femurs of these two rats were removed and cleaned of soft tissue remnants. The ends of the femur were cut and flushed four times with DMEM (GIBCO) (4 ml/femur total). The concentration of viable mononucleated cells was determined to be  $1.1 \times 10^7$  cells/ml. The remaining twenty-one rats were used for implantation. The rats were anesthetized with an intramuscular injection of approximately 0.45 ml of ketamine-xylazine. L4-L5 transverse processes were exposed through a dorsal midline skin incision and paravertebral muscle separation, stripped of periosteum by scraping, and decorticated with a burr until bleeding was observed from the transverse processes. 0.3 ml of the lyophilized synthetic graft was rehydrated for 1 minute in either physiological saline, bone marrow (BM) flush, or basic fibroblast growth factor (bFGF; 10 ng/ml) in saline and placed between the transverse processes in the fusion bed on each side of the spine. Seven rats received BM flush-soaked grafts, seven received bFGF-soaked grafts, while the remaining seven received grafts soaked in saline. The muscle pouch was closed with resorbable 4-0 Vicryl sutures and the skin was closed with staples. Buprenorphine (0.03 – 0.05 mg/kg) was administered for relieving postoperative pain and the animals were allowed access to food and water *ad libitum*. At 8 weeks, the rats were euthanized by  $\text{CO}_2$  and cervical dislocation.

## 2.4 Measurement of bFGF retention on grafts

Lyophilized synthetic grafts (0.3 ml) were rehydrated for 1 minute in bFGF solution (500  $\mu\text{g/ml}$ ). The concentration of bFGF remaining in the unbound bFGF solution was measured with a UV-Vis Spectrophotometer (Nanodrop 2000, Thermo Scientific). The percentage of bound bFGF was calculated after subtraction of bound bFGF from the original bFGF solution.

## 2.5 Radiographic monitoring

Bone formation in the host was monitored as a function of time through live imaging. Anterior-posterior (AP) digital radiographs (NAOMI; 365 dpi; 71  $\mu\text{m}$  pixel size; 50 kVp; 10  $\mu\text{As}$ ) were acquired at 0, 2, 4, 6, and 8 weeks post-implantation. Post-sacrifice, animals were also imaged via high-resolution X-ray films using a tabletop Faxitron X-ray machine.

## 2.6 Micro-computed tomography

Animals were imaged via whole-body micro-computed tomography ( $\mu\text{CT}$ ) (Skyscan1076, Skyscan, Belgium) in live animals at 8 weeks (pixel size: 36  $\mu\text{m}$ ; 100 kV; 1.0-mm Al filter) under anesthesia (2% isoflurane). Scans were reconstructed using NRecon software and analyzed via CTAn and DataViewer software (Skyscan). Bone (or hard tissue) volume percentage was calculated for each animal at 8 weeks from the reconstructed  $\mu\text{CT}$  scans using CTAn software. Bone morphometry was assessed as percentage of mineral volume compared to total graft volume (BV/TV) with CTAn software. Briefly, to selectively account for positive signals from minerals by eliminating background, a thresholding value was determined for native trabecular bone using the Otsu Threshold Method.

The fusion mass region on each side of the spine (left and right) was then isolated as a region of interest in each slice via visual inspection and the pre-determined threshold was applied. Bone density was quantified as percentage of volume occupied by bone (hard tissue with a pixel value exceeding the threshold) as compared to total tissue volume for each side. For each animal, bone volume percentage was expressed as the average of the bone volume percentage in the left and right side fusion mass, respectively.

## 2.7 Bone labeling with calcein fluorochrome

Calcein fluorochrome (Sigma Aldrich) labeling was used to identify newly calcified/forming bone tissues; freshly prepared calcein reagent was used for the injection. Briefly, calcein powder was dissolved in 2%  $\text{NaHCO}_3$  (diluted in physiological saline) to make a 3 mg/ml stock solution and filter-sterilized using a 0.22- $\mu\text{m}$  filter. The calcein solution was loaded into 3-ml syringes and injected into the athymic rats subcutaneously at 15 mg/kg body weight at week 6 (2 weeks before sacrifice at week 8).

## 2.8 Histology

Following sacrifice, the spines were excised from the animals along with surrounding soft tissue and fixed in 10% buffered formalin. Samples were decalcified for 1–2 weeks using Cal-EXII according to the manufacturer's instructions. Decalcified samples were embedded in methyl methacrylate, sectioned, and stained using hematoxylin and eosin (H&E). For immunohistochemical (IHC) staining of osteocalcin, rehydrated paraffin-embedded sections were washed in PBS, blocked, and incubated overnight with primary antibodies against osteocalcin (1:100; mouse monoclonal; Abcam) at 4°C. Following thorough washes, sections were immersed in 3% hydrogen peroxide (Acros Organics) and washed in PBS containing 0.1% Tween 20 (v/v). Sections were exposed to horseradish peroxidase (HRP)-conjugated secondary antibodies (1:100; goat anti-mouse, Santa Cruz Biotechnology) at room temperature for 60 minutes. After several washes, sections were developed in 3-3' diaminobenzidine (DAB) peroxidase substrate (Vector Laboratories) for 10 minutes.

Sections were imaged under a microscope in color mode under H-filter. Rat skin tissue was used as a negative control.

## 2.9 Manual Palpation

Following sacrifice, spines were extracted from animals and manually palpated to evaluate fusion. Movement of fused adjacent vertebra was compared to movement of unfused adjacent vertebra [20]. Spines were graded on a scale of 1–4, with 1 representing no fusion with substantial movement, 2 representing limited fusion with reduced movement, 3 representing substantial fusion with minimal movement, and 4 representing complete fusion with no detectable movement.

## 2.10 Lateral Bending

In addition to manual palpation and radiographic evaluation, fusion was evaluated using a custom-designed approach [21]. Briefly, explanted spines were placed in a custom-designed device capable of displacement-controlled lateral bending. Spines were anchored at the sacrum by three set screws and the L1 vertebral body was placed in the loading mechanism and allowed displacement of samples in the medial-lateral direction resulting in cantilever bending. Specifically, the L1 vertebral body was moved to three specific positions: bent left (–10 mm), neutral (0 mm), and bent right (+10 mm). Supplementary Figure S1 depicts right bending as an example. In each position, the spine was imaged using  $\mu$ CT (pixel size: 18  $\mu$ m, 70 kV, 1.0-mm Al filter), and converted to 3-D models using Mimics software. Six degrees-of-freedom 3-D segmental movements (3 rotational and 3 translational) were analyzed via Volume-Merge method [22].

## 2.11 Statistical analysis

Statistical analyses were carried out using Graphpad Prism 5. One-way analysis of variance (ANOVA) with Tukey post-hoc test was used to compare multiple groups. In the figures, groups with statistical significance are represented using different letters, i.e. groups with “a” are statistically significant to those with “b”. The *p*-values were obtained from each test.

# 3. Results

## 3.1 Macroporous mineralized grafts

The development and detailed characterization of the biomineralized matrix has been published previously [14, 15, 17, 18]. SEM characterization confirmed that the grafts exhibited interconnected pore structure (Fig. 1A). The matrix bound minerals had a plate-like morphology (Fig. 1A, inset). The elemental dispersive spectra (EDS) analysis of the graft revealed the presence of CaP minerals with a Ca/P ratio of 1.44 in the mineralized macroporous hydrogels (Fig. 1B). XRD analyses of the mineralized matrices suggested presence of a mixture of crystalline and semicrystalline minerals [18]. The CaP minerals of the mineralized matrix undergo a dynamic dissolution-precipitation responding to the  $\text{Ca}^{2+}$  and  $\text{PO}_4^{3-}$  in the milieu [15].

The overall development of the grafts and their *in vivo* implantation is depicted in Figure 1C. Minced porous materials were mineralized, lyophilized in 1-ml syringes, and rehydrated



for 1 minute with either saline, basic fibroblast growth factor (bFGF) solution, or bone marrow (BM) flush before being injected into the surgically created fusion beds in rats. The growth factor bFGF was chosen because a number of studies have shown its role in promoting bone formation [23–25]; furthermore, silencing the *bFGF* gene results in decreased bone formation [26]. Although the exact amount of bFGF adsorbed onto the mineralized grafts is unknown, our measurements indicate more than 80% of bFGF can be adsorbed onto the mineralized grafts from the soaking solution. The porous graft materials were injected into the decorticated transverse processes in the fusion bed on each side of the spine (white arrow). The ability of the grafts to support bone formation and assist fusion of the transverse processes was determined as a function of post-implantation time.

### 3.2 Radiographic analysis of hard tissue formation and mineral density

The presence of hard tissue formation in saline-soaked, bFGF-soaked, and BM flush-soaked grafts were imaged by X-ray radiography (Fig. 2A). No adverse reaction to the grafts was observed in any of the animals throughout the study period. X-ray radiographic analysis of the animals immediately post-implantation revealed that the grafts were not visible in any of the animals (Fig. 2A; red asterisks). In contrast to the immediate post-implantation radiographs, fusion masses of newly formed hard tissues were visible in some of the animals as early as 2 weeks (4 animals out of 7 in each group). By 4 weeks, all animals showed clear evidence of hard tissue formation, with progressively increasing mineral density observed at 6 and 8 weeks, respectively. Remarkably, *de novo* hard tissue formation was observed irrespective of whether the implants were soaked in saline, bFGF, or BM flush (Fig. 2A). Also, no observable difference could be discerned between animals within the three groups.

Micro-computed tomography ( $\mu$ CT) analyses corroborated the radiographic findings.  $\mu$ CT analyses after 8 weeks of implantation revealed hard tissue formation in all animals treated with implants irrespective of whether they were infused with saline, bFGF, or BM. Visual inspection of  $\mu$ CT scans indicated that the formation of new bone was restricted to the grafts (Fig. 2B and Supplementary Movies S1–3). Additionally, examination of transaxial cross-sectional views of the reconstructed 3-D images revealed that the newly formed bone is bridged with the decorticated transverse processes (Fig. 2B). Bone morphometric analysis from  $\mu$ CT imaging at 8 weeks post-implantation revealed the percentage of mineralized hard tissue, relative to total graft volume, to be 51% for saline group, 59% for bFGF group, and 54% for BM group, with bFGF significantly higher than saline and BM groups (Fig. 2C). While the graft fragments showed excellent hard tissue formation, spaces between the fragments of the grafts showed more sparse bone formation and less calcification.

### 3.3 Histological analysis of bone formation

Calcein labeling for calcium incorporation into newly formed tissue at 8 weeks post-implantation revealed consistent calcification with positive calcein signals for saline, bFGF, and BM groups, respectively (Fig. 3A). H&E staining for the decalcified sections within the fusion masses at 8 weeks post-implantation revealed woven bone matrix with osteoblast-like lining cells in all experimental groups (Fig. 3B; blue arrows). The bone tissue formation was further confirmed by immunostaining for osteocalcin, a bone specific protein. Significant osteocalcin immunostaining was detected in all the three groups: saline-, bFGF- and BM-

soaked groups (Fig. 3C). Lacunae-like cartilage structures were apparent in saline and BM groups (Fig. 3B; yellow arrows). No such cartilage-like structure was observed in grafts enriched with bFGF at the same experimental time point(s).

### 3.4 Evaluation of fusion through manual palpation

Despite its subjectivity, manual palpation has been touted as a gold standard for evaluation of spinal fusion in human patients [20]. Manual palpation of animals treated with the grafts revealed an average score of 2.9 for the saline group, 3.0 for the BM group, and 2.7 for the bFGF group, thus providing evidence of fusion in all groups, with no significant differences in fusion indices (Fig. 4A). In comparison, sham group (decortication only) consistently scored approximately 1, supporting the radiographic observations of lack of fusion and bone formation in the absence of exogenous grafts [21].

### 3.5 Lateral bending analysis of 3-D segmental movements

While the aforementioned measurements showed the formation of neo-bone tissue, it is important to quantitate the bridging of the neo-bone with the host transverse processes. To assess the functional integration of the neo-tissue with the native bone, 3-D segmental movements during lateral bending motions were determined. We quantified the 3-D segmental movements of the animals treated with implants after 8 weeks of implantation by using a technique developed by our group that involves lateral bending of the fused spines under controlled displacement along with a  $\mu$ CT-based 3-D kinematic analysis [21]. The total absolute value of rotation about the  $x$ -axis in lateral bending is defined as the 3-D lateral bending angular range of motion (ROM). A low ROM indicates bridging of the neo-bone tissue with the host transverse processes, thereby spinal fusion. In this study, spines treated with the synthetic grafts soaked with saline and BM showed a statistically significant reduction in lateral bending angular ROM compared to the sham surgery group ( $p < 0.05$ ), with lateral bending angular ROMs of approximately  $7.54 \pm 2.63^\circ$  and  $8.16 \pm 2.50^\circ$  for the saline and BM groups, respectively, compared to  $12.44 \pm 2.10^\circ$  observed for the sham surgery group (Fig. 4, B and C). The significant reduction in mobility for the saline and BM groups compared to sham suggests that the grafts were fused with the transverse processes through the bridging of newly formed bone. On the other hand, the bFGF group did not significantly reduce mobility compared to sham. Additionally, no significant differences were observed between the saline and BM groups, further supporting the results from the  $\mu$ CT and histological analyses that the saline-soaked grafts were able to promote bone tissue formation and fusion to a similar extent as the BM flush-soaked grafts.

## 4. Discussion

In this study, we examined the ability of synthetic biomineralized matrices to support *in vivo* bone formation and bridging of decorticated transverse process in a rodent model with the addition of BM flush or bFGF. Live radiographic imaging was used to monitor hard tissue formation for up to 8 weeks. X-ray images and  $\mu$ CT analyses of the grafts immediately following implantation showed the grafts themselves were not visible suggesting that the biomineralized matrices contained only small amounts of minerals. The subsequent fusion masses of hard tissue observed at the implantation site starting 2 weeks post-implantation

can thus be solely attributed to the formation of new hard tissue and not an artifact due to visualization of the mineralized grafts themselves.

H&E staining and calcein labeling, together with the immunostaining for osteocalcin, further confirm hard neo-bone tissue, which was restricted to the graft. It is important to note that several of the large graft fragments in the  $\mu$ CT images showed relatively higher calcification at the periphery compared to the center of the fragment, while smaller fragments showed similar levels of calcification throughout the entire fragment. The formation of an exterior shell has often been reported during bone induction in soft tissues, particularly when calcium phosphate matrices are used either in isolation or as carriers for osteoinductive growth factors [27, 28]. The histological analyses showed extensive tissue formation throughout the graft irrespective of the size of the fragments. Furthermore, the histological analyses showed bone formation even in graft fragments located in the center of the fusion mass, away from the transverse processes. The majority of bone tissue appeared to resemble woven bone. The presence of cartilaginous matrix in grafts infused with saline and bone marrow groups suggests that the bone tissue formation, as evident by bone matrix and immunostaining for osteocalcin, followed endochondral ossification for these groups.

While manual palpation may seem fairly subjective and susceptible to inter-observer and intra-observer variability, studies using manual palpation to assess posterolateral intertransverse process spinal fusion indeed show correlation with other methods, such as fine detail radiography and  $\mu$ CT for evaluation of fusion [29]. The results of manual palpation in this study indicate that all grafts irrespective of the biological additives were able to promote bridging of the graft assisted neo-bone tissue with the native transverse process). Results from the lateral bending quantitative analyses corroborated findings from the manual palpation. As evident from the 3-D lateral bending analyses, the saline-, and BM flush-infused grafts not only promoted neo-bone tissue formation, but also led to a 40% reduction in angular range of motion when compared to the corresponding sham surgery. Mechanical characterization thus corroborated the  $\mu$ CT and histological findings that the synthetic grafts assisted the bridging of the transverse process.

The contribution of BM-infused and bFGF-infused grafts towards the neo-bone tissue formation is dependent upon the extent of adsorbed/bound biological materials. Bone marrow flush is comprised of a large number of cytokines, growth factors, and cells, including MSCs. Determining the composition and concentration of the biological components within the BM flush-infused grafts is a challenge. Previously, we have shown that incorporation of 6-aminocaproic acid (6ACA) moieties improves the protein and growth factor-binding ability of various materials, including the antifouling materials [30]. Synthetic matrices containing 6ACA moieties have also been shown to promote adhesion and growth of human mesenchymal stem cells [31]. Biom mineralization should not have any negative effect on the ability of these materials to adsorb proteins and growth factors as a number of studies have shown that mineralization promotes adsorption of proteins and growth factors [32–34]. Measurements of bFGF adsorption onto the mineralized materials suggest that a majority of bFGF was adsorbed by the graft (>80%). This is consistent with other studies that showed high levels of bFGF adsorption by the CaP-based materials [35, 36].

It is particularly intriguing that the saline-soaked grafts lacking any biological additives promoted bone tissue formation similar to the grafts soaked with BM flush or bFGF, and that the material alone is osteoconductive. Osteoconduction may depend on the action of differentiated skeletal cells that may originate either in pre-existing osteoblasts or in cells recruited from precursor mesenchymal cells by osteoinduction [37]. Since we did not identify the cells that contributed to then neo-bone, the mineralized scaffolds either stimulated differentiation of recruited progenitor cells into osteoblasts or recruited endogenous osteoblasts *per se*, leading to the deposition of bone matrix and bone formation. The presence of host cells in the grafts is likely facilitated by bleeding of the transverse processes during surgical implantation of grafts. This suggests that the biomineralized matrices used in this study are osteoinductive and the material can convert osteoprogenitors into osteoblasts through endochondral ossification. Synthetic calcium-phosphate materials that facilitate ectopic bone formation in the absence of biologics or exogenous cells as demonstrated in our study have been observed by others [38–43]. The ability of biomineralized matrices to promote ectopic bone tissue formation could be attributed to physicochemical cues arising from the mineralized matrix. The biomineralized matrices used in this study contained apatite-like CaP minerals that can be easily dissociated into  $\text{Ca}^{2+}$  and  $\text{PO}_4^{3-}$  ions [44]. We and others have demonstrated the dissolution-precipitation of mineralized materials that leads to increased local  $\text{Ca}^{2+}$  and  $\text{PO}_4^{3-}$  concentrations within the immediate microenvironment of matrices promote osteogenic differentiation of osteoprogenitor cells *in vitro*, [13, 14, 45–47] and could play a role in osteoinduction by mineralized materials *in vivo* [13, 45, 48, 49]. Crystalline CaP minerals have demonstrated increasing dissolution rates in the order of hydroxyapatite (HA), biphasic calcium phosphate (BCP), and tricalcium phosphate (TCP) [47, 50] which proportionally promoted osteogenic differentiation of MSCs [51]. A direct comparison between HA, BCP, and TCP showed enhanced bone regeneration by TCP compared with BCP in the skeletal sites and no bone formation with HA [47]. In addition, the mineralized phase could also promote the selective adsorption and subsequent release of pro-angiogenic and pro-osteogenic growth factors from the surrounding physiological environment, such as vascular endothelial growth factors (VEGFs) and bone morphogenetic proteins (BMPs) [52–54], leading to their accumulation within the implant and fusion bed for osteoinduction.

Given the relative scarcity of biologic-independent synthetic matrices for bone induction, the consistent osteoinductivity displayed by the mineralized PEGDA-co-A6ACA grafts is highly encouraging and could potentially allow for their use in spinal fusion procedures without the need for any biologic additives, such as bone marrow aspirate, platelet-rich plasma, growth factors, and others. Synthetic materials that could promote bone tissue formation and fusion between native and neo-bone without the addition of biologics and exogenous cells are highly desirable and could be an alternative to current grafting strategies.

## 5. Conclusion

This work demonstrates the utility of novel synthetic bone grafts based on biomineralized porous matrices in an athymic rat posterolateral fusion model. Results from our study show that the biomineralized synthetic matrices were able to assist neo-bone tissue formation and promote posterolateral fusion as evidenced by radiographic, histological and lateral bending



analyses. These grafts were found to promote bone tissue formation and fusion irrespective of the presence of bone marrow flush or bFGF, as saline-soaked grafts *per se* were able to produce highly similar, statistically significant improvements when compared to sham surgery.

## Supplementary Material

Refer to Web version on PubMed Central for supplementary material.

## Acknowledgments

The authors gratefully acknowledge the financial support from National Institutes of Health (NIH, Grant 1 R01 AR063184-01A1).

## References

1. Faour O, Dimitriou R, Cousins CA, Giannoudis PV. The use of bone graft substitutes in large cancellous voids: any specific needs? *Injury*. 2011; 42(Suppl 2):S87–90. [PubMed: 21723553]
2. Rajae SS, Bae HW, Kanim LE, Delamarter RB. Spinal fusion in the United States: analysis of trends from 1998 to 2008. *Spine*. 2012; 37:67–76. [PubMed: 21311399]
3. Glassman SD, Howard J, Dimar J, Sweet A, Wilson G, Carreon L. Complications with recombinant human bone morphogenetic protein-2 in posterolateral spine fusion: a consecutive series of 1037 cases. *Spine*. 2011; 36:1849–54. [PubMed: 20838369]
4. Bhatia, SK., Bhatia, SR. Bioactive Devices. In: Lee, S., Henthorn, D., editors. *Materials in Biology and Medicine*. Boca Raton, FL: CRC Press; 2012. p. 149-60.
5. Carragee EJ, Hurwitz EL, Weiner BK. A critical review of recombinant human bone morphogenetic protein-2 trials in spinal surgery: emerging safety concerns and lessons learned. *The spine journal : official journal of the North American Spine Society*. 2011; 11:471–91. [PubMed: 21729796]
6. Kai T, Shao-qing G, Geng-ting D. In vivo evaluation of bone marrow stromal-derived osteoblasts-porous calcium phosphate ceramic composites as bone graft substitute for lumbar intervertebral spinal fusion. *Spine*. 2003; 28:1653–8. [PubMed: 12897487]
7. Lee YP, Jo M, Luna M, Chien B, Lieberman JR, Wang JC. The efficacy of different commercially available demineralized bone matrix substances in an athymic rat model. *Journal of spinal disorders & techniques*. 2005; 18:439–44. [PubMed: 16189457]
8. Tay BK, Le AX, Heilman M, Lotz J, Bradford DS. Use of a collagen-hydroxyapatite matrix in spinal fusion. A rabbit model. *Spine*. 1998; 23:2276–81. [PubMed: 9820906]
9. Okamoto S, Ikeda T, Sawamura K, Nagae M, Hase H, Mikami Y, et al. Positive effect on bone fusion by the combination of platelet-rich plasma and a gelatin beta-tricalcium phosphate sponge: a study using a posterolateral fusion model of lumbar vertebrae in rats. *Tissue engineering Part A*. 2012; 18:157–66. [PubMed: 21819268]
10. Yoshida T, Sakamoto A, Tsukamoto N, Nakayama K, Iwamoto Y. Establishment of an animal model of a pasteurized bone graft, with a preliminary analysis of muscle coverage or FGF-2 administration to the graft. *Journal of orthopaedic surgery and research*. 2009; 4:31. [PubMed: 19650934]
11. Jenis LG, Banco RJ. Efficacy of silicate-substituted calcium phosphate ceramic in posterolateral instrumented lumbar fusion. *Spine*. 2010; 35:E1058–63. [PubMed: 20479699]
12. Acharya NK, Kumar RJ, Varma HK, Menon VK. Hydroxyapatite-bioactive glass ceramic composite as stand-alone graft substitute for posterolateral fusion of lumbar spine: a prospective, matched, and controlled study. *Journal of spinal disorders & techniques*. 2008; 21:106–11. [PubMed: 18391714]
13. Phadke A, Shih YR, Varghese S. Mineralized synthetic matrices as an instructive microenvironment for osteogenic differentiation of human mesenchymal stem cells. *Macromolecular bioscience*. 2012; 12:1022–32. [PubMed: 22760917]

14. Shih YR, Hwang YS, Phadke A, Kang H, Hwang NS, Caro EJ, et al. Calcium phosphate-bearing matrices induce osteogenic differentiation of stem cells through adenosine signaling. *Proceedings of the National Academy of Sciences*. 2014; 111:990–5.
15. Kang H, Wen C, Hwang Y, Shih YR, Kar M, Seo SW, et al. Biom mineralized matrix-assisted osteogenic differentiation of human embryonic stem cells. *Journal of Materials Chemistry B*. 2014; 2:5676–88.
16. Kang H, Shih YR, Hwang Y, Wen C, Rao V, Seo T, et al. Mineralized gelatin methacrylate-based matrices induce osteogenic differentiation of human induced pluripotent stem cells. *Acta Biomaterialia*. 2014
17. Phadke A, Hwang Y, Kim SH, Kim SH, Yamaguchi T, Masuda K, et al. Effect of scaffold microarchitecture on osteogenic differentiation of human mesenchymal stem cells. *European Cells and Materials*. 2013; 25:114–29. [PubMed: 23329467]
18. Phadke A, Zhang C, Hwang Y, Vecchio K, Varghese S. Templated mineralization of synthetic hydrogels for bone-like composite materials: Role of matrix hydrophobicity. *Biomacromolecules*. 2010; 11:2060–8. [PubMed: 20690714]
19. Oyane A, Kim HM, Furuya T, Kokubo T, Miyazaki T, Nakamura T. Preparation and assessment of revised simulated body fluids. *Journal of biomedical materials research Part A*. 2003; 65:188–95. [PubMed: 12734811]
20. Boden SD, Schimandle JH, Hutton WC. An experimental lumbar intertransverse process spinal fusion model. Radiographic, histologic, and biomechanical healing characteristics. *Spine*. 1995; 20:412–20. [PubMed: 7747224]
21. Yamaguchi T, Inoue N, Sah RL, Lee Y-P, Taborek AP, Williams GM, et al. Micro-computed tomography-based three-dimensional kinematic analysis during lateral bending for spinal fusion assessment in a rat posterolateral lumbar fusion model. *Tissue Engineering Part C: Methods*. 2014
22. Ochia RS, Inoue N, Renner SM, Lorenz EP, Lim TH, Andersson GB, et al. Three-dimensional in vivo measurement of lumbar spine segmental motion. *Spine*. 2006; 31:2073–8. [PubMed: 16915091]
23. Nagai H, Tsukuda R, Yamasaki H, Mayahara H. Systemic injection of FGF-2 stimulates endocortical bone modelling in SAMP6, a murine model of low turnover osteopenia. *The Journal of veterinary medical science / the Japanese Society of Veterinary Science*. 1999; 61:869–75.
24. Nakamura Y, Tensho K, Nakaya H, Nawata M, Okabe T, Wakitani S. Low dose fibroblast growth factor-2 (FGF-2) enhances bone morphogenetic protein-2 (BMP-2)-induced ectopic bone formation in mice. *Bone*. 2005; 36:399–407. [PubMed: 15777655]
25. Kimoto T, Hosokawa R, Kubo T, Maeda M, Sano A, Akagawa Y. Continuous administration of basic fibroblast growth factor (FGF-2) accelerates bone induction on rat calvaria--an application of a new drug delivery system. *Journal of dental research*. 1998; 77:1965–9. [PubMed: 9839783]
26. Montero A, Okada Y, Tomita M, Ito M, Tsurukami H, Nakamura T, et al. Disruption of the fibroblast growth factor-2 gene results in decreased bone mass and bone formation. *The Journal of clinical investigation*. 2000; 105:1085–93. [PubMed: 10772653]
27. Hartman EH, Vehof JW, Spauwen PH, Jansen JA. Ectopic bone formation in rats: the importance of the carrier. *Biomaterials*. 2005; 26:1829–35. [PubMed: 15576157]
28. Matsushita N, Terai H, Okada T, Nozaki K, Inoue H, Miyamoto S, et al. A new bone-inducing biodegradable porous beta-tricalcium phosphate. *Journal of biomedical materials research Part A*. 2004; 70:450–8. [PubMed: 15293319]
29. Yee AJ, Bae HW, Friess D, Robbin M, Johnstone B, Yoo JU. Accuracy and interobserver agreement for determinations of rabbit posterolateral spinal fusion. *Spine*. 2004; 29:1308–13. [PubMed: 15187630]
30. Kabra H, Hwang Y, Lim HL, Kar M, Arya G, Varghese S. Biomimetic Material-Assisted Delivery of Human Embryonic Stem Cell Derivatives for Enhanced In Vivo Survival and Engraftment. *ACS Biomater Sci Eng*. 2015; 1:7–12. [PubMed: 26280019]
31. Ayala R, Zhang C, Yang D, Hwang Y, Aung A, Shroff SS, et al. Engineering the cell-material interface for controlling stem cell adhesion, migration, and differentiation. *Biomaterials*. 2011; 32:3700–11. [PubMed: 21396708]

32. LeGeros RZ. Calcium phosphate-based osteoinductive materials. Chemical reviews. 2008; 108:4742–53. [PubMed: 19006399]
33. Alam MI, Asahina I, Ohmamiuda K, Takahashi K, Yokota S, Enomoto S. Evaluation of ceramics composed of different hydroxyapatite to tricalcium phosphate ratios as carriers for rhBMP-2. Biomaterials. 2001; 22:1643–51. [PubMed: 11374466]
34. Liu Y, Hunziker EB, Layrolle P, De Bruijn JD, De Groot K. Bone morphogenetic protein 2 incorporated into biomimetic coatings retains its biological activity. Tissue engineering. 2004; 10:101–8. [PubMed: 15009935]
35. Perez RA, Kim TH, Kim M, Jang JH, Ginebra MP, Kim HW. Calcium phosphate cements loaded with basic fibroblast growth factor: delivery and in vitro cell response. Journal of biomedical materials research Part A. 2013; 101:923–31. [PubMed: 22962037]
36. Midy V, Rey C, Bres E, Dard M. Basic fibroblast growth factor adsorption and release properties of calcium phosphate. Journal of biomedical materials research. 1998; 41:405–11. [PubMed: 9659610]
37. Albrektsson T, Johansson C. Osteoinduction, osteoconduction and osseointegration. European spine journal : official publication of the European Spine Society, the European Spinal Deformity Society, and the European Section of the Cervical Spine Research Society. 2001; 10(Suppl 2):S96–101.
38. Selye H, Lemire Y, Bajusz E. Induction of bone, cartilage and hemopoietic tissue by subcutaneously implanted tissue diaphragms. Dev Genes Evol. 1960; 151:572–85.
39. Pek YS, Gao S, Arshad MS, Leck KJ, Ying JY. Porous collagen-apatite nanocomposite foams as bone regeneration scaffolds. Biomaterials. 2008; 29:4300–5. [PubMed: 18706690]
40. Seyedjafari E, Soleimani M, Ghaemi N, Shabani I. Nanohydroxyapatite-coated electrospin poly(L-lactide) nanofibers enhance osteogenic differentiation of stem cells and induce ectopic bone formation. Biomacromolecules. 2010; 11:3118–25. [PubMed: 20925348]
41. Barradas AM, Yuan H, van der Stok J, Le Quang B, Fernandes H, Chatterjee A, et al. The influence of genetic factors on the osteoinductive potential of calcium phosphate ceramics in mice. Biomaterials. 2012; 33:5696–705. [PubMed: 22594974]
42. Cheng L, Duan X, Xiang Z, Shi Y, Lu X, Ye F, et al. Ectopic bone formation cannot occur by hydroxyapatite/ $\beta$ -tricalcium phosphate bioceramics in green fluorescent protein chimeric mice. Appl Surf Sci. 2012:262.
43. Kawai T, Anada T, Honda Y, Kamakura S, Matsui K, Matsui A, et al. Synthetic octacalcium phosphate augments bone regeneration correlated with its content in collagen scaffold. Tissue engineering Part A. 2009; 15:23–32. [PubMed: 18637727]
44. Phadke A, Zhang C, Hwang Y, Vecchio K, Varghese S. Templated mineralization of synthetic hydrogels for bone-like composite materials: role of matrix hydrophobicity. Biomacromolecules. 2010; 11:2060–8. [PubMed: 20690714]
45. Chai YC, Roberts SJ, Schrooten J, Luyten FP. Probing the osteoinductive effect of calcium phosphate by using an in vitro biomimetic model. Tissue engineering Part A. 2011; 17:1083–97. [PubMed: 21091326]
46. Chai YC, Roberts SJ, Van Bael S, Chen Y, Luyten FP, Schrooten J. Multi-level factorial analysis of  $\text{Ca}^{2+}/\text{Pi}$  supplementation as bio-instructive media for in vitro biomimetic engineering of three-dimensional osteogenic hybrids. Tissue engineering Part C, Methods. 2012; 18:90–103. [PubMed: 21933019]
47. Yuan H, Fernandes H, Habibovic P, de Boer J, Barradas AM, de Ruiter A, et al. Osteoinductive ceramics as a synthetic alternative to autologous bone grafting. Proceedings of the National Academy of Sciences of the United States of America. 2010; 107:13614–9. [PubMed: 20643969]
48. Le Nihouannen D, Daculsi G, Saffarzadeh A, Gauthier O, Delplace S, Pilet P, et al. Ectopic bone formation by microporous calcium phosphate ceramic particles in sheep muscles. Bone. 2005; 36:1086–93. [PubMed: 15869915]
49. Muller P, Bulnheim U, Diener A, Luthen F, Teller M, Klinkenberg ED, et al. Calcium phosphate surfaces promote osteogenic differentiation of mesenchymal stem cells. Journal of cellular and molecular medicine. 2008; 12:281–91. [PubMed: 18366455]

50. Ducheyne P, Radin S, King L. The effect of calcium phosphate ceramic composition and, structure on in vitro behavior. I. Dissolution. *Journal of biomedical materials research*. 1993; 27:25–34. [PubMed: 8380596]
51. Barradas AM, Monticone V, Hulsman M, Danoux C, Fernandes H, Tahmasebi Birgani Z, et al. Molecular mechanisms of biomaterial-driven osteogenic differentiation in human mesenchymal stromal cells. *Integrative biology : quantitative biosciences from nano to macro*. 2013; 5:920–31. [PubMed: 23752904]
52. Lee JS, Suarez-Gonzalez D, Murphy WL. Mineral coatings for temporally controlled delivery of multiple proteins. *Advanced materials*. 2011; 23:4279–84. [PubMed: 22039597]
53. Yuan H, Zou P, Yang Z, Zhang X, De Bruijn JD, De Groot K. Bone morphogenetic protein and ceramic-induced osteogenesis. *Journal of materials science Materials in medicine*. 1998; 9:717–21. [PubMed: 15348928]
54. Suarez-Gonzalez D, Lee JS, Lan Levengood SK, Vanderby R Jr, Murphy WL. Mineral coatings modulate beta-TCP stability and enable growth factor binding and release. *Acta Biomater*. 2012; 8:1117–24. [PubMed: 22154864]



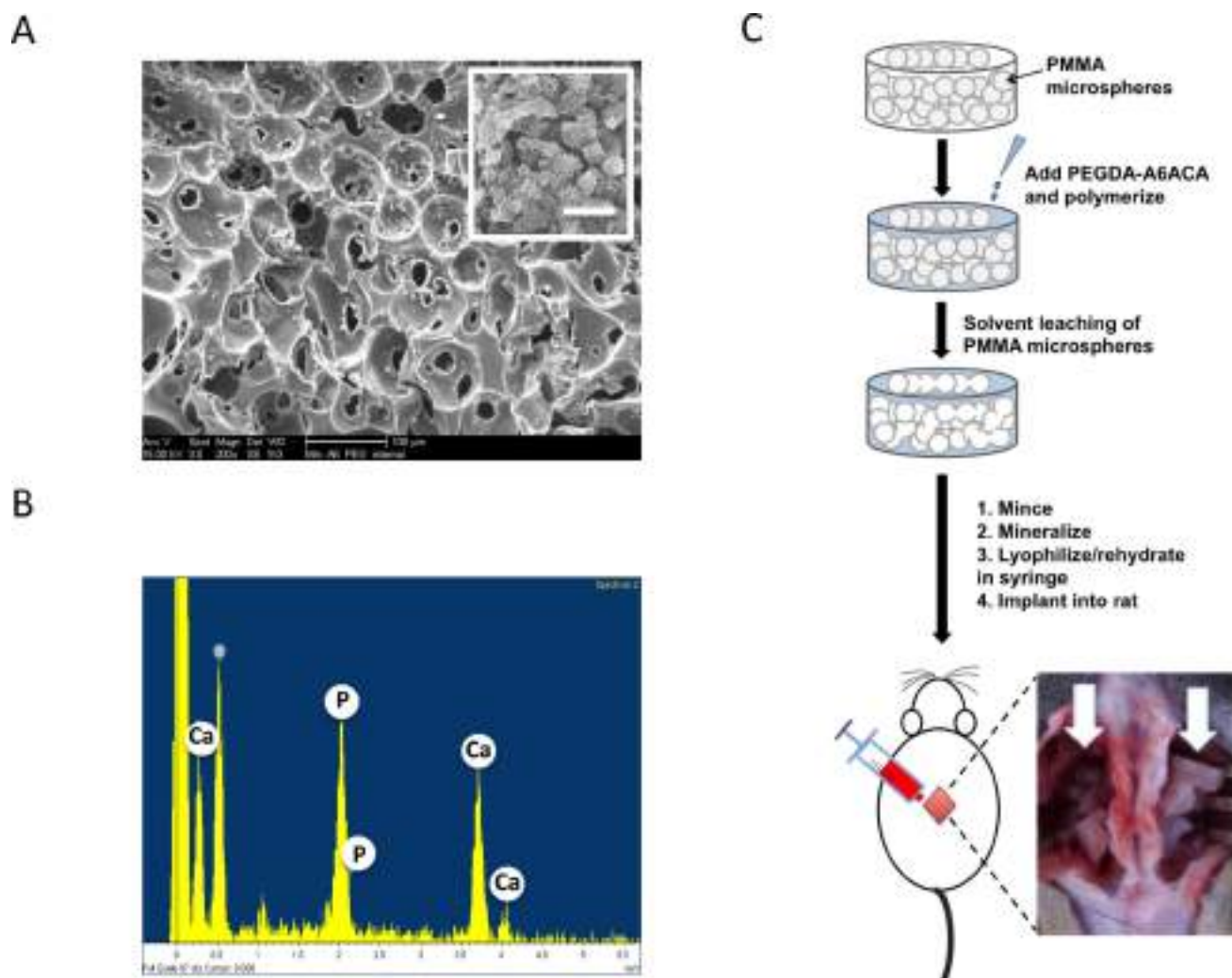


**Figure 1.**

Experimental procedure and characterization of mineralized macroporous matrices. (A) SEM images (inset shows high magnification image; Scale bar: 2  $\mu$ m). (B) EDS analysis for calcium and phosphate ions of mineralized PEGDA-A6ACA hydrogels. (C) Schematic representation of the experimental procedure. Preparation of sintered template of PMMA microspheres (PMMA microspheres: grey spheres), polymerization of PEGDA-A6ACA hydrogel matrix (PEGDA-A6ACA: light blue mass) around the PMMA template, and the leaching of PMMA template to obtain porous hydrogel matrices (white). The porous hydrogels were minced and mineralized to obtain biomineralized grafts. The grafts were loaded into the syringe, lyophilized and rehydrated in saline, basic fibroblast growth factor (bFGF), or bone marrow (BM) flush prior to implantation. Implantation of grafts in nude rats for posterolateral fusion with white arrows pointing to grafts placed on either side of the spine at L4-L5 following decortication of transverse processes.

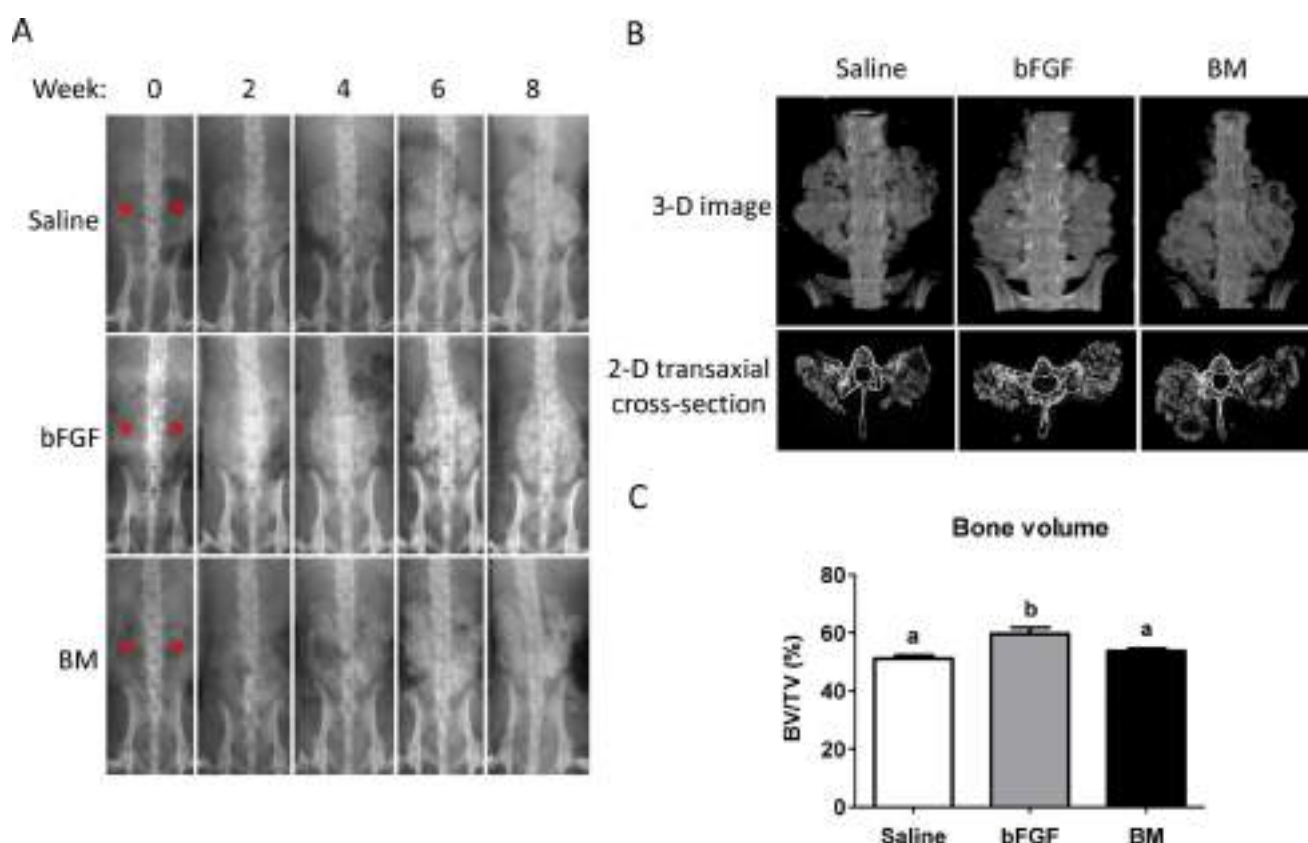


**Figure 2.** X-ray and micro-computerized tomography ( $\mu$ CT) analysis. (A) Representative images from X-ray radiography of live animals receiving grafts infused with saline, basic fibroblast growth factor (bFGF), or bone marrow (BM) flush indicate hard tissue formation as a function of post-implantation time for up to 8 weeks. Red asterisks indicate the locations of implanted grafts at week 0. (B) Three-dimensional (3-D) micro-computerized tomography ( $\mu$ CT) and transaxial cross-sectional images at 8 weeks after graft implantation. (C) Bone density in fusion mass for saline-, bFGF-, and BM-soaked groups quantified from  $\mu$ CT images. Different letters represent statistical significances, where “a” is statistically significant compared to “b”. Error bars represent standard error of the mean ( $n=7$ ,  $p<0.05$ ).

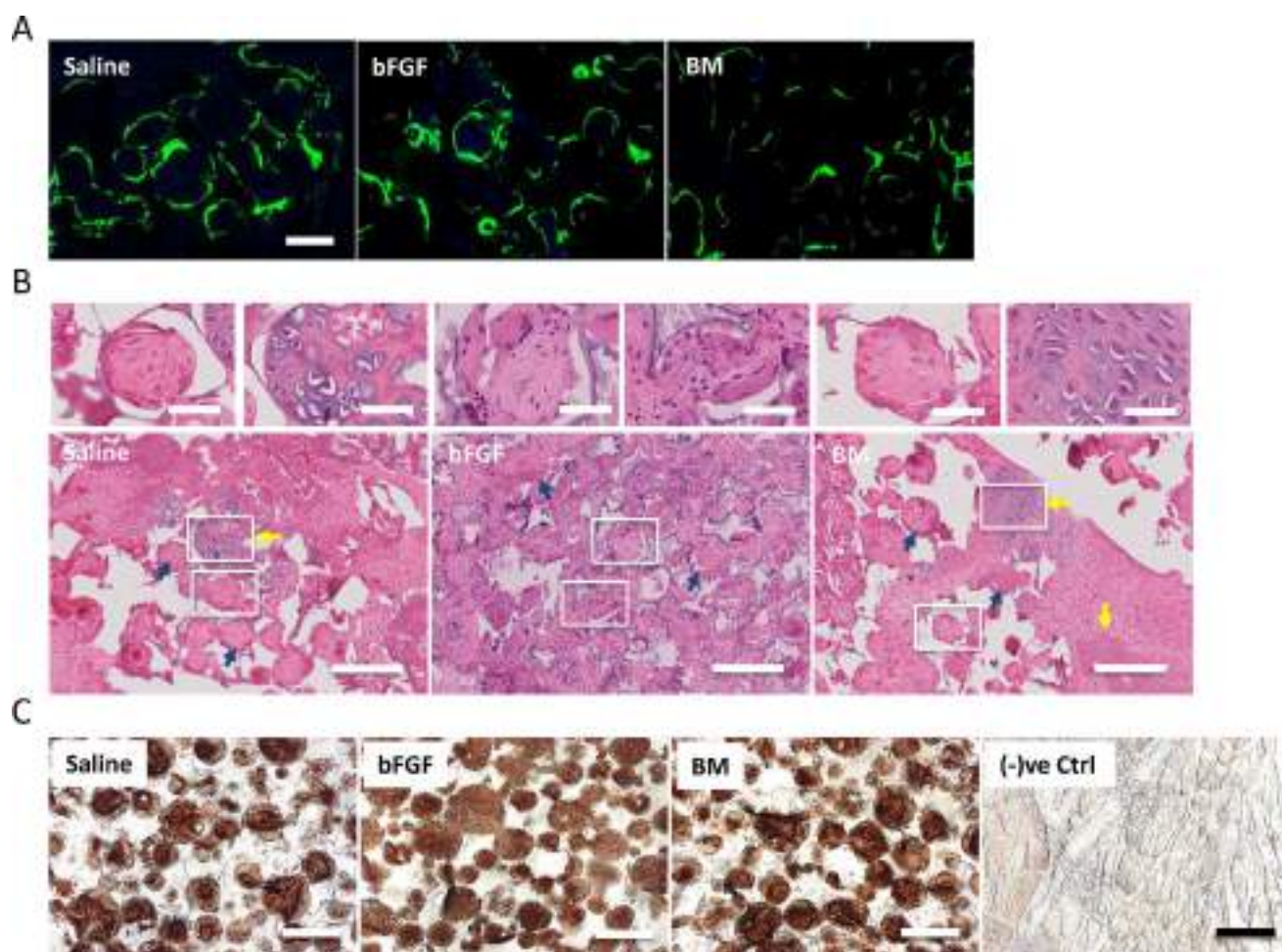


**Figure 3.**

Calcium deposition and histological staining for bone formation. (A) Calcein labeling suggests neo-calcium deposition in saline-, basic fibroblast growth factor (bFGF)-, and bone marrow (BM)-soaked grafts after 2 weeks of calcein uptake. Scale bar: 100  $\mu$ m. (B) Hematoxylin-eosin (H&E) staining of grafts infused with saline, bFGF, and BM after 8 weeks of implantation for neo-bone tissue formation. Evidence of bone formation through endochondral ossification is evident in saline and BM groups (yellow arrows). Woven bone matrices with osteoblastic cells (blue arrows) were found in all groups. Scale bar: 200  $\mu$ m. Magnified images on top are regions undergoing endochondral ossification or woven bone from regions highlighted by white borders. Scale bar: 50  $\mu$ m. (C) Immunohistochemical staining for osteocalcin in saline-, bFGF-, and BM-soaked grafts after 8 weeks of implantation. Rat skin tissues were used as negative control [(-)ve Ctrl]. Scale bar: 200  $\mu$ m.

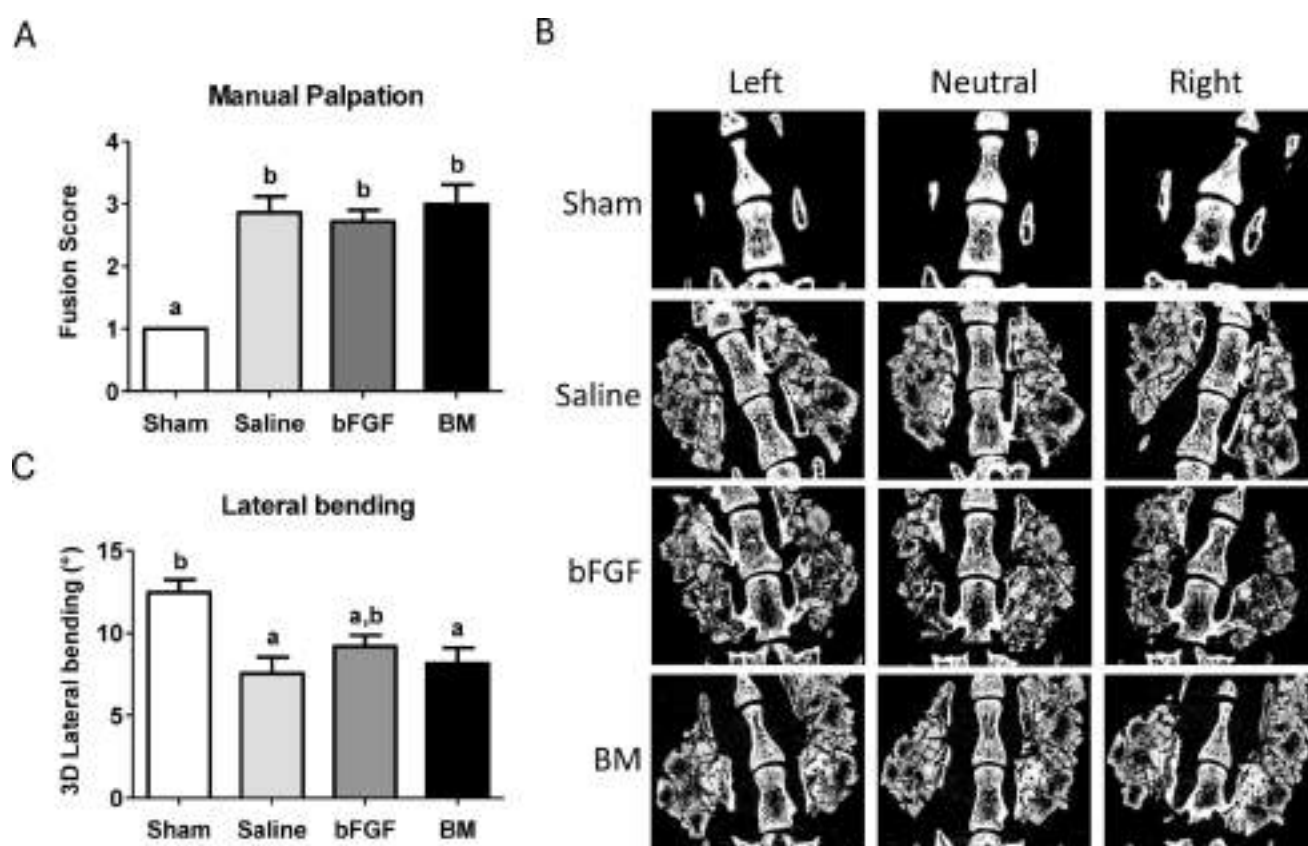


**Figure 4.** Analysis for spinal fusion. (A) Fusion score generated from manual palpation for each group; saline-, basic fibroblast growth factor (bFGF)-, and bone marrow (BM)-soaked grafts, after 8 weeks of implantation. Different letters represent statistical significance. Error bars represent standard error of the mean ( $n=7$ ,  $p<0.05$ ). (B) Micro-computed tomography ( $\mu$ CT) of sham, saline-soaked, bFGF-soaked and BM-soaked biomineralized grafts undergoing lateral bending measurements. Representative images at different positions during measurements for various groups after 8 weeks post-implantation. (C) Three-dimensional (3-D) lateral bending angles of spine with saline-, bFGF-, and BM-soaked grafts compared to sham surgery. Different letters represent statistical significances with “a” statistically significant to “b”. Error bars indicate standard error of the mean ( $n=7$ ,  $p<0.01$ ).



# Laminin-511 and -521 Enable Efficient In Vitro Expansion of Human Corneal Endothelial Cells

Naoki Okumura,<sup>1,2</sup> Kazuya Kakutani,<sup>1</sup> Ryohei Numata,<sup>1</sup> Makiko Nakahara,<sup>1</sup> Ursula Schlötzer-Schrehardt,<sup>3</sup> Friedrich Kruse,<sup>3</sup> Shigeru Kinoshita,<sup>2</sup> and Noriko Koizumi<sup>1</sup>

<sup>1</sup>Department of Biomedical Engineering, Faculty of Life and Medical Sciences, Doshisha University, Kyotanabe, Japan

<sup>2</sup>Department of Ophthalmology, Kyoto Prefectural University of Medicine, Kyoto, Japan

<sup>3</sup>Department of Ophthalmology, University of Erlangen-Nürnberg, Erlangen, Germany

Correspondence: Noriko Koizumi, Department of Biomedical Engineering, Faculty of Life and Medical Sciences, Doshisha University, Kyotanabe 610-0321, Japan; nkoizumi@mail.doshisha.ac.jp.

Submitted: July 4, 2014

Accepted: March 24, 2015

Citation: Okumura N, Kakutani K, Numata R, et al. Laminin-511 and -521 enable efficient in vitro expansion of human corneal endothelial cells. *Invest Ophthalmol Vis Sci*. 2015;56:2933–2942. DOI:10.1167/iov.14-15163

**PURPOSE.** The purpose of this study was to investigate the usefulness of laminin isoforms as substrates for culturing human corneal endothelial cells (HCECs) for clinical application of tissue engineering therapy.

**METHODS.** Expression of specific laminin chains in human corneal endothelium and Descemet's membrane was analyzed at the mRNA and protein levels. The effect of laminin-511 and -521 on cell adhesion and proliferation was evaluated. Recombinant laminin E8 fragments (E8s), which represent functionally minimal forms of laminins, were also evaluated for their effects on cell density and cellular phenotype. The potential involvement of  $\alpha\beta 1$  and  $\alpha 6\beta 1$  integrins in laminin signal transduction was also investigated using neutralizing antibodies.

**RESULTS.** Laminin-511 and -521 were expressed in Descemet's membrane and corneal endothelium. These laminin isoforms significantly enhanced the in vitro adhesion and proliferation, and differentiation of HCECs. A cell density of 2200 to 2400 cells/mm<sup>2</sup> was achieved when HCECs were cultured on laminin-511 or -521, whereas the density was only 1100 cells/mm<sup>2</sup> on an uncoated control. E8s also supported HCEC cultivation with a similar efficacy to that obtained with full-length laminin. Functional blocking of  $\alpha\beta 1$  and  $\alpha 6\beta 1$  integrins suppressed the adhesion of HCECs even in the presence of laminin-511.

**CONCLUSIONS.** Laminin-511 and -521 were the laminin isoforms present in Descemet's membrane, and these laminins modulate the adhesion and proliferation of CECs. Laminin E8s represent an ideal xeno-free defined substrate for the culture of CECs for clinical applications.

**Keywords:** corneal endothelial cells, laminin, cell culture, tissue engineering

The corneal endothelium maintains corneal transparency by pump and barrier functions.<sup>1</sup> However, corneal endothelial cells (CECs) are severely limited in their proliferative ability,<sup>2</sup> so that any damage to CECs causes a concurrent compensatory migration and enlargement of the remaining cells to cover the damaged area. When the density of CECs decreases due to pathological conditions or aging, the compromised endothelial pump function is compensated by an increase in the metabolic activity via ATP and by an increase in the total number of pump sites.<sup>3</sup> However, when the cell density decreases to a critical level, the metabolic pump function and the endothelial barrier can no longer counteract the stromal swelling pressure. Decompensation of the corneal endothelium resulting from various causes (e.g., Fuchs' corneal endothelial dystrophy, surgical trauma, and endotheliitis) ultimately leads to corneal edema, visual disturbance, and blindness.

Transplantation of donor corneas remains the only therapy for corneal endothelial dysfunction. Endothelial keratoplasty provides a less invasive and more efficient therapy for corneal endothelial disorders, but the worldwide shortage of donor corneas remains a persistent problem.<sup>4</sup> Several groups, including ours, have endeavored to overcome this shortage of donor tissue by exploring tissue engineering-based approaches using CEC cultivation.<sup>5–13</sup> However, in vitro expansion of CECs

poses difficulties due to the limited proliferative ability, undesired transformation to fibroblasts during culture, and senescence of cultured CECs.<sup>14–18</sup> Consequently, a cell culture protocol for clinical application has been investigated in the present study.

Laminin is a glycoprotein composed of three trimeric ( $\alpha$ ,  $\beta$ , and  $\gamma$ ) chains.<sup>19,20</sup> Fifteen laminin isoforms have been identified and are named according to the specific trimeric combination of their chains (e.g.,  $\alpha 1-5$ ,  $\beta 1-4$ , and  $\gamma 1-3$ ).<sup>20,21</sup> Laminins are the major basement membrane components responsible for modulating cellular functions such as migration, survival, proliferation, and differentiation.<sup>19,22</sup> The expression of laminin-411 and -511 in the corneal endothelial basement membrane, the Descemet's membrane, have been reported<sup>23,24</sup>; however, the laminin composition and its biological role are not fully understood.<sup>25</sup>

In the present study, we hypothesized that specific laminin isoforms expressed in Descemet's membrane may transduce biological signals to CECs, and that these signals may trigger the in vitro expansion of CECs for clinical use. Therefore, we investigated the expression of specific laminin isoforms in the Descemet's membrane of the human cornea and the potential of these laminins for in vitro expansion of CECs. We also screened the expression of integrins in CECs, as these

TABLE 1. Oligonucleotide Sequences of Laminins for RT-PCR

Gene	Sense Primer	Antisense Primer	Size (bp)
Laminin $\alpha 1$	5'-GAGTCCGTCTCTCTGGACATAG-3'	5'-CGTGGCATTCACAGGGTTGAC-3'	180
Laminin $\alpha 2$	5'-TGCTAGAATTTACCTCCGCTCG-3'	5'-GATCAAGTGGACAAGCCCTG-3'	203
Laminin $\alpha 3$	5'-CTCCAAAGGCCCAACTCAAG-3'	5'-CCATAACTGCCTCCTTAGTCTC-3'	304
Laminin $\alpha 4$	5'-CTTACGCAACACCACCGGATTC-3'	5'-CCTTCTTCCAAGCATTCTCCG-3'	140
Laminin $\alpha 5$	5'-GAGGACTGAAGTGAAAACCTCAA-3'	5'-CCACTGAAGTTGTAAATGGTG-3'	221
Laminin $\beta 1$	5'-GATGGTGAACCTTGATGAAAAGT-3'	5'-GGCTTATATCCTTTAGGAGTGA-3'	258
Laminin $\beta 2$	5'-GATGATCGCATCCAAGGGAC-3'	5'-GTCCAGAGTAGGGAGTCTCAG-3'	150
Laminin $\beta 3$	5'-CTCCTCTGCCTCTGTCTTCACAC-3'	5'-GACAAGCATGACCAAGCAGC-3'	233
Laminin $\beta 4$	5'-GGCAGGCTACTTTGGATTTC-3'	5'-GCTTGAGGGATCATCTGGAC-3'	204
Laminin $\gamma 1$	5'-GATGAGATGGTGACAGATCAAG-3'	5'-TTTCCAGTCTCTTCAATGGTAT-3'	199
Laminin $\gamma 2$	5'-ATCGAAGGTTACTGCGGAATC-3'	5'-GTAGCCAGAAGCACAATCCTG-3'	193
Laminin $\gamma 3$	5'-GGGATACAAGAGGGAGATGC-3'	5'-CATAGAAACCTGGCAAACAGC-3'	157

transmembrane receptors mediate binding and signal transduction between cells and laminins.<sup>19,22,26</sup> In addition, we examined laminin E8 fragments (E8s) as potential culture substrates for clinical applications. E8s are truncated proteins consisting of the C-terminal regions of the  $\alpha$ ,  $\beta$ , and  $\gamma$  chains and contain the laminin globular domains of the  $\alpha$  chain.<sup>27</sup> Our findings demonstrated that laminin E8s may represent an important component of a xeno-free defined substrate for human CEC (HCEC) culture and may promote the in vitro expansion of CECs for cell-based therapies.

## MATERIALS AND METHODS

### Ethics Statement

The human tissue specimens used in this study were handled in accordance with the tenets set forth in the Declaration of Helsinki. Informed written consent was obtained from the next of kin of all deceased donors with regard to eye donation for research. Human donor corneas were obtained from SightLife (<http://www.sightlife.org/>, Seattle, WA, USA). All tissue specimens were recovered under the tenets of the Uniform Anatomical Gift Act (UAGA) of the particular state in which the donor consent was obtained and the tissue recovered.

### Cell Culture

All human corneas were stored at 4°C in storage medium (Optisol-GS; Chiron Vision, Irvine, CA, USA) for less than 14 days prior to use. Primary cultures of CECs were established according to published protocols.<sup>16</sup> Briefly, Descemet's membranes containing the CECs were stripped from donor corneas and the membranes were digested with 1 mg/mL collagenase A at 37°C for 12 hours. The resulting CECs were seeded in one well of a 48-well plate. A total of six human donor corneas (from persons >40 years of age) were used for the experiment. Plates had previously been coated with laminin-511, -521, or -211. The culture medium was prepared according to published protocols.<sup>16</sup> First, human bone marrow-derived mesenchymal stem cells (BM-MSCs), provided by JCR Pharmaceuticals Co., Ltd. (Kobe, Japan), were cultured according to previously reported protocols. Briefly, BM-MSCs were plated at a density of  $1.3 \times 10^4$  cells/cm<sup>2</sup> and cultured for 24 hours in Dulbecco's Modified Eagle Medium (DMEM) supplemented with 10% fetal bovine serum (FBS), 100 U/mL penicillin, and 100  $\mu$ g/mL streptomycin. Then, basal medium for human CECs (HCECs) was prepared (OptiMEM-I, 8% FBS, 5 ng/mL epidermal growth factor, 20  $\mu$ g/mL ascorbic acid, 200 mg/L calcium chloride, 0.08% chondroitin sulfate, 50  $\mu$ g/mL gentamicin, and 10  $\mu$ M SB431542) and conditioned by

culturing BM-MSCs for 24 hours. Finally, the basal medium conditioned with BM-MSCs was collected for use as the culture medium for HCECs. The HCECs were cultured at 37°C in a humidified atmosphere containing 5% CO<sub>2</sub>, and the culture medium was changed every 2 days. Cell density was evaluated by phase contrast images analyzed using the KSS-400EB software (Konan Medical, Inc., Hyogo, Japan).

### Reverse Transcription PCR

Descemet's membranes containing CECs were stripped from three independent human donor corneas. Total RNA was extracted using the RNeasy Mini kit (Qiagen, Hilden, Germany). The quality of the RNA preparations was measured with a NanoDrop (Thermo Fisher Scientific, Inc., Waltham, MA, USA) spectrophotometer. First-strand cDNA was synthesized with 1  $\mu$ g of total RNA using a ReverTra Ace (Toyobo Corporation, Osaka, Japan) reverse transcriptase kit. The cDNA was subjected to PCR with the specific primers listed in Tables 1 and 2. Glyceraldehyde 3-phosphate dehydrogenase (GAPDH) was used as an internal control for gene analysis. PCR reactions were performed with Extaq DNA polymerase (Takara Bio, Inc., Otsu, Japan) under the following conditions: denaturation at 94°C for 30 seconds, 35 cycles of annealing at 54°C for 30 seconds, and elongation at 72°C for 30 seconds. The PCR products were separated by electrophoresis on 1.5% agarose gels, stained with ethidium bromide, and detected under ultraviolet illumination.

### Immunofluorescence

Corneas obtained from three independent donors were embedded in OCT compound, sectioned at a thickness of 6  $\mu$ m, and fixed in 4% paraformaldehyde for 5 minutes at room temperature. HCECs cultured in a 48-well cell culture plate were fixed in 4% paraformaldehyde for 10 minutes at room temperature. Nonspecific binding was blocked using 1% bovine serum albumin (BSA) for 30 minutes at room temperature. Primary antibodies against laminin  $\alpha 2$  (1:200), laminin  $\alpha 5$  (1:100), laminin  $\beta 1$  (1:200), laminin  $\beta 2$  (1:200), laminin  $\beta 3$  (1:500, Thermo Fisher Scientific, Inc.), laminin  $\gamma 1$  (1:200), Ki67 (1:400, Sigma-Aldrich Corp., St. Louis, MO, USA), Na<sup>+</sup>/K<sup>+</sup>-ATPase (1:200, Upstate Biotechnology, Lake Placid, NY, USA), and ZO-1 (1:200, Zymed Laboratories, South San Francisco, CA, USA) were used. Antibodies against laminin  $\alpha 2$ ,  $\alpha 5$ ,  $\beta 1$ ,  $\beta 2$ , and  $\gamma 1$  were a gift from Lydia Sorokin.<sup>28</sup> Either Alexa Fluor 488-conjugated goat anti-mouse (Life Technologies Corp., Carlsbad, CA, USA) or Alexa Fluor 594-conjugated goat anti-rabbit IgG (Life Technologies) were used as secondary antibodies at a 1:1000 dilution. Nuclei were stained with DAPI (Vector Laboratories, Burlingame, CA, USA). The slides were

TABLE 2. Oligonucleotide Sequences of Integrins for RT-PCR

Gene	Sense Primer	Antisense Primer	Size (bp)
<i>Integrin α1</i>	5'-GAAGAACCTCCTGAAACCCCTTT-3'	5'-TGATGTCATATTGGGGAATGAA-3'	254
<i>Integrin α2</i>	5'-TGATGGGACAGAAGTAACATGC-3'	5'-TGGACCAACATCTTCAAAACTG-3'	333
<i>Integrin α3</i>	5'-GCTCTGCCTTTGGTTTATCTGT-3'	5'-TTCCCACTAGAAGGTCTGGGTA-3'	257
<i>Integrin α4</i>	5'-ATATTCAGTCGGAGCTGGTCAT-3'	5'-GCATATTTGTCACTTCCAACGA-3'	338
<i>Integrin α5</i>	5'-TCCTCAGCAAGAATCTCAACAA-3'	5'-GTTGAGTCCCGTAACTCTGGTC-3'	304
<i>Integrin α6</i>	5'-AGCAAGGCAGATGGAATAATGT-3'	5'-CAGGGTAGGAATTTTCGATCAAG-3'	275
<i>Integrin α7</i>	5'-CAGGTCACCTTCTACCTCATCC-3'	5'-ACCGTGACCTCATACTTGACCT-3'	262
<i>Integrin α8</i>	5'-ATGGAAAATGTAACCAGGATGG-3'	5'-CAGTTATGAATGGGCAGAACAA-3'	265
<i>Integrin α9</i>	5'-CACTTTCAGCCCATCAATATCA-3'	5'-ACAGTGCTGCTGTTAGGCAAGAA-3'	305
<i>Integrin α10</i>	5'-ATCAGTGTGGTTCAGAGGGACT-3'	5'-GCCCTGGCTTTGTAGTATTGTC-3'	330
<i>Integrin α11</i>	5'-GGACACTGCTGACTACGTGAAG-3'	5'-GCGTGCTCTCTATGATGAAG-3'	294
<i>Integrin αE</i>	5'-TAGCAGTGAAGAAGCTGACGAG-3'	5'-TCTTTTCAGGAAGACGACAGTGA-3'	300
<i>Integrin αV</i>	5'-ATCTGTGAGGTCGAAACAGGAT-3'	5'-ACCTTGCCAATAAAAGCTACCA-3'	255
<i>Integrin αL</i>	5'-GAACCATTGACACCAGAAGTGA-3'	5'-TTCTTCAAACCCCAACTGTCTT-3'	341
<i>Integrin αM</i>	5'-GATCGGCTAAGAGAAGGACAGA-3'	5'-CATTGCCACAATTCTTCTCAAA-3'	330
<i>Integrin αX</i>	5'-CCAACATCTGCCTTTACATTGA-3'	5'-CGTGAAGTATCTCTGAGCATCG-3'	331
<i>Integrin αD</i>	5'-TTAACCAGATGAAGGGCTTTGT-3'	5'-GGTCTTTGTACTTCTGCCCATC-3'	296
<i>Integrin αIIb</i>	5'-GAAAAGACTGAGGAGGCTGAGA-3'	5'-GAGAAAATATCCGCAACTGGAG-3'	245
<i>Integrin β1</i>	5'-GCTGAAGACTATCCCATTGACC-3'	5'-ATTTCCAGATATGCGCTGTTTT-3'	321
<i>Integrin β2</i>	5'-TGATGGACCTCTCCTACTCCAT-3'	5'-GAAACTGGTTGGAGTTGTTGGT-3'	258
<i>Integrin β3</i>	5'-TGTTTACCACCTGATGCCAAGAC-3'	5'-TCCCATAAGCATCAACAATGAG-3'	308
<i>Integrin β4</i>	5'-GCTTCACACCTATTTCCCTGTC-3'	5'-GAAGGAAGGTTTCAGATGGATG-3'	316
<i>Integrin β5</i>	5'-GCTGGTGTTCACAACAGATGAT-3'	5'-ATCCCAGACTGACAACCTCCACT-3'	349
<i>Integrin β6</i>	5'-TGTGACTGTGGTGAATGTGTGT-3'	5'-CACCAGCTAGTTTGCACCTTGTC-3'	289
<i>Integrin β7</i>	5'-CACTTCAGACGACACATTCCAT-3'	5'-CCCAACTGCAGACTTAGGAATC-3'	250
<i>Integrin β8</i>	5'-GCATTATGTGACCAAACTTCA-3'	5'-ATTTCTTCAGGCTTCTCACGTC-3'	255

examined with a fluorescence microscope (TCS SP2 AOBs; Leica Microsystems, Wetzlar, Germany, or BZ-9000; Keyence, Osaka, Japan).

Cell Adhesion Assay

HCECs were seeded in 96-well plates and the numbers of adhered cells were measured 24 hours after seeding, using a CellTiter-Glo luminescent cell viability assay (Promega Corporation, Madison, WI, USA) according to the manufacturer's instructions. The number of adhered cells was determined using a Veritas microplate luminometer (Promega Corporation). Culture plates were coated with laminin-511, -521, and -211 (BioLamina, Sundbyberg, Sweden), type I collagen (Nitta Galatin, Inc., Osaka, Japan), and fibronectin (Wako Pure Chemical Industries, Ltd., Osaka, Japan; 20 µg/µL). The culture plate was also coated with FNC Coating mix (Athena Environmental Sciences, Inc., Baltimore, MD, USA), a commonly used coating reagent for cultivation of HCECs. The effect of laminin fragments on cell adhesion was examined using plates coated with laminin-521 or laminin E8 fragments (iMatrix-511; Nippi, Inc., Tokyo, Japan; 1.0, 2.0, 4.0 µg/cm<sup>2</sup>). The effect of the interaction between cellular integrins and laminins on cell adhesion was evaluated by seeding HCECs (5 × 10<sup>3</sup> cells/well) in 96-well plates coated with laminin-511 or 211 in the presence or absence of integrin-neutralizing antibodies (2 µg/mL): anti-α<sub>3</sub> integrin (Merck Millipore, Billerica, MA, USA), anti-α<sub>6</sub> integrin (Merck Millipore), and anti-β<sub>1</sub> integrin (R&D Systems, Inc., Minneapolis, MN, USA). Three hours after seeding, the numbers of adherent cells were determined with the CellTiter-Glo luminescent cell viability assay, as described above.

Cell Proliferation Assay

Cells were seeded at a density of 5000 cells/well in a 96-well plate and cultured for 24 hours, followed by incubation in serum-free media for an additional 24 hours (n = 6). DNA

synthesis was detected as incorporation of 5-bromo-2'-deoxyuridine (BrdU) into the Cell Proliferation Biotrak ELISA system, version 2, according to the manufacturer's instructions (Sigma-Aldrich Corp.). Briefly, cells were incubated with 10 mol/L BrdU for 24 hours at 37°C in a humidified atmosphere containing 5% CO<sub>2</sub>. The cultured cells were incubated with 10 µM BrdU labeling solution for 2 hours, and then incubated with 100 µL of monoclonal antibody against BrdU for 30 minutes. The BrdU absorbance was measured directly using a spectrophotometric microplate reader at a test wavelength of 450 nm.

Flow Cytometry

Expression of integrins was assessed by the Human Cell Surface Marker Screening Panel (BD Biosciences, Franklin Lakes, NJ, USA) according to manufacturer's protocol. HCECs at passages 2 through 5 were used for these experiments. Briefly, cultured HCECs were detached by treatment with Accutase (BD Biosciences) at 37°C, washed twice with PBS, passed through a BD Falcon 70-µm cell strainer (BD Biosciences), incubated in OptiMEM with the addition of 100 units/mL DNase for 15 minutes at room temperature, and resuspended in BD Pharmingen Stain Buffer (BD Biosciences) containing 5 mM EDTA. Cells were incubated with primary antibodies (integrin α<sub>1</sub>, integrin α<sub>2</sub>, integrin α<sub>3</sub>, integrin α<sub>6</sub>, integrin β<sub>1</sub>, mouse isotope IgG, and rat isotype IgG; BD Biosciences) at the dilution indicated by manufacturer's protocol for 30 minutes on ice. The cells were washed with BD Pharmingen Stain Buffer containing 5 mM EDTA and then incubated with AlexaFluor 647 conjugated goat anti-mouse IgG or goat anti-rat IgG (1:200 dilution, BD Biosciences) for 30 minutes. Cells were then washed with BD Pharmingen Stain Buffer containing 5 mM EDTA, fixed in BD Cytofix Fixation Buffer (BD Biosciences) for 10 minutes, and analyzed by flow cytometry using the BD FACSCant (BD Biosciences) and CellQuest Pro software (BD Biosciences).



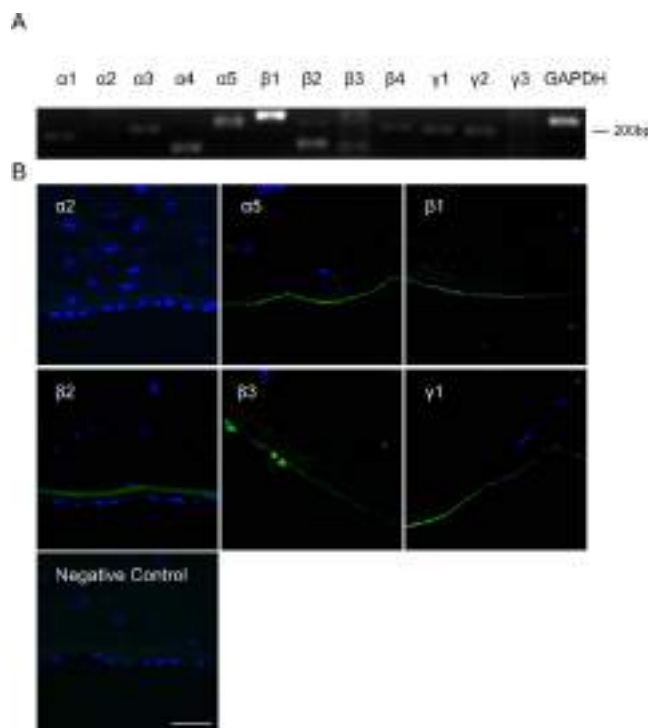


**FIGURE 1.** Laminin-511 and -521 are expressed in corneal endothelium and Descemet's membrane. (A) Expression of genes of laminin chains  $\alpha 1$ ,  $\alpha 2$ ,  $\alpha 3$ ,  $\alpha 4$ ,  $\alpha 5$ ,  $\beta 1$ ,  $\beta 2$ ,  $\beta 3$ ,  $\beta 4$ ,  $\gamma 1$ ,  $\gamma 2$ , and  $\gamma 3$  in the corneal endothelium were assessed by RT-PCR. (B) Expression of laminin  $\alpha 2$ ,  $\alpha 5$ ,  $\beta 1$ ,  $\beta 2$ ,  $\beta 3$ , and  $\gamma 1$  chains in donor Descemet's membrane were stained by immunohistochemistry. Scale bar: 50  $\mu$ m. The experiments were performed in triplicate.

### Immunoblotting

The CECs were seeded, with or without neutralizing integrin  $\alpha 3\beta 1$  and  $\alpha 6\beta 1$  antibodies, on a culture plate coated with laminin -511 or -211. A noncoated plate was used as a control. Three hours after seeding, the CECs were washed with ice-cold PBS, and then lysed with ice-cold radio immunoprecipitation assay (RIPA) buffer (Bio-Rad Laboratories, Hercules, CA, USA) buffer containing phosphatase inhibitor cocktail 2 and protease inhibitor cocktail. The lysates were centrifuged, and the supernatant representing total proteins was collected. An equal amount of protein was fractionated by SDS-PAGE, and polyvinylidene fluoride (PVDF) membranes were blocked with 3% nonfat dry milk, followed by an overnight incubation at 4°C with the following primary antibodies: phosphorylated focal adhesion kinase (FAK; 1:1000; Cell Signaling Technology, Inc., Danvers, MA, USA), FAK (1:1000; Cell Signaling Technology, Inc.), and GAPDH (1:3000; Abcam, Cambridge, UK). The blots were washed and incubated with horseradish peroxidase-conjugated secondary antibodies (1:5000; Cell Signaling Technology, Inc.). The blots were developed with luminal for enhanced chemiluminescence using the ECL Advanced Western Blotting Detection Kit (GE Healthcare, Piscataway, NJ, USA), and documented using an LAS4000S (Fuji Film, Tokyo, Japan) cooled charge-coupled-device camera gel documentation system. The relative density of the immunoblot bands was determined by Image J (National Institutes of Health, Bethesda, MD, USA) software. Relative fold differences were compared with the control values.

### Statistical Analysis

The statistical significance (*P*-value) of differences between mean values of the two-sample comparison was determined

with the Student's *t*-test. The statistical significance in the comparison of multiple sample sets was analyzed with Dunnett's multiple-comparisons test. Results are expressed as mean  $\pm$  SEM.

## RESULTS

### Expression of Laminin Isoforms in Corneal Endothelium and Descemet's Membrane

Expression patterns of laminin isotypes vary in different tissues; therefore, we analyzed the expression of specific laminin chains in human corneal endothelium and the Descemet's membrane at the mRNA and protein levels. Gene expression of laminin chains ( $\alpha 1$ ,  $\alpha 2$ ,  $\alpha 3$ ,  $\alpha 4$ ,  $\alpha 5$ ,  $\beta 1$ ,  $\beta 2$ ,  $\beta 3$ ,  $\beta 4$ ,  $\gamma 1$ ,  $\gamma 2$ , and  $\gamma 3$ ) was analyzed by RT-PCR in the corneal endothelium obtained from three independent donor corneas (Table 1). Laminin  $\alpha 5$ ,  $\beta 1$ ,  $\beta 2$ ,  $\beta 3$ ,  $\gamma 1$ , and  $\gamma 2$  chains were expressed in the corneal endothelium, while  $\alpha 1$ ,  $\alpha 2$ ,  $\alpha 3$ ,  $\alpha 4$ ,  $\beta 4$ , and  $\gamma 3$  were not expressed (Fig. 1A).

We then used immunohistochemistry to evaluate the presence of laminin chains expressed by endothelial cells in the Descemet's membrane. Immunostaining for laminin  $\alpha 5$ ,  $\beta 1$ ,  $\beta 2$ , and  $\gamma 1$  chains was evident as a linear staining pattern along the endothelial face of the Descemet's membrane (Fig. 1B), suggesting that laminin-511 and -521 represent the major laminin forms in the adult human Descemet's membrane.

### Effect of Laminin-511 and -521 on Cell Adhesion and Proliferation of HCECs

The detection of laminin-511 and -521 as the predominant laminin forms in the Descemet's membrane led to further evaluation of the suitability of these laminins as a substrate for in vitro expansion of HCECs. Primary HCECs seeded on laminin-511 and -521 formed a monolayer of cells with a hexagonal phenotype after 48 hours of culture. In contrast, control HCECs seeded on laminin-211 coated or uncoated culture plates formed patchy colonies rather than a confluent monolayer (Fig. 2A). The effect of laminin-511 and -521 on cell adhesion was evaluated by determining the numbers of adherent HCECs 24 hours after seeding. Incubation on laminin-511 and -521 coated plates increased the number of adherent cells 1.5-fold compared to uncoated controls, while laminin-211 had no effect on the number of adherent cells (Fig. 2B). The effect of laminins on HCEC proliferation was further assessed by measuring the incorporation of BrdU into the newly synthesized DNA. HCECs cultured on laminin-511 and -521 showed 2.6- to 3.2-fold increases in BrdU incorporation compared to the uncoated control. Of interest, HCECs cultured on laminin-211 demonstrated almost same proliferative potential when compared to HCECs cultured on uncoated control plates (Fig. 2C). In addition, laminin-511 and -521 increased percentage of Ki67-positive HCECs compared to the uncoated control and laminin-211 (Figs. 2D, 2E).

### Cell Density and Functional Phenotype of HCECs Cultured on Laminin-511 and -521

Cultured primary HCECs formed a contact inhibited monolayer of cells after 30 days of cultivation under all experimental conditions (Fig. 3A). A cell density of 2200 to 2400 cells/mm<sup>2</sup> was achieved when HCECs were cultured on laminin-511 or -521, whereas the density was only 1100 cells/mm<sup>2</sup> in uncoated control plates. Of interest, an increase in HCEC cell density similar to that seen with laminin-511 and -521 was observed following culture on laminin-211 (Fig. 3B).



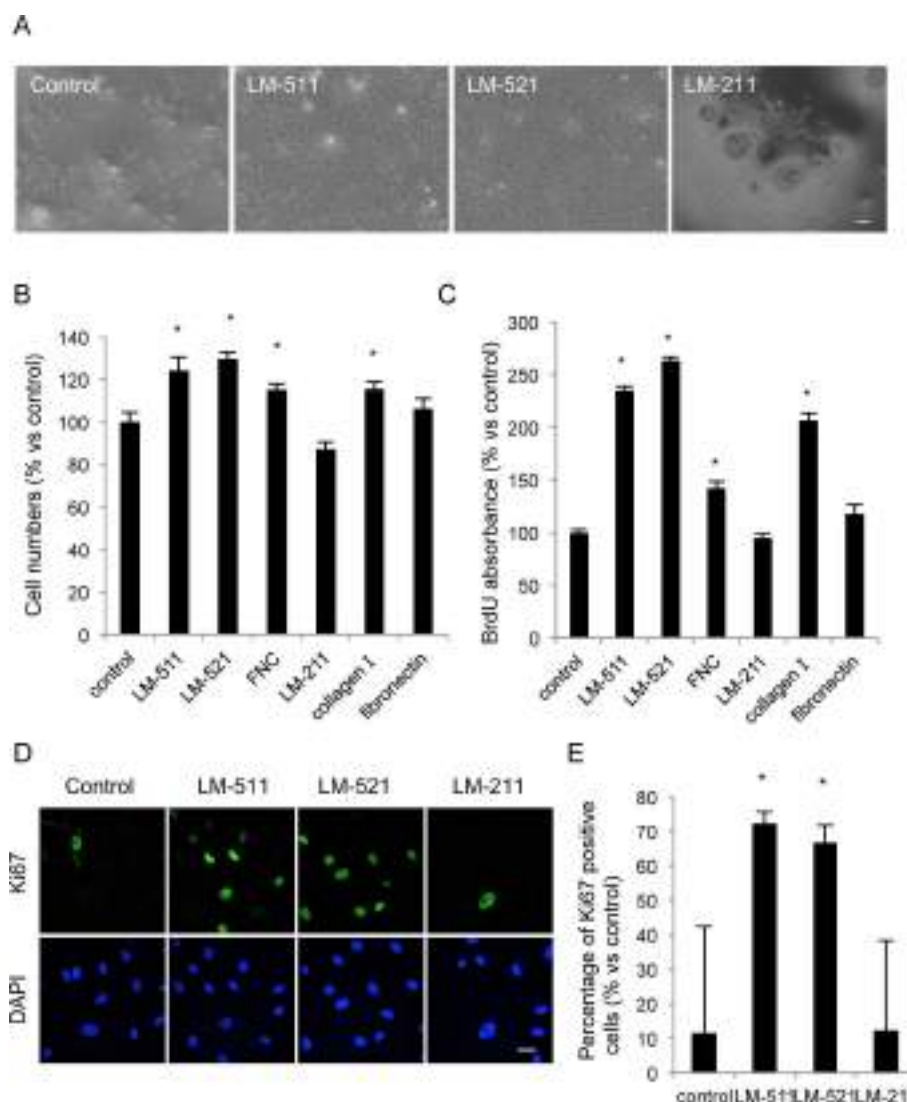


**FIGURE 2.** Laminin-511 and -521 enhance cell adhesion and proliferation of HCECs. **(A)** Phase-contrast images of HCECs cultured on plates coated with laminin-511 and -521 (Descemet's membrane type laminins) and laminin-211 (non-Descemet's membrane type laminin). *Scale bar:* 100  $\mu$ m. **(B)** The effect of laminins on cell adhesion was tested by seeding CECs at a density of  $5.0 \times 10^3$  cells/well, and the number of adhering CECs was determined with a CellTiter-Glo luminescent cell viability assay after 24 hours. The experiments were performed in triplicate.  $*P < 0.01$ . **(C)** The stimulating potency of laminins on cell proliferation was evaluated by seeding CECs at a density of  $5.0 \times 10^3$  cells/well. The proliferation of the CECs was evaluated by a BrdU incorporation assay after 24 hours of incubation with 10  $\mu$ M BrdU. The experiment was performed in duplicate.  $*P < 0.01$ . **(D, E)** CECs were seeded at a density of  $1.25 \times 10^4$  cells/cm<sup>2</sup> for 72 hours, and then expression of Ki67 was assessed by immunofluorescence staining. Ki67 positive cells were plotted as a graph. The experiment was performed in duplicate.  $*P < 0.01$ .

Culture on laminin-511 or -521 stimulated persistent expression and subcellular localization of Na<sup>+</sup>/K<sup>+</sup>-ATPase and ZO-1 at the plasma membrane. However, HCECs cultured on uncoated control plates showed partial loss of Na<sup>+</sup>/K<sup>+</sup>-ATPase and ZO-1 expression during culture (Fig. 3C). These data suggest that laminins present in the Descemet's membrane maintain the cell density and a functional cellular phenotype in vitro.

### Effect of Laminin E8 Fragments on Cell Culture of HCECs

We therefore examined the effect of laminin E8 fragments (E8s) on cell density and cellular phenotype of cultured HCECs. Laminin E8s are truncated proteins composed only of the  $\alpha$ ,  $\beta$ , and  $\gamma$  chain C-terminal regions, which include the active integrin binding site.<sup>29</sup> Culture on plates coated with

either laminin-511 or laminin-511-E8s resulted in a 1.3-fold increase in cell number compared to uncoated control plates 24 hours after cell seeding (Fig. 4A). Phase contrast images of confluent monolayers of primary HCECs derived from three independent donor corneas showed that HCECs cultured on laminin E8s assumed a hexagonal contact-inhibited phenotype while HCECs cultured on the FNC coating mix showed less hexagonality and had a greater size variation (Fig. 4B). The average cell density was significantly higher for HCECs cultured on laminin E8s than on FNC ( $2397.1 \pm 149.0$  cells/mm<sup>2</sup>,  $1203.3 \pm 209.7$  cells/mm<sup>2</sup>, respectively; Fig. 4C).

### Involvement of Integrin $\alpha 3 \beta 1$ and $\alpha 6 \beta 1$ in Mediating Binding to Laminins

Laminin isoforms bind to receptors expressed on the cell surface, including integrin receptors and nonintegrin receptors

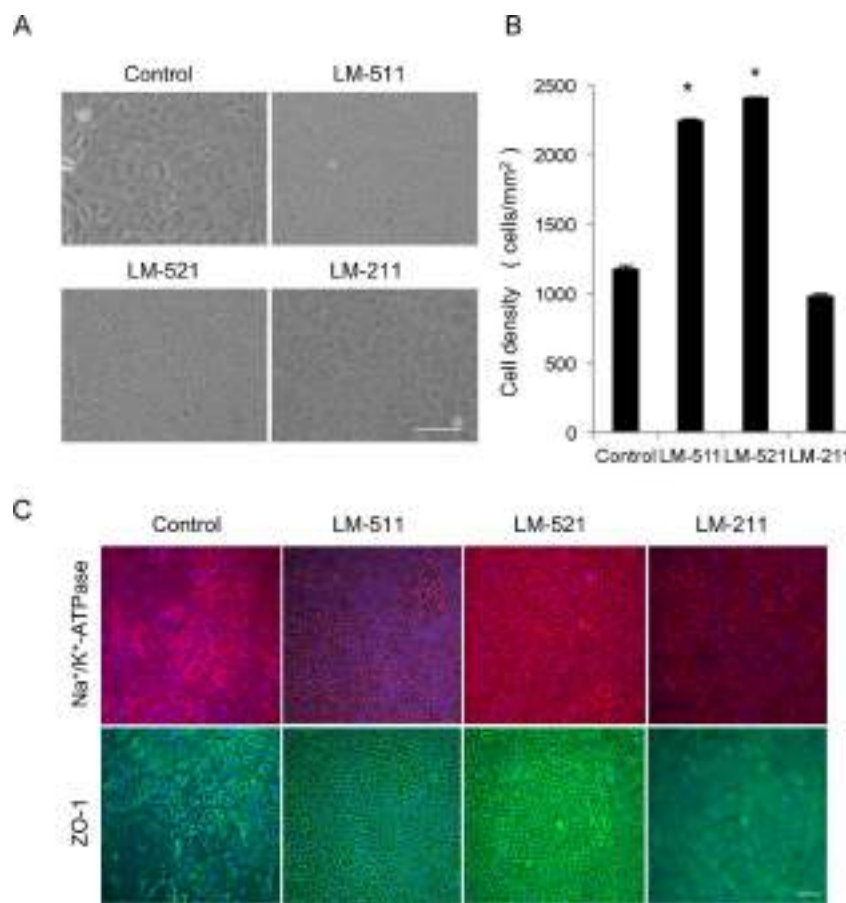


**FIGURE 3.** Laminin-511 and -521 maintain cell density and functional phenotype during cell culture. (A, B) CECs obtained from donor corneas were divided into four groups and seeded on a noncoated plate, or on plates coated with laminin-511, -521, or -211. Images show representative phase contrast images of CECs after 110 days cultivation. Graphs indicate the average cell densities of CECs. Scale bar: 100  $\mu$ m. \* $P < 0.01$ . (C) The functional phenotype was assessed by staining for ZO-1 and Na<sup>+</sup>/K<sup>+</sup>-ATPase at the plasma membrane in the CEC culture. Scale bar: 50  $\mu$ m. The experiments were performed in duplicate.

such as syndecans and dystroglycans. Various integrins are known to bind to laminins, so we first evaluated the expression of integrin chains in human corneal endothelium at the mRNA and protein levels. PCR analysis of donor corneal endothelium confirmed the expression of integrins  $\alpha 1$ ,  $\alpha 2$ ,  $\alpha 3$ ,  $\alpha 4$ ,  $\alpha 5$ ,  $\alpha 6$ ,  $\alpha 7$ ,  $\alpha 8$ ,  $\alpha 9$ ,  $\alpha 10$ ,  $\alpha 11$ ,  $\alpha V$ ,  $\alpha IIb$ ,  $\beta 1$ ,  $\beta 5$ , and  $\beta 8$  (Fig. 5A). We next assessed the protein expression of these integrins on the cell surface of cultured HCECs. Flow cytometry revealed expression of  $\alpha 1$ ,  $\alpha 2$ ,  $\alpha 3$ ,  $\alpha 6$ , and  $\beta 1$  integrin chains by the HCECs (Fig. 5B). The involvement of integrin  $\alpha 3\beta 1$  and  $\alpha 6\beta 1$  in activation of FAK was evaluated. Phosphorylation of FAK was enhanced in the HCECs cultured on the laminin-511 in comparison to the HCECs cultured on uncoated plate and laminin-211. However, functional blocking of  $\alpha 3\beta 1$  and  $\alpha 6\beta 1$  integrins by neutralizing antibodies suppressed phosphorylation of FAK of the HCECs cultured on laminin-511 (Fig. 5C). We then evaluated the effect of  $\alpha 3\beta 1$  integrin and  $\alpha 6\beta 1$  integrin on cell adhesion.  $\alpha 3\beta 1$  and  $\alpha 6\beta 1$  integrin neutralizing antibodies suppressed the adhesion of HCECs after 24 hours of seeding, even in the presence of laminin-511 (Fig. 5D). These findings indicate that laminins regulate HCEC adhesion through binding to integrin  $\alpha 3\beta 1$  and  $\alpha 6\beta 1$ .

## DISCUSSION

Corneal endothelial dysfunction is a major disorder requiring corneal transplantation.<sup>30</sup> Modern corneal transplantation

techniques such as Descemet's stripping automated endothelial keratoplasty (DSAEK) and Descemet's membrane endothelial keratoplasty (DMEK) are widely performed to replace damaged recipient corneal endothelium with healthy donor corneal endothelium.<sup>31,32</sup> The success of these techniques confirms that replacement of the corneal endothelium, rather than a full thickness corneal transplant, is sufficient for treating corneal endothelial dysfunction. It also raises the possibility of using tissue engineering therapy for treating corneal endothelial dysfunction by regenerating corneal endothelium alone rather than full thickness corneal tissue. Tissue engineering would have the distinct advantages of alleviating associated problems such as shortage of donors, primary graft failure, and technical difficulties in transplantation in severe cases.<sup>4</sup>

We previously reported that the corneal endothelium in rabbit and monkey corneal endothelial dysfunction models was regenerated by cell-based therapy without the need for a carrier.<sup>13</sup> Rho kinase inhibitor enhanced the adhesion of CECs onto the substrate,<sup>33</sup> so we injected cultured CECs into the anterior chamber together with a Rho kinase inhibitor in order to modulate cell adhesion properties. However, a serious technical bottleneck for tissue engineering therapy for corneal endothelial dysfunction is the ability to provide sufficient numbers of cultured CECs.<sup>14</sup> No protocol for culturing CECs for clinical use has been established, although several research groups, including ours, have been pursuing culture methods.<sup>14–16,34,35</sup> For instance, we demonstrated that conditioned

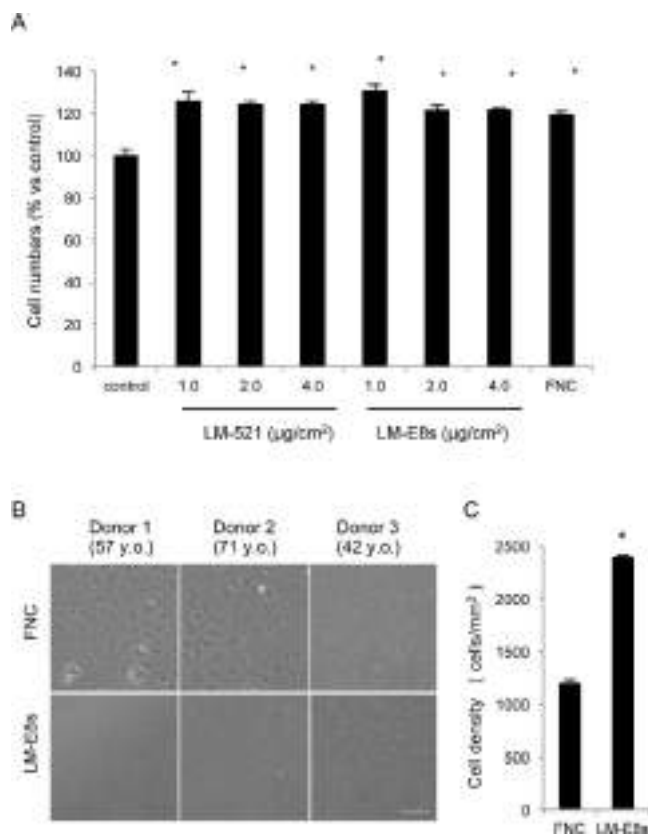


**FIGURE 4.** Laminin E8 fragments enable HCEC culture while maintaining cell density. **(A)** The effect of laminin E8s was evaluated by seeding CECs at a density of  $5.0 \times 10^3$  cells/well, and determining the number of adhered CECs with a CellTiter-Glo luminescent cell viability assay after 24 hours. Culture plates were coated with laminin-521 or laminin-511-E8s. The experiments were performed in triplicate.  $^*P < 0.01$ . **(B, C)** CECs obtained from three independent donors were cultured on FNC coating mix (a widely used coating reagent) or laminin 511-E8s. Phase contrast images depict CECs after 110 days cultivation. Graphs show the average cell densities of the CECs. Scale bar: 100  $\mu\text{m}$ .  $^*P < 0.01$ .

medium obtained from GMP-grade human BM-MSCs potentiated CEC proliferation.<sup>16</sup> We also reported that the inhibition of transforming growth factor- $\beta$  signaling counteracts the fibroblastic change under culture conditions.<sup>15</sup> These recently updated techniques have enabled efficient in vitro expansion of human CECs for clinical use, and we have recently obtained approval of the Japanese Ministry of Health, Labour, and Welfare and have initiated clinical research into cell-based therapy for corneal endothelial dysfunction patients at the Kyoto Prefectural University of Medicine (Clinical trial registration was obtained from UMIN000012534; <http://www.umin.ac.jp/english/>).

Typical culture substrates for CECs have included extracellular matrix (ECM) derived from bovine CECs<sup>36</sup> and FNC Coating Mix (Athena Environmental Sciences, Inc.).<sup>37</sup> We recently reported that a pericellular matrix prepared from human decidua-derived mesenchymal cells (PCM-DM) provides a xeno-free matrix substrate and enables efficient cell culture,<sup>38</sup> while avoiding the risk of contamination by xenogenic pathogens and immunogens from animal-derived matrixes. Interestingly, we noted that the use of PCM-DM enhanced the adhesion, migration, proliferation, and survival of CECs while maintaining cellular functions and cell density through integrin interactions.<sup>38</sup>

Integrins are receptors that sense changes in the extracellular environment and transmit that information.<sup>26</sup> We were therefore motivated to examine the effect of constituents of the Descemet's membrane extracellular matrix on CEC culture, since the Descemet's membrane provides the in vivo extracellular environment for CECs. The Descemet's membrane is formed by CECs that secrete the ECM, and is composed of type IV collagen, type VIII collagen, fibronectin, and laminin.<sup>39</sup> Its average thickness at birth is 3  $\mu\text{m}$  and it continuously increases in thickness throughout life.<sup>39</sup>

Laminins are the most potent molecules that determine cellular fate by binding to integrins,<sup>19,22</sup> while collagen and fibronectin have less effect on the adhesion of CECs when compared to FNC Coating Mix.<sup>38</sup> We therefore hypothesized that laminins present in the Descemet's membrane are pivotal for CEC culture. The expression of laminin  $\alpha 1$ ,  $\alpha 4$ ,  $\alpha 5$ ,  $\beta 1$ , and  $\gamma 1$  chains has been indicated in human fetal Descemet's membrane,<sup>25</sup> but the expression profile of laminin isoforms and their biological role in the corneal endothelium is unclear. Therefore, we examined the expression of laminin isoforms expressed in the Descemet's membrane and CECs and showed that laminin  $\alpha 5$ ,  $\beta 1$ ,  $\beta 2$ ,  $\beta 3$ ,  $\gamma 1$ , and  $\gamma 2$  chains were expressed in the corneal endothelium at the mRNA level. Laminin-511 and -521 were indicated as the isoforms expressed in the Descemet's membrane.

Several integrins ( $\alpha 2\beta 1$ ,  $\alpha 3\beta 1$ ,  $\alpha 5\beta 1$ , and  $\alpha 6\beta 1$ ) are present in human CECs,<sup>40</sup> and expression of  $\alpha v\beta 3$  integrin was reported in rat CECs during postnatal corneal maturation.<sup>41</sup> The  $\alpha v$  family integrins were shown to modulate bovine CEC adhesion to collagen.<sup>42</sup> However, evidence for a relationship between CECs and integrins is mostly indirect rather than direct and not much is known regarding integrin expression.<sup>43</sup> In the present study, we demonstrated that the  $\alpha 1$ , 2, 3, 6, and  $\beta 1$  subunits are expressed at the mRNA level and the protein is localized at the cell surface of the CECs. The neutralizing antibody experiments indicated that the  $\alpha 3\beta 1$  and  $\alpha 6\beta 1$  integrins are the ones that bind to CECs and transduce the signals. Reports that laminin globular modules of the laminin  $\alpha 5$  chain are recognized by  $\alpha 3\beta 1$ ,  $\alpha 6\beta 1$ ,  $\alpha 7\beta 1$ , and  $\alpha 6\beta 4$  integrins in various cell types provide further support for this assertion.<sup>26,44</sup> The laminin  $\alpha 5$  chain contains functional RGD sequences and mediates adhesion and migration.<sup>45</sup> Further studies, such as binding assays, are needed to confirm the direct interaction of these integrins and laminins in CECs.

FAK is a ubiquitously expressed cytoplasmic tyrosine kinase that regulates signals initiated by integrin-mediated ECM attachment.<sup>46,47</sup> In the present study, we showed that FAK in the CECs was activated by laminin-511, through  $\alpha 3\beta 1$  and  $\alpha 6\beta 1$  integrins, but not by laminin-211. Coincidentally, we also showed that laminin-511, but not laminin-211, enhances cell adhesion and proliferation, resulting in a higher cell density. These data suggest that the integrins expressed by CECs recognized specific laminin isoforms. Therefore, the signal that regulates cell fate may be triggered by FAK activation. FAK mediates cell spreading, adhesion, and migration by balancing the activation of Rho GTPases.<sup>48,49</sup> Though we reported that inhibiting the Rho-Rho kinase pathway enhances proliferation and adhesion of CECs,<sup>33</sup> detailed downstream signaling pathway of FAK in CECs should be studied further. The saturation density of the cultured CECs is also important, but suboptimal seeding density could result in a decrease in cell saturation density and a loss of proliferative potential.<sup>50</sup> Therefore, one possible explanation is that enhancement of HCEC adhesion by laminin-511 and -521 maintained the proliferative potential, which in turn enabled a higher saturation density, when compared to the HCECs cultured on uncoated control or laminin-211 coated surfaces in this study.

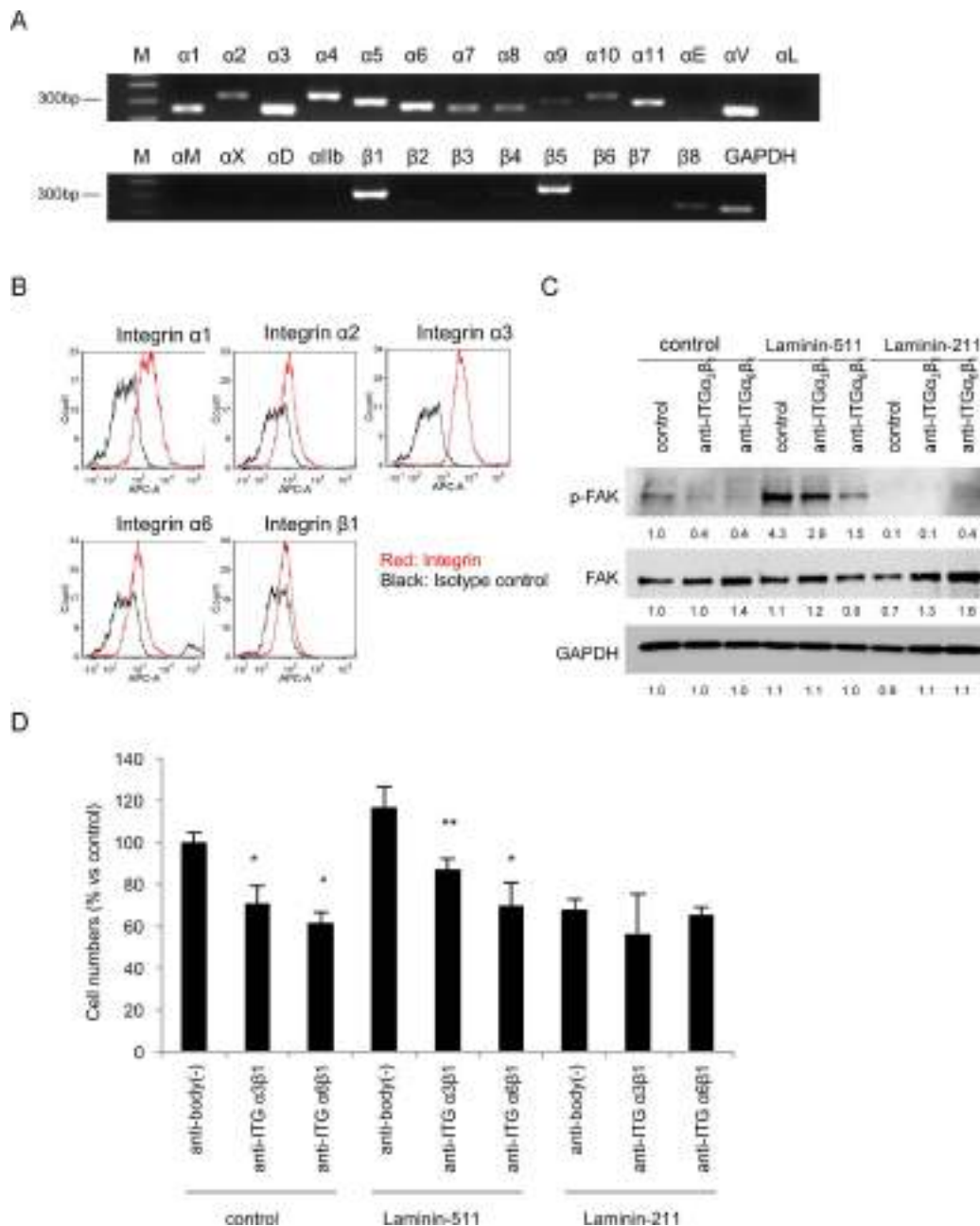


**FIGURE 5.** Interaction between laminins and HCECs is facilitated by integrin  $\alpha 3 \beta 1$  and  $\alpha 6 \beta 1$ . (A) The expression pattern of integrin  $\alpha$  and  $\beta$  chains in donor corneal endothelium was evaluated by PCR. (B) The expression of integrins detected by PCR was evaluated on the cell surface of cultured HCECs by flow cytometry. Three independent cultured CECs were used for the experiments. (C) The involvement of integrin  $\alpha 3 \beta 1$  and  $\alpha 6 \beta 1$  in activation of FAK was evaluated by functional blocking of with neutralizing antibodies. The CECs were seeded, with or without neutralizing integrin  $\alpha 3 \beta 1$  and  $\alpha 6 \beta 1$  antibodies, on a culture plate coated with laminin 511 or 211. A noncoated plate was used as a control. Phosphorylation of FAK and total FAK were evaluated by Western blotting after 3 hours. The experiments were performed in duplicate. (D) The involvement of integrin  $\alpha 3 \beta 1$  and  $\alpha 6 \beta 1$  in laminin-CECs interaction was evaluated by functional blocking of with neutralizing antibodies. The CECs were seeded at a density of  $5.0 \times 10^3$  cells/well with or without neutralizing integrin  $\alpha 3 \beta 1$  and  $\alpha 6 \beta 1$  antibodies, and the number of adhered CECs was determined by performing a CellTiter-Glo luminescent cell viability assay after 24 hours. The experiments were performed in triplicate. \* $P < 0.01$ .

A recent report indicated that deposition of collagen types III and XVI, agrin, TGFBI, and clusterin is altered in the Descemet's membrane of late-onset Fuchs' corneal endothelial dystrophy.<sup>51</sup> We demonstrated that ECM, which is not expressed in normal Descemet's membrane, does not activate FAK and does not support cell proliferation and adhesion. Consequently, the CECs of Fuchs' corneal endothelial dystrophy may possibly sense the alteration in ECM by integrins and

transduce a pathological signal from the ECM. However, this possibility requires further investigation.

The clinical application of laminin-511 and -521 still presents technical difficulties because laminins are large heterotrimeric proteins and require three independent vectors, coding the  $\alpha$ ,  $\beta$ , and  $\gamma$  chains, for production of a recombinant protein.<sup>29</sup> However, the recent report by Miyazaki et al.<sup>29</sup> that recombinant E8s of laminin isoforms support human embry-



onic stem cells suggests that laminin fragments may be a viable alternative to the native protein for CEC culture. E8s retain the integrin binding site that possess full binding capability to  $\alpha 6 \beta 1$  integrin, and then E8s are a functionally minimal form of laminin.<sup>29</sup> Recombinant E8s also do not present the risk of contamination with xenogenic pathogens and immunogens, so they offer a safe culture alternative.

In conclusion, we demonstrated that laminin-511 and -521 were the laminin isoforms present in the Descemet's membrane, and that these laminins modulate the adhesion and proliferation of CECs. Binding of these laminin isoforms to integrin  $\alpha 6 \beta 1$  and integrin  $\alpha 3 \beta 1$  may transduce functional signals from the microenvironment to the CECs. Lastly, the inclusion of laminin E8s may generate an ideal xeno-free defined substrate for the culture of CECs for clinical applications.

### Acknowledgments

The authors thank Lydia Sorokin for providing antibodies, Michio Hagiya for his invaluable advice about BM-MSCs, and Monty Montoya and Bernardino Iliakis (SightLife) for providing donor corneas.

Disclosure: **N. Okumura**, P; **K. Kakutani**, None; **R. Numata**, None; **M. Nakahara**, None; **U. Schlötzer-Schrehardt**, P; **F. Kruse**, P; **S. Kinoshita**, P; **N. Koizumi**, P

### References

- Bourne WM. Clinical estimation of corneal endothelial pump function. *Trans Am Ophthalmol Soc.* 1998;96:229-239, discussion 239-242.
- Joyce NC. Proliferative capacity of the corneal endothelium. *Prog Retin Eye Res.* 2003;22:359-389.
- Geroski DH, Matsuda M, Yee RW, Edelhauser HE. Pump function of the human corneal endothelium. Effects of age and cornea guttata. *Ophthalmology.* 1985;92:759-763.
- Tan DT, Dart JK, Holland EJ, Kinoshita S. Corneal transplantation. *Lancet.* 2012;379:1749-1761.
- Ishino Y, Sano Y, Nakamura T, et al. Amniotic membrane as a carrier for cultivated human corneal endothelial cell transplantation. *Invest Ophthalmol Vis Sci.* 2004;45:800-806.
- Mimura T, Yamagami S, Yokoo S, et al. Cultured human corneal endothelial cell transplantation with a collagen sheet in a rabbit model. *Invest Ophthalmol Vis Sci.* 2004;45:2992-2997.
- Sumide T, Nishida K, Yamato M, et al. Functional human corneal endothelial cell sheets harvested from temperature-responsive culture surfaces. *FASEB J.* 2006;20:392-394.
- Koizumi N, Sakamoto Y, Okumura N, et al. Cultivated corneal endothelial cell sheet transplantation in a primate model. *Invest Ophthalmol Vis Sci.* 2007;48:4519-4526.
- Lai JY, Chen KH, Hsiue GH. Tissue-engineered human corneal endothelial cell sheet transplantation in a rabbit model using functional biomaterials. *Transplantation.* 2007;84:1222-1232.
- Choi JS, Williams JK, Greven M, et al. Bioengineering endothelialized neo-corneas using donor-derived corneal endothelial cells and decellularized corneal stroma. *Biomaterials.* 2010;31:6738-6745.
- Liang Y, Liu W, Han B, et al. Fabrication and characters of a corneal endothelial cells scaffold based on chitosan. *J Materials Sci Materials Med.* 2011;22:175-183.
- Watanabe R, Hayashi R, Kimura Y, et al. A novel gelatin hydrogel carrier sheet for corneal endothelial transplantation. *Tissue Engin Part A.* 2011;17:2213-2219.
- Okumura N, Koizumi N, Ueno M, et al. ROCK inhibitor converts corneal endothelial cells into a phenotype capable of regenerating in vivo endothelial tissue. *Am J Pathol.* 2012;181:268-277.
- Peh GS, Beuerman RW, Colman A, Tan DT, Mehta JS. Human corneal endothelial cell expansion for corneal endothelium transplantation: an overview. *Transplantation.* 2011;91:811-819.
- Okumura N, Kay EP, Nakahara M, Hamuro J, Kinoshita S, Koizumi N. Inhibition of TGF-beta signaling enables human corneal endothelial cell expansion in vitro for use in regenerative medicine. *PLoS One.* 2013;8:e58000.
- Nakahara M, Okumura N, Kay EP, et al. Corneal endothelial expansion promoted by human bone marrow mesenchymal stem cell-derived conditioned medium. *PLoS One.* 2013;8:e69009.
- Walshe J, Harkin DG. Serial explant culture provides novel insights into the potential location and phenotype of corneal endothelial progenitor cells. *Exper Eye Res.* 2014;127:9-13.
- Kim E, Kim JJ, Hyon JY, et al. The effects of different culture media on human corneal endothelial cells. *Invest Ophthalmol Vis Sci.* 2014;55:5099-5108.
- Miner JH, Yurchenco PD. Laminin functions in tissue morphogenesis. *Ann Rev Cell Develop Biol.* 2004;20:255-284.
- Durbecq M. Laminins. *Cell Tissue Res.* 2010;339:259-268.
- Aumailley M, Bruckner-Tuderman L, Carter WG, et al. A simplified laminin nomenclature. *Matrix Biol.* 2005;24:326-332.
- Scheele S, Nystrom A, Durbecq M, Talts JE, Ekblom M, Ekblom P. Laminin isoforms in development and disease. *J Mol Med.* 2007;85:825-836.
- Ljubimov AV, Burgeson RE, Butkowski RJ, Michael AF, Sun TT, Kenney MC. Human corneal basement membrane heterogeneity: topographical differences in the expression of type IV collagen and laminin isoforms. *Lab Invest.* 1995;72:461-473.
- Kabosova A, Azar DT, Bannikov GA, et al. Compositional differences between infant and adult human corneal basement membranes. *Invest Ophthalmol Vis Sci.* 2007;48:4989-4999.
- Bystrom B, Virtanen I, Rousselle P, Gullberg D, Pedrosa-Domellof F. Distribution of laminins in the developing human eye. *Invest Ophthalmol Vis Sci.* 2006;47:777-785.
- Hynes RO. Integrins: bidirectional, allosteric signaling machines. *Cell.* 2002;110:673-687.
- Ido H, Harada K, Futaki S, et al. Molecular dissection of the alpha-dystroglycan- and integrin-binding sites within the globular domain of human laminin-10. *J Biol Chem.* 2004;279:10946-10954.
- Korpos E, Kadri N, Kappelhoff R, et al. The peri-islet basement membrane, a barrier to infiltrating leukocytes in type 1 diabetes in mouse and human. *Diabetes.* 2013;62:531-542.
- Miyazaki T, Futaki S, Suemori H, et al. Laminin E8 fragments support efficient adhesion and expansion of dissociated human pluripotent stem cells. *Nature Comm.* 2012;3:1236.
- Eye Bank Association of America. Eye Banking Statistical Report. Washington, DC: Eye Bank Association of America; 2012.
- Melles GR, Ong TS, Ververs B, van der Wees J. Preliminary clinical results of Descemet membrane endothelial keratoplasty. *Am J Ophthalmol.* 2008;145:222-227.
- Price MO, Price FW Jr. Endothelial keratoplasty: a review. *Clin Exper Ophthalmol.* 2010;38:128-140.
- Okumura N, Ueno M, Koizumi N, et al. Enhancement on primate corneal endothelial cell survival in vitro by a ROCK inhibitor. *Invest Ophthalmol Vis Sci.* 2009;50:3680-3687.
- Yamaguchi M, Ebihara N, Shima N, et al. Adhesion, migration, and proliferation of cultured human corneal endothelial cells by laminin-5. *Invest Ophthalmol Vis Sci.* 2011;52:679-684.
- Shima N, Kimoto M, Yamaguchi M, Yamagami S. Increased proliferation and replicative lifespan of isolated human corneal

- endothelial cells with L-ascorbic acid 2-phosphate. *Invest Ophthalmol Vis Sci.* 2011;52:8711–8717.
36. Miyata K, Drake J, Osakabe Y, et al. Effect of donor age on morphologic variation of cultured human corneal endothelial cells. *Cornea.* 2001;20:59–63.
  37. Zhu C, Joyce NC. Proliferative response of corneal endothelial cells from young and older donors. *Invest Ophthalmol Vis Sci.* 2004;45:1743–1751.
  38. Numata R, Okumura N, Nakahara M, et al. Cultivation of corneal endothelial cells on a pericellular matrix prepared from human decidua-derived mesenchymal cells. *PLoS One.* 2014;9:e88169.
  39. Gottsch JD, Zhang C, Sundin OH, Bell WR, Stark WJ, Green WR. Fuchs corneal dystrophy: aberrant collagen distribution in an L450W mutant of the COL8A2 gene. *Invest Ophthalmol Vis Sci.* 2005;46:4504–4511.
  40. Ljubimov AV, Huang ZS, Huang GH, et al. Human corneal epithelial basement membrane and integrin alterations in diabetes and diabetic retinopathy. *J Histochem Cytochem.* 1998;46:1033–1041.
  41. Joyce NC, Harris DL, Zieske JD. Mitotic inhibition of corneal endothelium in neonatal rats. *Invest Ophthalmol Vis Sci.* 1998;39:2572–2583.
  42. Rixen H, Kirkpatrick CJ, Schmitz U, Ruchatz D, Mittermayer C. Interaction between endothelial cells and basement membrane components. In vitro studies on endothelial cell adhesion to collagen types I, III, IV and high molecular weight fragments of IV. *Exper Cell Bio.* 1989;57:315–323.
  43. Stepp MA. Corneal integrins and their functions. *Exper Eye Res.* 2006;83:3–15.
  44. Kikkawa Y, Sasaki T, Nguyen MT, Nomizu M, Mitaka T, Miner JH. The LG1-3 tandem of laminin alpha5 harbors the binding sites of Lutheran/basal cell adhesion molecule and alpha3-beta1/alpha6beta1 integrins. *J Biol Chem.* 2007;282:14853–14860.
  45. Wondimu Z, Omrani S, Ishikawa T, et al. A novel monoclonal antibody to human laminin alpha5 chain strongly inhibits integrin-mediated cell adhesion and migration on laminins 511 and 521. *PLoS One.* 2013;8:e53648.
  46. Frame MC, Patel H, Serrels B, Lietha D, Eck MJ. The FERM domain: organizing the structure and function of FAK. *Nature Rev Mol Cell Bio.* 2010;11:802–814.
  47. Lee BY, Timpson P, Horvath LG, Daly RJ. FAK signaling in human cancer as a target for therapeutics. *Pharmacol Ther.* 2014;146:132–149.
  48. Tomar A, Lim ST, Lim Y, Schlaepfer DDA. FAK-p120RasGAP-p190RhoGAP complex regulates polarity in migrating cells. *J Cell Sci.* 2009;122:1852–1862.
  49. Schaller MD. Cellular functions of FAK kinases: insight into molecular mechanisms and novel functions. *J Cell Sci.* 2010;123:1007–1013.
  50. Peh GS, Toh KP, Ang HP, Seah XY, George BL, Mehta JS. Optimization of human corneal endothelial cell culture: density dependency of successful cultures in vitro. *BMC Res Notes.* 2013;6:176.
  51. Weller JM, Zenkel M, Schlotzer-Schrehardt U, Bachmann BO, Tourtas T, Kruse FE. Extracellular matrix alterations in late-onset Fuchs' corneal dystrophy. *Invest Ophthalmol Vis Sci.* 2014;55:3700–3708.

# SCIENTIFIC REPORTS

OPEN

## Density-gradient centrifugation enables the purification of cultured corneal endothelial cells for cell therapy by eliminating senescent cells

Naoki Okumura<sup>1</sup>, Ayaka Kusakabe<sup>1</sup>, Hiroatsu Hirano<sup>1</sup>, Ryota Inoue<sup>1</sup>, Yugo Okazaki<sup>1</sup>, Shinichiro Nakano<sup>1</sup>, Shigeru Kinoshita<sup>2</sup> & Noriko Koizumi<sup>1</sup>

Received: 06 July 2015

Accepted: 11 September 2015

Published: 07 October 2015

The corneal endothelium is essential for maintaining corneal transparency; therefore, corneal endothelial dysfunction causes serious vision loss. Tissue engineering-based therapy is potentially a less invasive and more effective therapeutic modality. We recently started a first-in-man clinical trial of cell-based therapy for treating corneal endothelial dysfunction in Japan. However, the senescence of corneal endothelial cells (CECs) during the serial passage culture needed to obtain massive quantities of cells for clinical use is a serious technical obstacle preventing the push of this regenerative therapy to clinical settings. Here, we show evidence from an animal model confirming that senescent cells are less effective in cell therapy. In addition, we propose that density-gradient centrifugation can eliminate the senescent cells and purify high potency CECs for clinical use. This simple technique might be applicable for other types of cells in the settings of regenerative medicine.

The cornea is transparent tissue exposed to the outer environment and serves as the transparent “window” of the eye to allow the entry of light. The corneal endothelium is responsible for maintenance of corneal transparency as a result of regulation by the corneal endothelium pump and barrier function. The proliferative ability of the corneal endothelium is severely limited<sup>1,2</sup>; consequently, severe damage to the corneal endothelium due to pathological conditions, such as endothelial corneal dystrophies and surgical trauma, impair corneal transparency and ultimately induce bullous keratopathy with serious vision loss. Corneal transplantation is currently the only therapeutic choice, but a worldwide shortage of donor corneas, the difficulty of the surgical procedure, and graft failure in both acute and chronic phases encourages researchers to develop tissue engineering-based therapies<sup>3</sup>.

A fundamental difficulty for the establishment of a tissue engineering-based therapy is the development of a cell cultivation protocol for clinical application<sup>4</sup>. Many researchers, including us, have devoted their efforts to establishing cell culture protocols<sup>5–11</sup>. Indeed, we are currently culturing CECs of Good Manufacturing Practice (GMP) grade in the cell-processing center for clinical applications<sup>4</sup>, and have successfully treated the patients with those cells (not published). However, an unresolved problem is the occurrence of cellular senescence, where the cells exhibit morphological changes such as cell enlargement, vacuolization, and multinucleus formation<sup>12,13</sup>, during serial passage culture aimed at generating massive numbers of cells for clinical use.

<sup>1</sup>Department of Biomedical Engineering, Faculty of Life and Medical Sciences, Doshisha University, Kyotanabe, Japan. <sup>2</sup>Department of Frontier Medical Science and Technology for Ophthalmology, Kyoto Prefectural University of Medicine, Kyoto, Japan. Correspondence and requests for materials should be addressed to N.K. (email: nkoizumi@mail.doshisha.ac.jp)

Here, we provide evidence to show that senescent phenotype CECs were less effective in cell-based therapy in an animal model and that non-senescent phenotype cells should be used clinically. We also proposed a simple procedure for purification of cultured human CECs (HCECs) by eliminating the senescent HCECs by density-gradient centrifugation.

## Results

**Senescent CECs *in vitro* and *in vivo*.** The cell density of the corneal endothelium is approximately 3000 cells/mm<sup>2</sup> at the age of 10–20 years, then it gradually decreases with aging at 0.3–0.6% per year, and pathological conditions induce the rapid loss of cell density<sup>14,15</sup>. Representative corneal endothelium images obtained by non-contact specular microscope showed that the cell density (CD) is lower in 89-year-old healthy elderly subjects than in 16-year-old healthy young subjects due to aging. Corneal trauma also induced the remaining cells to enlarge and flatten, associated with the cell density decrease (Fig. 1a). We successfully cultured HCECs that maintained a high CD and showed less variation in morphology (Fig. 1b; left). However, the numbers of low CD-HCECs with morphological senescence features, such as enlargement, flattening, vacuolization, and multiple nuclei, sometimes spontaneously increase after passaging the culture 5–8 times (Fig. 1b; right).

**Effect of cell density on cell therapy.** We were motivated to evaluate the effect of cell senescence on cell-based therapy and conducted experiments using a rabbit corneal endothelial dysfunction model. In accordance with our previous report<sup>16</sup>, corneal transparency was restored in endothelial dysfunction models by intracameral injection of high CD rabbit CECs (RCECs) with ROCK inhibitor, while the controls exhibited hazy corneas due to corneal endothelial dysfunction. Interestingly, senescent RCECs with low CD were able to restore corneal transparency similar to high-CD RCECs (Fig. 2a). However, the corneal thickness and corneal volume, which are indexes of corneal endothelial function, were significantly reduced in the eyes injected with high CD RCECs when compared to eyes injected with low-CD CECs (Fig. 2b,c). The corneal endothelium was regenerated following injection of either high- or low-CD CECs, but the CD of regenerated corneal endothelium was significantly higher in the eyes injected with high CD-CECs than with low-CD senescent CECs (2630.0 cells/mm<sup>2</sup> and 1137.0 cells/mm<sup>2</sup>, respectively) (Fig. 2d,e). In accordance with these clinical indicators, fluorescent staining demonstrated that the function-related markers Na<sup>+</sup>/K<sup>+</sup>-ATPase (pump function), ZO-1 (tight junction), and N-cadherin (adherent junction) were expressed in all regenerated CECs in eyes injected with high-CD CECs, while expression of these markers was partially disrupted in the CECs in eyes injected with low-CD CECs. Actin was distributed in the cell cortex similar to its distribution in healthy cells in the eyes injected with high-CD CECs, while cortical actin distribution showed irregularity, with stress fibers, in the eyes injected with low-CD CECs, suggesting that the functional and morphological recovery is poor when elicited by senescent cells (Fig. 2f).

**Phenotypic analysis of senescent cells.** Phenotypic analysis of senescent cells revealed enlargement and flattening in cells with low CD. RCECs underwent senescence spontaneously after 4–5 passages but formed monolayer sheet structures with cobblestone-like morphology and were used for the experiment (Fig. 3a). Expressions of ZO-1, which represents the barrier function, and of Na<sup>+</sup>/K<sup>+</sup>-ATPase, which represents pump function, were partially disrupted in low-CD CECs, while they were expressed in all high-CD CECs. Disruption of actin at the cell cortex was also observed, with the formation of stress fibers, but only in low-CD CECs (Fig. 3b). Cell adhesion and proliferation potencies were significantly decreased in low-CD CECs when compared to high-CD CECs (Fig. 3c–f).

**RCEC purification by density-gradient centrifugation.** Next, we hypothesized that senescent cells can be separated by density-gradient centrifugation according to their specific gravity because the senescent CECs are enlarged and flattened. Additionally, the cell size is believed to be the most valid indicator for corneal endothelial healthiness in clinical settings, which gave us reason to eliminate large cells as senescent cells. We tried to separate RCECs from a mixture of high-CD CECs and spontaneously-appearing senescent CECs into several fractions according to their specific gravity using OptiPrep™ Density Gradient Medium (Fig. 4a). Flow cytometry showed that CECs were separated according to cell size; i.e., the heavier specific gravity fraction included smaller diameter CECs and the lighter specific gravity fraction included the larger CECs (Fig. 4b). After seeding those cells, the CD was significantly higher in the CECs recovered from the 1.048 g/ml fraction than from the 1.018 and 1.033 g/ml fractions (Fig. 4c,d). In agreement with the smaller cell diameter of CECs recovered from the 1.048 g/ml fraction, the variation in cell size was smaller than those from 1.018 and 1.033 g/ml fractions after reaching confluence in culture. Additionally, the variation in cell size was smaller in the 1.048 g/ml fraction cells than in the control cells (Fig. 4e). Expressions of ZO-1 and Na<sup>+</sup>/K<sup>+</sup>-ATPase were partially disrupted in the control, whereas all cells recovered from the 1.048 g/ml fraction expressed these function-related proteins. Actin staining showed that cells recovered from 1.048 g/ml fraction were less variable in size and maintained their hexagonality (Fig. 4f).

**HCEC purification by density-gradient centrifugation.** We conducted experiments to evaluate whether cultured HCECs can be purified by separating out senescent cells by density-gradient



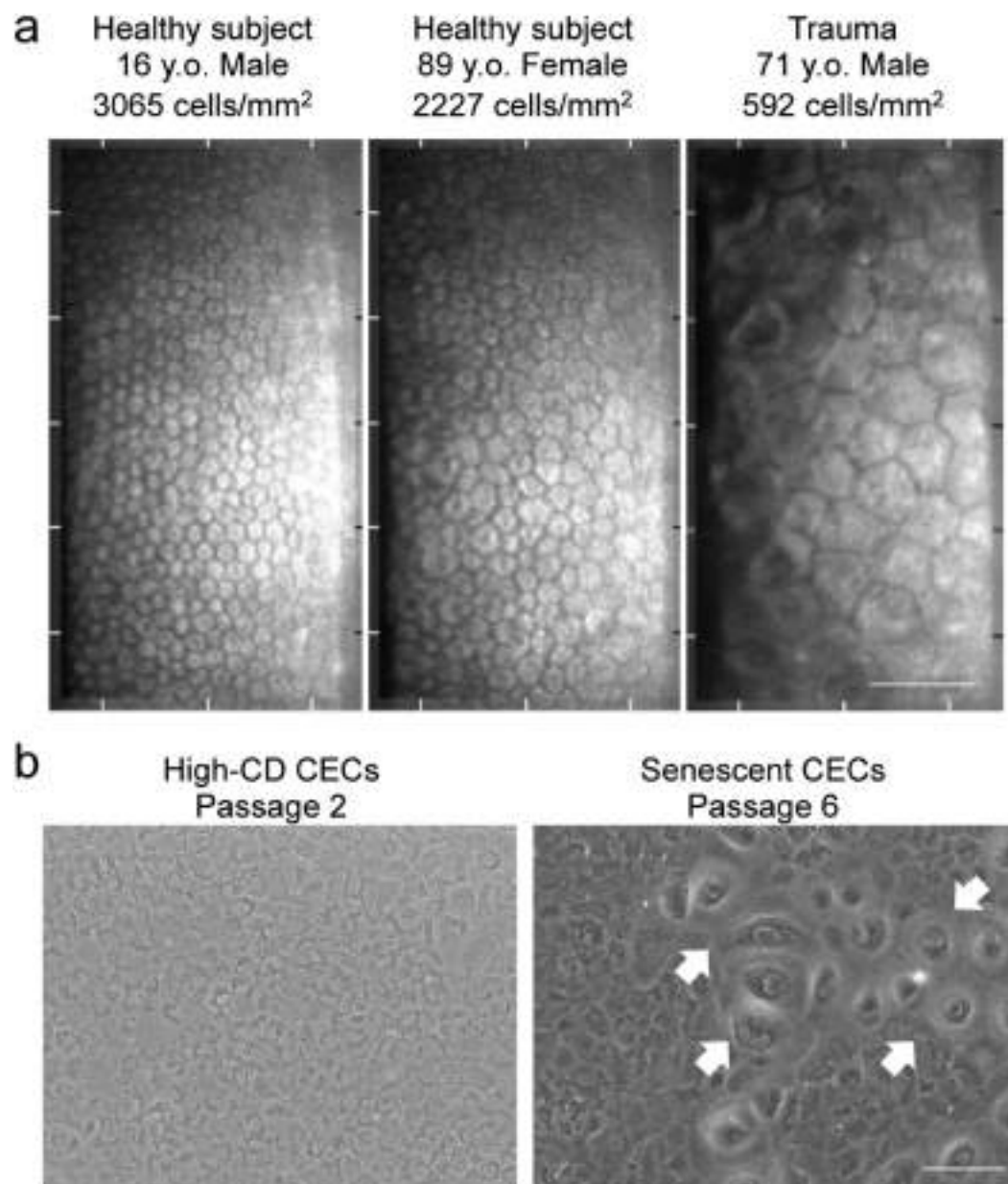


**Figure 1. Cellular senescence of CECs *in vivo* and *in vitro*.** (a) Representative corneal endothelium images obtained by non-contact specular microscopy are shown. Left: A 16-year-old healthy young subject, middle: An 89-year-old healthy elderly subject with relatively low cell density (CD) due to aging, and right: A 71-year-old with low CD CECs due to corneal trauma. Scale bar: 100  $\mu$ m. (b) HCECs were cultured from a human donor cornea and passaged for expansion culture. Left: representative phase contrast images of HCECs passaged 1 time after primary culture with high CD cells. Right: representative phase contrast images of HCECs passaged 6 times; senescent cells are visible within the cultured cell population. Arrows indicate senescent cells. Scale bar: 100  $\mu$ m.

centrifugation. HCECs recovered from the supernatant and from the precipitated pellet after centrifugation in 1.060 g/ml density gradient medium were subsequently cultured (Fig. 5a). Flow cytometry demonstrated a mean diameter of pellet-derived cells of 42.9  $\mu$ m, while that of supernatant-derived cells was 49.9  $\mu$ m (Fig. 5b). Culture of the separated cells gradient revealed that pellet-derived HCECs formed monolayer cell sheets with a hexagonal cobblestone-like phenotype with a CD of 1584.5 cells/mm<sup>2</sup> while the supernatant-derived HCECs had an elongated phenotype with a CD of 827.8 cells/mm<sup>2</sup> (Fig. 5c). The cell area was significantly smaller for the pellet-derived HCECs than for the supernatant-derived HCECs (Fig. 5d).

We also conducted experiments to optimize the specific gravity of the density gradient medium for removal of senescent cells from the HCECs for clinical application. Of note, HCECs recovered from the

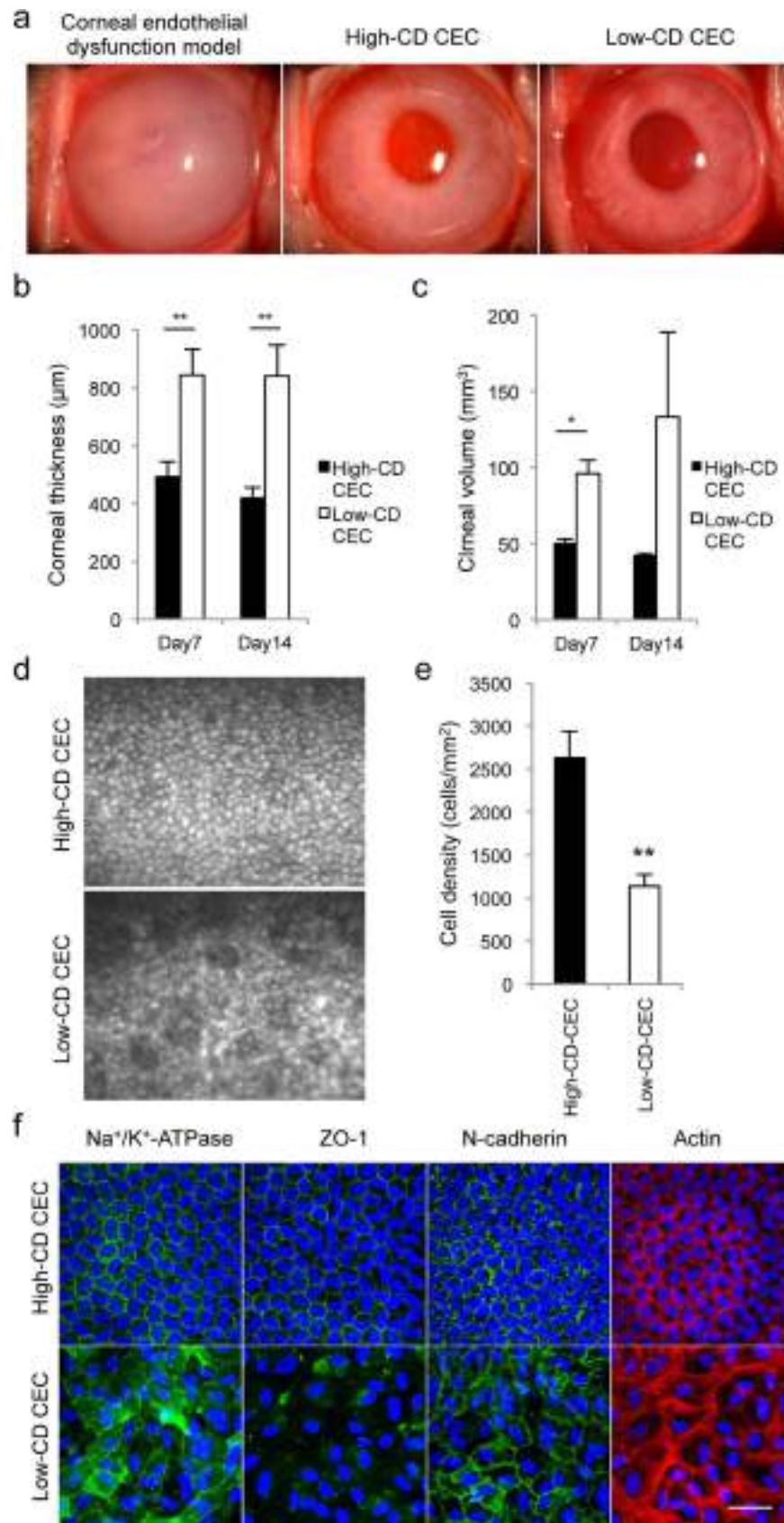


Figure 2. For legend see next page.

**Figure 2. Effect of cellular senescence on cell-based therapy in the corneal endothelial dysfunction rabbit model.** (a) The corneal endothelial dysfunction model was created by mechanically removing the rabbit corneal endothelium. A total of  $5.0 \times 10^5$  high-CD or low-CD RCECs was injected, together with ROCK inhibitor, into the anterior chamber, followed by maintenance in a face down position for 3 hours ( $n = 6$ ). The corneal endothelial dysfunction model in which RCECs were not injected was used as a control ( $n = 3$ ). Representative slit lamp photograph images are shown. Corneal transparency was restored in endothelial dysfunction models by intracameral injection of high CD RCECs with ROCK inhibitor, while the controls exhibited hazy corneas due to corneal endothelial dysfunction. Interestingly, senescent RCECs with low CD were also able to restore corneal transparency. (b, c) The mean central corneal thickness and corneal volume evaluated by Pentacam® at 7 and 14 days after cell injection are shown as a graph. The corneal thickness and corneal volume were significantly reduced in the eyes injected with high CD RCECs when compared to eyes injected with low-CD CECs. \* $P < 0.01$ , \*\* $P < 0.05$ . (d) Regenerated corneal endothelium following injection of high-CD and low-CD RCECs was evaluated by contact specular microscopy at 14 days. (e) The mean cell density of regenerated corneal endothelium was analyzed. The CD of the regenerated corneal endothelium was significantly higher in the eyes injected with high CD-CECs than with low-CD senescent CECs. \*\* $P < 0.05$ . (f) Function-related markers of CECs ( $\text{Na}^+/\text{K}^+$ -ATPase, ZO-1, and N cadherin) were immunostained in the regenerated corneal endothelium. Phalloidin staining was also performed to evaluate the actin cytoskeleton.  $\text{Na}^+/\text{K}^+$ -ATPase, ZO-1, and N-cadherin were expressed in all regenerated CECs in eyes injected with high-CD CECs, while expression of these markers was partially disrupted in the CECs in eyes injected with low-CD CECs. Actin was distributed in the cell cortex in the eyes injected with high-CD CECs, while cortical actin distribution showed irregularity and the presence of stress fibers in the eyes injected with low-CD CECs. Nuclei were stained with DAPI. Scale bar: 100  $\mu\text{m}$ .

pellet following centrifugation in the density gradient medium could be cultured with a normal cell passage procedure (Fig. 5e). The 1.065 g/ml density gradient medium enabled purification of HCECs with a cell density of 1924.3 cells/ $\text{mm}^2$  (Fig. 5f). Variation in the cell sizes of HCECs cultured from the pellet was smaller than in the control, suggesting that density gradient centrifugation minimizes the variation in cell size (Fig. 5g).

## Discussion

Regenerative medicine for treating corneal endothelial dysfunction has been anticipated to provide an alternative therapeutic choice to corneal transplantation<sup>3</sup>. Cultured sheet transplantation and cell-based therapy have been researched in animal models<sup>16–21</sup>. For instance, we showed that corneal endothelium can be regenerated in rabbit and monkey corneal endothelial dysfunction models by injecting a cultured CEC suspension combined with a Rho-associated kinase (ROCK) inhibitor<sup>16</sup>. In addition, we recently started a first-in-man clinical trial at Kyoto Prefectural University of Medicine after obtaining the necessary approval (Clinical trial registration: UMIN000012534)<sup>4</sup>. In this clinical trial, we isolated and cultured CECs from human donor corneas and injected them, together with ROCK inhibitor, into the anterior chamber of the patients (unpublished data).

No protocol specifically designed for clinical application can yet overcome the problems of the limited proliferative ability of CECs and their tendency to undergo fibroblastic transformation<sup>4</sup>. Consequently, our research group and others have been continuously striving towards the development of a successful culture method<sup>5,6,9–11,22,23</sup>. For instance, we reported that ROCK inhibitor<sup>5</sup> and conditioned medium obtained from GMP-grade human bone marrow-derived mesenchymal stem cells (BM-MSCs)<sup>8</sup> enhanced CEC proliferation. We also showed that the fibroblastic transformation of CECs is caused by activation of transforming growth factor beta ( $\text{TGF-}\beta$ ) signaling, and that inhibition of  $\text{TGF-}\beta$  signaling by small molecules enables CECs to counteract fibroblastic changes and maintain the endothelial phenotype<sup>9</sup>. One unresolved clinical issue is that several passages are required to obtain large numbers of cells (e.g.; 5 passages enables the treatment of 100–200 patients from 1 donor cornea), but serial passaging also leads to a senescent cell phenotype.

Morphological features of senescent cells usually include cell enlargement, flattening, vacuolization, and occasionally multinucleation<sup>12</sup>. Here, we demonstrated that senescent CECs can be separated by differences in specific gravity. Possible explanations include: 1) the lower nucleus/cytoplasm ratio of senescent CECs yields a lower specific density, as the larger volume of cytoplasm has a less dense internal structure than the nucleus; and 2) vacuolization of senescent CECs results in a lower specific gravity, as the vacuoles have a lower density than the rest of the cytoplasm. We also showed that low-CD CECs exhibited these senescence features, together with decreases in the expression of function-related proteins, adhesion potency, and proliferative ability. Cellular senescence can be induced by a variety of triggers in various cell types, and no definitive marker has been established; therefore, a set of criteria is required for each tissue<sup>12,13</sup>.

One potential biomarker for senescence of corneal endothelium is SA- $\beta$ -gal, an indicator of senescent cells, as it is expressed at higher levels in the corneal endothelium of elderly individuals than of young individual<sup>24</sup>. The expression of p21; the main driving force for the induction of the senescence program, and p16, a p21-independent senescence-determining molecule, are expressed at higher levels in older



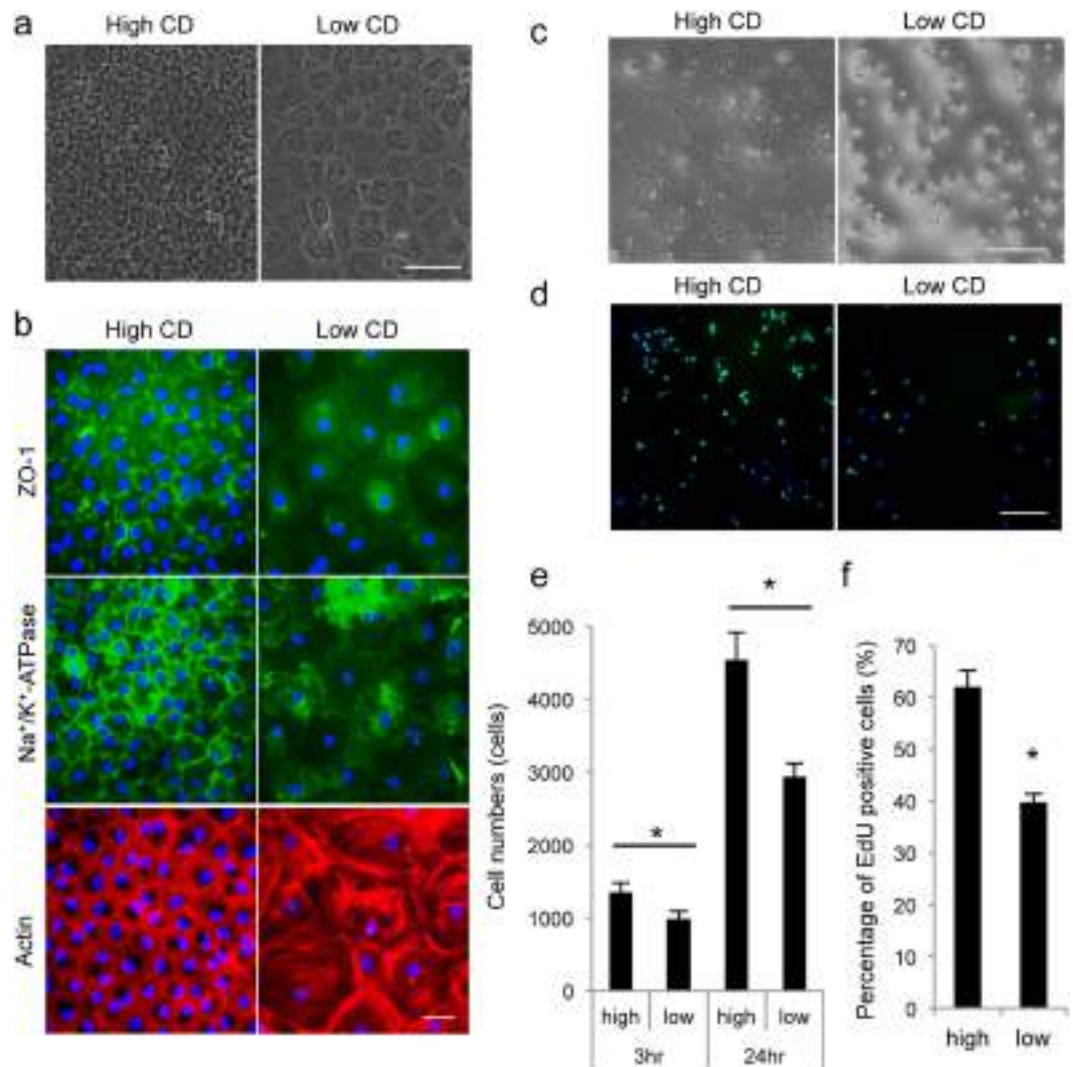


**Figure 3. Phenotypic analysis of low-CD RCECs.** (a) Representative phase contrast images of high-CD and low-CD RCECs are shown. RCECs with a CD of  $2540.4 \pm 64.9$  cells/mm<sup>2</sup> were used as high-CD cell and  $720.2 \pm 29.4$  cells/mm<sup>2</sup> were used as low-CD cells for this study. Scale bar: 100  $\mu$ m. (b) ZO-1, Na<sup>+</sup>/K<sup>+</sup>-ATPase and actin were stained in high-CD and low-CD RCECs. Nuclei were stained with DAPI. Expressions of ZO-1 and of Na<sup>+</sup>/K<sup>+</sup>-ATPase were partially disrupted in low-CD CECs, but these expressions occurred in all high-CD CECs. Disruption of actin at the cell cortex was also observed, along with the formation of stress fibers, but only in low-CD CECs. Scale bar: 50  $\mu$ m. (c) High-CD and low-CD RCECs were seeded at a density of  $5 \times 10^3$  cells/cm<sup>2</sup> and cultured for 24 hours. Scale bar: 50  $\mu$ m. (d) The effect of CD on cell proliferation was evaluated using 5-ethynyl-2'-deoxyuridine (EdU) Click-iT® imaging kits. (e) The number of attached cells was calculated using the CellTiter-Glo® Luminescent Cell Viability Assay at 3 and 24 hours after seeding (n = 6). The numbers of adhered cells were significantly lower in low-CD CECs than in high-CD CECs. \*P < 0.01. (f) EdU positive cells were counted after 9 hours of incubation (n = 3). The numbers of EdU positive cells were significantly lower in low-CD CECs than in high-CD CECs. \*P < 0.01. Experiments were performed in duplicate.

individuals than in younger individuals<sup>1,2</sup>. The evidence that low-CD CECs are senescent cells, as determined by an established set of criteria for corneal endothelial senescence, needs further investigation, but we propose that CD is a simple and practical criterion that can predict the outcome of corneal endothelial cell-based therapy.

Magnetic affinity cell separation (MACS)<sup>25</sup> and fluorescence-activated cell sorting (FACS)<sup>26</sup> were reported to purify cultured HCECs. However, these methods are not ideal for therapeutic application, because of drawbacks that include the use of antibodies, the cost issues to establish the GMP-grade MACS or FACS, and the fibroblastic transformation after cell dissociation for cell sorting. In the current study, we demonstrated that density-gradient centrifugation could purify CECs by eliminating the



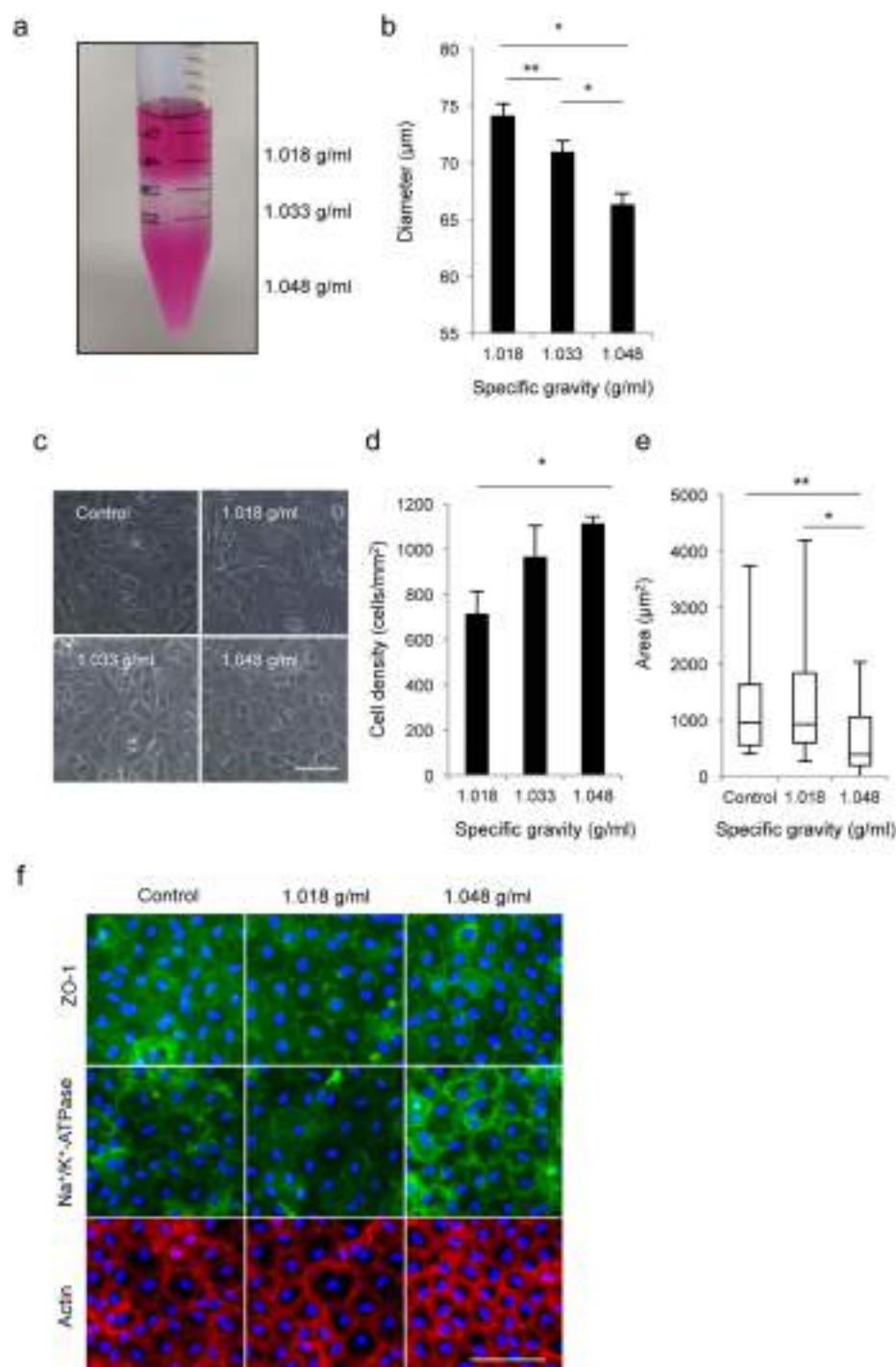


**Figure 4. Density-gradient centrifugation of RCECs.** (a) The cultured RCECs, including senescent RCECs with low-CD RCECs, were centrifuged through OptiPrep™ Density Gradient Medium at 800 g for 15 minutes. (b) The diameter of cells recovered from density gradient media with different specific gravity was evaluated by flow cytometry. RCECs were separated according to cell size. \* $P < 0.01$ , \*\* $P < 0.05$ . Experiments were performed in triplicate. (c) Cells recovered from density gradient media of different specific gravity were cultured for 2 weeks after cells reached confluence. Representative phase contrast images are shown. (d,e) Cell density and cell area were determined with Image J® (NIH) software. The CD was significantly higher in the CECs recovered from the 1.048 g/ml fraction than from the 1.018 and 1.033 g/ml fractions. The variation in cell size was smaller in the 1.048 g/ml fraction cells than in the control cells. \* $P < 0.01$ , \*\* $P < 0.05$ . Experiments were performed in triplicate. (f) Representative images of ZO-1,  $\text{Na}^+/\text{K}^+$ -ATPase, and actin staining are shown. Nuclei were stained with DAPI. Expressions of ZO-1 and  $\text{Na}^+/\text{K}^+$ -ATPase were partially disrupted in the control, whereas RCECs recovered from the 1.048 g/ml fraction fully expressed these function-related proteins. Scale bar: 100 μm.

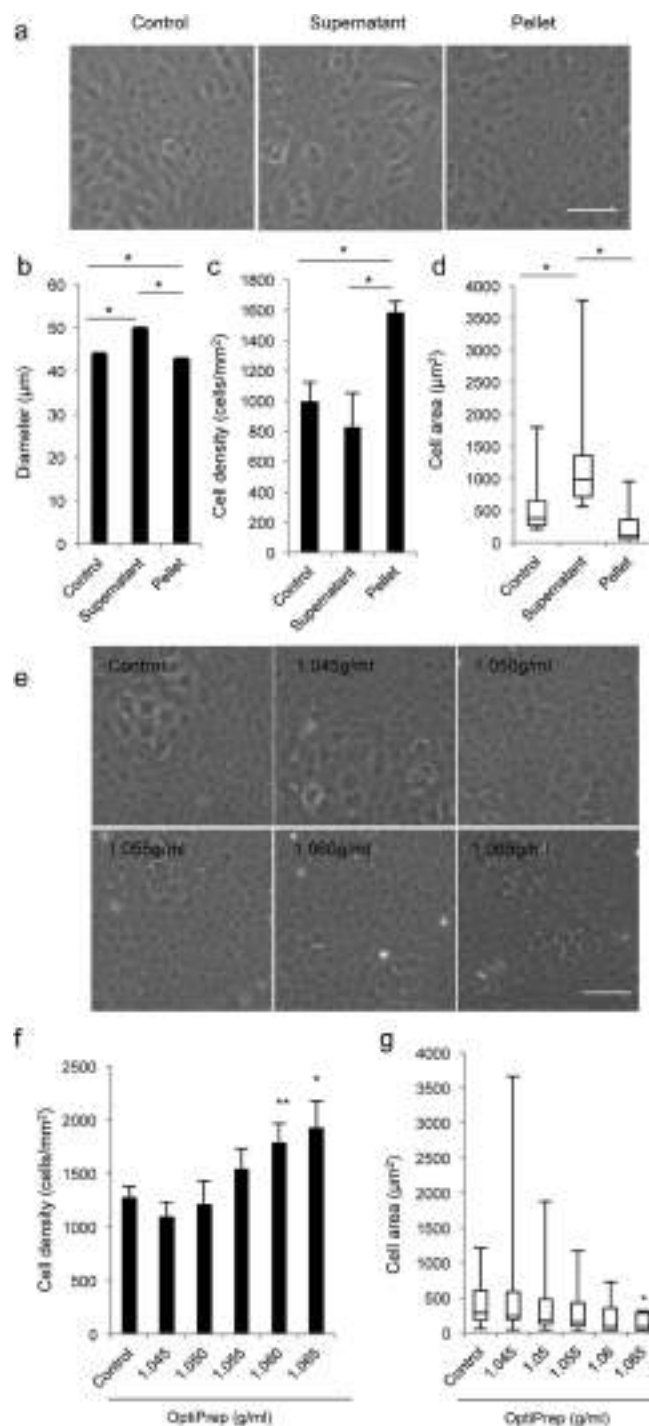


**Figure 5. Density-gradient centrifugation of HCECs.** (a) The cultured HCECs, including senescent cells with a low CD, were centrifuged through 1.060 g/ml density gradient medium at 800 g for 15 minutes. The cells recovered from supernatant and pellet were then seeded at the same cell numbers and cultured for 2 weeks after cells reached confluence. (b) The diameter of cells recovered from the supernatant and pellet were evaluated by flow cytometry. The mean diameter of the pellet-derived cells was 42.9 μm, while that of supernatant-derived cells was 49.9 μm. \* $P < 0.01$ . Experiments were performed in triplicate. (c,d) Cell density (CD) and cell area were determined with Image J® (NIH) software. The CD of pellet-derived HCECs was 1584.5 cells/mm<sup>2</sup>, while that of supernatant-derived HCECs was 827.8 cells/mm<sup>2</sup>. \* $P < 0.01$ . Experiments were performed in triplicate. (e) HCECs were centrifuged through 1.045, 1.050, 1.055, 1.060, and 1.065 g/ml density gradient medium at 800 g for 15 minutes. HCECs recovered from the pellet were seeded at the same cell numbers and cultured for 2 weeks after the cells reached confluence. (f,g) Cell density and cell area were determined with Image J® (NIH) software. The 1.065 g/ml density gradient medium enabled purification of HCECs with higher CD and less size variation. \* $P < 0.01$ , \*\* $P < 0.05$ .

senescent cells based on cell size. Senescent cells exhibit a senescence-associated secretory phenotype (SASP), and the SASP components can trigger senescence in neighboring cells in a paracrine manner<sup>12,27</sup>. This simple technique of density-gradient centrifugation is applicable for final cell preparation for the patient but can also be used for each passage procedure to eliminate senescent cells throughout the cultivation period. In conclusion, density-gradient centrifugation, by separating out senescent cells, will enable the purification of HCECs for cell based therapy for treating corneal endothelial dysfunction. This technique might also be applicable for other types of cells in the settings of regenerative medicine.

## Methods

**Ethics statement.** Animals were housed and treated in accordance with the ARVO Statement for the Use of Animals in Ophthalmic and Vision Research. The rabbit experiments were performed at Doshisha University (Kyoto, Japan) according to the protocol approved by that university's Animal Care and Use Committee (Approval No. A15011-2). Human donor corneas were obtained from SightLife™ (<http://www.sightlife.org/>, Seattle, WA) for research purposes.

**Cell Culture.** Thirty rabbit eyes were used for the rabbit CEC (RCEC) culture. The RCECs were cultivated as described previously<sup>16</sup>. Briefly, Descemet's membrane with RCECs was stripped and incubated in 0.6 U/mL of Dispase II (Roche Applied Science, Penzberg, Germany) to release the RCECs. The isolated RCECs were resuspended in culture medium and plated in 1 well of a 6-well plate coated with cell attachment reagent (FNC Coating Mix®, Athena Environmental Sciences, Inc., Baltimore, MD). All primary cell cultures and serial passages of RCECs were performed in growth medium composed of Dulbecco's modified Eagle's medium (Life Technologies Corp., Carlsbad, CA) supplemented with 10% fetal bovine serum (FBS), 50 U/mL penicillin, 50 µg/mL streptomycin, and 2 ng/mL fibroblast growth factor 2 (Life Technologies Corp.). Cultivated RCECs at passages 1 through 3 were used for all experiments. RCECs with a CD of  $2540.4 \pm 64.9$  cells/mm<sup>2</sup> were used as high-CD cells and those with a CD of  $720.2 \pm 29.4$  cells/mm<sup>2</sup> were used as low-CD cells for this study.

A total of six human donor corneas (from persons >40 years of age) were used for cultivation of human CECs (HCECs) by the protocol described previously. Briefly, Descemet's membranes containing the HCECs were stripped from donor corneas and the membranes were digested with 1 mg/mL collagenase A (Roche Applied Science) at 37°C for 12 h. The HCECs were seeded in one well of a 48-well plate. Plates had previously been coated with laminin E8 fragments (iMatrix-511; Nippi, Incorporated, Tokyo, Japan) ( $2.0 \mu\text{g}/\text{cm}^2$ )<sup>11</sup>. The culture medium was prepared according to published protocols<sup>8</sup>.

First, BM-MSCs were cultured according to previously reported protocols. Briefly, BM-MSCs were plated at a density of  $1.3 \times 10^4$  cells/cm<sup>2</sup> and cultured for 24 hours in DMEM supplemented with 10% FBS, 100 U/mL penicillin, and 100 µg/mL streptomycin. Then, basal medium for HCECs was prepared (OptiMEM-I (Life Technologies Corp.) containing 8% FBS, 5 ng/mL epidermal growth factor (Sigma-Aldrich Co., St. Louis, MO), 20 µg/mL ascorbic acid (Sigma-Aldrich Co.), 200 mg/L calcium chloride, 0.08% chondroitin sulfate (Wako Pure Chemical Industries, Ltd., Osaka, Japan), 50 µg/mL gentamicin, and 10 µM SB431542 (Merck Millipore, Billerica, MA)) and conditioned by culturing BM-MSCs for 24 hours. Finally, the basal medium conditioned with BM-MSCs was collected for use as the culture medium for HCECs.

**Injection of RCECs into a corneal endothelial dysfunction model.** The rabbit corneal endothelial dysfunction models were created following lens removal by mechanically scraping the corneal endothelium from the Descemet's membrane with a 20-gauge silicone needle (Soft Tapered Needle; Inami & Co., Ltd., Tokyo, Japan) as described previously<sup>16</sup>. A total of  $5.0 \times 10^5$  RCECs, suspended in 200 µl of DMEM supplemented with 100 µM of Y-27632 (Wako Pure Chemical Industries, Ltd.), was injected into the anterior chamber of the corneal endothelial dysfunction model and the eyes were kept in the face-down position for 3 hours under general anesthesia. Anterior segments and corneal endothelium were evaluated by slit-lamp microscopy and contact specular microscopy (Konan scanning slit specular microscope, Konan Medical, Nishinomiya, Japan) for 2 weeks. Corneal thickness and corneal volume were evaluated with a Pentacam® (OCULUS Optikgeräte GmbH, Wetzlar, Germany).

**Fluorescence staining.** Rabbit corneal specimens were fixed in 4% formaldehyde and incubated for 30 minutes in 1% bovine serum albumin (BSA) to block nonspecific binding. Corneas were examined by actin staining performed with a 1:400 dilution of Alexa Fluor® 546 conjugated Phalloidin (Life Technologies Corp.). For immunohistochemical analyses, specimens were incubated with primary antibodies against Na<sup>+</sup>/K<sup>+</sup>-ATPase (1:300, Upstate Biotechnology, Lake Placid, NY), ZO-1 (1:300, Life Technologies Corp.), and N-cadherin (1:300, BD Biosciences, San Jose, CA), and then Alexa Fluor® 488-conjugated goat anti-mouse (Life Technologies Corp.) was used as a secondary antibody at a 1:1000 dilution. Proliferative cells were evaluated by 5-ethynyl-2 Click-iT® EdU imaging kits (Life Technologies Corp.) according to the manufacturer's instructions. Briefly, the RCECs ( $1 \times 10^4$  cells/well) were cultured in a 96-well plate and incubated with 10 µM EdU for 6 h at 37°C. Following fixation with 4% paraformaldehyde and permeabilization with 0.3% Triton® X-100 (Nacalai Tesque, Kyoto, Japan), the RCECs were incubated with a reaction cocktail for 30 min at room temperature. Nuclei were stained with DAPI

(Vector Laboratories, Burlingame, CA). The slides were examined with a fluorescence microscope (TCS SP2 AOBS; Leica Microsystems, Wetzlar, Germany).

**Density-gradient centrifugation.** The cultured RCECs or HCECs were suspended in DMEM or Opti-MEM® Reduced Serum Medium, respectively. The OptiPrep™ Density Gradient Medium (Sigma-Aldrich Co.) was then added and the cells were centrifuged at 800 g for 15 minutes. RCECs or HCECs were recovered from the pellet or supernatant, respectively.

**Flow cytometry.** RCECs or HCECs recovered following density gradient centrifugation were suspended in DMEM or OptiMEM-I. Cells were evaluated by flow cytometry using the BD Accuri™ (BD Biosciences), and the cell diameter was determined using a SPHERO™ Flow Cytometry Size Standard Kit (Spherotech, Inc. Lake Forest, IL).

**Statistical analysis.** The statistical significance (P-value) of differences between mean values of the two-sample comparison was determined with the Student's t-test. The comparison of multiple sample sets was analyzed using Dunnett's multiple-comparison test. The values shown in the graphs represent the mean ± SEM.

## References

- Joyce, N. C. Proliferative capacity of the corneal endothelium. *Prog Retin Eye Res* **22**, 359–389 (2003).
- Joyce, N. C. Proliferative capacity of corneal endothelial cells. *Exp Eye Res* **95**, 16–23 (2012).
- Tan, D. T., Dart, J. K., Holland, E. J. & Kinoshita, S. Corneal transplantation. *Lancet* **379**, 1749–1761 (2012).
- Okumura, N., Kinoshita, S. & Koizumi, N. Cell-based approach for treatment of corneal endothelial dysfunction. *Cornea* **33** Suppl 11, S37–41 (2014).
- Okumura, N. *et al.* Enhancement on primate corneal endothelial cell survival *in vitro* by a ROCK inhibitor. *Investigative ophthalmology & visual science* **50**, 3680–3687 (2009).
- Shima, N., Kimoto, M., Yamaguchi, M. & Yamagami, S. Increased proliferation and replicative lifespan of isolated human corneal endothelial cells with L-ascorbic acid 2-phosphate. *Investigative ophthalmology & visual science* **52**, 8711–8717 (2011).
- Peh, G. S., Toh, K. P., Wu, F. Y., Tan, D. T. & Mehta, J. S. Cultivation of human corneal endothelial cells isolated from paired donor corneas. *PLoS one* **6**, e28310 (2011).
- Nakahara, M. *et al.* Corneal endothelial expansion promoted by human bone marrow mesenchymal stem cell-derived conditioned medium. *PLoS one* **8**, e69009 (2013).
- Okumura, N. *et al.* Inhibition of TGF- $\beta$  Signaling Enables Human Corneal Endothelial Cell Expansion *In Vitro* for Use in Regenerative Medicine. *PLoS one* **8**, e58000 (2013).
- Peh, G. S. *et al.* The effects of Rho-associated kinase inhibitor Y-27632 on primary human corneal endothelial cells propagated using a dual media approach. *Sci Rep* **5**, 9167 (2015).
- Okumura, N. *et al.* Laminin-511 and -521 enable efficient *in vitro* expansion of human corneal endothelial cells. *Investigative ophthalmology & visual science* **56**, 2933–2942 (2015).
- Munoz-Espin, D. & Serrano, M. Cellular senescence: from physiology to pathology. *Nature reviews. Molecular cell biology* **15**, 482–496 (2014).
- Burton, D. G. & Krizhanovsky, V. Physiological and pathological consequences of cellular senescence. *Cellular and molecular life sciences* : *CMLS* **71**, 4373–4386 (2014).
- Murphy, C., Alvarado, J., Juster, R. & Maglio, M. Prenatal and postnatal cellularity of the human corneal endothelium. A quantitative histologic study. *Investigative ophthalmology & visual science* **25**, 312–322 (1984).
- Bourne, W. M., Nelson, L. R. & Hodge, D. O. Central corneal endothelial cell changes over a ten-year period. *Investigative ophthalmology & visual science* **38**, 779–782 (1997).
- Okumura, N. *et al.* ROCK inhibitor converts corneal endothelial cells into a phenotype capable of regenerating *in vivo* endothelial tissue. *Am J Pathol* **181**, 268–277 (2012).
- Ishino, Y. *et al.* Amniotic membrane as a carrier for cultivated human corneal endothelial cell transplantation. *Investigative ophthalmology & visual science* **45**, 800–806 (2004).
- Mimura, T. *et al.* Cultured human corneal endothelial cell transplantation with a collagen sheet in a rabbit model. *Investigative ophthalmology & visual science* **45**, 2992–2997 (2004).
- Mimura, T., Yokoo, S., Araie, M., Amano, S. & Yamagami, S. Treatment of rabbit bullous keratopathy with precursors derived from cultured human corneal endothelium. *Investigative ophthalmology & visual science* **46**, 3637–3644 (2005).
- Sumide, T. *et al.* Functional human corneal endothelial cell sheets harvested from temperature-responsive culture surfaces. *FASEB J* **20**, 392–394 (2006).
- Koizumi, N. *et al.* Cultivated corneal endothelial cell sheet transplantation in a primate model. *Investigative ophthalmology & visual science* **48**, 4519–4526 (2007).
- Miyata, K. *et al.* Effect of donor age on morphologic variation of cultured human corneal endothelial cells. *Cornea* **20**, 59–63 (2001).
- Peh, G. S., Beuerman, R. W., Colman, A., Tan, D. T. & Mehta, J. S. Human corneal endothelial cell expansion for corneal endothelium transplantation: an overview. *Transplantation* **91**, 811–819 (2011).
- Mimura, T. & Joyce, N. C. Replication competence and senescence in central and peripheral human corneal endothelium. *Investigative ophthalmology & visual science* **47**, 1387–1396 (2006).
- Peh, G. S. *et al.* Optimization of human corneal endothelial cells for culture: the removal of corneal stromal fibroblast contamination using magnetic cell separation. *International journal of biomaterials* **2012**, 601302 (2012).
- Okumura, N. *et al.* Cell surface markers of functional phenotypic corneal endothelial cells. *Investigative ophthalmology & visual science* **55**, 7610–7618 (2014).
- Toussaint, O., Medrano, E. E. & von Zglinicki, T. Cellular and molecular mechanisms of stress-induced premature senescence (SIPS) of human diploid fibroblasts and melanocytes. *Experimental gerontology* **35**, 927–945 (2000).

## Acknowledgement

The authors thank Dr. Kentaro Kojima for providing patient data. This study was supported by the Program for the Strategic Research Foundation at Private Universities from MEXT (Koizumi N and Okumura N).



### Author Contributions

N.O., S.K. and N.K. conceived and designed the study. N.O., A.K., H.H., R.I., Y.O. and S.N. performed the experiments. N.O. drafted the article, and all authors revised the article and approved the final version to be published.

### Additional Information

**Competing financial interests:** The authors declare no competing financial interests.

**How to cite this article:** Okumura, N. *et al.* Density-gradient centrifugation enables the purification of cultured corneal endothelial cells for cell therapy by eliminating senescent cells. *Sci. Rep.* **5**, 15005; doi: 10.1038/srep15005 (2015).



This work is licensed under a Creative Commons Attribution 4.0 International License. The images or other third party material in this article are included in the article's Creative Commons license, unless indicated otherwise in the credit line; if the material is not included under the Creative Commons license, users will need to obtain permission from the license holder to reproduce the material. To view a copy of this license, visit <http://creativecommons.org/licenses/by/4.0/>

# Microstructural Analysis of Three-Dimensional Canal Network in the Rabbit Lumbar Vertebral Endplate

Tomonori Yamaguchi,<sup>1</sup> Shota Goto,<sup>1</sup> Yasuhiro Nishigaki,<sup>1</sup> Alejandro A. Espinoza Orías,<sup>2</sup> Won C. Bae,<sup>3</sup> Koichi Masuda,<sup>4</sup> Nozomu Inoue<sup>1,2</sup>

<sup>1</sup>Department of Biomedical Engineering, Faculty of Life and Medical Sciences, Doshisha University, Kyoto, Japan, <sup>2</sup>Department of Orthopedic Surgery, Rush University Medical Center, Chicago 60612, Illinois, <sup>3</sup>Department of Radiology, School of Medicine, University of California, San Diego, La Jolla 92103, California, <sup>4</sup>Department of Orthopaedic Surgery, School of Medicine, University of California, San Diego 92093, California

Received 27 November 2013; accepted 29 September 2014

Published online 3 November 2014 in Wiley Online Library (wileyonlinelibrary.com). DOI 10.1002/jor.22759

**ABSTRACT:** Insufficient nutrient supply through vertebral canal structures to the intervertebral disc (IVD) has been considered as an important contributor for disc degeneration. Despite previous canal structure characterization studies using histology, scanning electron microscopy, and angiography, among others, their three-dimensional (3D) topology inside the vertebral endplate remains poorly understood. This study aims to characterize the 3D canal structure in the rabbit lumbar vertebral endplate using micro computed tomography ( $\mu$ CT). Vertebral endplates were imaged using high-resolution  $\mu$ CT with  $1.4 \times 1.4 \times 1.8 \mu\text{m}$  voxel size. Diameter, length, orientation, and depth starting from the vertebral endplate surface were analyzed for each canal using individual 3D canal models from the vertebral endplate scans. In the layer underneath the vertebral endplate, at a mean depth of  $76.2 \mu\text{m}$ , longitudinally-oriented relatively short-length ( $57.6 \mu\text{m}$ ) and small diameter ( $45.7 \mu\text{m}$ ) canals were dominant. Large-scale canals with a mean diameter of  $152.1 \mu\text{m}$  running parallel to the endplate surface were isolated at the depth of  $224.1 \mu\text{m}$ . These canals were connected to both IVD and bone marrow spaces through vertically oriented canals. © 2014 Orthopaedic Research Society. Published by Wiley Periodicals, Inc. *J Orthop Res* 33:270–276, 2015.

**Keywords:** nutrient canal; vertebral endplate; intervertebral disc; bone morphology; spine

Low back pain is one of the most common health problems in adults.<sup>1</sup> Intervertebral disc (IVD) degeneration has been implicated as a major cause of back pain,<sup>2,3</sup> which also leads to secondary clinical problems, such as disc herniation, spinal stenosis, and degenerative spondylolisthesis.<sup>4</sup> Multiple conditions link with disc degeneration, including age,<sup>5</sup> genetic inheritance,<sup>6</sup> mechanical,<sup>7</sup> and systematic<sup>8</sup> factors, although its etiology and pathogenesis remain unclear.<sup>9</sup> Since the IVD is the largest avascular tissue in the body, insufficient IVD nutrition has been believed to be one of the important contributors for disc degeneration among those risk factors.<sup>2,10</sup>

There are two major pathways of nutrient supplies into the IVD: either through adjacent vertebral endplates or the annulus periphery.<sup>11</sup> Since nutrient supplies are normally restricted to the outmost layers of the annulus fibrosus in the adult disc,<sup>12</sup> the IVD relies primarily on nutrient transport through adjacent endplates. The endplate is characterized as a bilayer consisting of a hyaline cartilaginous layer on the IVD side and an osseous layer on the vertebral body side, both of which contribute to IVD integrity through biomechanical and nutritional functions.<sup>10–14</sup> There is evidence of canal structure penetration within the osseous region of the vertebral endplate into the cartilaginous endplate from the bone marrow space.<sup>9,15</sup> Through those canals, nutrients are supplied to the

IVD and waste products are removed from discs.<sup>10,13</sup> Therefore, microstructural changes in the endplate, such as cartilage endplate calcification and vertebral endplate sclerosis, have been considered to potentially influence the disc metabolic transport through the canals in the vertebral endplate.<sup>9,15–17</sup>

To date, active blood flow in the canals within the vertebral endplate has been confirmed using vascular tracers,<sup>18,19</sup> and the layered structure of the canal network with the large-scale transverse canals running parallel to the vertebral endplate has been observed.<sup>20</sup> Scanning electron microscopy has also shown various sizes of nutrient canals in the vertebral endplate.<sup>9</sup> However, the canal network architecture inside the vertebral endplate is yet to be quantitatively evaluated due to the canal system's complex three-dimensional (3D) structure.<sup>19,21</sup>

Based on previous observations on the vertebral endplate canal structure, we hypothesized that the canal network topology can be characterized through the canal size, orientation and depth. Furthermore, rabbit models have been well-established to study mechanisms of IVD degeneration and therapeutic interventions for IVD repair.<sup>22</sup> We believe that the microstructural changes of the vertebral endplate canal can be appropriately investigated using those models. Therefore, the purpose of this study was to analyze length, diameter, orientation angle, and depth of individual canals in the rabbit lumbar vertebral endplate using micro-computed tomography ( $\mu$ CT).

## MATERIALS AND METHODS

### Sample Preparation

The lumbar spines (L1–L6) from five Japanese white rabbits (male, 3–4 months old, 2.5–3.5 kg in body weight; Shimizu

Grant sponsor: Ministry of Education, Science, Sports and Culture, Japan, Grant-in-Aid for Scientific Research; Grant number: 22591645.

Correspondence to: Nozomu Inoue (T: +312-942-8151; F: +312-942-2040; E-mail: nozomu\_inoue@rush.edu)

© 2014 Orthopaedic Research Society. Published by Wiley Periodicals, Inc.

Laboratory Supplies Co, Ltd, Kyoto, Japan) were extracted after sacrifice following Institutional Animal Care and Use Committee protocol approval. Soft tissues, transverse processes, and posterior elements were then removed. A total of 25 bone-disc-bone (BDB) units were prepared by cutting vertebral bodies parallel to the vertebral endplate, including an IVD with the adjacent vertebral endplates. From these BDB units, 6 mm diameter samples from the central region of the BDB units were cored and stored at  $-20^{\circ}\text{C}$  until  $\mu\text{CT}$  scanning was conducted. In this study, we only focused the central region of endplates because the central region is believed to be the most important for nutrient transport to the IVD.<sup>18</sup>

### $\mu\text{CT}$ Imaging

Each sample was removed from the freezer before  $\mu\text{CT}$  scanning, and placed into a sample holder (6.0 mm inner diameter polypropylene tube with a wall thickness of 0.25 mm) on the rotating stage of the  $\mu\text{CT}$  scanner. Simultaneously, adjacent endplates cranial and caudal to the IVD were imaged using a high-resolution  $\mu\text{CT}$  scanner (SMX-160CTS, Shimadzu Co., Kyoto, Japan; maximum resolution:  $0.8\text{ }\mu\text{m}$ ).  $\mu\text{CT}$  scanning was performed at 66 kV with an in-plane resolution of  $1.4\text{ }\mu\text{m}$  and a slice interval of  $1.8\text{ }\mu\text{m}$ .

### Three-Dimensional (3D) Canal Model Creation

The  $\mu\text{CT}$  images were imported into a 3D reconstruction software package (Mimics 15.0; Materialise Inc., Leuven, Belgium). 3D vertebral endplate models were created based on the Otsu method,<sup>23</sup> employed to calculate a bone threshold value (Fig. 1A). The canals within the vertebral endplate were segmented by filling the canal space. 3D surface models of vertebral endplates were also segmented (Fig. 1B). Individual canals were manually separated to evaluate the microstructural parameters as described below (Fig. 2A). For the canals with one end in the endplate and opening to the vertebral endplate surface or bone marrow space, the starting point was defined at the canal end inside the endplate, and the ending point was defined at the opening. When the canals had openings at the bone marrow space and vertebral endplate surface, the starting point was set at the bone marrow opening site and the ending point was set at the vertebral endplate opening site. For the canals with both ends in the endplate, the starting point was set at the branching point from the larger canal and the ending point was set at the branching point at the smaller canal.

### Individual Canal Orientation

Individual canal orientation was evaluated against the vertebral endplate normal direction. Both the 3D endplate surface and the individual canal models were converted to point-cloud data sets. Eigenvectors of the 3D vertebral endplate surface point-cloud data sets were calculated using custom-written routines in MATLAB (MathWorks, Inc., Natick, MA) to obtain the endplate's normal vector. Individual canal orientation was determined by the eigenvector with the highest eigenvalue. The directionality of the eigenvector was adjusted to correspond to the direction from the starting point towards the ending point of individual canal described earlier. The angles ( $\theta$ , degrees) between the normal vector to the vertebral endplate towards the IVD and the eigenvector of each canal directing longitudinal direction of the canal were calculated using the dot product ( $0 \leq \theta \leq 180^{\circ}$ ).

### Length and Mean Diameter of the Individual Canals

Length [ $\mu\text{m}$ ] and volume [ $\mu\text{m}^3$ ] of each canal were measured using the 3D reconstruction software package. The mean cross-sectional area of each canal was calculated by volume/length and the mean diameter of each canal was determined by assuming the cross-section was circle.

### Individual Canal Depth

Individual canal depth was defined by the least distance between the centroid of each canal and the vertebral endplate surface in the vertebral endplate normal direction.

### Statistical Analysis

The canals were segregated into longitudinal and transverse canals by orientation angle bimodal distributions. The canal length and diameter were compared between the longitudinal canal and the transverse canal using unpaired *t*-tests. Ward's clustering analysis was used to categorize the individual canals based on distribution of canal diameter and angle or combinations of length and depth. Chi-square test was used to assess distribution of orientations among the clusters. All statistical analyses were performed using the StatView program (version 5.0; SAS Institute Inc., Cary, NC). Statistical significance was considered when  $p < 0.05$ . Data are presented as mean  $\pm$  standard deviation (SD).

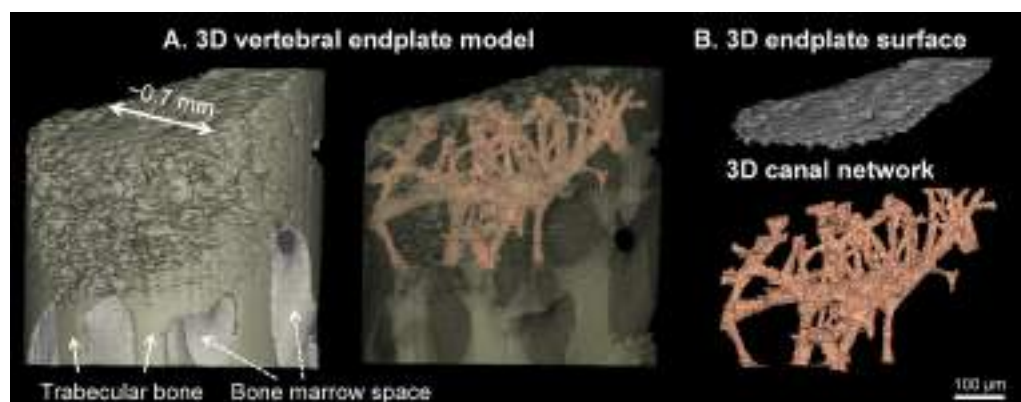


**Figure 1.** (A) Representative high-resolution  $\mu\text{CT}$ -based 3D canal network models in the rabbit lumbar vertebral endplate. (B) Representative 3D vertebral endplate surface and 3D canal network topology.

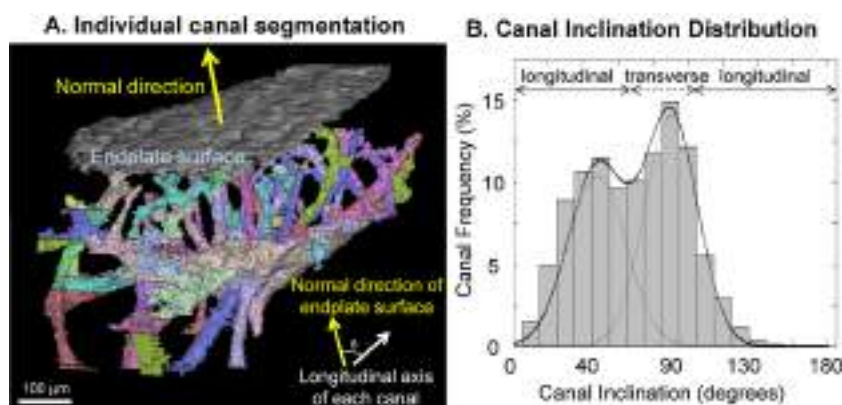


**Figure 2.** (A) Segmentation of individual canals in the vertebral endplate. Individual canals are depicted in different, unique colors. (B) Bimodal distribution of the canal inclination with its corresponding Gaussian curves.

## RESULTS

The  $\mu$ CT images revealed three damaged endplates (one cranial and two caudal endplates), possibly due to sample preparation procedure or storage; these samples were excluded from this study and the remaining samples ( $n=47$ ; 24 cranial endplates and 23 caudal endplates adjacent to the IVD) were used for analysis.

### Canal Orientations

Canal angles followed a bimodal distribution (Fig. 2B) and could be segregated into two distinct canal orientations: **the longitudinal canal** ( $0^\circ \leq \theta < 70^\circ$  and  $110^\circ < \theta \leq 180^\circ$ ) and **the transverse canal** ( $70^\circ \leq \theta \leq 110^\circ$ ). The longitudinal and transverse canals accounted for 58.3% and 41.7% of all canals, respectively. The mean inclinations of the longitudinal and transverse canals were  $47.7 \pm 26.4^\circ$  and  $87.3 \pm 10.0^\circ$ , respectively (Table 1).

### Mean Canal Length and Diameter

Table 1 shows the mean length and diameter of all canals, as well as a description by canal orientation. The transverse canals were significantly longer and wider than the longitudinal canals ( $p < 0.0001$ ). There were no other differences in these parameters.

### Canal Depth

The canal depth histogram showed a right-skewed distribution with a peak between 90–100  $\mu$ m (data not shown), and a mean depth of  $142.3 \pm 86.1 \mu$ m from the vertebral endplate surface.

### Canal Categorization

Based on Ward's clustering results, the canals running parallel to the vertebral endplate were termed

**large-scale transverse canals** (Figs. 3A, B). Furthermore, the canals connected to the bone marrow space were labeled as **marrow-contact canals**. The canals directly running through the vertebral endplate surface from the bone marrow space were especially categorized as **direct-connection canals** (Fig. 3C). Additionally, the canals existing in the surface region between the large-scale transverse canals and the vertebral endplate surface, were further sub-divided into three groups according to the Ward's clustering results: **surface-surface canal**, **surface-middle canal**, and **surface-deep canal** (Figs. 4A, B). A breakdown of canals classified by location and function is shown in Table 2. Figures 5 and 6 showed the depth dependency of the canal parameters and a proposed schematic detailing the classification resulting from the clustering analysis, respectively.

Chi-square tests showed significant differences in distribution of canal inclination among these canal sub-categories ( $p < 0.0001$ ).

The large-scale transverse canals were oriented at  $92.5 \pm 8.8^\circ$  from the normal direction of the vertebral endplate (Table 2). The direct-connection canal and the surface-surface canals had similar diameters ( $45.7 \pm 16.2 \mu$ m vs.  $44.3 \pm 11.2 \mu$ m, respectively), but the direct-connection canals were almost six-times as long (Table 2). All canals, with the exception of the large-scale and the marrow-contact canals had diameters between 40–50  $\mu$ m (Table 2).

A histogram plot of the surface-middle canal angles shows a large peak at 80–90° (Figure 4C), while the surface-surface and the surface-deep canal inclinations followed multimodal distributions (data not shown).

**Table 1.** Longitudinal and Transverse Canal 3D Topological Parameters

Canal	# of total canals (%)	Length ( $\mu$ m)	Diameter ( $\mu$ m)	Angle ( $^\circ$ )
Total	—	$99.8 \pm 73.6$	$50.5 \pm 22.1$	$64.2 \pm 28.8$
Longitudinal	58.3	$87.3 \pm 57.7^*$	$47.4 \pm 17.0$	$47.7 \pm 26.4$
Transverse	41.7	$117.2 \pm 88.4$	$54.9 \pm 27.2$	$87.3 \pm 10.0$

\* $p < 0.0001$ , compared to the transverse canals.



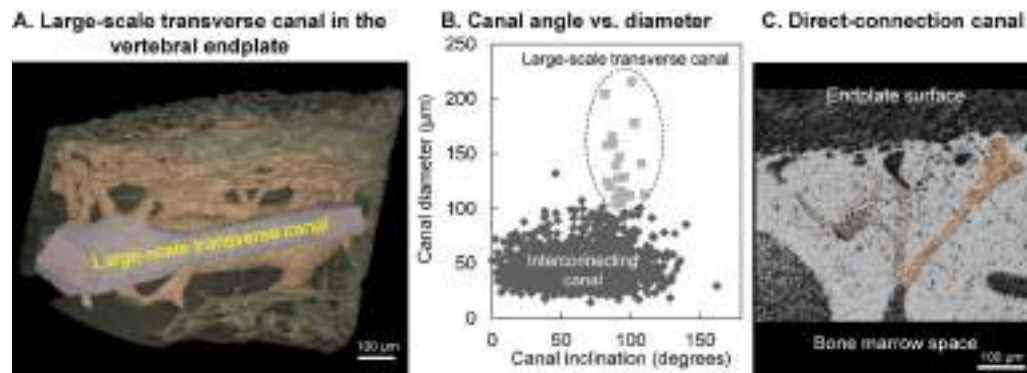


**Figure 3.** (A) Representative 3D canal network model with the large-scale transverse canal inside the vertebral endplate. (B) Categorization of the large-scale transverse canals according to Ward's cluster analysis. (C) Representative direct-connection canal directly connected from the bone marrow space to the vertebral endplate surface.

## DISCUSSION

The present study investigated the lumbar vertebral endplate 3D canal structure in a rabbit model in the region corresponding to the nucleus pulposus by means of  $\mu$ CT. Individual canals were isolated and characterized quantitatively by measuring their length, diameter, orientation angle, and depth starting from the endplate surface. The results revealed differences in the canal structure above and below the large-scale canals running parallel to the endplate surface.

In the layer underneath the vertebral endplate at a mean depth of 76.2  $\mu$ m, longitudinally oriented relatively short length (57.6  $\mu$ m) and small diameter (45.7  $\mu$ m) canals were dominant as described as **surface-surface canals** in the present study. Crock and Goldwasser studied circulation in the adult canine vertebral endplate using an intra-arterial infusion technique and reported the existence of the capillary bed at the disc-bone interface in the region of the nucleus pulposus.<sup>24</sup> Although the species are different, the canal structure we isolated underneath the endplate surface appears to correspond to the above-mentioned capillary bed, described as “sessile and discoid” and similar to the “suckers on the tentacles of an octopus.” In fact, the mean orientation of this canal

group measured in the present study was 62.9° in reference to the normal direction of the endplate surface – not precisely perpendicular to the endplate surface.

In spite of these detailed reports, blood supply to the capillary bed remains unclear. Clark investigated the structure of vascular channels in the subchondral plate of the tibial plateau, patellae and femoral condyle in humans, canines, and leporidae using scanning electron microscopy.<sup>25</sup> The author found that the capillaries ran through the subchondral plate in cylindrical channels surrounded by a concentric laminar structure similar to a Haversian system, but most of the channels were separated from the cartilage by a layer of bone. If such vascular system does exist in the vertebral endplate, it could be a source of vascular supply to the capillary bed underneath the endplate surface. In the present study, we isolated transversely oriented canals with a mean diameter of 50.5  $\mu$ m with a connection to the surface-surface canals, which may correspond to the cylindrical channels shown in the subchondral plate analogous to the Haversian system. Additional histological studies will be required to investigate if a Haversian system exists in the vertebral endplate.

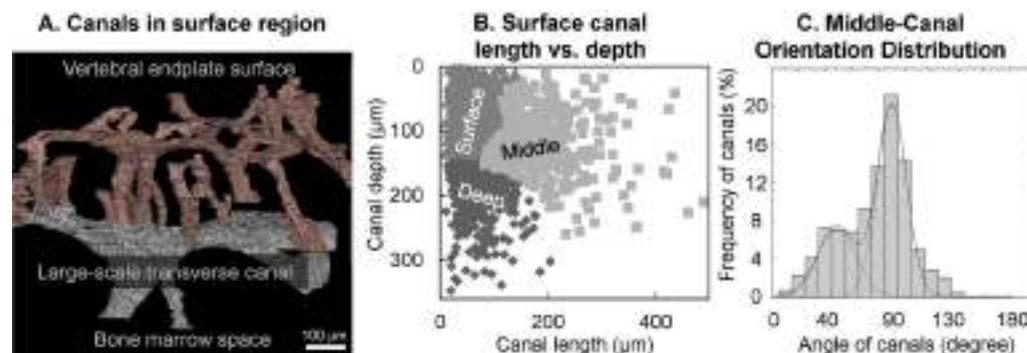


**Figure 4.** (A) Representative 3D canal network model in the surface region between the large-scale transverse canal and the vertebral endplate surface. (B) Categorization of the surface-surface, the surface-middle, and the surface-deep canals according to Ward's clustering analysis. (C) Histogram of the surface-middle canal angles with Gaussian curves.

**Table 2.** 3D Topological of the Canals Classified by Their Location and Function

Canal	Proportion of total canals (%)	Length ( $\mu\text{m}$ )	Diameter ( $\mu\text{m}$ )	Inclination ( $^{\circ}$ )	Depth from endplate surface ( $\mu\text{m}$ )
Surface-surface	23.2	$57.6 \pm 23.2$	$45.7 \pm 16.2$	$62.9 \pm 29.1$	$76.2 \pm 33.7$
Surface-middle	22.9	$169.6 \pm 68.6$	$50.5 \pm 17.0$	$72.7 \pm 25.9$	$115.6 \pm 43.5$
Surface-deep	36.7	$69.7 \pm 31.0$	$47.0 \pm 17.7$	$59.8 \pm 28.1$	$189.9 \pm 43.6$
Large-scale	1.3	$245.3 \pm 129.9$	$152.1 \pm 24.3$	$92.5 \pm 8.8$	$224.1 \pm 62.7$
Marrow-contact	15.6	$125.5 \pm 85.5$	$58.0 \pm 22.4$	$59.5 \pm 30.6$	$263.1 \pm 90.9$
Direct-connection	0.3	$332.5 \pm 50.1$	$44.3 \pm 11.2$	$53.1 \pm 37.9$	$117.3 \pm 48.2$

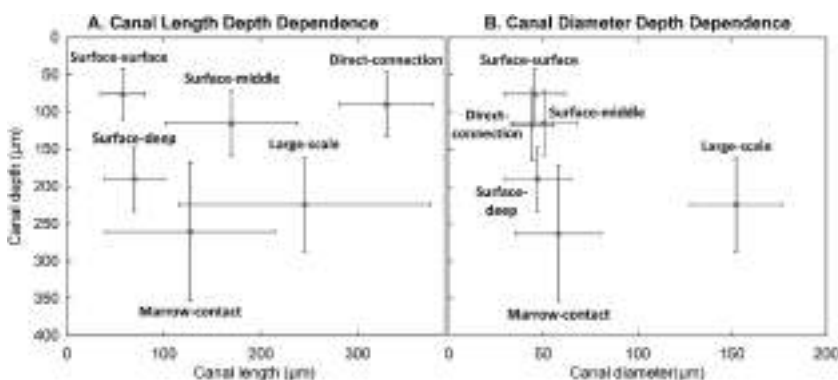
Crock and Goldwasser also described in detail the venous drainage system in the vertebral endplate.<sup>24</sup> They demonstrated that the subchondral postcapillary venous network connects to the aforementioned capillary bed at the disc-bone interface and the existence of an epiphyseal subarticular collecting vein system oriented parallel to the endplate surface. In the present study, we identified distinct large canals ( $245.3\mu\text{m}$  mean diameter) oriented parallel to the endplate surface ( $92.5^{\circ}$  with respect to the endplate normal vector) at a depth of  $189.9\mu\text{m}$  from the endplate surface, which appears to be a conduit for the epiphyseal subarticular collecting vein. The **surface-deep canals** described in the present study may correspond to the subchondral postcapillary venous network proposed by Crock and Goldwasser.<sup>24</sup> They also demonstrated the direct connection between the endplate surface and the epiphyseal subarticular collecting vein, which is also reported here.

In the deeper layer of the vertebral endplate, vertically-oriented large-diameter ( $58.0\mu\text{m}$ ) canals connecting between the bone marrow space and the large-scale transverse canal were identified in the present study and named **marrow-contact canals**. Although the connection between the epiphyseal subarticular collecting vein and bone marrow space has not been described before, the frequency of the **marrow-contact canals** was as high as 15.6% of the total number of the canals and they could play an important role as pathways between the bone marrow space and large central space within the endplate. Crock and Goldwasser described some canals directly connected

between the bone-disc interface and the bone marrow space,<sup>24</sup> which were also identified in the present study with a low frequency of 0.3% of the total canal number (Fig. 3D).

Because the current study focused on the development of a quantitative microstructural analysis technique to describe the 3D canal networks observed within the vertebral endplate, the normal rabbit disc was preferred to characterize the canal structure as an initial step to provide primary data of the vertebral endplate structure that can be later compared to degenerated discs in future studies. The analysis of the canal parameters in the present study illustrated a depth-dependent canal structure from the IVD side towards the bone marrow side of the vertebral endplate; however, connectivity among the canals was not analyzed in a quantitative manner. A quantitative analysis of the connectivity would provide more information on the flow of nutrients within the endplate. We noted varied canal topologies; however, the parameters used in the present study may have been too simplified to characterize the individual canal geometry in more detail. Future studies will include quantitative analyses of canal connectivity and more detailed individual canal topological analyses.

Recent computational analyses allow simulation of fluid flow through the endplate using microstructural 3D models of the endplate.<sup>26</sup> The information on the microstructure of the nutrition canals investigated in the current study could be used for these analyses to better understand nutrition transport phenomena through the endplate. The porosity of the endplate

**Figure 5.** Depth-dependent canal length (A) and diameter (B). Data is presented as mean  $\pm$  standard deviation (SD).

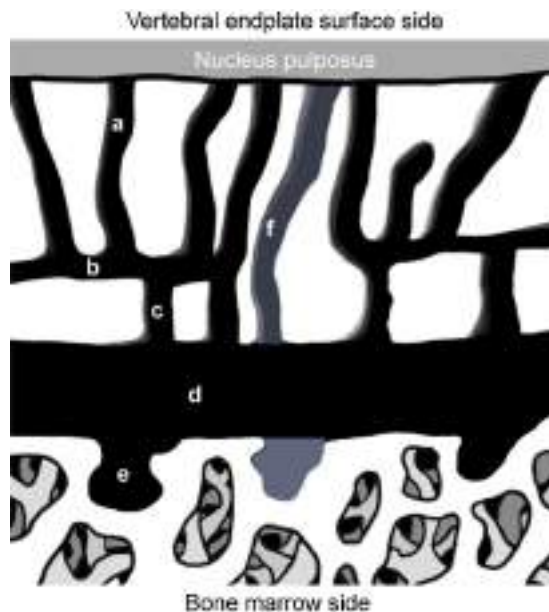


**Figure 6.** Proposed schematic of the 3D canal network in the central region of vertebral endplate based on the clustering analysis: (A) Surface-surface canal. (B) Surface-middle canal. (C) Surface-deep canal. (D) Large-scale transverse canal. (E) Marrow-contact canal. (F) Direct-connection canal.

has been reported as an important parameter to calculate permeability of the endplate.<sup>26</sup> The porosity of the endplate could be calculated by dividing the canal volume in the endplate, which we have measured, by the total volume of the endplate. However, we faced difficulties when the measuring the endplate total volume. Because the rabbit endplates connect to the trabeculae in the medullary cavity as shown in Figure 1, it is difficult to identify a clearly defined boundary between the endplate and bone marrow. These are the reasons that prevented us to from accurately determining the endplate total volume and, in turn, the endplate porosity in the current study. Future studies need to establish clear criteria to define the boundary between endplate and trabecular bone tissue in order to calculate appropriately both the endplate volume and thickness.

Since different morphologic characteristics of the rabbit lumbar spine have been reported in the literature,<sup>27</sup> future studies will analyze the microstructure of the canal in the human endplate using the same technique used in the current study.

## CONCLUSION

The present study revealed a distinct depth-dependent structure of the canal in the rabbit vertebral endplate characterized by length, diameter, and orientation of the individual canals. The large-scale transverse canals were isolated in the deeper layer of the endplate, which connected to both the IVD surface and bone marrow space. Such structures may play a role for collecting and redistributing the fluid within

the endplate. Although the microstructural analysis of the canal network in the vertebral endplate using the  $\mu$ CT technique only allows analysis of the bony structure, information of the 3D canal structure could provide essential information to understand nutrient pathways through the vertebral endplate.

## ACKNOWLEDGMENTS

This research was supported by the Ministry of Education, Science, Sports and Culture, Japan, Grants-in-Aid for Scientific Research (C) 22591645 and (C) 25462315.

## REFERENCES

1. Vos T, Flaxman AD, Naghavi M, et al. 2010. Years lived with disability (YLDs) for 1160 sequelae of 289 diseases and injuries 1990–2010: a systematic analysis for the Global Burden of Disease Study 2010. *Lancet* 380: 2163–2196.
2. Adams MA, Dolan P. 2012. Intervertebral disc degeneration: evidence for two distinct phenotypes. *J Anat* 221:497–506.
3. Luoma K, Riihimäki H, Luukkainen R, et al. 2000. Low back pain in relation to lumbar disc degeneration. *Spine* 25: 487–492.
4. An HS, Anderson PA, Haughton VM, et al. 2004. Introduction: disc degeneration: summary. *Spine* 29:2677–2678.
5. Miller JA, Schmatz C, Schultz AB. 1988. Lumbar disc degeneration: correlation with age, sex, and spine level in 600 autopsy specimens. *Spine* 13:173–178.
6. Battie MC, Videman T, Levalahti E, et al. 2008. Genetic and environmental effects on disc degeneration by phenotype and spinal level: a multivariate twin study. *Spine (Phila Pa 1976)* 33:2801–2808.
7. Videman T, Nurminen M, Troup JD. 1990. 1990 Volvo Award in clinical sciences. Lumbar spinal pathology in cadaveric material in relation to history of back pain, occupation, and physical loading. *Spine* 15:728–740.
8. Battie MC, Videman T, Gill K, et al. 1976. 1991 Volvo Award in clinical sciences. Smoking and lumbar intervertebral disc degeneration: an MRI study of identical twins. *Spine (Phila Pa)* 16:1015–1021.
9. Benneker LM, Heini PF, Alini M, et al. 2004. Young Investigator Award Winner: vertebral endplate marrow contact channel occlusions and intervertebral disc degeneration. *Spine* 30:167–173.
10. Lotz JC, Fields AJ, Liebenberg EC. 2013. The role of the vertebral end plate in low back pain. *Global Spine J* 03: 153–164.
11. Aoki J, Yamamoto I, Kitamura N, et al. 1987. End plate of the discovertebral joint: degenerative change in the elderly adult. *Radiology* 164:411–414.
12. Adams MA, Roughley PJ. 2006. What is intervertebral disc degeneration, and what causes it?. *Spine* 31:2151–2161.
13. Nguyen C, Poiraudou S, Rannou F. 2012. Vertebral subchondral bone. *Osteoporos Int* 23:S857–S860.
14. Broberg KB. 1983. On the mechanical behaviour of intervertebral discs. *Spine* 8:151–165.
15. Humzah MD, Soames RW. 1988. Human intervertebral disc: structure and function. *Anat Rec* 220:337–356.
16. Moore RJ. 2000. The vertebral end-plate: what do we know?. *Eur Spine J* 9:92–96.
17. Moore RJ. 2006. The vertebral endplate: disc degeneration, disc regeneration. *Eur Spine J* 15:S333–S337.
18. Nachemson A, Lewin T, Maroudas A, et al. 1970. In vitro diffusion of dye through the end-plates and the annulus

- fibrosus of human lumbar inter-vertebral discs. *Acta Orthop Scand* 41:589–607.
19. Gruber HE, Ashraf N, Kilburn J, et al. 2005. Vertebral endplate architecture and vascularization: application of micro-computerized tomography, a vascular tracer, and immunocytochemistry in analyses of disc degeneration in the aging sand rat. *Spine* 30:2593–2600.
  20. Crock HV, Yoshizawa H, Kame SK. 1973. Observations on the venous drainage of the human vertebral body. *J Bone Joint Surg Br* 55:528–533.
  21. Urban JP, Smith S, Fairbank JC. 2004. Nutrition of the intervertebral disc. *Spine* 29:2700–2709.
  22. Alini M, Eisenstein SM, Ito K, et al. 2008. Are animal models useful for studying human disc disorders/degeneration?. *Eur Spine J* 17:2–19.
  23. Otsu N. 1979. A threshold selection method from gray-level histogram. *IEEE Trans* 9:62–66.
  24. Crock HV, Goldwasser M. 1984. Anatomic studies of the circulation in the region of the vertebral end-plate in adult Greyhound dogs. *Spine* 9:702–706.
  25. Clark JM. 1990. The structure of vascular channels in the subchondral plate. *J Anat* 171:105–115.
  26. Malandrino Lacroix AD, Hellmich C, et al. 2014. Numerical studies about the possible influence of bony endplate micro-structure on the nutrition of the disc. *Osteoarthritis Cartilage* 22:1053–1060.
  27. O'Connell GD, Vresilovic EJ, Elliott DM. 2007. Comparison of animals used in disc research to human lumbar disc geometry. *Spine (Phila Pa 1976)* 32:328–333.



RESEARCH ARTICLE

# Autologous Transplantation of Oral Mucosal Epithelial Cell Sheets Cultured on an Amniotic Membrane Substrate for Intraoral Mucosal Defects

Takeshi Amemiya<sup>1\*</sup>, Takahiro Nakamura<sup>2,3</sup>, Toshiro Yamamoto<sup>1</sup>, Shigeru Kinoshita<sup>2</sup>, Narisato Kanamura<sup>1</sup>

**1** Department of Dental Medicine, Kyoto Prefectural University of Medicine, Graduate School of Medical Science, Kyoto, Japan, **2** Department of Ophthalmology, Kyoto Prefectural University of Medicine, Graduate School of Medical Science, Kyoto, Japan, **3** Research Center for Inflammation and Regenerative Medicine, Faculty of Life and Medical Sciences, Doshisha University, Kyoto, Japan

\* [amemiya@koto.kpu-m.ac.jp](mailto:amemiya@koto.kpu-m.ac.jp)



## OPEN ACCESS

**Citation:** Amemiya T, Nakamura T, Yamamoto T, Kinoshita S, Kanamura N (2015) Autologous Transplantation of Oral Mucosal Epithelial Cell Sheets Cultured on an Amniotic Membrane Substrate for Intraoral Mucosal Defects. PLoS ONE 10(4): e0125391. doi:10.1371/journal.pone.0125391

**Academic Editor:** Irina Kerkis, Instituto Butantan, BRAZIL

**Received:** September 2, 2014

**Accepted:** March 24, 2015

**Published:** April 27, 2015

**Copyright:** © 2015 Amemiya et al. This is an open access article distributed under the terms of the [Creative Commons Attribution License](https://creativecommons.org/licenses/by/4.0/), which permits unrestricted use, distribution, and reproduction in any medium, provided the original author and source are credited.

**Data Availability Statement:** All relevant data are within the paper.

**Funding:** This work supported by a Grant-in-Aid for Scientific Research (No. 21592535) from the Japan Society for the Promotion of Science (NK), and a Grant for Advanced Medical Treatment in Kyoto Prefectural University of Medicine (NK). The funders had no role in the study design, data collection and analysis, decision to publish, or preparation of the manuscript.

## Abstract

The human amniotic membrane (AM) is a thin intrauterine placental membrane that is highly biocompatible and possesses anti-inflammatory and anti-scarring properties. Using AM, we developed a novel method for cultivating oral mucosal epithelial cell sheets. We investigated the autologous transplantation of oral mucosal epithelial cells cultured on AM in patients undergoing oral surgeries. We obtained specimens of AM from women undergoing cesarean sections. This study included five patients without any history of a medical disorder who underwent autologous cultured oral epithelial transplantation following oral surgical procedures. Using oral mucosal biopsy specimens obtained from these patients, we cultured oral epithelial cells on an AM carrier. We transplanted the resultant cell sheets onto the oral mucosal defects. Patients were followed-up for at least 12 months after transplantation. After 2–3 weeks of being cultured on AM, epithelial cells were well differentiated and had stratified into five to seven layers. Immunohistochemistry revealed that the cultured cells expressed highly specific mucosal epithelial cell markers and basement membrane proteins. After the surgical procedures, no infection, bleeding, rejection, or sheet detachment occurred at the reconstructed sites, at which new oral mucous membranes were evident. No recurrence was observed in the long-term follow-up, and the postoperative course was excellent. Our results suggest that AM-cultured oral mucosal epithelial cell sheets represent a useful biomaterial and feasible method for oral mucosal reconstruction. However, our primary clinical study only evaluated their effects on a limited number of small oral mucosal defects.

**Competing Interests:** The authors have declared that no competing interests exist.

## Introduction

Although oral mucosal defects created by tumor surgery or traumatic injury are augmented by mucosal transplantation, open wounds may become infected or develop contraction and secondary dysfunction. In such cases, autologous mucosal grafts provide transplant materials for postoperative mucosal defects in the oral cavity. However, autologous mucous membrane grafts leave defects at the donor site, and it may be difficult to harvest sufficient oral mucosa for reconstruction. The ideal reconstruction material is an autologous tissue, the harvesting of which involves minimally invasive procedures at the donor site. Tissue engineering studies have addressed these issues. Small masses of healthy oral mucosa have been cultured into mucosal epithelial cell sheets for use as biomaterials [1]. Cultured oral epithelial cell sheet transplants have the potential to respond to a wide range of membrane defects and represent an effective method with wide applications in surgical augmentation.

The human amniotic membrane (AM) is a tissue that has attracted considerable interest as a cell culture substrate that facilitates the proliferation, differentiation, and functional organization of various cell types *in vitro* [2–9]. It is a thin membrane of parenchymal tissue that covers the outermost surface of the placenta, and is generally discarded after parturition. It can be collected almost aseptically from the placenta with few technical problems or ethical concerns, and has unique characteristics, including anti-inflammatory and anti-infection properties [10, 11]. AM has been utilized as a tissue in various surgical therapies for the following purposes: to prevent adhesion/scarring after skin transplants or abdominal surgeries; as a wound dressing to accelerate the healing of burns; and in ocular surface reconstruction [12–16].

We investigated the possibility of reconstructing oral mucosal defects using an autologous cultured mucosal epithelium. We previously reported that oral mucosal epithelial cells grown on AM represented a useful biomaterial and feasible method for oral mucosal reconstruction [4, 6, 7]. In the present study, we attempted oral mucosal reconstruction using autologous AM-cultured oral mucosal epithelial sheets in five patients with oral mucosal defects after dental surgery. The use of AM in transplanted epithelial sheets following oral surgery has not yet been documented. This study represents the first step towards assessing the feasibility of transplanting autologous AM-cultured oral mucosal epithelial cell sheets in the oral cavity.

## Materials and Methods

### Ethics statement

All experimental procedures and clinical applications introduced here were approved by the Medicine Research Ethics Committee of Kyoto Prefectural University, Kyoto, Japan (R-29). We obtained prior written informed consent from all patients in accordance with the *Declaration of Helsinki* for research involving human subjects. The individual in this manuscript has given written informed consent (as outlined in PLOS consent form) to publish these case details.

### Subjects

We investigated the autologous transplantation of oral mucosal epithelial cells cultured on AM in patients undergoing oral surgeries. The study included five patients without any history of a medical disorder who underwent autologous cultured oral mucosal epithelial transplantation at our university hospital following oral surgical procedures and who were available for a follow-up exceeding 12 months. The patients comprised three men and two women who ranged in age from 36–75 years and had oral leukoplakia, pleomorphic adenoma, and mucous cysts (Table 1).

**Table 1. Research patients who underwent amniotic membrane-cultured oral mucosal epithelial cell sheet transplantation.**

Case	Age	Sex	Diagnosis	Site	Defect size (L×W×D)	Follow-up
1	74	Female	Oral leukoplakia	Buccal mucosa	17×12×2	24 months
2	45	Female	Pleomorphic adenoma	Upper lip	12×9×4	12 months
3	36	Male	Mucous cyst	Lower lip	18×16×2	18 months
4	42	Male	Mucous cyst	Lower lip	12×12×5	12 months
5	75	Male	Mucous cyst	Upper lip	13×12×5	12 months

L: length, W: width, D: depth: in mm.

doi:10.1371/journal.pone.0125391.t001

## Preparation of the amniotic membrane

We obtained AM from women undergoing cesarean section. We collected tissue from AM for our clinical purposes. We sufficiently explained the proposed use to the women and obtained their informed consent. We washed the membranes under aseptic conditions with phosphate-buffered saline (PBS) containing 5 ml of 0.5% levofloxacin and stored them at  $-80^{\circ}\text{C}$  in Dulbecco's modified Eagle's medium (GIBCO/Invitrogen, Carlsbad, CA, USA) and glycerol (1:1, v/v; Wako Pure Chemical Industries, Ltd., Osaka, Japan). AM was thawed immediately before use for the oral epithelial cell culture and washed three times with PBS. In the oral epithelial cell cultures, membranes were deprived of their amniotic epithelial cells by incubating with 0.02% EDTA (Nacalai Tesque, Inc., Kyoto, Japan) at  $37^{\circ}\text{C}$  for 2 h to loosen cellular adhesion, followed by gentle scraping with a cell scraper (Nalge Nunc International, Naperville, IL, USA) to remove the amniotic epithelial cells.

## Cultivation of oral mucosal epithelial cells on the amniotic membrane

We performed an oral mucosal epithelial cell culture according to a previously reported procedure with a few modifications [6]. Briefly, epithelial cells were co-cultured with mitomycin-C (MMC)-treated NIH/3T3 cells. Confluent 3T3 cells were incubated with PBS containing 4  $\mu\text{g}/\text{ml}$  MMC ( $37^{\circ}\text{C}$ , 2 h) in 5%  $\text{CO}_2$ :95% atmospheric air to inhibit cell proliferation, rinsed with PBS to remove the MMC, trypsinized, and inoculated ( $2 \times 10^4$  cells/ $\text{cm}^2$ ) into cell culture dishes.

We obtained oral mucosal biopsy specimens (approximately 3 mm in length) from each patient under local anesthesia 2–3 weeks before each surgical procedure for the oral epithelial cell sheet cultures on AM. Briefly, we carefully examined the oral mucosa and selected a biopsy site at the healthy mucogingival junction of the lower molar area or buccal mucosa. We injected 2% lidocaine hydrochloride containing epinephrine around the biopsy site to provide infiltration anesthesia. We made incisions of approximately 3  $\text{mm}^2$  to create a biopsy site. We then obtain a sample containing submucosal connective tissue. We sutured the surgical wound with 3–0 surgical silk and removed all sutures 1 week later. We confirmed that the patients had negative results for various infections (including hepatitis B and C, syphilis, human immunodeficiency virus, Creutzfeldt-Jakob disease, and West Nile fever) on serum tests before performed biopsies.

We immersed the oral mucosal biopsy specimens in PBS containing 50 IU/ml penicillin-streptomycin for 10 min at room temperature (RT), incubated them with 1.2 IU dispase ( $37^{\circ}\text{C}$ , 1 h), and treated them with 0.05% trypsin-ethylenediaminetetraacetic acid (RT, 10 min) to separate the cells. Enzyme activity was eliminated by washing the specimens with culture medium. We centrifuged the cells twice at 1000 revolutions per minute for 5 min and suspended the cell pellet in culture medium at  $1 \times 10^5$  cells/ $\text{cm}^2$ . We seeded the oral mucosal epithelial cells onto

AM, left them to rest on cell culture plate inserts (Corning Inc., Corning, NY, USA), and then co-cultured them with MMC-treated 3T3 cells. The culture medium consisted of a 1:1 mixture of Dulbecco's modified Eagle's medium, Ham's F-12 medium, and defined keratinocyte growth medium (ArBlast Co., Ltd., Kobe, Japan) supplemented with 5 µg/ml insulin, 10 ng/ml human recombinant epidermal growth factor, 50 IU/ml penicillin-streptomycin, and 5% autologous serum. We obtained autologous serum from all patients according to Nakamura *et al.* [17]. Blood samples (approximately 30 ml) were collected from the antecubital vein, centrifuged, and filtered under aseptic conditions, yielding approximately 10 ml of serum.

We submerged oral epithelial cells grown on AM in culture medium for approximately 2 weeks and then exposed them to air (i.e., air-lifting) for approximately 1 week. We incubated the cultures at 37°C in a 5% CO<sub>2</sub>:95% air incubator and changed the medium once daily.

## Immunohistochemistry

We performed immunohistochemical studies according to previously described methods [6]. We compared the cytoarchitectures and protein expression patterns of stained sections of oral mucosa and oral mucosal epithelial cells cultured on AM. Briefly, oral mucosal samples and AM-cultured oral mucosal epithelial cells were embedded in Tissue-Tek (Qiagen N.V., Venlo, Limburg, The Netherlands) compound, quick-frozen, and stored at −80°C. We prepared 8-µm-thick frozen sections from these stored specimens.

We fixed samples with acetone at 4°C for 10 min and then washed them in PBS at RT for 10 min. To block nonspecific binding, we incubated all specimens with 1% bovine serum albumin (Nacalai Tesque, Inc.) at RT for 20 min. We incubated the samples with the appropriate primary antibodies, presented in Table 2, at RT for 1 h, and rinsed them with PBS containing 0.15% Triton X-100. We subsequently incubated the samples at RT for 1 h with the appropriate secondary antibodies; namely fluorescein isothiocyanate-conjugated donkey anti-mouse immunoglobulin G antibodies (Molecular Probes, Inc., Eugene, OR, USA). We washed them again with PBS and mounted them under coverslips with an anti-fading medium (Vectashield; Vector Laboratories, Inc., Burlingame, CA, USA) containing propidium iodide as a nuclear counterstain for examination by confocal microscopy (Fluoview; Olympus Corporation, Tokyo, Japan).

**Table 2. Primary antibodies and their sources.**

Primary antibodies	Dilution	Sources
Mouse monoclonal cytokeratin 4	×200	Novocastra Laboratories, Newcastle-on-Tyne, UK
Mouse monoclonal cytokeratin 13	×200	Novocastra Laboratories, Newcastle-on-Tyne, UK
Mouse monoclonal cytokeratin 1	×40	Novocastra Laboratories, Newcastle-on-Tyne, UK
Mouse monoclonal cytokeratin 10	×50	Novocastra Laboratories, Newcastle-on-Tyne, UK
Mouse monoclonal integrin alpha 6	×200	Chemicon International, Inc., Temecula, CA, USA
Mouse monoclonal integrin beta 4	×500	Chemicon International, Inc., Temecula, CA, USA
Mouse monoclonal integrin alpha 3	×500	Chemicon International, Inc., Temecula, CA, USA
Mouse monoclonal integrin beta 1	×500	Chemicon International, Inc., Temecula, CA, USA
Mouse monoclonal laminin 5	×100	Chemicon International, Inc., Temecula, CA, USA
Mouse monoclonal laminin alpha 5 chain	×200	Chemicon International, Inc., Temecula, CA, USA
Mouse monoclonal collagen VII	×100	Chemicon International, Inc., Temecula, CA, USA

doi:10.1371/journal.pone.0125391.t002



## Surgical procedures

We established an approximately 2-mm safety margin around the lesion, used a CO<sub>2</sub> gas laser under local anesthesia to dissect the mucosa, and then detached the lesion. We transplanted the AM-cultured oral mucosal epithelial cell sheet onto the oral mucosal defect region after oral surgery and secured it with 7–0 nylon sutures (Prolene; Ethicon, Inc., Somerville, NJ, USA). We used fluorescein staining of the cultured oral epithelial sheets to confirm their quality. We also performed a tie-over dressing. We removed the threads on postoperative day 7.

## Results

### Cell morphology and keratin expression of oral epithelial cells cultured on the amniotic membrane

After 2–3 weeks, the oral epithelial cells cultured on AM histomorphologically showed five to seven stratification layers of measurable thickness. The basal cells of the cultured epithelium were cuboidal, whereas the superficial cells were flattened ([Fig 1A](#)). Immunohistochemically, the oral epithelial cells stained positive for antibodies specific to the mucosal epithelium, e.g., keratins 4 and 13 ([Fig 1B and 1C](#)), which was consistent with our earlier findings [3]. Conversely, keratins 1 and 10 were not expressed in any layer ([Fig 1D and 1E](#)).

The oral mucosal epithelia revealed stratified cell layers ([Fig 1F](#)) and the expression of keratins 4 and 13 was evident throughout the oral mucosal epithelial layers ([Fig 1G and 1H](#)). In contrast, keratins 1 and 10 were not expressed at detectable levels in any layer ([Fig 1I and 1J](#)).

### Expression of basement membrane proteins in oral mucosal epithelial cells cultured on the amniotic membrane

Immunohistochemical analyses of AM-cultured oral mucosal epithelial cells and oral mucosal epithelia demonstrated linearly positive staining for integrin alpha-6 beta-4 ([Fig 2A, 2B, 2H and 2I](#)), integrin alpha-3 beta-1 ([Fig 2C, 2D, 2J and 2K](#)), laminin 5 ([Fig 2E and 2L](#)), laminin alpha 5 chain ([Fig 2F and 2M](#)), and collagen VII ([Fig 2G and 2N](#)) on the basement membrane side. Expression patterns were similar between the cultured oral mucosal epithelial sheets and the *in vivo* oral mucosa.

### Transplanted amniotic membrane-cultured oral mucosal epithelial cell sheets

Autologous AM-cultured oral mucosal epithelial cell sheets were successfully generated for all five patients. Clinically, AM-cultured oral mucosal epithelial cell sheets had sufficient strength to be handled. In all cases, we observed that the transplanted sheets adhered to the mucosal defects ([Figs 3A–3C, 4A–4C and 5A–5C](#)). One week after surgery, no infection, bleeding, or sheet detachment was evident at the transplanted sites. The transplanted cell sheets were visible to the naked eye as adherent to the graft beds, and were distinguishable from the surrounding adjacent mucosa ([Figs 3D, 4D and 5D](#)).

At 1 month, the mucosal defects were well-epithelialized and had been replaced by transplanted oral epithelial sheets. They were macroscopically indistinguishable from the surrounding mucosa ([Figs 3E, 4E and 5E](#)). We did not detect recurrence macroscopically in the long-term follow-up, which exceeded 12 months, and all patients had an excellent postoperative course ([Figs 3F, 4F and 5F](#)). Cases 1 and 2 were reported previously ([Figs 3 and 4](#)) [4, 7], and the long-term follow-up of these cases was performed in this study.

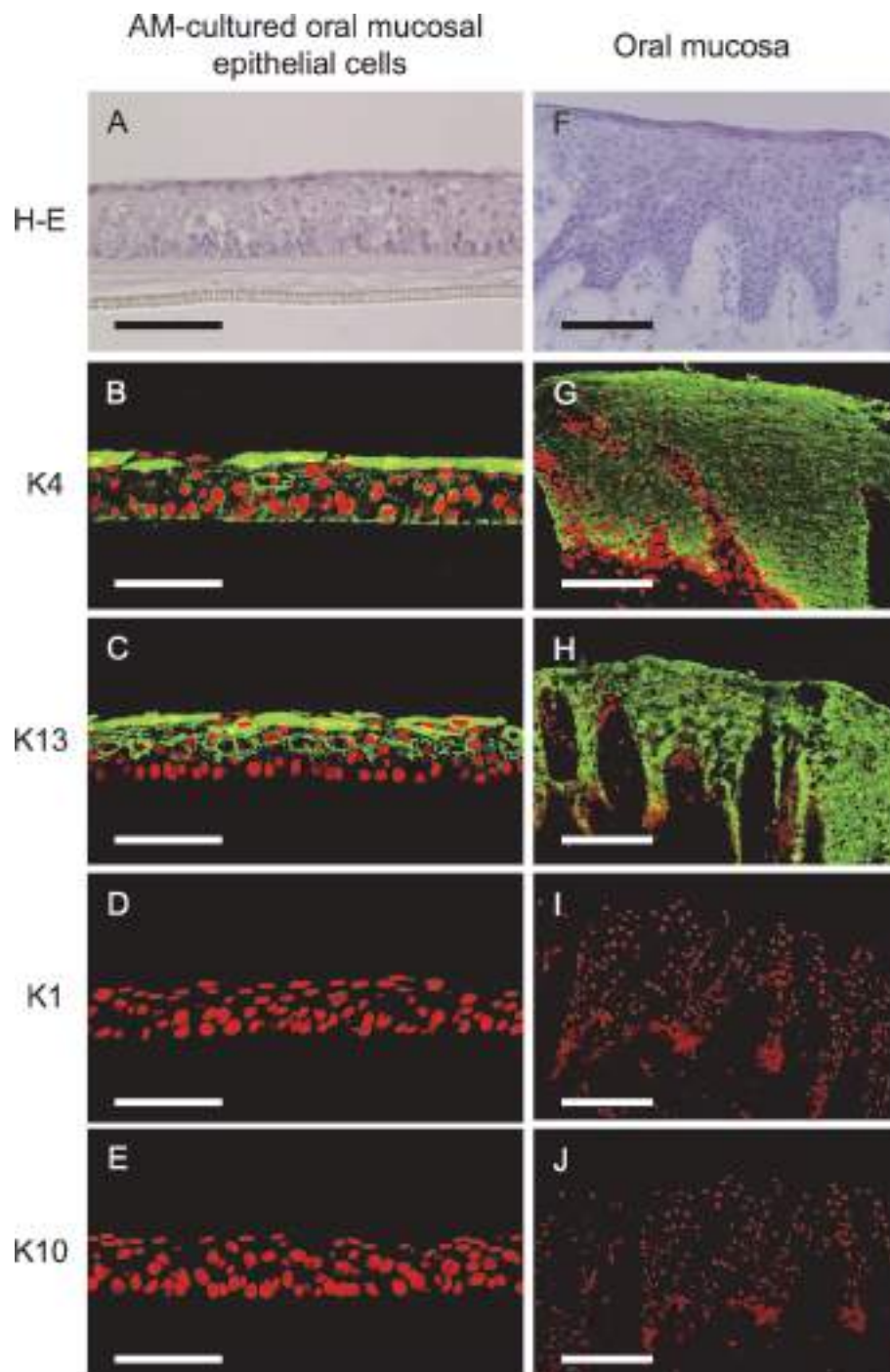


**Fig 1. Morphology and keratin expression patterns of amniotic membrane-cultured oral mucosal epithelial cells and the oral mucosa.** Light micrographs of amniotic membrane (AM)-cultured oral mucosal epithelial cells and the *in vivo* oral mucosa stained with hematoxylin and eosin as well as representative immunohistochemical staining results of AM-cultured oral mucosal epithelial cells and the *in vivo* oral mucosa. Culture oral mucosal epithelial cells grew well on AM, exhibiting five to seven differentiated, stratified layers with a measurable thickness (A). Keratins 4 and 13 were expressed by AM-cultured oral mucosal epithelial cells (B and C). These keratins were expressed in all epithelial layers of the oral mucosa (G and H). Conversely, keratins 1 and 10 were not expressed in any layer of AM-cultured oral mucosal epithelial cells (D and E) or oral epithelial cells (I and J). Nuclei are stained with propidium iodide (red). Scale bars: (A–E) 100  $\mu$ m, (F–J) 200  $\mu$ m.

doi:10.1371/journal.pone.0125391.g001

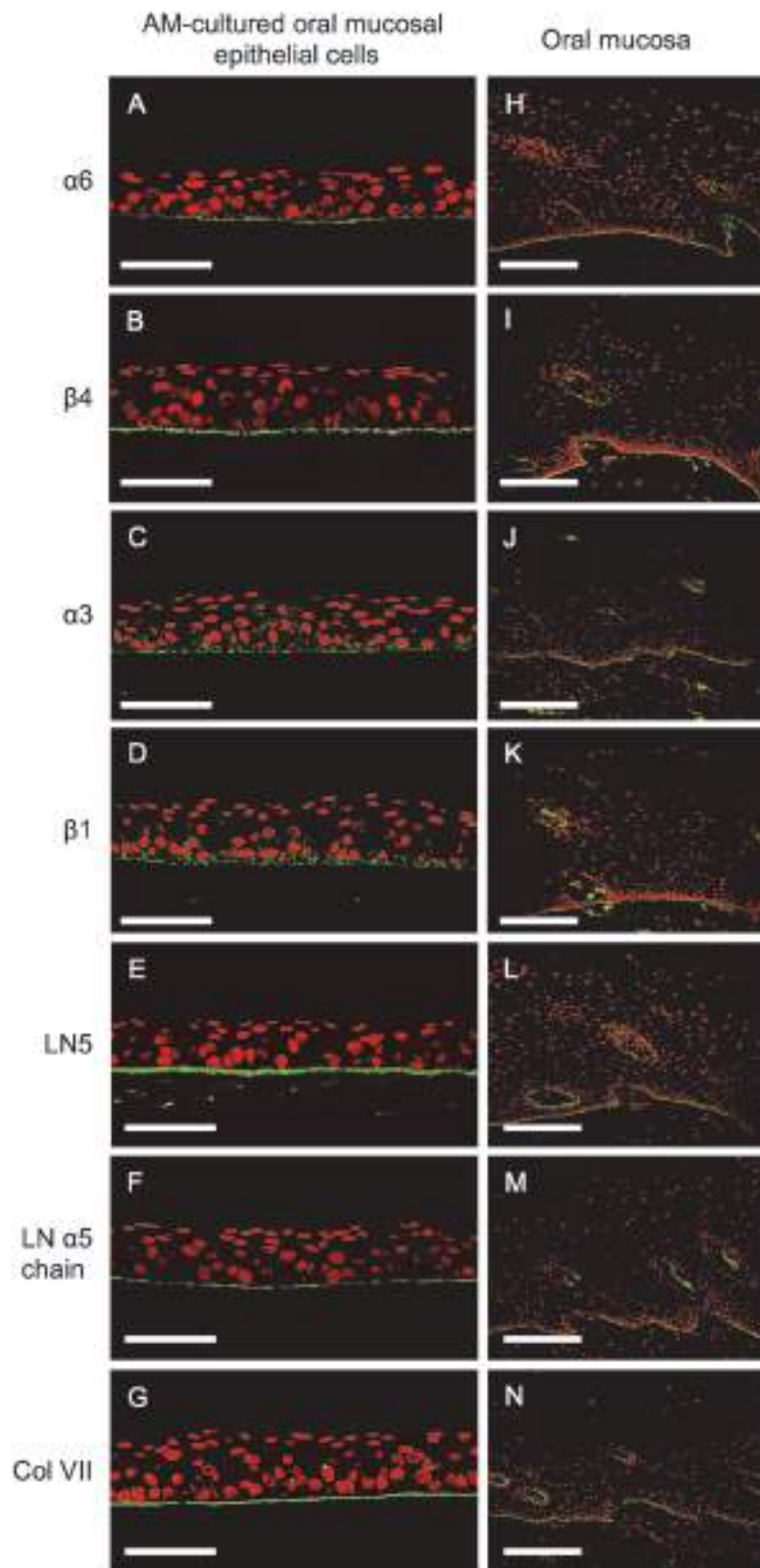


**Fig 2. Expression of basement membrane proteins in amniotic membrane-cultured oral mucosal epithelial cells and the oral mucosa.** Representative immunohistochemical results. Positive staining for integrins alpha-6 beta-4 and alpha-3 beta-1, laminin 5, the laminin alpha 5 chain, and collagen VII was evident on the basement membrane side of the cultured oral mucosal epithelial cell layer (A–G) and the basement membrane of the oral mucosa (H–N). Nuclei are stained with propidium iodide (red). Scale bars: (A–G) 100  $\mu$ m, (H–N) 200  $\mu$ m.

doi:10.1371/journal.pone.0125391.g002

## Discussion

The acquisition of transplantable cultured structures requires a combination of stem cells, an adequate extracellular matrix, and growth factors. Cultured oral epithelial cell sheets have been developed for mucosal defects; however, these epithelial sheets lack substrates and are fragile and difficult to handle for grafting [1]. The important element in oral grafting is a substrate that supports the oral epithelial cells. Selecting a substrate with biocompatibility, stability, and mechanical properties is important for tissue engineering. We used AM as a key substrate for the growth of oral mucosal epithelial cells and performed preliminary clinical studies on AM-cultured oral mucosal epithelial cell sheets [17] for intraoral mucosal defects. To the best of our knowledge, this is the first study to have successfully transplanted these cells into the oral cavity.

AM is a thin placental membrane that retains amniotic fluid and is easily attainable. Morphologically, AM consists of a monostratal amniotic epithelium on a basement membrane of a specific parenchymal thickness. Immunohistochemically, collagens III and IV and laminin are expressed in the amniotic basement membrane; collagens are also expressed in the parenchyma [18–20]. In addition, AM contains many growth factors, including epidermal growth factor, keratinocyte growth factor, hepatocyte growth factor, and basic fibroblast growth factor [21], and exhibits anti-inflammatory [22] and antibacterial properties [23]. The biologically active peptides in AM have significant roles in epithelial cell proliferation. Our results demonstrated

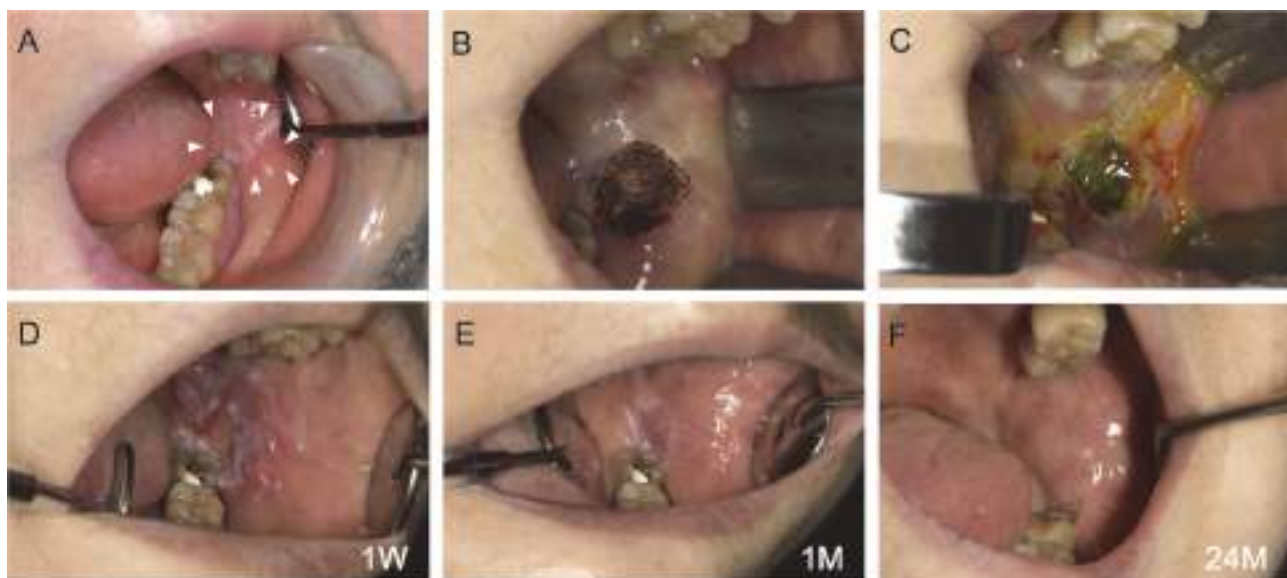


**Fig 3. Autotransplantation procedure for an oral mucosal defect after surgery for oral leukoplakia: Case 1.** A lesion measuring 15  $\times$  10  $\times$  2 mm was detected in the left buccal mucosa (A). The lesion was excised using a CO<sub>2</sub> laser under local anesthesia (B). The amniotic membrane (AM)-cultured oral mucosal epithelial cell sheet was applied and sutured in place (C). One week after surgery, the transplanted sheets had adhered to the graft bed (D). Approximately 1 month after surgery, the mucosal defect had been replaced by the transplanted AM-cultured oral mucosal epithelial cell sheet (E). After 24 months, there was no postoperative recurrence (F).

doi:10.1371/journal.pone.0125391.g003



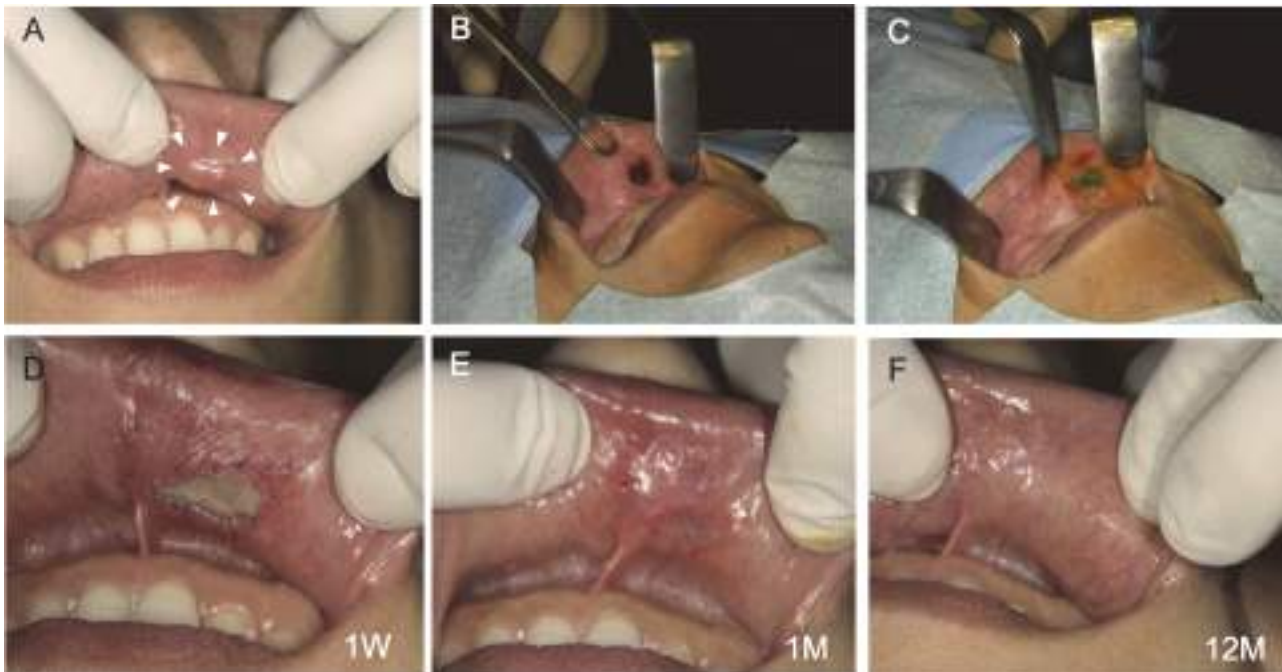


**Fig 4. Autotransplantation procedure for an oral mucosal defect after surgery for pleomorphic adenoma: Case 2.** A lesion measuring  $10 \times 7 \times 4$  mm was detected below the left mucosa of the upper lip (A). The lesion was excised to the depth of the subepithelial tissues using a CO<sub>2</sub> laser under local anesthesia (B). An amniotic membrane (AM)-cultured oral mucosal epithelial cell sheet was applied to the oral mucosal defect and sutured in place (C). The sutures were removed 1 week after surgery. The transplanted site did not show infection, bleeding, or sheet detachment, and had adhered to the graft bed (D). Approximately 1 month after surgery, the mucosal defect had been replaced by the transplanted AM-cultured oral mucosal epithelial cell sheet (E). After 12 months, there was no postoperative recurrence (F).

doi:10.1371/journal.pone.0125391.g004

that AM is suitable for culturing oral mucosal epithelial cells, suggesting that it is a useful tissue for normal cell proliferation and differentiation. Although little is known about its mechanism of action, it can be expected to elicit a relatively mild immune response. Several advantages of the clinical use of AM as a tissue have been reported in the field of surgical procedures. It has also been used in the fields of reconstructive and dental surgery, dermatology, and ophthalmology, and significant evidence of its success has been reported [13, 14, 24]. In addition, AM can be used not only as a transplant material but also as a substrate for cell culture [1–9, 15, 17, 24, 25].

An important element in oral mucosal reconstruction is the scaffold that supports the cells. In our previous study, we focused on AM as a scaffold to facilitate the growth of oral epithelial cells and successfully transplanted AM-cultured autologous mucosal epithelial cells onto intraoral mucosal defects in animals [6]. No rejection or inflammatory reactions occurred, underscoring the potential use of AM as a graft material. Nakamura *et al.* [17, 26] produced AM-cultured oral epithelial cell sheets as an extracellular matrix. They obtained good clinical results using these sheets to treat severe intractable corneal disorders. We previously confirmed the detachment/removal of amniotic epithelial cells was using electron microscopy [27]. We did not quantify DNA in AM after the removal of epithelial cells (i.e., denuded AM); however, we succeeded in clinically applying denuded AM and autologous oral mucosal epithelial cells to ocular surface reconstruction in patients with intractable corneal/conjunctival diseases [26]. No serious adverse events developed after transplantation over a long-term follow-up [17].

To the best of our knowledge, no previous studies have documented the use of AM as a scaffold for human oral mucosal epithelial cell sheets; therefore, it was unclear whether these cells

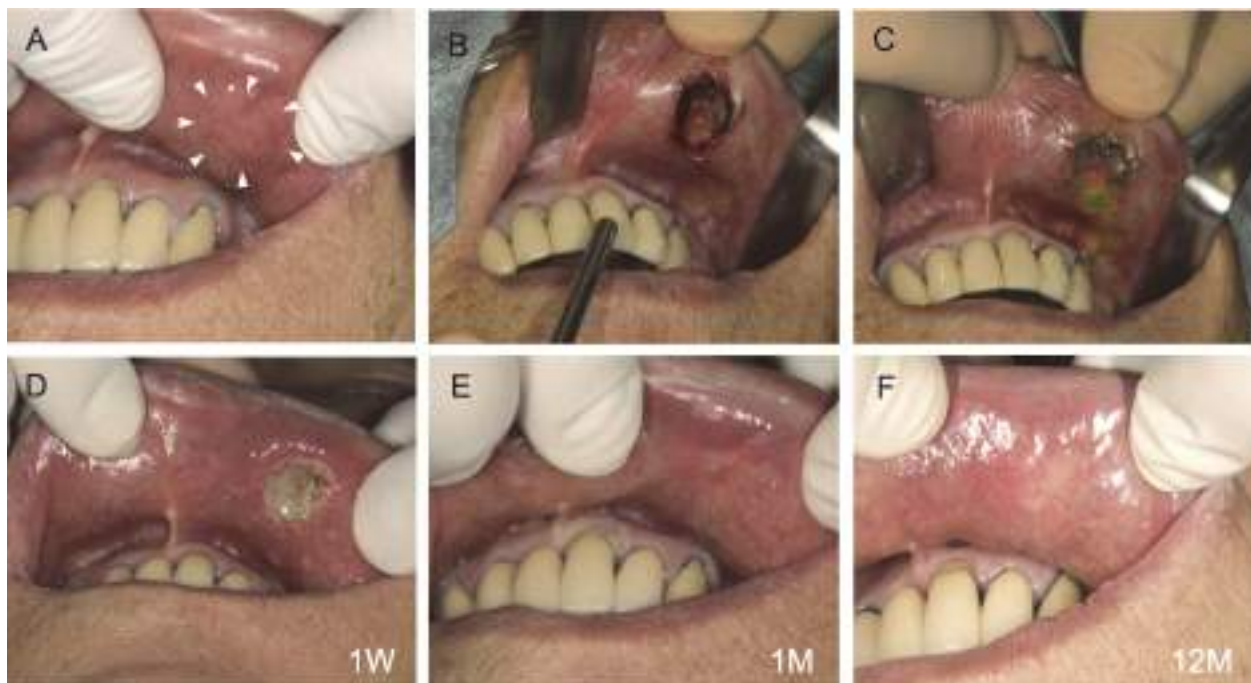


**Fig 5. Autotransplantation procedure for an oral mucosal defect after surgery for a mucous cyst: Case 5.** A lesion measuring  $11 \times 10 \times 5$  mm was detected below the left mucosa of the upper lip (A). The lesion was excised to the depth of the subepithelial tissues using a CO<sub>2</sub> laser under local anesthesia (B). An amniotic membrane (AM)-cultured oral mucosal epithelial cell sheet was applied to the oral mucosal defect and sutured in place (C). The sutures were removed 1 week after surgery. The transplanted sheets had adhered to the graft bed (D). Approximately 1 month after surgery, the mucosal defect had been replaced with the transplanted AM-cultured oral mucosal epithelial cell sheet (E). After 12 months, there was no postoperative recurrence (F).

doi:10.1371/journal.pone.0125391.g005

had the ability to proliferate efficiently or differentiate appropriately on AM. Furthermore, it had not been determined whether oral mucosal epithelial cells grown on AM were an effective biomaterial for reconstructing oral mucosal defects in clinical settings. Collection of the oral mucosa (biopsy) is associated with the risk of developing various postoperative complications, including pain, swelling, bleeding, and functional disorders. Thus, we explained the possible development of these complications to the patients undergoing biopsy and obtained their consent. We also avoided the risk of postoperative complications and cicatrization of the donor site by reducing the size of the biopsy specimen as much as possible (approximately 3 mm in length). In addition, we strictly followed the course by administering oral antibiotics to prevent infection and anti-inflammatory analgesics to reduce pain and confirmed the absence of abnormal findings such as secondary infection. No serious postoperative complication developed and patient satisfaction was high. We previously compared cultures of oral mucosal epithelial cells between media containing autologous serum and general fetal bovine serum [25]. Cell growth within autologous serum and fetal bovine serum was equivalent; oral mucosal epithelial cells cultured with autologous serum on AM expressed mucosa-specific keratins 4 and 13, and the basement membrane (integrin alpha-6, beta-4, and beta-1; collagen VII; and laminin 5) and hemidesmosomes were present.

We immunohistochemically analyzed the oral epithelial cells cultured on AM to examine the ability of this scaffold material to maintain the characteristics of the oral mucosa, namely, cell proliferation and basal cell attachment to the underlying substrate. The cultivation of oral mucosal epithelia on AM at the air-liquid interface facilitated the construction of multilayered sheets of an epithelium that resembled the native epithelium and showed signs of differentiation such as basement membrane formation and cytokeratin expression [15, 28, 29]. Human

oral epithelial cells cultured for 3 weeks on AM manifested five to seven differentiated, stratified layers; however, stratification was insufficient and complete cornification was rarely observed. We chose a 2–3-week culture period in this study based on our earlier findings that cell growth decreased in longer cultures [3, 6, 7, 15]. Immunohistochemically, keratins 4 and 13 are highly specific mucosal epithelial cell markers [30–33], whereas keratins 1 and 10 are cornified epidermis markers [31, 33, 34]. Our immunohistochemical results indicated that AM-cultured human oral epithelial sheets expressed keratins 4 and 13, but not 1 or 10, which was consistent with the findings of our earlier animal experiment [6]. This showed that AM-cultured oral mucosal epithelial cells maintained many of the phenotypic characteristics of oral mucosal epithelia *in vivo*.

An ideal engineered oral mucosa closely resembling a normal oral mucosa should consist of a continuous basement membrane that separates the lamina propria and epithelium [35], with a stratified squamous epithelium on the basement membrane [1]. Integrins alpha-3 beta-1 and alpha-6 beta-4, which are specific receptors for laminin 5, are widely distributed in the basement membranes of epithelial tissues, and laminin 5 has two functional domains capable of binding these integrins and collagen VII on basal cells to form anchoring fibrils [36, 37]. Collagen VII and the laminin alpha 5 chain are major components of basement membranes, and collagen VII localizes exclusively to the basement membrane zone. Integrin alpha-6 beta-4 is a specific component of hemidesmosomes [38].

Since integrin alpha-6 beta-4 and alpha-3 beta-1, laminin 5, the laminin alpha 5 chain, and collagen VII were expressed in the basal layer of AM-cultured oral mucosal epithelial cell sheets, these results indicated that AM-cultured oral mucosal epithelial cell sheets maintained the properties of the mucous membrane. The reaction products of these proteins were confined to basal epithelial cells adherent to AM with hemidesmosome attachments and produced the basement membrane of the oral mucosal epithelia in culture.

Clinically, a key point for successfully cultivating oral epithelial sheets is understanding how basal cells attach to the underlying AM, and these findings encouraged us to perform the transplantation of AM-cultured oral epithelial cells. Therefore, the transplantation of AM-cultured oral mucosal epithelial cells may be considered advantageous because rapid epithelialization occurs following transplantation; this makes the transplanted site very stable and avoids post-operative infections, both of which are important factors for the successful clinical application of this procedure. In the present study, we clinically applied AM-cultured oral mucosal epithelial cell sheets and encountered no problems in the strength of the cell sheets or their applicability during surgery. No complications such as immunological rejection or infection occurred in any patient.

Izumi *et al.* [39] reported that cultured oral mucosal epithelial grafts enhanced the maturation of the underlying submucosal layer and were associated with rapid epithelial coverage in intraoral applications. In our study, we could not obtain histological samples from the transplanted areas. Macroscopically, the transplanted sheets were visible to the naked eye as adherent to the graft beds and were distinguishable from the adjacent mucosa at 1 week. After 1 month, the mucosal defects were well-epithelialized and had been replaced by the transplanted oral epithelial sheets. The transplanted oral epithelial sheets became macroscopically indistinguishable from the surrounding mucosa over time, suggesting that AM-cultured oral mucosal epithelial cell sheets were successfully engrafted onto the oral mucosal defects.

In conclusion, we succeeded in growing oral epithelial cells on AM and performing the autologous transplantation of these cells onto intraoral mucosal defects. This primary clinical study evaluated a limited number of small oral mucosal defects. In future studies, we aim to examine the utility of AM-cultured oral mucosal epithelial sheets on lesions of an extensive size, depth, and in different regions in a larger number of patients.

## Acknowledgments

The authors would like to thank Tomoko Horikiri and Sachiko Mano for assisting with the culturing procedures.

## Author Contributions

Conceived and designed the experiments: TA TN SK NK. Performed the experiments: TA TN TY NK. Analyzed the data: TA TN. Contributed reagents/materials/analysis tools: TA TN TY SK NK. Wrote the paper: TA.

## References

1. Moharamzadeh K, Brook IM, Van Noort R, Scutt AM, Thornhill MH. Tissue-engineered oral mucosa: a review of the scientific literature. *J Dent Res*. 2007; 86: 115–124. PMID: [17251509](#).
2. Amemiya T, Yamamoto T, Oseko F, Nakamura T, Kinoshita S, Kanamura N. Development of rabbit oral mucosal epithelium cells and periodontal ligament cells sheet using the amniotic membrane. *J Jpn Assoc Regenerative Dent*. 2003; 1: 25–35.
3. Amemiya T, Nakamura T, Oseko F, Yamamoto T, Fukushima A, Nakanishi A, et al. Human oral epithelial and periodontal ligament cells sheets cultured on human amniotic membrane for oral reconstruction. *J Oral Tissue Engin*. 2004; 1: 89–96.
4. Yamamoto T, Amemiya T, Nakanishi A, Nakamura T, Kinoshita S, Kanamura N. Usefulness for a cultured human oral epithelial cell sheet on human amniotic membrane following removal of minor salivary gland tumor surgery. *J Oral Tissue Engin*. 2007; 5: 54–58.
5. Amemiya T, Adachi K, Nishigaki M, Yamamoto T, Kanamura N. Experiences of preclinical use of periodontal ligament-derived cell sheet cultured on human amniotic membrane. *J Oral Tissue Engin*. 2008; 6: 106–112.
6. Amemiya T, Nakamura T, Yamamoto T, Kinoshita S, Kanamura N. Immunohistochemical study of oral epithelial sheets cultured on amniotic membrane for oral mucosal reconstruction. *Biomed Mater Eng*. 2010; 20: 37–45. doi: [10.3233/BME-2010-0613](#) PMID: [20448302](#).
7. Amemiya T, Nakamura T, Yamamoto T, Kinoshita S, Kanamura N. Tissue engineering by transplantation of oral epithelial sheets cultivated on amniotic membrane for oral mucosal reconstruction. *Inflam Regener*. 2010; 30: 176–180.
8. Amemiya T, Adachi K, Akamatsu Y, Nishigaki M, Oseko F, Yamamoto T, et al. Immunohistochemical study of human periodontal ligament-derived cells cultured on amniotic membrane. *Jpn J Conserv Dent*. 2010; 53: 214–221.
9. Adachi K, Amemiya T, Nakamura T, Honjo K, Kumamoto S, Yamamoto T, et al. Human periodontal ligament cell sheets cultured on amniotic membrane substrate. *Oral Dis*. 2014; 20: 582–590. doi: [10.1111/odi.12176](#) PMID: [24112848](#)
10. Talmi YP, Sigler L, Inge E, Finkelstein Y, Zohar Y. Antibacterial properties of human amniotic membranes. *Placenta*. 1991; 12: 285–288. PMID: [1754577](#).
11. Hao Y, Ma DH, Hwang DG, Kim WS, Zhang F. Identification of antiangiogenic and antiinflammatory proteins in human amniotic membrane. *Cornea*. 2000; 19: 348–352. PMID: [10832697](#).
12. Colococho G, Graham WP 3rd, Greene AE, Matheson DW, Lynch D. Human amniotic membrane as a physiologic wound dressing. *Arch Surg*. 1974; 109: 370–373. PMID: [4604542](#)
13. Trelford JD, Trelford-Sauder M. The amnion in surgery, past and present. *Am J Obstet Gynecol*. 1979; 134: 833–845. PMID: [380345](#).
14. Tseng SC, Prabhasawat P, Barton K, Gray T, Meller D. Amniotic membrane transplantation with or without limbal allografts for corneal surface reconstruction in patients with limbal stem cell deficiency. *Arch Ophthalmol*. 1998; 116: 431–441. PMID: [9565039](#).
15. Nakamura T, Endo K, Cooper LJ, Fullwood NJ, Tanifuji N, Tsuzuki M, et al. The successful culture and autologous transplantation of rabbit oral mucosal epithelial cells on amniotic membrane. *Invest Ophthalmol Vis Sci*. 2003; 44: 106–116. PMID: [12506062](#).
16. Samandari MH, Yaghmaei M, Ejlali M, Moshref M, Saffar AS. Use of amniotic membrane as a graft material in vestibuloplasty: a preliminary report. *Oral Surg Oral Med Oral Pathol Oral Radiol Endod*. 2004; 97: 574–578. PMID: [15153868](#).
17. Nakamura T, Takeda K, Inatomi T, Sotozono C, Kinoshita S. Long-term results of autologous cultivated oral mucosal epithelial transplantation in the scar phase of severe ocular surface disorders. *Br J Ophthalmol*. 2011; 95: 942–946. doi: [10.1136/bjo.2010.188714](#) PMID: [21097786](#).



18. Modesti A, Scarpa S, D'Orazi G, Simonelli L, Caramia FG. Localization of type IV and V collagens in the stroma of human amnion. *Prog Clin Biol Res*. 1989; 269: 459–463. PMID: [2740400](#).
19. Nanaev AK, Rukosuev VS, Shirinsky VP, Milovanov AP, Domogatsky SP, Duance VC, et al. Confocal and conventional immunofluorescent and immunogold electron microscopic localization of collagen types III and IV in human placenta. *Placenta*. 1991; 12: 573–595. PMID: [1805200](#).
20. Malak TM, Ockleford CD, Bell SC, Dalgleish R, Bright N, Macvicar J. Confocal immunofluorescence localization of collagen types I, III, IV, V and VI and their ultrastructural organization in term human fetal membranes. *Placenta*. 1993; 14: 385–406. PMID: [8248033](#).
21. Koizumi NJ, Inatomi TJ, Sotozono CJ, Fullwood NJ, Quantock AJ, Kinoshita S. Growth factor mRNA and protein in preserved human amniotic membrane. *Curr Eye Res*. 2000; 20: 173–177. PMID: [10694891](#).
22. Hao Y, Ma DH, Hwang DG, Kim WS, Zhang F. Identification of antiangiogenic and antiinflammatory proteins in human amniotic membrane. *Cornea*. 2000; 19: 348–352. PMID: [10832697](#).
23. Talmi YP, Sigler L, Inge E, Finkelstein Y, Zohar Y. Antibacterial properties of human amniotic membranes. *Placenta*. 1991; 12: 285–288. PMID: [1754577](#).
24. Kesting MR, Wolff KD, Nobis CP, Rohleder NH. Amniotic membrane in oral and maxillofacial surgery. *Oral Maxillofac Surg*. 2014; 18: 153–164. doi: [10.1007/s10006-012-0382-1](#) PMID: [23242942](#).
25. Nakamura T, Ang LP, Rigby H, Sekiyama E, Inatomi T, Sotozono C, et al. The use of autologous serum in the development of corneal and oral epithelial equivalents in patients with Stevens-Johnson syndrome. *Invest Ophthalmol Vis Sci*. 2006; 47: 909–916. PMID: [16505023](#).
26. Nakamura T, Inatomi T, Sotozono C, Amemiya T, Kanamura N, Kinoshita S. Transplantation of cultivated autologous oral mucosal epithelial cells in patients with severe ocular surface disorders. *Br J Ophthalmol*. 2004; 88: 1280–1284. PMID: [15377551](#).
27. Cooper LJ, Kinoshita S, German M, Koizumi N, Nakamura T, Fullwood NJ. An investigation into the composition of amniotic membrane used for ocular surface reconstruction. *Cornea*. 2005; 24: 722–729. PMID: [16015093](#).
28. Rosdy M, Clauss LC. Terminal epidermal differentiation of human keratinocytes grown in chemically defined medium on inert filter substrates at the air-liquid interface. *J Invest Dermatol*. 1990; 95: 409–414. PMID: [1698886](#).
29. Rosdy M, Pisani A, Ortonne JP. Production of basement membrane components by a reconstructed epidermis cultured in the absence of serum and dermal factors. *Br J Dermatol*. 1993; 129: 227–234. PMID: [8286218](#).
30. Clausen H, Moe D, Buschard K, Dabelsteen E. Keratin proteins in human oral mucosa. *J Oral Pathol*. 1986; 15: 36–42. PMID: [2418182](#).
31. Cooper D, Sun TT. Monoclonal antibody analysis of bovine epithelial keratins. Specific pairs as defined by coexpression. *J Biol Chem*. 1986; 261: 4646–4654. PMID: [2420789](#).
32. Juhl M, Reibel J, Stoltze K. Immunohistochemical distribution of keratin proteins in clinically healthy human gingival epithelia. *Scand J Dent Res*. 1989; 97: 159–170. PMID: [2468178](#).
33. Feghali-Assaly M, Sawaf MH, Ouhayoun JP. In situ hybridization study of cytokeratin 4, 13, 16 and 19 mRNAs in human developing junctional epithelium. *Eur J Oral Sci*. 1997; 105: 599–608. PMID: [9469612](#).
34. Shabana AH, Ouhayoun JP, Sawaf MH, Forest N. Cytokeratin patterns of human oral mucosae in histiotypic culture. *Arch Oral Biol*. 1991; 36: 747–758. PMID: [1720953](#).
35. Black AF, Bouez C, Perrier E, Schlotmann K, Chapuis F, Damour O. Optimization and characterization of an engineered human skin equivalent. *Tissue Eng*. 2005; 11: 723–733. PMID: [15998214](#).
36. Maragou P, Bazopoulou-Kyrkanidou E, Panotopoulou E, Kakarantza-Angelopoulou E, Sklavounou-Andrikopoulou A, Kotaridis S. Alteration of integrin expression in oral squamous cell carcinomas. *Oral Dis*. 1999; 5: 20–26. PMID: [10218037](#).
37. Nishiyama T, Amano S, Tsunenaga M, Kadoya K, Takeda A, Adachi E, et al. The importance of laminin 5 in the dermal-epidermal basement membrane. *J Dermatol Sci*. 2000; 24 Suppl: S51–59. PMID: [11137397](#).
38. Stepp MA, Spurr-Michaud S, Tisdale A, Elwell J, Gipson IK. Alpha 6 beta 4 integrin heterodimer is a component of hemidesmosomes. *Proc Natl Acad Sci USA*. 1990; 87: 8970–8974. PMID: [2247472](#).
39. Izumi K, Feinberg SE, Iida A, Yoshizawa M. Intraoral grafting of an ex vivo produced oral mucosa equivalent: a preliminary report. *Int J Oral Maxillofac Surg*. 2003; 32: 188–197. PMID: [12729781](#).

# Effect of the Rho Kinase Inhibitor Y-27632 on Corneal Endothelial Wound Healing

Naoki Okumura,<sup>1,2</sup> Ryota Inoue,<sup>1</sup> Yugo Okazaki,<sup>1</sup> Shinichiro Nakano,<sup>1</sup> Hiroko Nakagawa,<sup>\*,2</sup> Shigeru Kinoshita,<sup>2,3</sup> and Noriko Koizumi<sup>1</sup>

<sup>1</sup>Department of Biomedical Engineering, Faculty of Life and Medical Sciences, Doshisha University, Kyotanabe, Japan

<sup>2</sup>Department of Ophthalmology, Kyoto Prefectural University of Medicine, Kyoto, Japan

<sup>3</sup>Department of Frontier Medical Science and Technology for Ophthalmology, Kyoto Prefectural University of Medicine, Kyoto, Japan

Correspondence: Noriko Koizumi, Department of Biomedical Engineering, Faculty of Life and Medical Sciences, Doshisha University, Kyotanabe 610-0321, Japan; nkoizumi@mail.doshisha.ac.jp.

\*Deceased May 27, 2015.

Submitted: June 29, 2015

Accepted: August 7, 2015

Citation: Okumura N, Inoue R, Okazaki Y, et al. Effect of the Rho kinase inhibitor Y-27632 on corneal endothelial wound healing. *Invest Ophthalmol Vis Sci*. 2015;56:6067–6074. DOI:10.1167/iovs.15-17595

**PURPOSE.** The purpose of this study was to investigate the feasibility of using Rho-associated kinase (ROCK) inhibitor eye drops for treating severe corneal endothelial damage due to surgical invasion.

**METHODS.** A rabbit corneal endothelial damage model was created by mechanically scraping half the area of the corneal endothelium of eighteen eyes of Japanese white rabbits. A selective ROCK inhibitor, Y-27632 (10 mM), was applied topically for 2 weeks, and then the anterior segment was evaluated by slitlamp microscopy. The corneal endothelium was evaluated by phalloidin staining and immunohistochemical analysis. We then conducted pilot clinical research and applied Y-27632 eye drops topically to three patients who exhibited severe corneal edema due to corneal endothelial damage.

**RESULTS.** In the corneal endothelial damage rabbit model, more Ki67-positive cells were detected in Y-27632-treated eyes than in control eyes. Five of six corneas became transparent in Y-27632-treated eyes, whereas zero of six corneas became transparent in the control eyes ( $P < 0.01$ ). Actin fibers were distributed at the cell cortex in the eyes treated with Y-27632, whereas actin distribution was partially disrupted, and stress fibers were observed in control eyes. N-cadherin and Na<sup>+</sup>/K<sup>+</sup>-ATPase were expressed in almost all cells in Y-27632-treated eyes, but expression decreased in control eyes. Preliminary human cases confirmed that ROCK inhibitor eye drops were considerably effective for treatment of corneal edema associated with cataract surgery.

**CONCLUSIONS.** ROCK inhibitor may be developed as an eye drop for treating acute corneal endothelial damage to prevent progression of bullous keratopathy. (University Hospital Medical Information Network Clinical Trial Registry no. UMIN000003625; www.umin.ac.jp/ctr)

Keywords: bullous keratopathy, corneal endothelial cells, PBK, ROCK inhibitor

In the United States, pseudophakic bullous keratopathy (PBK) has been the most frequent indicator for corneal transplantation from 1980 to 2005 and has accounted for 28.4% of the corneal transplantations from 2001 to 2005.<sup>1</sup> More recently, the Eye Bank Association of America reported that 14,153 corneas (21.3%) were provided for treatment of Fuchs' endothelial corneal dystrophy and 8244 corneas (12.4%) were provided for post-cataract surgery edema among a total of 66,305 corneas in 2013.<sup>2</sup> In Asian countries, as in Western countries, cataract surgery is a leading cause of demand for corneal transplantation.<sup>1,3–5</sup> For instance, PBK and aphakic bullous keratopathy (ABK) accounted for 23.4% of corneal transplantations in Singapore from 1991 to 2006,<sup>6</sup> 44.4% in Japan from 1999 to 2001,<sup>7</sup> and 25.5% in India from 1987 to 1995.<sup>8</sup>

The corneal endothelium is critical for maintaining homeostatic corneal transparency, which it accomplishes by pump and barrier functions. However, the proliferative ability of corneal endothelial cells (CECs) is severely limited,<sup>9</sup> so any trauma to the corneal endothelium decreases corneal endothelial cell density due to compensatory migration and spreading

of the remaining cells. When corneal endothelial cell density decreases to a critical level (500–1000 cells/mm<sup>2</sup>), the cornea exhibits haziness, with edema, due to decompensation of the corneal endothelial function. No pharmaceutical intervention is available to reverse this corneal endothelial damage, and the only therapeutic choice is still corneal transplantation.<sup>10</sup>

However, we recently showed that a Rho-associated kinase (ROCK) inhibitor can be useful in treating corneal endothelial dysfunction. In 2009, we demonstrated that the selective ROCK inhibitor Y-27632 showed unique effects on cultured CECs, including (1) promotion of proliferation, (2) enhancement of cell adhesion, and (3) suppression of apoptosis.<sup>11</sup> Our subsequent studies revealed that administration of ROCK inhibitor in the form of eye drops promotes CEC proliferation in rabbit and monkey in vivo models.<sup>12,13</sup> In addition to animal experiments, we conducted a clinical trial of ROCK inhibitor eye drops in combination with a 2-mm-diameter transcorneal freezing procedure for treatment of human corneal endothelial dysfunction patients.<sup>13,14</sup> In that clinical trial, we showed that Y-27632 eye drops effectively reduced corneal edema in

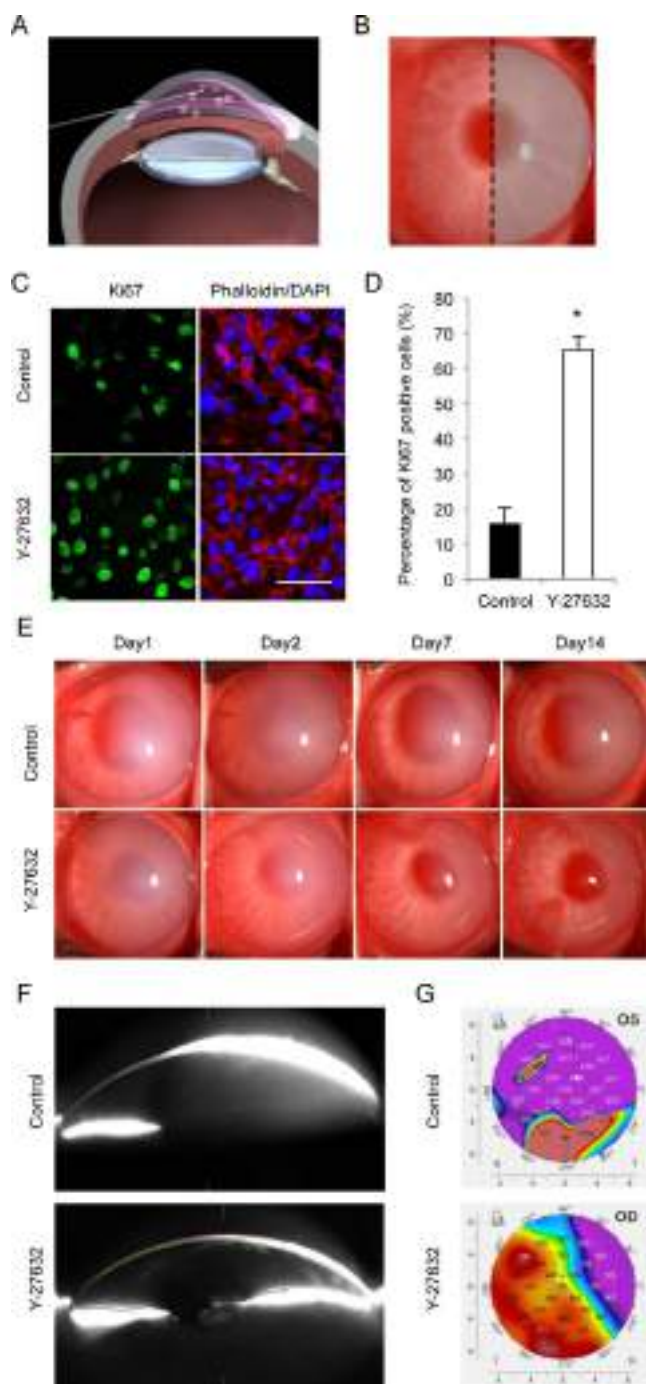


**FIGURE 1.** Effect of Y-27632 on wound healing in a corneal endothelial damage rabbit model. (A) Schematic shows removal of the corneal endothelium using a 20-gauge silicone needle to create a corneal endothelial damage model to mimic surgical trauma. (B) Half of the area of the corneal endothelium was mechanically scraped (indicated in gray) and confirmed by 0.04% trypan blue staining. The experimenter who created the endothelial damage model was blinded to the subsequent treatment with Y-27632 or vehicle. Y-27632 (10 mM) diluted in PBS (50  $\mu$ L) was applied topically 6 times daily, whereas PBS was applied 6 times daily as a control. (C, D) The effect of Y-27632 eye drop on proliferation of corneal endothelium was evaluated by Ki67 staining after 2 days ( $n = 3$ ). Ki67-positive cells were counted in the pupil center. \* $P < 0.01$ . (E) Corneal transparency was assessed by slit-lamp microscopy for 14 days ( $n = 6$ ). Representative anterior segment images are shown. (F, G) Anterior segment was also evaluated by Pentacam. Representative Scheimpflug images and corneal thickness maps obtained by Pentacam HR are shown. Values in the corneal thickness map are indicated in micrometers.

patients with early stage Fuchs' endothelial corneal dystrophy, who exhibited central edema with relatively healthy corneal endothelium remaining at the peripheral area.<sup>13</sup> Those findings led us to hypothesize that a ROCK inhibitor could be an effective pharmaceutical treatment for those patients whose corneal endothelium was severely damaged by cataract surgery despite having a certain number of relatively healthy CECs.

In the present study, we tested the feasibility of using ROCK-inhibitor eye drops for treating severe corneal endothelial damage due to cataract surgery. We showed that ROCK inhibitor eye drops promote wound healing of severe corneal endothelial damage in a rabbit model by enhancing proliferation of the remaining CECs. We also performed a pilot clinical research study and showed that ROCK inhibitor eye drops were considerably effective in patients who exhibited corneal edema after cataract surgery.

## MATERIALS AND METHODS

### Animal Experiment Approval

In all experiments, animals were housed and treated in accordance with the Association for Research in Vision and Ophthalmology Statement for the Use of Animals in Ophthalmic and Vision Research. Rabbit experiments were performed at Doshisha University (Kyoto, Japan) according to the protocol approved by the University's Animal Care and Use Committee (approval no. A15012).

### Fluorescence Staining

Rabbit corneal specimens were fixed in 4% formaldehyde and incubated in 1% bovine serum albumin for 30 minutes at room temperature to block nonspecific binding. The effect of the ROCK inhibitor on cell proliferation was evaluated by Ki67 staining using anti-mouse Ki67 antibody diluted 1:200 (Sigma-Aldrich Corp., St. Louis, MO, USA). Alexa Fluor 488-conjugated goat anti-mouse immunoglobulin G (IgG; 1:1000 dilution; Life Technologies Corp., Carlsbad, CA, USA) was used as a secondary antibody. Reconstructed corneal endothelium was investigated by conducting immunohistochemical analyses of N-cadherin (1:300 dilution; BD Biosciences, San Jose, CA, USA) and Na<sup>+</sup>/K<sup>+</sup>-ATPase (1:300 dilution; Upstate Biotechnology, Lake Placid, NY, USA). Alexa Fluor 488-conjugated goat anti-mouse (Life Technologies) was used as a secondary antibody at 1:1000 dilution. Cell morphology was evaluated after actin staining with a Alexa Fluor 594-conjugated phalloidin diluted 1:400 (Life Technologies). Nuclei were stained with 4',6-diamidino-2-phenylindole (DAPI; Vector Laboratories, Burlingame, CA, USA). The slides were viewed with fluorescence microscopy (model TCS SP2 AOBS; Leica Microsystems, Wetzlar, Germany).

### Rabbit Corneal Endothelial Damage Model

A rabbit corneal endothelial damage model was created to mimic surgical trauma by removing the lenses of 18 eyes of 9 Japanese white rabbits, using a series 20000 Legacy surgical system (Alcon, Inc., Fort Worth, TX, USA), under general anesthesia; this procedure deepened the anterior chamber. One week after lens removal, half of the area of the corneal endothelium was mechanically scraped from Descemet's membrane with a 20-gauge silicone needle (Soft tapered needle; Inami and Co., Ltd., Tokyo, Japan) (Figs. 1A, 1B). The scraped area was confirmed by 0.04% trypan blue staining. One eye of each rabbit was used for Y-27632 treatment, and the contralateral eye served as the control. The corneal endothelium of both eyes was damaged to reduce the number of



rabbits required for the study and for correct evaluation of the effect, because wound healing varied depending on the individual rabbit. This procedure was confirmed not to induce complete blindness or any severe general adverse effects. The experimenter who created the endothelial damage model was blinded to subsequent treatment with Y-27632 or vehicle.

### Administration of Y-27632 Eye Drops in the Corneal Endothelial Damage Model

Y-27632 (10 mM) diluted in phosphate-buffered saline (PBS; 50  $\mu$ L) was applied topically four times daily to nine eyes of the corneal endothelial damage model, whereas PBS was applied four times daily to nine eyes as a control. The effect of Y-27632 eye drops on proliferation of the corneal endothelium after 2 days was evaluated by staining with Ki67 ( $n = 3$  samples). Corneal transparency was assessed with slit-lamp microscopy for 14 days ( $n = 6$ ). Corneal thickness was evaluated by using a Pentacam system (Oculus; Optikergeräte GmbH, Wetzlar, Germany). Corneal endothelium was evaluated by contact specular microscopy (scanning slit specular microscope; Konan Medical, Nishinomiya, Japan).

### Organ Culture

For rabbit cornea organ culture experiments, twenty rabbit eyes were purchased from the Funakoshi Corp. (Tokyo, Japan). Half the area of the corneal endothelium from ten corneas was mechanically scraped without removing Descemet's membrane. Then, five of these corneas were incubated at 37°C for 48 hours with Dulbecco's modified Eagle's medium (DMEM) supplemented with Y-27632 (10  $\mu$ M), while five corneas were incubated with DMEM alone as control. The proliferative ability of the corneal stroma was evaluated by mechanically removing half the area of the corneal endothelium of ten corneas along with Descemet's membrane. A total of five corneas were incubated at 37°C for 48 hours with DMEM supplemented with Y-27632 (10  $\mu$ M), while three corneas were incubated with DMEM alone as control. After 48 hours, the corneas were stained with Ki67 and phalloidin. The area of corneal endothelium or Descemet's membrane removed was confirmed by 0.04% trypan blue staining in preliminary experiments.

### Pilot Human Clinical Trial of ROCK Inhibitor Eye Drops

The pilot human clinical trial performed in this study was conducted in accordance with tenets of Declaration of Helsinki. This study was performed according to a protocol approved by the Institutional Review Board of Kyoto Prefectural University of Medicine (approval number C-626-2). Clinical trial registration was obtained from University Hospital Medical Information Network, Clinical Trial Registry no. UMIN000003625; [www.umin.ac.jp/ctr](http://www.umin.ac.jp/ctr). Prior to this, a phase 1 clinical study of Y-27632 eye drops involving ten healthy volunteers was conducted (approval number C-626-1), which confirmed that 10 mM Y-27632 applied six times a day for 7 days caused no systemic or local side effects. After proper informed consent was obtained, three eyes of three patients were enrolled in this study, which ran from October 2012.

All three patients had undergone cataract surgery, and severe corneal edema had subsequently developed due to corneal endothelial damage. In two patients, more than half of Descemet's membrane area was detached accidentally and was removed during phacoemulsification (cases 1 and 2). In 1 patient, an iris cyst was observed with low corneal endothelial cell density due to an old corneal trauma, and one third to one

half of the corneal endothelial area was damaged caused by dissection of the iris cyst during cataract surgery (case 3). For all patients, 1 mM of Y-27632 was administered in the form of an eye drop six times daily for 4 months, followed by four times daily for 2 additional months.

### Statistical Analysis

Statistical significance ( $P$  value) of differences in the mean values of the two-sample comparison was determined with Student's  $t$ -test. Values shown in the graphs represent means  $\pm$  SEM.

## RESULTS

### Effect of Y27632 on Cell Proliferation During Wound Healing in a Rabbit Model

Administration of 10 mM Y-27632 in the form of eye drops to the corneal endothelial damage model was followed 48 hours later by evaluation of the Ki67-positive cells in the wounded area at the center of cornea. The control eye showed approximately 13% of the cell population of Ki67-positive corneas, whereas the Y-27632-treated eyes showed approximately 65% Ki67-positive cells (Figs. 1C, 1D). Actin staining showed that Y-27632-treated eyes had an endothelial phenotype in which actin was distributed at the cell cortex, whereas control eyes showed irregular patterns of actin fibers.

### Effect of Y-27632 on Wound Healing in a Rabbit Model

Representative slit-lamp microscopy demonstrated that control eyes exhibited stromal edema due to corneal endothelial dysfunction, especially where the corneal endothelium had initially been removed. On the other hand, eyes treated with Y-27632 eye drops exhibited clear corneas after 2 weeks. (Fig. 1E). Slitlamp microscopy revealed no adverse effects in the corneal epithelium or the stroma. Scheimpflug images and corneal thickness maps obtained with a Pentacam HR also demonstrated that control eyes showed substantial corneal edema while Y-27632 treated eyes showed less corneal edema (Figs. 1F, 1G).

We also evaluated the regenerated corneal endothelium by contact specular microscopy, which demonstrated that control eyes showed blurred corneal endothelial images from the border (center of the cornea) to the damaged area. However, the regenerated corneal endothelium observed in Y-27632 treated eyes formed a hexagonal monolayer, although the corneal endothelial cell density tended to be lower in the damaged area than in undamaged areas (Fig. 2A). Cell density was almost the same in the undamaged area of eyes treated with Y-27632 as in the control eyes, implying that enhanced wound healing by Y-27632 occurs mainly by promoted cell proliferation rather than by migration (Fig. 2B). Phalloidin staining showed that corneal endothelium at the border area in the eyes treated with Y-27632 had a hexagonal and monolayer morphology and that actin fibers were distributed at the cell cortex. However, control eyes showed partial disruption of the cortical actin and contained stress fibers. N-cadherin (a marker of adherence junctions) and Na<sup>+</sup>/K<sup>+</sup>-ATPase (a marker of pump function) were expressed in almost all cells in the Y-27632-treated eyes, but expression was decreased in control eyes, suggesting that the ROCK inhibitor enhanced functional recovery as well as morphological recovery (Fig. 2C). No Ki67 expression was observed in Y-27632-treated eyes or control eyes after 2 weeks, suggesting that corneal endothelial



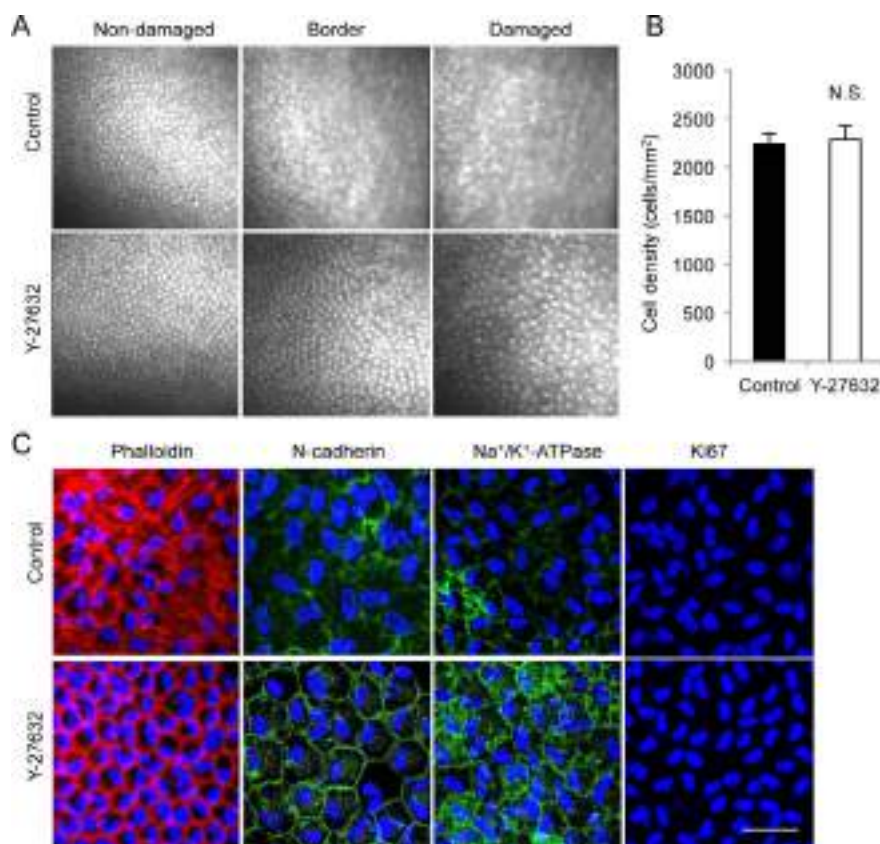


**FIGURE 2.** Regenerated corneal endothelium of a rabbit model treated with Y-27632. (A) The corneal endothelium of the corneal endothelial damage rabbit model was evaluated by contact specular microscopy after 14 days. Undamaged areas, borders (pupil center), and damaged areas were evaluated in all animals ( $n = 6$ ). (B) Corneal endothelial cell density in the undamaged area of the rabbit model was evaluated after 14 days. (C) Regenerated corneal endothelium was evaluated histologically after 14 days. Morphology was evaluated using actin staining performed with Alexa Fluor 594-conjugated phalloidin. Functional recovery was analyzed by immunostaining for N-cadherin and  $\text{Na}^+/\text{K}^+$ -ATPase. Cell proliferation status was analyzed by Ki67 immunostaining. Nuclei were stained with DAPI. Representative images of pupil centers are shown. Scale bar: 50  $\mu\text{m}$ .

cell proliferation was suppressed, even following treatment with Y-27632, when the remaining CECs covered the damaged area and cell-cell contact was established (Fig. 2C).

### Effect of Y-27632 on Wound Healing in an Organ Culture Model

We conducted organ culture experiments to determine whether the ROCK inhibitor enhances cell proliferation and migration onto the corneal stroma, as occurs onto Descemet's membrane. Half of the corneal endothelium (Fig. 1B) was removed with or without Descemet's membrane. The numbers of Ki67-positive cells were counted 48 hours after organ culture in the absence or presence of Y-27632. In eyes where the corneal endothelium was removed without Descemet's membrane, as in the *in vivo* model, 12.8% of the cells observed at the border site in the controls were Ki67-positive cells, whereas 41.7% were Ki67-positive cells in the Y-27632 treated eyes (Fig. 3B). In the eyes where the corneal endothelium was removed with the Descemet's membrane, 11.8% of the control cells were Ki67 positive, while 47.5% of the Y-27632-treated cells were Ki67 positive (Fig. 3C). The corneal endothelium that regenerated onto the corneal stroma had hexagonal cells in a monolayer in the eyes where the Descemet's membrane was removed, similar to the eyes where the Descemet's membrane was left intact (Fig. 3A).

### Pilot Human Clinical Research of ROCK Inhibitor Eye Drops for Treatment of Acute Corneal Endothelial Damage due to Cataract Surgery

We conducted pilot clinical research to determine whether ROCK inhibitor eye drops could rescue the acute corneal endothelial damage due to cataract surgery. An 84-year-old female (case 1) treated with cataract surgery had undergone phacoemulsification performed by her previous physician. During the surgery, Descemet's membrane had spontaneously detached from the upper incision tunnel, and more than two thirds was aspirated. A foldable IOL was implanted in the capsular bag. She was referred to the cornea clinic of Kyoto Prefectural University of Medicine due to severe corneal edema caused by the loss of corneal endothelium (Fig. 4A). Visual acuity in the right eye was counting fingers. Contact specular microscopy revealed no corneal endothelium at the corneal center owing to edema, but the lower peripheral cornea remained clear and contained relatively healthy-looking endothelial cells at a cell density of 2653 cells/mm<sup>2</sup> (Fig. 4C). The patient was treated with 1 mM Y-27632 eye drops six times daily for 4 months and four times for 2 months. At 2 weeks, the cornea had recovered its clarity, and the patient's visual acuity had improved to 20/20 at 3 months (Fig. 4A). Contact specular microscopy showed that the corneal endothelium was regenerated directly onto stroma at 3 months where Descemet's membrane had been removed (Fig. 4B, Descemet's

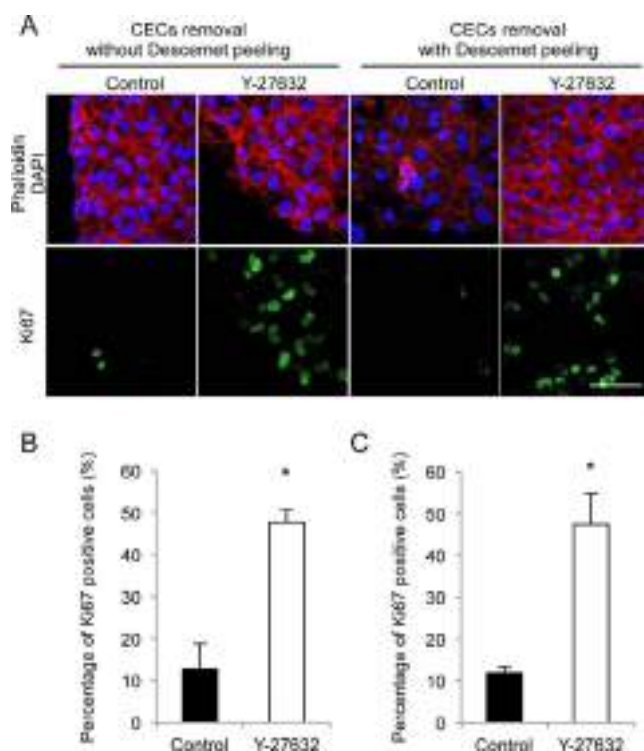


**FIGURE 3.** Effect of Y-27632 on wound healing in an organ culture model. (A) Half of the area of corneal endothelium samples from 10 corneas was mechanically scraped without Descemet's membrane removal. Then, five corneas were incubated with DMEM supplemented with Y-27632 (10  $\mu$ M) for 48 hours, while three corneas were incubated with DMEM as controls. Likewise, half of the area of the corneal endothelium of 10 corneas was mechanically removed along with Descemet's membrane. Then, five corneas were incubated with DMEM supplemented with Y-27632 (10  $\mu$ M) for 48 hours, while three corneas were incubated with DMEM as control. After 48 hours, Ki67 and phalloidin staining were performed. Nuclei were stained with DAPI. Scale bar: 50  $\mu$ m. (B) Effect of Y-27632 on proliferation of CECs was evaluated by Ki67 staining after 2 days. Ki67-positive cells were counted at the wound edge ( $n = 3$ ). Results are shown of Ki67 analysis of organ-cultured corneas in which the corneal endothelium was mechanically scraped with remaining Descemet's membrane intact. (C) Result are shown of Ki67 analysis of organ cultured cornea in which corneal endothelium was mechanically scraped along with removal of Descemet's membrane. \* $P < 0.01$ . All experiments were performed in duplicate.

removal line is indicated as a white dotted line). Although the regenerated corneal endothelium had a lower cell density than the undamaged area, the cell density of the undamaged area (2732 cells/mm<sup>2</sup>) did not decrease after cataract surgery (Fig. 4C), suggesting that wound healing occurred by a combination of proliferation and migration and not just by migration.

Case 2 patient is similar that in case 1: an 84-year-old female underwent phacoemulsification, and more than two thirds of Descemet's membrane was spontaneously detached from the upper incision tunnel and was aspirated. This patient also recovered corneal clarity after administration of 1 mM Y-27632 eye drops six times daily for 4 months and four times for 2 months.

A 71-year-old male (case 3) was diagnosed with an iris cyst due to an ocular trauma that had occurred approximately 50 years previously (Fig. 4D). The iris cyst was attached to the corneal endothelium and corneal endothelial cell density was 508 cells/mm<sup>2</sup> (Fig. 4E). The patient felt a visual disturbance due to cataract progression, so the cystic iris was dissected from the cornea and standard phacoemulsification was

performed following IOL implantation. After the surgery, corneal edema was observed due to corneal endothelial damage, with a visual acuity of 20/63 (Fig. 4D). The patient was treated with the 1 mM Y-27632 eye drops four times daily for 3 months, and the cornea became clear, with a visual acuity of 20/25 (3 months) (Fig. 4D). The central corneal thickness was reduced to 611  $\mu$ m after surgery and to 503  $\mu$ m at 3 months. The central corneal endothelial cell density was approximately 500 cells/mm<sup>2</sup> and was not observable after cataract surgery due to corneal edema but was observed again after therapy with ROCK inhibitor eye drops at a density of approximately 500 cells/mm<sup>2</sup> (Fig. 4E).

## DISCUSSION

ROCK was originally discovered as a target of the small GTP-binding protein RhoA.<sup>15</sup> The Rho-binding domain within the coiled-coil region of ROCK was identified, but multiple contact points where several molecules can activate or inhibit ROCK were subsequently demonstrated.<sup>16–18</sup> As ROCK mediates various cellular events, such as cell shape, motility, adhesion, and proliferation, ROCK signaling activation is involved in numerous diseases.<sup>15</sup> Therefore, ROCK attracted research interest as a potential therapeutic target for vascular disease, cancer, neuronal degenerative disease, asthma, and glaucoma.<sup>19,20</sup> Several pharmaceutical companies have started clinical trials to develop ROCK inhibitors as next-generation therapeutic agents.<sup>19</sup> Indeed, fasudil was approved for the treatment of cerebral vasospasm in Japan and China in 1995<sup>21</sup> and ripasudil was approved for the treatment of glaucoma in Japan in 2014.<sup>22</sup>

Earlier researchers reported that inactivation of Rho by C3 blocks G<sub>1</sub>/S progression in 3T3 fibroblasts, suggesting that activation of Rho facilitates cell-cycle progression,<sup>23</sup> although the cellular responses regulated by ROCK are now known to be cell-type-dependent.<sup>20</sup> In CECs, we demonstrated that inhibition of Rho/ROCK signaling promotes cell proliferation.<sup>11</sup> We also showed that a ROCK inhibitor works via phosphatidylinositol 3-kinase signaling that subsequently regulates two proteins of the G<sub>1</sub> phase of the cell cycle.<sup>24</sup> ROCK inhibitor upregulates cyclin D and downregulates p27<sup>kip1</sup> (p27), and then both activities promote G<sub>1</sub>/S progression of CECs.<sup>24</sup> On the other hand, Pipparelli et al.<sup>25</sup> reported that ROCK signaling inhibition by Y-27632 did not induce proliferation of CECs. However, Peh et al.<sup>26</sup> reported that Y-27632 increased cell proliferation and increased overall cell yield 1.96 to 3.36 fold.<sup>26</sup> They also suggested that CECs derived from young donors were more responsive to Y-27632; thus, the results of Pipparelli et al.<sup>25</sup> are likely explainable by a different status of the cornea.<sup>26</sup>

We also used a partial corneal endothelial damage model of rabbits and monkeys in previous studies and showed that when the central corneal endothelium was damaged by transcorneal freezing, ROCK inhibitor administration in the form of eye drops enhanced cell proliferation and wound healing of the damaged corneal endothelium.<sup>12,13,24</sup> However, the limitation of this experimental model was that the permeability of the pharmaceutical agents to the corneal endothelium was artificially enhanced, because the corneal epithelium was removed as well as the endothelium by transcorneal freezing. In the current study, we mechanically removed half of the area of the corneal endothelium to mimic acute mechanical trauma occurring during cataract surgery. In agreement with the findings from the previous transcorneal freezing model, the ROCK inhibitor eye drops administered in the current model enhanced CEC proliferation and facilitated regeneration of the transparent cornea.

The other question in line with clinical settings is whether a ROCK inhibitor promotes cell proliferation of the remaining



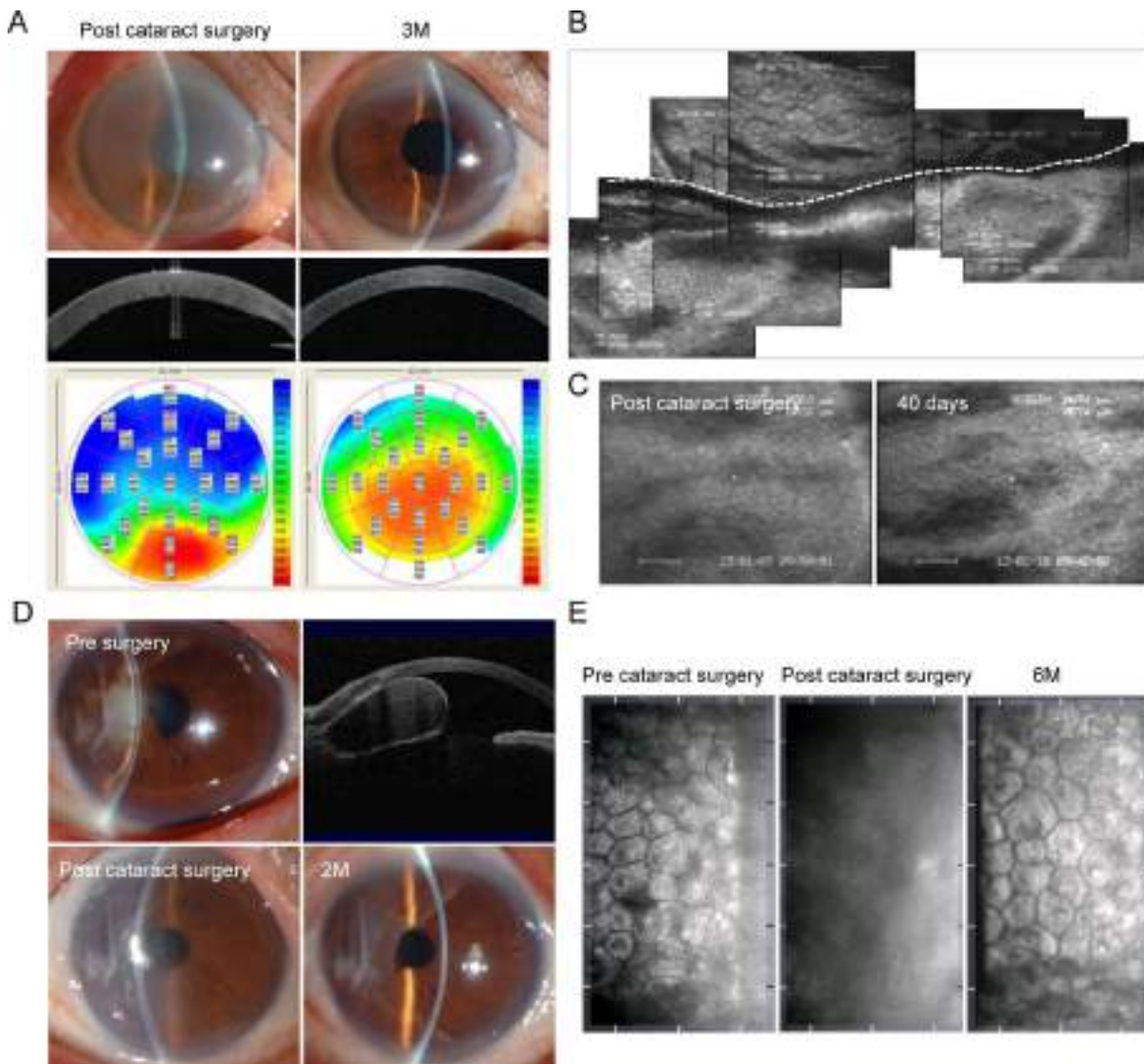


**FIGURE 4.** Pilot clinical research of ROCK inhibitor eye drops for the acute corneal endothelial damage due to cataract surgery. (A) An 84-year-old female (case 1) with a diagnosis of cataract underwent phacoemulsification. During the surgery, Descemet's membrane was spontaneously detached from the upper incision tunnel, and over two thirds of the membrane was aspirated. The patient was referred to the cornea clinic of Kyoto Prefectural University of Medicine due to severe corneal edema (*upper left*: slitlamp microscope image; *middle left*: Scheimpflug image; *lower left*: corneal thickness maps). The patient was treated with 1 mM Y-27632 eye drops for 6 months (*upper right*: anterior segment image; *middle right*: Scheimpflug image; *lower right*: corneal thickness maps). (B) Panoramic image of corneal endothelium evaluated by contact specular microscopy after 3 months. Descemet's removal line is indicated as a *white dotted line*. (C) Lower, undamaged corneal endothelium was evaluated by contact specular microscopy. (D) A 71-year-old male (case 3) with a diagnosis of iris cyst due to ocular trauma occurring approximately 50 years previously (*upper left*: slit-lamp microscopy; *upper right*: anterior OCT). The cystic iris was dissected from the cornea, and standard phacoemulsification was performed following IOL implantation. For corneal edema due to corneal endothelial decompensation, the patient was treated with the 1 mM Y-27632 eye drops for 6 months. Slit-lamp view is shown after the surgery (*lower left*) and Y-27632 treatment (*lower right*). (E) Central corneal endothelial cell density, approximately 500 cells/mm<sup>2</sup>, was not observable after cataract surgery due to corneal edema, and then it was observed again after treatment with ROCK inhibitor eye drops, where a density of approximately 500 cells/mm<sup>2</sup> was achieved.

CECs onto a bare corneal stroma, because Descemet's membrane can detach spontaneously and be removed during cataract surgery in a certain number of cases. Detachment of Descemet's membrane can further impair the healing of wounded corneal endothelium, as Descemet's membrane is a basement membrane of the corneal endothelium. We answered this question by using organ culture experiments, which demonstrated that the ROCK inhibitor promoted proliferation and regeneration of the remaining CECs to almost the same level on Descemet's membrane and the stroma under our ex vivo experimental conditions. Coincidentally, the ROCK inhibitor showed effectiveness in two patients whose Desce-

met's membrane were removed during surgery. In those cases, the corneal endothelium was regenerated onto a bare corneal stroma, suggesting that the ROCK inhibitor can be applied to corneal endothelial damage occurring in cases where Descemet's membrane is accidentally removed.

Corneal transplantation is the only definitive treatment for PBK, although conjunctival flap,<sup>27</sup> phototherapeutic keratectomy,<sup>28</sup> collagen cross-linking,<sup>29</sup> therapeutic contact lens,<sup>30</sup> and topical hyperosmotic agents<sup>31</sup> have been used to reduce pain. No clinically practical medical therapy has been developed, although pharmaceutical agents such as EGF,<sup>32</sup> PDGF,<sup>33</sup> FGF-2,<sup>34</sup> and small interfering RNA (siRNA) of

connexin 43<sup>35</sup> have been shown to promote the proliferative capacity of CECs. Here, we showed clinical cases where a ROCK inhibitor seemed to be effective in wound healing of corneal endothelium and in avoidance of development of PBK.

This study had a number of limitations: the cases are very preliminary, no vehicle control cases were included, and patients without treatment were not followed. Nevertheless, this is the first report to show that pharmaceutical agents can be effective in the treatment of post-cataract surgical corneal edema, and the findings encourage us to conduct a randomized clinical trial. Recently, ripasudil, a selective ROCK inhibitor, was approved in Japan for the treatment of glaucoma and ocular hypertension.<sup>22</sup> Several preclinical and clinical research studies have shown that ROCK inhibitors do not have severe adverse side effects when applied locally and systemically, suggesting that ROCK inhibitors can be applied as eye drops.<sup>36–44</sup> Hence, future studies to evaluate the specific form of ROCK inhibitor among numerous kinds of agents that possess the highest potency for enhancement of cell proliferation of CECs will enable promising development of eye drops for the treatment of corneal endothelial damage.

The number of corneal transplantations for PBK in the United States has shown a decline since the late 1990s, perhaps because (1) cataract surgery techniques and devices have developed very rapidly (e.g., phacoemulsification, viscoelastics, and biocompatible intraocular lenses), and (2) most surgeons have completed the learning curve for phacoemulsification.<sup>1</sup> Indeed, the complication rate of PBK was estimated at up to 0.3% of cataract surgeries in 1994,<sup>45</sup> and a recent review showed that endothelial cell loss during cataract surgery is <100 cells/mm<sup>2</sup>.<sup>46</sup> However, although data indicating the prevalence of PBK in developing countries are not well elucidated, physicians should still remain aware of PBK/ABK, given that cataract accounts for 51% of the global causes of blindness according to the World Health Organization, and numerous cataract patients are waiting for surgery.<sup>47</sup> If pharmaceutical agents such as ROCK inhibitors can be applied to reduce post-surgical corneal edema, the incidence of PBK/ABK will be minimized.

In summary, we have demonstrated that ROCK inhibitor eye drops promote wound healing by enhancing cell proliferation of CECs in a rabbit model. We also show in preliminary human cases that post cataract surgical corneal edema can be treated with ROCK inhibitor eye drops. These data encourage us to develop ROCK inhibitor eye drops for acute corneal endothelial damage, such as that occurring after invasive ocular surgery and surgery for high risk cases, in order to reduce the incidence of PBK/ABK.

### Acknowledgments

The authors thank Tsutomu Inatomi and Kanae Miyamoto for collecting clinical data.

Supported by Program for the Strategic Research Foundation at Private Universities from MEXT (NK, NO).

SK holds a patent, no. 5657252, for Rho-associated kinase (ROCK) inhibitor for corneal endothelium. NO and NK are listed as inventors on the patent.

Disclosure: **N. Okumura**, P; **R. Inoue**, None; **Y. Okazaki**, None; **S. Nakano**, None; **H. Nakagawa**, None; **S. Kinoshita**, P; **N. Koizumi**, P

### References

- Ghosheh FR, Cremona FA, Rapuano CJ, et al. Trends in penetrating keratoplasty in the United States 1980-2005. *Int Ophthalmol*. 2008;28:147–153.
- Eye Bank Association of America. 2013 *Eye Banking Statistical Report*. Washington, DC; Eye Bank Association of America; 2013.
- Al-Yousuf N, Mavrikakis I, Mavrikakis E, Daya SM. Penetrating keratoplasty: indications over a 10 year period. *Br J Ophthalmol*. 2004;88:998–1001.
- Keenan TD, Jones MN, Rushton S, et al. Trends in the indications for corneal graft surgery in the United Kingdom: 1999 through 2009. *Arch Ophthalmol*. 2012;130:621–628.
- Cunningham WJ, Brookes NH, Twohill HC, et al. Trends in the distribution of donor corneal tissue and indications for corneal transplantation: the New Zealand National Eye Bank Study 2000-2009. *Clin Exp Ophthalmol*. 2012;40:141–147.
- Tan DT, Janardhanan P, Zhou H, et al. Penetrating keratoplasty in Asian eyes: the Singapore Corneal Transplant Study. *Ophthalmology*. 2008;115:975–982.
- Shimazaki J, Amano S, Uno T, Maeda N, Yokoi N. National survey on bullous keratopathy in Japan. *Cornea*. 2007;26:274–278.
- Dandona L, Naduvilath TJ, Janarthanan M, Ragu K, Rao GN. Survival analysis and visual outcome in a large series of corneal transplants in India. *Br J Ophthalmol*. 1997;81:726–731.
- Joyce NC. Proliferative capacity of the corneal endothelium. *Prog Retin Eye Res*. 2003;22:359–389.
- Tan DT, Dart JK, Holland EJ, Kinoshita S. Corneal transplantation. *Lancet*. 2012;379:1749–1761.
- Okumura N, Ueno M, Koizumi N, et al. Enhancement on primate corneal endothelial cell survival in vitro by a ROCK inhibitor. *Invest Ophthalmol Vis Sci*. 2009;50:3680–3687.
- Okumura N, Koizumi N, Ueno M, et al. Enhancement of corneal endothelium wound healing by Rho-associated kinase (ROCK) inhibitor eye drops. *Br J Ophthalmol*. 2011;95:1006–1009.
- Okumura N, Koizumi N, Kay EP, et al. The ROCK inhibitor eye drop accelerates corneal endothelium wound healing. *Invest Ophthalmol Vis Sci*. 2013;54:2493–2502.
- Koizumi N, Okumura N, Ueno M, Nakagawa H, Hamuro J, Kinoshita S. Rho-associated kinase inhibitor eye drop treatment as a possible medical treatment for Fuchs corneal dystrophy. *Cornea*. 2013;32:1167–1170.
- Riento K, Ridley AJ. Rocks: multifunctional kinases in cell behaviour. *Nat Rev Mol Cell Biol*. 2003;4:446–456.
- Sebbagh M, Renvoize C, Hamelin J, Riche N, Bertoglio J, Breard J. Caspase-3-mediated cleavage of ROCK I induces MLC phosphorylation and apoptotic membrane blebbing. *Nat Cell Biol*. 2001;3:346–352.
- Coleman ML, Sahai EA, Yeo M, Bosch M, Dewar A, Olson MF. Membrane blebbing during apoptosis results from caspase-mediated activation of ROCK I. *Nat Cell Biol*. 2001;3:339–345.
- Blumenstein L, Ahmadian MR. Models of the cooperative mechanism for Rho effector recognition: implications for RhoA-mediated effector activation. *J Biol Chem*. 2004;279:53419–53426.
- Liao JK, Seto M, Noma K. Rho kinase (ROCK) inhibitors. *J Cardiovasc Pharmacol*. 2007;50:17–24.
- Olson MF. Applications for ROCK kinase inhibition. *Curr Opin Cell Biol*. 2008;20:242–248.
- Suzuki Y, Shibuya M, Satoh S, Sugimoto Y, Takakura K. A postmarketing surveillance study of fasudil treatment after aneurysmal subarachnoid hemorrhage. *Surg Neurol*. 2007;68:126–131.
- Garnock-Jones KP. Ripasudil: first global approval. *Drugs*. 2014;74:2211–2215.
- Olson MF, Ashworth A, Hall A. An essential role for Rho, Rac, and Cdc42 GTPases in cell cycle progression through G1. *Science*. 1995;269:1270–1272.



24. Okumura N, Nakano S, Kay EP, et al. Involvement of cyclin D and p27 in cell proliferation mediated by ROCK inhibitors Y-27632 and Y-39983 during corneal endothelium wound healing. *Invest Ophthalmol Vis Sci.* 2014;55:318-329.
25. Pipparelli A, Arsenijevic Y, Thuret G, Gain P, Nicolas M, Majo F. ROCK inhibitor enhances adhesion and wound healing of human corneal endothelial cells. *PLoS One.* 2013;8:e62095.
26. Peh GS, Adnan K, George BL, et al. The effects of Rho-associated kinase inhibitor Y-27632 on primary human corneal endothelial cells propagated using a dual media approach. *Sci Rep.* 2015;5:9167.
27. Gundersen T. Conjunctival flaps in the treatment of corneal disease with reference to a new technique of application. *Arch Ophthalmol.* 1958;60:880-888.
28. Rosa N, Cennamo G. Phototherapeutic keratectomy for relief of pain in patients with pseudophakic corneal edema. *J Refract Surg.* 2002;18:276-279.
29. Arora R, Manudhane A, Saran RK, Goyal J, Goyal G, Gupta D. Role of corneal collagen cross-linking in pseudophakic bullous keratopathy: a clinicopathological study. *Ophthalmology.* 2013;120:2413-2418.
30. Takahashi GH, Leibowitz HM. Hydrophilic contact lenses in corneal disease. 3. Topical hypertonic saline therapy in bullous keratopathy. *Arch Ophthalmol.* 1971;86:133-137.
31. Insler MS, Benefield DW, Ross EV. Topical hyperosmolar solutions in the reduction of corneal edema. *CLAO J.* 1987;13:149-151.
32. Hoppenreijns VP, Pels E, Vrensen GF, Oosting J, Treffers WE. Effects of human epidermal growth factor on endothelial wound healing of human corneas. *Invest Ophthalmol Vis Sci.* 1992;33:1946-1957.
33. Hoppenreijns VP, Pels E, Vrensen GF, Treffers WE. Effects of platelet-derived growth factor on endothelial wound healing of human corneas. *Invest Ophthalmol Vis Sci.* 1994;35:150-161.
34. Lu J, Lu Z, Reinach P, et al. TGF-beta2 inhibits AKT activation and FGF-2-induced corneal endothelial cell proliferation. *Exp. Cell Res.* 2006;312:3631-3640.
35. Nakano Y, Oyamada M, Dai P, Nakagami T, Kinoshita S, Takamatsu T. Connexin43 knockdown accelerates wound healing but inhibits mesenchymal transition after corneal endothelial injury in vivo. *Invest Ophthalmol Vis Sci.* 2008;49:93-104.
36. Honjo M, Tanihara H, Inatani M, et al. Effects of rho-associated protein kinase inhibitor Y-27632 on intraocular pressure and outflow facility. *Invest Ophthalmol Vis Sci.* 2001;42:137-144.
37. Tokushige H, Inatani M, Nemoto S, et al. Effects of topical administration of y-39983, a selective rho-associated protein kinase inhibitor, on ocular tissues in rabbits and monkeys. *Invest Ophthalmol Vis Sci.* 2007;48:3216-3222.
38. Tokushige H, Waki M, Takayama Y, Tanihara H. Effects of Y-39983, a selective Rho-associated protein kinase inhibitor, on blood flow in optic nerve head in rabbits and axonal regeneration of retinal ganglion cells in rats. *Curr Eye Res.* 2011;36:964-970.
39. Williams RD, Novack GD, van Haarlem T, Kopczynski C; Group ARPAS. Ocular hypotensive effect of the Rho kinase inhibitor AR-12286 in patients with glaucoma and ocular hypertension. *Am J Ophthalmol.* 2011;152:834-841. e831.
40. Tanihara H, Inoue T, Yamamoto T, et al. Phase 1 clinical trials of a selective Rho kinase inhibitor, K-115. *JAMA Ophthalmol.* 2013;131:1288-1295.
41. Tanihara H, Inoue T, Yamamoto T, et al. Phase 2 randomized clinical study of a Rho kinase inhibitor, K-115, in primary open-angle glaucoma and ocular hypertension. *Am J Ophthalmol.* 2013;156:731-736.
42. Van de Velde S, Van Bergen T, Sijnave D, et al. AMA0076, a novel, locally acting Rho kinase inhibitor, potentially lowers intraocular pressure in New Zealand white rabbits with minimal hyperemia. *Invest Ophthalmol Vis Sci.* 2014;55:1006-1016.
43. Tanihara H, Inoue T, Yamamoto T, et al. Intra-ocular pressure-lowering effects of a Rho kinase inhibitor, ripasudil (K-115), over 24 hours in primary open-angle glaucoma and ocular hypertension: a randomized, open-label, crossover study. *Acta Ophthalmol.* 2015;93:e254-260.
44. Tanihara H, Inoue T, Yamamoto T, et al. Additive intraocular pressure-lowering effects of the Rho kinase inhibitor ripasudil (K-115) combined with timolol or latanoprost: a report of 2 randomized clinical trials. *JAMA Ophthalmol.* 2015;133:755-761.
45. Powe NR, Schein OD, Gieser SC, et al. Synthesis of the literature on visual acuity and complications following cataract extraction with intraocular lens implantation. Cataract Patient Outcome Research Team. *Arch Ophthalmol.* 1994;112:239-252.
46. Van den Bruel A, Gailly J, Devriese S, Welton NJ, Shortt AJ, Vrijens F. The protective effect of ophthalmic viscoelastic devices on endothelial cell loss during cataract surgery: a meta-analysis using mixed treatment comparisons. *Br J Ophthalmol.* 2011;95:5-10.
47. World Health Organization. Global data on visual impairments. 2010;1-12.

# Phenotypic Investigation of Regenerated Epithelial Cells After Gonococcal Corneal Perforation: A Clinical, Histological, and Immunohistochemical Study

Passara Jongkhajornpong, MD,\*† Takahiro Nakamura, MD, PhD,\*‡ Chie Sotozono, MD, PhD,\* Tsutomu Inatomi, MD, PhD,\* and Shigeru Kinoshita, MD, PhD\*‡

**Purpose:** To determine the characteristics of regenerated epithelial cells after severe gonococcal infection after corneal perforation.

**Methods:** Pathological tissue was obtained from the cornea at the time of surgery. Hematoxylin and eosin staining and immunohistochemical analysis were performed for cytoskeletal keratins (K12, K13, and K15), basement membrane and junctional markers (laminin 5, ZO-1 and Desmoplakin), and proliferative and mesenchymal markers (Ki67,  $\alpha$ -SMA, and vimentin).

**Results:** A 42-year-old patient with severe gonococcal keratoconjunctivitis rapidly progressed to corneal perforation during administration of intensive topical and systemic antibiotics. After conservative treatment, the perforation healed and 5- × 3-mm corneal ectasia occurred with localized iris attachment. Complete closure of the cornea was confirmed by a negative Seidel test. After lamellar keratoplasty to improve corneal integrity and to prevent secondary glaucoma, the pathological tissue revealed a poorly organized epithelial layer at the regenerated ectatic area. The regenerated epithelial cells clearly expressed K12, ZO-1, and Desmoplakin with underlying laminin 5 (+) basement membrane. K15 and Ki67 expressions were observed predominantly at the limbal area but not in the regenerated area.  $\alpha$ -SMA and vimentin were sporadically expressed in the underlying connective tissue.

**Conclusions:** We speculate that the process of epithelial wound healing at the site of corneal perforation was responsible for migration of the surrounding epithelial cells. Although the regenerated cells expressed several cytokeratins and junctional markers, they remained disorganized and fragile.

**Key Words:** phenotype, epithelial cell, corneal perforation, gonococcal infection

(*Cornea* 2015;34:1508–1512)

Corneal perforation is one of the most severe complications occurring after infectious keratitis.<sup>1</sup> *Neisseria gonorrhoeae* is a species of gram-negative diplococci bacteria that causes sexually transmitted diseases. *Gonococcus* can invade the intact corneal epithelium, leading to corneal perforation within 24 hours if the patient is left untreated or receives inappropriate treatment. Both systemic and topical antibiotics are required for treatment. In case of corneal perforation, surgical treatment is necessary to restore ocular integrity. Recently, McElnea et al<sup>2</sup> reviewed a case of corneal perforation from *Neisseria gonorrhoeae*, for which they performed deep lamellar keratoplasty. Although necrotic tissue was removed, the histopathology has not been documented. Another group reported the histopathology of corneal tissue after surgical treatment of gonococcal corneal perforation, which revealed destruction of the corneal stroma and fibrosis in some cells across the perforated area.<sup>3</sup> However, little is known about the biological characteristics of cells in the perforated area.

The purpose of this study was to investigate clinical presentation and ocular findings in a patient with perforated severe gonococcal keratitis and to identify the histological and cell biological phenotypes of the regenerated epithelium. This is the first study to describe the structure of regenerated epithelial cells after severe gonococcal keratitis with corneal perforation.

## CASE REPORT

### Clinical History and Ocular Findings

A 42-year-old man was referred from a local clinic because of severe subacute conjunctivitis with purulent discharge that was intractable to topical antibiotics. A conjunctival swab culture was performed at the general hospital, and it revealed *N. gonorrhoeae* after three days. Corneal melting progressed rapidly and became profoundly thin (5 × 3 mm in size) with central perforation. The Seidel test was positive. The anterior chamber appeared shallow, with localized iris attachment to the posterior cornea at the site of perforation. The patient was treated with fortified ceftriaxone eye drops every hour and with intravenous ceftriaxone (1 g) once a day

Received for publication May 5, 2015; revision received June 3, 2015; accepted June 4, 2015. Published online ahead of print July 23, 2015.

From the \*Department of Ophthalmology, Kyoto Prefectural University of Medicine, Kyoto, Japan; †Department of Ophthalmology, Ramathibodi Hospital, Mahidol University, Bangkok, Thailand; and ‡Department of Frontier Medical Science and Technology for Ophthalmology, Kyoto Prefectural University of Medicine, Kyoto, Japan.

The authors have no funding or conflicts of interest to disclose.

Supplemental digital content is available for this article. Direct URL citations appear in the printed text and are provided in the HTML and PDF versions of this article on the journal's Web site ([www.corneajrnl.com](http://www.corneajrnl.com)).

Reprints: Takahiro Nakamura, MD, PhD, Department of Frontier Medical Science and Technology for Ophthalmology, Kyoto Prefectural University of Medicine, 465 Kajii-cho, Kamigyo-ku, Kyoto 602-0841, Japan (e-mail: [tnakamur@koto.kpu-m.ac.jp](mailto:tnakamur@koto.kpu-m.ac.jp)).

Copyright © 2015 Wolters Kluwer Health, Inc. All rights reserved.

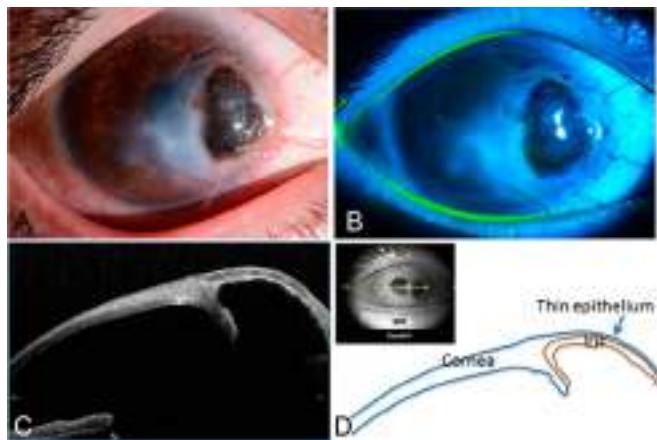


**FIGURE 1.** Slit-lamp examination and anterior segment optical coherent tomography (AS-OCT). A, A profoundly thin and ectatic area with iris adhesion was observed at the temporal cornea. B, Fluorescein staining showed a negative Seidel test, indicating no epithelial defect. C, AS-OCT (horizontal scan across pathological area) showed marked corneal thinning with iris attachment. D, The diagram outlines the iris and corneal structures; blue line = cornea, brown line = iris.

for 1 week. After 1 week of treatment, corneal infiltration had visibly improved, and the perforated area was totally closed. The cornea surrounding the ulcer developed haze with vascularized ingrowth (Fig. 1A). The Seidel test was negative, indicating no leakage of aqueous humor from the anterior chamber (Fig. 1B). Anterior segment optical coherence tomography (CASIA; Tomey Corporation, Aichi, Japan) revealed a protruding area with iris adherence, corresponding to the location of the previously perforated area (Figs. 1C, D). Three weeks after corneal perforation, lamellar keratoplasty was performed to restore corneal integrity and to prevent secondary glaucoma. Lamellar keratoplasty

was performed using a 7.2-mm manual trephine and a Golf/Scleral knife to dissect the base of the lesion at the depth of three-fourths of the corneal thickness. Intraoperatively, the corneal tissue was thoroughly separated from the adhered iris in a single continuous piece. The requirement was to dissect from the surrounding margin and to preserve the depth of the anterior chamber as close to the perforation area as possible. We debrided an atrophic iris and sutured for the purpose of creating a deep anterior chamber. The lamellar donor graft was then sutured, and the anterior chamber was re-formed. No serious intraoperative or postoperative complications were noted, and no recurrence of infection was detected at 4 months after operation. The visual acuity was 0.03 and 0.07 before and after operation, respectively. Because of the involvement of the optical axis, we plan to perform an optical penetrating keratoplasty after 6 to 12 months of the clinical course.

## Histopathology

The pathological tissue included partial thickness of the sclera, limbus, and cornea, with a very thin cornea at the middle part of the tissue (Figs. 2A, B). The specimen from lamellar surgery comprised 2 layers of corneal epithelium and corneal stroma. The epithelial layer was readily identified at the limbus and cornea. The corneal epithelium consisted of 6 to 14 stratified layers at the limbal region, gradually decreasing to 3 to 5 layers at the peripheral cornea, and finally to 2 to 3 layers at the site of perforation (Figs. 2C–E). Poor organization of epithelial cells was observed at the perforated area. The cellular margin and nuclear structure were obscured, in contrast to the clear configuration at the peripheral cornea and the limbus. We could not identify the Bowman layer beneath the epithelial layer. No gram-negative diplococci were detected at high magnification, but numerous inflammatory cells were observed in the connective tissue at the limbus, some of them scattered at the anterior corneal stroma. Collagen lamellae were absent at the perforated area, and only thin connective tissue was observed beneath the epithelial layer. Irregular surface alignment was noted along the perforated area.

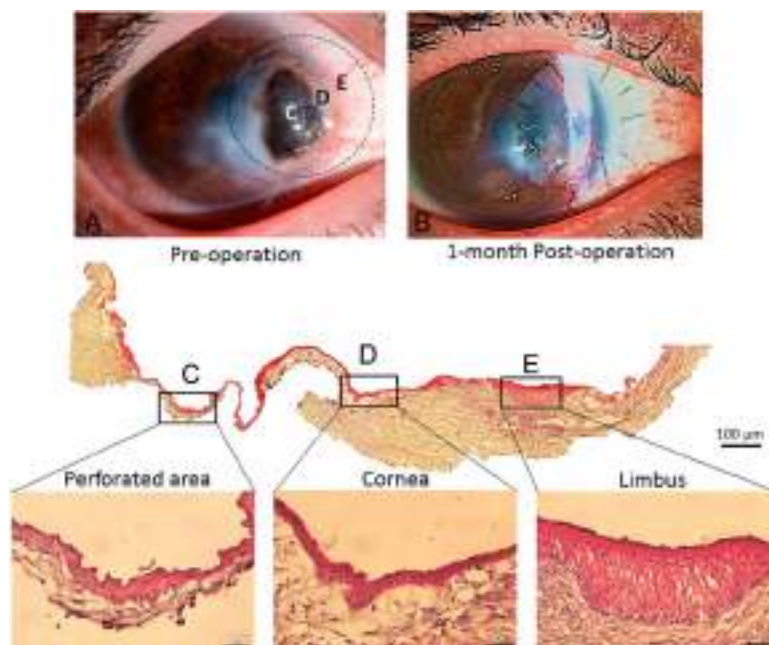


**FIGURE 2.** Representative slit-lamp photographs and corresponding histopathological findings [hematoxylin and eosin staining (H&E)] at the same locations. C = perforated area; D = peripheral cornea; E = limbus. Preoperative slit-lamp findings with the labeled area (A). Slit-lamp finding at 1 month after operation (B). H&E staining showed the disorganized epithelial layer with an irregular basement membrane and supporting cells beneath the perforated area (C); a well-organized epithelial layer with a smooth basement membrane and increased stromal cells at the peripheral cornea (D); and 6 to 12 well-organized layers of stratified squamous epithelial cells at the limbus (E). Scale bar = 20  $\mu$ m.

## Immunohistochemistry

Immunohistochemical studies followed our previously described method (see Table, Supplemental Digital Content 1, <http://links.lww.com/ICO/A295>).<sup>4</sup>

### Cytokeratin Markers

K12, identifying the corneal epithelial phenotype, was markedly expressed along the epithelial layer at the limbal area, peripheral cornea, and in a regenerated membrane (Figs. 3A–C). K13, which is a nonkeratinized epithelial maker, did not express in the renewed epithelial cells (Figs. 3D–F). K15, identifying the basal limbal cells, was frequently expressed at the limbus and peripheral cornea; no expression was observed in the renewed epithelial cells (Figs. 3G–I).

### Basement Membrane and Cell Junction Markers

Laminin 5 was clearly expressed along the whole corneal tissue (Figs. 4A–C). However, an irregular expression pattern was observed beneath the renewed epithelial layer. ZO-1 expression condensed at the superficial epithelial layer of the limbus, peripheral cornea, and the regenerated area (Figs. 4D–F). Positive staining was also observed as a punctate pattern in the subsuperficial layers. Desmoplakin, a component of the zonula adherens, was generally expressed at the cellular margin of epithelium cells, in all layers from the limbus to the renewed epithelial cells, but an irregular weaving pattern was observed only at the renewed area (Figs. 4G–I).

### Proliferative and Mesenchymal Markers

Ki67 was intermittently expressed in the basal and suprabasal layers of the limbal epithelium and rarely expressed in the peripheral cornea (Figs. 5A–C). No expression was observed in the renewed membrane. Both  $\alpha$ -SMA and vimentin, which are mesenchymal markers, were generally expressed in the stroma of the limbus and cornea, and in the connective tissue beneath the renewed epithelial layer (Figs. 5D–I).

## DISCUSSION

Corneal perforation after severe infection is not uncommon, especially in cases of gonococcal infection. Although it is known that after a corneal wound occurs, adjacent corneal epithelial cells will start to migrate into the perforated area to begin the healing cascade, what happens histologically and biologically at the perforation site in the *in vivo* human cornea has not been well determined. In this study, we have reported for the first time a comprehensive comparison of clinical, histological, and cell biological findings of the corneal perforation healing process.

In this case, it was possible to obtain intact pathological corneal tissue from lamellar keratoplasty. In contrast to penetrating keratoplasty, lamellar keratoplasty has proved more beneficial for the treatment of severe gonococcal keratitis in terms of less immunological response, better

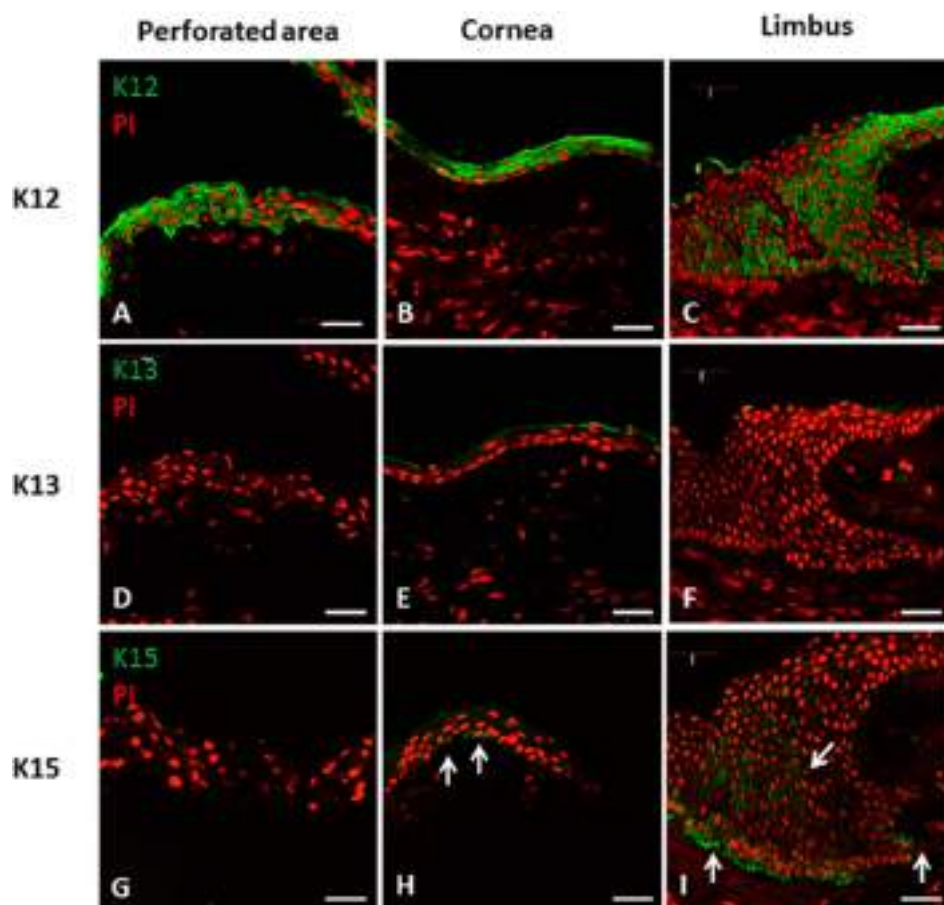


**FIGURE 3.** Immunohistochemistry of cytokeratin (K) markers. K12 was observed at the epithelial layer of the perforated area, cornea, and limbus (A–C). No K13 was detected from the entire corneal tissue. D–F, K15 was observed at the basal epithelium of the limbal area and the peripheral cornea, and sporadically observed at suprabasal cells of the limbus (arrows) (E–F). Scale bar = 50  $\mu$ m; red = PI, green = target markers.



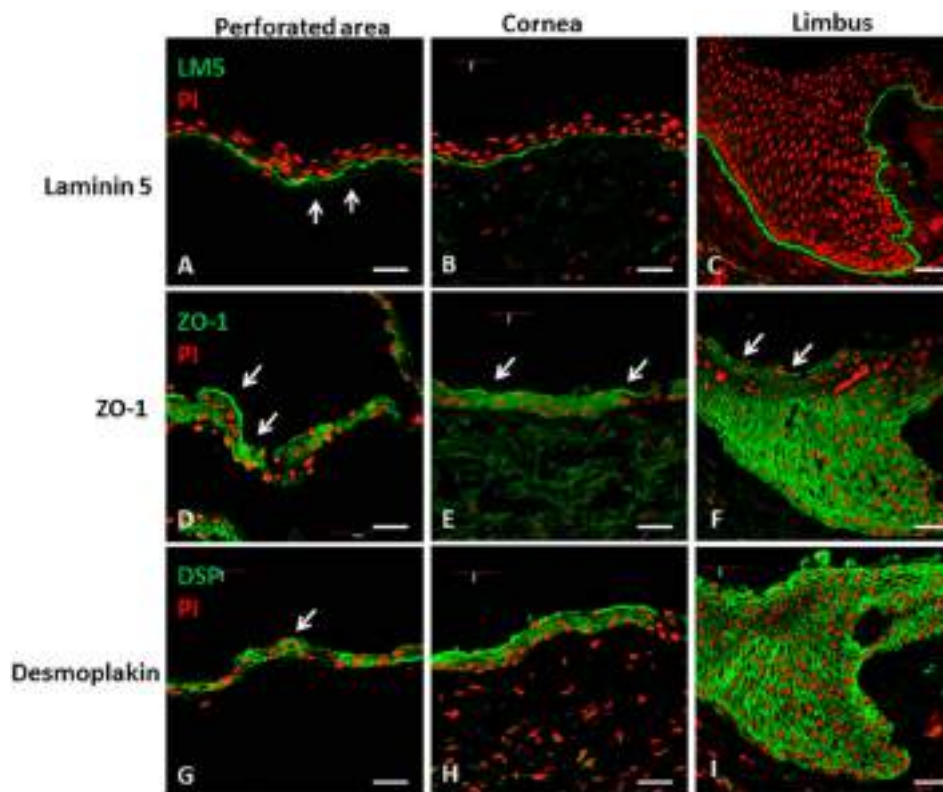


**FIGURE 4.** Immunohistochemistry of the basement membrane and cell junction markers. Laminin 5 was expressed along the basement membrane of the perforated area, cornea, and limbus (A–C). ZO-1 was densely expressed at the apical cells (arrows) in all areas (D–F). Desmoplakin (DSP) was observed throughout the corneal and limbal epithelium layer, but an irregular weaving pattern (arrow) was noticed at the perforated area (G–I). Scale bar = 50  $\mu$ m; red = PI, green = target markers.

wound strength, and less impact on anterior chamber architecture.

K12 is specific for the corneal epithelial phenotype.<sup>5</sup> Unlike K12, K13 indicates a nonkeratinized epithelial phenotype, which is highly expressed in conjunctival epithelial cells.<sup>6</sup> In this study, the regenerated epithelial cells clearly expressed K12 but not K13, indicating a corneal epithelial phenotype. K15 was identified as the key cytokeratin for limbal basal cells, staining predominantly at the basal layer and declining in suprabasal layers. For the central area of the cornea, K15 is rarely observed.<sup>7</sup> As we expected, K15 expression was negative at the perforated area, which was located at the paracentral cornea, corresponding to the K15 expression pattern in the previous study.<sup>7</sup>

The most important function of corneal epithelial cells is to maintain a viable barrier between the cornea and surrounding environment by means of tight junctions. ZO-1 is the membrane-associated protein component of the tight junction complex. In a transverse section of the human corneal epithelium, ZO-1 was found mostly in the apical cells, with very fine staining in the wing and basal cells.<sup>8</sup> We demonstrated a similar pattern of ZO-1 expression, although the wing and basal cells also clearly expressed ZO-1 in this study. Various observations of ZO-1 in subsuperficial layers may imply the effect of prompt formation of tight junctions after corneal injury.<sup>9</sup> Moreover, it has been reported that a tight junction is re-formed at the time of most rapid recovery as compared with other cellular junctions.<sup>10</sup> In our patient, the expression of ZO-1 corresponded to the clinical finding of

a negative Seidel test. Furthermore, although we clearly observed the expression of desmoplakin at the renewed epithelial cells, the irregularity of desmoplakin expression indicated that the cell junctions required a longer time to achieve good arrangement.

Laminin 5 is the major component of the corneal epithelial basement membrane, which is secreted by the epithelial basal cells of the corneal epithelium and requires more than 1 week to be rebuilt after epithelial debridement.<sup>11</sup> In the present case, expression of laminin 5 was observed at the limbus and along the corneal epithelial layer, including the renewed epithelial sheet. However, irregularity of alignment was detected, particularly at the area of renewal. It was known that irregularity of the basement membrane could cause the epithelial layer to be disorganized.<sup>12</sup> We speculated that the irregular line of the basement membrane in this study might account for the disorganization in the epithelial layers above.

The physical strength and stability of the cornea depends largely on stromal integrity and not only on the formation of epithelial tight junctions. For this reason, we observed the extreme protrusion of the previously perforated area by both slit-lamp examination and anterior segment optical coherence tomography, using vimentin and  $\alpha$ -SMA to indicate stromal keratocytes and myofibroblasts, respectively. We observed strong expression of vimentin and  $\alpha$ -SMA at the connective tissue beneath the renewed epithelial layer, indicating that myofibroblasts or activated keratocytes play a major role in stromal wound healing after corneal perforation.

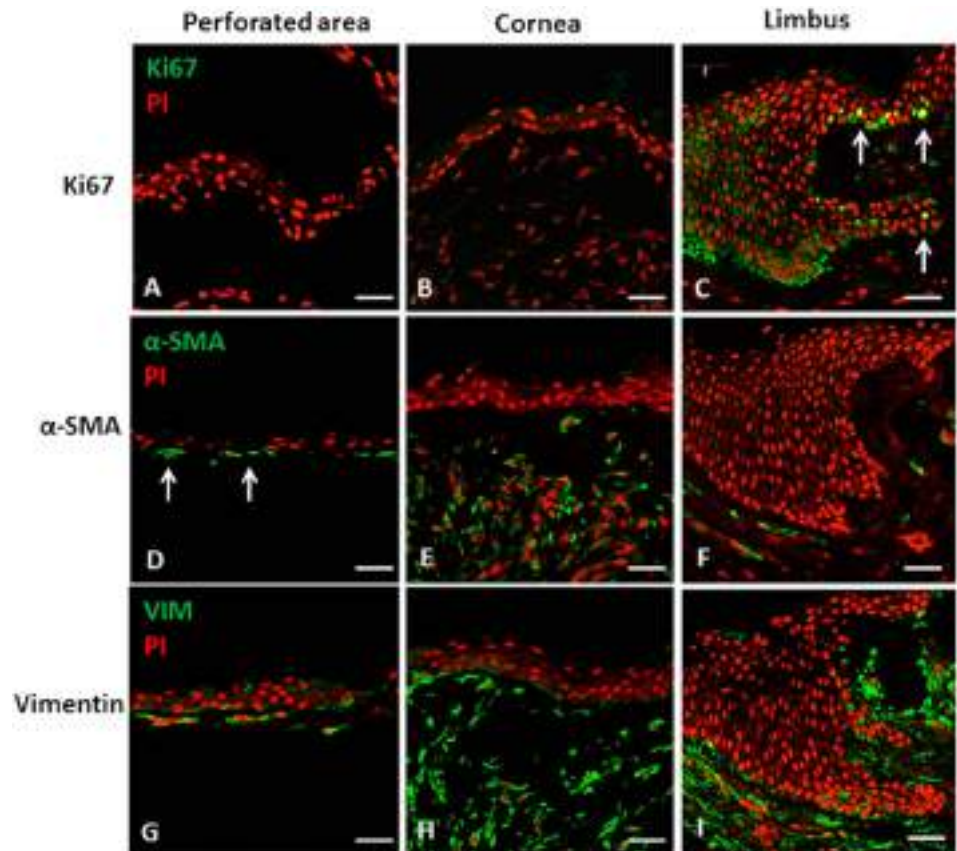


**FIGURE 5.** Immunohistochemistry of proliferative and mesenchymal markers. Ki67 was frequently observed only at the limbal area (arrows) (C).  $\alpha$ -SMA was sporadically observed beneath the perforated area (arrows) but was generally observed at the peripheral cornea and limbus (D–F). Vimentin (VIM) expression was similar to  $\alpha$ -SMA (G–I). In addition, positive staining of vimentin was also intermittently observed at basal cells in the limbal region (arrow) (I). Scale bar = 50  $\mu$ m; red = PI, green = target markers.

In conclusion, we elucidated the clinical, histological, and cell biological characteristics of the regenerated epithelium after corneal perforation caused by severe gonococcal keratitis. The regenerated epithelium remained delicate and disorganized even when the healing process was complete, suggesting a need to raise awareness of this issue. Our findings have important basic and clinical implications and provide valuable insight into the corneal wound-healing mechanism after perforation.

## REFERENCES

- Prajna NV, Srinivasan M, Lalitha P, et al. Differences in clinical outcomes in keratitis due to fungus and bacteria. *JAMA Ophthalmol.* 2013;131:1088–1089.
- McElnea E, Stapleton P, Khan S, et al. Challenges in the management of Neisseria gonorrhoeae keratitis. *Int Ophthalmol.* 2014. [epub ahead of print].
- Kawashima M, Kawakita T, Den S, et al. Surgical management of corneal perforation secondary to gonococcal keratoconjunctivitis. *Eye (Lond).* 2009;23:339–344.
- Nakamura T, Hamuro J, Takaishi M, et al. LRIG1 inhibits STAT3-dependent inflammation to maintain corneal homeostasis. *J Clin Invest.* 2014;124:385–397.
- Chen WY, Mui MM, Kao WW, et al. Conjunctival epithelial cells do not transdifferentiate in organotypic cultures: expression of K12 keratin is restricted to corneal epithelium. *Curr Eye Res.* 1994;13:765–778.
- Ramirez-Miranda A, Nakatsu MN, Zarei-Ghanavati S, et al. Keratin 13 is a more specific marker of conjunctival epithelium than keratin 19. *Mol Vis.* 2011;17:1652–1661.
- Yoshida S, Shimmura S, Kawakita T, et al. Cytokeratin 15 can be used to identify the limbal phenotype in normal and diseased ocular surfaces. *Invest Ophthalmol Vis Sci.* 2006;47:4780–4786.
- Ban Y, Cooper LJ, Fullwood NJ, et al. Comparison of ultrastructure, tight junction-related protein expression and barrier function of human corneal epithelial cells cultivated on amniotic membrane with and without air-lifting. *Exp Eye Res.* 2003;76:735–743.
- Suzuki K, Saito J, Yanai R, et al. Cell-matrix and cell-cell interactions during corneal epithelial wound healing. *Prog Retin Eye Res.* 2003;22:113–133.
- Wang Y, Chen M, Wolosin JM. ZO-1 in corneal epithelium; stratal distribution and synthesis induction by outer cell removal. *Exp Eye Res.* 1993;57:283–292.
- Nishida T. Cornea. In: Krachmer JH, Mannis MJ, Holland EJ, eds. *Cornea*. 2nd ed. Philadelphia, PA: Elsevier; 2005:3–26.
- Fukuda K, Chikama T, Nakamura M, et al. Differential distribution of subchains of the basement membrane components type IV collagen and laminin among the amniotic membrane, cornea, and conjunctiva. *Cornea.* 1999;18:73–79.

# Rho-Associated Kinase Inhibitor Eye Drop (Ripasudil) Transiently Alters the Morphology of Corneal Endothelial Cells

Naoki Okumura,<sup>1</sup> Yugo Okazaki,<sup>1</sup> Ryota Inoue,<sup>1</sup> Shinichiro Nakano,<sup>1</sup> Nigel J. Fullwood,<sup>2</sup> Shigeru Kinoshita,<sup>3</sup> and Noriko Koizumi<sup>1</sup>

<sup>1</sup>Department of Biomedical Engineering, Faculty of Life and Medical Sciences, Doshisha University, Kyotanabe, Japan

<sup>2</sup>Biomedical and Life Sciences, School of Health and Medicine, Lancaster University, Lancaster, United Kingdom

<sup>3</sup>Department of Frontier Medical Science and Technology for Ophthalmology, Kyoto Prefectural University of Medicine, Kyoto, Japan

Correspondence: Noriko Koizumi, Department of Biomedical Engineering, Faculty of Life and Medical Sciences, Doshisha University, Kyotanabe 610-0321, Japan; nkoizumi@mail.doshisha.ac.jp.

Submitted: August 5, 2015

Accepted: October 28, 2015

Citation: Okumura N, Okazaki Y, Inoue R, et al. Rho-associated kinase inhibitor eye drop (ripasudil) transiently alters the morphology of corneal endothelial cells. *Invest Ophthalmol Vis Sci*. 2015;56:7560-7567. DOI:10.1167/iovs.15-17887

**PURPOSE.** Ripasudil (Glanatec), a selective Rho-associated coiled coil-containing protein kinase (ROCK) inhibitor, was approved in Japan in September 2014 for the treatment of glaucoma and ocular hypertension. The purpose of this study was to investigate the effect of ripasudil eye drops on corneal endothelial morphology, as ROCK signaling is known to modulate the actin cytoskeleton.

**METHODS.** Morphological changes in the corneal endothelium were evaluated in human subjects by specular and slit-lamp microscopy, following topical administration of ripasudil. We also used a rabbit model to evaluate the effect of ripasudil on clinical parameters of the corneal endothelium. Twenty-four hours after ripasudil application, corneal specimens were evaluated by phalloidin staining, immunohistochemical analysis, and electron microscopy.

**RESULTS.** Specular microscopy revealed morphological changes in human eyes, and slit-lamp microscopy showed guttae-like findings. The rabbit model showed morphological changes similar to those seen in human eyes after ripasudil administration. Electron microscopy demonstrated that these alterations are due to the formation of protrusions along the cell-cell borders, but this formation is transient. Expression of corneal endothelial function-related markers was not disrupted; corneal thickness and corneal volume were not changed; and no cell death was observed following ripasudil administration.

**CONCLUSIONS.** Ripasudil induces transient guttae-like findings in humans, most likely due to protrusion formation along intracellular borders caused by the reduction in actomyosin contractility of the corneal endothelial cells. No severe adverse effects were observed. Physicians should be aware that ROCK inhibitors can cause these guttae-like findings, to avoid misdiagnosing patients as having Fuchs endothelial corneal dystrophy. (www.umin.ac.jp/ctr number, UMIN000018340.)

**Keywords:** ROCK inhibitor, ripasudil, corneal endothelial cells

Glaucoma, a progressive optic neuropathy, causes visual field loss and is one of the major causes of secondary blindness.<sup>1,2</sup> Research confirms that the progression of visual field loss due to glaucomatous optic neuropathy is suppressed by reducing intraocular pressure (IOP); consequently, the main goal of glaucoma treatment is to reduce IOP.<sup>3,4</sup> A number of pharmaceutical agents, such as prostaglandin analogues,  $\beta$ -blockers, carbonic anhydrase inhibitors, and  $\alpha$ 2-agonists, are used in clinical settings, but IOP is not well controlled by the currently available drugs in a certain number of patients.<sup>4</sup> Development of new therapeutic agents therefore remains eagerly anticipated.

Rho-associated coiled coil-containing protein kinase (ROCK) inhibitors and other drugs that modulate the actin cytoskeleton are reported to reduce IOP by promoting aqueous humor outflow through the trabecular meshwork.<sup>5-12</sup> A selective ROCK inhibitor, Y27632, altered the distribution of actin stress fibers and cell-substrate adhesion of cultured trabecular

meshwork and Schlemm's canal cells.<sup>8,10,13</sup> Topical administration of ROCK inhibitor eye drops also reduced IOP in rabbit and monkey models by increasing the outflow capacity,<sup>8,14</sup> a unique mechanism among conventional IOP-lowering drugs.<sup>8,9,15</sup> In addition, a clinical study demonstrated that the ROCK inhibitors SNJ-1656 (Y39983)<sup>16,17</sup> and AR-12286<sup>18</sup> reduced IOP in healthy volunteers, as well as in patients with glaucoma and ocular hypertension.

Ripasudil (GLANATEC), a selective ROCK inhibitor, was approved in Japan in September 2014 for the treatment of glaucoma and ocular hypertension.<sup>15</sup> Ripasudil exhibited IOP-lowering effects in rabbits and monkeys,<sup>19</sup> and phase 1 clinical trials showed that ripasudil reduced IOP in healthy adult volunteers.<sup>20</sup> In addition, randomized clinical studies showed that 0.4% ripasudil reduced IOP in patients with primary open-angle glaucoma and ocular hypertension.<sup>21</sup>

Wato et al.<sup>22</sup> observed morphological changes in the corneal endothelium by noncontact specular microscopy following



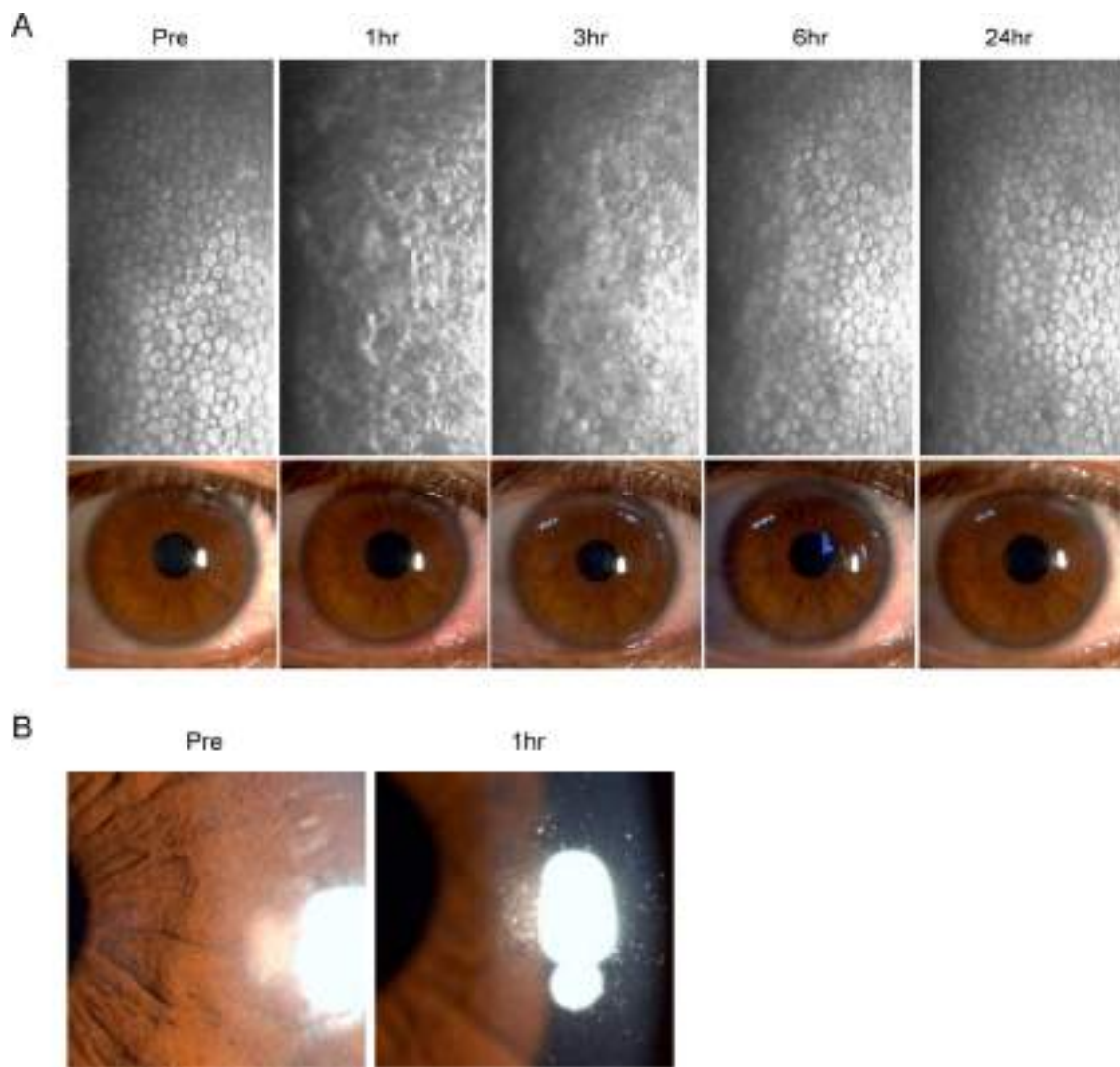


**FIGURE 1.** Pseudo guttae-like morphological changes in human corneal endothelium induced by ripasudil eye drops. **(A)** Noncontact specular microscopy image and slit-lamp photograph of a healthy subject administered one drop of 0.4% ripasudil. **(B)** Slit-lamp photograph demonstrating pseudo guttae of healthy subject 1 hour after topical administration of 0.4% ripasudil.

instillation of ripasudil in cynomolgus monkeys; however, the reasons for these changes are not yet well elucidated. The corneal endothelium is a nonregenerative tissue, and severe damage can cause vision loss due to corneal edema.<sup>23</sup> Therefore, further investigation is required to evaluate this effect of ripasudil eye drops on the corneal endothelium. The aim of the current study was to perform a pathological investigation of corneal endothelial cells (CECs) to elucidate how ripasudil administration induces the observed morphological changes in the corneal endothelium.

## MATERIALS AND METHODS

### Ethics Statement

Animals were housed and treated in accordance with the ARVO Statement for the Use of Animals in Ophthalmic and Vision Research. The rabbit experiments were performed at Doshisha University (Kyoto, Japan), according to the protocol approved by that university's Animal Care and Use Committee (Approval No. 0831). The human data were obtained in accordance with the tenets set forth in the Declaration of Helsinki.

### Ripasudil Administration in Human Subjects

The effect of ripasudil eye drops (GLANATEC ophthalmic solution 0.4%; Kowa Company, Ltd., Nagoya, Japan) on corneal endothelium was examined in two human subjects (46-year-old female and 38-year-old male) who had no corneal diseases. Each was administered one drop of ripasudil to the right eye, and the corneal endothelium was observed by noncontact specular microscopy and slit-lamp microscopy at specific time points: before administration and 1, 3, 6, and 24 hours after a single dose of ripasudil. This study was performed according to a protocol approved by the Institutional Review Board of Doshisha University. Clinical trial registration was obtained from UMIN UMIN000018340 (<http://www.umin.ac.jp/english/>).

### Ripasudil Administration in a Rabbit Model

A single dose of ripasudil was administered into the right eyes of nine rabbits. Anterior segments and corneal endothelium were evaluated by slit-lamp microscopy and contact specular microscope (Konan scanning slit specular microscope; Konan Medical, Nishinomiya, Japan) for 24 hours. Corneal thickness,



corneal volume, and corneal refractive power were evaluated with a Pentacam (OCULUS Optikgeräte GmbH, Wetzlar, Germany). Intraocular pressure was determined with a Tonovet (icare Finland, Vantaa, Finland) ( $n = 5$ ). Corneal specimens obtained from four rabbits were used for analysis by scanning electron microscopy and transmission electron microscopy. For repeated-dose administration, ripasudil was administered into the right eye of three rabbits twice daily for 7 days, and the corneal endothelium was evaluated by contact specular microscopy and histological analysis.

### Fluorescent Staining

Rabbit corneal specimens were fixed in 4% formaldehyde and incubated for 30 minutes at room temperature in 1% bovine serum albumin (BSA) to block nonspecific binding. The actin fibers were evaluated by examining the corneas after actin staining with a 1:400 dilution of Alexa Fluor 488-conjugated phalloidin (Life Technologies Corp., Carlsbad, CA, USA). The effect on function-related proteins was investigated by immunohistochemical analyses of ZO-1, N-cadherin, and  $\text{Na}^+/\text{K}^+$ -ATPase using primary antibodies against Zona Occludens 1 (ZO-1; 1:200; Zymed Laboratories, South San Francisco, CA, USA), N-cadherin (1:200, Zymed Laboratories), and  $\text{Na}^+/\text{K}^+$ -ATPase (1:200; Upstate Biotechnology, Lake Placid, NY, USA). Alexa Fluor 488-conjugated goat anti-mouse (Life Technologies Corp.) was used as a secondary antibody at a 1:1000 dilution.

The effect of ripasudil on cell death was examined in corneas obtained from five rabbits 24 hours after administration of ripasudil. The specimens were stained with annexin V and propidium iodide (PI) by incubating with annexin V-fluorescein isothiocyanate (FITC; 1:200; Zymed Laboratories) and PI (1:200, Zymed Laboratories) for 30 minutes at 37°C, followed by fixation in 4% formaldehyde. As a positive control, 10  $\mu\text{M}$  staurosporine was injected into anterior chamber in two rabbits and corneas were recovered after 24 hours. Nuclei were stained with 4',6-diamidino-2-phenylindole (DAPI) (Vector Laboratories, Burlingame, CA, USA). The slides were examined with a fluorescence microscope (TCS SP2 AOBS; Leica Microsystems, Wetzlar, Germany).

### Scanning Electron Microscopy

The effect of ripasudil on corneal endothelial morphology was evaluated in corneal specimens obtained from four rabbits at 1, 3, and 24 hours after a single dose of ripasudil or control. Excised corneas were fixed in 2.5% glutaraldehyde and 2% paraformaldehyde in 0.1 M Sørensen buffer (pH 7.2–7.4) for at least 3 hours at room temperature. The samples were washed in the buffer, postfixed with 1% aqueous osmium tetroxide, dehydrated through an ascending ethanol series, and transferred to hexamethyldisilazane (HMDS) (Agar Scientific, Stansted, UK), which was allowed to sublimate off. The samples were mounted on stubs, sputter-coated with gold, and examined by scanning electron microscopy (model 5600; JEOL Ltd., Tokyo, Japan).

### Transmission Electron Microscopy

Corneal specimens were obtained from four rabbits at 1, 3, and 24 hours after a single dose of ripasudil or control. The samples were washed in 0.1 M Sørensen buffer, fixed with 2.5% glutaraldehyde and 2% paraformaldehyde in 0.1 M Sørensen buffer, and postfixed with 1% osmium tetroxide. After dehydration in an ascending ethanol series and acetone, the samples were infiltrated and embedded in epoxy resin. Ultrathin sections were collected on uncoated copper grids and double stained with uranyl acetate and lead. Sections were

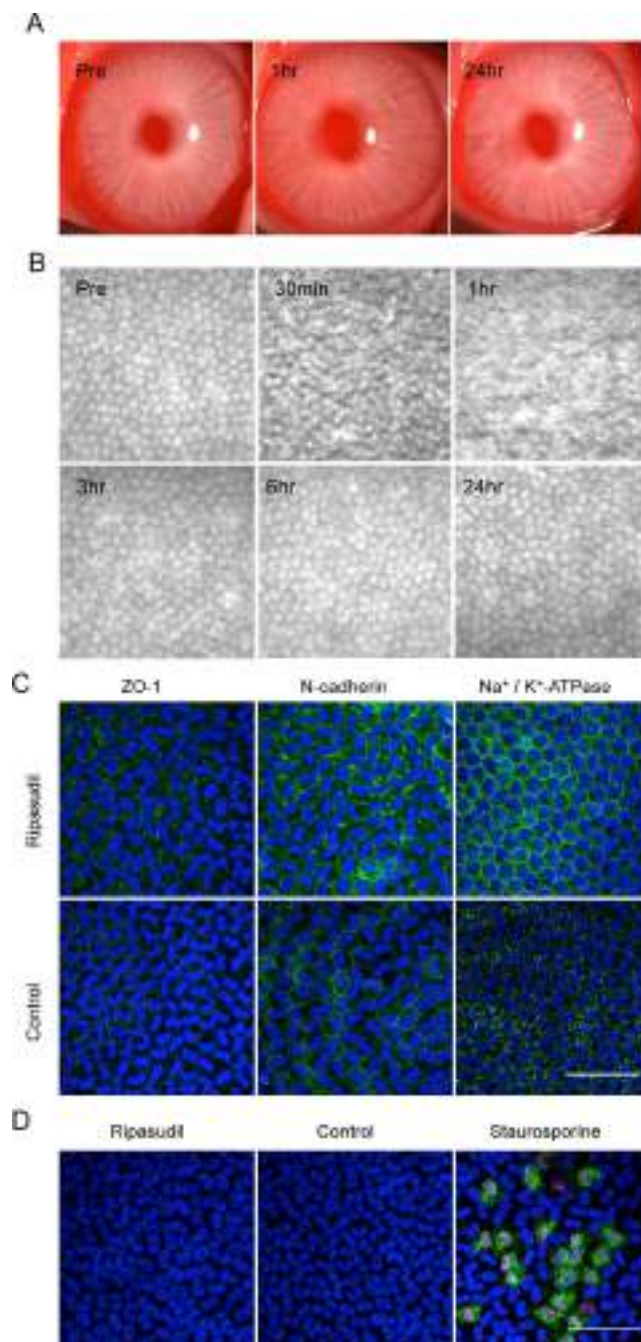


**FIGURE 2.** Slit-lamp microscopy, contact specular microscopy, and histological evaluation of rabbit corneal endothelium after single-dose administration of ripasudil eye drops. (A) 0.4% ripasudil was administered topically as an eye drop in five rabbits, followed by slit-lamp microscopy evaluation. (B) Endothelial morphology was evaluated by contact specular microscopy after administration of 0.4% ripasudil. Representative images obtained from five independent rabbits are shown. (C) Corneas recovered from five rabbits 24 hours after administration of 0.4% ripasudil were stained with phalloidin. Expression of the function-related proteins ZO-1, N-cadherin, and  $\text{Na}^+/\text{K}^+$ -ATPase was also evaluated by immunofluorescence staining. Nuclei were stained with DAPI. Scale bar: 50  $\mu\text{m}$ . (D) To evaluate the effect of ripasudil, corneas from five rabbits recovered 24 hours after administration of 0.4% ripasudil were stained with annexin V and PI. Staurosporine was injected into the anterior chamber to induce apoptosis as a positive control. Nuclei were stained with DAPI. Scale bar: 50  $\mu\text{m}$ .

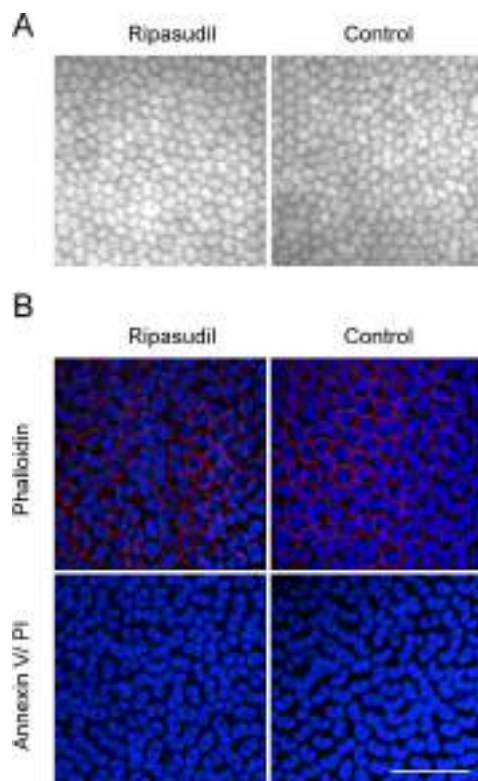


**FIGURE 3.** The effect of repeated-dose administration of 0.4% ripasudil on rabbit corneal endothelium. (A) For repeated-dose administration, 0.4% ripasudil was administered twice daily for 7 days in three rabbits, and the corneal endothelium was examined by contact specular microscopy. (B) To evaluate cell morphology, the corneal endothelium was stained with phalloidin. Annexin V and PI staining was performed to evaluate the effect of ripasudil on corneal endothelial cell death. Nuclei were stained with DAPI. Scale bar: 50  $\mu$ m.

examined with a transmission electron microscope (JEM-1400Plus; JEOL Ltd.) equipped with a charge-coupled device camera.

### Statistical Analysis

The Student's *t*-test was used to determine statistical significance (*P* value) of differences between mean values of the two-sample comparison. Results are expressed as mean  $\pm$  SEM.

## RESULTS

### Effect of Ripasudil Eye Drops on Corneal Endothelium in Human Subjects

Noncontact specular microscopy demonstrated an indistinct cell border after 1 hour. The cell border was still slightly indistinct after 3 hours and was distinct once again by 6 hours; no pathological changes, such as distinct cell borders and cell loss, were observed at 24 hours after administration (Fig. 1A). Conjunctival injection, which was previously reported as a possible adverse effect of ROCK inhibitors, was observed coincident to the morphological changes in the corneal endothelium at 3 hours (Fig. 1A). A guttae-like appearance of the cornea was observed by slit-lamp microscopy after 1 to 3 hours of treatment, but this resolved within 24 hours (Fig. 1B). These changes were observed similarly in both human subjects.

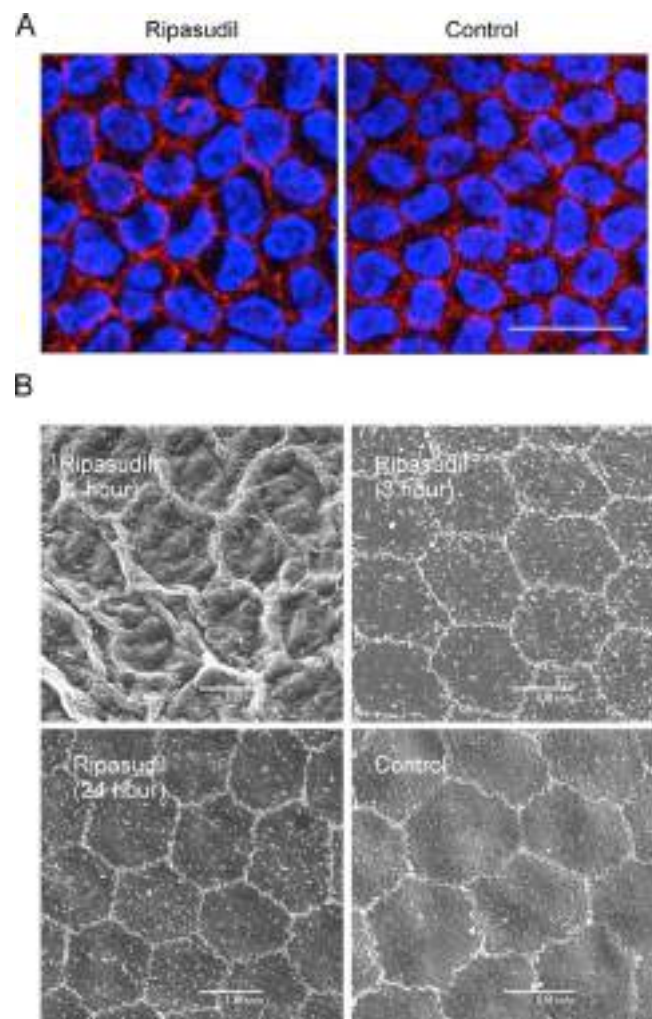


**FIGURE 4.** Morphological evaluation of rabbit corneal endothelium after treatment with ripasudil eye drops. (A) 0.4% ripasudil was topically administered to the rabbit eye, and 1 hour after treatment the cornea and control cornea were recovered. Actin fibers were stained by phalloidin. Scale bar: 50  $\mu$ m. (B) Corneas were recovered from rabbits 1, 3, and 24 hours after administering a single dose of 0.4% ripasudil. Rabbit corneal endothelium was evaluated by scanning electron microscopy. Images were representative of two independent rabbits for every time point. Scale bar: 10  $\mu$ m.

### Effect of Ripasudil Eye Drops on Rabbit Corneal Endothelium

A histological analysis of corneal endothelium following treatment with ripasudil was conducted on a rabbit model. Slit-lamp microscopy showed no severe adverse corneal effects such as corneal edema, but contact specular microscopy showed that the cell border of the corneal endothelium became indistinct by 30 minutes to 1 hour after dosing (Figs. 2A, 2B). Similar to the finding in human subjects, it recovered within 3 to 6 hours, and no morphological changes or cell losses were observed 24 hours after administration. At 24 hours after administration, the expression of the function-related proteins ZO-1 (tight junction), N-cadherin (adherence junction), and Na<sup>+</sup>/K<sup>+</sup>-ATPase (pump function) was well preserved in the normal phenotypes (Fig. 2C). Annexin V and PI staining showed no induction of apoptosis or cell death by ripasudil administration (Fig. 2D). Ripasudil administration twice daily for 7 days in the rabbit model caused no



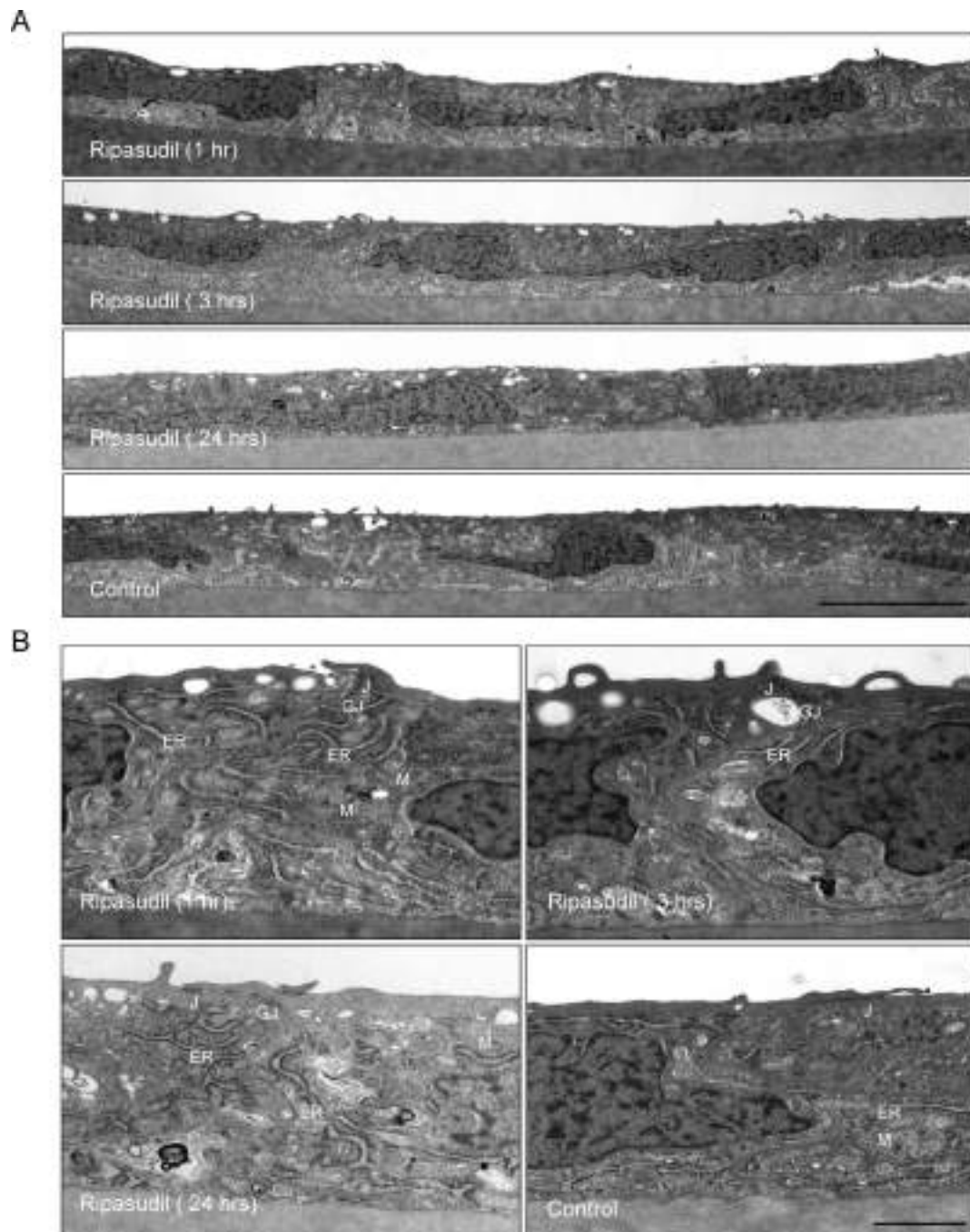


**FIGURE 5.** Transmission electron microscopy of rabbit corneal endothelium after treatment with ripasudil eye drops. (A, B) Corneas administered ripasudil were recovered after 1, 3, and 24 hours. Rabbit corneal endothelium was then evaluated by transmission electron microscopy. Images are representative of two independent rabbits for every time point. J, intact junctional complexes (tight junction and adherens junction); GJ, gap junction; M, mitochondria; ER, endoplasmic reticulum. Scale bars: 5  $\mu$ m (A); 1  $\mu$ m (B).

morphological changes, as determined by contact specular microscopy (Fig. 3A) and phalloidin staining (Fig. 3B). In addition, no annexin V- and PI-positive cells were observed (Fig. 3B).

The ROCK inhibitors regulate the actin cytoskeleton, so we next examined the expression pattern of actin in the corneal endothelium. Phalloidin staining revealed a distribution of actin fibers at the cell cortex in both ripasudil-treated and control eyes, and no obvious differences were observed 24 hours after administration (Fig. 4A). However, scanning electron microscopy demonstrated the formation of protrusions along the cell

borders, which recovered by 3 hours (Fig. 4B). Transmission electron microscopy also revealed the formation of protrusions at the cell border of the corneal endothelium, which also reverted to the control level within 24 hours (Fig. 5A). Tight junctions, adherence junctions, and gap junctions were present, even at 1 hour when specular microscopy revealed indistinct cell borders, and retention of adhesion on Descemet's membrane was unchanged (Fig. 5B). Organelles such as mitochondria and endoplasmic reticulum were unaltered morphologically by ripasudil administration throughout the 24-hour study.

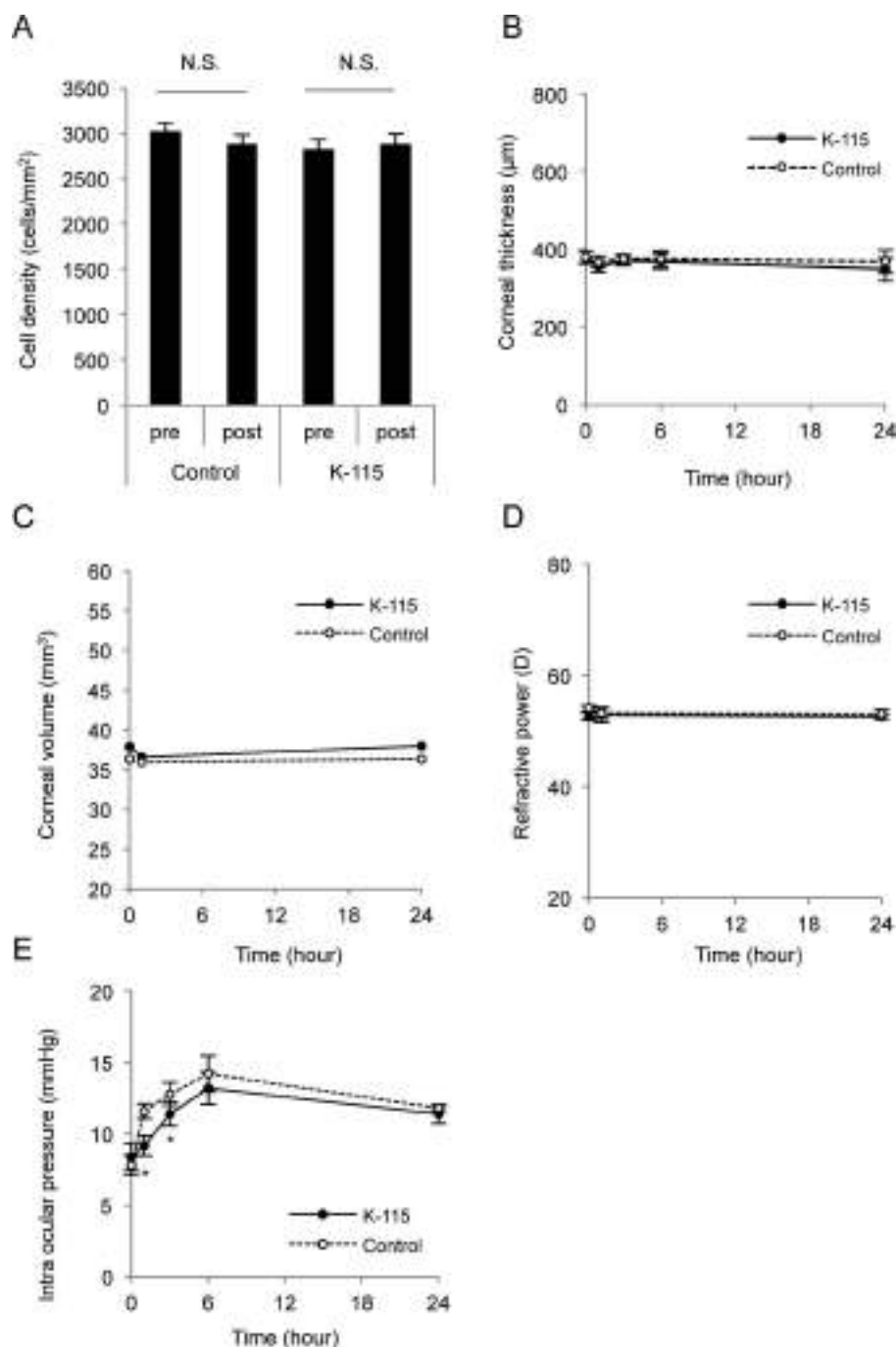


**FIGURE 6.** Evaluation of rabbit clinical parameters after treatment with ripasudil eye drops. (A) 0.4% ripasudil was administered topically as an eye drop in the right eyes of five rabbits, and corneal endothelial cell density was evaluated by contact specular microscopy after 24 hours. (B) Corneal thickness of rabbit after ripasudil administration was evaluated with an ultrasound pachymeter. (C, D) The effect of ripasudil on corneal volume and refractive power was evaluated by Pentacam. (E) Intraocular pressure of rabbits was measured by Tonovet after treatment with 0.4% ripasudil. \* $P < 0.01$ .

We next evaluated the clinical parameters in the rabbit model that undergo changes if corneal endothelial function is damaged. Corneal endothelial cell density, determined by contact specular microscopy, was not decreased by ripasudil (Fig. 6A). Corneal thickness and corneal volume, which are maintained by the barrier and pump functions of the corneal endothelium, were not significantly changed by ripasudil (Figs. 6B, 6C). The lack of any significant changes in refractive power also demonstrated that corneal shape was preserved, despite the formation of protrusions at the cell border (Fig. 6D). The

IOP was significantly lower at 1 and 3 hours after treatment, showing the effect of ripasudil against glaucoma (Fig. 6E).

## DISCUSSION

The ROCK isoforms ROCK1 and ROCK2 were originally discovered as a target of the small Guanosine-5'-triphosphate (GTP)-binding protein RhoA.<sup>24</sup> The Rho-binding domain within the coiled-coil region of ROCK was identified, but subsequent



research revealed that several molecules activate or inhibit ROCK via multiple contact points.<sup>25–28</sup> ROCK mediates various important cellular functions, such as cell shape, motility, adhesion, and proliferation.<sup>24</sup> Active Rho-GTP binds to ROCK and increases the phosphorylation of a number of downstream target proteins, such as myosin light chain (MLC), Lin-11/Isl-1/Mec-3 kinase (LIMK), and MLC phosphatase complex of type 1 (MYPT1). This is followed by stabilization of filamentous actin and an increase in the actin-myosin contractile force.<sup>24,29</sup> ROCK has attracted the interest of researchers as a potential therapeutic target for various diseases, such as cancer, neuronal degenerative disease, asthma, cardiovascular disease, and hypertension, as well as glaucoma.<sup>28,30</sup> In fact, fasudil was approved in Japan and China for the treatment of cerebral vasospasm in 1995.<sup>28</sup> To our knowledge, ripasudil is the first approved ROCK inhibitor eye drop for the treatment of glaucoma and ocular hypertension.<sup>15</sup>

Ripasudil is anticipated to alter cytoskeletal contraction of the trabecular meshwork and Schlemm's canal cells to increase outflow of aqueous humor<sup>15,16,19</sup>; therefore, several types of ocular cells can be affected. For instance, the high occurrence of hyperemia is a common symptom after topical administration of ROCK inhibitors.<sup>14,16,18</sup> Coincidentally, slight to mild conjunctival hyperemia was observed in more than half of the participants in ripasudil clinical trials.<sup>20,21</sup> This hyperemia is thought to arise because of conjunctival vessel dilation due to alteration of vascular endothelial cells.<sup>16</sup> However, the hyperemia was transient, and no conjunctival hemorrhage, which occurred in animal experiments,<sup>14</sup> was observed in the clinical studies, suggesting the safety of ripasudil eye drops.<sup>31</sup>

In this study, we showed that ripasudil eye drops caused morphological changes in the corneal endothelium as observed by noncontact specular microscopy. Of importance, this change was also recognized as guttae-like findings by slit-lamp microscopy. Guttae are collagenous excrescences of the corneal endothelial basement membrane (Descemet's membrane) and are observed in as many as 5% of the population aged over 40.<sup>32</sup> They are also typical features of Fuchs endothelial corneal dystrophy.<sup>33</sup> To avoid misdiagnosing a patient as having Fuchs endothelial corneal dystrophy, physicians should be aware that guttae-like findings can be caused by ROCK inhibitor eye drops.

We investigated these guttae-like findings further using the rabbit model and demonstrated that they are induced by the formation of mild protrusions along the cell-cell borders. Protrusion formation is considered an effect of ripasudil, because ROCK inhibitors modulate the actin cytoskeleton in various types of cells. We have also reported that ROCK inhibitors alter the cell morphology of cultured CECs.<sup>34</sup> A pharmacodynamics study revealed that ripasudil has high intraocular permeability and that it penetrates into all eye tissues except the lens,<sup>19</sup> suggesting that ripasudil affects the corneal endothelium. Tian and his colleagues<sup>7</sup> reported that intracameral infusion of H-7 to monkey eyes induced morphological change in the corneal endothelium, observed by specular microscopy, and membrane ruffling along the intracellular borders, as observed by SEM.<sup>7</sup> H-7 is a serine-threonine kinase inhibitor that inhibits actomyosin contractility and eventually produces cellular relaxation.<sup>5–7,35</sup> Taken together, alteration of corneal endothelium borders by ripasudil and other actin cytoskeleton-modulating drugs is suggested to be a common feature of these drugs.

The corneal endothelium is essential for maintaining corneal clarity via its barrier function that suppresses the overflow of aqueous humor into the corneal stroma. Transmission electron microscopy demonstrated that tight junctions, adherence junctions, and gap junctions were present 1 hour after ripasudil administration, and the corneal thickness

and volume were unchanged. This suggests that the barrier function of the corneal endothelium was not disrupted. ROCK inhibitors can change the localization of junctional proteins and increase the permeability of Schlemm's canal,<sup>11</sup> but this difference may be explained by the fact that the effects of ROCK inhibitors depend on the cell types.<sup>28</sup> One remaining question is the effect of long-term use of ripasudil eye drops on the corneal endothelium in clinical settings. We have shown that morphological changes are transient in this animal model, but careful evaluation in human patients is needed.

In conclusion, we have demonstrated that ripasudil induces transient guttae-like findings in humans, most likely due to protrusion formation along intracellular borders caused by the reduction in actomyosin contractility of the CECs. Physicians should appreciate that ROCK inhibitors can cause these guttae-like findings in order to avoid misdiagnosing patients as having Fuchs endothelial corneal dystrophy.

### Acknowledgments

The authors thank Masato Asahiyama and Keisuke Itagaki for technical support for transmission electron microscopy.

Supported by Program for the Strategic Research Foundation at Private Universities from MEXT (NK, NO).

Disclosure: **N. Okumura**, None; **Y. Okazaki**, None; **R. Inoue**, None; **S. Nakano**, None; **N.J. Fullwood**, None; **S. Kinoshita**, None; **N. Koizumi**, None

### References

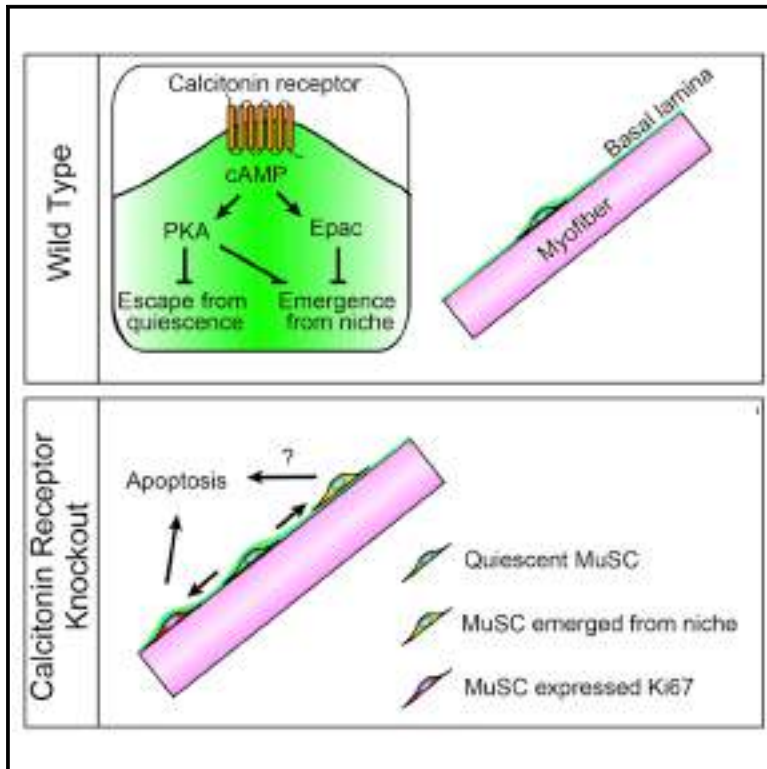
1. Quigley HA, Broman AT. The number of people with glaucoma worldwide in 2010 and 2020. *Br J Ophthalmol*. 2006;90:262–267.
2. Tham YC, Li X, Wong TY, Quigley HA, Aung T, Cheng CY. Global prevalence of glaucoma and projections of glaucoma burden through 2040: a systematic review and meta-analysis. *Ophthalmology*. 2014;121:2081–2090.
3. The Advanced Glaucoma Intervention Study (AGIS): 7. The relationship between control of intraocular pressure and visual field deterioration. The AGIS Investigators. *Am J Ophthalmol*. 2000;130:429–440.
4. Kass MA, Heuer DK, Higginbotham EJ, et al. The Ocular Hypertension Treatment Study: a randomized trial determines that topical ocular hypotensive medication delays or prevents the onset of primary open-angle glaucoma. *Arch Ophthalmol*. 2002;120:701–713, discussion 829–830.
5. Tian B, Kaufman PL, Volberg T, Gabelt BT, Geiger B. H-7 disrupts the actin cytoskeleton and increases outflow facility. *Arch Ophthalmol*. 1998;116:633–643.
6. Tian B, Gabelt BT, Peterson JA, Kiland JA, Kaufman PL. H-7 increases trabecular facility and facility after ciliary muscle disinsertion in monkeys. *Invest Ophthalmol Vis Sci*. 1999;40:239–242.
7. Tian B, Sabanay I, Peterson JA, Hubbard WC, Geiger B, Kaufman PL. Acute effects of H-7 on ciliary epithelium and corneal endothelium in monkey eyes. *Curr Eye Res*. 2001;22:109–120.
8. Honjo M, Tanihara H, Inatani M, et al. Effects of rho-associated protein kinase inhibitor Y-27632 on intraocular pressure and outflow facility. *Invest Ophthalmol Vis Sci*. 2001;42:137–144.
9. Rao PV, Deng P, Sasaki Y, Epstein DL. Regulation of myosin light chain phosphorylation in the trabecular meshwork: role in aqueous humour outflow facility. *Exp Eye Res*. 2005;80:197–206.
10. Koga T, Koga T, Awai M, Tsutsui J, Yue BY, Tanihara H. Rho-associated protein kinase inhibitor, Y-27632, induces alterations in adhesion, contraction and motility in cultured human trabecular meshwork cells. *Exp Eye Res*. 2006;82:362–370.

11. Kameda T, Inoue T, Inatani M, et al. The effect of Rho-associated protein kinase inhibitor on monkey Schlemm's canal endothelial cells. *Invest Ophthalmol Vis Sci*. 2012;53:3092-3103.
12. Inoue T, Tanihara H. Rho-associated kinase inhibitors: a novel glaucoma therapy. *Prog Retin Eye Res*. 2013;37:1-12.
13. Rao PV, Deng PF, Kumar J, Epstein DL. Modulation of aqueous humor outflow facility by the Rho kinase-specific inhibitor Y-27632. *Invest Ophthalmol Vis Sci*. 2001;42:1029-1037.
14. Tokushige H, Inatani M, Nemoto S, et al. Effects of topical administration of Y-39983, a selective rho-associated protein kinase inhibitor, on ocular tissues in rabbits and monkeys. *Invest Ophthalmol Vis Sci*. 2007;48:3216-3222.
15. Garnock-Jones KP. Ripasudil: first global approval. *Drugs*. 2014;74:2211-2215.
16. Tanihara H, Inatani M, Honjo M, Tokushige H, Azuma J, Araie M. Intraocular pressure-lowering effects and safety of topical administration of a selective ROCK inhibitor, SNJ-1656, in healthy volunteers. *Arch Ophthalmol*. 2008;126:309-315.
17. Inoue T, Tanihara H, Tokushige H, Araie M. Efficacy and safety of SNJ-1656 in primary open-angle glaucoma or ocular hypertension. *Acta Ophthalmol*. 2015;93:e393-e395.
18. Williams RD, Novack GD, van Haarlem T, Kopczynski C. Ocular hypotensive effect of the Rho kinase inhibitor AR-12286 in patients with glaucoma and ocular hypertension. *Am J Ophthalmol*. 2011;152:834-841, e831.
19. Isobe T, Mizuno K, Kaneko Y, Ohta M, Koide T, Tanabe S. Effects of K-115, a rho-kinase inhibitor, on aqueous humor dynamics in rabbits. *Curr Eye Res*. 2014;39:813-822.
20. Tanihara H, Inoue T, Yamamoto T, Kuwayama Y, Abe H, Araie M. Phase 1 clinical trials of a selective Rho kinase inhibitor, K-115. *JAMA Ophthalmol*. 2013;131:1288-1295.
21. Tanihara H, Inoue T, Yamamoto T, Kuwayama Y, Abe H, Araie M. Phase 2 randomized clinical study of a Rho kinase inhibitor, K-115, in primary open-angle glaucoma and ocular hypertension. *Am J Ophthalmol*. 2013;156:731-736.
22. Wato E, Omichi K, Yoneyama S, Tanaka M, Kagawa M, Amano Y. Safety evaluation of morphological changes in corneal endothelial cells induced by K-115 in cynomolgus monkeys. *Fundam Toxicol Sci*. 2014;1:39-47.
23. Tan DT, Dart JK, Holland EJ, Kinoshita S. Corneal transplantation. *Lancet*. 2012;379:1749-1761.
24. Riento K, Ridley AJ. Rocks: multifunctional kinases in cell behaviour. *Nat Rev Mol Cell Biol*. 2003;4:446-456.
25. Sebbagh M, Renvoize C, Hamelin J, Riche N, Bertoglio J, Breard J. Caspase-3-mediated cleavage of ROCK I induces MLC phosphorylation and apoptotic membrane blebbing. *Nat Cell Biol*. 2001;3:346-352.
26. Coleman ML, Sahai EA, Yeo M, Bosch M, Dewar A, Olson MF. Membrane blebbing during apoptosis results from caspase-mediated activation of ROCK I. *Nat Cell Biol*. 2001;3:339-345.
27. Blumenstein L, Ahmadian MR. Models of the cooperative mechanism for Rho effector recognition: implications for RhoA-mediated effector activation. *J Biol Chem*. 2004;279:53419-53426.
28. Olson MF. Applications for ROCK kinase inhibition. *Curr Opin Cell Biol*. 2008;20:242-248.
29. Scott RW, Olson MF. LIM kinases: function, regulation and association with human disease. *J Mol Med (Berl)*. 2007;85:555-568.
30. Liao JK, Seto M, Noma K. Rho kinase (ROCK) inhibitors. *J Cardiovasc Pharmacol*. 2007;50:17-24.
31. Tanihara H, Inoue T, Yamamoto T, et al. Intra-ocular pressure-lowering effects of a Rho kinase inhibitor, ripasudil (K-115), over 24 hours in primary open-angle glaucoma and ocular hypertension: a randomized, open-label, crossover study. *Acta Ophthalmol*. 2015;93:e254-e260.
32. Lorenzetti DW, Uotila MH, Parikh N, Kaufman HE. Central cornea guttata. Incidence in the general population. *Am J Ophthalmol*. 1967;64:1155-1158.
33. Zhang J, Patel DV. The pathophysiology of Fuchs' endothelial dystrophy—a review of molecular and cellular insights. *Exp Eye Res*. 2015;130:97-105.
34. Okumura N, Ueno M, Koizumi N, et al. Enhancement on primate corneal endothelial cell survival in vitro by a ROCK inhibitor. *Invest Ophthalmol Vis Sci*. 2009;50:3680-3687.
35. Birrell GB, Hedberg KK, Habliston DL, Griffith OH. Protein kinase C inhibitor H-7 alters the actin cytoskeleton of cultured cells. *J Cell Physiol*. 1989;141:74-84.

# Cell Reports

## Calcitonin Receptor Signaling Inhibits Muscle Stem Cells from Escaping the Quiescent State and the Niche

### Graphical Abstract



### Authors

Masahiko Yamaguchi, Yoko Watanabe, Takuji Ohtani, ..., Shin'ichi Takeda, Hiroshi Yamamoto, So-ichiro Fukada

### Correspondence

fukada@phs.osaka-u.ac.jp

### In Brief

Muscle stem cells express calcitonin receptor, a hormone receptor, but its physiological role is unclear. Yamaguchi et al. demonstrate that the calcitonin receptor is important in maintaining muscle stem cells in the quiescent state and in their niche.

### Highlights

- The calcitonin receptor (Calcr) maintains the adult MuSC pool
- The Calcr-cAMP-PKA pathway keeps MuSCs in their quiescent state
- Loss of Calcr allows emergence of MuSCs from their niche
- Calcr-cAMP-PKA and -Epac signaling inhibits emergence of MuSCs from their niche



# Calcitonin Receptor Signaling Inhibits Muscle Stem Cells from Escaping the Quiescent State and the Niche

Masahiko Yamaguchi,<sup>1,7</sup> Yoko Watanabe,<sup>1,7</sup> Takuji Ohtani,<sup>1,7</sup> Akiyoshi Uezumi,<sup>2</sup> Norihisa Mikami,<sup>1</sup> Miki Nakamura,<sup>1</sup> Takahiko Sato,<sup>3</sup> Masahito Ikawa,<sup>4</sup> Mikio Hoshino,<sup>5</sup> Kunihiro Tsuchida,<sup>2</sup> Yuko Miyagoe-Suzuki,<sup>6</sup> Kazutake Tsujikawa,<sup>1</sup> Shin'ichi Takeda,<sup>6</sup> Hiroshi Yamamoto,<sup>1</sup> and So-ichiro Fukada<sup>1,\*</sup>

<sup>1</sup>Laboratory of Molecular and Cellular Physiology, Graduate School of Pharmaceutical Sciences, Osaka University, 1-6 Yamadaoka, Suita, Osaka 565-0871, Japan

<sup>2</sup>Division for Therapies Against Intractable Diseases, Institute for Comprehensive Medical Science, Fujita Health University, 1-98 Dengakugakubo, Kutsukake, Toyoake, Aichi 470-1192, Japan

<sup>3</sup>Department of Ophthalmology, Kyoto Prefectural University of Medicine, Kyoto 602-8566, Japan

<sup>4</sup>Research Institute for Microbial Diseases, Osaka University, 3-1 Yamadaoka, Suita, Osaka 565-0871, Japan

<sup>5</sup>Department of Biochemistry and Cellular Biology, National Institute of Neuroscience, National Center of Neurology and Psychiatry, 4-1-1 Ogawa-Higashi, Kodaira, Tokyo 187-8502, Japan

<sup>6</sup>Department of Molecular Therapy, National Institute of Neuroscience, National Center of Neurology and Psychiatry, 4-1-1 Ogawa-Higashi, Kodaira, Tokyo 187-8502, Japan

<sup>7</sup>Co-first author

\*Correspondence: [fukada@phs.osaka-u.ac.jp](mailto:fukada@phs.osaka-u.ac.jp)

<http://dx.doi.org/10.1016/j.celrep.2015.08.083>

This is an open access article under the CC BY-NC-ND license (<http://creativecommons.org/licenses/by-nc-nd/4.0/>).

## SUMMARY

Calcitonin receptor (Calcr) is expressed in adult muscle stem cells (muscle satellite cells [MuSCs]). To elucidate the role of Calcr, we conditionally depleted Calcr from adult MuSCs and found that impaired regeneration after muscle injury correlated with the decreased number of MuSCs in Calcr-conditional knockout (cKO) mice. Calcr signaling maintained MuSC dormancy via the cAMP-PKA pathway but had no impact on myogenic differentiation of MuSCs in an undifferentiated state. The abnormal quiescent state in Calcr-cKO mice resulted in a reduction of the MuSC pool by apoptosis. Furthermore, MuSCs were found outside their niche in Calcr-cKO mice, demonstrating cell relocation. This emergence from the sublamina niche was prevented by the Calcr-cAMP-PKA and Calcr-cAMP-Epac pathways downstream of Calcr. Altogether, the findings demonstrated that Calcr exerts its effect specifically by keeping MuSCs in a quiescent state and in their location, maintaining the MuSC pool.

## INTRODUCTION

Adult stem cells are maintained in a reversible quiescent state (or G0) and reside in a specific microenvironment referred to as a niche. Quiescent adult stem cells show low levels of transcriptional activity and energy production (Freter et al., 2010; Rodgers et al., 2014). In culture, serum deprivation forces many types of cells to enter a G0-like dormancy. Given that the quiescent state

is a transient state that results from escaping the cell cycle due to the absence of growth factor, it had been assumed that the quiescent state is a “passive,” rather than an “active,” state. However, recent evidence suggests that quiescence is not merely a passive state (Cheung and Rando, 2013).

Quiescent adult stem cells specifically or highly express coding and non-coding genes in a G0-specific manner not observed in activated or proliferating progenitors (Cheung et al., 2012; Codega et al., 2014; Fukada et al., 2007; Tumber et al., 2004; Venezia et al., 2004). In addition, a recent study showed that many kinds of G-protein-coupled receptors (GPCRs) are expressed more abundantly in quiescent neural stem cells (NSCs) than in activated NSCs: two ligands (sphingosine-1-phosphate [S1P] and prostaglandin D<sub>2</sub> [PGD<sub>2</sub>]) of these GPCRs inhibit activation of quiescent NSCs ex vivo (Codega et al., 2014). On the other hand, two secondary messengers of GPCR, Gs $\alpha$  and Gq/11 $\alpha$ , are required in stem-cell-like chondrocytes to maintain the quiescent or undifferentiated state (Chagin et al., 2014). Thus, GPCR-mediated signaling may be a common pathway to keep some types of adult stem cells from escaping the quiescent and undifferentiated state. However, their cellular receptors have not been fully identified in adult stem cells.

Adult muscle stem cells, also known as muscle satellite cells (MuSCs), are responsible for skeletal muscle regeneration after injury to the muscle. During postnatal development, MuSCs enter the G0-phase quiescent state and are maintained in the niche between the basal lamina and sarcolemma (the cell membrane of myofibers). By utilizing highly purified quiescent MuSCs and microarray analyses, we previously identified a GPCR receptor, *calcitonin receptor* (*Calcr*), as a “quiescence” gene in MuSCs (Fukada et al., 2007). *Calcr* is one of seven transmembrane-domain receptors known to regulate homeostasis of the



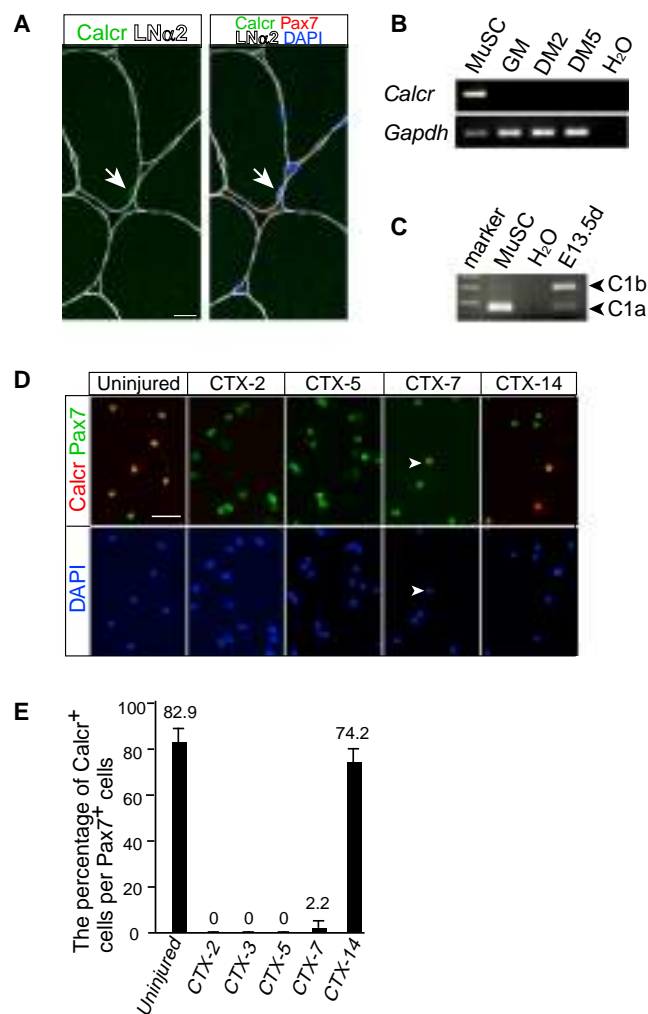


**Figure 1. Expression of Calcitonin Receptor in Muscle Stem Cells**  
(A) Calcr (green) expression was detected on Pax7<sup>+</sup> (red) cells locating beneath the basal lamina (white; LN $\alpha$ 2 laminin  $\alpha$ 2). Arrow indicates a Calcr<sup>+</sup>Pax7<sup>+</sup> MuSC.  
(B) *Calcr* mRNA was detected in freshly isolated MuSCs, but not in MuSCs cultured in growth medium for 3 days (GM) or cells additionally cultured in differentiation medium for 2 (DM2) or 5 days (DM5). As a negative control, the cDNA template was omitted from the reaction (H<sub>2</sub>O).  
(C) The PCR product of C1b mRNA is 111 bp longer than that of C1a. Ladder size markers (100 bp) are shown (marker). Mouse embryo (E13.5) or H<sub>2</sub>O were used as positive and negative controls, respectively.  
(D) Mononuclear cells were prepared from uninjured, regenerating muscle 2, 5, 7, or 14 days after CTX injection, and sorted myogenic cells on glass slides were immediately stained with anti-Calcr (red), Pax7 (green), and DAPI (blue).  
(E) The graph indicates percentages of Calcr<sup>+</sup> cells in Pax7<sup>+</sup> cells during regeneration. Arrowheads indicate Calcr and Pax7 double-positive cells on the seventh day.  
Scale bars, 10  $\mu$ m (A) and 50  $\mu$ m (D).

calcium level in blood (Becker et al., 2002). Osteoclasts abundantly express Calcr receptor, and the Calcr ligand, calcitonin, inhibits osteoclast-mediated bone resorption by disrupting actin organization (Suzuki et al., 1996). Although the relevance of Calcr in the bone system is well studied, the roles of Calcr in other loco-

motive tissues, including skeletal muscle, have not been investigated. In the present study, we aimed to identify the physiological consequences of Calcr depletion in MuSCs using *Calcr* conditional knockout mice and MuSC-specific Cre recombinase-expressing mice.

## RESULTS

### Calcitonin Receptor Is Expressed Exclusively in Quiescent Muscle Stem Cells

In our previous study, we compared the gene expression profile of quiescent MuSCs with those of activated and proliferating MuSCs (myoblasts) and non-myogenic cells (Fukada et al., 2007). We found 63 MuSC-specific quiescence genes in skeletal muscle, and *calcitonin receptor* (*Calcr*) was one of them. As shown in Figure 1A, we confirmed that MuSCs (stained positive for paired box 7 [Pax7]) expressed Calcr at the protein level (Figure 1A). Myogenic cells cultured in a proliferating or differentiating condition, on the other hand, did not show any detectable *Calcr* mRNA (Figure 1B). In rodents, two known major isoforms of *Calcr* mRNA, C1a (osteoclast type, lacking exon 10) and C1b (found in brain), are generated by alternative splicing (Sexton et al., 1993). Here, the MuSCs expressed the C1a isoform (Figure 1C).

Next, we examined the level of Calcr protein expression during regeneration after injury to the muscle by cardiotoxin (CTX) injection. We directly isolated myogenic cells from uninjured and regenerating muscle at six recovery time points. Consistent with our previous study using tissue sections (Fukada et al., 2007), approximately 80% of Pax7<sup>+</sup> cells (indicating MuSCs) from uninjured muscle expressed Calcr (Figures 1D and 1E). However, while Pax7<sup>+</sup> cells from regenerating muscle 2–5 days after CTX injection were completely negative for Calcr, we observed Pax7<sup>+</sup>/Calcr<sup>+</sup> double-positive cells on day 7 post CTX injury (Figure 1D). Approximately 2% of Pax7<sup>+</sup> cells expressed Calcr on day CTX-7, and the percentage had increased significantly to 74.2% on the 14th day after CTX injection (the time point by which most cellular regeneration is presumed to have taken place) (Figure 1E).

### Depleting Calcitonin Receptor Reduces Muscle Stem Cell Pool

We generated *Calcr*-floxed mice (Figures S1A and S1B) and crossed them with *Pax7*<sup>CreERT2/+</sup> mice (Figure 2A) to generate *Pax7*<sup>CreERT2/+</sup>;*Calcr*<sup>flox/flox</sup> mice (cKO). In these mice, genetic inactivation of *Calcr* was induced by tamoxifen (Tm) administration. Because Pax7 is specifically expressed in MuSCs of adult skeletal muscle, the effect of depletion of Calcr by the Tm injection was limited to MuSCs. Two or 5 weeks after the Tm injection into older than 8-week-old cKO mice, less than 1% of the cells expressed Calcr in cKO-MuSCs (Figure 2B; Cont > 80% versus cKO < 1%). mRNA transcriptional depletion was also confirmed in these mice (Figure S1C).

We then investigated the role of Calcr in MuSCs. First, we detected a decreased number of MuSCs after Tm treatment in cKO mice using fluorescence-activated cell sorting (FACS) (Figures 2C and 2D). At 16 weeks after Tm treatment, the MuSC fraction was decreased approximately 35%–80% in

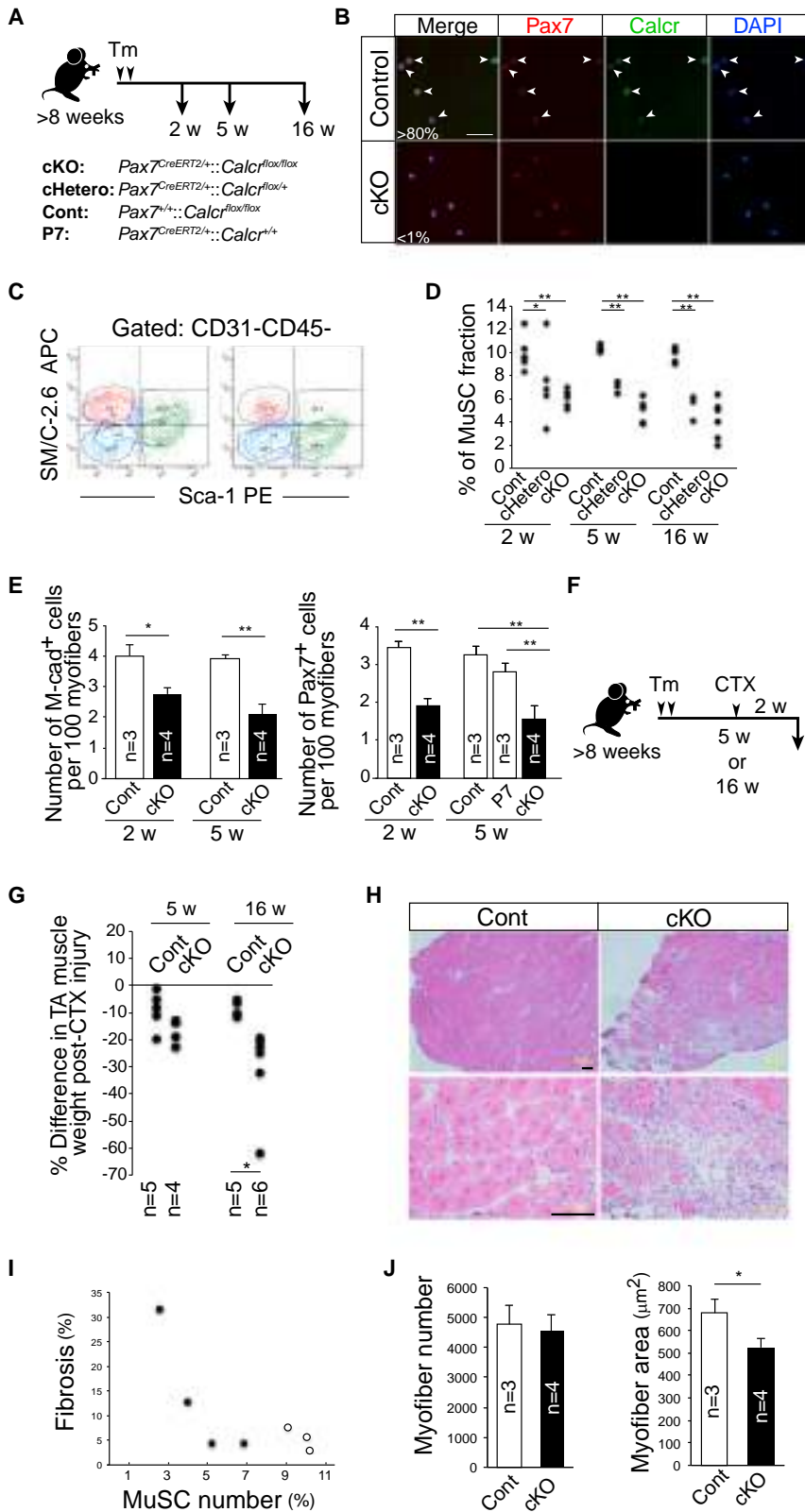


**Figure 2. Calcitonin Receptor Is Necessary to Maintain Adult MuSC Pool**

(A) The cartoon indicates the time course for analysis of mice after tamoxifen (Tm) injection. *Calcr<sup>flax/flax</sup>* (Cont), *Pax7<sup>CreERT2/+</sup>::Calcr<sup>+/+</sup>* (P7), *Pax7<sup>CreERT2/+</sup>::Calcr<sup>flax/+</sup>* (cHetero), and *Pax7<sup>CreERT2/+</sup>::Calcr<sup>flax/flax</sup>* (cKO) mice were used in the following studies. All mice were treated with Tm. (B) Freshly isolated MuSCs were stained with antibodies against Pax7 (red) and Calcr (green). Arrowheads indicate cells positive for both Calcr and Pax7.

(C) FACS profiles of mononuclear cells derived from Cont (left) or cKO (right) muscles 16 weeks after Tm injection. The profiles were gated for CD31<sup>−</sup>CD45<sup>−</sup> fractions.

(D) The y axis shows the percentages of Cont, cHetero, and cKO-MuSC fractions after Tm injection as indicated in the x axis. Each black circle indicates the results of one mouse.

(E) The y axis indicates the numbers of M-cadherin<sup>+</sup> or Pax7<sup>+</sup> cells per 100 cross-sectional TA myofibers in Cont, P7, and cKO after Tm injection at indicated weeks in the x axis.

(F) Time course for analysis of cKO mice after Tm and CTX injection.

(G) The y axis shows the difference in TA muscle weight after regeneration per opposite uninjured muscle. Each black circle indicates the result of one mouse.

(H) H&E staining of TA muscles of Cont or cKO mice treated with Tm after 16 weeks.

(I) Correlation between fibrosis area and MuSC number. Open or closed circles indicate Cont or cKO mice, respectively.

(J) The y axis indicates the number or area of myofibers.

The number of mice used is shown in each graph (E, G, and J). \**p* < 0.05, \*\**p* < 0.01 (D, E, and G). Scale bars, 50 μm (B) and 100 μm (H).

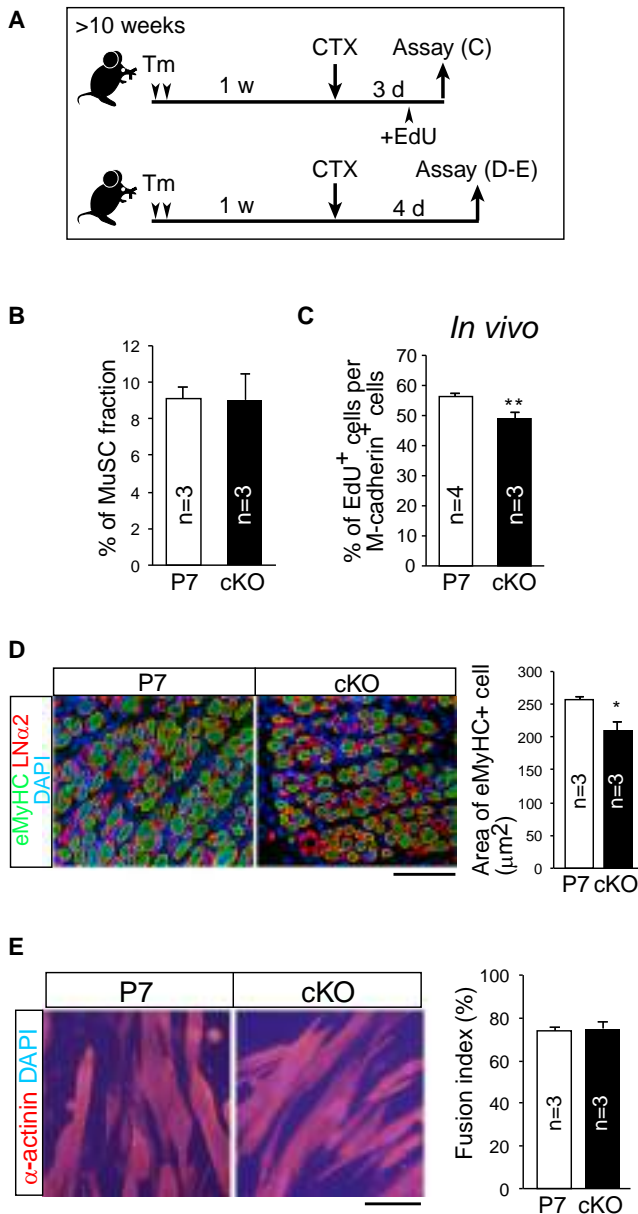


**Figure 3. Loss of Calcr Secondarily Affects MuSC Proliferation**  
(A) Time course for analysis of cKO mice after Tm or CTX injection.  
(B) The y axis indicates the percentage of the MuSC fraction.  
(C) The y axis shows the mean percentage of EdU<sup>+</sup> cells in M-cadherin<sup>+</sup> cells.  
(D) Immunostaining of embryonic myosin heavy chain (eMyHC, green), laminin  $\alpha$ 2 (red), and DAPI (blue) in injured muscle 4 days after CTX injection. The y axis shows the eMyHC<sup>+</sup> area.  
(E) Myotubes were stained with anti-sarcomeric  $\alpha$ -actinin antibody (red) and DAPI (blue). The y axis shows the percentage of fusion index.  
Scale bars, 100  $\mu$ m (D and E).

cKO mice compared with the control mice. Heterozygous mice (*Pax7*<sup>CreERT2/+::Calcr<sup>flox/+</sup>, cHetero) also showed a decrease in the MuSC fraction, although the decrease in the MuSC number was less than that of cKO mice (Figure 2D). Moreover, we quantified the number of MuSCs by immunohistochemical studies,</sup>

providing further evidence that the quantity of MuSCs decreased in cKO mice (Figure 2E).

The significant decrease in the MuSC pool affected the skeletal muscle weight following injury (Fukada et al., 2011). We measured the muscle weight 2 weeks after CTX injection (Figure 2F). Five weeks after Tm injection, cKO mice demonstrated only a tendency toward a smaller muscle weight recovery (Figure 2G). The cKO group 16 weeks post Tm injection exhibited a significantly smaller muscle weight recovery, though there was individual variation. For example, one mouse recovered only 40% of the muscle weight on the injured side compared to the contralateral side, but another recovered 70% (Figure 2G). The reduction in MuSC numbers correlated with the weight loss and increased fibrotic area (Figures 2H and 2I; Figure S2). When the number of MuSCs retained was greater than 5% of all muscle-derived mononuclear cells in cKO mice, as analyzed by FACS, the mice did not exhibit an increase in fibrotic area nor a decrease in myofiber number. The myofiber area, on the other hand, consistently decreased in all cKO mice, regardless of the individual variance in muscle weight (Figure 2J).

### Loss of Calcitonin Receptor Affects Proliferation of Muscle Stem Cells

As shown in Figure 1, proliferating myoblasts did not express Calcr. However, it is possible that the absence of Calcr in MuSCs exerts a secondary effect on the regenerative processes. In order to further examine the effect of Calcr loss in MuSCs after injury, we investigated mice 1 week after Tm injection because these mice still have a similar number of MuSCs as the control mice, while Calcr mRNA was significantly depleted (Figures 3A and 3B; Figure S1C).

The proliferation of MuSC-derived myoblasts in cKO mice, visualized using EdU and M-cadherin antibodies, was inferior to that of control myoblasts (Figure 3C). The area of newly generated myotubes, as shown in Figure 3D by immunostaining, also decreased in cKO samples. We then tested the cellular capacity to form myotubes ex vivo by staining and found, in contrast, that there was no morphological difference between the control group and the cKO group (Figure 3E). The results suggest that the presence of Calcr in MuSCs is secondarily necessary for muscle regeneration following injury.

### Calcitonin Receptor Signaling Maintains Quiescent State via cAMP/PKA Pathway

Both quiescent and undifferentiated states are characteristic of adult stem cells, and the impairment of these states results in exhaustion of the adult stem cell pool, including MuSCs (Bjornson et al., 2012; Cheung et al., 2012; Imayoshi et al., 2010; Mourikis et al., 2012). In addition, consistent with our previous data (Fukada et al., 2007), Calcr ligands (elcatonin and calcitonin) inhibited the activation of quiescent MuSCs ex vivo (Figure 4A; Figure S3A). This effect was Calcr dependent because the inhibition was not observed in cKO-MuSCs (Figure 4A). It could be speculated that the impairment of the quiescent or undifferentiated condition in cKO-MuSCs was attributable to the loss of the MuSC pool and reduced proliferation. Hence, we studied the in vivo dormancy of cKO-MuSCs by quantifying the expression level of Ki67 (a non-quiescence marker) in freshly isolated

MuSCs. As shown in Figure 4B, the expression of *Ki67* mRNA was higher in the order of cKO, cHetero, and control MuSCs 2 weeks after the Tm injection. Expression of non-quiescence marker *Ki67* protein was higher in cKO-MuSCs compared to control cells relatively soon after the Tm injection (Figure 4C). The expression levels of several other cell-cycle-related genes, *Ccna2*, *Ccnd1*, and *Skp2*, were also elevated in cKO-MuSCs 2 weeks post Tm injection. (Figure 4D).

The increase in expression of *Ki67*/cell-cycle-related genes (Figure 4D) and in vivo decrease in proliferation (Figure 3C) may seem contradictory. In cKO mice, about 60% of *Ki67*<sup>+</sup> cells were positive for EdU (Figures 4E and 4F), and at early analyses (24-hr culture), the number of EdU<sup>+</sup> cells in cKO-MuSC was higher than that of the control mice (Figure 4G). However, consistent with in vivo results (Figure 3C), after 72-hr culture, the number of proliferating EdU<sup>+</sup> cells in cKO mice had decreased (Figure 4H). Collectively, it can be suggested that MuSCs escaped dormancy in the absence of *Calcr* and that the loss of the *Calcr*-mediated mechanism secondarily affects the proliferation of MuSCs-derived daughter cells, myoblasts.

Next, we sought to reveal the downstream pathway of *Calcr*. *Calcr* is a GPCR and uses *Gsα* protein, which increases the intracellular level of cAMP in osteoclasts (Suzuki et al., 1996). We confirmed that when *Calcr* was retrovirally expressed in myoblasts, the ligand raised the intracellular cAMP levels in *Calcr*-expressing C2C12 cells (Figure 4I). To further clarify the effects of cAMP as a downstream initiator of *Calcr* signaling, we tested two cAMP activators, dibutyl-AMP ([dbcAMP] an analog of cAMP) and forskolin (an activator of adenylate cyclase), and both cAMP activators were found to suppress the activation of quiescent MuSCs ex vivo (Figure 4J; Figure S3B). In addition, the expressions of cell-cycle-related genes were suppressed in 24-hr-cultured MuSCs treated with elcatonin or dbcAMP (Figure 4K).

To further study the downstream effects on cAMP, either a protein kinase A (PKA)-specific cAMP analog (6-bnz-cAMP) or an exchange protein directly activated by cAMP (Epac)-specific cAMP analog (8-CPT-cAMP) targets of cAMP (de Rooij et al., 1998) was applied to freshly isolated MuSCs. As shown in Figure 4J, only the PKA-specific analog inhibited the activation (EdU uptake) of MuSCs. Pretreatment with a PKA-specific inhibitor negated the effect of *Calcr* signaling in freshly isolated MuSCs cultured with elcatonin, a *Calcr* ligand (Figure 4L). Hence, these results suggest that the *Calcr*-cAMP-PKA pathway maintains the quiescent state of MuSCs in adult skeletal muscle.

### Calcitonin Receptor Signaling Has No Impact on Myogenic Differentiation

We next examined the effect of *Calcr* signaling on myogenic differentiation. In contrast to the elevated *Ki67* expression level, freshly isolated cKO-MuSCs exhibited no significant elevation of myogenic genes (*Pax7*, *Myf5*, *MyoD*, or *myogenin*) compared to the control MuSCs (Figure 5A). In vivo and ex vivo protein expressions of *MyoD* also did not differ between control and cKO-MuSCs (Figure 5B; Figure S4A). Furthermore, although a ligand-dependent suppression of proliferation was observed in retrovirally *Calcr*-expressing primary myoblasts (Figure 5C),

neither *MyoD* expression nor myotube formation was inhibited by *Calcr* signaling in the primary myoblasts (Figures 5D and 5E) and in a C2C12 cell line (Figures S4B and S4C). Moreover, no evidence of accelerated myogenic differentiation was observed in cKO mice carrying a Cre-inducible yellow fluorescent protein (YFP) reporter gene (cKO-YFP; *Pax7*<sup>CreERT2/+</sup>; *Calcr*<sup>flox/flox</sup>; *Rosa26R*<sup>YFP/YFP or YFP/+</sup>). In this model, YFP<sup>+</sup> myofibers increase when a YFP-labeled MuSC differentiates and fuses with a myofiber. We found that the number of YFP<sup>+</sup> myofibers in cKO-YFP mice was similar to that of the control mice (YFP; *Pax7*<sup>CreERT2/+</sup>; *Calcr*<sup>+/+</sup>; *Rosa26R*<sup>YFP/YFP or YFP/+</sup>) (Figure 5F).

If the number of cells in the MuSC pool was decreased by a mechanism other than premature myogenic differentiation, it can be assumed that are two other ways by which the cKO-MuSC pool decreases. One is transdifferentiation of MuSCs into non-myogenic cells, and the other is cell death. As shown in Figure 5G, although almost all YFP<sup>+</sup> mononuclear cells in control and cKO-YFP mice expressed *Pax7*, apoptotic cells could be detected more frequently in cKO mice (Figure 5H). We also observed apoptosis in *Ki67*<sup>+</sup> cells only in cKO-MuSCs (Figure 5I). Thus, *Calcr* signaling is necessary to maintain the quiescent state of adult MuSCs, but it is not necessary to maintain the undifferentiated state (Figure 5J).

### Calcitonin Receptor Signaling Inhibits Emergence of Muscle Stem Cells from Niche

During the study using the YFP-reporter mice, MuSCs residing within the interstitial areas were unexpectedly observed in cKO-YFP mice 5 weeks after Tm injection, though in small numbers (approximately 4%) (Figure 6). Such cells had not been reported previously in normal mice. Since MuSCs were originally defined by their location of residence (Mauro, 1961), this result indicates that MuSCs moved from their niches to the interstitial areas in a steady state when *Calcr* is absent.

To examine the effect of *Calcr* signaling on the location change of MuSCs, we conducted a single-myofiber culture that allowed observation of the MuSCs locating beneath the basal lamina. At the beginning of culture, all MuSCs were located beneath the basal lamina (not shown), but approximately half of the MuSCs had emerged from their niche and located outside of the basal lamina within 24 hr of culture. Although cell division of the relocated MuSCs was not observed within the 24 hr, adding *Calcr* ligand significantly suppressed their movement to the outside of the basal lamina from the surface of myofibers (Figures 7A–7C).

We then similarly examined the effects of *Calcr* signaling on MuSC relocation. Although PKA and Epac activators exerted different effects on MuSC activation in the EdU-uptake assay (Figure 4J), dbcAMP, a PKA activator, and an Epac activator exerted effects similar to that of elcatonin (Figure 7C). To further study the contribution of PKA or Epac to the *Calcr* signaling effects, isolated single myofibers were pretreated with each inhibitor and then pulsed with elcatonin for 1 hr. After removing reagents, single myofibers were cultured for 24 hr (Figure 7D). The elcatonin treatment significantly inhibited the emergence of MuSCs from their niches (Figures 7E and 7F). Both PKA and Epac inhibitors rescued the suppressive effect of elcatonin



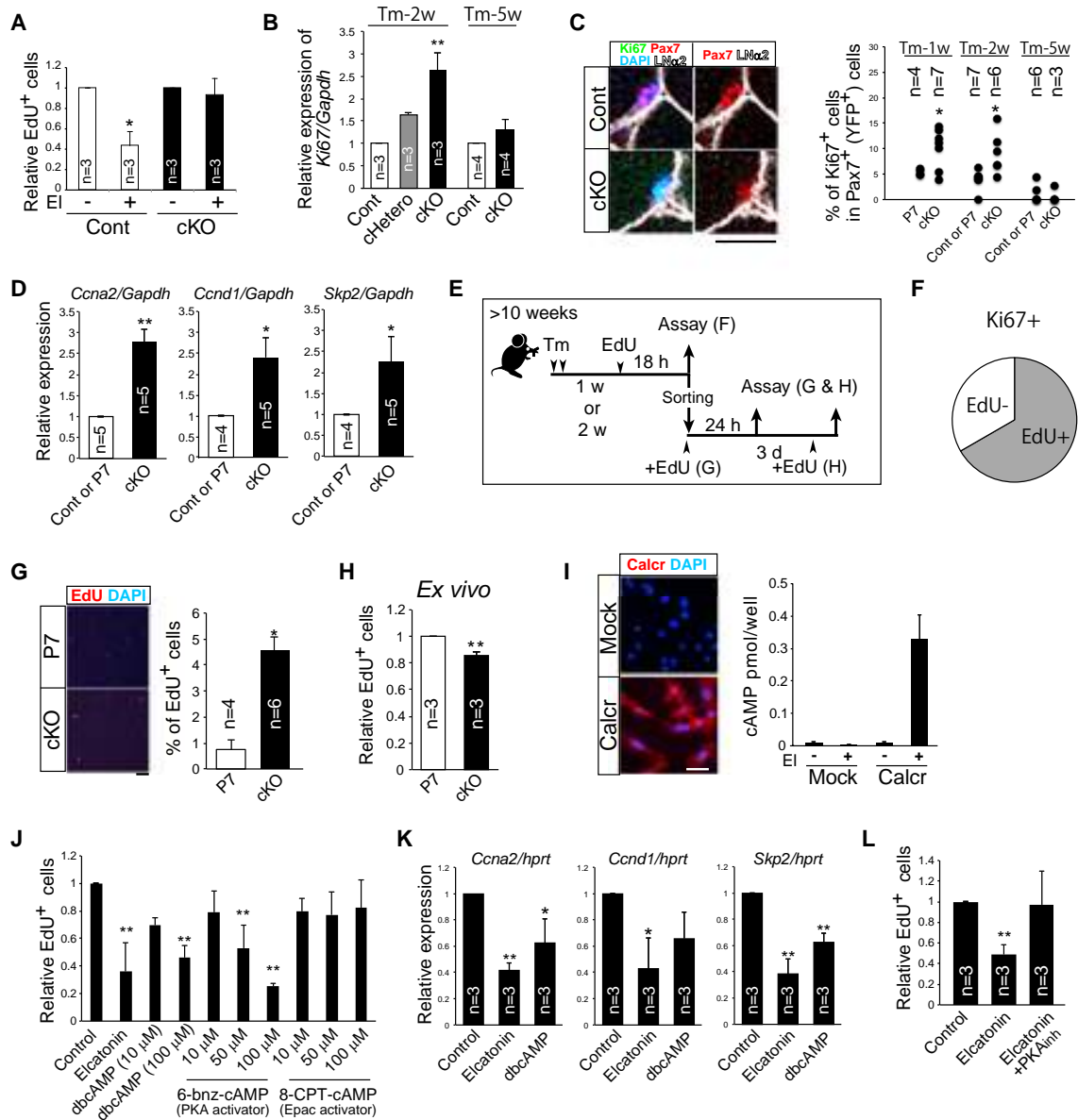


**Figure 4. Calcitonin Receptor Signaling Regulates Quiescence of Muscle Stem Cells via cAMP/PKA Pathway**

(A) Relative percentage of EdU<sup>+</sup> cells in freshly isolated MuSCs cultured for 2 days with or without elcatonin (El). The cells were prepared from Cont (white) or cKO (black) mice 2 weeks after Tm injection.

(B) Relative expression of *Ki67* mRNA in freshly isolated MuSCs derived from Cont (white), cHetero (gray), or cKO (black) mice 2 weeks or 5 weeks after Tm injection.

(C) TA muscle sections were stained with antibodies against *Ki67* (green), *Pax7* (red), and laminin  $\alpha 2$  (white; LN $\alpha 2$ ). The graph represents the proportion of *Ki67*<sup>+</sup> cells in *Pax7*<sup>+</sup> cells in Cont, P7, or cKO mice 1–5 weeks after Tm injection.

(D) Relative expressions of *Ccna2*, *Ccnd1*, and *Skp2* mRNA in freshly isolated MuSCs were compared in Cont, P7 (white), or cKO (black) mice 2 weeks after Tm injection.

(E) Time course for analysis of cKO mice after Tm injection.

(F) Percentage of EdU<sup>+</sup> cell in *Ki67*<sup>+</sup> cells in cKO mice 1 week after Tm injection.

(G) Percentage of EdU<sup>+</sup> cells after culturing ex vivo for 24 hr.

(H) Percentage of EdU<sup>+</sup> cells after culturing ex vivo for 3 days.

(I) C2C12 cells were infected with Calcr-carrying (Calcr) or control (Mock) retrovirus, and the infected cells were sorted by GFP fluorescence and then stained with antibody against Calcr (red). The graph indicates the amount of cAMP in control or Calcr-expressing C2C12 cells treated or untreated with elcatonin (El); n = 3 in each group.

(J) Relative numbers of EdU<sup>+</sup> cells in freshly isolated MuSC cultured for 2 days in the absence or presence of elcatonin, dbcAMP, 6-bnz-cAMP (PKA activator), or 8-CPT-cAMP (Epac activator) at indicated concentrations; n = 3–4 in each group.

(legend continued on next page)

(Figures 7E and 7F). Furthermore, a larger number of cKO-MuSCs emerged from the niche than control MuSCs (Figure 7G shows the ratio to the control).

In this myofiber culture model, MuSCs are said to escape from the niche and then start to proliferate (Siegel et al., 2009). We did find, however, that Ki67<sup>+</sup> cells in cKO-MuSCs remained beneath the basal lamina (Figure 4C). We believe that the escapes from the niche and from quiescence are not sequential events. Our present study demonstrated that Calcr signaling has two separate roles: Calcr signaling inhibits the escape of MuSCs from quiescence by the cAMP-PKA pathway, and Calcr signaling inhibits the emergence of MuSCs from the niche by the cAMP-PKA and cAMP-Epac pathway (Figure 7H).

## DISCUSSION

Our current study highlights the roles of calcitonin receptors (Calcrs) in MuSCs. Our results indicate that Calcr signaling holds the MuSCs in a quiescent state and in the niche. Calcr signaling, on the other hand, exerted no effect in the undifferentiated state of MuSCs. Further, apoptotic cells were observed in Ki67<sup>+</sup> cKO-MuSCs. As a result, the number of MuSCs decreased, followed by a reduction of muscle weight after post-injury regeneration. There was a discrepancy between the upregulated cell cycle genes and a decrease in the MuSC pool. Similar results for *Dicer*-mutated or Notch-signaling-mutated mice have been reported, however (Bjornson et al., 2012; Cheung et al., 2012; Fukada et al., 2011; Mourikis et al., 2012). For example, Mourikis et al. (2012) indicated that *Rbp-J* knockout MuSCs expressed Ki67, but the majority of them terminally differentiated without passing through the cell cycle S-phase. In *Dicer*-mutated MuSCs, the impaired quiescence resulted in cell death by apoptosis. Collectively, these abnormal quiescent states might affect subsequent MuSC survival.

We propose that Calcr-cAMP-PKA or Epac signaling is an “active” signaling pathway for maintaining the quiescence of MuSCs. Our results strongly suggest that G0-quiescent adult stem cells require active signaling pathways to maintain their pool. Although it is well known that increasing the cAMP concentration inside a cell results in growth inhibition in many types of cells (Stork and Schmitt, 2002) or arrest of the reversible cell cycle in a few types of cells (Dransfield et al., 2001; L’Allemain et al., 1997; Stambrook and Velez, 1976), the relationship between the quiescent state of adult stem cells and the cAMP pathway has largely been unknown. Two recent studies imply that the GPCR-cAMP pathway may be a common signaling pathway to maintain some types of adult stem cells. Specifically, Chagin et al. (2014) reported Gs $\alpha$  and Gq/11 $\alpha$  proteins play an essential role in maintaining quiescent stem-like chondrocytes via parathyroid hormone-related protein receptors (PPRs). Gs $\alpha$  is a heterotrimeric subunit that activates adenylate

cyclase and is activated by GPCRs like PPRs and Calcr that increase cAMP. Another study demonstrated that the abundant expression of GPCRs in quiescent NSCs and their activation can be inhibited by S1P and PGD<sub>2</sub> (Codega et al., 2014). Both S1P and PGD<sub>2</sub> have the potential to increase intracellular cAMP levels (Davaile et al., 2000; Regan et al., 1994); thus, GPCR-mediated cAMP accumulation may be a common mechanism to regulate the dormancy of adult stem cells in some tissues.

Recently, Sato et al. reported that both miR-195 and miR-497 induce cell cycle arrest by targeting the cell cycle genes *Cdc25* and *Ccnd* (Sato et al., 2014). As shown in the present study, the Calcr-cAMP pathway inhibited the expression of *Ccna2*, *Ccnd1*, and *Skp2*. *Ccna2*, a gene with the CREB-binding sequence (Kamiya et al., 2007), is commonly suppressed in adult stem cells (Cheung and Rando, 2013). CREB is the major target of PKA, and Calcr signaling activates CREB transcriptional activity. *Ccnd1* is also a well-known target of CREB. On the other hand, the expressions of cyclin-dependent kinase inhibitors (*p21*, *p27*, and *p57*) and *Spry1* (one critical regulator for maintaining MuSCs) did not change in cKO-MuSC (Figure S5). Although we did not specifically show that suppressing cyclin-related gene expression is required to maintain stem cells in a quiescent state, expression of Calcr/cAMP/PKA-mediated cyclin-related genes (*Ccna2*, *Ccnd1*, *Skp2*, etc.) is a potential mechanism by which MuSCs are maintained in a quiescent state.

One of our unexpected results was the observation of MuSCs in the interstitial space. Because we used a lineage-tracing model, the result clearly indicated that MuSCs had emerged from their niche. The small numbers of interstitial MuSCs implies that they either undergo cell death or return to sublaminal niches. While both phenomena are possible, the precise mechanism is still unknown. Notably, the discovery of the unusual residence of MuSCs suggests the existence of active signaling pathways involved in keeping MuSCs in their niches. Intriguingly, Jockusch and Voigt (2003) stated that MuSCs can exit from their niche in undamaged muscle. They transplanted intact skeletal muscle tissue by differentially labeling the graft, host skeletal myofibers, and MuSCs (which they refer to as myogenic precursor cells) and observed that donor-derived MuSCs migrated toward and fused with the host myofibers and vice versa (Jockusch and Voigt, 2003), although it took more than 7 weeks before the fused myofibers were observed. Further, we did not find interstitial YFP<sup>+</sup> cells in *Pax7<sup>CreERT2/+</sup>;Calcr<sup>+/+</sup>;Rosa26R<sup>YFP</sup>* mice in high quantity, demonstrating that very few MuSCs move from one myofiber to another in a physiological condition. Our results demonstrate the necessity of external active signaling pressure to prevent the exodus of MuSCs from their niche.

Calcitonin is the best-characterized ligand of Calcr, but there is a difference between Calcr null and calcitonin null mice. The

(K) Relative expressions of *Ccna2*, *Ccnd1*, and *Skp2* mRNA were compared among non-, elcatonin-, or dbcAMP-treated MuSCs freshly isolated after culturing for 24 hr.

(L) Relative numbers of EdU<sup>+</sup> cells in freshly isolated MuSCs cultured for 2 days in the absence or presence of elcatonin and PKA inhibitor (20  $\mu$ M). The y axis indicates means with  $\pm$  SE (n = 3).

Scale bars, 10  $\mu$ m (C) and 50  $\mu$ m (G and I). The number of mice used is shown in each graph (A–D, G, H, K, and L). \*p < 0.05, \*\*p < 0.01 (A–D, G, H, and J–L).

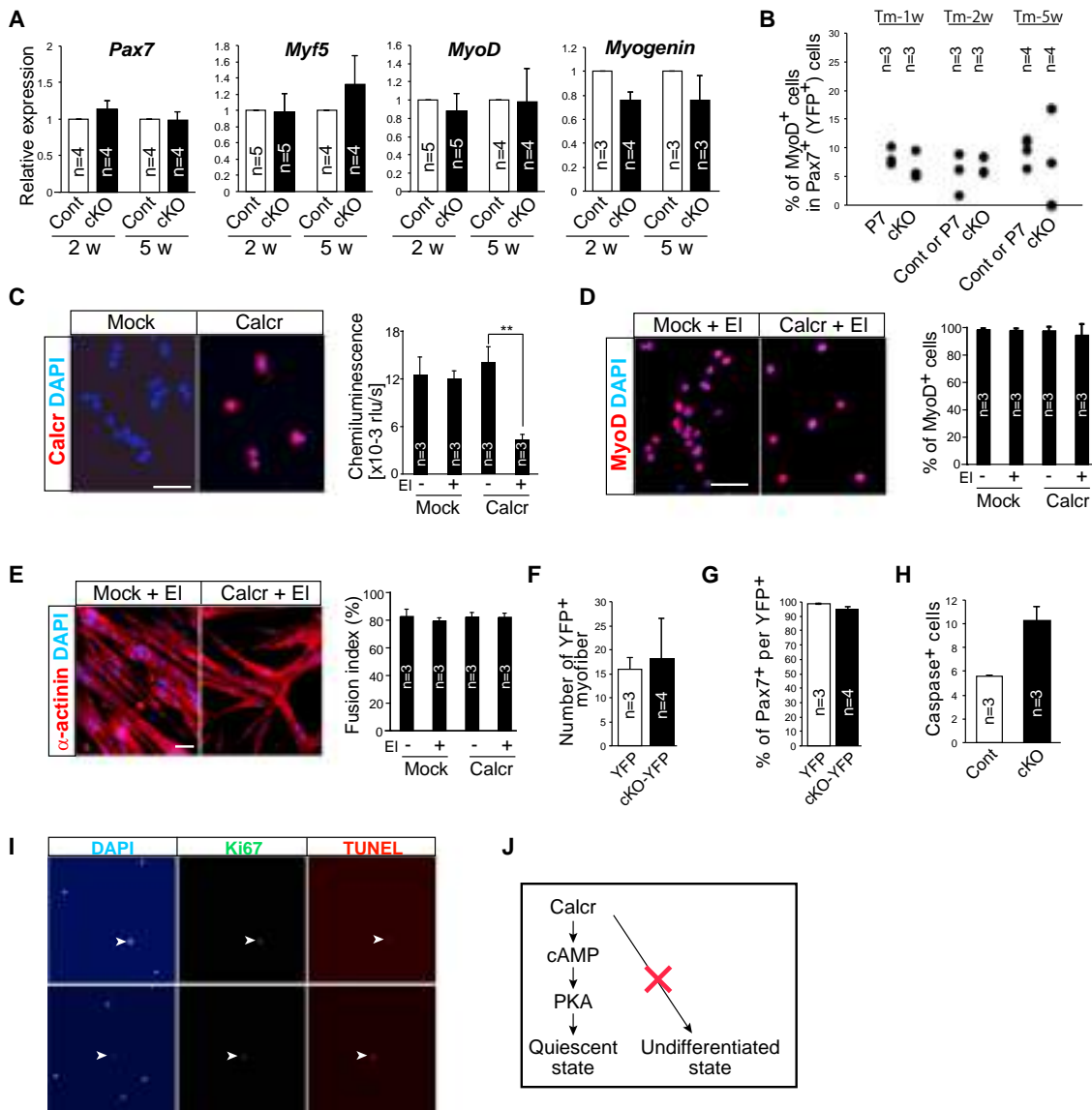


**Figure 5. Calcinonin Receptor Signaling Has No Impact on Expression and Differentiation of Myogenic Genes**

(A) Relative expressions of *Pax7*, *Myf5*, *MyoD*, and *myogenin* mRNA in freshly isolated MuSCs derived from Cont (white) or cKO (black) 2 or 5 weeks after Tm injection.

(B) The proportion of MyoD<sup>+</sup> cells in Pax7<sup>+</sup> (or YFP<sup>+</sup>) cells in Cont, P7, or cKO mice 1–5 weeks after Tm injection.

(C) The expression of Calcr (red) in control primary myoblasts (Mock) or Calcr vector-infected cells (Calcr). Nuclei were stained with DAPI (blue). The graph shows the frequency of BrdU<sup>+</sup> cells when each type of cell was cultured with or without elcatonin (EI) for 24 hr. \*\*p < 0.01.

(D and E) The frequency of MyoD<sup>+</sup> cells (D) or fusion index (E) in control (Mock) or Calcr vector-infected cells (Calcr) treated with or without elcatonin (EI). The graph shows the percentages of MyoD<sup>+</sup> cells or multinuclear cell per total nuclei. Myotubes were stained with anti- $\alpha$ -actinin (red).

(F) Numbers of YFP<sup>+</sup> myofibers in YFP (white) or cKO-YFP (black) mice 5 weeks after Tm injection.

(G) Frequency of Pax7<sup>+</sup> cells per YFP<sup>+</sup> mononuclear cells in YFP (white) or cKO-YFP (black) mice 5 weeks after Tm injection.

(H) Apoptotic cells (caspase<sup>+</sup>) were measured by FACS in freshly isolated MuSCs derived from Cont (white) or cKO (black) 2 weeks after Tm injection.

(I) Apoptotic cells (TUNEL<sup>+</sup>) in Ki67<sup>+</sup> cells of cKO-MuSC 2 weeks after Tm injection. Arrowheads indicate Ki67<sup>+</sup>TUNEL<sup>+</sup> cells.

(J) A model of calcitonin receptor signaling in a quiescent or undifferentiated state in MuSCs. The number of mice used is shown in each graph. Scale bars, 50  $\mu$ m (C–E and I). Values are means  $\pm$  SE.

Calcr null condition is embryonically lethal (Dacquin et al., 2004), but calcitonin null mice are viable (Hoff et al., 2002), indicating that Calcr has other ligands besides calcitonin. In fact, calcitonin receptor and receptor-activity-modifying proteins can serve as

receptors for amylin, a member of the calcitonin family co-secreted with insulin by pancreatic beta cells (Christopoulos et al., 1999). Amylin inhibits the activation of quiescent MuSCs ex vivo just like calcitonin (Figure S6). Moreover, Katafuchi

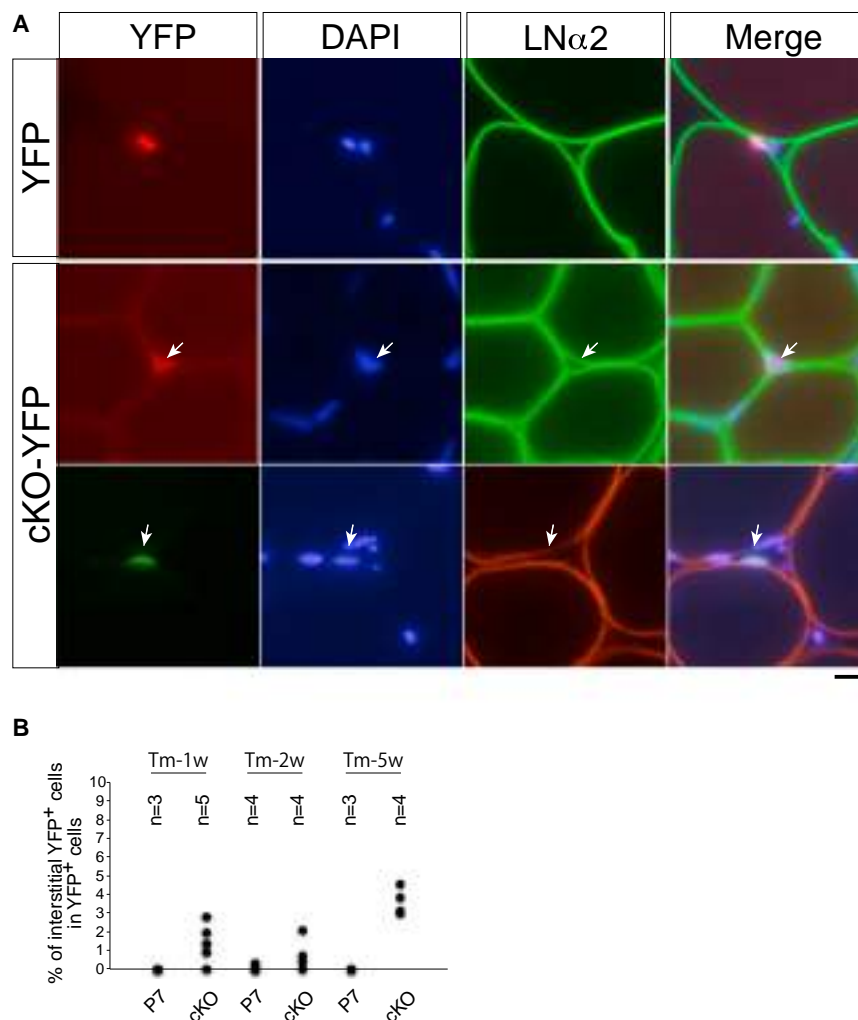


**Figure 6. Detection of Interstitial Muscle Stem Cells in Calcr-Depleted Mice**

(A) All YFP<sup>+</sup> cells were detected beneath the basal lamina in control (YFP) mice, but cKO-YFP mice have YFP<sup>+</sup> cells located outside the basal lamina 5 weeks after Tm injection. Arrow indicates interstitial YFP<sup>+</sup> cells. Scale bar, 10  $\mu$ m.

(B) Percentage of interstitial YFP<sup>+</sup> cells 1–5 weeks after Tm injection. The number of mice used is shown in the graph.

489 are critical regulators, studies on the transcriptional regulation locus of *Calcr* genes will lead to in-depth understanding of molecular mechanisms in the quiescence, activation, and self-renewal of MuSCs.

In conclusion, we showed that *Calcr* plays two roles in sustaining the muscle stem cell pool, specifically, the regulation of dormancy and the location of stem cells. Although there still may be other *Calcr* ligands to be discovered, the blood level of the most potent ligand known, calcitonin, decreases during aging (Shamoni et al., 1980). The expression of *Calcr* on osteocytes also disappears with age (Gooi et al., 2014). In the elderly population, it is relatively common to observe sarcopenia, a significant loss of skeletal muscle mass. Age-related loss of bone density is also well-known, specifically in postmenopausal woman, and *Calcr* is a treatment target for osteoporosis. *Calcr* itself and its signaling pathway could become a shared molecular target in preventing age-related functional decline in the musculoskeletal system.

## EXPERIMENTAL PROCEDURES

### Generation of *Calcr*<sup>fllox</sup> Mice

A conditional knockout vector for *Calcitonin receptor* (PRPG00131 B F08) was purchased from KOMP (Knockout Mouse Project: <https://www.komp.org/>). ENSMUSE00000136685 (exon 6) and ENSMUSE00000136688 (exon 7) were floxed by the loxP sequence (Figure S1). The linearized targeting vector was introduced into embryonic stem cells (Fujihara et al., 2013). Colonies that had undergone homologous recombination were detected by PCR analysis with specific primers provided by KOMP. Mice with the *calcitonin receptor flox* allele were generated in our facility. The neomycin cassette was removed by crossing with CAG-Flip transgenic mice (Rodríguez et al., 2000).

### Mice

*Pax7*<sup>CreERT2/+</sup> (Lepper et al., 2009) and *Rosa26*<sup>EYFP/+</sup> (Srinivas et al., 2001) mice were obtained from Jackson Laboratories. *Pax7*<sup>CreERT2/+</sup> mice were injected twice (24 hr apart) intraperitoneally with 200–300  $\mu$ l Tm (20 mg/ml; Sigma-Aldrich #T5648) dissolved in sunflower seed oil 5% ethanol (Mourikis et al., 2012). Control mice were also treated with Tm in this study. All procedures for experimental animals were approved by the Experimental Animal Care

et al. (2003) have identified another calcitonin receptor ligand named calcitonin receptor-stimulating peptide (CRSP) in the pig. Although a gene corresponding to CRSP has not been found in humans and mice, it is possible there is still an unidentified *Calcr* ligand that functions in MuSCs.

In addition to coding RNA, non-coding RNA plays essential roles in stem cells. One non-coding RNA, miRNA, requires Dicer for its biogenesis. By utilizing conditional *Dicer* mutant mice, Cheung et al. (2012) found the loss of the MuSC pool in *Pax7*<sup>CreERT2/+</sup>::*Dicer*<sup>fllox/fllox</sup> mice. They also identified a quiescent MuSC-specific miRNA, mir-489. Notably, mir-489 is located in intron 4 of the mouse *calcitonin receptor* gene, which was not affected in our mouse construct. Along with mRNA expression of *Calcr*, mir-489 also decreased when MuSCs are activated. Furthermore, Cheung et al. (2012) also identified the target of mir-489, *Dek*. In our analyses, mir-489 expression in *Calcr* cKO-MuSCs was approximately 40% of that in control MuSCs, though *Dek* expression was not changed significantly (Figure S7). *Calcr* signaling directly inhibited activation and emergence of MuSCs from niches ex vivo. Thus, the phenotype of cKO most likely did not depend on mir-489. Because both *Calcr* and mir-



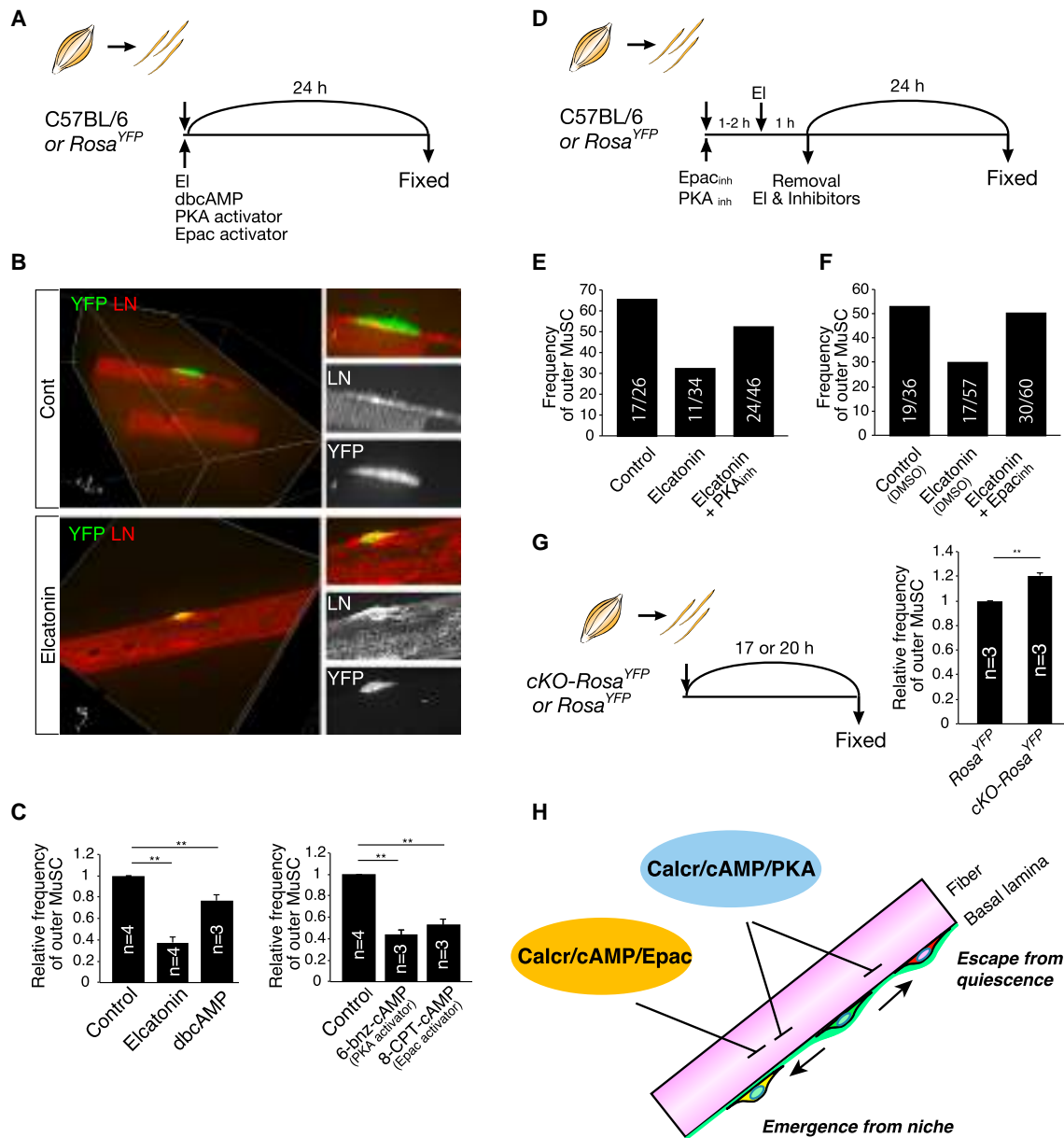


**Figure 7. Calcinonin Receptor Signaling Suppresses Emergence of Muscle Stem Cell from the Niche**

(A and B) Isolated single myofibers were cultured with or without elcatonin or each activator (100  $\mu$ M) for 24 hr in GM (A) and then fixed and stained with anti-YFP ( $Rosa26R^{YFP}$ ), Pax7 (C57BL/6), and LN (laminin) (B).

(C) Relative numbers of MuSCs locating outside the LN after culturing with or without elcatonin, dbcAMP (100  $\mu$ M), 6-Bnz-cAMP (100  $\mu$ M), or 8-CPT-cAMP (100  $\mu$ M) for 24 hr in GM.

(D) Isolated single myofibers were pretreated with or without PKA inhibitor or Epac inhibitor for 1–2 hr. The single myofibers were additionally cultured with or without elcatonin for 1 hr. After removing each inhibitor and elcatonin, all myofibers were cultured in GM for 24 hr and then fixed and stained with anti-YFP ( $Rosa26R^{YFP}$ ), Pax7 (C57BL/6), and LN antibodies.

(E and F) Frequency of MuSCs locating outside the laminin after culturing with or without elcatonin, PKA inhibitor (E; 20  $\mu$ M), or Epac inhibitor (F; 10  $\mu$ M) for 24 hr in GM. Similar results were obtained by independent experiments.

(G) Isolated single myofibers derived from control ( $Rosa26R^{YFP}$ ) and cKO ( $cKO-Rosa26R^{YFP}$ ) mice were cultured in GM for 17–20 hr and then fixed and stained with anti-YFP and -LN antibodies. The graph indicates the frequency of MuSCs locating outside the laminin in control ( $Rosa26R^{YFP}$ ) and cKO ( $cKO-Rosa26R^{YFP}$ ) mice.

(H) Putative roles of Calcr in muscle stem cells.

The number of mice (C and G) or MuSCs (E and F) analyzed is shown in the graph. \*\*p < 0.01 (C and G).

and Use Committee at Osaka University. PCR-based genotyping was performed with the DNA using the primers listed in Table S1.

### Muscle Injury

Tibialis anterior muscles were damaged by injecting 2.5  $\mu$ l per g of mouse body weight of 10  $\mu$ M CTX (Wako Pure Chemical Industries) in saline. When mononuclear cells were prepared from injured muscles, CTX was injected into tibialis anterior (50  $\mu$ l), gastrocnemius (150  $\mu$ l), and quadriceps femoris (100  $\mu$ l) muscles.

### Real-Time PCR

Total RNA was extracted from sorted or cultured cells using a QIAGEN RNeasy Mini Kit according to the manufacturer's instructions (QIAGEN) and then reverse-transcribed into cDNA using a QuantiTect Reverse Transcription Kit (QIAGEN). Specific forward and reverse primers for optimal amplification in real-time PCR of reverse transcribed cDNAs are listed in Table S1.

### Muscle Fixation and Histological Analysis

Isolated tibialis anterior muscles were frozen in liquid nitrogen-cooled isopentane (Wako Pure Chemicals Industries). In order to prevent YFP protein leaking, these muscles were fixed in 4% paraformaldehyde (PFA) for 30 min, immersed sequentially in 10% and 20% sucrose/PBS, and then frozen in isopentane cooled with liquid nitrogen. Transverse cryosections (10  $\mu$ m) were stained with H&E.

### Immunohistochemistry

For immunohistochemical studies, transverse cryosections (6  $\mu$ m) were fixed with 4% PFA for 10 min. After blocking with 5% skim milk, sections were stained with primary antibodies. Detailed information on antibodies used in this study is listed in Table S2. In order to block endogenous mouse IgG, a M.O.M. kit (Vector Laboratories) was used for Pax7 or eMyHC staining. After the first staining at 4°C overnight, sections were reacted with secondary antibodies (Molecular Probes). The signals were recorded photographically using a confocal laser scanning microscope system TCS-SP5 (Leica Microsystems) or a fluorescence microscope BX51 (Olympus) equipped with a DP70 CCD camera (Olympus).

### Preparation and FACS Analyses of Skeletal-Muscle-Derived Mononuclear Cells

Mononuclear cells from uninjured limb muscles were prepared using 0.2% collagenase type II (Worthington Biochemical). Mononuclear cells derived from skeletal muscle were stained with FITC-conjugated anti-CD31, -CD45, PE-conjugated anti-Sca-1, and biotinylated-SM/C-2.6 (Fukada et al., 2004) antibodies. Cells were then incubated with streptavidin-labeled allophycocyanin (BD Biosciences) on ice for 30 min and resuspended in PBS containing 2% FBS and 2  $\mu$ g/ml propidium iodide. Cell sorting was performed using a FACS Aria II flow cytometer (BD Immunocytometry Systems). In the case of Rosa26<sup>EYFP</sup> mice, MuSCs were isolated by YFP fluorescence without any staining.

### Cytospin and Immunocytochemistry

FACS-sorted cells were collected on glass slides by Cytospin (Thermo Fisher Scientific) and then fixed with 4% PFA for 10 min. Cultured cells were also fixed with 4% PFA for 10 min. After permeabilization by 0.25% Triton X-100 and blocking with 5% skim milk, the cells were stained with primary antibodies at 4°C overnight and then reacted with secondary antibodies (Molecular Probes).

### Cell Culture

MuSCs were cultured in a growth medium (GM) of high-glucose DMEM ([DMEM-HG] Sigma-Aldrich) containing 20% FBS (Cell Culture Bioscience, Nichirei Biosciences), 2.5 ng/ml bFGF (PeproTech), and penicillin (100 U/ml)-streptomycin (100  $\mu$ g/ml) (Gibco BRL) on culture dishes coated with Matrigel (BD Biosciences). Differentiation was induced in differentiation medium (DM) containing DMEM-HG, 5% horse serum, and penicillin-streptomycin for 3–4 days.

### EdU-Uptake Assay

EdU was detected following the protocol supplied by the manufacturer (Molecular Probes). Detailed information on reagents used in this study is described in Supplemental Experimental Procedures.

### Single Myofiber Culture and Staining

Single myofibers were isolated from extensor digitorum longus muscles following the previously described protocol (Rosenblatt et al., 1995) and cultured for 24 hr in GM without attaching to the culture dish. Fixation and immunostaining followed described protocols (Collins-Hooper et al., 2012; Shin et al., 2009). To capture the 3D structure in single myofiber studies, the stained myofibers were visualized using a BZ-X700 fluorescence microscope (Keyence).

### Detection of Apoptotic Cells

For FACS analyses of apoptotic cells, a Vybrant FAM Caspase-3 and -7 Assay Kit was used by following the provided protocol (Molecular Probes). Apoptotic cells were detected immunohistochemically by rhodamine fluorescence using an ApopTag Red In Situ Apoptosis Detection Kit (Chemicon).

### Retroviral Vector Preparation

A full-length C1a-type Calcr cDNA was amplified by real-time PCR, and the PCR product was sequenced and cloned into a bicistronic retrovirus construct, pMXs-IRES/GFP (Nosaka et al., 1999), which contains IRES and therefore simultaneously expresses Calcr and GFP. The viral particles were prepared as described (Morita et al., 2000).

### Quantitation of cAMP

After infection with retroviral vectors, GFP<sup>+</sup> C2C12 cells were sorted and plated on 96-well dishes at a density of 2,000–3,000 cells and cultured for 1 day. Cells were then stimulated with elcatonin (0.1 U/ml) in GM for 3 hr, and the amount of cAMP in the cells was quantified using a cAMP-Screen System (Applied Biosystems).

### Statistics

Values were expressed as means  $\pm$  SE. Statistical significance was assessed by Student's t test. In comparisons of more than two groups, non-repeated-measures analysis of variance (ANOVA) followed by the Bonferroni test (versus control) or SNK test (multiple comparisons) were used. A probability of less than 5% ( $p < 0.05$ ) or 1% ( $p < 0.01$ ) was considered statistically significant.

### SUPPLEMENTAL INFORMATION

Supplemental Information includes Supplemental Experimental Procedures, seven figures, and two tables and can be found with this article online at <http://dx.doi.org/10.1016/j.celrep.2015.08.083>.

### AUTHOR CONTRIBUTIONS

S.F. was responsible for designing and performing the experiments, analysing the data, and writing the manuscript; M.Y., M.I., K.T., H.Y., and S.F. contributed to generation of Calcr<sup>fllox</sup> mice. M.Y., Y.W., T.O., T.S., and S.F. performed the analyses of Pax7<sup>CreERT2</sup>:Calcr<sup>fllox</sup> or Pax7<sup>CreERT2</sup>:Calcr<sup>fllox</sup>;Rosa26<sup>YFP</sup> mice. Y.W. and S.F. did ex vivo analyses of BrdU- or EdU-uptake. N.M. designed experiments for using PKA or Epac activator or inhibitor. T.O. and M.N. did single myofiber and regeneration experiments. A.U., K.T., M.H., Y.M.-S., and S.T. provided reagents and materials.

### ACKNOWLEDGMENTS

We thank Yoko Esaki and Kiyo Kawata of NPO Biotechnology Research and Development for technical assistance in generating Calcr<sup>fllox</sup> mice, A.F. Stewart for permitting use of CAG-Flpe transgenic mice, and Prof. Toshio Kitamura for providing the pMXs vector and packaging cells. We also thank Prof. Shahragim Tajbakhsh for technical advice. We appreciate the KOMP project for Calcr targeting vectors. This work was supported by a JSPS KAKENHI grant,

a Grant-in Aid for Young Scientists (S.F.), an Intramural Research Grant (S.F.) for Neurological and Psychiatric Disorders of NCNP, and the Takeda Science Foundation (S.F.).

Received: August 20, 2014

Revised: June 9, 2015

Accepted: August 31, 2015

Published: October 1, 2015

## REFERENCES

- Becker, K., Muller, B., Nylen, E., Cohen, R., White, J., and Snider, J. (2002). Calcitonin Gene Family of Peptides, Second Edition, *Volume 1* (New York: Academic Press).
- Bjornson, C.R., Cheung, T.H., Liu, L., Tripathi, P.V., Steeper, K.M., and Rando, T.A. (2012). Notch signaling is necessary to maintain quiescence in adult muscle stem cells. *Stem Cells* 30, 232–242.
- Chagin, A.S., Vuppapapati, K.K., Kobayashi, T., Guo, J., Hirai, T., Chen, M., Offermanns, S., Weinstein, L.S., and Kronenberg, H.M. (2014). G-protein stimulatory subunit alpha and Gq/11α G-proteins are both required to maintain quiescent stem-like chondrocytes. *Nat. Commun.* 5, 3673.
- Cheung, T.H., and Rando, T.A. (2013). Molecular regulation of stem cell quiescence. *Nat. Rev. Mol. Cell Biol.* 14, 329–340.
- Cheung, T.H., Quach, N.L., Charville, G.W., Liu, L., Park, L., Edalati, A., Yoo, B., Hoang, P., and Rando, T.A. (2012). Maintenance of muscle stem-cell quiescence by microRNA-489. *Nature* 482, 524–528.
- Christopoulos, G., Perry, K.J., Morfis, M., Tilakaratne, N., Gao, Y., Fraser, N.J., Main, M.J., Foord, S.M., and Sexton, P.M. (1999). Multiple amylin receptors arise from receptor activity-modifying protein interaction with the calcitonin receptor gene product. *Mol. Pharmacol.* 56, 235–242.
- Codega, P., Silva-Vargas, V., Paul, A., Maldonado-Soto, A.R., Deleo, A.M., Pastrana, E., and Doetsch, F. (2014). Prospective identification and purification of quiescent adult neural stem cells from their in vivo niche. *Neuron* 82, 545–559.
- Collins-Hooper, H., Woolley, T.E., Dyson, L., Patel, A., Potter, P., Baker, R.E., Gaffney, E.A., Maini, P.K., Dash, P.R., and Patel, K. (2012). Age-related changes in speed and mechanism of adult skeletal muscle stem cell migration. *Stem Cells* 30, 1182–1195.
- Dacquin, R., Davey, R.A., Laplace, C., Levasseur, R., Morris, H.A., Goldring, S.R., Gebre-Medhin, S., Galson, D.L., Zajac, J.D., and Karsenty, G. (2004). Amylin inhibits bone resorption while the calcitonin receptor controls bone formation in vivo. *J. Cell Biol.* 164, 509–514.
- Davaille, J., Gallois, C., Habib, A., Li, L., Mallat, A., Tao, J., Levade, T., and Lottersztajn, S. (2000). Antiproliferative properties of sphingosine 1-phosphate in human hepatic myofibroblasts. A cyclooxygenase-2 mediated pathway. *J. Biol. Chem.* 275, 34628–34633.
- de Rooij, J., Zwartkruis, F.J., Verheijen, M.H., Cool, R.H., Nijman, S.M., Wittinghofer, A., and Bos, J.L. (1998). Epac is a Rap1 guanine-nucleotide-exchange factor directly activated by cyclic AMP. *Nature* 396, 474–477.
- Dransfield, D.T., Griner, R.D., Ray, S., Keskinetepe, M., and Bollag, W.B. (2001). 8-Cl-adenosine induces growth arrest without differentiation of primary mouse epidermal keratinocytes. *J. Invest. Dermatol.* 117, 1588–1593.
- Freter, R., Osawa, M., and Nishikawa, S. (2010). Adult stem cells exhibit global suppression of RNA polymerase II serine-2 phosphorylation. *Stem Cells* 28, 1571–1580.
- Fujihara, Y., Kaseda, K., Inoue, N., Ikawa, M., and Okabe, M. (2013). Production of mouse pups from germline transmission-failed knockout chimeras. *Transgenic Res.* 22, 195–200.
- Fukada, S., Higuchi, S., Segawa, M., Koda, K., Yamamoto, Y., Tsujikawa, K., Kohama, Y., Uezumi, A., Imamura, M., Miyagoe-Suzuki, Y., et al. (2004). Purification and cell-surface marker characterization of quiescent satellite cells from murine skeletal muscle by a novel monoclonal antibody. *Exp. Cell Res.* 296, 245–255.
- Fukada, S., Uezumi, A., Ikemoto, M., Masuda, S., Segawa, M., Tanimura, N., Yamamoto, H., Miyagoe-Suzuki, Y., and Takeda, S. (2007). Molecular signature of quiescent satellite cells in adult skeletal muscle. *Stem Cells* 25, 2448–2459.
- Fukada, S., Yamaguchi, M., Kokubo, H., Ogawa, R., Uezumi, A., Yoneda, T., Matev, M.M., Motohashi, N., Ito, T., Zolkiewska, A., et al. (2011). Hes1 and Hes3 are essential to generate undifferentiated quiescent satellite cells and to maintain satellite cell numbers. *Development* 138, 4609–4619.
- Gooi, J.H., Chia, L.Y., Walsh, N.C., Karsdal, M.A., Quinn, J.M., Martin, T.J., and Sims, N.A. (2014). Decline in calcitonin receptor expression in osteocytes with age. *J. Endocrinol.* 227, 181–191.
- Hoff, A.O., Catala-Lehnen, P., Thomas, P.M., Priemel, M., Rueger, J.M., Nasonkin, I., Bradley, A., Hughes, M.R., Ordonez, N., Cote, G.J., et al. (2002). Increased bone mass is an unexpected phenotype associated with deletion of the calcitonin gene. *J. Clin. Invest.* 110, 1849–1857.
- Imayoshi, I., Sakamoto, M., Yamaguchi, M., Mori, K., and Kageyama, R. (2010). Essential roles of Notch signaling in maintenance of neural stem cells in developing and adult brains. *J. Neurosci.* 30, 3489–3498.
- Jockusch, H., and Voigt, S. (2003). Migration of adult myogenic precursor cells as revealed by GFP/nLacZ labelling of mouse transplantation chimeras. *J. Cell Sci.* 116, 1611–1616.
- Kamiya, K., Sakakibara, K., Ryer, E.J., Hom, R.P., Leof, E.B., Kent, K.C., and Liu, B. (2007). Phosphorylation of the cyclic AMP response element binding protein mediates transforming growth factor beta-induced downregulation of cyclin A in vascular smooth muscle cells. *Mol. Cell. Biol.* 27, 3489–3498.
- Katafuchi, T., Kikumoto, K., Hamano, K., Kangawa, K., Matsuo, H., and Minamino, N. (2003). Calcitonin receptor-stimulating peptide, a new member of the calcitonin gene-related peptide family. Its isolation from porcine brain, structure, tissue distribution, and biological activity. *J. Biol. Chem.* 278, 12046–12054.
- L'Allemain, G., Lavoie, J.N., Rivard, N., Baldin, V., and Pouyssegur, J. (1997). Cyclin D1 expression is a major target of the cAMP-induced inhibition of cell cycle entry in fibroblasts. *Oncogene* 14, 1981–1990.
- Lepper, C., Conway, S.J., and Fan, C.M. (2009). Adult satellite cells and embryonic muscle progenitors have distinct genetic requirements. *Nature* 460, 627–631.
- Mauro, A. (1961). Satellite cell of skeletal muscle fibers. *J. Biophys. Biochem. Cytol.* 9, 493–495.
- Morita, S., Kojima, T., and Kitamura, T. (2000). Plat-E: an efficient and stable system for transient packaging of retroviruses. *Gene Ther.* 7, 1063–1066.
- Mourikis, P., Sambasivan, R., Castel, D., Rocheteau, P., Bizzarro, V., and Tajbakhsh, S. (2012). A critical requirement for notch signaling in maintenance of the quiescent skeletal muscle stem cell state. *Stem Cells* 30, 243–252.
- Nosaka, T., Kawashima, T., Misawa, K., Ikuta, K., Mui, A.L., and Kitamura, T. (1999). STAT5 as a molecular regulator of proliferation, differentiation and apoptosis in hematopoietic cells. *EMBO J.* 18, 4754–4765.
- Regan, J.W., Bailey, T.J., Pepperl, D.J., Pierce, K.L., Bogardus, A.M., Donello, J.E., Fairbairn, C.E., Kedzie, K.M., Woodward, D.F., and Gil, D.W. (1994). Cloning of a novel human prostaglandin receptor with characteristics of the pharmacologically defined EP2 subtype. *Mol. Pharmacol.* 46, 213–220.
- Rodgers, J.T., King, K.Y., Brett, J.O., Cromie, M.J., Charville, G.W., Maguire, K.K., Brunson, C., Mastey, N., Liu, L., Tsai, C.R., et al. (2014). mTORC1 controls the adaptive transition of quiescent stem cells from G0 to G(Alert). *Nature* 510, 393–396.
- Rodríguez, C.I., Buchholz, F., Galloway, J., Sequerra, R., Kasper, J., Ayala, R., Stewart, A.F., and Dymecki, S.M. (2000). High-efficiency deleter mice show that FLPe is an alternative to Cre-loxP. *Nat. Genet.* 25, 139–140.
- Rosenblatt, J.D., Lunt, A.I., Parry, D.J., and Partridge, T.A. (1995). Culturing satellite cells from living single muscle fiber explants. *In Vitro Cell. Dev. Biol. Anim.* 31, 773–779.
- Sato, T., Yamamoto, T., and Sehara-Fujisawa, A. (2014). miR-195/497 induce postnatal quiescence of skeletal muscle stem cells. *Nat. Commun.* 5, 4597.

- Sexton, P.M., Houssami, S., Hilton, J.M., O'Keeffe, L.M., Center, R.J., Gillespie, M.T., Darcy, P., and Findlay, D.M. (1993). Identification of brain isoforms of the rat calcitonin receptor. *Mol. Endocrinol.* 7, 815–821.
- Shamonki, I.M., Frumar, A.M., Tataryn, I.V., Meldrum, D.R., Davidson, B.H., Parthemore, J.G., Judd, H.L., and Deftos, L.J. (1980). Age-related changes of calcitonin secretion in females. *J. Clin. Endocrinol. Metab.* 50, 437–439.
- Shinin, V., Gayraud-Morel, B., and Tajbakhsh, S. (2009). Template DNA-Strand Co-Segregation and Asymmetric Cell Division in Skeletal Muscle Stem Cells, *Volume 482* (Humana Press).
- Siegel, A.L., Atchison, K., Fisher, K.E., Davis, G.E., and Cornelison, D.D. (2009). 3D timelapse analysis of muscle satellite cell motility. *Stem Cells* 27, 2527–2538.
- Srinivas, S., Watanabe, T., Lin, C.S., William, C.M., Tanabe, Y., Jessell, T.M., and Costantini, F. (2001). Cre reporter strains produced by targeted insertion of EYFP and ECFP into the ROSA26 locus. *BMC Dev. Biol.* 1, 4.
- Stambrook, P.J., and Velez, C. (1976). Reversible arrest of Chinese hamster V79 cells in G2 by dibutyryl AMP. *Exp. Cell Res.* 99, 57–62.
- Stork, P.J., and Schmitt, J.M. (2002). Crosstalk between cAMP and MAP kinase signaling in the regulation of cell proliferation. *Trends Cell Biol.* 12, 258–266.
- Suzuki, H., Nakamura, I., Takahashi, N., Ikuhara, T., Matsuzaki, K., Isogai, Y., Hori, M., and Suda, T. (1996). Calcitonin-induced changes in the cytoskeleton are mediated by a signal pathway associated with protein kinase A in osteoclasts. *Endocrinology* 137, 4685–4690.
- Tumbar, T., Guasch, G., Greco, V., Blanpain, C., Lowry, W.E., Rendl, M., and Fuchs, E. (2004). Defining the epithelial stem cell niche in skin. *Science* 303, 359–363.
- Venezia, T.A., Merchant, A.A., Ramos, C.A., Whitehouse, N.L., Young, A.S., Shaw, C.A., and Goodell, M.A. (2004). Molecular signatures of proliferation and quiescence in hematopoietic stem cells. *PLoS Biol.* 2, e301.





## Review

## Ocular surface reconstruction using stem cell and tissue engineering



Takahiro Nakamura<sup>a,\*</sup>, Tsutomu Inatomi<sup>b</sup>, Chie Sotozono<sup>b</sup>, Noriko Koizumi<sup>b</sup>,  
Shigeru Kinoshita<sup>a</sup>

<sup>a</sup> Department of Frontier Medical Sciences and Technology for Ophthalmology, Kyoto Prefectural University of Medicine, Kyoto, Japan

<sup>b</sup> Ophthalmology, Kyoto Prefectural University of Medicine, Kyoto, Japan

## ARTICLE INFO

## Article history:

Received 29 April 2015

Received in revised form

8 July 2015

Accepted 8 July 2015

Available online 15 July 2015

## Keywords:

Ocular surface

Stem cell

Tissue engineering

Growth factor

Severe ocular surface disease

Regenerative medicine

## ABSTRACT

Most human sensory information is gained through eyesight, and integrity of the ocular surface, including cornea and conjunctiva, is known to be indispensable for good vision. It is believed that severe damage to corneal epithelial stem cells results in devastating ocular surface disease, and many researchers and scientists have tried to reconstruct the ocular surface using medical and surgical approaches. Ocular surface reconstruction via regenerative therapy is a newly developed medical field that promises to be the next generation of therapeutic modalities, based on the use of tissue-specific stem cells to generate biological substitutes and improve tissue functions. The accomplishment of these objectives depends on three key factors: stem cells, which have highly proliferative capacities and longevities; the substrates determining the environmental niche; and growth factors that support them appropriately. This manuscript describes the diligent development of ocular surface reconstruction using tissue engineering techniques, both past and present, and discusses and validates their future use for regenerative therapy in this field.

© 2015 Elsevier Ltd. All rights reserved.

## Contents

1. Introduction .....	188
2. Ocular surface reconstruction .....	188
2.1. Conjunctival transplantation, keratoepithelioplasty and limbal transplantation .....	188
2.2. Cultivated limbal epithelial transplantation (CLET) .....	189
2.2.1. The history of creating corneal epithelial sheets .....	189
2.2.2. Development of CLET .....	189
2.2.3. Clinical outcomes of autologous CLET .....	190
2.2.4. Clinical outcomes of allogenic CLET .....	190
2.2.5. Phenotypic investigation of allogenic CLET .....	191
2.3. Cultivated oral mucosal epithelial transplantation (COMET) .....	191
2.3.1. Development of COMET .....	191
2.3.2. Clinical outcomes of autologous COMET .....	192
2.3.3. Phenotypic investigation of autologous COMET .....	193
2.3.4. Surgical variations .....	193
2.4. Recent pre-clinical trial .....	195
3. Stem cells .....	195
3.1. Concept of corneal epithelial stem cell .....	196
3.1.1. XYZ hypothesis .....	196
3.1.2. Limbal stem cell theory .....	196
3.1.3. Oligopotent stem cells .....	197

\* Corresponding author. Department of Frontier Medical Sciences and Technology for Ophthalmology, Kyoto Prefectural University of Medicine, 465 Kajii-cho, Kamigyo-ku, Kyoto 602-0841, Japan.

E-mail address: [tnakamur@koto.kpu-m.ac.jp](mailto:tnakamur@koto.kpu-m.ac.jp) (T. Nakamura).

3.2.	Candidate limbal stem cell markers .....	197
3.3.	Single cell-based clonal analysis .....	198
3.3.1.	Gene expression profiling of holoclone-type stem cells .....	198
3.3.2.	miRNA profiling of holoclone-type stem cells .....	200
4.	Tissue engineering .....	200
4.1.	Amniotic membrane (AM) .....	200
4.1.1.	Naive AM .....	200
4.1.2.	Dried AM .....	201
4.2.	Fibrin and the temperature-sensitive dish .....	202
4.3.	Development of novel cultured substrates .....	202
4.4.	Bio-adhesive .....	203
5.	Growth factors .....	203
5.1.	Feeder layer factor .....	203
5.2.	Serum factor .....	204
5.3.	Development of feeder-free and serum-free systems .....	204
6.	Future directions .....	204
	References .....	204

## 1. Introduction

The concept of an “ocular surface” is widely recognized in the field of ophthalmology, and our understanding of the role of ocular surface biology and immunology has been greatly improved by the numerous research studies carried out in this field (Thoft and Friend, 1979). Although the normal ocular surface comprises only 1/6 of the outer wall of the eye, it supports several of the eye's major functions, as it is covered with highly specialized corneal and conjunctival epithelia, formed by two phenotypically different types of epithelial cell. Over the past thirty years, several scientific discoveries such as the identification of corneal epithelial stem cells, the establishment of novel methods in epithelial culturing and the understanding of extracellular matrices and growth factors have enabled a novel surgical approach to treatment of ocular surface disorders, using regenerative medicine.

Based on tissue engineering, regenerative medicine is a newly developed area that uses somatic stem cells to generate biological substitutes and improve tissue functions (Langer and Vacanti, 1993). Success depends on three key factors: stem cells, extracellular matrices and growth factors. A variety of trials are currently in development, based on the utilization of stem cells and appropriate substrates to produce substitutes capable of reconstructing damaged and diseased tissues. In the field of ophthalmology, the production of tissue organs *in vitro* shows great promise, especially with regard to the anterior segment of the eye (Pellegrini et al., 1997).

Severe ocular surface disease (OSD) due to thermal and chemical burns, Stevens-Johnson syndrome (SJS), ocular cicatricial pemphigoid (OCP) or other conditions currently poses a serious clinical challenge for ophthalmologists worldwide. In these cases, the corneal epithelial stem cells located in the corneal limbus are destroyed, and coverage of the corneal surface by invading neighboring conjunctival epithelial cells results in neovascularization, chronic inflammation, ingrowth of fibrous tissue and stromal scarring. This severely compromises the ocular surface and seriously diminishes visual acuity (Chiou et al., 1998; Kinoshita et al., 2001; Tseng, 1989). Conventional treatment methods have generally proved unsatisfactory, and the long-term consequences of these ocular disorders are devastating. Clinically useful and effective surgical techniques for ocular surface reconstruction (OSR) are therefore needed for such patients.

In this present paper, we describe the history, recent advances, current developments and future challenges relating to OSR in both its basic science and clinical aspects, as well as providing novel

clinical information for the treatment of severe OSD.

## 2. Ocular surface reconstruction

The concept of OSR is widely accepted in the field of ophthalmology, and our understanding of the role of the ocular surface has been greatly improved by numerous research studies. Various surgical procedures have been developed over the past 30 years to treat and reconstruct severely damaged or diseased ocular surface epithelia.

### 2.1. Conjunctival transplantation, keratoepithelioplasty and limbal transplantation

The concept of OSR was first reported in relation to an autologous conjunctival transplantation for unilateral chemical injury in Thoft's description of conjunctival tissue transplantation for unilaterally affected chemical injuries (Thoft, 1977). The surgery was performed by removing pathological scarred tissue from a patient's corneal surface and placing four pieces of conjunctival autograft taken from the contralateral eye at the limbus in order to reconstruct the cornea by regenerating conjunctival epithelial cells from these autografts. Subsequently, Thoft described the similar surgical technique of keratoepithelioplasty (Thoft, 1984), which employed a different tissue source (donor corneal lenticles) to regenerate corneal epithelial cells. Although the concept of corneal epithelial stem cells was not established at that time, the cell-level biological differences between regenerated corneal and conjunctival epithelia were known. Over time, keratoepithelioplasty has gradually gained acceptance despite initial disputes among researchers because it is a form of epithelial allograft (Kaufman, 1984). In fact, keratoepithelioplasty has proved to be dramatically effective in treating peripheral corneal ulcers, including Mooren's ulcer (Kinoshita et al., 1991), supplying both a regenerated corneal epithelium and an appropriate corneal substrate for inhibiting conjunctival invasion onto the cornea. Sun's group proposed the corneal limbal stem cell concept (Schmermer et al., 1986), which had a tremendous impact on the development of keratoepithelioplasty, leading to autologous limbal transplantation (LT) (Kenyon and Tseng, 1989). Tsai and Tseng then introduced allogenic LT, aimed at achieving a permanent lifespan for regenerated corneal epithelium by means of stem cell transplantation, although intensive immunosuppressive therapy was also needed (Tsai and Tseng, 1994). These surgical procedures are classed as “cellular surgery”—a form of primitive regenerative

medicine—as they are a form of *in vivo* expansion of corneal epithelial cells. Significantly, Kim and Tseng subsequently reported that amniotic membrane (AM) transplantation was capable of inhibiting pathological subepithelial scarring in OSR (Kim and Tseng, 1995). Since that time, AM transplantation combined with limbal allografts has been used to treat certain challenging occurrences of severe OSD (Tsubota et al., 1996).

## 2.2. Cultivated limbal epithelial transplantation (CLET)

While corneal epithelial transplantations (including keratoplasty and LT) have indisputably contributed to improved clinical outcomes for OSR in a range of clinical situations, an autologous LT needs quite a large section of limbal tissue from the healthy eye and cannot be applied if the disease is bilateral. In order to improve the surgical results of OSR for severe OSD, CLET needs to be developed *in vitro* from a small portion of limbal epithelium (Fig. 1).

### 2.2.1. The history of creating corneal epithelial sheets

In the initial stages of OSR during the 1980s, at least two investigative approaches were adopted in attempting to create an epithelial sheet. One was the direct sampling of corneal epithelial sheets, using dispare and gentle mechanical treatment. In rabbit experiments, the corneal epithelial sheet, taken directly from the *in vivo* cornea, attached itself to the corneal stroma but peeled away easily during lid movement, making it quite difficult to preserve the corneal surfaces (Gipson and Grill, 1982).

A second approach was to develop a cultivated epithelial cell sheet. In dermatological research, Green successfully established a procedure for cultivating epidermal cell sheets (Rheinwald and Green, 1975), focusing particular attention on the tissue-engineered cultivated corneal epithelial cell sheet. The cultivation

of corneal epithelial cells on the scraped rabbit corneal stroma was examined by Friend et al. (1982), and several other substrates, such as collagen matrix and hydrogel coated with fibronectin, were also investigated in developing this procedure (Kobayashi and Ikada, 1991; Minami et al., 1993). However, until 1997, there were no clinical reports regarding the success of OSR using the cultivated corneal epithelial cell sheets, probably because of the poor understanding of surrounding corneal epithelial stem cell cultivation and/or its proper substrate. Some groups tried to reconstruct all three layers of corneal tissue—a “corneal equivalent”—using cell-lines arranged by natural and synthetic polymers (Griffith et al., 1999). This kind of corneal equivalent is now available for use in testing experimental drug toxicity and efficacy but not for clinical use (because of the use of immortalized cell lines).

### 2.2.2. Development of CLET

From the mid-1990s, attention has focused on the development of regenerative corneal epithelial cell therapy using tissue-engineered techniques as a new approach to OSR. The first successful OSR procedure using autologous CLET for patients with unilateral OSD was reported by Pellegrini et al. (Pellegrini et al., 1997). They developed a surgical method to reconstruct stratified corneal epithelial cell sheets on petrolatum gauze or a soft contact lens as carrier, treating two patients. It seems likely that their success can be accounted for by their adoption of a well-recognized epidermal keratinocyte-culturing method, including the use of mouse-derived 3T3 feeder layers to maintain epithelial stem cells. Since then, scientists worldwide have sought to devise novel and better methods for OSR. Again, in considering reconstruction of the ocular surface, the three key elements are the cell source and its proper substrate and growth factors. Following establishment of a suitable substrate, many researchers investigated the use of AM, fibrin and a temperature-responsive culture dish as carrier

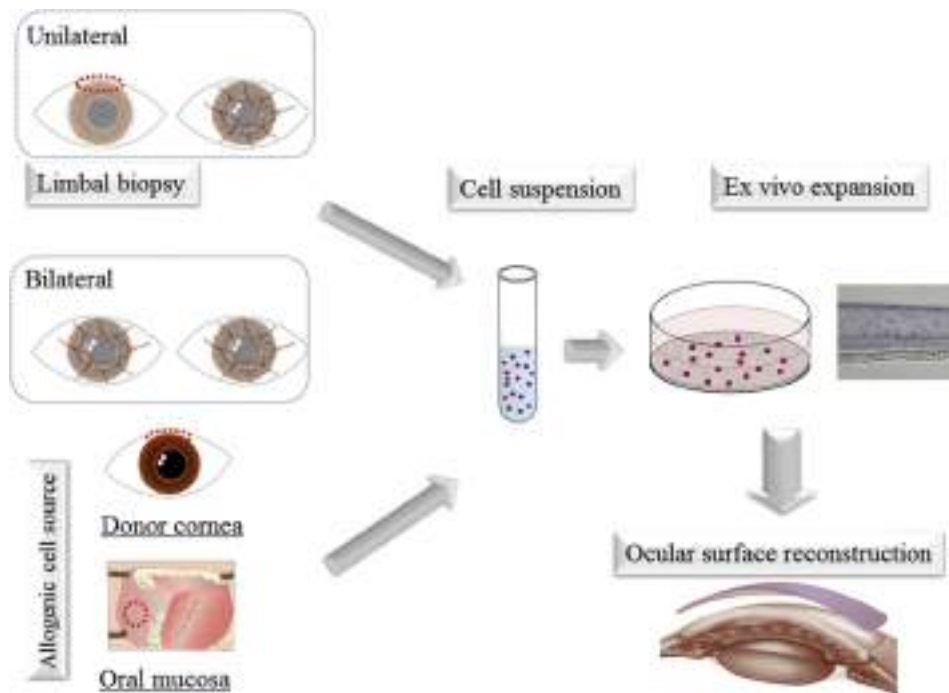


**Fig. 1.** Conceptual diagram of OSR via regenerative therapy. For patients with unilateral severe OSD, autologous corneal limbal epithelial cells from a biopsy of the uninjured eye (dashed circle) are used for cell culturing. For patients with bilateral severe OSD, allogenic cell sources (donor cornea or autologous oral mucosa) are used for cell culturing. The resultant cell suspensions were seeded onto the proper substrate under appropriate *in vitro* conditions. Finally, we successfully tissue-engineered the cultured sheet and transplanted it to the diseased corneal surface.

(Koizumi et al., 2000a; Nishida et al., 2004a; Rama et al., 2001; Tsai et al., 2000). From a clinical perspective, AM can serve not only as a proper epithelial carrier but also as a healthy substrate to cover a damaged ocular surface; the success of CLET using AM has been reported by a majority of groups worldwide (Baylis et al., 2011; Zhao and Ma, 2015). In addition, Sangwan has recently reported a novel surgical technique that combines AM transplantation and cultivation of small limbal explant with fibrin glue (Sangwan et al., 2012).

### 2.2.3. Clinical outcomes of autologous CLET

The ideal therapy for unilateral severe OSD—as caused, for instance, by thermal and chemical burns—is the use of autologous cultivated limbal epithelial sheets, with harvesting of much smaller pieces of limbal biopsy to prevent damage to the healthy or uninjured eye. With this in mind, several researchers have reported the successful use of autologous CLET for OSR (Grueterich et al., 2002; Nakamura et al., 2004b; Sangwan et al., 2003; Schwab et al., 2000; Tsai et al., 2000). These initial reports offer hope to patients with unilateral lesions or severe ocular surface damage. Long-term clinical assessment of autologous CLET was reported by Rama (Rama et al., 2010), confirming that autologous cultivated limbal stem cells represent an adequate long-term source for tissue-engineered transplants; clinical results reported success at up to 10 years in more than 75% of the patients treated. Importantly, this demonstrates the relationship between clinical results and the

percentage of p63 (+) cells in cultivated graft. (Cultures in which p63-bright cells accounted for more than 3% of the total number of clonogenic cells were associated with successful transplantation in 78% of patients. In contrast, cultures in which such cells made up 3% or less of the total number of cells were associated with successful transplantation in only 11% of patients). In our long-term clinical cases (mean period 48 months; longest follow-up period 80 months), autologous CLET successfully reconstructed the corneal surface, but all cases showed varying degrees of mild superficial conjunctivalization extending from the limbal region (Fig. 2). These long-term clinical results strongly support the conclusion that tissue-engineered autologous CLET can be useful for reconstructing the ocular surface in cases of unilateral severe OSD. We further posit that the cultivation of limbal epithelial cells harvested from much smaller specimens is possible but difficult to achieve using conventional culturing techniques; these must be further developed to produce a sufficiently stratified epithelium that will hopefully include limbal stem cells.

### 2.2.4. Clinical outcomes of allogeneic CLET

Although autologous CLET is the safest and most reliable procedure, bilaterally affected severe OSD cannot be treated by this means. In order to treat these bilateral cases, we have developed allogeneic CLET, using AM as a culture substrate (Kinoshita et al., 2004; Koizumi et al., 2001a). While acute-phase patients with persistent epithelial defects received allogeneic CLET for the

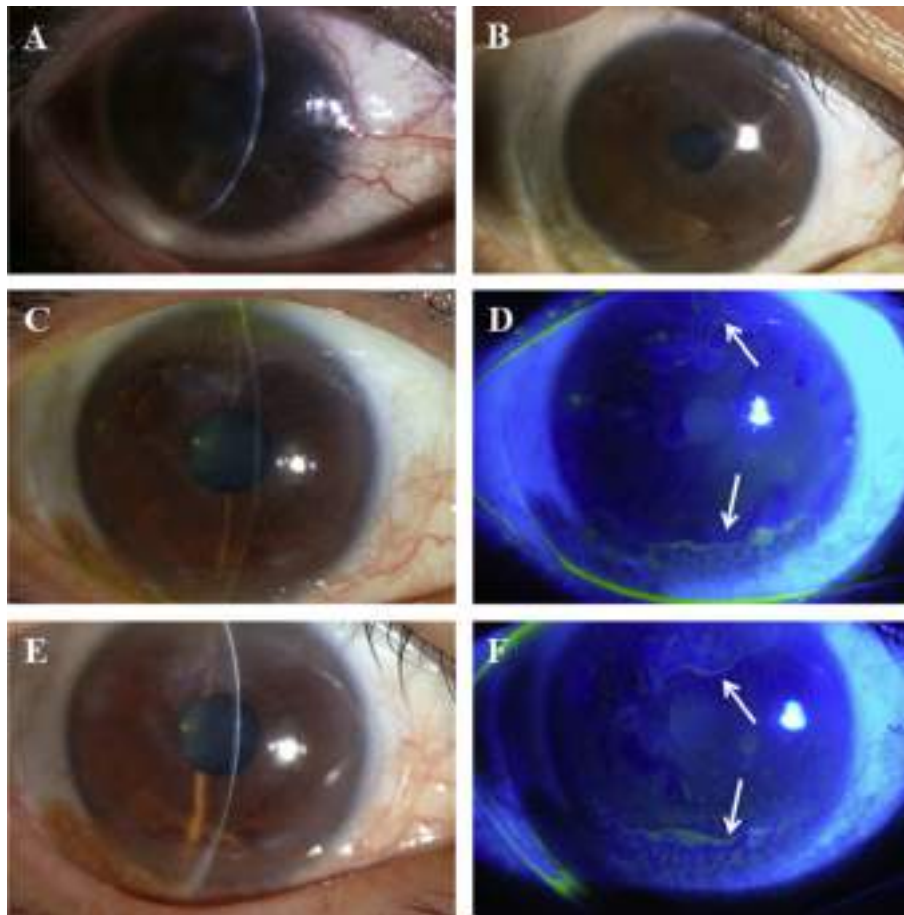


**Fig. 2.** Representative long-term clinical results of autologous CLET in patient with chemical injury. (A) Before transplantation, the eye manifested severe destruction of the ocular surface, with conjunctivalization and neovascularization. Postoperative appearance at 1 year (B), 5 years (C, D) and 7 years (E, F) shows a relatively smooth, epithelialized corneal surface with minimal corneal scarring and inflammation. During long-term follow-up, varying degrees of mild peripheral conjunctivalization were observed (D, F; white arrows).



purpose of covering the corneal surface and reducing ocular surface inflammation, chronic-phase patients received CLET to improve visual acuity. We have transplanted allogeneic cultivated corneal limbal epithelial cells in 39 eyes of 36 patients with severe OSD, including acute and chronic phases of SJS, OCP and thermal and chemical injuries (Fig. 3). During the postoperative 1–3 years, most of the transplanted sheets successfully survived on the ocular surfaces and maintained their transparency with the aid of immunosuppressive treatments.

It is worth noting that, in acute-phase patients, the severe preoperative ocular surface inflammation that had not been controlled by conventional treatments decreased rapidly post transplantation (Koizumi et al., 2001b); in chronic-phase patients, long-term visual outcome and epithelial stability varied. In a case of severe chemical injury, the transplanted corneal epithelial sheet was found to be transparent and stable as much as 10 years after transplantation, with only minimal conjunctival inflammation during the follow-up period. On the other hand, in SJS patients, mild to moderate ocular surface inflammation and subsequent rejection occurred after allogeneic CLET. While subconjunctival fibrosis had not progressed in SJS, conjunctival scarring (symblepharon and shortening of the conjunctival fornix) had progressed in OCP. Our clinical observations confirmed that the phenotypes of transplanted cells gradually changed from donor to host epithelial cells over a couple of years, but subepithelial scarring and neovascularization did not progress. This phenomenon can be explained as a mild rejection of the transplanted corneal epithelial cells. For that reason, we strongly believe that postoperative management, especially immunosuppressive therapy, is critical in ensuring survival of the transplanted graft. Although graft survival was brief in some chronic cases, the ocular surface maintained its transparency and patients gained better visual function in comparison to their condition before surgery. Importantly, it was noted that the rejected cultivated transplants were easily removed from patients' ocular surfaces at the time of second surgery, and the exposed corneal stroma were found to be fairly transparent, with fewer scarring

changes (Nakamura et al., 2003c).

### 2.2.5. Phenotypic investigation of allogenic CLET

Although our clinical assessments of allogenic CLET yielded favorable outcomes from the perspective of corneal stabilization, long-term phenotypic analyses of allogenic corneal epithelial transplants to the ocular surface would be required to confirm the direct evidence of graft survival. To this end, we compared our clinical observations with the results of long-term cell biological phenotype analysis of allogeneic CLET (Nakamura et al., 2010) (Fig. 4). In that report, we noted that, in clinical conjunctival phenotypic grafts, the transplanted cells were gradually replaced by surrounding conjunctival epithelial cells. In contrast, clinical corneal phenotypic grafts demonstrated that transplanted cells could indeed survive for a long period of time. Those findings have valuable clinical implications and provide novel information on allogeneic CLET, suggesting reasons for the phenotypic diversities of these grafts.

### 2.3. Cultivated oral mucosal epithelial transplantation (COMET)

As severe OSD is mostly bilateral, ophthalmologists worldwide have no choice but to select allogeneic LT or CLET, resulting in intensive and prolonged postoperative immunosuppressive therapy. These drawbacks have led us to examine whether the ocular surface could be reconstructed by using an autologous mucosal epithelium of non-ocular surface origin. In so doing, we (and other groups) have developed COMET as a substitute for corneal epithelial cells (Nakamura et al., 2003a, 2004a; Nakamura and Kinoshita, 2003; Nishida et al., 2004b).

#### 2.3.1. Development of COMET

In the past, several groups have investigated the possibility of using oral mucosa for OSR. Ballen used oral mucosal grafts that included both epithelial and subepithelial tissues in both human and rabbit eyes, finding that they vascularized heavily with early fibrosis (Ballen, 1963). Gipson et al. transplanted oral mucosal

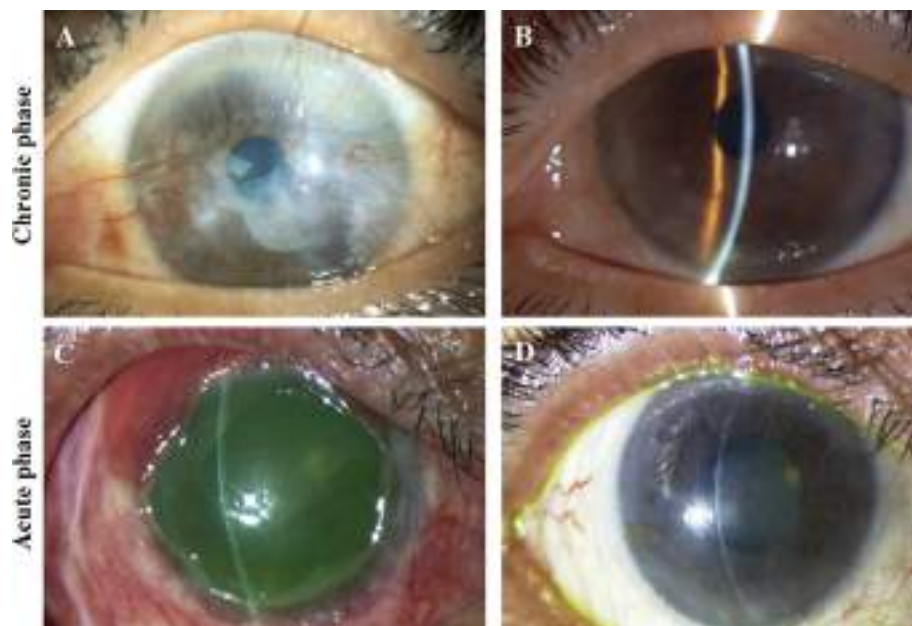


**Fig. 3.** Representative clinical results of allogenic CLET in patient with chronic (A, B) and acute (C, D) phase of chemical injury. Before transplantation, the eyes manifested conjunctivalization with corneal scarring (A) and persistent epithelial defects surrounded by inflammatory subconjunctival fibrosis (C). At 6 years (B) and 2 years (D) post-transplantation, the ocular surface was stable, without epithelial defects. Modified with permission from Kinoshita et al. (2004).

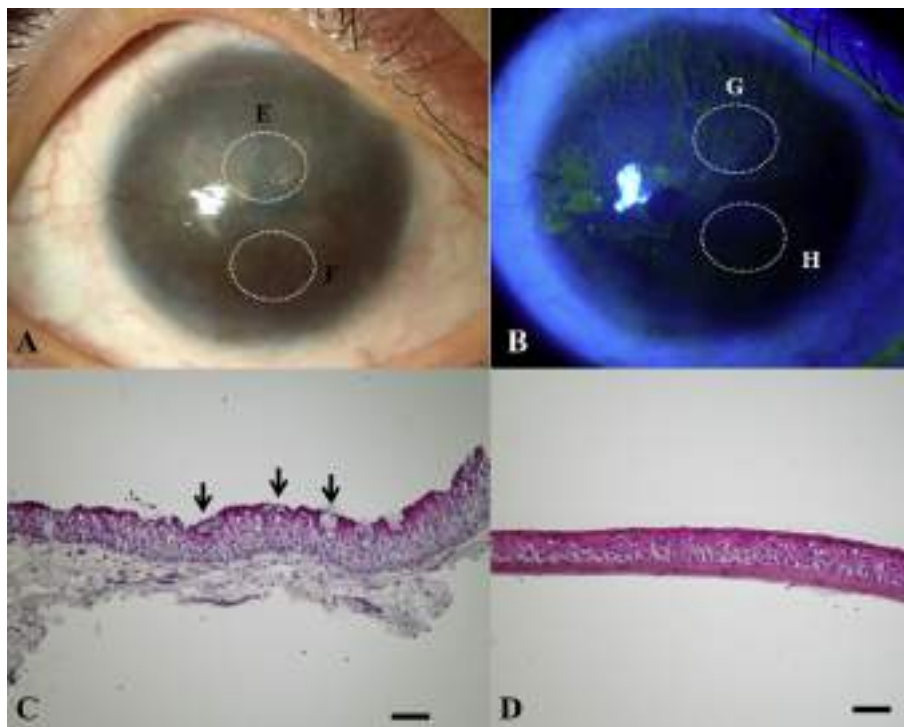


**Fig. 4.** Representative slit-lamp photographs after allogeneic CLET in patient with SJS. Slit-lamp examination revealed that the upper part of the corneal surface was apparently covered with conjunctiva (A; white circle E). However, slit-lamp examination revealed that the lower-nasal part of the corneal surface was still transparent (A; white circle F). Fluorescein staining showed a comparatively clear demarcation between corneal and conjunctival phenotypes (B). The corneal phenotype area showed comparatively smooth epithelium with no fluorescein staining (B; white circle H), but the conjunctival phenotype area revealed light and stippled staining with fluorescein. (B; white circle G). The cross-section of white circle E disclosed 5 to 6 stratified layers of conjunctival-like epithelial cells and also included goblet-cell-like cells (black arrows) (C). Cross-section of white circle F showed 5 to 6 stratified cell layers and cornea-like epithelial cells (D). Scale bars: C, D = 50  $\mu$ m. Modified with permission from Nakamura et al. (2010).

epithelial cells freed by Dispase II treatment of underlying connective tissue onto the rabbit ocular surface (Gipson et al., 1986). They reported that it was feasible to transplant *in vivo* oral mucosal epithelium to corneal-limbal areas but that it was not maintained in central corneal regions. By general consensus, the character of epithelial cell is thought to depend on the underlying substrate, and AM is a good substrate for cultivating mucosal epithelium (Fig. 5). Based on these considerations, we first propose that oral mucosal epithelial cells cultivated on AM may be able to differentiate into cornea-like epithelial cells under cell culture conditions (Nakamura et al., 2003a; Nakamura and Kinoshita, 2003). After intensive investigations, we successfully generated a well-stratified and differentiated rabbit and human cultivated oral mucosal epithelial sheet that appeared very similar to normal *in vivo* corneal epithelium, successfully performing autologous transplantation of these cells onto rabbit corneas (Fig. 5). These results demonstrate that human cultivated oral mucosal epithelial sheets can function as an ocular surface epithelium and that COMET is a feasible method of OSR.

### 2.3.2. Clinical outcomes of autologous COMET

In light of these experimental results, this method was initially applied to six eyes of four patients with severe OSD, and the ocular surfaces were successfully reconstructed (Nakamura et al., 2004a) (Fig. 6). During follow-up ( $13.8 \pm 2.9$  months), visual acuity showed improvement in all eyes, and the ocular surface remained stable. Although all eyes showed peripheral neovascularization with epithelial thickening, use of this novel tissue-engineering technique generated from autologous oral mucosa avoids the need to administer intensive and prolonged immunosuppressive therapy, so reducing the risk of postoperative complications.

We reported long-term clinical data on 19 eyes that received COMET (mean follow-up period 55 months; longest follow-up period 90 months) (Nakamura et al., 2011) (Fig. 6). The study included 19 eyes of 17 patients in the chronic phase of severe OSD; clinical results were evaluated and graded on a scale according to severity (Sotozono et al., 2007). Clinical safety was evaluated in cases of persistent epithelial defect (PED), ocular hypertension and infections. During follow-up, best-corrected visual acuity was improved in 18 eyes (95%), and visual acuity at the postoperative 36th month was improved in 10 eyes (53%). During the follow-up period, clinical conjunctivalization was significantly inhibited, and corneal opacification tended to improve. All eyes showed various degrees of superficial corneal vascularization, but this gradually reduced, and its activity was comparatively stable from 6 months after surgery. Symblepharon formation was also significantly inhibited; 7 of the 19 eyes showed PED at least once during the long-term follow-up. Ocular hypertension was observed in a total of 3 eyes. Corneal infection was observed mainly within 6 months after transplantation, and methicillin-resistant staphylococcus aureus was found to be the only cause of infection. Most recently, in order to clarify the effectiveness, disease-specific results and safety of COMET, all of the clinical data of all 72 patients treated with COMET since 2002 were analyzed (Sotozono et al., 2013). The findings of this retrospective study confirmed that long-term visual improvement can be obtained in end-stage severe OSDs, and that COMET offered substantial visual improvement even for patients with severe tear deficiency. The findings also showed that patients with corneal blindness resulting from severe OSDs such as SJS benefited from critical improvement of visual acuity. It was concluded that COMET is a safe and effective treatment for improvement of the

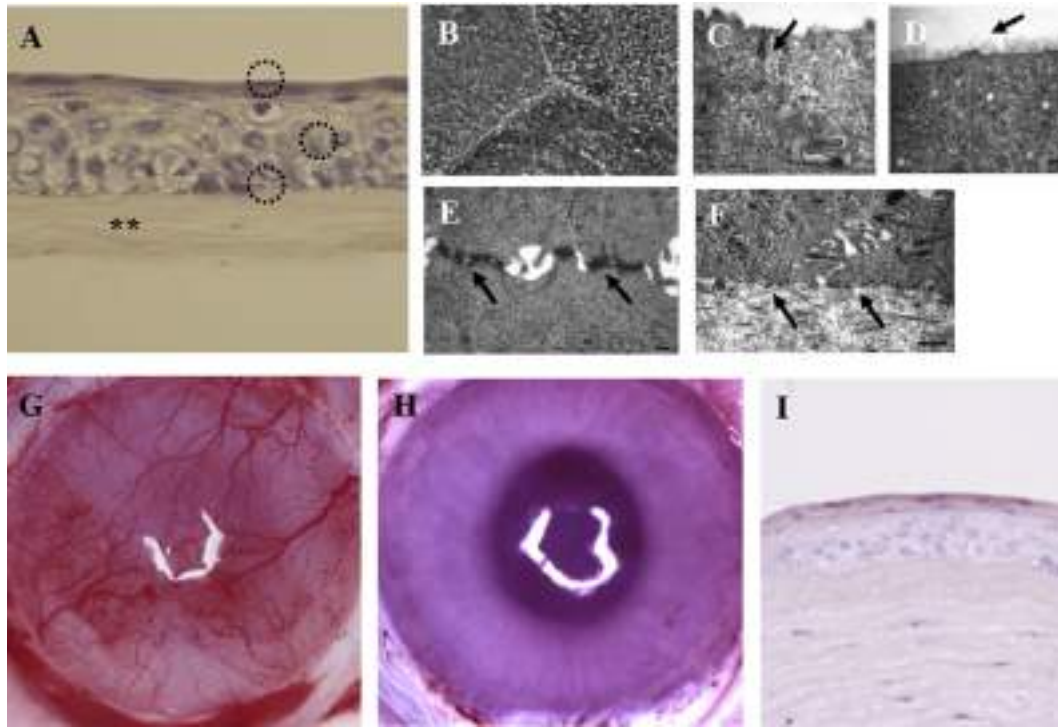


**Fig. 5.** Development of COMET. (A) The rabbit-cultivated oral mucosal epithelial sheet on AM had 4 to 5 layers of stratified, well-differentiated cells and appeared very similar to normal corneal epithelium. The apical surface of the cells was covered with numerous microvilli (B). In the superficial cell layer, what appeared to be tight junctions were evident between neighboring cells (C, arrow). The apical surface of the most superficial cells was covered with a glycocalyx-like material (D, arrow). The cultivated epithelial cells had numerous desmosomal junctions (E, arrows) and were attached to a basement membrane with hemi-desmosomes (F, Arrows). (G) Representative slit-lamp photographs of rabbit eye taken before transplantation and 10 days after transplantation (H). Before transplantation, the eye had total limbal stem cell destruction (G). Ten days after surgery, the corneal surface of the rabbit eye was covered with clear cultivated oral mucosal epithelium (H). The transplanted grafts adhered well to the host corneal stroma, with no evidence of subepithelial cell infiltration or stromal oedema (I). Modified with permission from Kinoshita et al. (2004), Nakamura et al. (2003).

visual prognosis of patients with severe OSD and that preexisting neovascularization and symblepharon were the prognostic factors. Because we have not precisely determined the clinical advantage and disadvantages of CLET and COMET, further clinical comparison of CLET and COMET is needed to develop a future clinical protocol for severe OSD.

In addition, Nishida et al. reported the success of OSR using carrier-free cultivated oral mucosal epithelial sheet in patients with severe OSD (Nishida et al., 2004b), but its long-term clinical outcomes are as yet unknown. Satake et al. reported that transplantation of cultivated oral mucosal epithelial sheets is a reliable procedure for reconstruction of a stable ocular surface (Satake et al., 2011). They also demonstrated that, during long-term follow-up, epithelialization of the corneal surface is very important both for obtaining a reliable long-term clinical results and in achieving a lower incidence of postoperative complications. In our own work, COMET was found to enable sustained reconstruction of the ocular surface epithelium in patients with severe OSD; management of postoperative PED and neovascularization may further increase the clinical efficacy of this type of surgery.

### 2.3.3. Phenotypic investigation of autologous COMET

Although our long-term clinical assessments of autologous COMET have yielded favorable results from the perspective of ocular surface stabilization, longevity and phenotypic analyses of cultivated oral mucosal epithelial sheets on the corneal surface are still required. As the effects of failed and successful grafts on the corneal surface remained unknown, we compared our clinical observations with the results of long-term cellular phenotype analysis of autologous COMET (Nakamura et al., 2007b) (Fig. 7). Our clinical,

ultrastructural and cell biological examinations showed that the process of graft failure after COMET was responsible for the loss of transplanted cultivated oral mucosal epithelial sheets, and that this is followed by invasion of the corneal surface by the surrounding conjunctival epithelial cells. In the clinically successful transplanted eyes, transplanted cultivated oral epithelial cells survived and were found to have adapted well to the host corneal tissues (keratin 3 [+], Muc5ac [-]); there was no infiltration by inflammatory cells, nor was there any dissolution of the AM substrate. Based on our immunohistochemical results alone, we cannot determine whether cultivated oral epithelial cells can transdifferentiate into the corneal cell lineage. In addition, for successful COMET, it is essential to involve oral mucosal epithelial stem/progenitor cells in the cultivated sheet if long-term graft survival is to be expected. We previously reported that p75 was exclusively expressed in the basal cell layer of both the tips of the papillae and the deep rete ridges, and that these immunostaining patterns suggested a cluster organization (Nakamura et al., 2007a). Thus, we demonstrated that p75 may represent a novel marker for oral keratinocyte stem cell-containing populations. Unfortunately, we have yet to examine how many p75 (+) cells are involved in the transplanted graft, so further clinical study using the proper validation of the transplanted graft is needed to clarify this point. Studies are currently underway in our laboratory to shed further light on this observation. Our findings have valuable basic and clinical implications and provide useful insights into the mechanisms of both graft failure and graft survival after COMET.

### 2.3.4. Surgical variations

Severe OSD is sometimes accompanied by severe corneal



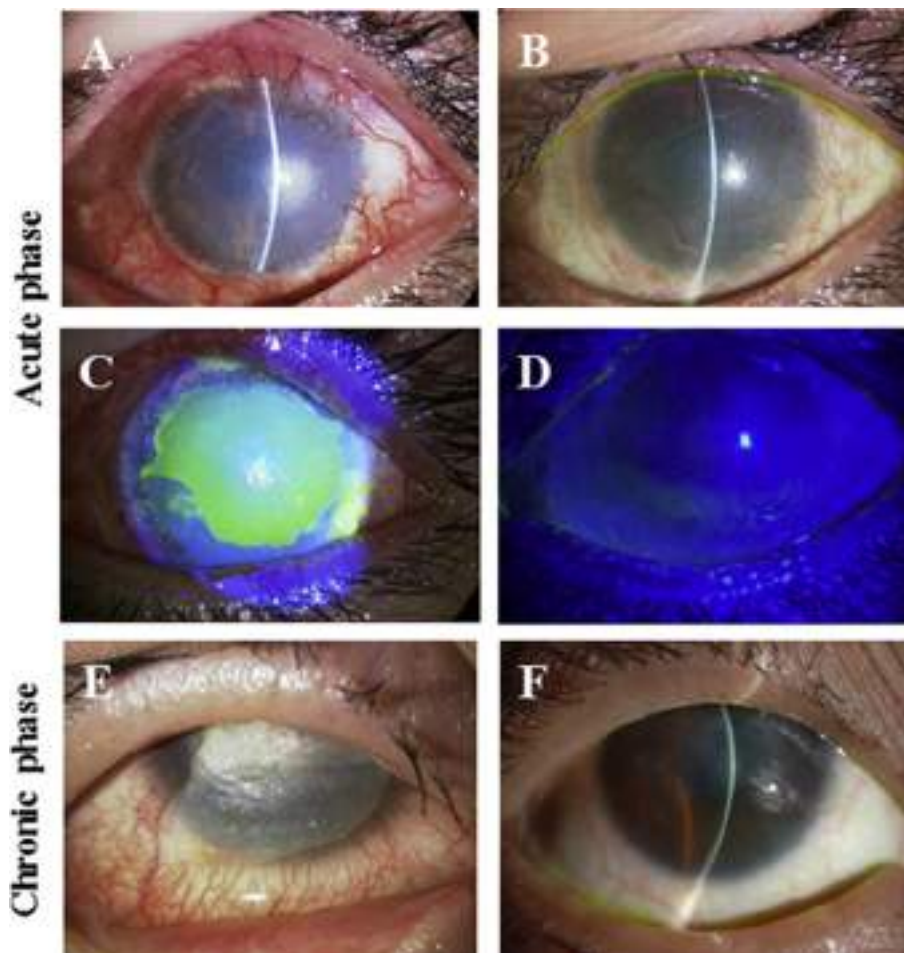


**Fig. 6.** Clinical outcomes of autologous COMET. Representative slit-lamp photographs taken before transplantation without (A) and with fluorescein (C) in patients with acute phase of chemical burn. Before transplantation, the eye manifested persistent epithelial defects surrounded by inflammatory subconjunctival fibrosis. The photographs were taken 17 months after transplantation without (B) and with fluorescein (D). The ocular surface was covered with transplanted cells and was stable without defects. (E, F) Long-term clinical progress of representative patient with severe OSD arising from SJS. Before transplantation, all eyes manifested severe destruction of the ocular surface with limbal stem cell deficiency (E). Postoperative appearance at 50 (F) months shows a relatively smooth, epithelialized corneal surface with minimal corneal neovascularization, scarring and inflammation. Modified with permission from Nakamura et al. (2004a), Nakamura et al. (2011).

stromal opacity and scarring. PKP without epithelial transplantation certainly results in PED because of the limited lifespan of the corneal epithelium in patients with severe OSD. To improve the clinical outcome of these patients, their reconstructed cornea must be provided with a more stable epithelial supply such as cultivated epithelial stem/progenitor cell transplantation. Based on these findings, we proposed a two-step surgical strategy that applies a combination of COMET and PKP (Inatomi et al., 2006) (Fig. 8). In this procedure, PKP was performed around 6 months after the initial COMET; the ocular surface was found to be stable, and the donor cornea remained transparent after COMET. These clinical findings suggested that this surgical treatment may be useful for maintenance of the reconstructed ocular surface by providing cultivated oral mucosal epithelial stem/progenitor cells around the corneal graft.

Varying degrees of symblepharon formation (conjunctival shortening) and entropion frequently occur in patients with severe OSD. The resultant abnormal eyelid can often exacerbate severe OSD, as eyelid margin rotation or structural abnormalities disturb corneal wetting. Malfunction of the conjunctival fornix as a result of symblepharon formation can cause severe OSD such as

dry eye, resulting from cicatricial entropion and restriction of ocular motility, making it necessary to reconstruct not only the ocular surface but also the eyelid formation in these patients. In previously reported clinical results of using the combination of COMET and eyelid surgery (Takeda et al., 2011), the ocular surfaces were successfully reconstructed with COMET and eyelid surgery in all 3 patients, with no serious complications during surgery (Fig. 8). The results of this clinical trial demonstrate that the combined procedure of COMET and eyelid surgery is a useful approach for treatment of severe OSD with associated eyelid abnormality.

In our clinical trials, COMET was used in two different transplantation scenarios: to reconstruct the corneal surface of a severe case of OSD, and to reconstruct the conjunctival fornix in patients with severe OSD-related symblepharon formation. In our clinical work, COMET was also used to reconstruct the conjunctival fornix and proved successful in treating severe OSD (Fig. 8). However, abnormal postoperative fibrovascular proliferation caused by primary severe OSD (SJS and OCP) must be considered in detail, as this remains critical to the long-term clinical prognosis.



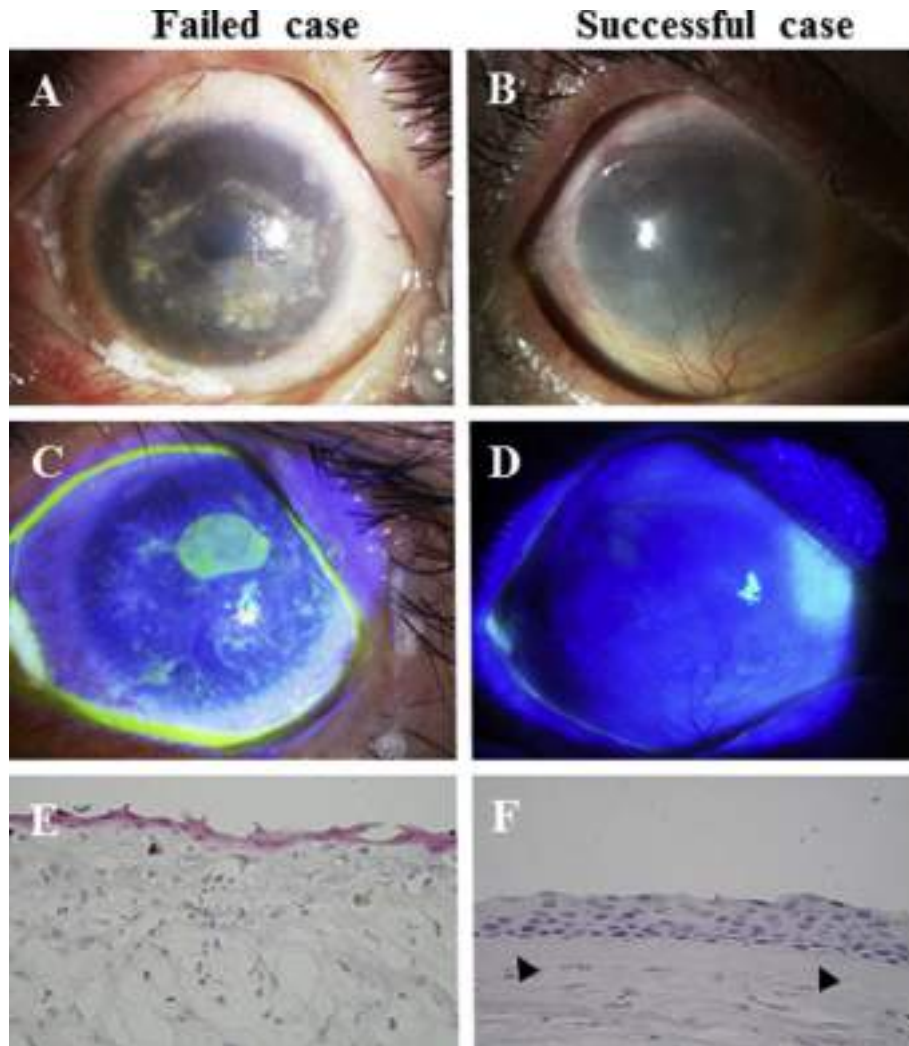


**Fig. 7.** Representative illustrations of samples from failed and successful COMET grafts. (A, C) 16 months after COMET, recurrent, small, persistent epithelial defects developed in a patient with SJS. (E) In cross-section, most areas showed 2 to 5 stratified layers and disorganized epithelium; microscopically, the AM substrate could not be observed. (B, D) Slit-lamp examination showed that the ocular surface was successfully reconstructed by COMET in a patient with chemical injury. Although in the successfully treated eye the ocular surface was stable and uniform and free of inflammation after initial transplantation, severe preoperative corneal stromal opacity that strongly affected these patients' visual acuity led us to perform PKP. (F) Microscopically, most areas contained 5 to 6 stratified layers of cells and cornea-like (cultivated oral mucosal epithelial sheet) epithelial cells on AM substrate (arrows) (original magnification:  $\times 200$ ). Modified with permission from Nakamura et al. (2007b).

#### 2.4. Recent pre-clinical trial

In view of these clinical trials, tissue-engineered CLET and COMET currently stand as established methods in the field of OSR. In an aim to further improve these surgical procedures, many groups worldwide have tried to develop treatments that use novel cell sources such as embryonic stem cells (Homma et al., 2004), mesenchymal stem cells (Ma et al., 2006), epidermal stem cells (Yang et al., 2008), immature dental-pulp stem cells (Monteiro et al., 2009), hair follicle bulge-derived stem cells (Meyer-Blazejewski et al., 2011) and umbilical cord stem cells (Reza et al., 2011). Most recently, we reported an attempt to overcome the problems of treating severe OSD with the most severe dry eye by transplanting a tissue-engineered cultivated nasal mucosal epithelial cell sheet to supply functional goblet cells and to stabilize and reconstruct the ocular surface (Kobayashi et al., 2015). This study represents a first step towards evaluating the use of tissue-engineered goblet cell transplantation of non-ocular surface origin for OSR. As a result of translational research and developments in the field of

regenerative medicine for OSR, innovative advances have been made in the basic understanding and development of new therapeutic modalities such as the transplantation of tissue-engineered cultivated epithelial stem cell sheets. We strongly believe that an understanding of stem cell biology is crucial in developing the next generation of OSR, and we are hopeful that our efforts will enable treatment of all currently intractable forms of severe OSD.

#### 3. Stem cells

It is generally believed that stem cells are critical for supplying and maintaining homeostasis within tissues or organs and for regenerating damaged tissues or organs. Based on previous studies, criteria for epithelial stem cells provide that they are relatively undifferentiated both biologically and morphologically, possess a high capacity for long-term self-renewal, are stimulated to proliferate in response to external stimuli and are usually located in well-protected, highly vascularized and innervated areas (Hall and Watt, 1989; Lajtha, 1979; Lavker and Sun, 1982; Leblond, 1981; Potten and



**Fig. 8.** (A–C) OSR with combination of COMET and PKP in patients with SJS. (A) Preoperative total conjunctivalization with severe symblepharon and partial parakeratinization. (B) Two months after initial COMET surgery. (C) Three months after PKP with cataract surgery. (D, E) Conjunctival fornix reconstruction with COMET in patients with idiopathic OSD. (D) Preoperative total conjunctivalization with severe symblepharon. (E) Six months after COMET, conjunctival fornix was successfully reconstructed. Modified with permission from Inatomi et al. (2006). (F, G) Representative illustrations of OSR using the combination of COMET and eyelid surgery in patients with thermal injury. (F) Preoperatively, there was persistent epithelial defect (PED), symblepharon and scarred entropion of the upper-eyelid. (G) Fifty months after surgery, the ocular surfaces were successfully reconstructed with COMET and eyelid surgery. Modified with permission from Takeda et al. (2011).

Loeffler, 1990). In relation to OSR, many scientists worldwide have been examining the molecular mechanism of corneal stem cells in order to better understand the role of corneal homeostasis, as well as to elucidate the most useful approach to OSR. In clinical situations, the quality of a tissue-engineered transplant is known to be the key to success, and the selection of a large number of highly proliferating stem/progenitor cells enhances the reproducibility, quality and longevity of these transplants. It follows that basic understanding of corneal epithelial stem cells is of importance for the development and clinical evaluation of OSR.

### 3.1. Concept of corneal epithelial stem cell

#### 3.1.1. XYZ hypothesis

As with other tissues and organs, the corneal epithelium must be maintained by corneal epithelial stem cells. The mechanism of corneal epithelial maintenance was first proposed as the XYZ hypothesis by Thoft et al. (Thoft and Friend, 1983). Describing as X the proliferation of corneal basal epithelial cells, the centripetal movement of peripheral cells as Y and the epithelial cell loss from the cell surface as Z, maintenance of the corneal epithelium can be defined by the equation:  $X + Y = Z$ . This clearly states that if the corneal epithelium is to be maintained, cell loss must be arranged by cell replacement. Using this hypothesis, it is possible to classify both diseases and treatments according to the specific component involved. Examining the X, Y and Z variables led to the limbal stem cell theory and to new insights into the pathogenesis and treatment of severe OSD.

#### 3.1.2. Limbal stem cell theory

The presumed location of corneal epithelial stem cells in the limbus was first reported by Schermer et al., using a rabbit model (Schermer et al., 1986). Based on the cornea-specific keratin expression pattern, they proposed that corneal epithelial stem cells are located in the limbal regions, and that corneal basal cells correspond to “transient amplifying cells” in the diagram of “stem cells ~ transient amplifying cells ~ terminally differentiated cells”. Subsequently, using 3H-thymidine labeling in mice, Cotsarelis et al. reported that label-retaining, slow-cycling cells are located only in the limbal region and that no such cells can be observed in the central corneal epithelium, suggesting that corneal epithelial stem cells are located in the limbus (Cotsarelis et al., 1989). The results of these cutting-edge investigations led to the advancement of limbal stem cell theory in understanding the pathogenesis of severe OSD and to clinical applications for OSR. However, we must exercise care in interpreting those results because the concept of “limbal stem cells” somehow differs from embryonic stem cells, induced pluripotent stem cells, hematopoietic stem cells and neural stem cells. In addition, although extensive experiments have been performed to test limbal stem cell theory, there is as yet no direct evidence that human corneal epithelial stem cells are located only in the limbal regions. While we completely agree that the limbus is an important area in the maintenance of corneal homeostasis, it is not impossible that a population of corneal stem cells may exist in the peripheral or central cornea, in much the same way as peripheral blood contains some stem cells. For that reason, continuous careful observation and direct examination will be needed to

establish a proper understanding of limbal stem cell theory. The subject was well summarized and discussed in the excellent recent review (West et al., 2015).

### 3.1.3. Oligopotent stem cells

This well-established limbal stem cell theory presented challenges in discussing the location of the corneal epithelial stem cells. Using mouse models, Majo et al. demonstrated that central corneal epithelium could be serially transplanted for a long period of time, with capability for multipotential differentiation and unlimited cellular proliferation, implying that corneal epithelial stem cells were located not only in the limbal region but also in the central cornea (Majo et al., 2008). It is now known that the limbal region is not only the niche for corneal epithelial stem cells. Kawakita et al. reported that the central corneal epithelium can maintain itself when separated from the limbus in rabbits (Kawakita et al., 2011), and Chang et al. also showed that both human limbal and central corneal epithelial cells are capable of forming spheres in cultures that have stem cell properties (Chang et al., 2011). In examining this hypothesis, we found that the cornea still maintained its transparency six months after peripheral corneal and limbal epithelial ablation in rabbits, without inflammation and conjunctivalization (Fig. 9). Additionally, Bi et al. recently reported that human central corneal epithelial cells have *in vivo* self-healing ability under pathological conditions without support from limbal stem cells (Bi et al., 2013). While these findings require further detailed scrutiny, they may yet lead to reconsideration of the concept of corneal epithelial stem cells and of the cell source for OSR.

### 3.2. Candidate limbal stem cell markers

In terms both of basic knowledge and clinical practice, many scientists worldwide have been investigating the molecular marker for cornea epithelial stem cells in order to better understand the physiological maintenance of the cornea, and to identify the most useful tools for OSR. In the clinical setting, the quality and longevity of the cultivated epithelial transplant is known to be the key to success, and the manipulation of a large number of highly proliferating stem/progenitor cells using cell biological markers promotes the longevity of these transplants. Many putative corneal epithelial stem cell markers (e.g. p63, ABCG2, Integrin  $\alpha$ 9, Keratin 15, N-cadherin, NGF/TrkA, Integrin  $\alpha$ 6/CD71, Hes1, p75, Nectin 3, Importin 13, Nucleostemin, CD38/157, Lrig1, ABCB5, WNT7A) have been reported worldwide (Di Girolamo et al., 2008; Hayashi et al., 2008, 2007; Horenstein et al., 2009; Kawashima et al., 2009; Ksander et al., 2014; Kusanagi et al., 2009; Nakamura et al., 2014, 2008a; Ouyang et al., 2014; Pajooohesh-Ganji et al., 2006; Pellegrini et al., 2001; Qi et al., 2008; Wang et al., 2009; Watanabe et al., 2004; Yoshida et al., 2006) (Fig. 10). We posit that, in our work, most of these stem cell markers were expressed not only in the limbal region but also in the conjunctival basal cells. In that light, the appropriate corneal epithelial stem cell markers for use in OSR remain in need of further detailed investigation. We further consider that the current process for isolating cells must severely damage the cell's potential. In order to select the large number of stem cells needed for manipulation of the cultured sheet, innovative tissue-engineered technology is required. This important issue is seen

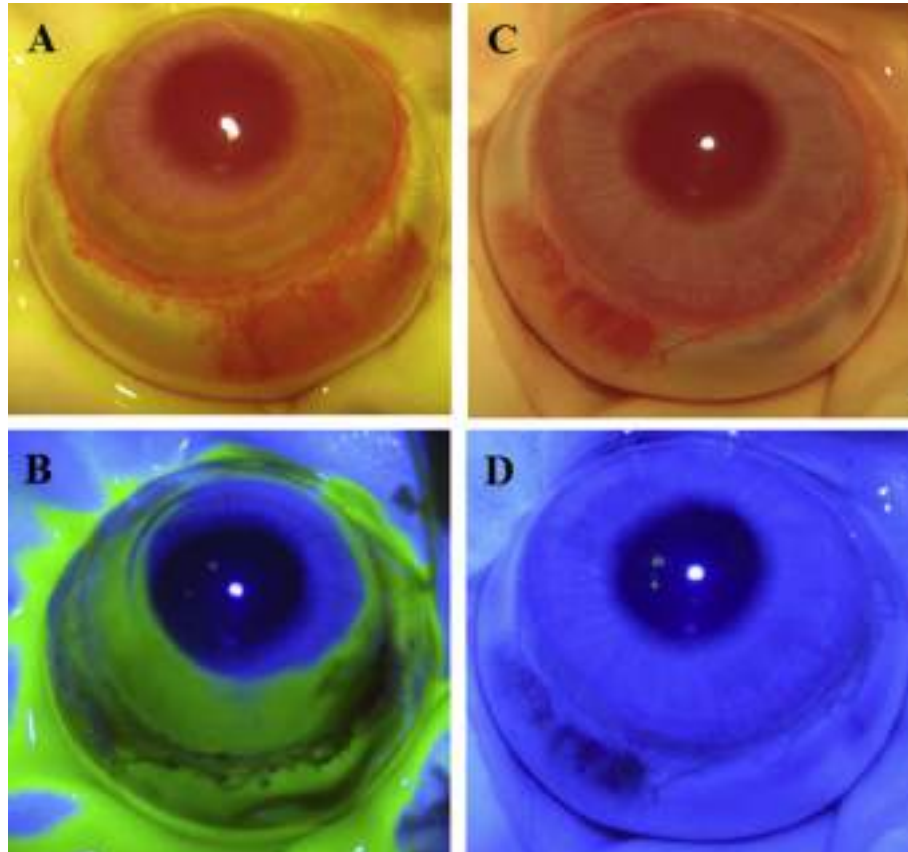


**Fig. 9.** Representative slit-lamp photographs of peripheral and limbal epithelial ablation in rabbits with or without fluorescein. (A, B) Immediately after ablation, fluorescein staining was clearly observed in all peripheral and limbal areas. (C, D) 6 months after ablation, cornea still maintained its transparency without inflammation or neovascularization.



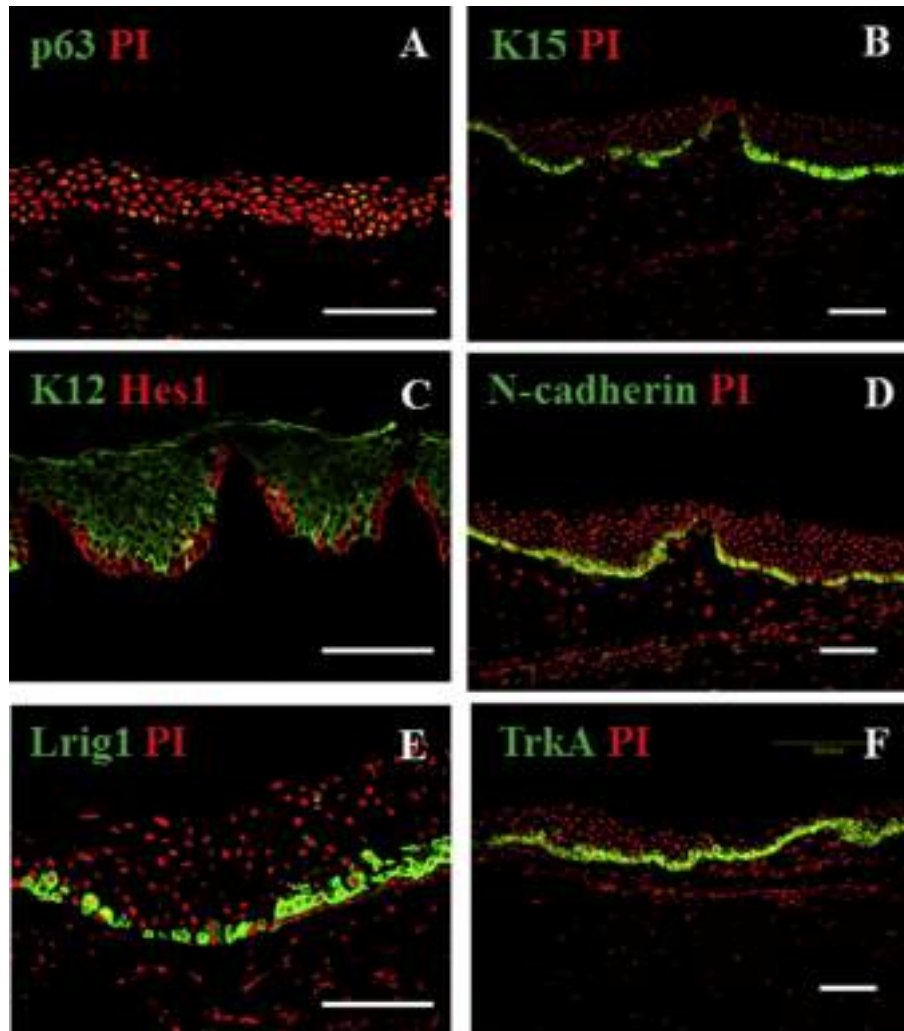


**Fig. 10.** Expression of proposed corneal epithelial stem cell markers. Immunohistochemistry for p63(A), Keratin 15(B), Hes1(C), N-cadherin(D), Lrig1(E) and TrkA(F) in human limbal region. Each marker (green) is clearly expressed in the basal cells of the limbus. Scale bars: 100  $\mu$ m.

as the first step towards the next generation of OSR using real corneal epithelial stem cells.

### 3.3. Single cell-based clonal analysis

It has been reported that one of the characteristics of epithelial stem cells is their greater proliferative capacity as compared to differentiated cells, using *in vitro* colony-forming efficiency assay from single cell. By means of this assay, Barrandon et al. previously reported the existence of three types of epidermal keratinocytes with different self-renewal capacities (Barrandon and Green, 1987). While holoclones (stem cells) have the highest reproductive capacity, in paraclones (transient amplifying cells), terminal differentiation is observed within a few generations (Fig. 11). Similar observations have subsequently been reported for the ocular surface epithelium (cornea and conjunctiva) (Pellegrini et al., 1999). They demonstrated that corneal epithelial stem cells are segregated in the limbal region while conjunctival epithelial stem cells are uniformly distributed in bulbar and fornical conjunctiva. We also reported that holoclone-type stem cells, previously identified in the skin and the ocular surface, were present in human oral mucosal epithelium, and that the low-affinity neurotrophin receptor p75 is a potential marker of oral keratinocyte stem/progenitor cells

(Nakamura et al., 2007a).

#### 3.3.1. Gene expression profiling of holoclone-type stem cells

In seeking an insight into the molecular mechanism of the human corneal epithelial stem cell, the gene expression profile of corneal epithelium was first reported by Nishida et al. (Kinoshita et al., 2001; Nishida et al., 1996). Subsequently, several groups conducted investigations using up-to-date experimental procedures such as microarray and deep RNA sequencing (Bath et al., 2013; Figueira et al., 2007; Kulkarni et al., 2010; Nakatsu et al., 2013; Takacs et al., 2011; Utheim et al., 2009). However, the molecular mechanism and gene expression profile of holoclone-type corneal epithelial stem cells remain entirely unknown. In order to gain better understanding of the molecular mechanisms responsible for corneal homeostasis, we performed gene expression profiling of holoclone-type human corneal epithelial stem cells, using DNA chip analysis (Nakamura et al., 2014) (Table 1). Among the up-regulated genes in this assay, we focused on Lrig1 for further investigation because of its unique expression pattern in the ocular surface epithelium.

Lrig1 is a transmembrane glycoprotein, recently reported as a potential master regulator of epidermal and intestinal epithelial stem cells (Jensen and Watt, 2006; Powell et al., 2012; Suzuki et al.,



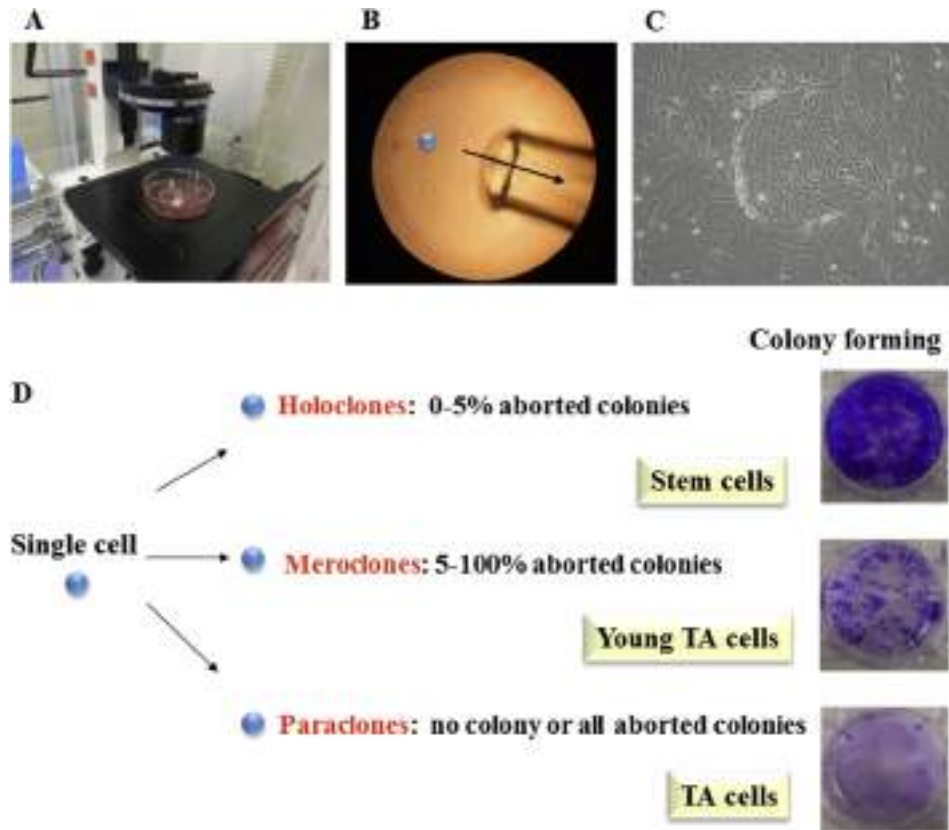


**Fig. 11.** Schema of single cell-based clonal analysis. (A, B) Using special equipment in the culture lab, a single cell can be manipulated under the microscope. (C) A colony can be formed from a single cell on the 3T3 feeder cells. (D) Holoclones (stem cells) have the highest reproductive capacity; in paraclones (transient amplifying (TA) cells), terminal differentiation is observed within a few generations.

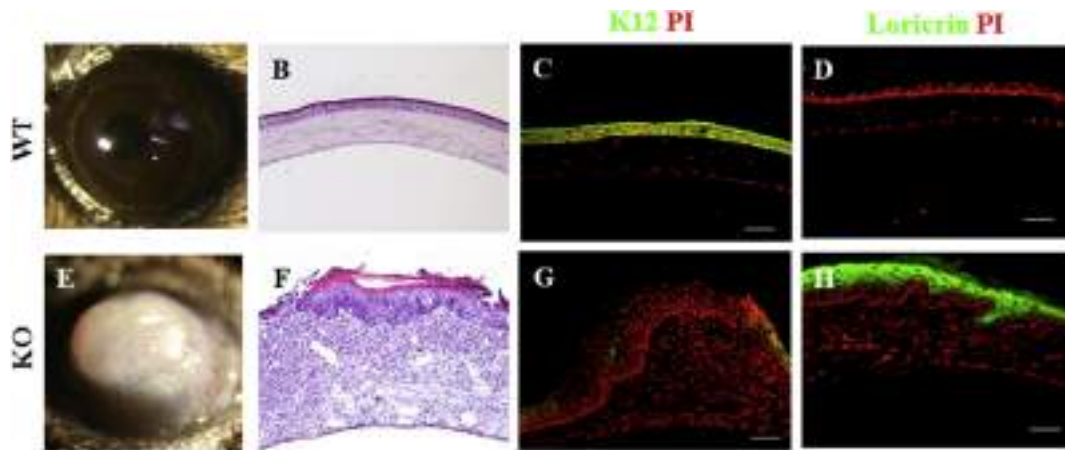


**Fig. 12.** Loss of Lrig1 results in a cell-fate change from corneal to keratinized epithelium. Slit-lamp photographs of Lrig1 wild-type (WT) (A) and knockout (KO) (E) mice corneas, and their histological appearances with hematoxylin and eosin staining (B, F). Lrig1 KO corneas formed corneal plaques with massive neovascularization and intense infiltration of inflammatory cells (E). Histological examination revealed extensive thickening and pathological keratinization of the corneal epithelium, with inflammation of the underlying corneal stroma (F). Immunostaining for keratin 12 and loricrin in Lrig1 WT (C, D) and KO (G, H) corneas. While the epithelium of the WT corneas specifically expressed keratin 12 (C), that of the Lrig1 KO corneas had gradually lost keratin 12 (D) and gained loricrin expression (H). Scale bars: 100  $\mu$ m. Modified with permission from Nakamura et al. (2014).

2002; Wong et al., 2012). We demonstrated that Lrig1 was highly expressed in holoclone-type corneal epithelial stem cells and that it was essential for maintenance of the corneal epithelium during repair (Nakamura et al., 2014) (Fig. 12). Loss of Lrig1 impaired wound-induced corneal replacement and resulted in a cell-fate change from non-keratinized to keratinized epithelium.

Interestingly, we discovered that Lrig1 controlled corneal homeostasis by negatively regulating the novel Stat3-dependent inflammatory pathway. Furthermore, corneal maintenance was arranged not only by corneal epithelial stem cells but also by bone marrow-derived inflammatory cells, whose functions and roles are well-regulated by the Lrig1-Stat3 inflammatory pathway (Fig. 13).

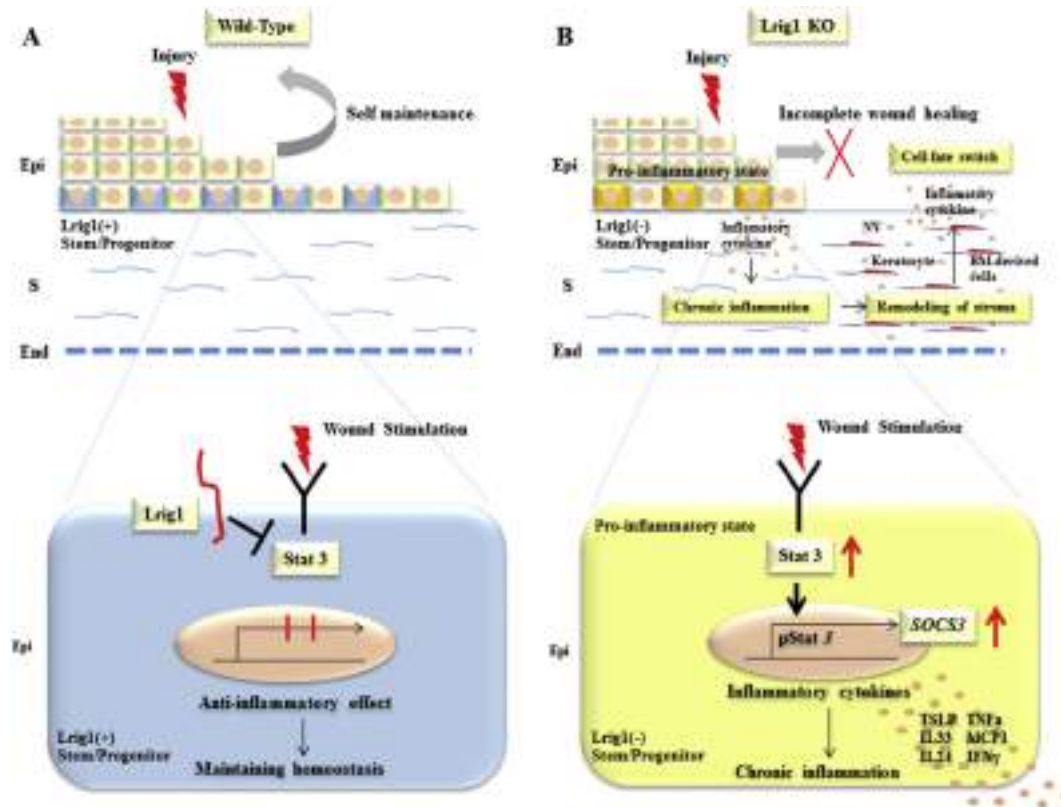


**Fig. 13.** Model of the function of Lrig1 in corneal homeostasis. (A) Normally, the cornea is self-maintained by Lrig1 (+) corneal stem/progenitor cells post-injury. Corneal transparency is maintained via negative regulation of the Stat3-dependent inflammatory pathway by Lrig1. (B) Loss of Lrig1 causes the pro-inflammatory state in Lrig1 (–) corneal stem/progenitor cells and impairs delayed/incomplete wound healing. Loss of Lrig1 activates the Stat3-dependent inflammatory pathway and induces chronic inflammation, resulting in remodeling of the corneal stroma. Inductive bone marrow-derived cells secrete inflammatory cytokines and cause cell-fate changes to keratinized epithelium. Epi: corneal epithelium; S: corneal stroma; End: corneal endothelium; NV: neovascularization. Modified with permission from Nakamura et al. (2014).

These findings provide new insights into the underlying homeostatic regulation of Lrig1 (+) corneal epithelial stem cells and serve as a target for therapeutic exploitation, including OSR.

### 3.3.2. miRNA profiling of holoclone-type stem cells

Recently, particular attention has focused on microRNAs (miRNAs), a newly identified form of non-coding, regulatory RNA that modulate gene expression post-transcriptionally (He and Hannon, 2004). These play an important role in regulating a range of physiological and pathological processes, including cell proliferation, migration and differentiation processes, stem cell maintenance. Although some studies have addressed the function and role of miRNAs in the corneal epithelium (Lee et al., 2011; Lin et al., 2013; Shalom-Feuerstein et al., 2012; Yu et al., 2008), little is yet known about the molecular mechanism of miRNAs in corneal homeostasis. To better understand the subject, we performed miRNA profiling of holoclone-type corneal epithelial stem cells. Among the up-regulated miRNAs in this assay, we focused on several sets of miRNAs (1246, 3687, 4284 etc.) for further investigation. Extensive investigations are currently underway to clarify the molecular pathway of corneal epithelial stem cells by miRNAs. This basic understanding of corneal epithelial stem cells from different points of view holds promise for future regenerative therapy, including OSR.

## 4. Tissue engineering

When considering the development of OSR using tissue engineering, there are three important factors: 1) the cell source

including stem cells, 2) a suitable biocompatible substrate and 3) suitable growth factors. In the past 20 years, this newly developed field of research has shown promising translational potential in the use of stem cells and biomaterials to generate biological substitutes and improve tissue functions. Successful generation of tissue-engineered sheet for OSR is highly dependent on the quality of underlying substrates. A useful substrate for OSR should have a highly biocompatible, non-immunogenic and non-inflammatory character, and should maintain corneal transparency and mechanical stability and promote cell adhesion and proliferation. Many cell substrates, such as biological scaffolds (e.g. AM), biosynthetic scaffolds (e.g. Fibrin, collagen) and synthetic scaffolds (e.g. temperature-responsive dish, contact lens), have been proposed as useful for OSR. Among these, AM is the most widely-used and represents the current gold standard substrate for OSR.

### 4.1. Amniotic membrane (AM)

#### 4.1.1. Naive AM

Human AM is the innermost layer of the fetal sac and is composed of a monolayer of amniotic epithelial cells, a thick basement membrane and a subjacent avascular stroma. It has been used in surgical materials and biological dressing for the epidermal field (Trelford and Trelford-Sauder, 1979). In the context of OSR, previous studies have indicated AM's potential for conjunctival reconstruction in cases of severe OSD (De RÖTH, 1940). A number of AM's characteristics make it a good fit for use in OSR; it contains various growth factors and cytokines inducing epithelialization and wound healing (Koizumi et al., 2000b), has anti-scarring and anti-

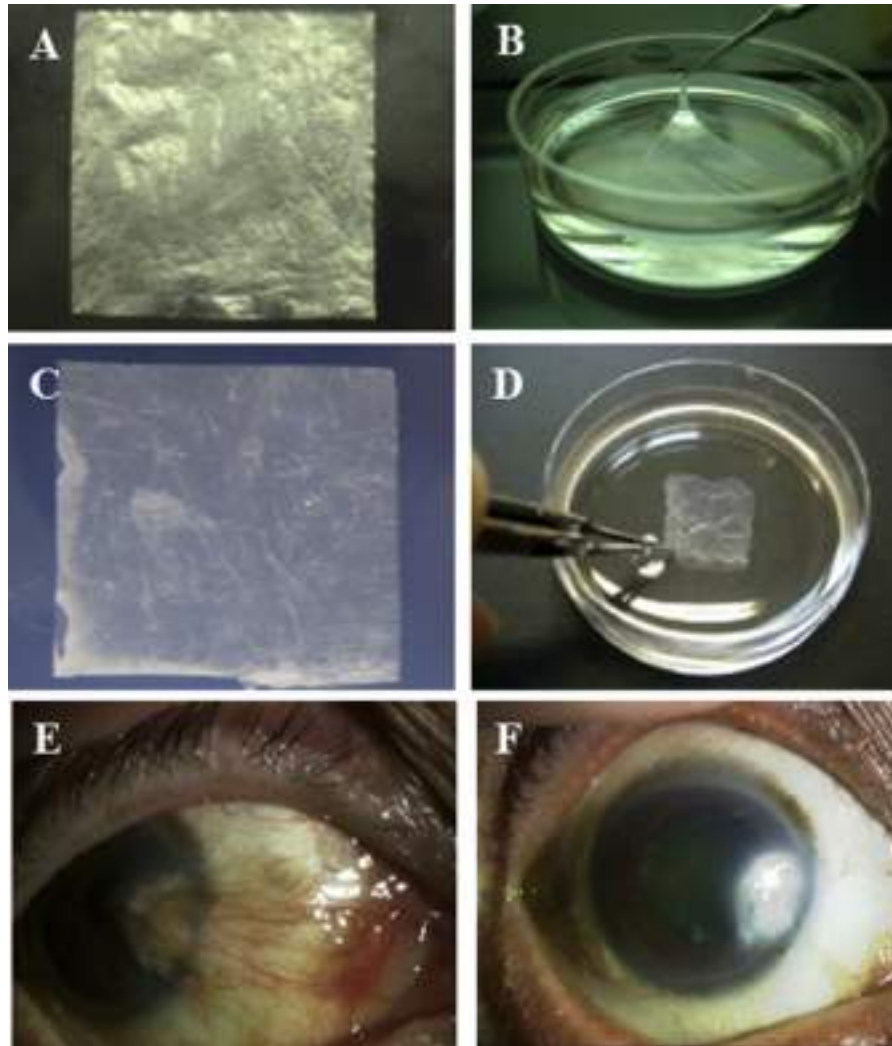


**Fig. 14.** Development of dried AM. (A) The sterilized, freeze-dried AM was wafer-like and very light and thin. (B) It became smooth and flexible on hydration. (C) Visually, trehalose-treated freeze-dried AM was similar to freeze-dried AM in the dry condition. (D) Trehalose-treated freeze-dried AM was smoother and more flexible than freeze-dried AM in the wet condition. Representative slit-lamp photographs taken before the sterilized, freeze-dried AM transplantation (E) and at 24 months after transplantation (F). Before transplantation, eyes manifested fibrovascular overgrowth of degenerative conjunctiva onto the cornea (E). At 24 months after transplantation, fibrosis was markedly suppressed, and the conjunctival surface was stable without inflammation (F). Modified with permission from Nakamura et al. (2004b), Nakamura et al. (2006b), Nakamura et al. (2008b).

inflammatory properties (Solomon et al., 2001; Tseng et al., 1999) and resembles the basement membrane of the corneal epithelium (Endo et al., 2004). From these basic and clinical observations, AM has come to be seen as an appropriate substrate for use in OSR. Clinical results of CLET and COMET using an AM substrate are encouraging, although there are still several variations and arguments in respect of its use. For example, there is no standard protocol to prepare the AM, and it also has donor-dependent variability and regional variations both physiologically and biologically. These concerns have prompted us to develop alternative substrates for OSR.

#### 4.1.2. Dried AM

As mentioned above, AM has unique properties that can be useful in treating severe OSD. However, some biological and logistical issues remain. To date, a majority of ophthalmologists have used cryopreserved AM under conditions that are as sterile as possible; complete sterilization cannot be achieved using existing procedures. For clinical use, AM should ideally be sterile and free of

contamination, and also be easily to obtain and preserve at room temperature; cryopreservation of AM needs an expensive and bulky deep freezer. To overcome these problems, we have successfully produced sterilized, freeze-dried AM using our own unique protocol (under vacuum conditions and vacuum-packed at room temperature with gamma-irradiation), and this biomaterial has been successfully used as a substrate in OSR (Nakamura et al., 2004c) (Fig. 14). On the basis of these results, we applied this biomaterial to OSR for patients with pterygium (Nakamura et al., 2006b). This prototype freeze-dried AM was improved by use of trehalose to protect its physical properties during the freezing process (Nakamura et al., 2008b). Most recently, Okabe et al. reported that hyper-dry AM, using far-infrared rays, depression of air and microwaves with  $\gamma$ -ray irradiation, is a useful biomaterial for tissue engineering (Okabe et al., 2014). In view of the particular focus on pathogenic organisms in recent years, suitable sterilization of both native and dried AM is vital, and these developments will contribute to the next generation of AM, using tissue engineering techniques. Following strict regulation in Japan, we are now trying



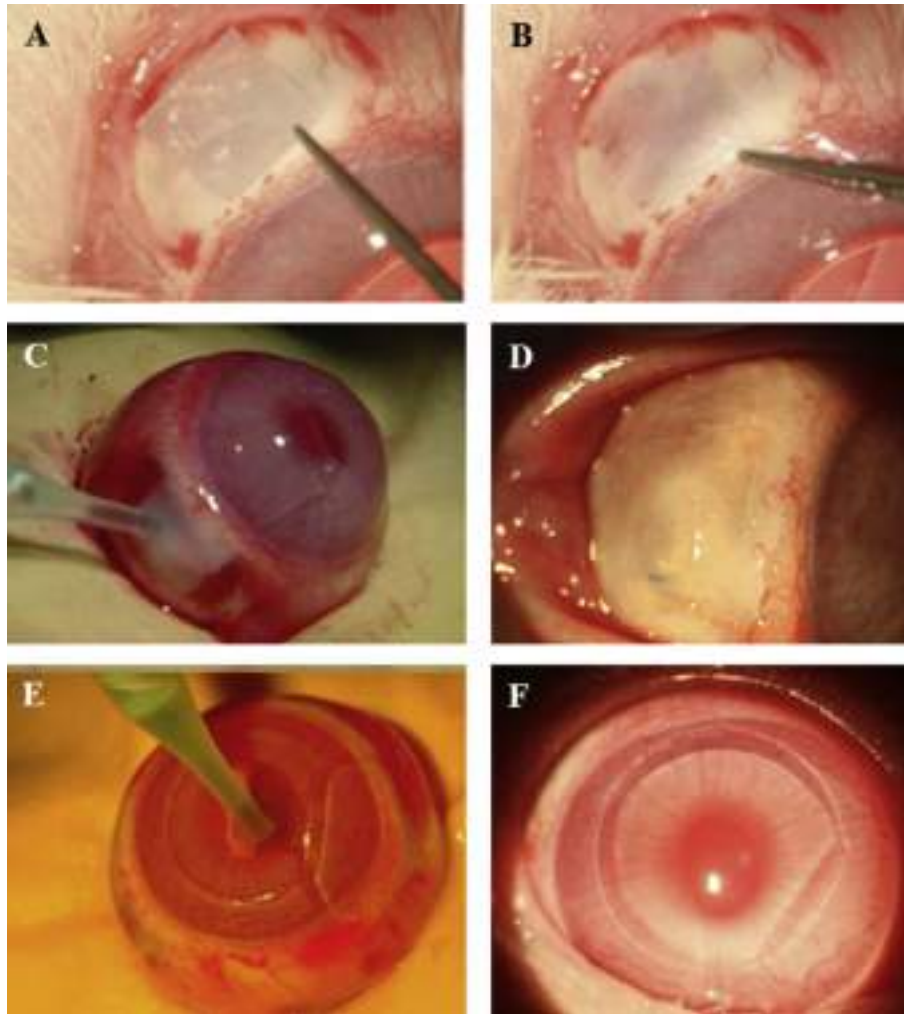


**Fig. 15.** Development of bio-adhesives. (A, B) Representative photos of fibrin glue-coated freeze-dried AM transplantation. FCFD-AM adhered immediately after transplantation onto the bare sclera, before fibrin glue-coated freeze-dried AM transplantation (A) and after fibrin glue-coated freeze-dried AM transplantation (B). Representative photographs of sutureless AM transplantation (C, D) and lamellar therapeutic keratoplasty (E, F) using chemically-defined bioadhesive. Modified with permission from Sekiyama et al. (2007), Takaoka et al. (2008), Takaoka et al. (2009).

to set up an AM banking center to organize the preparation and spread of AM.

#### 4.2. Fibrin and the temperature-sensitive dish

Another promising substrate for clinical use in OSR is fibrin and the temperature-sensitive culture dish. The usefulness of a serum-derived fibrin substrate for cultured corneal epithelial cells has previously been reported (Hirayama et al., 2012; Rama et al., 2001, 2010). As fibrin substrate is absorbed after CLET and COMET, this method has some clinical benefits, in that the cultivated epithelial sheet can be transplanted directly onto the corneal surface. Although fibrin has achieved successful clinical outcomes, safety and logistical problems remain, such as the risk of disease transmission after operations (e.g. human parvovirus B19, prions) (Hino et al., 2000).

Another unique tissue-engineered technique has been developed using a temperature-sensitive culture dish for corneal epithelial cells (Nishida et al., 2004a, 2004b). This is an original system that allows the cultivated epithelium to be detached from the culture dish by changing the temperature. Both of these substrates (fibrin and the temperature-sensitive dish) may be more suitable for transplantation than AM because AM will remain

permanently on the transplanted area if severe postoperative inflammation does not occur. However, since the ocular surface (including epithelium and subjacent stroma) is severely damaged in patients with severe OSD, we need to reconstruct the subjacent corneal stroma as well as the epithelial layer. In considering the biological clinical aspects, AM can serve as both an epithelial layer and as a healthy substrate covering a damaged corneal stroma. Further comparative clinical studies are needed to establish which substrate is most effective.

#### 4.3. Development of novel cultured substrates

Although AM, fibrin and the temperature-sensitive culture dish have been widely used for OSR, a variety of alternative substrates suitable for generating tissue-engineered cultured sheet have been examined in preclinical or clinical applications. Among biosynthetic scaffolds, the cross-linked collagen scaffold (Dravida et al., 2008), fibroin membrane (Chirila et al., 2008), myogel extracted from skeletal muscle (Francis et al., 2009), collagen vitrigel (McIntosh Ambrose et al., 2009), compressed collagen (Levis et al., 2010; Mi et al., 2010), keratin films (Reichl et al., 2011) and chitosan hydrogels (Groluk et al., 2012) have all been studied. In the area of synthetic scaffolds, medical-use contact lenses (Di Girolamo et al.,



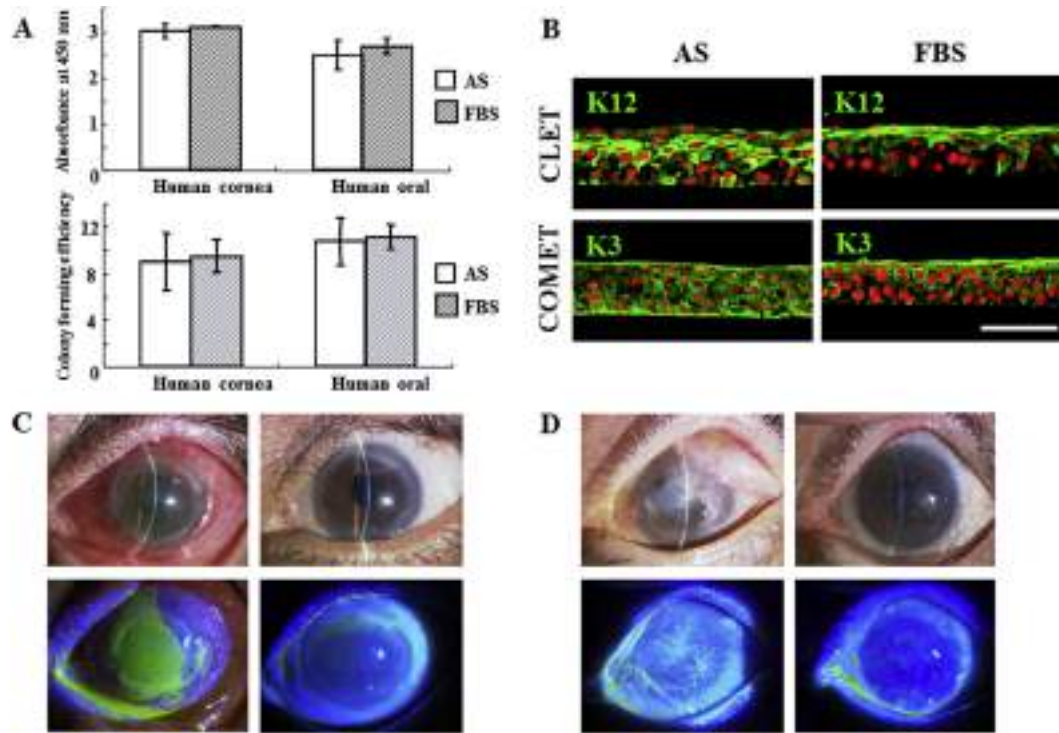


**Fig. 16.** Development of autologous serum-derived CLET and COMET. (A) BrdU proliferation assay and colony-forming efficiencies (CFE) showed that the proliferation indices and CFE of human corneal and oral mucosal epithelium cultivated using autologous serum (AS) and fetal bovine serum (FBS) were almost similar. (B) The expression patterns of K12 and K3 were similar in cultivated corneal and oral mucosal epithelial sheets derived from AS- and FBS-supplemented culture systems. (C) Representative clinical outcomes of autologous serum-derived CLET in patients with OCP. (D) Representative clinical outcomes of autologous serum-derived COMET in patients with OCP. Modified with permission from Nakamura et al. (2006a), Ang et al. (2006), Nakamura et al. (2006c).

**Table 1**  
Upregulated genes in holoclone-type corneal keratinocytes (selected).

Gene symbol	Gene title	Proposed function
<i>NLRP2</i>	NLR family, pyrin domain containing 2	Activation of proinflammatory caspases
<i>IL24</i>	Interleukin 24	Anti-proliferative property
<i>PTX3</i>	Pentraxin-related gene, rapidly induced by IL-1 beta	Regulation of innate resistance to pathogens
<i>CALD1</i>	Caldesmon 1	Actin- and myosin-binding protein
<i>KLK6</i>	Kallikrein 6 (neurosin, zyme)	Serine protease
<i>CRISP2</i>	Cysteine-rich secretory protein 2	Regulation of ion channels' activity
<i>JPH3</i>	Junctophilin 3	Stabilization of the junctional membrane
<i>MUM1</i>	Melanoma associated antigen (mutated) 1	DNA damage response pathway
<i>LRIG1</i>	Leucine-rich repeats and Ig-like domains 1	Epidermal and intestinal stem cell marker
<i>MTSS1</i>	Metastasis suppressor 1	Cancer progression
<i>KRT19</i>	Keratin 19	Organization of myofibers
<i>LRP11</i>	Low density lipoprotein receptor-related protein 11	Receptor activity
<i>DEFB4</i>	Defensin, beta 4	Antibacterial activity
<i>LGR5</i>	Leucine-rich repeat-containing G protein-coupled receptor 5	Intestinal and hair follicle stem cell marker
<i>KRT24</i>	Keratin 24	Structural constituent of cytoskeleton

2009), nanofibers (Sharma et al., 2011; Zajicova et al., 2010) and electrospun 3D scaffolds (Ortega et al., 2013) have also been examined. In addition, biological scaffolds such as lens capsule (Galal et al., 2007) and decellular corneal stroma (Shafiq et al., 2012) have been investigated. All these proposed substrates have potential advantages and disadvantages, and careful investigation

is again needed before treating patients with severe OSD using these substrates.

#### 4.4. Bio-adhesive

Among established OSR protocols, the most standard method of AM transplantation, CLET and COMET using AM carrier involve suturing, which is time-consuming and is associated with disadvantages that include suture abscesses, granuloma formation and tissue necrosis. To overcome these problems, sutureless transplantation, using proper tissue-engineered bio-adhesive, is ideal for developing next-generation OSR. There have previously been some studies of sutureless techniques for OSR using fibrin glue (Szurman et al., 2006); we initially developed a novel sutureless technique for AM transplantation by generating a fibrin glue-coated dried AM (Sekiya et al., 2007) (Fig. 15). Fibrin is derived from serum, so if a non-biologic and defined bio-adhesive can be successfully developed, it would prove ideal for safe and simple OSR. On that basis, we developed AM transplantation for OSR using a chemically defined bio-adhesive that is safe, biocompatible and biodegradable (Takaoka et al., 2008) (Fig. 15). Based on those results, we foresee the use of chemically defined bio-adhesives in a range of sutureless transplantations, including CLET, COMET and lamellar keratoplasty (Takaoka et al., 2009). We are currently applying this technique for lamellar keratoplasty, and the clinical results are quite promising so far.

### 5. Growth factors

#### 5.1. Feeder layer factor

Based on the pioneering culture method by Rheinwald and

Green, long-term survival and serial expansion of epidermal stem cells is possible if the epithelial cells are co-cultured with mouse-derived 3T3 feeder layer (Rheinwald and Green, 1975). Since that time, 3T3 feeder cells have become the most widely-used for culturing corneal epithelial cells. The exclusion of animal material from the culture system offers significant clinical advantages for OSR, reducing the risk of transmission of animal-derived infections or unknown pathogens. Various candidate human-derived feeder cells such as MRC-5, amniotic epithelium, adipose tissue, mesenchymal stem cells and dermal fibroblast have been examined for their usefulness in generating cultivated epithelial sheet (Chen et al., 2007; Notara et al., 2007; Oie et al., 2010; Omoto et al., 2009; Sugiyama et al., 2008). However, widespread use of these culture systems has been hindered by the standardization of culture protocols because of the variable culture conditions of feeder cells.

### 5.2. Serum factor

The previously preferred method of cultivating epithelial sheets also requires the use of xenobiotic materials such as fetal bovine serum (FBS) in the culture system. However, the use of FBS in the culturing system is a major clinical concern, as bovine spongiform encephalopathy cannot be detected by any known assay. The use of autologous serum (AS) as an alternative to FBS is therefore significantly safer, excluding the need for bovine material in the culture process. Initially, we tried to determine whether AS from patients with severe OSD was as effective in supporting cell proliferation and differentiation in cultivated corneal and oral mucosal epithelial cells as culture methods using FBS (Nakamura et al., 2006a) (Fig. 16). We found that an AS-supplemented culture protocol was effective in supporting the proliferation of human corneal and oral mucosal epithelial cells, as well as the development of transplantable cultivated corneal and oral mucosal epithelial sheets. Based on these findings, we adapted this method for clinical application and reported the successful clinical use of cultivated corneal and oral mucosal epithelial sheets (Ang et al., 2006; Nakamura et al., 2006c). These clinical reports make important suggestions and represent progress in the pursuit of completely xenobiotic-free tissue-engineered transplants. In addition, we know from our clinical work that AS sometimes has donor-dependent variations (e.g. disease or age) that must be kept in view.

### 5.3. Development of feeder-free and serum-free systems

In light of the above mentioned factors, the development of feeder-free and serum-free culturing systems might be ideal for the next generation of OSR using tissue-engineering techniques. Yokoo et al. reported the generation of a cultivated corneal epithelial cell sheet for OSR in a completely serum-free and feeder-free culture system containing epidermal growth factor and B-27 (Yokoo et al., 2008). More recently, Miyashita et al. reported the long-term maintenance of corneal epithelial stem/progenitor cells using Rho Kinase inhibitor and keratinocyte growth factor (Miyashita et al., 2013). We believe that these studies represent an important step in the development of real feeder-free and serum-free transplantable cultivated epithelial sheets for safe and ideal OSR.

## 6. Future directions

Corneal regeneration has long been one of the great challenges for ophthalmologists and vision scientists worldwide. With advances in basic research in regenerative medicine and tissue engineering, great progress has been made in the fundamental

understanding and development of novel therapeutic modalities such as CLET and COMET. However, although CLET and COMET currently represent the safest and most reliable form of newly developed transplantation, several issues remain to be overcome. First, autologous CLET is to date the most promising treatment for reconstructing the ocular surface in cases of unilateral severe OSD. However, in our long-term follow-up, we certainly observed some incidence of mild conjunctivalization in peripheral corneas. The current cultivated corneal epithelial sheet could not absolutely reproduce the corneal limbal niche, and recreation of the functional corneal limbal niche using innovative tissue-engineering technology may be needed to properly develop this surgical tool. In contrast, treatment of patients with bilateral severe OSD requires either allogeneic CLET or autologous COMET, depending on patient variables (e.g. type of disease, age). In the case of CLET, the risk of postoperative rejection must be addressed, requiring a basic knowledge of the immunological background of allogeneic OSR and an appropriate protocol for postoperative management, especially with regard to immunosuppressive therapy. In the case of COMET, we must exercise caution because the cultivated oral mucosal epithelial sheet is not identical to *in vivo* corneal epithelium. This requires a basic understanding of epithelial cell biology in trying to characterize the cell source to be used. One candidate approach is to identify a novel, non-ocular surface cell source for use in OSR. The other candidate approach is to develop innovative genetically-modified biotechnology using induced-pluripotent stem cells or direct reprogramming. We strongly believe that greater knowledge of proposed and established surgical modalities, stem cell behavior, the surrounding extracellular matrix and beneficial growth factors will provide a foundation for the further development of treatments for severe OSD.

## References

- Ang, L.P., Nakamura, T., Inatomi, T., Sotozono, C., Koizumi, N., Yokoi, N., Kinoshita, S., 2006. Autologous serum-derived cultivated oral epithelial transplants for severe ocular surface disease. *Arch. Ophthalmol.* 124, 1543–1551.
- Ballen, P.H., 1963. Mucous membrane grafts in chemical (lye) burns. *Am. J. Ophthalmol.* 55, 302–312.
- Barrandon, Y., Green, H., 1987. Three clonal types of keratinocyte with different capacities for multiplication. *Proc. Natl. Acad. Sci. U. S. A.* 84, 2302–2306.
- Bath, C., Muttuvolu, D., Emmersen, J., Vorum, H., Hjortdal, J., Zachar, V., 2013. Transcriptional dissection of human limbal niche compartments by massive parallel sequencing. *PLoS One* 8, e64244.
- Baylis, O., Figueiredo, F., Henein, C., Lako, M., Ahmad, S., 2011. 13 years of cultured limbal epithelial cell therapy: a review of the outcomes. *J. Cell Biochem.* 112, 993–1002.
- Bi, Y., Bock, F., Zhou, Q., Cursiefen, C., 2013. Central corneal epithelium self-healing after ring-shaped glycerol-cryopreserved lamellar keratoplasty in Terrien marginal degeneration. *Int. J. Ophthalmol.* 6, 251–252.
- Chang, C.Y., McGhee, J.J., Green, C.R., Sherwin, T., 2011. Comparison of stem cell properties in cell populations isolated from human central and limbal corneal epithelium. *Cornea* 30, 1155–1162.
- Chen, Y.T., Li, W., Hayashida, Y., He, H., Chen, S.Y., Tseng, D.Y., Kheirkhah, A., Tseng, S.C., 2007. Human amniotic epithelial cells as novel feeder layers for promoting ex vivo expansion of limbal epithelial progenitor cells. *Stem Cells* 25, 1995–2005.
- Chiou, A.G., Florakis, G.J., Kazim, M., 1998. Management of conjunctival cicatrizing diseases and severe ocular surface dysfunction. *Surv. Ophthalmol.* 43, 19–46.
- Chirila, T., Barnard, Z., Zainuddin, H., Harkin, D.G., Schwab, I.R., Hirst, L., 2008. Bombyx mori silk fibroin membranes as potential substrata for epithelial constructs used in the management of ocular surface disorders. *Tissue Eng. Part A* 14, 1203–1211.
- Cotsarelis, G., Cheng, S.Z., Dong, G., Sun, T.T., Lavker, R.M., 1989. Existence of slow-cycling limbal epithelial basal cells that can be preferentially stimulated to proliferate: implications on epithelial stem cells. *Cell* 57, 201–209.
- De RÖTH, A., 1940. Plastic repair of conjunctival defects with fetal membrane. *Arch. Ophthalmol.* 23, 522–525.
- Di Girolamo, N., Bosch, M., Zamora, K., Coroneo, M.T., Wakefield, D., Watson, S.L., 2009. A contact lens-based technique for expansion and transplantation of autologous epithelial progenitors for ocular surface reconstruction. *Transplantation* 87, 1571–1578.
- Di Girolamo, N., Sarris, M., Chui, J., Cheema, H., Coroneo, M.T., Wakefield, D., 2008. Localization of the low-affinity nerve growth factor receptor p75 in human

- limbal epithelial cells. *J. Cell Mol. Med.* 12, 2799–2811.
- Dravida, S., Gaddipati, S., Griffith, M., Merrett, K., Lakshmi Madhira, S., Sangwan, V.S., Vemuganti, G.K., 2008. A biomimetic scaffold for culturing limbal stem cells: a promising alternative for clinical transplantation. *J. Tissue Eng. Regen. Med.* 2, 263–271.
- Endo, K., Nakamura, T., Kawasaki, S., Kinoshita, S., 2004. Human amniotic membrane, like corneal epithelial basement membrane, manifests the alpha5 chain of type IV collagen. *Invest. Ophthalmol. Vis. Sci.* 45, 1771–1774.
- Figueira, E.C., Di Girolamo, N., Coroneo, M.T., Wakefield, D., 2007. The phenotype of limbal epithelial stem cells. *Invest. Ophthalmol. Vis. Sci.* 48, 144–156.
- Francis, D., Abberton, K., Thompson, E., Daniell, M., 2009. Myogel supports the ex vivo amplification of corneal epithelial cells. *Exp. Eye Res.* 88, 339–346.
- Friend, J., Kinoshita, S., Thoft, R.A., Eliason, J.A., 1982. Corneal epithelial cell cultures on stromal carriers. *Invest. Ophthalmol. Vis. Sci.* 23, 41–49.
- Galal, A., Perez-Santonja, J.J., Rodriguez-Prats, J.L., Abad, M., Alio, J., 2007. Human anterior lens capsule as a biologic substrate for the ex vivo expansion of limbal stem cells in ocular surface reconstruction. *Cornea* 26, 473–478.
- Gipson, I.K., Geggel, H.S., Spurr-Michaud, S.J., 1986. Transplant of oral mucosal epithelium to rabbit ocular surface wounds in vivo. *Arch. Ophthalmol.* 104, 1529–1533.
- Gipson, I.K., Grill, S.M., 1982. A technique for obtaining sheets of intact rabbit corneal epithelium. *Invest. Ophthalmol. Vis. Sci.* 23, 269–273.
- Griffith, M., Osborne, R., Munger, R., Xiong, X., Doillon, C.J., Laycock, N.L., Hakim, M., Song, Y., Watsky, M.A., 1999. Functional human corneal equivalents constructed from cell lines. *Science* 286, 2169–2172.
- Grolik, M., Szczubialka, K., Wowra, B., Dobrowolski, D., Orzechowska-Wylegala, B., Wylegala, E., Nowakowska, M., 2012. Hydrogel membranes based on genipin-cross-linked chitosan blends for corneal epithelium tissue engineering. *J. Mater. Sci. Mater. Med.* 23, 1991–2000.
- Grueterich, M., Espana, E.M., Touhami, A., Ti, S.E., Tseng, S.C., 2002. Phenotypic study of a case with successful transplantation of ex vivo expanded human limbal epithelium for unilateral total limbal stem cell deficiency. *Ophthalmology* 109, 1547–1552.
- Hall, P.A., Watt, F.M., 1989. Stem cells: the generation and maintenance of cellular diversity. *Development* 106, 619–633.
- Hayashi, R., Yamato, M., Saito, T., Oshima, T., Okano, T., Tano, Y., Nishida, K., 2008. Enrichment of corneal epithelial stem/progenitor cells using cell surface markers, integrin alpha6 and CD71. *Biochem. Biophys. Res. Commun.* 367, 256–263.
- Hayashi, R., Yamato, M., Sugiyama, H., Sumide, T., Yang, J., Okano, T., Tano, Y., Nishida, K., 2007. N-Cadherin is expressed by putative stem/progenitor cells and melanocytes in the human limbal epithelial stem cell niche. *Stem Cells* 25, 289–296.
- He, L., Hannon, G.J., 2004. MicroRNAs: small RNAs with a big role in gene regulation. *Nat. Rev. Genet.* 5, 522–531.
- Hino, M., Ishiko, O., Honda, K.I., Yamane, T., Ohta, K., Takubo, T., Tatsumi, N., 2000. Transmission of symptomatic parvovirus B19 infection by fibrin sealant used during surgery. *Br. J. Haematol.* 108, 194–195.
- Hirayama, M., Satake, Y., Higa, K., Yamaguchi, T., Shimazaki, J., 2012. Transplantation of cultivated oral mucosal epithelium prepared in fibrin-coated culture dishes. *Invest. Ophthalmol. Vis. Sci.* 53, 1602–1609.
- Homma, R., Yoshikawa, H., Takeno, M., Kurokawa, M.S., Masuda, C., Takada, E., Tsubota, K., Ueno, S., Suzuki, N., 2004. Induction of epithelial progenitors in vitro from mouse embryonic stem cells and application for reconstruction of damaged cornea in mice. *Invest. Ophthalmol. Vis. Sci.* 45, 4320–4326.
- Horenstein, A.L., Sizzano, F., Lusso, R., Besso, F.G., Ferrero, E., Deaglio, S., Corno, F., Malavasi, F., 2009. CD38 and CD157 ectoenzymes mark cell subsets in the human corneal limbus. *Mol. Med.* 15, 76–84.
- Inatomi, T., Nakamura, T., Kojima, M., Koizumi, N., Sotozono, C., Kinoshita, S., 2006. Ocular surface reconstruction with combination of cultivated autologous oral mucosal epithelial transplantation and penetrating keratoplasty. *Am. J. Ophthalmol.* 142, 757–764.
- Jensen, K.B., Watt, F.M., 2006. Single-cell expression profiling of human epidermal stem and transit-amplifying cells: Lrig1 is a regulator of stem cell quiescence. *Proc. Natl. Acad. Sci. U. S. A.* 103, 11958–11963.
- Kaufman, H.E., 1984. Keratoplasty for the replacement of damaged corneal epithelium. *Am. J. Ophthalmol.* 97, 100–101.
- Kawakita, T., Higa, K., Shimmura, S., Tomita, M., Tsubota, K., Shimazaki, J., 2011. Fate of corneal epithelial cells separated from limbus in vivo. *Invest. Ophthalmol. Vis. Sci.* 52, 8132–8137.
- Kawashima, M., Kawakita, T., Yoshida, S., Shimmura, S., Tsubota, K., 2009. Nucleostemin as a possible progenitor marker of corneal epithelial cells. *Mol. Vis.* 15, 1162–1168.
- Kenyon, K.R., Tseng, S.C., 1989. Limbal autograft transplantation for ocular surface disorders. *Ophthalmology* 96, 709–722 discussion 722–723.
- Kim, J.C., Tseng, S.C., 1995. Transplantation of preserved human amniotic membrane for surface reconstruction in severely damaged rabbit corneas. *Cornea* 14, 473–484.
- Kinoshita, S., Adachi, W., Sotozono, C., Nishida, K., Yokoi, N., Quantock, A.J., Okubo, K., 2001. Characteristics of the human ocular surface epithelium. *Prog. Retin Eye Res.* 20, 639–673.
- Kinoshita, S., Koizumi, N., Nakamura, T., 2004. Transplantable cultivated mucosal epithelial sheet for ocular surface reconstruction. *Exp. Eye Res.* 78, 483–491.
- Kinoshita, S., Ohashi, Y., Ohji, M., Manabe, R., 1991. Long-term results of keratoplasty in Mooren's ulcer. *Ophthalmology* 98, 438–445.
- Kobayashi, H., Ikada, Y., 1991. Corneal cell adhesion and proliferation on hydrogel sheets bound with cell-adhesive proteins. *Curr. Eye Res.* 10, 899–908.
- Kobayashi, M., Nakamura, T., Yasuda, M., Hata, Y., Okura, S., Iwamoto, M., Nagata, M., Fullwood, N.J., Koizumi, N., Hisa, Y., Kinoshita, S., 2015. Ocular surface reconstruction with a tissue-engineered nasal mucosal epithelial cell sheet for the treatment of severe ocular surface diseases. *Stem Cells Transl. Med.* 4, 99–109.
- Koizumi, N., Inatomi, T., Quantock, A.J., Fullwood, N.J., Dota, A., Kinoshita, S., 2000a. Amniotic membrane as a substrate for cultivating limbal corneal epithelial cells for autologous transplantation in rabbits. *Cornea* 19, 65–71.
- Koizumi, N., Inatomi, T., Sotozono, C., Fullwood, N.J., Quantock, A.J., Kinoshita, S., 2000b. Growth factor mRNA and protein in preserved human amniotic membrane. *Curr. Eye Res.* 20, 173–177.
- Koizumi, N., Inatomi, T., Suzuki, T., Sotozono, C., Kinoshita, S., 2001a. Cultivated corneal epithelial stem cell transplantation in ocular surface disorders. *Ophthalmology* 108, 1569–1574.
- Koizumi, N., Inatomi, T., Suzuki, T., Sotozono, C., Kinoshita, S., 2001b. Cultivated corneal epithelial transplantation for ocular surface reconstruction in acute phase of Stevens-Johnson syndrome. *Arch. Ophthalmol.* 119, 298–300.
- Ksander, B.R., Kolovou, P.E., Wilson, B.J., Saab, K.R., Guo, Q., Ma, J., McGuire, S.P., Gregory, M.S., Vincent, W.J., Perez, V.L., Cruz-Guilloty, F., Kao, W.W., Call, M.K., Tucker, B.A., Zhan, Q., Murphy, G.F., Lathrop, K.L., Alt, C., Mortensen, L.J., Lin, C.P., Zieske, J.D., Frank, M.H., Frank, N.Y., 2014. ABCB5 is a limbal stem cell gene required for corneal development and repair. *Nature* 511, 353–357.
- Kulkarni, B.B., Tighe, P.J., Mohammed, I., Yeung, A.M., Powe, D.G., Hopkinson, A., Shanmuganathan, V.A., Dua, H.S., 2010. Comparative transcriptional profiling of the limbal epithelial crypt demonstrates its putative stem cell niche characteristics. *BMC Genomics* 11, 526.
- Kusanagi, R., Umamoto, T., Yamato, M., Matsuzaki, Y., Nishida, K., Kobayashi, Y., Fukai, F., Okano, T., 2009. Nectin-3 expression is elevated in limbal epithelial side population cells with strongly expressed stem cell markers. *Biochem. Biophys. Res. Commun.* 389, 274–278.
- Lajtha, L.G., 1979. Stem cell concepts. *Differentiation* 14, 23–34.
- Langer, R., Vacanti, J.P., 1993. Tissue engineering. *Science* 260, 920–926.
- Lavker, R.M., Sun, T.T., 1982. Heterogeneity in epidermal basal keratinocytes: morphological and functional correlations. *Science* 215, 1239–1241.
- Leblond, C.P., 1981. The life history of cells in renewing systems. *Am. J. Anat.* 160, 114–158.
- Lee, S.K., Teng, Y., Wong, H.K., Ng, T.K., Huang, L., Lei, P., Choy, K.W., Liu, Y., Zhang, M., Lam, D.S., Yam, G.H., Pang, C.P., 2011. MicroRNA-145 regulates human corneal epithelial differentiation. *PLoS One* 6, e21249.
- Levis, H.J., Brown, R.A., Daniels, J.T., 2010. Plastic compressed collagen as a biomimetic substrate for human limbal epithelial cell culture. *Biomaterials* 31, 7726–7737.
- Lin, D., Halilovic, A., Yue, P., Bellner, L., Wang, K., Wang, L., Zhang, C., 2013. Inhibition of miR-205 impairs the wound-healing process in human corneal epithelial cells by targeting KIR4.1 (KCNJ10). *Invest. Ophthalmol. Vis. Sci.* 54, 6167–6178.
- Ma, Y., Xu, Y., Xiao, Z., Yang, W., Zhang, C., Song, E., Du, Y., Li, L., 2006. Reconstruction of chemically burned rat corneal surface by bone marrow-derived human mesenchymal stem cells. *Stem Cells* 24, 315–321.
- Majo, F., Rochat, A., Nicolas, M., Jaoude, G.A., Barrandon, Y., 2008. Oligopotent stem cells are distributed throughout the mammalian ocular surface. *Nature* 456, 250–254.
- McIntosh Ambrose, W., Salahuddin, A., So, S., Ng, S., Ponce Marquez, S., Takezawa, T., Schein, O., Elisseff, J., 2009. Collagen vitrigel membranes for the in vitro reconstruction of separate corneal epithelial, stromal, and endothelial cell layers. *J. Biomed. Mater. Res. B Appl. Biomater.* 90, 818–831.
- Meyer-Blazejewski, E.A., Call, M.K., Yamanaka, O., Liu, H., Schlötzer-Schrehardt, U., Kruse, F.E., Kao, W.W., 2011. From hair to cornea: toward the therapeutic use of hair follicle-derived stem cells in the treatment of limbal stem cell deficiency. *Stem Cells* 29, 57–66.
- Mi, S., Chen, B., Wright, B., Connon, C.J., 2010. Ex vivo construction of an artificial ocular surface by combination of corneal limbal epithelial cells and a compressed collagen scaffold containing keratocytes. *Tissue Eng. Part A* 16, 2091–2100.
- Minami, Y., Sugihara, H., Oono, S., 1993. Reconstruction of cornea in three-dimensional collagen gel matrix culture. *Invest. Ophthalmol. Vis. Sci.* 34, 2316–2324.
- Miyashita, H., Yokoo, S., Yoshida, S., Kawakita, T., Yamagami, S., Tsubota, K., Shimmura, S., 2013. Long-term maintenance of limbal epithelial progenitor cells using rho kinase inhibitor and keratinocyte growth factor. *Stem Cells Transl. Med.* 2, 758–765.
- Monteiro, B.G., Serafim, R.C., Melo, G.B., Silva, M.C., Lizier, N.F., Maranduba, C.M., Smith, R.L., Kerkis, A., Cerruti, H., Gomes, J.A., Kerkis, I., 2009. Human immature dental pulp stem cells share key characteristic features with limbal stem cells. *Cell Prolif.* 42, 587–594.
- Nakamura, T., Ang, L.P., Rigby, H., Sekiyama, E., Inatomi, T., Sotozono, C., Fullwood, N.J., Kinoshita, S., 2006a. The use of autologous serum in the development of corneal and oral epithelial equivalents in patients with Stevens-Johnson syndrome. *Invest. Ophthalmol. Vis. Sci.* 47, 909–916.
- Nakamura, T., Endo, K., Cooper, L.J., Fullwood, N.J., Tanifuji, N., Tsuzuki, M., Koizumi, N., Inatomi, T., Sano, Y., Kinoshita, S., 2003a. The successful culture and autologous transplantation of rabbit oral mucosal epithelial cells on amniotic membrane. *Invest. Ophthalmol. Vis. Sci.* 44, 106–116.
- Nakamura, T., Endo, K., Kinoshita, S., 2007a. Identification of human oral keratinocyte stem/progenitor cells by neurotrophin receptor p75 and the role of



- neurotrophin/p75 signaling. *Stem Cells* 25, 628–638.
- Nakamura, T., Hamuro, J., Takaishi, M., Simmons, S., Maruyama, K., Zaffalon, A., Bentley, A.J., Kawasaki, S., Nagata-Takaoka, M., Fullwood, N.J., Itami, S., Sano, S., Ishii, M., Barrandon, Y., Kinoshita, S., 2014. LRIG1 inhibits STAT3-dependent inflammation to maintain corneal homeostasis. *J. Clin. Invest.* 124, 385–397.
- Nakamura, T., Inatomi, T., Cooper, L.J., Rigby, H., Fullwood, N.J., Kinoshita, S., 2007b. Phenotypic investigation of human eyes with transplanted autologous cultivated oral mucosal epithelial sheets for severe ocular surface diseases. *Ophthalmology* 114, 1080–1088.
- Nakamura, T., Inatomi, T., Sekiyama, E., Ang, L.P., Yokoi, N., Kinoshita, S., 2006b. Novel clinical application of sterilized, freeze-dried amniotic membrane to treat patients with pterygium. *Acta Ophthalmol. Scand.* 84, 401–405.
- Nakamura, T., Inatomi, T., Sotozono, C., Amemiya, T., Kanamura, N., Kinoshita, S., 2004a. Transplantation of cultivated autologous oral mucosal epithelial cells in patients with severe ocular surface disorders. *Br. J. Ophthalmol.* 88, 1280–1284.
- Nakamura, T., Inatomi, T., Sotozono, C., Ang, L.P., Koizumi, N., Yokoi, N., Kinoshita, S., 2006c. Transplantation of autologous serum-derived cultivated corneal epithelial equivalents for the treatment of severe ocular surface disease. *Ophthalmology* 113, 1765–1772.
- Nakamura, T., Inatomi, T., Sotozono, C., Koizumi, N., Kinoshita, S., 2004b. Successful primary culture and autologous transplantation of corneal limbal epithelial cells from minimal biopsy for unilateral severe ocular surface disease. *Acta Ophthalmol. Scand.* 82, 468–471.
- Nakamura, T., Kinoshita, S., 2003. Ocular surface reconstruction using cultivated mucosal epithelial stem cells. *Cornea* 22, S75–S80.
- Nakamura, T., Koizumi, N., Tsuzuki, M., Inoki, K., Sano, Y., Sotozono, C., Kinoshita, S., 2003c. Successful regrafting of cultivated corneal epithelium using amniotic membrane as a carrier in severe ocular surface disease. *Cornea* 22, 70–71.
- Nakamura, T., Ohtsuka, T., Sekiyama, E., Cooper, L.J., Kokubu, H., Fullwood, N.J., Barrandon, Y., Kageyama, R., Kinoshita, S., 2008a. Hes1 regulates corneal development and the function of corneal epithelial stem/progenitor cells. *Stem Cells* 26, 1265–1274.
- Nakamura, T., Sekiyama, E., Takaoka, M., Bentley, A.J., Yokoi, N., Fullwood, N.J., Kinoshita, S., 2008b. The use of trehalose-treated freeze-dried amniotic membrane for ocular surface reconstruction. *Biomaterials* 29, 3729–3737.
- Nakamura, T., Sotozono, C., Bentley, A.J., Mano, S., Inatomi, T., Koizumi, N., Fullwood, N.J., Kinoshita, S., 2010. Long-term phenotypic study after allogeneic cultivated corneal limbal epithelial transplantation for severe ocular surface diseases. *Ophthalmology* 117, 2247–2254.
- Nakamura, T., Takeda, K., Inatomi, T., Sotozono, C., Kinoshita, S., 2011. Long-term results of autologous cultivated oral mucosal epithelial transplantation in the scar phase of severe ocular surface disorders. *Br. J. Ophthalmol.* 95, 942–946.
- Nakamura, T., Yoshitani, M., Rigby, H., Fullwood, N.J., Ito, W., Inatomi, T., Sotozono, C., Shimizu, Y., Kinoshita, S., 2004c. Sterilized, freeze-dried amniotic membrane: a useful substrate for ocular surface reconstruction. *Invest. Ophthalmol. Vis. Sci.* 45, 93–99.
- Nakatsu, M.N., Vartanyan, L., Vu, D.M., Ng, M.Y., Li, X., Deng, S.X., 2013. Preferential biological processes in the human limbus by differential gene profiling. *PLoS One* 8, e61833.
- Nishida, K., Adachi, W., Shimizu-Matsumoto, A., Kinoshita, S., Mizuno, K., Matsubara, K., Okubo, K., 1996. A gene expression profile of human corneal epithelium and the isolation of human keratin 12 cDNA. *Invest. Ophthalmol. Vis. Sci.* 37, 1800–1809.
- Nishida, K., Yamato, M., Hayashida, Y., Watanabe, K., Maeda, N., Watanabe, H., Yamamoto, K., Nagai, S., Kikuchi, A., Tano, Y., Okano, T., 2004a. Functional bioengineered corneal epithelial sheet grafts from corneal stem cells expanded ex vivo on a temperature-responsive cell culture surface. *Transplantation* 77, 379–385.
- Nishida, K., Yamato, M., Hayashida, Y., Watanabe, K., Yamamoto, K., Adachi, E., Nagai, S., Kikuchi, A., Maeda, N., Watanabe, H., Okano, T., Tano, Y., 2004b. Corneal reconstruction with tissue-engineered cell sheets composed of autologous oral mucosal epithelium. *N. Engl. J. Med.* 351, 1187–1196.
- Notara, M., Haddow, D.B., MacNeil, S., Daniels, J.T., 2007. A xenobiotic-free culture system for human limbal epithelial stem cells. *Regen. Med.* 2, 919–927.
- Oie, Y., Hayashi, R., Takagi, R., Yamato, M., Takayanagi, H., Tano, Y., Nishida, K., 2010. A novel method of culturing human oral mucosal epithelial cell sheet using post-mitotic human dermal fibroblast feeder cells and modified keratinocyte culture medium for ocular surface reconstruction. *Br. J. Ophthalmol.* 94, 1244–1250.
- Okabe, M., Kitagawa, K., Yoshida, T., Suzuki, T., Waki, H., Koike, C., Furuichi, E., Katou, K., Nomura, Y., Uji, Y., Hayashi, A., Saito, S., Nikaido, T., 2014. Hyperdry human amniotic membrane is useful material for tissue engineering: physical, morphological properties, and safety as the new biological material. *J. Biomed. Mater. Res. A* 102, 862–870.
- Omoto, M., Miyashita, H., Shimamura, S., Higa, K., Kawakita, T., Yoshida, S., McGrogan, M., Shimazaki, J., Tsubota, K., 2009. The use of human mesenchymal stem cell-derived feeder cells for the cultivation of transplantable epithelial sheets. *Invest. Ophthalmol. Vis. Sci.* 50, 2109–2115.
- Ortega, I., Ryan, A.J., Deshpande, P., MacNeil, S., Claeysens, F., 2013. Combined microfabrication and electrospinning to produce 3-D architectures for corneal repair. *Acta Biomater.* 9, 5511–5520.
- Ouyang, H., Xue, Y., Lin, Y., Zhang, X., Xi, L., Patel, S., Cai, H., Luo, J., Zhang, M., Yang, Y., Li, G., Li, H., Jiang, W., Yeh, E., Lin, J., Pei, M., Zhu, J., Cao, G., Zhang, L., Yu, B., Chen, S., Fu, X.D., Liu, Y., Zhang, K., 2014. WNT7A and PAX6 define corneal epithelium homeostasis and pathogenesis. *Nature* 511, 358–361.
- Pajooesh-Ganji, A., Pal-Ghosh, S., Simmens, S.J., Stepp, M.A., 2006. Integrins in slow-cycling corneal epithelial cells at the limbus in the mouse. *Stem Cells* 24, 1075–1086.
- Pellegrini, G., Dellambra, E., Golisano, O., Martinelli, E., Fantozzi, I., Bondanza, S., Ponzin, D., McKeon, F., De Luca, M., 2001. p63 identifies keratinocyte stem cells. *Proc. Natl. Acad. Sci. U. S. A.* 98, 3156–3161.
- Pellegrini, G., Golisano, O., Paterna, P., Lambiase, A., Bonini, S., Rama, P., De Luca, M., 1999. Location and clonal analysis of stem cells and their differentiated progeny in the human ocular surface. *J. Cell Biol.* 145, 769–782.
- Pellegrini, G., Traverso, C.E., Franzi, A.T., Zingirian, M., Cancedda, R., De Luca, M., 1997. Long-term restoration of damaged corneal surfaces with autologous cultivated corneal epithelium. *Lancet* 349, 990–993.
- Potten, C.S., Loeffler, M., 1990. Stem cells: attributes, cycles, spirals, pitfalls and uncertainties. Lessons for and from the crypt. *Development* 110, 1001–1020.
- Powell, A.E., Wang, Y., Li, Y., Poulin, E.J., Means, A.L., Washington, M.K., Higginbotham, J.N., Juchheim, A., Prasad, N., Levy, S.E., Guo, Y., Shyr, Y., Aronow, B.J., Haigis, K.M., Franklin, J.L., Coffey, R.J., 2012. The pan-ErbB negative regulator Lrig1 is an intestinal stem cell marker that functions as a tumor suppressor. *Cell* 149, 146–158.
- Qi, H., Li, D.Q., Shine, H.D., Chen, Z., Yoon, K.C., Jones, D.B., Pflugfelder, S.C., 2008. Nerve growth factor and its receptor TrkA serve as potential markers for human corneal epithelial progenitor cells. *Exp. Eye Res.* 86, 34–40.
- Rama, P., Bonini, S., Lambiase, A., Golisano, O., Paterna, P., De Luca, M., Pellegrini, G., 2001. Autologous fibrin-cultured limbal stem cells permanently restore the corneal surface of patients with total limbal stem cell deficiency. *Transplantation* 72, 1478–1485.
- Rama, P., Matuska, S., Paganoni, G., Spinelli, A., De Luca, M., Pellegrini, G., 2010. Limbal stem-cell therapy and long-term corneal regeneration. *N. Engl. J. Med.* 363, 147–155.
- Reichl, S., Borrelli, M., Geerling, G., 2011. Keratin films for ocular surface reconstruction. *Biomaterials* 32, 3375–3386.
- Reza, H.M., Ng, B.Y., Gimeno, F.L., Phan, T.T., Ang, L.P., 2011. Umbilical cord lining stem cells as a novel and promising source for ocular surface regeneration. *Stem Cell Rev.* 7, 935–947.
- Rheinwald, J.G., Green, H., 1975. Serial cultivation of strains of human epidermal keratinocytes: the formation of keratinizing colonies from single cells. *Cell* 6, 331–343.
- Sangwan, V.S., Basu, S., MacNeil, S., Balasubramanian, D., 2012. Simple limbal epithelial transplantation (SLET): a novel surgical technique for the treatment of unilateral limbal stem cell deficiency. *Br. J. Ophthalmol.* 96, 931–934.
- Sangwan, V.S., Vemuganti, G.K., Iftikhar, G., Bansal, A.K., Rao, G.N., 2003. Use of autologous cultured limbal and conjunctival epithelium in a patient with severe bilateral ocular surface disease induced by acid injury: a case report of unique application. *Cornea* 22, 478–481.
- Satake, Y., Higa, K., Tsubota, K., Shimazaki, J., 2011. Long-term outcome of cultivated oral mucosal epithelial sheet transplantation in treatment of total limbal stem cell deficiency. *Ophthalmology* 118, 1524–1530.
- Schermer, A., Galvin, S., Sun, T.T., 1986. Differentiation-related expression of a major 64K corneal keratin in vivo and in culture suggests limbal location of corneal epithelial stem cells. *J. Cell Biol.* 103, 49–62.
- Schwab, I.R., Reyes, M., Isseroff, R.R., 2000. Successful transplantation of bioengineered tissue replacements in patients with ocular surface disease. *Cornea* 19, 421–426.
- Sekiyama, E., Nakamura, T., Kurihara, E., Cooper, L.J., Fullwood, N.J., Takaoka, M., Hamuro, J., Kinoshita, S., 2007. Novel sutureless transplantation of bioadhesive-coated, freeze-dried amniotic membrane for ocular surface reconstruction. *Invest. Ophthalmol. Vis. Sci.* 48, 1528–1534.
- Shafiq, M.A., Gemeinhart, R.A., Yue, B.Y., Djalilian, A.R., 2012. Decellularized human cornea for reconstructing the corneal epithelium and anterior stroma. *Tissue Eng. Part C Methods* 18, 340–348.
- Shalom-Feuerstein, R., Serró, L., De La Forest Divonne, S., Petit, I., Aberdam, E., Camargo, L., Damour, O., Vigouroux, C., Solomon, A., Gaggioli, C., Itskovitz-Eldor, J., Ahmad, S., Aberdam, D., 2012. Pluripotent stem cell model reveals essential roles for miR-450b-5p and miR-184 in embryonic corneal lineage specification. *Stem Cells* 30, 898–909.
- Sharma, S., Mohanty, S., Gupta, D., Jassal, M., Agrawal, A.K., Tandon, R., 2011. Cellular response of limbal epithelial cells on electrospun poly-epsilon-caprolactone nanofibrous scaffolds for ocular surface bioengineering: a preliminary in vitro study. *Mol. Vis.* 17, 2898–2910.
- Solomon, A., Rosenblatt, M., Monroy, D., Ji, Z., Pflugfelder, S.C., Tseng, S.C., 2001. Suppression of interleukin 1alpha and interleukin 1beta in human limbal epithelial cells cultured on the amniotic membrane stromal matrix. *Br. J. Ophthalmol.* 85, 444–449.
- Sotozono, C., Ang, L.P., Koizumi, N., Higashihara, H., Ueta, M., Inatomi, T., Yokoi, N., Kaido, M., Dogru, M., Shimazaki, J., Tsubota, K., Yamada, M., Kinoshita, S., 2007. New grading system for the evaluation of chronic ocular manifestations in patients with Stevens-Johnson syndrome. *Ophthalmology* 114, 1294–1302.
- Sotozono, C., Inatomi, T., Nakamura, T., Koizumi, N., Yokoi, N., Ueta, M., Matsuyama, K., Miyakoda, K., Kaneda, H., Fukushima, M., Kinoshita, S., 2013. Visual improvement after cultivated oral mucosal epithelial transplantation. *Ophthalmology* 120, 193–200.
- Sugiyama, H., Maeda, K., Yamato, M., Hayashi, R., Soma, T., Hayashida, Y., Yang, J., Shirakabe, M., Matsuyama, A., Kikuchi, A., Sawa, Y., Okano, T., Tano, Y., Nishida, K., 2008. Human adipose tissue-derived mesenchymal stem cells as a novel feeder layer for epithelial cells. *J. Tissue Eng. Regen. Med.* 2, 445–449.



- Suzuki, Y., Miura, H., Tanemura, A., Kobayashi, K., Kondoh, G., Sano, S., Ozawa, K., Inui, S., Nakata, A., Takagi, T., Tohyama, M., Yoshikawa, K., Itami, S., 2002. Targeted disruption of LIG-1 gene results in psoriasiform epidermal hyperplasia. *FEBS Lett.* 521, 67–71.
- Szurman, P., Warga, M., Grisanti, S., Roters, S., Rohrbach, J.M., Aisenbrey, S., Kaczmarek, R.T., Bartz-Schmidt, K.U., 2006. Sutureless amniotic membrane fixation using fibrin glue for ocular surface reconstruction in a rabbit model. *Cornea* 25, 460–466.
- Takacs, L., Toth, E., Losonczy, G., Szanto, A., Bahr-Ivacevic, T., Benes, V., Berta, A., Vereb, G., 2011. Differentially expressed genes associated with human limbal epithelial phenotypes: new molecules that potentially facilitate selection of stem cell-enriched populations. *Invest. Ophthalmol. Vis. Sci.* 52, 1252–1260.
- Takeda, K., Nakamura, T., Inatomi, T., Sotozono, C., Watanabe, A., Kinoshita, S., 2011. Ocular surface reconstruction using the combination of autologous cultivated oral mucosal epithelial transplantation and eyelid surgery for severe ocular surface disease. *Am. J. Ophthalmol.* 152, 195–201.
- Takaoka, M., Nakamura, T., Sugai, H., Bentley, A.J., Nakajima, N., Fullwood, N.J., Yokoi, N., Hyon, S.H., Kinoshita, S., 2008. Sutureless amniotic membrane transplantation for ocular surface reconstruction with a chemically defined bioadhesive. *Biomaterials* 29, 2923–2931.
- Takaoka, M., Nakamura, T., Sugai, H., Bentley, A.J., Nakajima, N., Yokoi, N., Fullwood, N.J., Hyon, S.H., Kinoshita, S., 2009. Novel sutureless keratoplasty with a chemically defined bioadhesive. *Invest. Ophthalmol. Vis. Sci.* 50, 2679–2685.
- Thoft, R.A., 1977. Conjunctival transplantation. *Arch. Ophthalmol.* 95, 1425–1427.
- Thoft, R.A., 1984. Keratoepithelioplasty. *Am. J. Ophthalmol.* 97, 1–6.
- Thoft, R.A., Friend, J., 1983. The X, Y, Z hypothesis of corneal epithelial maintenance. *Invest. Ophthalmol. Vis. Sci.* 24, 1442–1443.
- Thoft, R.A., Friend, J., 1979. The Ocular Surface. *International Ophthalmology Clinics*. Trelford, J.D., Trelford-Sauder, M., 1979. The amnion in surgery, past and present. *Am. J. Obstet. Gynecol.* 134, 833–845.
- Tsai, R.J., Li, L.M., Chen, J.K., 2000. Reconstruction of damaged corneas by transplantation of autologous limbal epithelial cells. *N. Engl. J. Med.* 343, 86–93.
- Tsai, R.J., Tseng, S.C., 1994. Human allograft limbal transplantation for corneal surface reconstruction. *Cornea* 13, 389–400.
- Tseng, S.C., 1989. Concept and application of limbal stem cells. *Eye* 3 (Pt 2), 141–157.
- Tseng, S.C., Li, D.Q., Ma, X., 1999. Suppression of transforming growth factor-beta isoforms, TGF-beta receptor type II, and myofibroblast differentiation in cultured human corneal and limbal fibroblasts by amniotic membrane matrix. *J. Cell Physiol.* 179, 325–335.
- Tsubota, K., Satake, Y., Ohyama, M., Toda, I., Takano, Y., Ono, M., Shinozaki, N., Shimazaki, J., 1996. Surgical reconstruction of the ocular surface in advanced ocular cicatricial pemphigoid and Stevens-Johnson syndrome. *Am. J. Ophthalmol.* 122, 38–52.
- Utheim, T.P., Raeder, S., Olstad, O.K., Utheim, O.A., de La Paz, M., Cheng, R., Huynh, T.T., Messelt, E., Roald, B., Lyberg, T., 2009. Comparison of the histology, gene expression profile, and phenotype of cultured human limbal epithelial cells from different limbal regions. *Invest. Ophthalmol. Vis. Sci.* 50, 5165–5172.
- Wang, H., Tao, T., Tang, J., Mao, Y.H., Li, W., Peng, J., Tan, G., Zhou, Y.P., Zhong, J.X., Tseng, S.C., Kawakita, T., Zhao, Y.X., Liu, Z.G., 2009. Importin 13 serves as a potential marker for corneal epithelial progenitor cells. *Stem Cells* 27, 2516–2526.
- Watanabe, K., Nishida, K., Yamato, M., Umemoto, T., Sumide, T., Yamamoto, K., Maeda, N., Watanabe, H., Okano, T., Tano, Y., 2004. Human limbal epithelium contains side population cells expressing the ATP-binding cassette transporter ABCG2. *FEBS Lett.* 565, 6–10.
- West, J.D., Dorà, N.J., Collinson, J.M., 2015. Evaluating alternative stem cell hypotheses for adult corneal epithelial maintenance. *World J. Stem Cells* 7, 281–299.
- Wong, V.W., Stange, D.E., Page, M.E., Buczacki, S., Wabik, A., Itami, S., van de Wetering, M., Poulson, R., Wright, N.A., Trotter, M.W., Watt, F.M., Winton, D.J., Clevers, H., Jensen, K.B., 2012. Lrig1 controls intestinal stem-cell homeostasis by negative regulation of ErbB signalling. *Nat. Cell Biol.* 14, 401–408.
- Yang, X., Moldovan, N.I., Zhao, Q., Mi, S., Zhou, Z., Chen, D., Gao, Z., Tong, D., Dou, Z., 2008. Reconstruction of damaged cornea by autologous transplantation of epidermal adult stem cells. *Mol. Vis.* 14, 1064–1070.
- Yoshida, S., Shimmura, S., Kawakita, T., Miyashita, H., Den, S., Shimazaki, J., Tsubota, K., 2006. Cytokeratin 15 can be used to identify the limbal phenotype in normal and diseased ocular surfaces. *Invest. Ophthalmol. Vis. Sci.* 47, 4780–4786.
- Yokoo, S., Yamagami, S., Usui, T., Amano, S., Araie, M., 2008. Human corneal epithelial equivalents for ocular surface reconstruction in a complete serum-free culture system without unknown factors. *Invest. Ophthalmol. Vis. Sci.* 49, 2438–2443.
- Yu, J., Ryan, D.G., Getsios, S., Oliveira-Fernandes, M., Fatima, A., Lavker, R.M., 2008. MicroRNA-184 antagonizes microRNA-205 to maintain SHIP2 levels in epithelia. *Proc. Natl. Acad. Sci. U. S. A.* 105, 19300–19305.
- Zajicova, A., Pokorna, K., Lencova, A., Krulova, M., Svobodova, E., Kubinova, S., Sykova, E., Pradny, M., Michalek, J., Svobodova, J., Munzarova, M., Holan, V., 2010. Treatment of ocular surface injuries by limbal and mesenchymal stem cells growing on nanofiber scaffolds. *Cell Transpl.* 19, 1281–1290.
- Zhao, Y., Ma, L., 2015. Systematic review and meta-analysis on transplantation of ex vivo cultivated limbal epithelial stem cell on amniotic membrane in limbal stem cell deficiency. *Cornea* 34, 592–600.

# SCIENTIFIC REPORTS

OPEN

## Rho kinase inhibitor enables cell-based therapy for corneal endothelial dysfunction

Received: 06 January 2016

Accepted: 27 April 2016

Published: 18 May 2016

Naoki Okumura<sup>1</sup>, Yuji Sakamoto<sup>2</sup>, Keita Fujii<sup>1</sup>, Junji Kitano<sup>1</sup>, Shinichiro Nakano<sup>1</sup>, Yuki Tsujimoto<sup>1</sup>, Shin-ichiro Nakamura<sup>3</sup>, Morio Ueno<sup>4</sup>, Michio Hagiya<sup>4</sup>, Junji Hamuro<sup>4</sup>, Akifumi Matsuyama<sup>5</sup>, Shingo Suzuki<sup>6</sup>, Takashi Shiina<sup>6</sup>, Shigeru Kinoshita<sup>4,7</sup> & Noriko Koizumi<sup>1</sup>

The corneal endothelium maintains corneal transparency; consequently, its dysfunction causes severe vision loss. Tissue engineering-based therapy, as an alternative to conventional donor corneal transplantation, is anticipated to provide a less invasive and more effective therapeutic modality. We conducted a preclinical study for cell-based therapy in a primate model and demonstrated regeneration of the corneal endothelium following injection of cultured monkey corneal endothelial cells (MCECs) or human CECs (HCECs), in combination with a Rho kinase (ROCK) inhibitor, Y-27632, into the anterior chamber. We also evaluated the safety and efficacy of Good Manufacturing Practice (GMP)-grade HCECs, similar to those planned for use as transplant material for human patients in a clinical trial, and we showed that the corneal endothelium was regenerated without adverse effect. We also showed that CEC engraftment is impaired by limited substrate adhesion, which is due to actomyosin contraction induced by dissociation-induced activation of ROCK/MLC signaling. Inclusion of a ROCK inhibitor improves efficiency of engraftment of CECs and enables cell-based therapy for treating corneal endothelial dysfunction as a clinically relevant therapy.

The corneal endothelium maintains corneal transparency by a pump and barrier function that reduces the aqueous humor flow into corneal stroma. Consequently, endothelial dysfunction causes severe vision loss. Any damage to the corneal endothelium due to pathological status, such as Fuchs endothelial corneal dystrophies and surgical trauma, is compensated by migration and spreading of the remaining corneal endothelial cells (CECs)<sup>1</sup>. However, once the cell density (2500–3000 cells/mm<sup>2</sup> in healthy individuals) drops lower than a critical level (<1000 cells/mm<sup>2</sup>), decompensation of endothelial function induces corneal haziness<sup>2</sup>.

Corneal transplantation is the only therapeutic choice for treating corneal endothelial dysfunction, but is hampered by a shortage of donor corneas, the difficulty of the surgical procedure, and graft failure in acute and chronic phases. Therefore, researchers are actively seeking to develop tissue engineering based therapeutics<sup>3,4</sup>. For instance, some investigators, including us, have cultured CECs on scaffolds in the form of a sheet, and have shown in animal models that corneal endothelial dysfunction can be treated by sheet transplantation<sup>5–7</sup>. In addition to sheet transplantation, we have demonstrated that a Rho kinase (ROCK) inhibitor, Y-27632, improves the engraftment of transplanted CECs and that injection of CECs in the form of a cell suspension can regenerate the corneal endothelium<sup>8</sup>.

This paper reports a preclinical study for corneal endothelial cell-based therapy conducted in a cynomolgus monkey model. Corneal endothelium was regenerated by injection of cultured monkey CECs (MCECs) and human CECs (HCECs), in combination with the ROCK inhibitor, and the regeneration occurred without adverse effects, such as rejection, secondary glaucoma, or aberrant ectopic cell transplantation. We also showed that CEC engraftment is impaired by actomyosin contraction induced by cell dissociation through activation of Rho/

<sup>1</sup>Department of Biomedical Engineering, Faculty of Life and Medical Sciences, Doshisha University, Kyotanabe, Japan. <sup>2</sup>Research Laboratory, Senju Pharmaceutical Co., Ltd., Kobe, Japan. <sup>3</sup>Research Center of Animal Life Science, Shiga University of Medical Science, Otsu, Japan. <sup>4</sup>Department of Ophthalmology, Kyoto Prefectural University of Medicine, Kyoto, Japan. <sup>5</sup>Platform of Therapeutics for Rare Disease, National Institutes of Biomedical Innovation, Health and Nutrition, Osaka, Japan. <sup>6</sup>Department of Molecular Life Science, Division of Basic Medical Science and Molecular Medicine, Tokai University School of Medicine, Isehara, Japan. <sup>7</sup>Department of Frontier Medical Science and Technology for Ophthalmology, Kyoto Prefectural University of Medicine, Kyoto, Japan. Correspondence and requests for materials should be addressed to N.K. (email: nkoizumi@mail.doshisha.ac.jp)

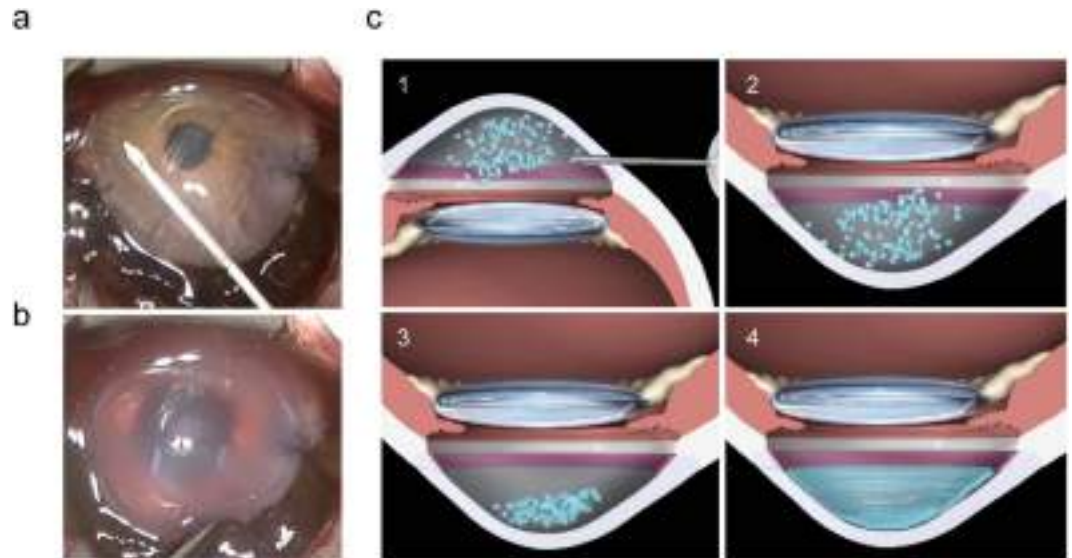


**Figure 1. Cultured corneal endothelial cell (CEC) injection in the corneal endothelial dysfunction model.** (a) To create monkey corneal endothelial dysfunction models, the corneal endothelium was completely scraped from the Descemet's membrane with a 20-gauge silicone needle. CECs ( $5.0 \times 10^5$  cells), suspended in  $200 \mu\text{l}$  of DMEM supplemented with  $100 \mu\text{M}$  of Y-27632 (a ROCK inhibitor), were injected into the anterior chamber with a 26-gauge needle. (b) After confirmation of the absence of leakage of the injected CECs, the eyes were kept in the face-down position for 3 hours with the monkeys under general anesthesia. (c) Schematic images show the cultured CEC injection procedure. (1) injection of cultured CECs with ROCK inhibitor into the anterior chamber, (2) face-down position for CECs to sink down to the anterior chamber side of the cornea, (3) animal is maintained in the face-down position for 3 hours, (4) regeneration of corneal endothelium by injected cultured CECs.

ROCK/MLC signaling. Inclusion of a ROCK inhibitor enhances the adhesion to the extracellular matrix (ECM) by counteracting this cascade. Taken together, the results from this preclinical study in a primate model demonstrate that ROCK inhibitors enhance cell engraftment, thereby enabling CEC injection as a clinically relevant cell-based therapy for treating corneal endothelial dysfunction.

## Results

**Cultivated MCEC injection in combination with a ROCK inhibitor in a monkey model.** We completely removed the corneal endothelium to generate the corneal endothelial dysfunction model. We then injected cultured MCECs ( $5.0 \times 10^5$  cells) into the anterior chamber using a 26G needle and confirmed the absence of leakage of injected cells from the wound (Fig. 1a,b). The schematic images in Fig. 1c show the surgical procedure: (1) cultured CEC injection in combination with the ROCK inhibitor into the anterior chamber, (2) face-down position to allow CECs to sink to the Descemet's membrane, (3) the face-down position is maintained for 3 hours to attach CECs onto the Descemet's membrane, and (4) the corneal endothelium is ultimately regenerated by the injected CECs. The corneas of control monkeys, in which no MCECs were injected, and corneas of monkeys in which MCECs were injected without ROCK inhibitor, showed hazy corneas due to corneal endothelial dysfunction after 14 days. On the other hand, MCEC injection in combination with the ROCK inhibitor restored corneal transparency (Fig. 2a and Supplemental Fig. 1).

Scheimpflug images obtained by a Pentacam<sup>TM</sup> instrument showed that an anatomically normal cornea was successfully regenerated by MCEC injection with the ROCK inhibitor, whereas corneal edema due to corneal endothelial dysfunction was induced by MCEC injection without the ROCK inhibitor (Fig. 2b). Due to severe corneal edema, Scheimpflug images were not obtained for the control eyes. Corneal thickness, which is an important index of corneal endothelial function, was significantly thinner in monkeys injected with MCECs with the ROCK inhibitor than in monkeys injected with MCECs without the ROCK inhibitor and in the control monkeys (Fig. 2c). We continued observing 2 monkeys for 1 year to evaluate the safety and efficacy of this cell-based therapy. Monkeys injected with MCECs with the ROCK inhibitor maintained corneal transparency, whereas monkeys injected only with MCECs exhibited hazy corneas after 1 year of treatment (Fig. 2d). Of the two monkeys treated with MCECs with the ROCK inhibitor, both showed a cell density higher than  $2000 \text{ cell/mm}^2$  (Fig. 2e). In the control eyes and eyes injected with MCECs without ROCK inhibitor, no images were obtained with non-contact specular microscopy due to corneal haziness.

The regenerated corneal endothelium had a monolayer hexagonal morphology and expressed function-related proteins, such as  $\text{Na}^+/\text{K}^+$ -ATPase and ZO-1 (Fig. 2f). No local adverse effects were observed, such as intraocular pressure elevation, abnormal accumulation of injected cells, or rejection. No systemic adverse responses occurred, such as abnormalities in blood tests, weight loss, or abnormal behaviors (data not shown).

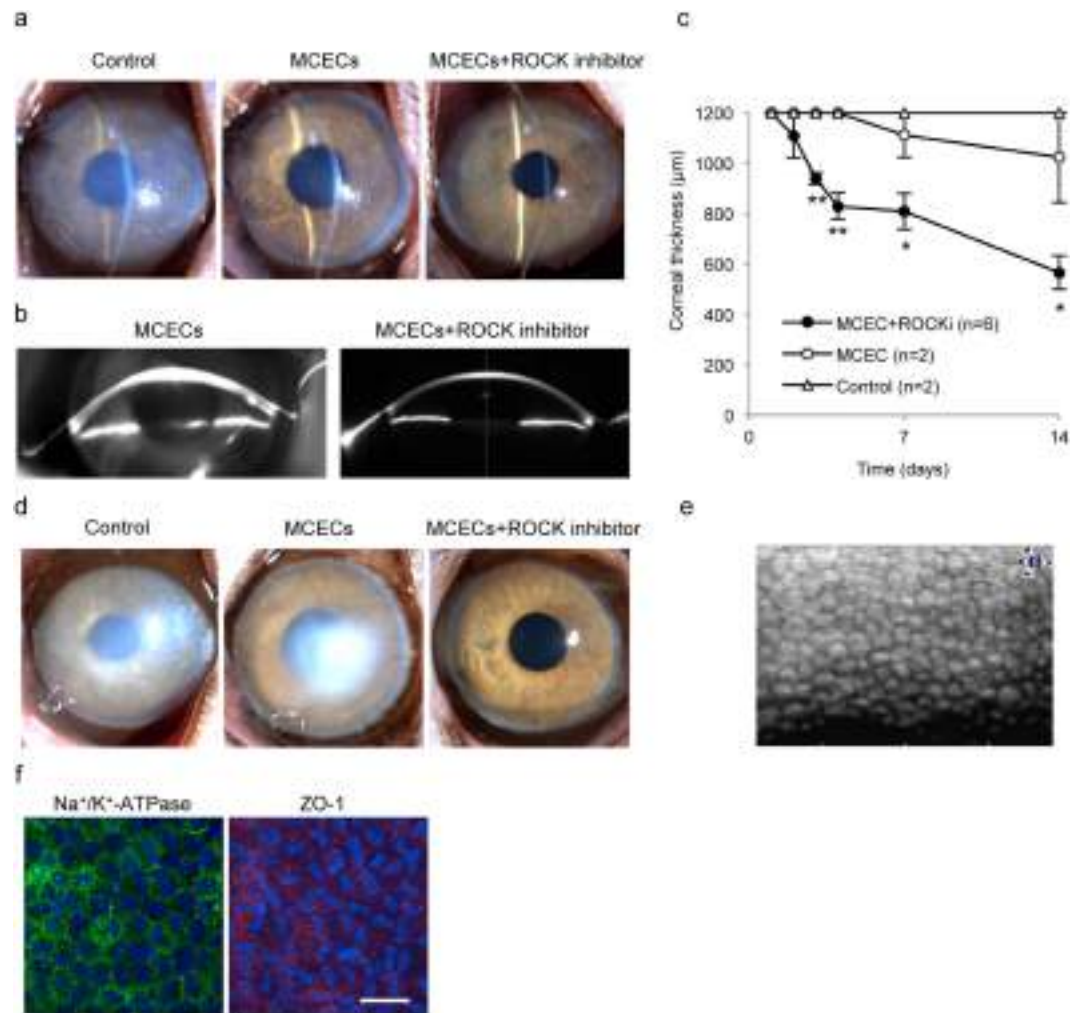


**Figure 2.** Preclinical research of cultured monkey corneal endothelial cell (MCEC) injection in combination with a ROCK inhibitor in a monkey corneal endothelial dysfunction model. (a) A representative slit-lamp image shows the monkey corneal endothelial dysfunction model (left) (n = 2). A representative slit-lamp image shows the corneal endothelial dysfunction model following injection of MCECs ( $5.0 \times 10^5$  cells) suspended in  $200 \mu\text{l}$  of DMEM without (middle) (n = 2) or with (right) (n = 6) the ROCK inhibitor Y-27632. All images were obtained 14 days after treatment. (b) Scheimpflug images were obtained from monkeys injected with MCECs without or with Y-27632, obtained with a Pentacam<sup>®</sup> instrument at 14 days after cell injection. (c) The mean central corneal thickness was evaluated by ultrasound pachymetry. \*P < 0.01, \*\*P < 0.05. (d) Representative slit-lamp images were obtained from monkeys injected with MCECs without or with Y-27632. Images were obtained 1 year after injection (n = 2). (e) Regenerated corneal endothelium was evaluated by non-contact specular microscopy 1 year after treatment in a monkey injected MCECs with the ROCK inhibitor Y-27632. Note that no image was obtained for the monkey injected with MCECs without Y-27632. (f) Immunostaining of function-related markers was determined in CECs (Na<sup>+</sup>/K<sup>+</sup>-ATPase and ZO-1) in regenerated corneal endothelium. Nuclei were stained with DAPI. Scale bar:  $100 \mu\text{m}$ .

**Cultivated HCEC injection in the monkey model.** We then evaluated the effect of cultured HCECs in a monkey corneal endothelial dysfunction model. The standard procedure for treating corneal endothelial dysfunction in clinical settings is Descemet's stripping automated endothelial keratoplasty (DSAEK), so we also transplanted human donor corneas using a DSAEK procedure for comparison with the HCEC injections. As was observed with MCEC injection, HCEC injection without a ROCK inhibitor did not regenerate a transparent cornea. By contrast, HCEC injection with a ROCK inhibitor regenerated a transparent cornea by 1 week after treatment (Fig. 3a). Slitlamp microscopy revealed that corneas treated with HCECs in combination with ROCK inhibitor were as transparent as the human cornea transplanted using the DSAEK procedure (Fig. 3a). The mean corneal thickness was thinner in eyes treated with HCECs and the ROCK inhibitor than in the other two groups (Fig. 3b and Supplemental Table 1). Rejection was observed in some of the HCEC-injected eyes and DSAEK eyes due to the xeno transplantation, but the eyes injected only with HCECs and without ROCK inhibitor, where rejection did not occur, showed hazy corneas, whereas the eyes injected with HCECs in combination with the ROCK inhibitor, where rejection did not occur, retained transparent corneas for 48 days (Fig. 3c).



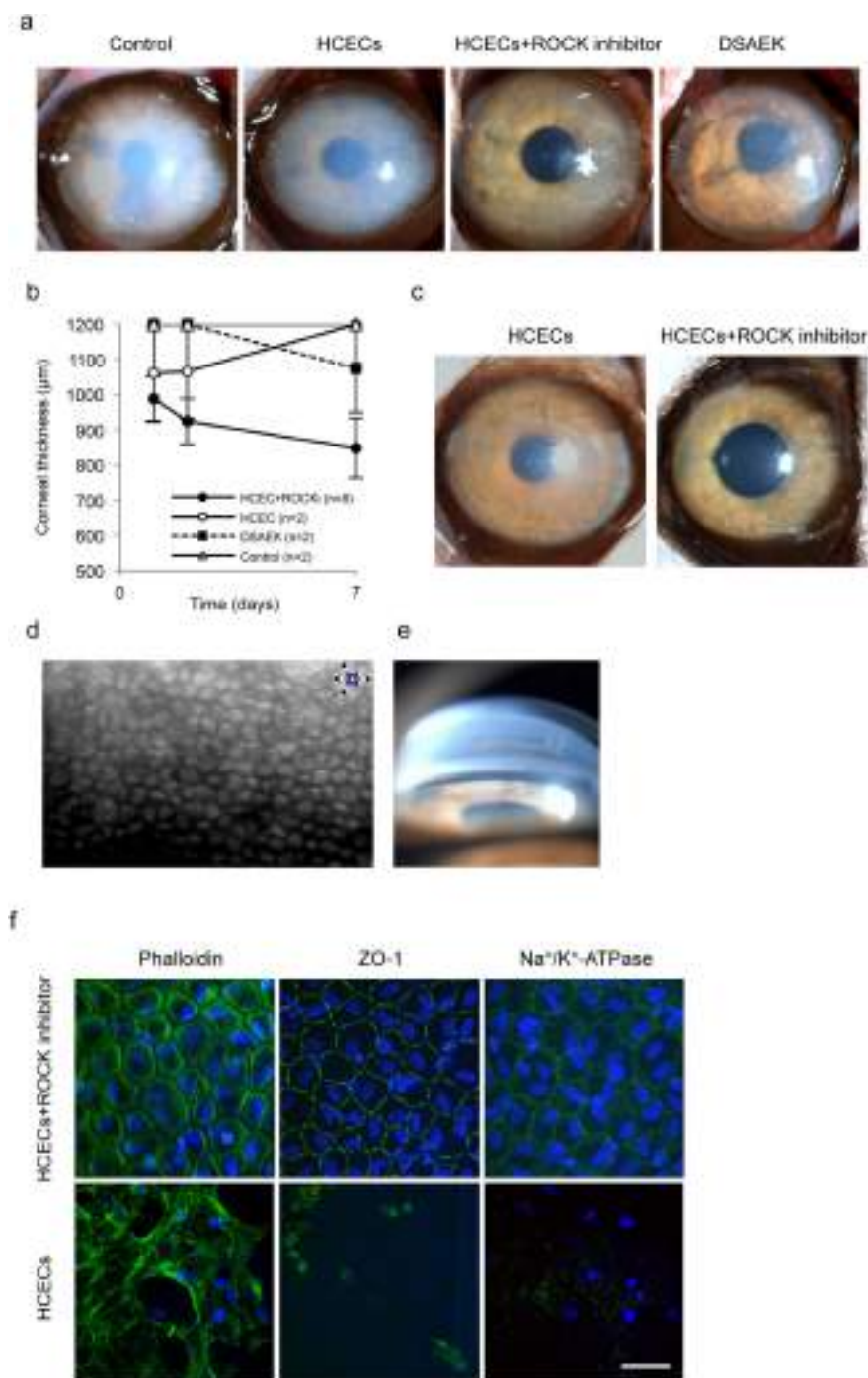


**Figure 3.** Preclinical research of cultured human corneal endothelial cell (HCEC) injection in combination with a ROCK inhibitor in a monkey corneal endothelial dysfunction model. (a) Representative slit-lamp images were obtained for the monkey corneal endothelial dysfunction model ( $n = 2$ ). A monkey injected with HCECs ( $5.0 \times 10^5$  cells) without the ROCK inhibitor Y-27632 ( $n = 2$ ), a monkey injected with HCECs ( $5.0 \times 10^5$  cells) and Y-27632 ( $n = 8$ ), and a monkey transplanted with a human donor cornea according to DSAEK procedure ( $n = 2$ ) are shown. All images were obtained 7 days after treatment. (b) Mean central corneal thickness was evaluated by ultrasound pachymetry. (c) Representative slit-lamp images were obtained for monkeys injected with HCECs without or with Y-27632. The images were obtained 3 months after injection ( $n = 2$ ). (d) An image of the regenerated corneal endothelium was obtained by non-contact specular microscopy 3 months after treatment in a monkey injected with HCECs in combination with Y-27632. Note that no image was obtained for monkeys injected with HCECs without Y-27632. (e) An angle image was obtained with a gonioscopy lens 3 months after treatment of a monkey injected with HCECs in combination with Y-27632. (f) Cell morphology of regenerated corneal endothelium was evaluated by phalloidin staining. Function-related markers of CECs ( $\text{Na}^+/\text{K}^+$ -ATPase and ZO-1) showed immunostaining in the regenerated corneal endothelium. Nuclei were stained with DAPI. Scale bar:  $100 \mu\text{m}$ .

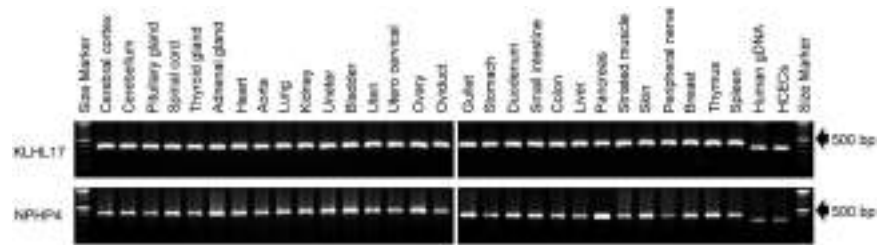


**Figure 4. Biodistribution tests in a monkey corneal endothelial dysfunction model.** PCR product sizes were compared between genomic DNAs derived from 29 different tissues from cynomolgus monkeys, and genomic DNA derived from HCECs and human genomic DNA in KLHL17 and NPHP4 genes.

Specular microscopy demonstrated that eyes treated with HCECs in combination with the ROCK inhibitor had a regenerated corneal endothelium in the form of a hexagonal monolayer, with a cell density of 2890 cell/mm<sup>2</sup> (Fig. 3d). Gonioscopy revealed no cell aggregation or peripheral anterior synechia. Coincidentally, no intraocular pressure elevation was observed, although secondary glaucoma is a possible adverse effect of cell injection into the anterior chamber (Fig. 3e). Fluorescent staining showed that the corneal endothelium regenerated by injected HCECs was hexagonal and a monolayer, and it expressed barrier and pump function-related proteins when HCECs were injected in combination with the ROCK inhibitor. By contrast, few fibroblastic cells were observed and function-related protein expression was lost in the eyes injected only with HCECs without ROCK inhibitor (Fig. 3f).

We initiated the culture of HCECs of Good Manufacturing Practice (GMP) grade in the cell-processing center at the Kyoto Prefectural University of Medicine, using the protocol required for clinical application (Supplement Fig. 2a). We then injected GMP-grade HCECs with ROCK inhibitor to 6 monkeys as a rehearsal (a so-called cold run). Representative slitlamp and Scheimpflug images showed that the cornea became transparent and regenerated an anatomically normal cornea without corneal edema, suggesting that the HCECs cultured by the protocol for clinical application should function *in vivo* (Supplement Fig. 2b,c). Fluorescent staining also showed that the corneal endothelium regenerated by GMP-grade HCECs was hexagonal and expressed function-related proteins (Supplement Fig. 2d).

**Systemic distribution assessment.** One possible adverse effect of cell-based therapy is an aberration due to the delivery of transplanted cells to other organs. We therefore evaluated the distribution of the injected HCECs in monkey organs 2 weeks after the HCEC injection. Macroscopic images and sectional analysis of organs showed no tissue abnormality and no aberrant ectopic cell transplantation ( $n = 6$ ) (Supplement Figs 3 and 4). The injected HCECs were labeled with DiI fluorescence, but no DiI positive cells were observed in any organs except the corneal endothelium (data not shown).

We also evaluated the presence of HCECs in the corneal endothelium and other tissues using two primer sets (KLHL17 and NPHP4) that differ in the PCR product lengths in humans and cynomolgus monkeys. The 331 bp PCR products were observed in human genomic DNA and HCECs, but only the 403 bp PCR products of KLHL17 were observed in tissues of the cynomolgus monkey. Similarly, the 317 bp PCR products of NPHP4 were observed in human genomic DNA and HCECs, but the 412 bp products were observed in all tissues of the cynomolgus monkey (Fig. 4 and Supplement Fig. 5). A preliminary study was conducted to determine the detection threshold for the PCR products from human KLHL17 cells using a series of two-fold dilutions of human genomic DNA samples. The PCR products were detected using  $>39$  pg samples of human genomic DNA as PCR templates in the first PCR amplification. The second PCR amplification was run with 1  $\mu$ L of the PCR products obtained from the first PCR amplification. Hence, theoretically, if even a single human cell was included in the PCR templates, the PCR products would be detected after the second PCR amplification. These results indicate that injected HCEC-derived cells were not present in any monkey organs other than the regenerated corneal endothelium.

#### A ROCK inhibitor enhances cell adhesion by suppressing the Rho/ROCK/MLC signaling cascade.

Phase contrast images showed that MCECs seeded without the ROCK inhibitor tended to be floating (non-adhering), with a round shape, whereas MCECs seeded with a ROCK inhibitor attached to the culture plate and showed extensive cell spreading (Fig. 5a). The actin cytoskeleton was well stretched and vinculin expression was promoted when the ROCK inhibitor was supplied with the MCECs (Fig. 5b,c). The cell size was significantly smaller in MCECs seeded without the ROCK inhibitor than with the ROCK inhibitor, even after 24 hours, suggesting that actin contraction is highly sustained by cell dissociation (Fig. 5d).

Examination of the phosphorylation of MLC showed it to be highly sustained in control MCECs and suppressed by ROCK inhibitor treatment of MCECs (Fig. 5e). Dissociation by EGTA also caused phosphorylation of MLC (Fig. 5f). The MCECs seeded on a non-adhesion plate, which maintained the cells in a dissociated state, showed phosphorylation of MLC even after 24 hours of seeding, whereas MCECs seeded on a normal culture plate exhibited less phosphorylation of MLC (Fig. 5g). These results indicate that cell dissociation induces phosphorylation of MLC and induces actin contraction in MCECs.

We also evaluated the effect of inhibiting MLC activity on adhesion of MCECs. Expression of vinculin was promoted by blebbistatin (an inhibitor of MLC) in a similar fashion to that seen in response to the ROCK inhibitor (Fig. 5h–j), as was phosphorylation of FAK and paxillin (Fig. 5k). The numbers of adhered MCECs were

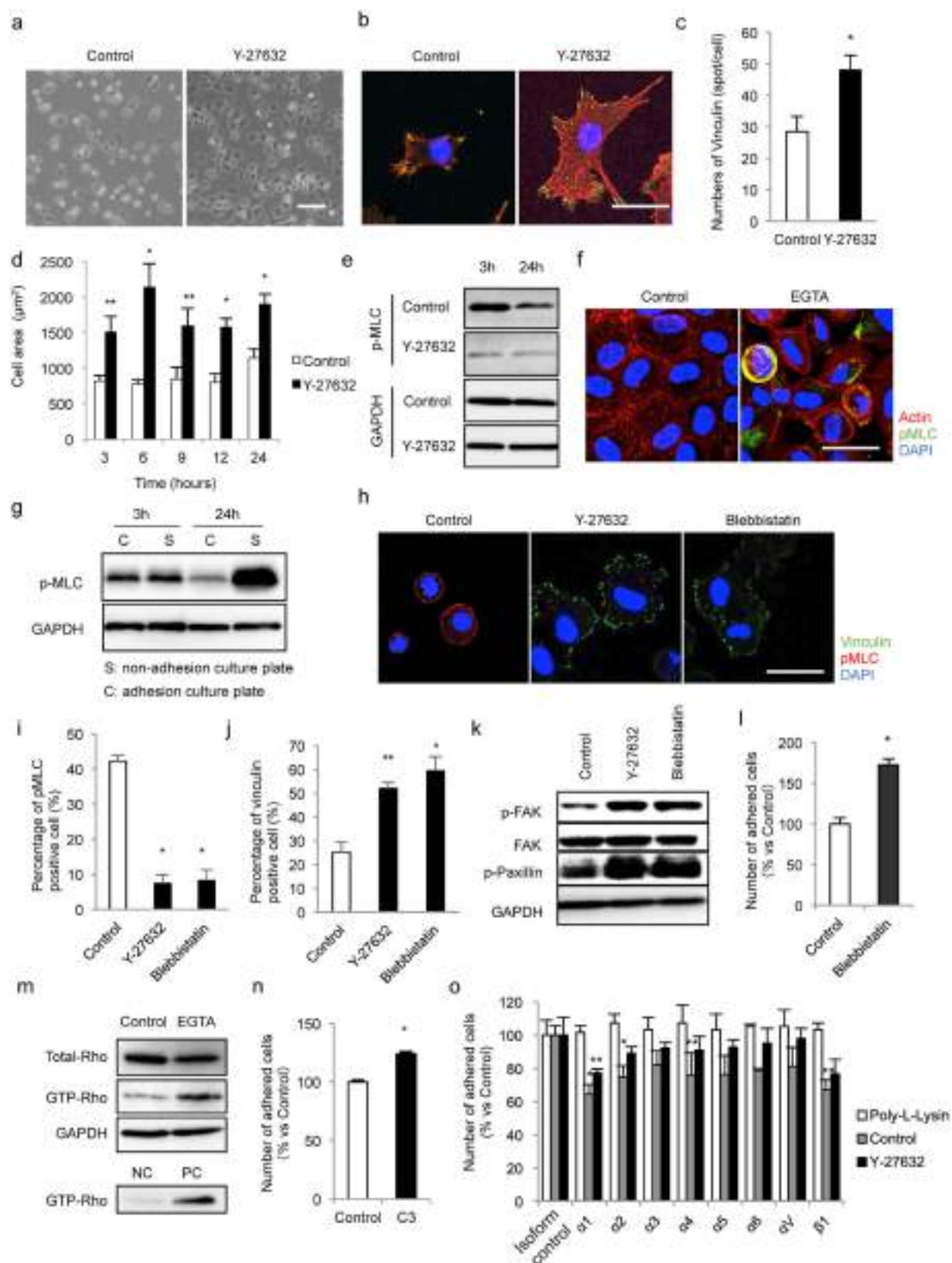


**Figure 5.** The molecular pathway by which ROCK inhibitor improves cell adhesion onto a substrate. (a) Phase contrast images show MCECs seeded onto culture plates after 3 hours. (b–d) MCECs seeded without or with Y-27632 were stained with phalloidin and an antibody for vinculin. The mean amount of vinculin per cell was evaluated. The mean cell area was smaller in control MCECs than in Y-27632-treated MCECs. \*P < 0.01, \*\*P < 0.05. (e) MLC was phosphorylated in control cells, even after 24 hours, while MLC phosphorylation was suppressed in MCECs treated with Y-27632. (f) Cell dissociation was induced by EGTA treatment, and phosphorylation of MLC was evaluated by immunostaining. (g) MCECs were seeded on non-

adhesion culture plates or adhesion culture plate, and phosphorylation of MLC was evaluated by western blotting. MLC phosphorylation was sustained in MCECs seeded on non-adhesion culture plates, while it was suppressed in MCECs seeded on adhesion culture plates. (h–j) MCECs were seeded and expression of vinculin and phosphorylated MLC was evaluated by immunostaining. Control MCECs expressed phosphorylated MLC without expression of vinculin, whereas phosphorylation of MLC was suppressed in MCECs treated with a ROCK inhibitor (Y-27632) and an MLC inhibitor (blebbistatin) associated with expression of vinculin. \* $P < 0.01$ , \*\* $P < 0.05$ . (k) MCECs were seeded and the effect of inhibition of MLC on focal adhesion molecule activity was evaluated by western blotting. (l) MCECs were seeded with or without blebbistatin and adhered numbers of MCECs were evaluated with the CellTiter-Glo™ luminescent cell viability assay after 24 hours. (m) Cell dissociation was induced by EGTA treatment, and activity of RhoA was evaluated by a pull-down assay. GTP-bound active RhoA was highly expressed in dissociated MCECs. (n) MCECs were seeded with or without C3 (a Rho inhibitor) and the numbers of adhered MCECs were evaluated by the CellTiter-Glo™ luminescent cell viability assay after 24 hours. (o) The involvement of integrins on cell adhesion enhancement by Y-27632 was evaluated by seeding MCECs in the presence or absence of integrin-neutralizing antibodies, and the numbers of adherent cells were determined. \* $P < 0.01$ , \*\* $P < 0.05$ .

enhanced by blebbistatin treatment (Fig. 5l), implying that activation of MLC negatively regulates cell adhesion. When we induced cell dissociation with an EGTA treatment, the GTP-bound RhoA was highly recognized by a pull down assay, suggesting that cell dissociation induced the activation of RhoA. In turn, inhibition of RhoA activity by C3 significantly enhanced cell adhesion (Fig. 5m,n).

We also showed that functional blocking of integrins by neutralizing antibodies counteracted the cell adhesion enhanced by the ROCK inhibitor but not by poly-L-lysine, suggesting that the ROCK inhibitor enhances cell adhesion through interactions between the focal adhesion complex and integrins (Fig. 5o). Cell dissociation therefore appeared to upregulate a RhoA/ROCK/MLC pathway and actin contraction impeded cell adhesion. However, inhibiting the phosphorylation of MLC by a ROCK inhibitor suppressed cell shrinkage by relaxing actin contraction and then promoting the focal adhesion complex (Fig. 6).

## Discussion

The low efficiency of engraftment and loss of phenotype after transplantation due to the absence of cell/cell and cell/ECM interactions *in vivo* impairs organ reconstruction in various tissues<sup>9–11</sup>. Researchers have therefore been exploring the use of various techniques, such as artificial scaffolds, biologically active molecules, and ECM coatings, to improve cell retention and survival<sup>12–14</sup>. In the present study, we defined the inhibition of ROCK signaling as a novel target for improving engraftment in the setting of cell-based therapy. We showed that CECs recovered from a culture plate for cell therapy undergo dissociation-induced Rho/ROCK/MLC signaling activation, which then impairs cell engraftment. Inhibition of ROCK therefore enhances cell engraftment and maintains the phenotype of the transplanted cells. Similar to our findings, Ohgushi and colleagues reported that human embryonic stem cells are vulnerable to apoptosis following dissociation due to ROCK-dependent hyperactivation of actomyosin, and that Rho-GEF (guanine nucleotide exchange factor), containing a functional Rac-GAP (GTPase activating protein) domain, is an indispensable regulator of Rho/ROCK/myosin activation<sup>15</sup>. The dissociation-induced cellular response varies with the cell type, but our findings should encourage researchers to evaluate and modulate dissociation-induced Rho/ROCK activation to improve cell engraftment efficiency in the settings of cell-based therapies in other organs.

We previously demonstrated that a ROCK inhibitor promotes the adhesion of cultured MCECs<sup>16</sup>, and a subsequent report by another group has also confirmed that a ROCK inhibitor improved the attachment of HCECs<sup>17</sup>. In 2012, we showed that use of ROCK inhibitor enables efficient cell engraftment in rabbit corneal endothelial dysfunction models and in a very preliminarily monkey model<sup>8</sup>. However, the rabbit corneal endothelium has a proliferative ability that is lacking in humans<sup>18,19</sup>, leaving the possibility that the proliferation of injected rabbit CECs seen after transplantation and the subsequent reconstruction of the corneal endothelium, would not be expected to occur in humans. We employed the present primate model to confirm or eliminate this possibility, because this model resembles the human corneal endothelium in terms of its very limited proliferative potency<sup>18,19</sup>. The use of this monkey model demonstrated that injection of either monkey or human CECs in combination with a ROCK inhibitor reconstructed the monkey corneal endothelium.

Corneal endothelial dysfunction has been treated by full-thickness corneal transplantation (penetrating keratoplasty) for more than 90 years, but more selective corneal endothelial replacement such as Descemet's stripping endothelial keratoplasty (DSEK) and Descemet's membrane endothelial keratoplasty (DMEK) were developed in the last decade<sup>3,20</sup>. In addition, graft rejection rates during first 2 years after corneal transplantation were 1% in DMEK and 5–14% in DSEK<sup>20–27</sup> suggesting that simple replacement of the corneal endothelium induce fewer episodes of rejection and that the stroma, but not corneal endothelium, mainly triggers antigenic recognition and responses<sup>20</sup>. The clinically successful outcomes of DSEK and DMEK imply that reconstruction of the corneal endothelium is a definitive treatment that can replace full thickness corneal replacement, and that further corneal endothelium reconstruction by cell-based therapy is a clinically relevant approach.

At present, HCECs are isolated from donor corneas and cultured for research purposes<sup>28</sup>, but several substantial technical obstacles remain, such as limited proliferative ability, vulnerable transformation with loss of functions, and senescence that prohibits efficient *in vitro* expansion for clinical use<sup>16,29–34</sup>. Indeed, no protocol specifically designed for clinical application has been established, although our research group and others are continually striving towards the development of a successful culture method<sup>29,30,31,34</sup>. For instance, we reported that a conditioned medium obtained from GMP-grade human bone marrow-derived mesenchymal stem cells



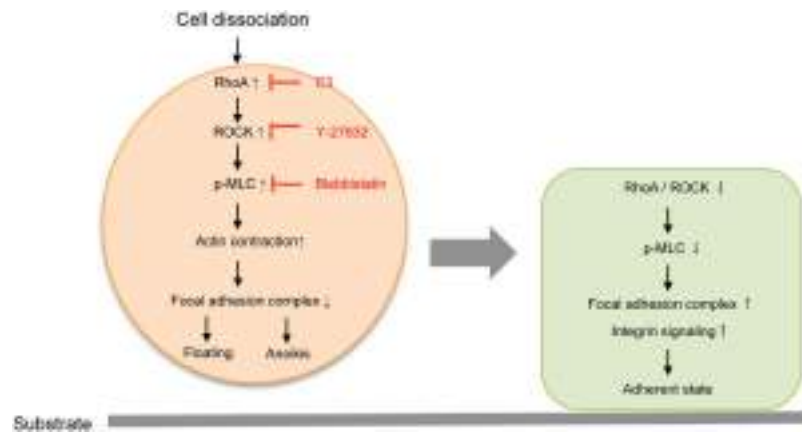


**Figure 6.** The molecular pathway by which a ROCK inhibitor treatment improves cell engraftment of CECs. (Right) Cell dissociation during the harvesting of CECs from culture plate activates RhoA/ROCK/MLC pathways. Activation of this pathway suppresses activation of the focal adhesion complex, and subsequently inhibits cell adhesion while inducing anoikis. (Left) By contrast, inhibition of actomyosin activation by a ROCK inhibitor activates the focal adhesion complex and enhances cell/ECM adhesion.

(BM-MSCs) enhanced CEC proliferation<sup>33</sup> and that inhibition of transforming growth factor beta (TGF- $\beta$ ) signaling activation by small molecules maintains the functional phenotype by counteracting fibroblastic transformation<sup>32</sup>. Based on these findings, we are currently culturing HCECs of Good Manufacturing Practice (GMP) grade in the cell-processing center for use in clinical applications<sup>35</sup>.

In the United States, the U.S. Food and Drug Administration (FDA) regulates regenerative medicine products through the Center for Biologics Evaluation and Research (CBER) and other countries also have similar systems<sup>36</sup>. Working with the FDA requirements<sup>11</sup>, we tested the safety and efficacy of GMP-grade HCECs in the same fashion as we intend to use in the transplantation of these cells into human patients in clinical trials. We have now established a culture protocol for clinical use. Notably, based on this current preclinical research, in 2013, we initiated a first-in-man clinical trial of cell-based therapy to treat corneal endothelial dysfunction at the Kyoto Prefectural University of Medicine, after obtaining the necessary approval (Clinical trial registration: UMIN000012534) from the Japanese Ministry of Health, Labour and Welfare.

The major safety concern of any regenerative medicine product is the potential for tumor formation<sup>36</sup>. There is a spectrum of risk (e.g., differentiated somatic cells have a lower risk than undifferentiated embryonic stem cells), so product-specific evaluation is necessary as a preclinical testing strategy<sup>36</sup>. In the current study, comparison of the numbers of injected CECs and the cell density of the regenerated corneal endothelium revealed that 40–50% of the injected CECs adhered to the cornea. The residual cells were then considered to have the potential to flow out by aqueous flow to other organs via the veins. We therefore examined the distribution of transplanted CECs in multiple organs of monkey disease models and showed that no CECs were observed by fluorescein labeling tracing and PCR at 2 weeks after transplantation (although perfect *in vivo* monitoring of delivered cells is surprisingly challenging). One possible explanation is that any cells that flowed out were removed by the host immune system; however, the duration of the follow-up period used here was not sufficient to conclude that these residual cells do not hold any risk of tumorigenicity. Therefore, diligent feedback from clinical trials—by evaluating possible side effects, such as host immune response and pulmonary embolism—will be needed to ensure patient safety and protect vulnerable populations.

In conclusion, inhibiting the dissociation-induced actomyosin activation by a ROCK inhibitor improves the efficiency of engraftment of CECs and enables cell-based approaches for treating corneal endothelial dysfunction as a clinically relevant therapy.

## Methods

**Ethics statement.** Animals were housed and treated in accordance with the ARVO Statement for the Use of Animals in Ophthalmic and Vision Research. The monkey experiments were performed at the Research Center for Animal Life Science at Shiga University of Medical Science (Otsu, Japan) according to the protocol approved by that university's Animal Care and Use Committee (Approval No. 2012-1-6H). Human donor corneas were obtained from SightLife<sup>TM</sup> (<http://www.sightlife.org/>, Seattle, WA) for research purposes.

**Cell Culture.** Ten corneas from 5 cynomolgus monkeys (3 to 5 years-of-age; estimated equivalent human age: 5 to 20 years) housed at NISSEI BILIS Co., Ltd. and Eve Bioscience, Co., Ltd. were used for the MCEC culture. The MCECs were cultivated as described previously<sup>7</sup>. Briefly, the Descemet's membrane with MCECs was stripped and incubated in 1 mg/mL collagenase A (Roche Applied Science, Penzberg, Germany). The isolated MCECs were resuspended in culture medium and seeded on culture plates coated with FNC Coating Mix<sup>®</sup> (Athena Environmental Sciences, Inc., Baltimore, MD). All primary cell cultures and serial passages of MCECs were performed in a growth medium composed of Dulbecco's modified Eagle's medium (Life Technologies Corp., Carlsbad, CA) supplemented with 10% fetal bovine serum (FBS), 50 U/mL penicillin, 50  $\mu$ g/mL streptomycin,

and 2 ng/mL fibroblast growth factor 2 (Life Technologies Corp.). MCECs at passages 2 through 8 were used for these experiments.

A total of ten human donor corneas were used for cultivation of HCECs by the protocol described previously<sup>32,33</sup>. Briefly, the Descemet's membranes containing the HCECs were stripped, followed by digestion with 1 mg/mL collagenase A for 12 hours. The HCECs were seeded and cultured in HCEC culture medium prepared according to published protocols. Basal medium, composed of OptiMEM-I (Life Technologies Corp.), 8% FBS, 5 ng/mL epidermal growth factor (Sigma-Aldrich Co., St. Louis, MO), 20 µg/mL ascorbic acid (Sigma-Aldrich Co.), 200 mg/L calcium chloride, 0.08% chondroitin sulfate (Wako Pure Chemical Industries, Ltd., Osaka, Japan), 50 µg/mL gentamicin, and 10 µM SB431542 (Merck Millipore, Billerica, MA), was conditioned by culturing human bone marrow-derived mesenchymal stem cells (BM-MSCs) for 24 hours. The basal medium conditioned with BM-MSCs was collected for use as the culture medium for HCECs. HCECs at passages 2 through 5 were used for these experiments.

**Injection of CECs into a monkey corneal endothelial dysfunction model.** The monkey corneal endothelial dysfunction model was created by scraping the corneal endothelium completely from the Descemet's membrane with a 20-gauge silicone needle (Soft Tapered Needle; Inami & Co., Ltd., Tokyo, Japan) while the animal was under general anesthesia, as described previously<sup>8</sup>. The MCEC injection experiments were conducted on the following 3 groups: 1) MCECs ( $5.0 \times 10^5$  cells) were suspended in 200 µl of DMEM supplemented with 100 µM of Y-27632 (ROCK inhibitor; Wako Pure Chemical Industries, Ltd.) and injected into the anterior chamber ( $n = 6$ ), 2) MCECs ( $5.0 \times 10^5$  cells) were suspended in 200 µl of DMEM and injected into the anterior chamber ( $n = 2$ ), and 3) no MCECs were injected ( $n = 2$ ). The HCEC injection experiments were conducted on the following 4 groups: 1) HCECs ( $5.0 \times 10^5$  cells) were suspended in 200 µl of OptiMEM-I supplemented with 100 µM of Y-27632 (Wako Pure Chemical Industries, Ltd.) and injected into the anterior chamber ( $n = 8$ ), 2) HCECs ( $5.0 \times 10^5$  cells) were suspended in 200 µl of OptiMEM-I and injected into the anterior chamber ( $n = 2$ ), 3) human pre-cut donor corneas were transplant using a DSAEK procedure ( $n = 2$ ), and 4) no HCECs were injected ( $n = 2$ ). The eyes were kept in the face-down position for 3 hours under general anesthesia, except for the eyes of monkeys that underwent DSAEK. The corneal transparency and thickness of the anterior segments were evaluated by slitlamp microscopy. A Pentacam® (OCULUS Optikgeräte GmbH, Wetzlar, Germany) instrument was used to visualize the corneal shape. Corneal thickness was determined with an ultrasound pachymeter (SP-2000; Tomey, Nagoya, Japan), and the mean of 10 measured values was calculated (up to a maximum thickness of 1200 µm, the instrument's maximum reading). Intraocular pressure was determined by a Tonovet® (icare Finland, Vantaa, Finland) instrument. The corneal endothelium was evaluated by non-contact specular microscopy (FA-3809, Konan Medical, Nishinomiya, Japan). Eyes that exhibited clinical features such as the presence of keratic precipitates, progression of corneal edema, and conjunctival injection were diagnosed as having undergone graft rejection.

**Immunohistochemistry.** Samples were fixed for 20 min with 4% paraformaldehyde and excess paraformaldehyde was removed by washing with Dulbecco's phosphate-buffered saline (PBS). The samples were permeabilized with 0.3% Triton® X-100 (Nacalai Tesque, Kyoto, Japan), and then incubated with 1% bovine serum albumin (BSA) to block nonspecific binding. Specimens were incubated with primary antibodies against Na<sup>+</sup>/K<sup>+</sup>-ATPase (1:300, Upstate Biotechnology, Lake Placid, NY), ZO-1 (1:300, Life Technologies Corp.), and N-cadherin (1:300, BD Biosciences, San Jose, CA), connexin 43 (1:300, Life Technologies Corp.), and vinculin (Merck Millipore, Billerica, MA). Alexa Fluor® 488- or 594- conjugated goat anti-mouse (Life Technologies Corp.) antibodies were used as secondary antibodies at a 1:1000 dilution. Actin staining was performed by incubation with a 1:400 dilution of Alexa Fluor® 488- or 546- conjugated Phalloidin (Life Technologies Corp.). Nuclei were stained with DAPI (Vector Laboratories, Burlingame, CA). The slides were examined with a fluorescence microscope (TCS SP2 AOBS; Leica Microsystems, Wetzlar, Germany).

**Immunoblotting.** The MCECs were washed with ice-cold PBS, lysed with ice-cold RIPA buffer containing phosphatase inhibitor cocktail 2 (Sigma-Aldrich Co., St. Louis, MO) and protease inhibitor cocktail (Roche Applied Science, Penzberg, Germany), and then centrifuged. The supernatant representing total proteins was collected and fractionated by SDS-PAGE. The proteins were then transferred to PVDF membranes and blocked with 3% non-fat dry milk, followed by an overnight incubation at 4 °C with the following primary antibodies: phosphorylated focal adhesion kinase (FAK) (1:1000; Cell Signaling Technology, Inc., Danvers, MA), FAK (1:1000; Cell Signaling Technology), phosphorylated MLC (Merck Millipore, Billerica, MA), phosphorylated paxillin (1:1000; Cell Signaling Technology), and GAPDH (1:3000; Abcam, Cambridge, UK). The blots were probed with horseradish peroxidase-conjugated secondary antibodies (1:5000; Cell Signaling Technology), followed by development with luminal for enhanced chemiluminescence using the ECL Advanced Western Blotting Detection Kit (GE Healthcare, Piscataway, NJ), and documentation by an LAS4000S (Fuji Film, Tokyo, Japan) cooled charge-coupled-device camera gel documentation system. Molecular weight markers (Bio-Rad, California) were run alongside all samples. The relative density of the immunoblot bands was determined by Image J® (NIH) software.

**Rho pull down assay.** The RhoA activation was evaluated by a Rho activation assay (Merck Millipore, Billerica, MA) according to the manufacturer's protocol. MCECs were cultured to a confluent state, and dissociated by incubation in serum-free medium supplemented with 3 mM EGTA (Nacalai Tesque) for 16 hours. The MCECs were washed with ice-cold PBS, lysed with ice-cold Mg<sup>2+</sup> Lysis/Wash Buffer (Merck Millipore) containing phosphatase inhibitor cocktail 2 (Sigma-Aldrich Co.), and then agitated. Samples were then reacted with Rho Assay Reagent (Merck Millipore) to bond GTP-Rho. The supernatant representing total proteins was collected

and immunoblotting was performed described as above. Anti-Rho, clone 55, (3:1000; Merck Millipore) was used as the primary antibody.

**Cell adhesion assay.** The involvement of integrins in the enhancement of cell adhesion by the ROCK inhibitor was evaluated by seeding MCECs ( $5 \times 10^3$  cells/well) in 96-well plates in the presence or absence of integrin-neutralizing antibodies (2 µg/mL): anti- $\alpha 1$  integrin (Merck Millipore, Billerica, MA), anti- $\alpha 2$  integrin (Merck Millipore, Billerica, MA), anti- $\alpha 3$  integrin (Merck Millipore, Billerica, MA), anti- $\alpha 4$  integrin (Merck Millipore, Billerica, MA), anti- $\alpha 5$  integrin (Merck Millipore, Billerica, MA), anti- $\alpha 6$  integrin (Merck Millipore, Billerica, MA), anti- $\alpha V$  integrin (Merck Millipore, Billerica, MA), anti- $\alpha 6$  integrin (Merck Millipore), and anti- $\beta 1$  integrin (R&D systems Inc., Minneapolis, MN). The effect of inhibiting phosphorylation of MLC and RhoA activity on cell adhesion was also evaluated by seeding MCECs with blebbistatin (10 µM) and C3 (300 ng/ml), respectively. Three hours after seeding, the numbers of adherent cells were determined with the CellTiter-Glo™ luminescent cell viability assay (Promega Corporation, Madison, WI) according to the manufacturer's instructions. The number of adhered cells was determined using a Veritas™ microplate luminometer (Promega Corporation).

**PCR method.** Genomic DNAs from cynomolgus monkey tissues were extracted using the DNeasy Blood & Tissue kit (Qiagen, Hilden, Germany), and the quality was measured with a NanoDrop® spectrophotometer (Thermo Fisher Scientific Inc., Waltham, MA). The KLHL17 and NPHP4 genes, which differ in length in humans and cynomolgus monkeys, were selected by a detailed search between human and rhesus monkey reference sequences (GRCh37/hg19 and MGSC Merged 1.0/rheMac2) released in the UCSC website (<http://genome.ucsc.edu/index.html>) for designation of primers. Two new primer sets in KLHL17 and NPHP4 genes were designed in exon 7 and exon 8 (PCR product sizes: 331 bp in human and 403 bp in cynomolgus monkey) and intron 11 (PCR product sizes: 317 bp in human and 412 bp in cynomolgus monkey), respectively, with the following primers: KLHL17 (KLHL17\_F1: 5'- TGGTGGCCTCCATGTCCAC-3' and KLHL17\_R1: 5'- CTACCTGTTCAGGCAGGAG-3'), NPHP4 (NPHP4\_F1: 5'- GGTGCTTCCCAAATACTACT-3' and NPHP4\_R1: 5'- GGTAAGCTTCCATTTCAGGA-3'). The fixing of the PCR products sizes in humans was confirmed by the 1000 genome website (<http://www.1000genomes.org>). In brief, the 20 µL amplification reaction volume contained 20 ng of genomic DNA, 0.4 units of KOD FX polymerase (TOYOBO, Osaka, Japan), 2 × PCR buffer, 2 mM of each dNTP and 0.5 µM of each primer. The cycling parameters were as follows: an initial denaturation of 94 °C/2 min followed by 30 cycles of 98 °C/10 sec, 62 °C/15 sec and 68 °C/30 sec. The irreducible minimum HCECs were detected by performing two repeats of the PCR amplification process. The second PCR amplification was run with 1 µL of PCR products obtained from the first PCR amplification. The PCR reactions were performed using the thermal cycler GeneAmp PCR system 9700 (Applied Biosystems/Life Technologies/Thermo Fisher Scientific, Foster City, CA). The PCR products were separated by electrophoresis on 1.0% agarose gels, stained with ethidium bromide, and detected under ultraviolet illumination.

**Statistical analysis.** The statistical significance (P-value) of differences between mean values of the two-sample comparison was determined with the Student's t-test. The comparison of multiple sample sets was analyzed using Dunnett's multiple-comparison test. The values shown in the graphs represent the mean ± SEM.

## References

- Joyce, N. C. Proliferative capacity of corneal endothelial cells. *Experimental eye research* **95**, 16–23 (2012).
- Bourne, W. M. Clinical estimation of corneal endothelial pump function. *Trans Am Ophthalmol Soc* **96**, 229–239; discussion 239–242 (1998).
- Tan, D. T., Dart, J. K., Holland, E. J. & Kinoshita, S. Corneal transplantation. *Lancet* **379**, 1749–1761 (2012).
- Patel, S. V. Graft survival and endothelial outcomes in the new era of endothelial keratoplasty. *Experimental eye research* **95**, 40–47 (2012).
- Mimura, T. *et al.* Cultured human corneal endothelial cell transplantation with a collagen sheet in a rabbit model. *Invest Ophthalmol Vis Sci* **45**, 2992–2997 (2004).
- Ishino, Y. *et al.* Amniotic membrane as a carrier for cultivated human corneal endothelial cell transplantation. *Invest Ophthalmol Vis Sci* **45**, 800–806 (2004).
- Koizumi, N. *et al.* Cultivated corneal endothelial cell sheet transplantation in a primate model. *Invest Ophthalmol Vis Sci* **48**, 4519–4526 (2007).
- Okumura, N. *et al.* ROCK inhibitor converts corneal endothelial cells into a phenotype capable of regenerating *in vivo* endothelial tissue. *Am J Pathol* **181**, 268–277 (2012).
- van der Bogt, K. E. *et al.* Comparison of different adult stem cell types for treatment of myocardial ischemia. *Circulation* **118**, S121–129 (2008).
- Wu, Y. M., Joseph, B., Berishvili, E., Kumaran, V. & Gupta, S. Hepatocyte transplantation and drug-induced perturbations in liver cell compartments. *Hepatology* **47**, 279–287 (2008).
- Harding, J. & Mirochnitchenko, O. Preclinical studies for induced pluripotent stem cell-based therapeutics. *The Journal of biological chemistry* **289**, 4585–4593 (2014).
- Hibino, N. *et al.* Evaluation of the use of an induced pluripotent stem cell sheet for the construction of tissue-engineered vascular grafts. *The Journal of thoracic and cardiovascular surgery* **143**, 696–703 (2012).
- Yang, J. J., Liu, J. F., Kurokawa, T., Kitada, K. & Gong, J. P. Hydrogels as feeder-free scaffolds for long-term self-renewal of mouse induced pluripotent stem cells. *Journal of tissue engineering and regenerative medicine* **9**, 375–388 (2015).
- Forbes, S. J., Gupta, S. & Dhawan, A. Cell therapy for liver disease: From liver transplantation to cell factory. *Journal of hepatology* **62**, S157–169 (2015).
- Ohgushi, M. *et al.* Molecular pathway and cell state responsible for dissociation-induced apoptosis in human pluripotent stem cells. *Cell stem cell* **7**, 225–239 (2010).
- Okumura, N. *et al.* Enhancement on primate corneal endothelial cell survival *in vitro* by a ROCK inhibitor. *Invest Ophthalmol Vis Sci* **50**, 3680–3687 (2009).

17. Peh, G. S. *et al.* The effects of Rho-associated kinase inhibitor Y-27632 on primary human corneal endothelial cells propagated using a dual media approach. *Sci Rep* **5**, 9167 (2015).
18. Matsubara, M. & Tanishima, T. Wound-healing of the corneal endothelium in the monkey: a morphometric study. *Jpn J Ophthalmol* **26**, 264–273 (1982).
19. Matsubara, M. & Tanishima, T. Wound-healing of corneal endothelium in monkey: an autoradiographic study. *Jpn J Ophthalmol* **27**, 444–450 (1983).
20. Price, F. W. Jr. & Price, M. O. Evolution of endothelial keratoplasty. *Cornea* **32** Suppl 1, S28–32 (2013).
21. Allan, B. D., Terry, M. A., Price, F. W. Jr., Price, M. O., Griffin, N. B. & Claesson, M. Corneal transplant rejection rate and severity after endothelial keratoplasty. *Cornea* **26**, 1039–1042 (2007).
22. Price, M. O., Jordan, C. S., Moore, G. & Price, F. W. Jr. Graft rejection episodes after Descemet stripping with endothelial keratoplasty: part two: the statistical analysis of probability and risk factors. *The British journal of ophthalmology* **93**, 391–395 (2009).
23. Dapena, I., Ham, L., Netukova, M., van der Wees, J. & Melles, G. R. Incidence of early allograft rejection after Descemet membrane endothelial keratoplasty. *Cornea* **30**, 1341–1345 (2011).
24. Anshu, A., Price, M. O. & Price, F. W. Jr. Risk of corneal transplant rejection significantly reduced with Descemet's membrane endothelial keratoplasty. *Ophthalmology* **119**, 536–540 (2012).
25. Li, J. Y., Terry, M. A., Goshe, J., Shamie, N. & Davis-Boozer, D. Graft rejection after Descemet's stripping automated endothelial keratoplasty: graft survival and endothelial cell loss. *Ophthalmology* **119**, 90–94 (2012).
26. Wu, E. I., Ritterband, D. C., Yu, G., Shields, R. A. & Seedor, J. A. Graft rejection following descemet stripping automated endothelial keratoplasty: features, risk factors, and outcomes. *American journal of ophthalmology* **153**, 949–957 e941 (2012).
27. Hjortdal, J., Pedersen, I. B., Bak-Nielsen, S. & Ivarsen, A. Graft rejection and graft failure after penetrating keratoplasty or posterior lamellar keratoplasty for fuchs endothelial dystrophy. *Cornea* **32**, e60–63 (2013).
28. Joyce, N. C. Proliferative capacity of the corneal endothelium. *Prog Retin Eye Res* **22**, 359–389 (2003).
29. Peh, G. S., Toh, K. P., Wu, F. Y., Tan, D. T. & Mehta, J. S. Cultivation of human corneal endothelial cells isolated from paired donor corneas. *PLoS One* **6**, e28310 (2011).
30. Peh, G. S., Beuerman, R. W., Colman, A., Tan, D. T. & Mehta, J. S. Human corneal endothelial cell expansion for corneal endothelium transplantation: an overview. *Transplantation* **91**, 811–819 (2011).
31. Shima, N., Kimoto, M., Yamaguchi, M. & Yamagami, S. Increased proliferation and replicative lifespan of isolated human corneal endothelial cells with L-ascorbic acid 2-phosphate. *Invest Ophthalmol Vis Sci* **52**, 8711–8717 (2011).
32. Okumura, N., Kay, E. P., Nakahara, M., Hamuro, J., Kinoshita, S. & Koizumi, N. Inhibition of TGF-beta Signaling Enables Human Corneal Endothelial Cell Expansion *in vitro* for Use in Regenerative Medicine. *PLoS One* **8**, e58000 (2013).
33. Nakahara, M. *et al.* Corneal endothelial expansion promoted by human bone marrow mesenchymal stem cell-derived conditioned medium. *PLoS One* **8**, e69009 (2013).
34. Okumura, N. *et al.* Laminin-511 and -521 enable efficient *in vitro* expansion of human corneal endothelial cells. *Invest Ophthalmol Vis Sci* **56**, 2933–2942 (2015).
35. Okumura, N., Kinoshita, S. & Koizumi, N. Cell-based approach for treatment of corneal endothelial dysfunction. *Cornea* **33** Suppl 11, S37–41 (2014).
36. Bailey, A. M. Balancing tissue and tumor formation in regenerative medicine. *Science translational medicine* **4**, 147fs128 (2012).

## Acknowledgements

This study was supported by the Highway Program for realization of regenerative medicine (Kinoshita and Koizumi) and the Program for the Strategic Research Foundation at Private Universities from MEXT (Koizumi N and Okumura N). The authors thank Mr. Takahiro Nakagawa, Mr. Ikuo Kawamoto, Mr. Yuki Hosoda, and Mr. Shunsuke Watanabe for their invaluable assistance with experiments.

## Author Contributions

N.O., M.U., M.H., J.H., A.M., T.S., S.K. and N.K. conceived and designed the study. N.O., Y.S., K.F., J.K., S.N., Y.T., S.N., S.S., T.S. and N.K. performed the experiments. N.O. and T.S. drafted the article, and all authors revised the article and approved the final version to be published.

## Additional Information

**Supplementary information** accompanies this paper at <http://www.nature.com/srep>

**Competing financial interests:** Shigeru Kinoshita obtained a patent regarding the application of ROCK inhibitor for corneal endothelium (registration number: 5657252). N. O. and N. K. are listed as inventors of the patent.

**How to cite this article:** Okumura, N. *et al.* Rho kinase inhibitor enables cell-based therapy for corneal endothelial dysfunction. *Sci. Rep.* **6**, 26113; doi: 10.1038/srep26113 (2016).



This work is licensed under a Creative Commons Attribution 4.0 International License. The images or other third party material in this article are included in the article's Creative Commons license, unless indicated otherwise in the credit line; if the material is not included under the Creative Commons license, users will need to obtain permission from the license holder to reproduce the material. To view a copy of this license, visit <http://creativecommons.org/licenses/by/4.0/>



RESEARCH ARTICLE

# Generation and Feasibility Assessment of a New Vehicle for Cell-Based Therapy for Treating Corneal Endothelial Dysfunction

Naoki Okumura<sup>1</sup>, Kazuya Kakutani<sup>1</sup>, Ryota Inoue<sup>1</sup>, Daiki Matsumoto<sup>1</sup>, Tomoki Shimada<sup>1</sup>, Makiko Nakahara<sup>1</sup>, Yumiko Kiyanagi<sup>2</sup>, Takehiro Itoh<sup>2</sup>, Noriko Koizumi<sup>1\*</sup>

**1** Department of Biomedical Engineering, Faculty of Life and Medical Sciences, Doshisha University, Kyotanabe, Japan, **2** Cell Science & Technology Institute, Inc., Sendai, Japan

\* [nkoizumi@mail.doshisha.ac.jp](mailto:nkoizumi@mail.doshisha.ac.jp)



## OPEN ACCESS

**Citation:** Okumura N, Kakutani K, Inoue R, Matsumoto D, Shimada T, Nakahara M, et al. (2016) Generation and Feasibility Assessment of a New Vehicle for Cell-Based Therapy for Treating Corneal Endothelial Dysfunction. PLoS ONE 11(6): e0158427. doi:10.1371/journal.pone.0158427

**Editor:** Alexander V. Ljubimov, Cedars-Sinai Medical Center; UCLA School of Medicine, UNITED STATES

**Received:** February 27, 2016

**Accepted:** June 15, 2016

**Published:** June 29, 2016

**Copyright:** © 2016 Okumura et al. This is an open access article distributed under the terms of the [Creative Commons Attribution License](https://creativecommons.org/licenses/by/4.0/), which permits unrestricted use, distribution, and reproduction in any medium, provided the original author and source are credited.

**Data Availability Statement:** Underlying participant-level data was provided in a supporting information file.

**Funding:** Program for the Strategic Research Foundation at Private Universities from Ministry of Education, Culture, Sports, Science and Technology [http://www.mext.go.jp/a\\_menu/koutou/shinkou/07021403/002/002/1218299.htm](http://www.mext.go.jp/a_menu/koutou/shinkou/07021403/002/002/1218299.htm).

**Competing Interests:** The authors have declared that no competing interests exist.

## Abstract

The corneal endothelium maintains corneal transparency by its pump and barrier functions; consequently, its decompensation due to any pathological reason causes severe vision loss due to corneal haziness. Corneal transplantation is the only therapeutic choice for treating corneal endothelial dysfunction, but associated problems, such as a shortages of donor corneas, the difficulty of the surgical procedure, and graft failure, still need to be resolved. Regenerative medicine is attractive to researchers as a means of providing innovative therapies for corneal endothelial dysfunction, as it now does for other diseases. We previously demonstrated the successful regeneration of corneal endothelium in animal models by injecting cultured corneal endothelial cells (CECs) in combination with a Rho kinase (ROCK) inhibitor. The purpose of the present study was to optimize the vehicle for clinical use in cell-based therapy. Our screening of cell culture media revealed that RELAR medium promoted CEC adhesion. We then modified RELAR medium by removing hormones, growth factors, and potentially toxic materials to generate a cell therapy vehicle (CTV) composed of amino acid, salts, glucose, and vitamins. Injection of CECs in CTV enabled efficient engraftment and regeneration of the corneal endothelium in the rabbit corneal endothelial dysfunction model, with restoration of a transparent cornea. The CECs retained >85% viability after a 24 hour preservation as a cell suspension in CTV at 4°C and maintained their potency to regenerate the corneal endothelium in vivo. The vehicle developed here is clinically applicable for cell-based therapy aimed at treating the corneal endothelium. Our strategy involves the generation of vehicle from a culture medium appropriate for a given cell type by removing materials that are not favorable for clinical use.

## Introduction

The cornea serves as the window of the eye, and its transparency is critical for vision. One function of the corneal endothelium is the maintenance of corneal transparency, which is

controlled by the regulation of aqueous humor flow to the corneal stroma by the pump and barrier functions of the corneal endothelium. Corneal endothelial cells (CECs) have very limited proliferative ability and rarely show mitosis in humans after birth [1–3]. The CECs continuously decrease in number at a rate of 0.6% per year throughout life [4], but this rate is sufficiently low to maintain the function of the corneal endothelium. However, severe damage to the corneal endothelium induces irreversible decompensation of endothelial function and leads to corneal haziness. Fuchs endothelial corneal dystrophies and decompensation following cataract surgery are the leading causes of corneal endothelial dysfunction [5].

Corneal transplantation is only therapeutic choice for treating corneal endothelial dysfunction [6]. Penetrating keratoplasty, which involves replacement of the full-thickness cornea, including the corneal endothelial layer, with a donor cornea has been performed since 1905 [6]. New surgical procedures have recently been introduced, including Descemet's stripping endothelial keratoplasty (DSEK) and Descemet's membrane endothelial keratoplasty (DMEK), where the diseased layer alone is selectively replaced instead of a full-thickness replacement. These procedures have undergone rapid development and have shown an explosive spread [7–11]. However, the problems associated with corneal transplantation, such as the shortage of donor corneas, the difficulty of the surgical procedure, and the incidence of graft failure in acute and chronic phases, have led researchers to devise new and less problematic strategies to provide less invasive and more effective therapy.

Regenerative medicine is now attracting researchers as a future innovative therapy for a number of diseases in many medical fields, including ophthalmology. For example, several groups have reported the successful transplantation of cultured corneal endothelial sheets in animal models [12–14]. However, the technical difficulty of transplanting a flexible sheet to the anterior chamber and the development of an artificial clinically applicable carrier are obstacles that limit corneal endothelial sheet transplantation. We have sought to overcome these obstacles through cell-based regenerative medicine. Our finding that a Rho kinase (ROCK) inhibitor enhanced the adhesion of cultured CECs to a substrate [15] suggested the possibility that ROCK inhibitors could be useful in cell-based therapy [16]. We used rabbit and monkey corneal endothelial dysfunction models to demonstrate the successful regeneration of corneal endothelium following the injection of cultured CECs in combination with a ROCK inhibitor [16].

In the current study, we conducted experiments to generate an optimized CEC vehicle for cell-based therapy aimed at treating corneal endothelial dysfunction. Our screening of various types of cell culture media revealed that RELAR medium promoted the cell adhesion property of CECs. We then used RELAR medium as a basis for generation of a cell therapy vehicle (CTV) by removing materials that are not favorable for clinical use. We then evaluated the feasibility of injecting CECs in CTV into a rabbit corneal endothelial dysfunction model, and we showed that the corneal endothelium was regenerated without any adverse effects.

## Materials and Methods

### Ethics statement

Human corneas were handled in accordance with the tenets set forth in the Declaration of Helsinki. Informed written consent in regard to eye donation for research was obtained from the next of kin of deceased donors. Donor corneas were obtained from SightLife™ (Seattle, WA). All tissue was recovered under the tenets of the Uniform Anatomical Gift Act (UAGA) of the particular state in which the donor consent was obtained and the tissue was recovered. The rabbit experiments were performed at Doshisha University (Kyoto, Japan) according to the protocol approved by Doshisha University Animal Experiment Committee (Approval No. A15011-2).

## Rabbit CECs Culture

Twenty rabbit eyes were purchased from the Funakoshi Co., Ltd. (Tokyo, Japan). The rabbit CECs (RCECs) were cultivated as described previously [16]. Briefly, Descemet's membrane with RCECs was stripped and incubated in 0.6 U/mL of Dispase II (Roche Applied Science, Penzberg, Germany). The RCECs isolated from the Descemet's membrane were seeded in 1 well of a 6-well plate coated with FNC Coating Mix<sup>®</sup> (Athena Environmental Sciences, Inc., Baltimore, MD). The RCECs were cultured in a growth medium composed of Dulbecco's modified Eagle's medium (Life Technologies Corp., Carlsbad, CA) supplemented with 10% fetal bovine serum (FBS), 50 U/mL penicillin, 50 µg/mL streptomycin, and 2 ng/mL fibroblast growth factor 2 (Life Technologies Corp.). Cultivated RCECs were used at passages 1 through 3 for all experiments.

## Human CEC Cultures

Four human donor corneas (from persons >40 years of age) were used for human CEC (HCEC) cultivation, as described previously [17]. Briefly, Descemet's membranes containing the HCECs were stripped from the corneas and the membranes were incubated with 1 mg/mL collagenase A (Roche Applied Science) at 37°C for 12 hours. The HCECs were then seeded in one well of a 48-well plate coated with laminin E8 fragments (iMatrix-511; Nippi, Incorporated, Tokyo, Japan) (2.0 µg/cm<sup>2</sup>) [17] [17]. The culture medium was prepared according to published protocols. First, basal medium was prepared, consisting of OptiMEM-I (Life Technologies Corp., Carlsbad, CA), 8% FBS, 5 ng/mL epidermal growth factor (Sigma-Aldrich Co., St. Louis, MO), 20 µg/mL ascorbic acid (Sigma-Aldrich Co.), 200 mg/L calcium chloride, 0.08% chondroitin sulfate (Wako Pure Chemical Industries, Ltd., Osaka, Japan), 50 µg/mL gentamicin, and 10 µM SB431542 (Merck Millipore, Billerica, MA). This basal medium was then conditioned by culturing human bone marrow-derived mesenchymal stem cells (BM-MSCs) for 24 hours. Finally, the conditioned basal medium was collected for use as the culture medium for HCECs. Cultivated HCECs were used at passages 3 through 6 for the experiments.

## Evaluation of cell adhesion and survival

HCECs were seeded in the following media supplemented with 8% FBS at a density of  $5.0 \times 10^3$  cells/cm<sup>2</sup> per well on a 96-well plate and cultured for 24 hours: OptiMEM-I, DMEM, RELAR medium (Cell Science & Technology Institute, Inc., Sendai, Japan), BME (Life Technologies Corp.), MEM (Life Technologies Corp.), MEM $\alpha$  (Life Technologies Corp.), M199 (Life Technologies Corp.), and F12/DMEM (Life Technologies Corp.). The effect of a ROCK inhibitor was evaluated by adding 100 µM Y-27632 (Wako Pure Chemical Industries, Ltd.) to the medium. RELAR medium is a modified type of RITC80-7 medium that contains supplemental serum substitutes, hormones and growth factors [18]. The CTV was prepared based on the composition of RITC80-7/RELAR medium by removing bioactive materials, such as hormones and growth factors and other possibly toxic materials. The CTV was generated and provided by Cell Science & Technology Institute, Inc. The composition of CTV is shown in S1 Table. Opeguard-MA Intraocular Irrigation Solution (Senju Pharmaceutical Co., Ltd., Osaka, Japan) and Ringer's solution (Otsuka Pharmaceutical Co., Ltd., Tokyo, Japan) were used to provide a comparison with solutions that are approved for clinical use. The numbers of adhered HCECs on the culture plate were evaluated using the CellTiter-Glo<sup>®</sup> Luminescent Cell Viability Assay and a Veritas<sup>™</sup> Microplate Luminometer (Promega, Fitchburg, Wisconsin). Six samples were prepared for each group.

## Injection of CECs into a corneal endothelial dysfunction model

Twenty-one rabbits were used in this experiment. One eye of each rabbit was used and fellow eye was not used to avoid blindness. The rabbit corneal endothelial dysfunction model was

created as described previously [16]. Briefly, the lens was removed to deepen the anterior chamber and the corneal endothelium was mechanically scraped from the Descemet's membrane with a 20-gauge silicone needle (Soft Tapered Needle; Inami & Co., Ltd., Tokyo, Japan). A total of  $5.0 \times 10^5$  RCECs, suspended in 200  $\mu$ l of Opeguard-MA Intraocular Irrigation Solution, DMEM, or CTV—all supplemented with 100  $\mu$ M Y-27632 (Wako Pure Chemical Industries, Ltd.)—was injected into the anterior chamber of the corneal endothelial dysfunction model and the animals were kept in the face-down position for 3 hours under general anesthesia. As a control, cell-free CTV supplemented with 100  $\mu$ M Y-27632 was injected ( $n = 3$ ). The anterior segments were evaluated by slit-lamp microscopy with a Pentacam<sup>®</sup> (OCULUS Optikgeräte GmbH, Wetzlar, Germany) instrument for 2 weeks. Corneal thickness was determined with an ultrasound pachymeter (SP-2000; Tomey, Nagoya, Japan), and the mean of 10 measured values was calculated (up to a maximum thickness of 1200  $\mu$ m, the instrument's maximum reading). Intraocular pressure was determined with a Tonovet<sup>®</sup> (icare Finland, Vantaa, Finland) instrument. The corneal endothelium was evaluated by contact specular microscopy (Konan scanning slit specular microscope, Konan Medical, Nishinomiya, Japan).

Corneal endothelium regeneration by preserved RCECs was evaluated in the rabbit corneal endothelial dysfunction model ( $n = 3$ ), and anterior segments were evaluated for 2 weeks. The preserved RCECs were prepared after harvesting from a culture plate by treatment with 0.05% Trypsin-EDTA (Life Technologies) for 5 minutes at 37°C. A total of  $5.0 \times 10^5$  RCECs were suspended in 100  $\mu$ l of CTV and preserved for 24 hours at 4°C. A 100  $\mu$ l volume of CTV, supplemented with 200  $\mu$ M of Y-27632, was then added and the preserved RCECs were gently mixed by pipetting to obtain a preparation of  $5.0 \times 10^5$  RCECs suspended in 200  $\mu$ l of CTV including Y-27632 (final concentration; 100  $\mu$ M) for cell injection into the rabbit model. Cell-free CTV supplemented with 100  $\mu$ M of Y-27632 was injected as control ( $n = 3$ ). The ability of HCECs to regenerate corneal endothelium was evaluated by injecting  $1.0 \times 10^6$  HCECs (suspended in 200  $\mu$ l CTV supplemented with 100  $\mu$ M Y-27632) into the rabbit corneal endothelial dysfunction model ( $n = 3$ ), and corneal specimens were evaluated after 48 hours.

## Staining

Rabbit corneal specimens were fixed in 4% formaldehyde and incubated for 30 minutes in 1% bovine serum albumin (BSA) to block nonspecific binding. Samples were incubated overnight at 4°C with antibodies against Na<sup>+</sup>/K<sup>+</sup>-ATPase (1:300, Upstate Biotechnology, Lake Placid, NY), ZO-1 (1:300, Life Technologies Corp., Carlsbad, CA), and N-cadherin (1:300, BD Biosciences, San Jose, CA). Alexa Fluor<sup>®</sup> 488-conjugated goat anti-mouse (Life Technologies) was used as a secondary antibody at a 1:1000 dilution. Cell morphology was evaluated after actin staining with a 1:400 dilution of Alexa Fluor<sup>®</sup> 594-conjugated phalloidin (Life Technologies). Nuclei were stained with DAPI (Dojindo Laboratories, Kumamoto, Japan). The samples were examined with a fluorescence microscope (TCS SP2 AOBS; Leica Microsystems, Wetzlar, Germany).

## Statistical analysis

The statistical significance (*P*-value) for mean values in two-sample comparisons was determined with the Student's *t*-test. The statistical significance of comparisons of multiple sample sets was analyzed with Dunnett's multiple-comparisons test. Results were expressed as mean  $\pm$  SEM.

## Results

### Generation of the CEC injection vehicle

We screened the effect of various cell culture media on HCEC adhesion compared with adhesion in OptiMEM-I, a standard culture medium used for HCEC culture by several researchers,



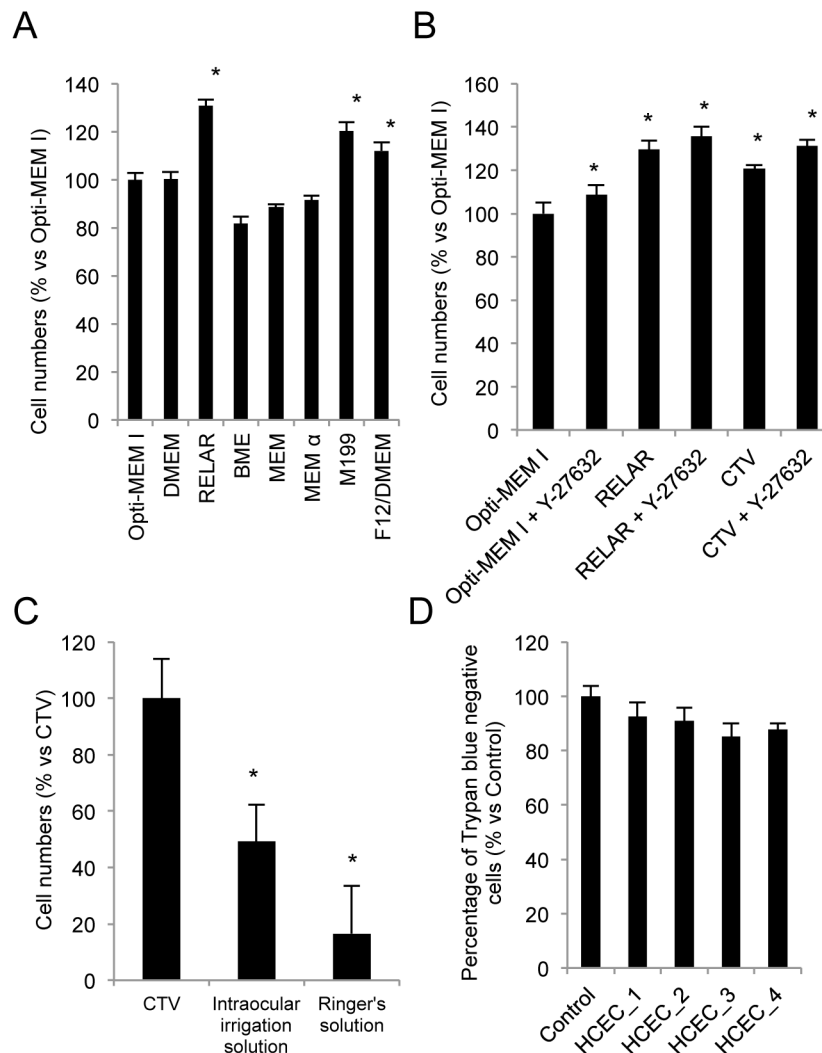


**Fig 1. Generation of a human corneal endothelium cell (HCEC) vehicle for cell therapy.** (A) Effect of various media types on HCEC adhesion to the substrate. HCECs were seeded with media without supplementation with FBS, and then the numbers of adhering cell were evaluated after 24 hours. RELAR, M199, and F12/DMEM media significantly enhanced cell adhesion when compared to OptiMEM-I.  $*p < 0.01$ . (B) The cell therapy vehicle (CTV) was generated based on RELAR medium but with removal of materials such as hormones, growth factors, and other materials with possible toxicity. The numbers of adhered cells increased by 120.7% with CTV when compared to OptiMEM-I, although cell adhesion tended to be lower than with RELAR. However, HCECs seeded with the Y-27632 ROCK inhibitor showed a similar level of cell adhesion in RELAR and CTV (135.6% and 131.1% vs OptiMEM-I without Y-27632, respectively).  $*p < 0.01$ . (C) The numbers of adhered HCECs were significantly lower in liquid Opeguard-MA Intraocular Irrigation Solution (used for intraocular surgery) and Ringer's solution (used for intravenous drip infusion) than with CTV.  $*p < 0.01$ . (D) Cell viability of HCECs was evaluated by Trypan blue staining after preservation in CTV for 24 hours at 4°C. HCECs derived from 4 independent donors and preserved in CTV showed a greater than 85% exclusion of Trypan blue. All experiments were performed in at least triplicate.

doi:10.1371/journal.pone.0158427.g001

including us [17, 19]. HCEC adhesion was significantly enhanced in RELAR, M199, and F12/DMEM media (Fig 1A). RELAR medium was then further examined to test its applicability as a vehicle for cell injection therapy for corneal endothelial dysfunction.

RELAR medium was originally developed for serum-free culture of human renal proximal tubular epithelial cells. It is a modified RITC80-7 medium, additionally supplemented with

some serum substitutes, hormones and growth factors. Hormones and growth factors, and especially mixtures of these, are not favored for clinical use if they are not necessary. Therefore, we removed those materials from the medium to generate the CTV. Cell adhesion was promoted by 120.7% by CTV, while it was promoted by 129.7% in comparison to OptiMEM-I. However, when HCECs were seeded with a ROCK inhibitor, the numbers of adhered cells were almost same in RELAR medium and in CTV (135.6% and 131.1%, respectively) (Fig 1B). The effects of representative liquids allowed for use in humans were also evaluated: Opeguard-MA Intraocular Irrigation Solution that is used for intraocular surgery and Ringer's solution that is used for intravenous drip infusion. The numbers of adhered HCECs were significantly lower in these clinically used liquids than with CTV (Fig 1C).

The ability to preserve HCECs for a certain time is critical for transportation of HCECs from a cell culture facility to the operating room in a clinical setting. Therefore, we assessed cell viability of the HCECs after preservation in CTV for 24 hours at 4°C. All four lots of HCECs from independent donors exhibited viability higher than 85% (Fig 1D).

### RCEC injection using CTV as a vehicle in the rabbit corneal endothelial dysfunction model

We conducted experiments using the rabbit corneal endothelial dysfunction model to evaluate the feasibility of using CTV as a vehicle for CEC transplantation. Control eyes showed hazy corneas due to corneal endothelial dysfunction. Injection of RCECs in Opeguard-MA Intraocular Irrigation Solution as an injection vehicle resulted in a slightly less hazy cornea than the control but a transparent cornea was not regenerated. This suggested that an injection vehicle, rather than an intraocular irrigation solution used in eye surgery, would be required for cell-based therapy. We previously reported [16] that corneal transparency was restored in the endothelial dysfunction model by intracameral injection of RCECs suspended in DMEM supplemented with Y-27632. Similarly, in the present case, intracameral injection of RCECs suspended in CTV supplemented with Y-27632 restored corneal transparency (Fig 2A). The central corneal thickness, which is one of the critical clinical indicators of corneal endothelial health, was restored to an almost normal value in the eyes in which RCECs were transplanted using DMEM or CTV (Fig 2B).

The IOP was also examined to check for possible elevation due to formation of cell aggregates in the eye as a possible complication. The IOP remained in the normal range throughout the 2 weeks of the study in all groups (Fig 2C). Immunofluorescent staining demonstrated that the function-related markers  $\text{Na}^+/\text{K}^+$ -ATPase (pump function), ZO-1 (tight junction), and N-cadherin (adherent junction) were expressed along the cell cortex in all regenerated CECs in eyes in both the DMEM and CTV groups. Actin staining revealed that the regenerated corneal endothelium was a sheet-like structure of hexagonal cells. The control eyes had a few fibroblastic transformed cells with no expression of the function-related markers and the intraocular irrigation solution group had a lower density of cells with only partial expression of the function-related markers (Fig 2D). The cell density of the regenerated corneal endothelium was similar in the eyes injected with RCECs in DMEM or in CTV (Fig 2E).

### Feasibility of RCEC preservation using CTV

We evaluated whether RCECs preserved for 24 hours would still be useful for transplantation. The RCECs were harvested from the culture plate and suspended in CTV for 24 hours at 4°C. Y-27632 was then added to the RCECs and they were injected into the anterior chamber of the rabbit corneal endothelial dysfunction model (Fig 3A). Slitlamp microscopy showed that the eyes transplanted with preserved RCECs developed transparent corneas, while control eyes

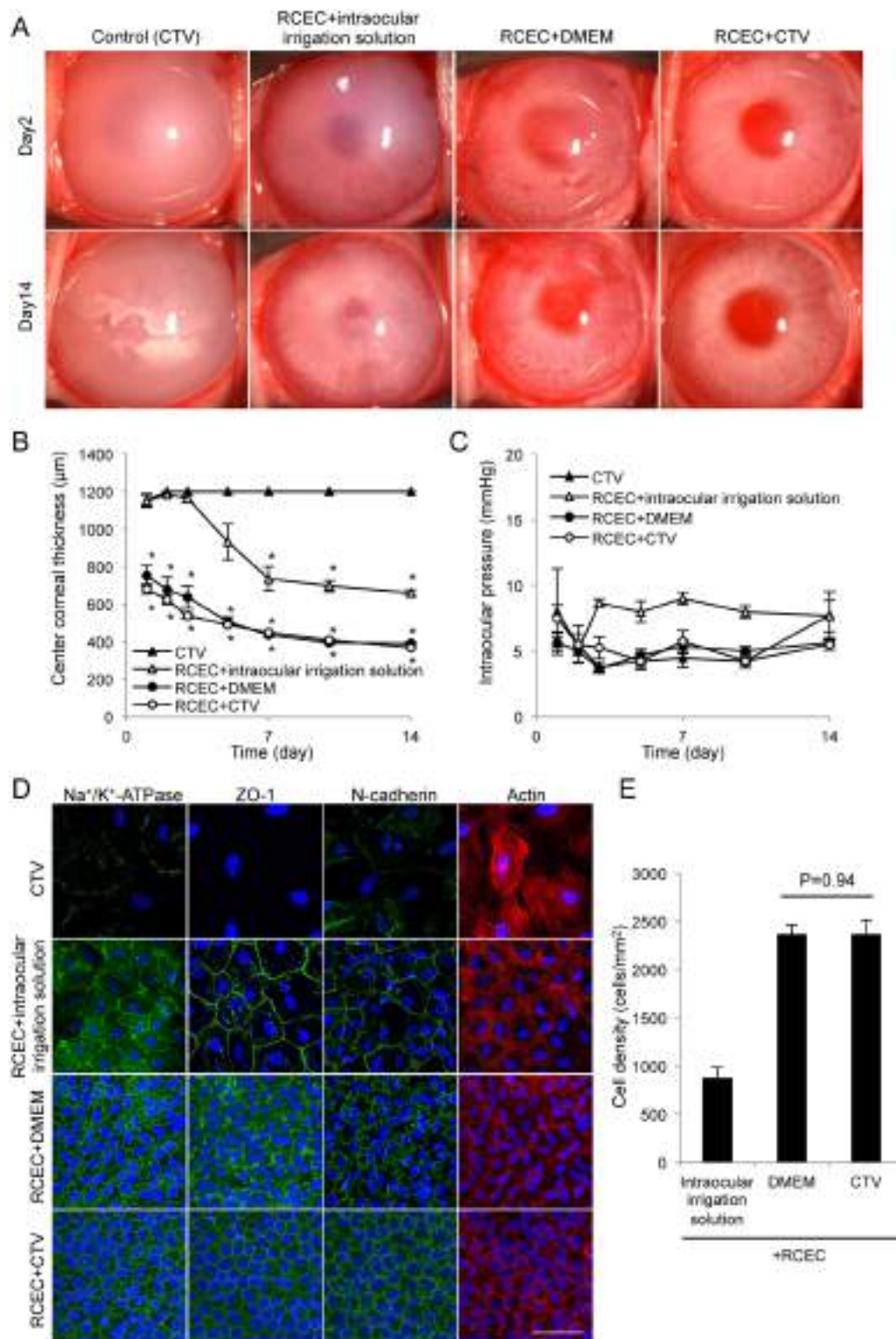


**Fig 2. Rabbit corneal endothelium cell (RCEC) injection with cell therapy vehicle (CTV) enables regeneration of corneal endothelium.** (A) A total of  $5.0 \times 10^5$  RCECs, suspended in 200  $\mu\text{l}$  of intraocular irrigation solution, DMEM, or CTV supplemented with 100  $\mu\text{M}$  Y-27632 was injected into the anterior chamber of the rabbit corneal endothelial dysfunction model ( $n = 3$ ). CTV (200  $\mu\text{l}$ ) supplemented with 100  $\mu\text{M}$  Y-27632 was injected into the anterior chamber of the rabbit corneal endothelial dysfunction model as a control ( $n = 3$ ).

Corneal transparency was restored by intracameral injection of RCECs suspended in either DMEM or CTV, while control eyes exhibited hazy corneas due to corneal endothelial dysfunction. (B) Central corneal thickness was evaluated with an ultrasound pachymeter and was restored to almost a normal value in the eyes transplanted with RCECs in DMEM or CTV. Eyes injected with RCECs in intraocular irrigation solution showed a thicker central corneal thickness when compared to eyes injected with RCECs in DMEM or CTV. (C) Intraocular pressure (IOP) elevation due to formation of cell aggregates in the eye is a possible complication and was evaluated with a Tonovet<sup>®</sup>. The IOP remained in the normal range throughout the 2 weeks of the study in all groups. (D) Regenerated corneal endothelium was evaluated by immunofluorescent staining 2 weeks after cell transplantation. The function-related markers Na<sup>+</sup>/K<sup>+</sup>-ATPase (pump function), ZO-1 (tight junction), and N-cadherin (adherent junction) were expressed in all regenerated CECs in eyes from both the DMEM and CTV groups. Actin staining showed hexagonal regenerated corneal endothelial cells. By contrast, control eyes had few fibroblastic transformed cells and lacked expression of the function-related markers. Scale bar: 50  $\mu$ m. (E) Cell density of regenerated corneal endothelium formed by injecting RCECs was the same for cells suspended in DMEM and CTV, while cells suspended in intraocular irrigation solution showed lower cell density (Fig 2E).

doi:10.1371/journal.pone.0158427.g002

injected with vehicle exhibited hazy corneas (Fig 3B). Scheimpflug images obtained with a Pentacam<sup>™</sup> instrument showed the successful regeneration of an anatomically normal cornea similar to a healthy cornea by RCEC injection, whereas the control eyes showed corneal edema due to corneal endothelial dysfunction (Fig 3C). A color map of corneal thickness demonstrated that preserved RCECs regenerated normal corneal thickness from the center to the periphery of the cornea, while the control eyes showed thick corneas (Fig 3D). The corneal volume was normal level after injection of preserved RCECs (Fig 3E). The central corneal thickness, evaluated with an ultrasound pachymeter, was normal after 1–2 weeks in the eyes injected with preserved RCECs (Fig 3F). A representative image of regenerated corneal endothelium examined by contact specular microscopy showed a hexagonal monolayer sheet structure, but no image was obtained in the control eyes (Fig 3G).

## Histological assessment of the corneal endothelium regenerated by RCECs and HCECs after preservation

Immunofluorescent staining demonstrated that the function-related markers Na<sup>+</sup>/K<sup>+</sup>-ATPase, ZO-1, and N-cadherin were expressed in all regenerated CECs in eyes injected with preserved RCECs. The distribution of actin in the cell cortex was similar to that in healthy cells in the eyes injected with RCECs. On the other hand, control eyes, which showed fibroblastic morphology, showed no expression of function-related markers (Fig 4A).

We also investigated the feasibility of using HCECs after preservation in CTV. HCECs preserved for 24 hours in CTV were injected into the rabbit corneal endothelial dysfunction model. Immunofluorescent staining showed that the HCECs regenerated corneal endothelium that expressed function-related markers and showed a normal morphology (Fig 4B).

## Discussion

We recently obtained approval from the Japanese Ministry of Health, Labour, and Welfare to treat corneal endothelial dysfunction with cell-based therapy and started the first-in-human clinical trial in 2014 at Kyoto Prefectural University of Medicine (Clinical trial registration: UMIN000012534). This clinical trial uses cultured HCECs suspended in a vehicle consisting of modified OptiMEM-I supplemented with ROCK inhibitor, which are injected into the anterior chamber of the patients following removal of the diseased corneal endothelium. We are currently focusing our efforts on optimizing the original protocol of the principal investigator-initiated clinical trial to begin a sponsor-initiated clinical trial [20].

The use of intraocular irrigation solutions is allowed by regulatory authorities in intra ocular surgeries such as cataract surgery and vitreo-retinal surgery and are widely utilized. These



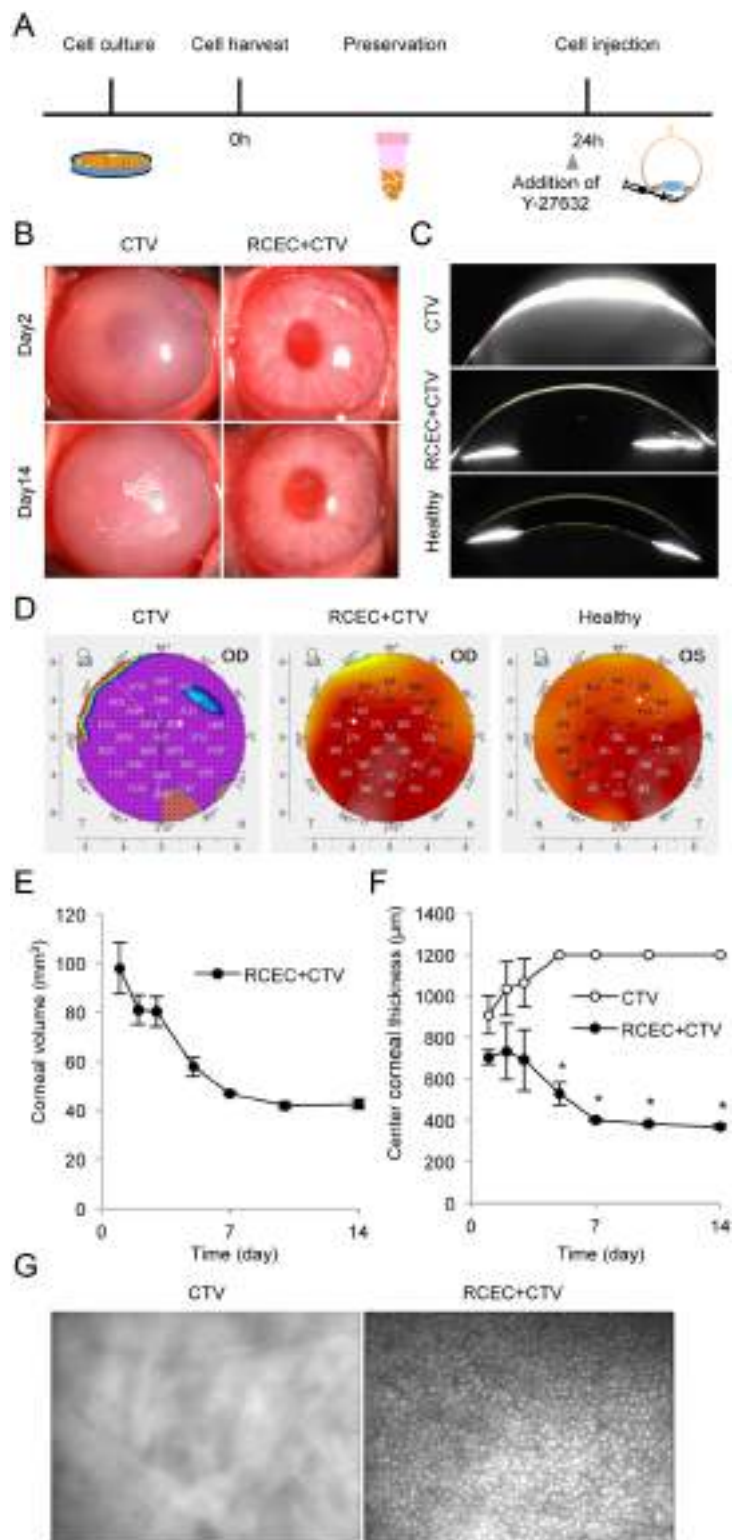


**Fig 3. Rabbit corneal endothelium cells (RCECs) preserved in CTV regenerate corneal endothelium.** (A) Schematic image showing the protocol for assessment of the feasibility of cell preservation in CTV. RCECs were harvested from the culture plate and suspended in CTV for 24 hours at 4°C, the ROCK inhibitor, Y-27632, was added to the RCECs before injection, and RCECs were injected into the anterior chamber of the rabbit corneal endothelial dysfunction model (n = 3). As a control, CTV supplemented with Y-27632 was

injected into the rabbit corneal endothelial dysfunction model ( $n = 3$ ). (B) Slitlamp microscopy showed that a transparent cornea was formed by the preserved RCECs, while the control eyes injected with vehicle alone exhibited hazy corneas. (C) Scheimpflug images showed the restoration of an anatomically normal cornea similar to a healthy cornea following injection of preserved RCECs. Control eyes injected with vehicle only exhibited corneal edema due to corneal endothelial dysfunction. (D) Corneal thickness was evaluated with a Pentacam<sup>®</sup>. The color map showing corneal thickness demonstrated that eyes injected with preserved RCECs exhibited normal thicknesses throughout the center to the periphery, whereas control eyes exhibited thick corneas after 2 weeks. (E) Corneal volumes evaluated with a Pentacam<sup>®</sup> showed normal levels after RCEC injection. (F) Central corneal thickness evaluated with an ultrasound pachymeter showed that eyes injected with preserved RCECs had corneas of normal thickness. (G) Regenerated corneal endothelium was examined *in vivo* by contact specular microscopy. A hexagonal monolayer sheet structure was observed in the eyes injected with preserved RCECs, whereas no similar structure was observed in the control eyes.

doi:10.1371/journal.pone.0158427.g003

intraocular irrigation solutions, which are combinations of buffers and antioxidants, were developed to mimic the composition of the aqueous and vitreous humor to maintain the integrity of the intraocular tissues. The physiological assessment of these solutions was focused on providing safety to the corneal endothelium, as damage to the corneal endothelium causes

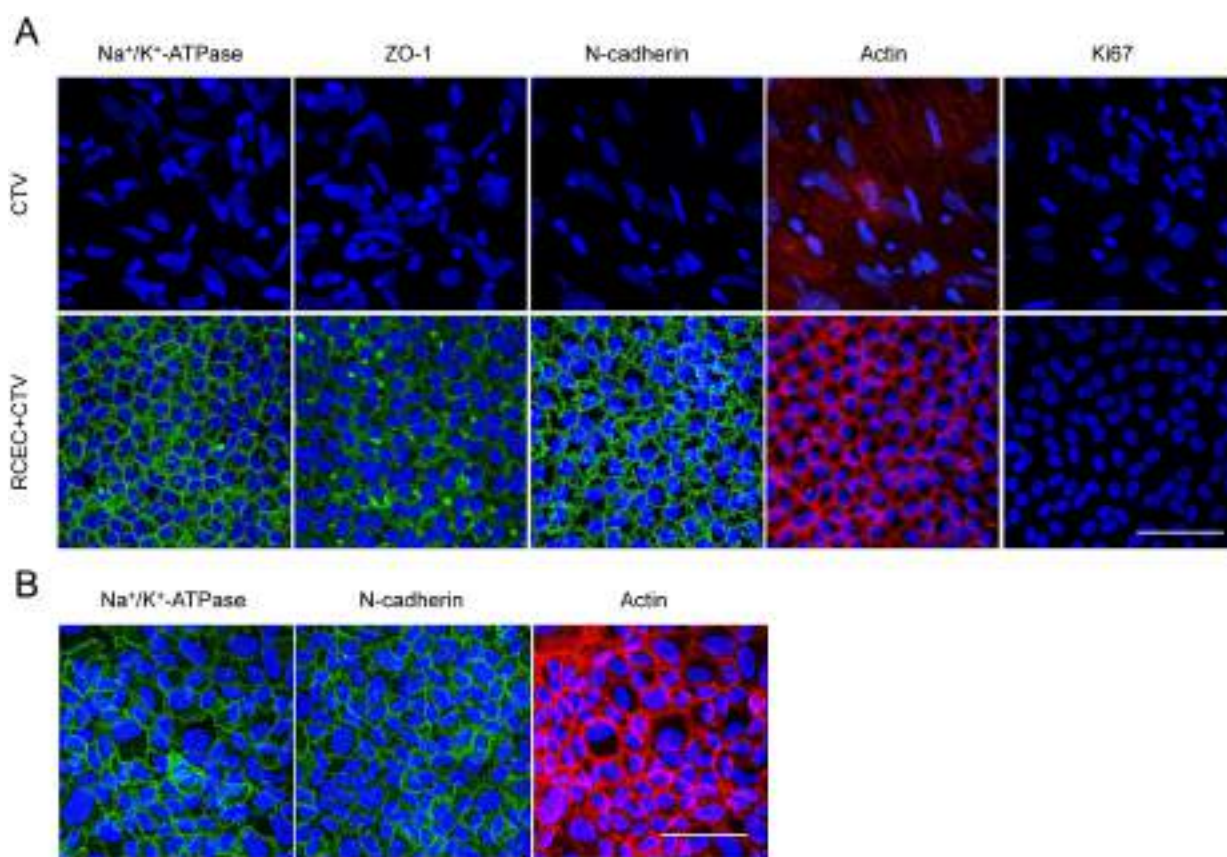


**Fig 4. Histological assessment of corneal endothelium regenerated by injection of RCECs and HCECs after preservation in CTV.** (A) Regenerated corneal endothelium was evaluated by immunofluorescent staining 2 weeks after cell transplantation. The function-related markers Na<sup>+</sup>/K<sup>+</sup>-ATPase, ZO-1, and N-cadherin were expressed in the corneal endothelium of the eyes injected with RCECs after 24 hours of preservation. Actin similar to that seen in healthy cells was observed along the cell cortex in the eyes injected with RCECs. Fibroblastic cells without function-related markers were observed. Scale bar: 50  $\mu$ m. (B) Feasibility of using HCECs after preservation in CTV was evaluated by injecting HCECs preserved for 24 hours in CTV into the rabbit corneal endothelial dysfunction model ( $n = 3$ ). Immunofluorescence staining showed that corneal endothelium was regenerated by the injected HCECs and expressed Na<sup>+</sup>/K<sup>+</sup>-ATPase and N-cadherin. Actin staining showed that the regenerated corneal endothelium in the rabbit eyes had a normal morphology consisting of a monolayer of hexagonal cells. Scale bar: 500  $\mu$ m.

doi:10.1371/journal.pone.0158427.g004

irreversible corneal haziness [21–23]. Intraocular irrigation solutions are assumed to be safe for cell-based therapy, but our current findings indicate that they hamper CEC adhesion onto substrates.

This finding suggests that an intraocular irrigation solution itself is unsuitable for use as a vehicle for cell-based therapy and that an optimized vehicle is important for the regeneration of the corneal endothelium. Our approach to generate a new vehicle was as follows: 1) screen the effects of various culture media on CEC adhesion, 2) generate a new vehicle by removing materials that are not favorable for clinical use, and 3) evaluate the feasibility of the vehicle in an animal disease model.

HCECs have limited proliferative ability and undergo transformation into a fibroblastic phenotype. Researchers have long recognized the difficulty of HCEC culture and have devoted their efforts to culture HCECs that can be used for research purposes and in regenerative medicine [17, 24–30]. Several culture media, such as F12, M199, SHEM, DMEM, and OptiMEM-I, were proposed as HCEC culture media when supplemented with materials such as serum and various growth factors [13, 24, 25, 27]. However, Zhu and colleagues, in a screening study of several culture media, demonstrated that OptiMEM-I promoted attachment and a moderate proliferative response [26]. We demonstrated the successful expansion of HCECs and suppression of fibroblastic transformation in an OptiMEM-I based culture medium [17, 19, 31]. A further screening of media modified from Eagle's minimum essential media (EMEM), like OptiMEM-I, showed that RELAR medium promoted the best HCEC adhesion among the media tested. However, media modified from EMEM, such as OptiMEM-I and RELAR, include hormones and growth factors, whereas EMEM contains amino acids, salts, glucose, and vitamins [32]. We generated CTV by removing hormones, growth factors, and potentially toxic materials to minimize the possible risk for the patients, although the amount of hormones and growth factors is probably sufficiently low to avoid causing adverse events such as carcinogenicity and other systemic disorders.

In the clinical setting, CECs will be cultured and harvested in a Good Manufacturing Practice (GMP) grade cell processing center (CPC), and will be transported to each facility. Thus, cell stability must be maintained for a certain time to enable transportation from the CPC to hospital. In this study, HCECs retained more than 85% viability after 24 hours of preservation in CTV, and the preserved RCECs and HCECs restored the corneal endothelium in the rabbit model of corneal dysfunction, confirming the efficacy of CEC preservation in CTV. However, possible adverse effects caused by dead cells generated during preservation should be carefully assessed.

Land et al. showed that human recombinant superoxide dismutase reduced the rejection episodes after renal allografts in a randomized double-blind trial [33]. They hypothesized that antioxidants suppressed the ischemia/reperfusion injury of the graft and then reduced the immunogenicity of the graft [33]. This phenomenon is currently explained by the concept of damage-associated molecular patterns (DAMPs) that trigger inflammatory responses against danger stimuli [34, 35]. The release of DAMPs by tissue stress or injury was confirmed to play an important role in the pathophysiology of a wide range of diseases [36–40]. In the current study, no adverse events, such as severe inflammation or rejection, were observed in rabbit model, but the possibility of an inflammatory response caused by CECs damaged during preservation should be further investigated.

In conclusion, we generated a CTV composed of amino acids, salts, glucose, and vitamins but without hormones, growth factors, and or potentially toxic materials for use for the treatment of corneal endothelial dysfunction using cell-based therapy. We also showed that CTV enabled the preservation of CECs for subsequent injection and that the preserved CECs restored a transparent cornea in rabbit model of corneal dysfunction. The current strategy for

generation of a vehicle from a culture medium by removing materials that are unfavorable for clinical use is fast and practical and can be applied to cell-based therapy in other fields.

## Supporting Information

**S1 File. Participant-level data.** This supporting information file provides participant-level data.  
(XLSX)

**S1 Table. Composition table of cell therapy vehicle (CTV).** This supporting table provides composition of CTV.  
(PDF)

## Author Contributions

Conceived and designed the experiments: NO TI NK. Performed the experiments: NO KK RI DM TS MN. Analyzed the data: NO KK RI DM TS MN NK. Contributed reagents/materials/analysis tools: YK TI NK. Wrote the paper: NO.

## References

- Joyce NC. Proliferative capacity of the corneal endothelium. *Prog Retin Eye Res* 2003; 22: 359–389. PMID: [12852491](#)
- Joyce NC. Cell cycle status in human corneal endothelium. *Exp Eye Res* 2005; 81: 629–638. PMID: [16054624](#)
- Joyce NC. Proliferative capacity of corneal endothelial cells. *Exp Eye Res* 2012; 95: 16–23. doi: [10.1016/j.exer.2011.08.014](#) PMID: [21906590](#)
- Bourne WM, Nelson LR, Hodge DO. Central corneal endothelial cell changes over a ten-year period. *Invest Ophthalmol Vis Sci* 1997; 38: 779–782. PMID: [9071233](#)
- Eye Bank Association of America. Eye Banking Statistical Report. Washington, DC 2013.
- Tan DT, Dart JK, Holland EJ, Kinoshita S. Corneal transplantation. *Lancet* 2012; 379: 1749–1761. doi: [10.1016/S0140-6736\(12\)60437-1](#) PMID: [22559901](#)
- Sumide T, Nishida K, Yamato M, Ide T, Hayashida Y, Watanabe K, et al. Functional human corneal endothelial cell sheets harvested from temperature-responsive culture surfaces. *FASEB J* 2006; 20: 392–394. PMID: [16339916](#)
- Patel SV. Graft survival and endothelial outcomes in the new era of endothelial keratoplasty. *Exp Eye Res* 2012; 95: 40–47. doi: [10.1016/j.exer.2011.05.013](#) PMID: [21689649](#)
- Price MO, Price FW Jr. Descemet's membrane endothelial keratoplasty surgery: update on the evidence and hurdles to acceptance. *Curr Opin Ophthalmol* 2013; 24: 329–335. doi: [10.1097/ICU.0b013e32836229ab](#) PMID: [23680758](#)
- Veldman PB, Terry MA, Straiko MD. Evolving indications for Descemet's stripping automated endothelial keratoplasty. *Curr Opin Ophthalmol* 2014; 25: 306–311. doi: [10.1097/ICU.0000000000000073](#) PMID: [24871355](#)
- Kruse FE, Schrehardt US, Tourtas T. Optimizing outcomes with Descemet's membrane endothelial keratoplasty. *Curr Opin Ophthalmol* 2014; 25: 325–334. doi: [10.1097/ICU.0000000000000072](#) PMID: [24871356](#)
- Mimura T, Yamagami S, Yokoo S, Usui T, Tanaka K, Hattori S, et al. Cultured human corneal endothelial cell transplantation with a collagen sheet in a rabbit model. *Invest Ophthalmol Vis Sci* 2004; 45: 2992–2997. PMID: [15326112](#)
- Ishino Y, Sano Y, Nakamura T, Cannon CJ, Rigby H, Fullwood NJ, et al. Amniotic membrane as a carrier for cultivated human corneal endothelial cell transplantation. *Invest Ophthalmol Vis Sci* 2004; 45: 800–806. PMID: [14985293](#)
- Koizumi N, Sakamoto Y, Okumura N, Okahara N, Tsuchiya H, Torii R, et al. Cultivated corneal endothelial cell sheet transplantation in a primate model. *Invest Ophthalmol Vis Sci* 2007; 48: 4519–4526. PMID: [17898273](#)



15. Okumura N, Ueno M, Koizumi N, Sakamoto Y, Hirata K, Hamuro J, et al. Enhancement on primate corneal endothelial cell survival in vitro by a ROCK inhibitor. *Invest Ophthalmol Vis Sci* 2009; 50: 3680–3687. doi: [10.1167/iops.08-2634](https://doi.org/10.1167/iops.08-2634) PMID: [19387080](https://pubmed.ncbi.nlm.nih.gov/19387080/)
16. Okumura N, Koizumi N, Ueno M, Sakamoto Y, Takahashi H, Tsuchiya H, et al. ROCK inhibitor converts corneal endothelial cells into a phenotype capable of regenerating in vivo endothelial tissue. *Am J Pathol* 2012; 181: 268–277. doi: [10.1016/j.ajpath.2012.03.033](https://doi.org/10.1016/j.ajpath.2012.03.033) PMID: [22704232](https://pubmed.ncbi.nlm.nih.gov/22704232/)
17. Okumura N, Kakutani K, Numata R, Nakahara M, Schlotzer-Schrehardt U, Kruse F, et al. Laminin-511 and -521 enable efficient in vitro expansion of human corneal endothelial cells. *Invest Ophthalmol Vis Sci* 2015; 56: 2933–2942. doi: [10.1167/iops.14-15163](https://doi.org/10.1167/iops.14-15163) PMID: [26024079](https://pubmed.ncbi.nlm.nih.gov/26024079/)
18. Yamane I, Kan M, Hoshi H, Minamoto Y. Primary culture of human diploid cells and its long-term transfer in a serum-free medium. *Exp Cell Res* 1981; 134: 470–474. PMID: [7274342](https://pubmed.ncbi.nlm.nih.gov/7274342/)
19. Okumura N, Kay EP, Nakahara M, Hamuro J, Kinoshita S, Koizumi N. Inhibition of TGF-beta Signaling Enables Human Corneal Endothelial Cell Expansion In Vitro for Use in Regenerative Medicine. *PLoS One* 2013; 8: e58000. doi: [10.1371/journal.pone.0058000](https://doi.org/10.1371/journal.pone.0058000) PMID: [23451286](https://pubmed.ncbi.nlm.nih.gov/23451286/)
20. Okumura N, Kinoshita S, Koizumi N. Cell-based approach for treatment of corneal endothelial dysfunction. *Cornea* 2014; 33 Suppl 11: S37–41. doi: [10.1097/ICO.0000000000000229](https://doi.org/10.1097/ICO.0000000000000229) PMID: [25188790](https://pubmed.ncbi.nlm.nih.gov/25188790/)
21. Glasser DB, Matsuda M, Ellis JG, Edelhauser HF. Effects of intraocular irrigating solutions on the corneal endothelium after in vivo anterior chamber irrigation. *Am J Ophthalmol* 1985; 99: 321–328. PMID: [3976807](https://pubmed.ncbi.nlm.nih.gov/3976807/)
22. Araie M, Shirasawa E, Hikita M. Effect of oxidized glutathione on the barrier function of the corneal endothelium. *Invest Ophthalmol Vis Sci* 1988; 29: 1884–1887. PMID: [3192379](https://pubmed.ncbi.nlm.nih.gov/3192379/)
23. Araie M, Shirasawa E, Ohashi T. Intraocular irrigating solutions and permeability of the blood-aqueous barrier. *Arch Ophthalmol* 1990; 108: 882–885. PMID: [2350292](https://pubmed.ncbi.nlm.nih.gov/2350292/)
24. Engelmann K, Friedl P. Optimization of culture conditions for human corneal endothelial cells. *In Vitro Cell Dev Biol* 1989; 25: 1065–1072. PMID: [2592302](https://pubmed.ncbi.nlm.nih.gov/2592302/)
25. Engelmann K, Friedl P. Growth of human corneal endothelial cells in a serum-reduced medium. *Cornea* 1995; 14: 62–70. PMID: [7712739](https://pubmed.ncbi.nlm.nih.gov/7712739/)
26. Zhu C, Joyce NC. Proliferative response of corneal endothelial cells from young and older donors. *Invest Ophthalmol Vis Sci* 2004; 45: 1743–1751. PMID: [15161835](https://pubmed.ncbi.nlm.nih.gov/15161835/)
27. Li W, Sabater AL, Chen YT, Hayashida Y, Chen SY, He H, et al. A novel method of isolation, preservation, and expansion of human corneal endothelial cells. *Invest Ophthalmol Vis Sci* 2007; 48: 614–620. PMID: [17251457](https://pubmed.ncbi.nlm.nih.gov/17251457/)
28. Peh GS, Toh KP, Wu FY, Tan DT, Mehta JS. Cultivation of human corneal endothelial cells isolated from paired donor corneas. *PLoS One* 2011; 6: e28310. doi: [10.1371/journal.pone.0028310](https://doi.org/10.1371/journal.pone.0028310) PMID: [22194824](https://pubmed.ncbi.nlm.nih.gov/22194824/)
29. Shima N, Kimoto M, Yamaguchi M, Yamagami S. Increased proliferation and replicative lifespan of isolated human corneal endothelial cells with L-ascorbic acid 2-phosphate. *Invest Ophthalmol Vis Sci* 2011; 52: 8711–8717. doi: [10.1167/iops.11-7592](https://doi.org/10.1167/iops.11-7592) PMID: [21980003](https://pubmed.ncbi.nlm.nih.gov/21980003/)
30. Peh GS, Beuerman RW, Colman A, Tan DT, Mehta JS. Human corneal endothelial cell expansion for corneal endothelium transplantation: an overview. *Transplantation* 2011; 91: 811–819. doi: [10.1097/TP.0b013e3182111f01](https://doi.org/10.1097/TP.0b013e3182111f01) PMID: [21358368](https://pubmed.ncbi.nlm.nih.gov/21358368/)
31. Nakahara M, Okumura N, Kay EP, Hagiya M, Imagawa K, Hosoda Y, et al. Corneal endothelial expansion promoted by human bone marrow mesenchymal stem cell-derived conditioned medium. *PLoS One* 2013; 8: e69009. doi: [10.1371/journal.pone.0069009](https://doi.org/10.1371/journal.pone.0069009) PMID: [23894393](https://pubmed.ncbi.nlm.nih.gov/23894393/)
32. Eagle H. Amino acid metabolism in mammalian cell cultures. *Science* 1959; 130: 432–437. PMID: [13675766](https://pubmed.ncbi.nlm.nih.gov/13675766/)
33. Land W, Schneeberger H, Schleibner S, Illner WD, Abendroth D, Rutili G, et al. The beneficial effect of human recombinant superoxide dismutase on acute and chronic rejection events in recipients of cadaveric renal transplants. *Transplantation* 1994; 57: 211–217. PMID: [8310510](https://pubmed.ncbi.nlm.nih.gov/8310510/)
34. Seong SY, Matzinger P. Hydrophobicity: an ancient damage-associated molecular pattern that initiates innate immune responses. *Nat Rev Immunol* 2004; 4: 469–478. PMID: [15173835](https://pubmed.ncbi.nlm.nih.gov/15173835/)
35. Schaefer L. Complexity of danger: the diverse nature of damage-associated molecular patterns. *J Biol Chem* 2014; 289: 35237–35245. doi: [10.1074/jbc.R114.619304](https://doi.org/10.1074/jbc.R114.619304) PMID: [25391648](https://pubmed.ncbi.nlm.nih.gov/25391648/)
36. Piccinini AM, Midwood KS. DAMPening inflammation by modulating TLR signalling. *Mediators Inflamm* 2010; 2010.
37. Rosin DL, Okusa MD. Dangers within: DAMP responses to damage and cell death in kidney disease. *J Am Soc Nephrol* 2011; 22: 416–425. doi: [10.1681/ASN.2010040430](https://doi.org/10.1681/ASN.2010040430) PMID: [21335516](https://pubmed.ncbi.nlm.nih.gov/21335516/)

38. Kang R, Lotze MT, Zeh HJ, Billiar TR, Tang D. Cell death and DAMPs in acute pancreatitis. *Mol Med* 2014; 20: 466–477. doi: [10.2119/molmed.2014.00117](https://doi.org/10.2119/molmed.2014.00117) PMID: [25105302](https://pubmed.ncbi.nlm.nih.gov/25105302/)
39. Broggi A, Granucci F. Microbe- and danger-induced inflammation. *Mol Immunol* 2015; 63: 127–133. doi: [10.1016/j.molimm.2014.06.037](https://doi.org/10.1016/j.molimm.2014.06.037) PMID: [25037632](https://pubmed.ncbi.nlm.nih.gov/25037632/)
40. Turner NA. Inflammatory and fibrotic responses of cardiac fibroblasts to myocardial damage associated molecular patterns (DAMPs). *J Mol Cell Cardiol* 2015.

# In Vivo Measurement of Vertebral Endplate Surface Area Along the Whole-Spine

Maho Kishimoto,<sup>1</sup> Koji Akeda,<sup>2</sup> Akihiro Sudo,<sup>2</sup> Alejandro A. Espinoza Orías,<sup>3</sup> Nozomu Inoue<sup>3</sup>

<sup>1</sup>Faculty of Medical and Life Sciences, Doshisha University, Kyoto, Japan, <sup>2</sup>Department of Orthopaedic Surgery, Mie University Graduate School of Medicine, Tsu City, Japan, <sup>3</sup>Department of Orthopedic Surgery, Rush University Medical Center, Chicago, Illinois

Received 15 December 2015; accepted 22 June 2016

Published online 7 July 2016 in Wiley Online Library (wileyonlinelibrary.com). DOI 10.1002/jor.23354

**ABSTRACT:** Accurate determination of vertebral endplate surface area and diameters plays an important role in surgical procedures, spinal implant design and sizing. The objective of this study was to contribute with baseline information on the endplate geometrical parameters using subject-based 3D whole-spine computed tomography (CT) models based on myelogram CT images taken of 49 patients with spinal disorders. Superior and inferior bony endplate mesh-models were created from said 3D CT models and endplate geometrical parameters including total polygon-mesh areas, projected areas and antero posterior and transverse diameters of each endplate were measured. The position of each endplate was determined by the cumulative distance along the spinal column with respect to C2. Endplate area and diameters were analyzed by gender, spinal level, age and correlation with spinal position. Males had larger endplates than females at all levels ( $p < 0.05$ ) but S1. While endplate areas and transverse diameters increased with age at C3–L5 in females, these increases were not consistent through the whole-spine and even decreases with age were found at T1–T3 in males. There was a strong linear correlation between endplate area and spinal position in males and females with correlation coefficient values of  $r = 0.938$  and  $r = 0.911$ , respectively. However, multiple comparisons of the geometrical parameters through the whole-spine revealed localized reduction of the anteroposterior or transverse diameters at T4 and L5–S1 levels. These regional and age-related changes in endplate dimensions should be taken into account for safe interventional treatments at these sites. © 2016 Orthopaedic Research Society. Published by Wiley Periodicals, Inc. J Orthop Res 34:1418–1430, 2016.

**Keywords:** endplate; surface area; endplate dimension, spine; computed tomography; three-dimensional measurement

Accurate knowledge of vertebral endplate morphology is important to better understand its structure-function relationships,<sup>1–4</sup> with respect to its influence and role in intervertebral disc degeneration, and to design proper surgical procedures, tissue-engineered disc replacement constructs and spinal implants.<sup>5,6</sup> Measurement of the endplate surface area provides essential information to be used for estimation of stress and pressure in intervertebral discs, estimation of disc volume and adequate sizing of spinal implants. To date, these endplate morphological parameters have been gathered mainly by means of planar methods.<sup>6–13</sup> Since the endplate actually has complex three-dimensional (3D) geometry, questions arise about whether appropriate 3D endplate surface models are necessary for accurate measurements of any morphological parameter, including the surface area. Information on the endplate surface area spanning the entire human spine is limited in the literature. To the best of the authors' knowledge, currently there is no in vivo study providing results of 3D-based endplate surface area measurements.

Continuous increases in endplate dimensions along the spine have been reported in the literature.<sup>6,7,14,15</sup> We hypothesize that the endplate area increases as a function of distal distance from C2 downwards, by increasing the size within the same vertebral body and/or between the endplates consisting of an intervertebral disc. The objective of this study was to contribute with

baseline information on endplate area of the whole-spine in both males and females using subject-based 3D whole-spine computed tomography (CT) models.

## METHODS

### Subjects

This IRB-approved study was conducted on 49 patients (male 25, female 24; range 22–88 years, average age 61.8 years old, Table 1). The patients were suspected to have spinal stenosis and/or spinal cord disorders and confirmatory whole-spine CT myelographic measurements were ordered by the attending surgeon. The mean heights of the male and female patients were  $165.1 \pm 8.9$  cm (mean  $\pm$  SD) and  $150.6 \pm 7.2$  cm, respectively. The mean weights of the male and female patients were  $61.6 \pm 12.7$  kg and  $56.7 \pm 23.7$  kg, respectively. The patients received whole-spine myelography CT imaging (tube voltage: 120 kV, tube current:  $84.6 \pm 11.8$  mAs, pixel size:  $0.39 \pm 0.07$  mm, field of view:  $197.4 \pm 33.3$  mm, matrix:  $512 \times 512$ , slice increment: 1.0 mm, slice thickness: 1.0 mm), and were diagnosed as: Lumbar spinal canal stenosis ( $n = 27$ ), lumbar disc herniation ( $n = 14$ ), cervical spondylosis ( $n = 3$ ), cervical spondylotic radiculopathy ( $n = 2$ ), cervical spondylotic myelopathy ( $n = 1$ ), low back pain ( $n = 1$ ), and lumbar disc disease ( $n = 1$ ).

### Creation of 3D Endplate Surface Models

CT images were reconstructed using a commercial 3D reconstruction software package (Mimics 16.0; Materialise Inc., Leuven, Belgium). Segmentation of each vertebra was performed using a threshold level of 226 Hounsfield Units and 3D whole-spine polygon-mesh models from C1 to S1 were created based on this data. The surface of the 3D polygon model was smoothed by using the "Wrap function" in the software package with the smallest detail level of 1.0 mm. Both superior and inferior endplates (relative to each vertebral body) were further segmented from each

Grant sponsor: NIH/NCCIH; Grant number: R01 AT006692.

Correspondence to: Nozomu Inoue (T: +1-312-942-8151; F: +1-312-942-2040; E-mail: nozomu\_inoue@rush.edu)

© 2016 Orthopaedic Research Society. Published by Wiley Periodicals, Inc.

**Table 1.** Study Population Categorized by Gender and Age

Age	Male ( <i>n</i> = 25)	Female ( <i>n</i> = 24)
20s	2	0
30s	1	2
40s	4	1
50s	4	4
60s	8	7
70s	5	6
80s	1	4

vertebral 3D model allowing for the creation of individual superior and inferior endplate polygon-mesh models. Whenever manifest cases of osteophytes were present, they were not included in the endplate model. A total of 2,352 endplate models were created from 1,176 vertebral bodies of C2 through S1 (Fig. 1).

#### Endplate Surface Area Measurements

For each endplate surface model, the mean normal vector was calculated by averaging the normal vectors of its

individual mesh elements (Fig. 2). The angle between the mean normal vector and the normal vector of an individual polygon mesh element was calculated by means of the dot product and the polygon elements with a normal vector oriented less than  $90^\circ$  were included for area measurements. The following two methods were implemented to enable automatic endplate surface-area calculations using a custom-written routine in Microsoft Visual C++ under Microsoft Foundation Class (MFC) programming environment.

#### Polygon Surface Area Measurement

The surface area of the endplate model was calculated by summation of individual polygon area through the entire surface of the endplate model.<sup>7,16</sup>

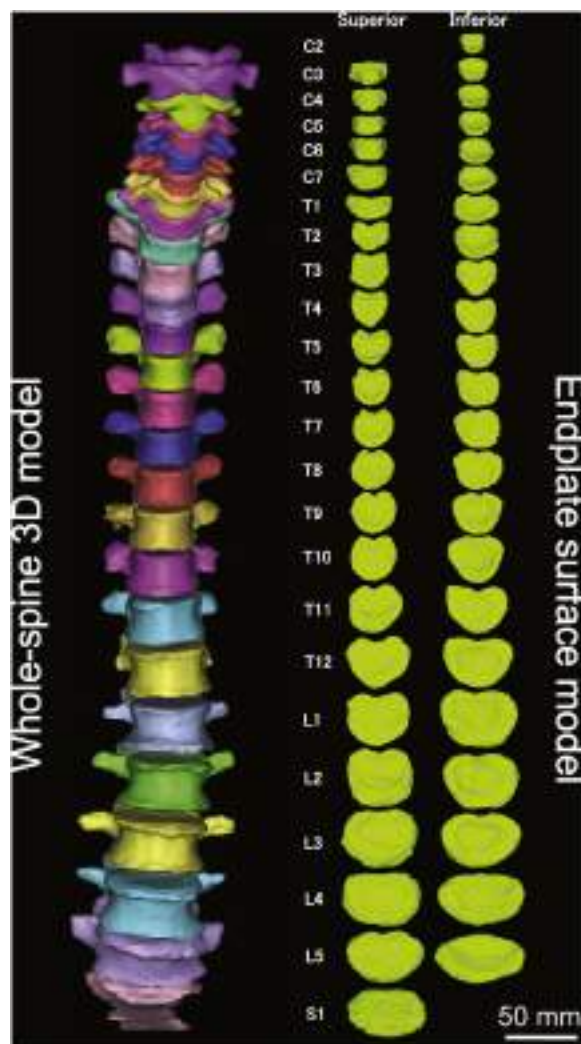
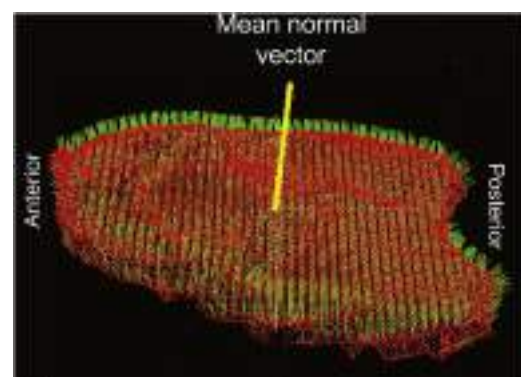
#### Projected Surface Area Measurement

Each polygon element of the endplate mesh model was projected on a plane perpendicular to the mean normal vector of its corresponding endplate (Fig. 2). The projected surface area of the endplate was calculated by summation of individual polygon element projected surface area magnitudes.

#### Endplate Diameter Measurements and Endplate Area Calculation by Elliptical Approximation

In order to compare the endplate area with that estimated by a conventional method based on elliptical approximation, anteroposterior (AP) and transverse diameters were measured. Since the area by elliptical approximation is a planar area, the projected model was used for measurement of the diameters and the elliptical approximation area was compared with the projected area.

Anatomical axes and planes for individual endplates were determined by each endplate eigenvectors of using custom software. The most posterior point was automatically determined in the midsagittal plane. The most anterior and the most lateral points of the model were also automatically determined based on the local anatomical axes. The AP diameter was determined by measuring the distances in space from the most posterior point to the coronal plane and from the most anterior point to the coronal plane using vector algebra. Similarly, the transverse diameter was determined by measuring the distances in space from the most lateral points for both sides to the sagittal plane using vector algebra. These procedures were used because the most anterior point and the most lateral points did not always exist on the sagittal plane or coronal plane, respectively. The

**Figure 1.** Whole-spine 3D model and endplate surface models.**Figure 2.** Endplate polygon-mesh model and the mean normal vector for the endplate surface model. Red lines: Polygon element sides. Green lines: Normal vector of individual polygon elements. Yellow line: Mean normal vector.



endplate area was calculated using the AP and transverse diameters by elliptical approximation as follows:

$$\text{Elliptical approximation area (elliptical area)} = (\text{AP diameter}/2) \times (\text{transverse diameter}/2) \times \pi.$$

### Determination of Endplate Position

In order to analyze the endplate as a function of distance from the inferior endplate of C2, the spinal position was determined as the sum of vertebral body height(s) and the intervening intervertebral disc height(s) toward the endplate of interest (Fig. 3).<sup>7</sup> The centroid of each endplate was located on the corresponding endplate point-cloud dataset model. The vertebral body height was determined by the distance between the centroids of superior and inferior endplates within the corresponding vertebral body. Similarly, the intervertebral disc height was determined by the distance between the centroid of inferior endplate in the cranial vertebral body and the centroid of the superior endplate of the caudal vertebral body. The distance to each endplate was normalized value by cranio-caudal distance (C2-S1) and presented as a percentage (%).

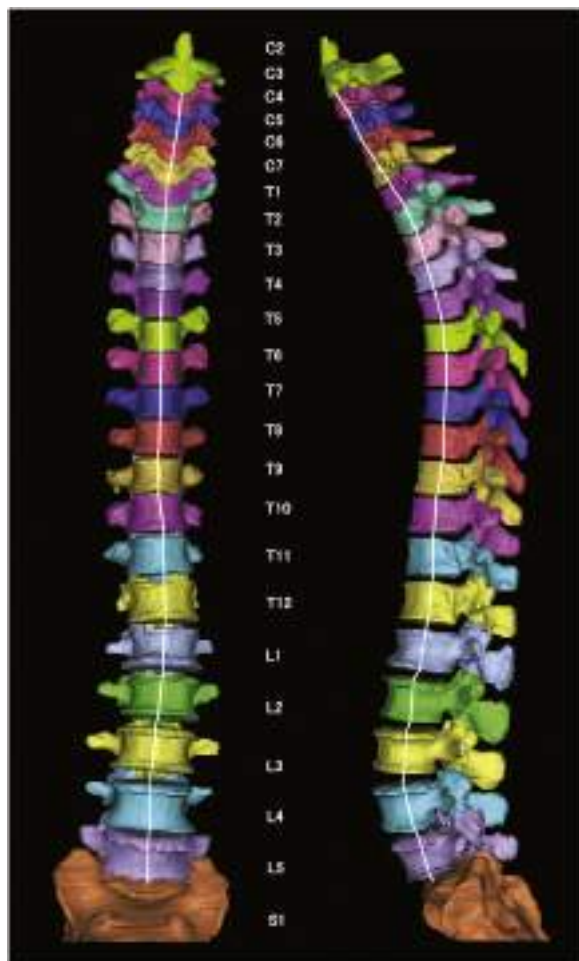


**Figure 3.** Spinal position determined by distance from centroid of the inferior C2 endplate. White lines show the cumulative distance path from the inferior endplate of C2 to the superior endplate of S1.

### Statistical Analysis

Gender effects were compared with unpaired Student's *t*-tests. Level and age effects were sought by ANOVA with Fisher's PLSD post hoc tests using SPSS Statistics v. 23 (IBM, Armonk, NY). The superior versus inferior endplate areas for each vertebral body, the superior versus inferior endplate areas for each intervertebral disc, polygon surface area versus projected area and the projected area versus elliptical area were compared with paired Student's *t*-tests. Correlation between the endplate area versus the spinal position was analyzed by simple linear regression analysis. Correlation between the endplate area and diameters versus age at each one of the spinal positions was analyzed by simple linear regression analysis. Significance level was set at  $p < 0.05$ . Results are presented as mean  $\pm$  SD.

## RESULTS

### Endplate Polygon-Mesh Surface Area

The endplate polygon-mesh surface area was larger in males on both the superior and inferior endplates at all levels, with the exception of S1. The inferior endplate area was higher as compared with the superior endplate area within the same vertebral body at C3, C5, T1 through L2 and L4 (Fig. 4A). Within the intervertebral disc, the area of the inferior endplate of the cranial vertebral body (cranial endplate for the disc) was higher than the area of the superior endplate of the caudal vertebral body (caudal endplate for the disc) at the C5/C6, T1/T2 through T6/T7, T8/T9, and L4/L5 discs, while lower at T11/T12, T12/L1, and L2/L3 (Fig. 4A). Strong linear correlations were found between the endplate area versus the spinal length both in males and females with correlation coefficient values of  $r = 0.938$  and  $r = 0.911$ , respectively (Fig. 5A, B).

The results of multiple comparisons among the spinal levels showed significant increases within three consecutive levels at C3 and T3-L2 levels in superior endplates and at C3, C5-C7, and T3-L2 levels in the inferior endplate in males, and at C3 and T4-L3 levels in the superior endplate and at C2, C6-C7, and T3-L3 levels in the inferior endplate in females (Fig. 6). Significant decreases were noted between L4 and L5 in the inferior endplate in both males and females (Fig. 6).

### Endplate Projected Surface Area

The endplate projected area was larger in males on both the superior and inferior endplates at all levels aside from S1. The inferior endplate area was higher when compared against the superior endplate area within the same vertebral body at C3, C4, C5, T1 through L2 and L4, but lower at L5 (Fig. 4B). Within the intervertebral disc, the projected area of the inferior endplate of the cranial vertebral body (cranial endplate for the disc) was larger than with the areas of the superior endplate of the caudal vertebral body (caudal endplate for the disc) at the C2/C3, C4/C5, C7/T1 through T6/T7, T8/T9, L4/L5, and L5/S1 discs, while lower at T11/T12, T12/L1, and L2/L3. Strong linear correlations were found between the endplate area versus the spinal distance both in males and females

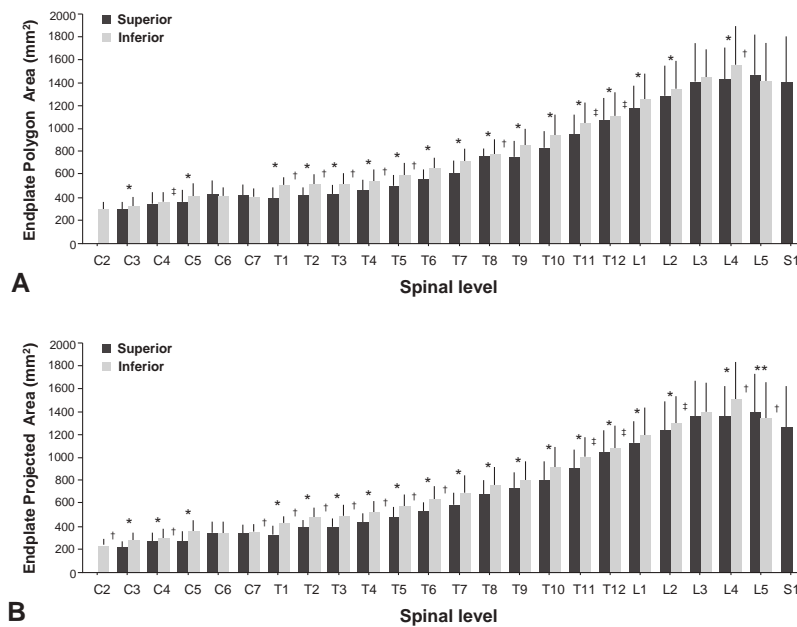


**Figure 4.** Endplate area by spinal level and anatomical site (superior or inferior). A: Endplate polygon area. B: Endplate projected area. \*Inferior > superior within a vertebral body ( $p < 0.05$ ), <sup>†</sup>Inferior of cranial vertebral body > superior of caudal vertebral body ( $p < 0.05$ ), <sup>‡</sup>Inferior of cranial vertebral body < superior of caudal vertebral body ( $p < 0.05$ ) (mean  $\pm$  SD).

with correlation coefficient values of  $r = 0.943$  and  $r = 0.922$ , respectively (Fig. 5C, D).

The results of multiple comparisons among the spinal levels showed significant increases within three consecutive levels at C3, C4, and T3-L2 levels in superior endplates and at C2, C3, C6, C7, and T2-L2 levels in the inferior endplate in males, and at C3 and T4-L2 levels in the superior endplate and at C3, C6-C7, and T4-L2 levels in the inferior endplate in females (Fig. 6). Significant decreases were noted between L3-L5 versus S1 in the superior endplate and between

L3-L4 versus L5 in the inferior endplate in males, and between L5 versus S1 in the superior endplate and between L4 versus L5 in the inferior endplate in females (Fig. 6).

#### Endplate Polygon-Mesh Surface Area Versus Endplate Projected Surface Area

The polygon-mesh surface area (3D surface) was larger than the projected area (planar surface) at all endplates. Overall, the polygon surface area/projected surface area ratio was  $1.06 \pm 0.05$ . When the results

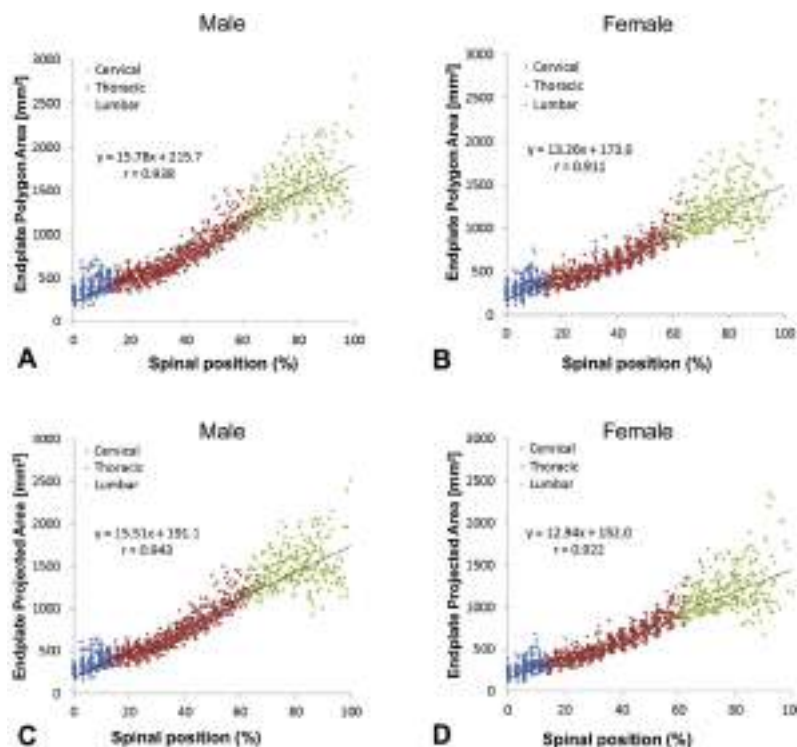


**Figure 5.** Correlations between endplate area and spinal length: A: Endplate polygon area versus spinal position in males. B: Endplate polygon area versus spinal position in females. C: Endplate projected area versus spinal position in males. D: Endplate projected versus spinal position in females.

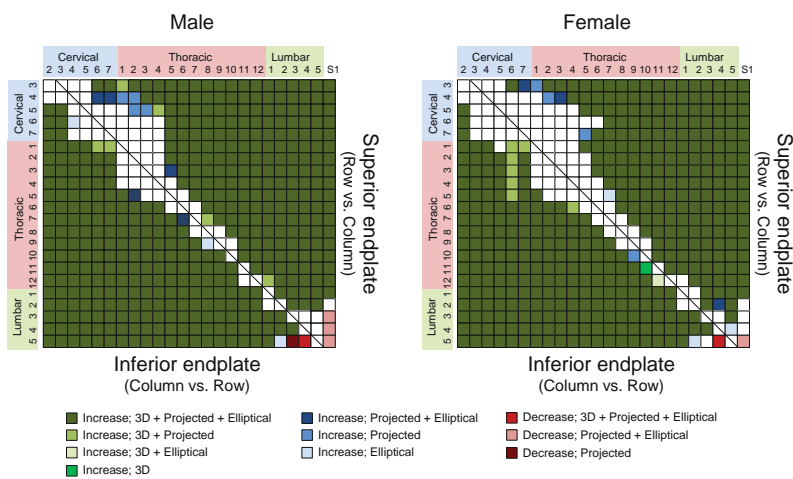


**Figure 6.** Results of multiple comparisons of endplate areas among the spinal levels by Fisher's PLSD test ( $p < 0.05$ ) by spinal level and anatomical site (superior or inferior). 3D: Endplate polygon surface area. Projected: Endplate projected area. Elliptical: Endplate surface area by elliptical approximation. The color of the matrix squares represents the largest change between column/row element pairs.

were segregated by cervical, thoracic and lumbar anatomical location, the ratios were  $1.12 \pm 0.06$ ,  $1.04 \pm 0.03$  and  $1.04 \pm 0.04$ , respectively. The mean ratios in the superior and inferior endplates were  $1.07 \pm 0.06$  and  $1.05 \pm 0.04$ , respectively, and the mean ratio in the superior endplate was higher than that in the inferior endplate (Table 2).

The endplate projected surface area shows more significant differences, including: Larger inferior than superior endplates within the same vertebral body at C4, smaller inferior than superior endplates within the same vertebral body at L5, larger inferior than superior endplates in the adjacent caudal vertebral body at the C2/C3, C4/C5, and C7/T1 disc levels, and smaller inferior than superior endplates in the adjacent caudal vertebral body at the L5/S1 disc level, as compared with the polygon-mesh surface area.

#### Endplate AP Diameter

The endplate AP diameter was larger in males on both the superior and inferior endplates at all levels except superior endplate at L5. The inferior endplate AP diameter was higher as compared with the superior endplate AP diameter within the same vertebral body at C3 through T9, L1, and L4 (Fig. 7A). Within the intervertebral disc, the AP diameter of the inferior endplate of the cranial vertebral body (cranial endplate for the disc) was higher than the AP diameter of the superior endplate of the caudal vertebral body (caudal endplate for the disc) at the C2/C3 through T5/T6, L4/5, and L5/S1 discs, while lower at T10/T11 through L2/L3 (Fig. 7A).

The results of multiple comparisons among the spinal levels showed significant increases within three consecutive levels at C3, C5, and C7-T12 levels in superior endplates and at C2, C3, T1-T7, and T12-L3 levels in the inferior endplate in males, and at C3, C5, and T4-L2 levels in the superior endplate and at C2, C3, and C7-L1 levels in the inferior endplate in females (Fig. 8). Significant decreases were noted between L2-L4 versus S1 and between L4 versus L5 in the superior endplate in males, and between L5 versus

S1 in the superior endplate between and C5 versus C7 and between L4 versus L5 in the inferior endplate in females (Fig. 8).

#### Endplate Transverse Diameter

The endplate transverse diameter was larger in males on both the superior and inferior endplates at all levels, with the exception of superior endplates of C3 through C6 and inferior endplates of C4 and C5. The inferior endplate transverse diameter was higher as compared with the superior endplate transverse diameter within the same vertebral body at C6 through L4 (Fig. 7B). Within the intervertebral disc, the transverse diameter of the inferior endplate of the cranial vertebral body (cranial endplate for the disc) was lower than the transverse diameter of the superior endplate of the caudal vertebral body (caudal endplate for the disc) at the C3/C4 through C7/T1 discs, while higher at T1/T11 through L1/L2 and L3/L4 through L5/S1 (Fig. 7B).

The results of multiple comparisons among the spinal levels showed significant increases within three consecutive levels at C3, C5, and T2-T12 levels in superior endplates and at C2, C3, T1-T7, and T12-L3 levels in the inferior endplate in males, and at C3, C5, and T4-L2 levels in the superior endplate and at C2, C3, and C7-L1 levels in the inferior endplate in females (Fig. 8). Significant decreases were noted between T1 versus T3-T4, between L2-L4 versus S1 and between L4 versus L5 in the superior endplate and between T1-T2 versus T4 in the inferior endplate in males, and between L5 versus S1 in the superior endplate between and C5 versus C7 and between L4 versus L5 in the inferior endplate in females (Fig. 8).

#### Endplate Surface Area by Elliptical Approximation

The endplate surface area estimated by elliptical approximation using the AP and transverse diameters was smaller than the projected area (planar surface) at all endplates except L5 inferior endplates in both genders. Overall, the elliptical approximation

**Table 2.** Spine Length, Endplate Polygon Area, Endplate Projected Area and Polygon Area/Projected Area Ratio by Spinal Level, Site, and Gender

Level	Site	Spinal Position (mm)		Polygon-Mesh Surface Area (mm <sup>2</sup> )		Projected Area (mm <sup>2</sup> )		Polygon Area/Projected Area	
		Male	Female	Male	Female	Male	Female	Male	Female
C2	Inf	0.0	0.0	314.9 (55.1)	265.3 (52.3)	282.9 (44.3)	237.8 (43.8)	1.11 (0.06)	1.11 (0.05)
C3	Sup	3.3 (0.8)	2.7 (0.7)	307.7 (64.8)	265.0 (72.5)	259.2 (45.2)	224.6 (56.0)	1.18 (0.07)	1.17 (0.06)
	Inf	19.0 (1.2)	16.6 (1.3)	347.8 (74.1)	295.0 (71.8)	320.2 (61.1)	268.4 (57.4)	1.08 (0.04)	1.09 (0.04)
C4	Sup	22.0 (1.8)	19.4 (1.7)	376.9 (118.1)	303.3 (77.7)	324.1 (100.5)	258.9 (58.9)	1.16 (0.07)	1.16 (0.06)
	Inf	37.5 (2.6)	33.0 (2.5)	383.4 (88.8)	324.5 (75.4)	356.6 (79.9)	298.1 (68.8)	1.07 (0.04)	1.09 (0.02)
C5	Sup	40.6 (3.1)	35.5 (2.7)	394.9 (113.3)	320.3 (95.1)	337.8 (94.6)	273.0 (77.1)	1.17 (0.07)	1.17 (0.06)
	Inf	55.6 (4.0)	49.1 (3.1)	443.6 (94.9)	370.3 (115.7)	413.4 (86.6)	342.6 (104.6)	1.07 (0.04)	1.08 (0.03)
C6	Sup	58.6 (4.6)	51.3 (3.2)	469.0 (123.0)	390.4 (114.6)	414.3 (107.9)	340.9 (99.4)	1.13 (0.05)	1.15 (0.06)
	Inf	73.6 (5.7)	65.4 (4.2)	456.5 (62.6)	355.5 (75.8)	425.1 (58.0)	328.8 (72.0)	1.07 (0.04)	1.08 (0.03)
C7	Sup	76.7 (6.2)	68.4 (4.5)	465.0 (87.9)	364.2 (75.9)	416.6 (75.9)	324.7 (66.3)	1.12 (0.03)	1.12 (0.04)
	Inf	93.3 (7.1)	83.4 (5.5)	452.4 (64.8)	360.7 (53.0)	424.4 (64.1)	329.5 (47.2)	1.07 (0.03)	1.09 (0.03)
T1	Sup	96.7 (7.6)	86.9 (5.6)	441.3 (73.8)	348.6 (82.1)	404.4 (63.9)	314.7 (69.0)	1.09 (0.04)	1.10 (0.04)
	Inf	115.1 (8.5)	103.7 (6.5)	541.0 (62.4)	449.2 (74.4)	504.8 (58.8)	412.6 (67.0)	1.07 (0.02)	1.09 (0.03)
T2	Sup	118.9 (8.8)	106.9 (6.7)	458.4 (62.3)	369.0 (68.5)	423.7 (53.9)	340.8 (57.0)	1.08 (0.04)	1.08 (0.03)
	Inf	137.8 (9.6)	124.1 (7.5)	566.0 (59.2)	460.8 (72.4)	526.7 (52.3)	424.8 (64.9)	1.07 (0.03)	1.08 (0.02)
T3	Sup	141.2 (10.0)	127.3 (7.6)	467.0 (69.5)	380.9 (71.4)	434.9 (57.2)	355.5 (61.2)	1.07 (0.04)	1.07 (0.03)
	Inf	160.1 (10.7)	144.5 (8.5)	576.1 (62.3)	471.1 (78.5)	545.4 (59.6)	441.6 (70.8)	1.06 (0.02)	1.07 (0.03)
T4	Sup	163.4 (11.2)	147.6 (8.5)	509.9 (72.1)	410.2 (71.4)	481.4 (62.5)	384.7 (61.2)	1.06 (0.02)	1.06 (0.02)
	Inf	182.6 (11.9)	165.1 (9.4)	592.1 (77.8)	499.3 (97.5)	567.8 (74.0)	472.7 (86.5)	1.04 (0.02)	1.05 (0.02)
T5	Sup	185.8 (12.1)	168.1 (9.4)	552.4 (76.8)	450.9 (89.5)	529.3 (73.4)	428.0 (79.5)	1.04 (0.02)	1.05 (0.02)
	Inf	205.6 (12.8)	186.1 (10.4)	637.7 (88.9)	541.8 (108.4)	616.9 (83.9)	520.7 (99.8)	1.03 (0.02)	1.04 (0.02)
T6	Sup	208.7 (13.1)	189.0 (10.5)	603.8 (83.2)	491.2 (80.3)	583.4 (78.3)	470.7 (69.7)	1.03 (0.02)	1.04 (0.02)
	Inf	229.2 (13.6)	207.3 (11.7)	702.7 (88.6)	590.7 (89.2)	686.2 (88.1)	572.3 (81.3)	1.02 (0.01)	1.03 (0.02)
T7	Sup	232.2 (13.7)	210.3 (11.9)	675.4 (83.3)	556.7 (84.4)	661.1 (83.5)	540.0 (76.7)	1.02 (0.01)	1.03 (0.02)
	Inf	253.0 (14.4)	229.1 (12.9)	777.7 (105.4)	638.1 (98.6)	764.9 (105.8)	621.6 (91.1)	1.02 (0.01)	1.03 (0.02)
T8	Sup	256.6 (14.5)	232.5 (13.2)	772.8 (108.9)	627.2 (91.7)	755.7 (105.9)	606.3 (83.8)	1.02 (0.01)	1.03 (0.03)
	Inf	277.6 (15.0)	251.8 (13.9)	859.4 (110.4)	683.1 (123.1)	844.6 (108.2)	663.9 (112.2)	1.02 (0.01)	1.03 (0.02)
T9	Sup	281.5 (15.2)	255.3 (14.0)	842.4 (112.0)	660.4 (100.2)	824.2 (110.5)	642.3 (94.6)	1.02 (0.01)	1.03 (0.02)
	Inf	303.3 (15.9)	275.0 (15.0)	936.8 (110.9)	738.7 (106.8)	917.1 (109.4)	719.9 (101.9)	1.02 (0.01)	1.03 (0.02)
T10	Sup	307.5 (16.1)	278.5 (15.4)	919.9 (111.6)	733.9 (97.3)	901.6 (109.0)	715.1 (90.2)	1.02 (0.01)	1.03 (0.02)
	Inf	330.4 (17.0)	299.5 (16.4)	1,052.7 (152.2)	835.5 (131.4)	1,030.8 (150.5)	816.6 (125.7)	1.02 (0.01)	1.02 (0.02)
T11	Sup	335.4 (17.4)	303.8 (16.5)	1,047.2 (855.1)	855.1 (136.0)	1,025.9 (126.8)	832.8 (126.5)	1.02 (0.01)	1.03 (0.02)
	Inf	359.7 (18.5)	326.2 (17.7)	1,163.0 (157.4)	908.1 (157.2)	1,140.0 (150.1)	887.5 (153.3)	1.02 (0.01)	1.02 (0.02)
T12	Sup	365.2 (18.9)	331.2 (17.6)	1,178.2 (147.3)	965.7 (170.0)	1,159.5 (142.8)	944.4 (162.9)	1.02 (0.01)	1.02 (0.01)
	Inf	391.3 (20.2)	355.4 (18.8)	1,220.7 (126.6)	995.5 (189.8)	1,193.2 (123.6)	966.4 (182.1)	1.02 (0.01)	1.03 (0.02)
L1	Sup	397.5 (20.3)	361.2 (19.0)	1,280.1 (153.6)	1,056.2 (191.5)	1,252.2 (144.9)	1,023.3 (170.0)	1.02 (0.01)	1.03 (0.03)
	Inf	424.7 (21.4)	385.9 (20.6)	1,371.9 (172.6)	1,143.4 (218.0)	1,340.2 (166.2)	1,106.4 (203.8)	1.02 (0.01)	1.03 (0.02)
L2	Sup	432.4 (21.7)	393.0 (20.6)	1,447.3 (191.6)	1,124.4 (213.5)	1,410.2 (179.6)	1,096.2 (199.9)	1.03 (0.02)	1.02 (0.01)
	Inf	459.9 (22.9)	419.2 (21.8)	1,493.6 (198.6)	1,195.3 (201.9)	1,457.6 (193.4)	1,160.9 (185.8)	1.02 (0.01)	1.03 (0.02)
L3	Sup	468.8 (23.4)	426.8 (21.7)	1,582.4 (271.0)	1,246.8 (261.2)	1,539.3 (252.2)	1,202.2 (219.0)	1.03 (0.02)	1.03 (0.03)
	Inf	496.7 (24.7)	452.9 (23.4)	1,592.4 (213.6)	1,291.4 (183.6)	1,551.2 (204.3)	1,248.9 (167.6)	1.03 (0.01)	1.03 (0.02)
L4	Sup	505.4 (24.3)	460.9 (23.9)	1,581.9 (216.4)	1,273.8 (251.3)	1,528.4 (204.6)	1,223.5 (218.6)	1.03 (0.02)	1.04 (0.03)
	Inf	532.9 (25.7)	486.8 (25.2)	1,699.8 (283.0)	1,408.0 (325.7)	1,641.5 (257.4)	1,356.4 (306.5)	1.03 (0.02)	1.04 (0.02)
L5	Sup	540.9 (25.8)	494.0 (24.9)	1,579.1 (251.7)	1,357.7 (402.3)	1,504.4 (223.5)	1,292.4 (370.9)	1.05 (0.03)	1.05 (0.02)
	Inf	567.5 (27.3)	518.8 (26.2)	1,560.7 (283.9)	1,272.8 (294.6)	1,476.5 (263.8)	1,203.7 (269.6)	1.06 (0.03)	1.06 (0.02)
S1	Sup	575.4 (27.5)	526.2 (26.3)	1,505.4 (372.4)	1,303.4 (413.7)	1,371.2 (322.4)	1,157.0 (330.3)	1.10 (0.05)	1.12 (0.07)

Mean (SD). Sup, superior endplate; Inf, inferior endplate.

area/projected surface area ratio was  $0.92 \pm 0.05$ . When the results were sub-divided by cervical, thoracic and lumbar anatomical location, the ratios were  $0.93 \pm 0.05$ ,  $0.93 \pm 0.05$  and  $0.91 \pm 0.05$ , respectively. The ratio was largest in the lumbar spine and followed

by cervical spine and thoracic spine. The mean ratios in the superior and inferior endplates were  $0.94 \pm 0.05$  and  $0.91 \pm 0.05$ , respectively, and the mean ratio in the inferior endplate was higher than that in the superior endplate (Table 3).



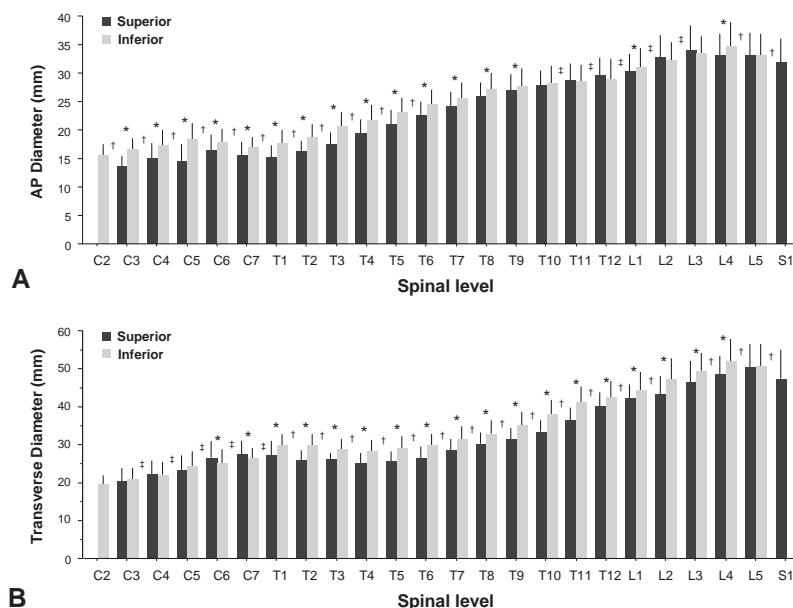


**Figure 7.** Endplate diameters by spinal level and anatomical position (superior or inferior). A: Anteroposterior (AP) diameter. B: Transverse diameter. \*Inferior > superior within a vertebral body ( $p < 0.05$ ), \*\*Inferior < superior within a vertebral body ( $p < 0.05$ ), †Inferior of cranial vertebral body > superior of caudal vertebral body ( $p < 0.05$ ), ‡Inferior of cranial vertebral body < superior of caudal vertebral body ( $p < 0.05$ ) (mean  $\pm$  SD).

#### Effects of Age on the Endplate Polygon-Mesh Surface Area, Endplate Projected Area, AP Diameter, Transverse Diameter, and Endplate Area by Elliptical Approximation

The geometrical parameters reported in the present study including the endplate polygon-mesh surface area, endplate projected area, AP diameter, transverse diameter and endplate area by elliptical approximation decreased from the 60s and 70s to the 80s with peaks in the 70s. For this reason, the linear regression analyses at individual spinal level and sites were performed on the subjects younger than 80 years old. The endplate areas, either polygon-mesh surface area, endplate projected area, or calculated by elliptical approximation, showed weak ( $0.2 < r < 0.4$ ,  $r$ ; correlation efficient) or moderate ( $0.4 \leq r \leq 0.6$ ) positive correlation with age at all sites with exception of one or two sites in females. In males, however, positive correlations were found only in 15–21 sites out of 46 sites. At the superior endplates of T1, T2, and T3, weak or moderate negative correlations were found in the endplate areas regardless of the measurement methods.

The AP diameter in females showed positive correlations at continuous levels and sites at cervical-thoracic junction (inferior endplate of C6 to superior endplate of T2) and lumbar spine (inferior endplate of L1 to inferior endplate of L5). In males, while a positive correlation was found at the upper cervical spine (inferior endplate of C2 to superior endplate of C4), the endplates with positive correlations were seen sporadically. Further, a negative correlation between the AP diameter and age was found at the superior endplate of T2 in males. The transverse diameter increased with age at all endplates but one site in females and most of the cervical levels and T7-L3 levels in males. Negative correlations between the transverse diameter and age were found T1 superior endplate through T3 superior endplate in males. This region of negative correlation changed to the aforementioned the region with positive correlation (T7-L3) via a transitional region of T4-T6 with mixed negative-positive correlation efficient values ( $r$ ) although their absolute values were less than 0.2 (Table 4).

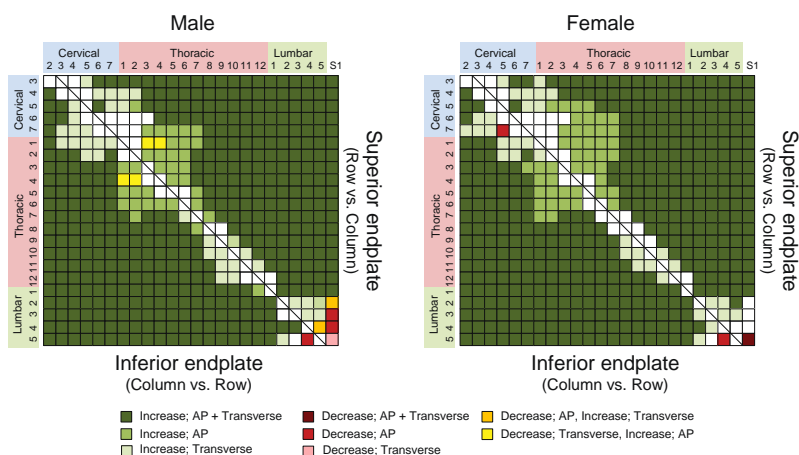


**Figure 8.** Results of multiple comparisons of endplate anteroposterior (AP) and transverse diameters among the spinal levels by Fisher's PLSD test ( $p < 0.05$ ) by spinal level and anatomical site (superior or inferior). AP, AP diameter; Transverse, Transverse diameter. The color of the matrix squares represents the largest change between column/row element pairs.

**Table 3.** Antero-Posterior (AP) Diameter, Transverse Diameter, Endplate Area by Elliptical Approximation and Elliptical Area/Projected Area Ratio by Spinal Level, Site, and Gender

Level	Site	AP Diameter (mm)		Transverse Diameter (mm)		Elliptical Area (mm <sup>2</sup> )		Elliptical Area/Projected Area	
		Male	Female	Male	Female	Male	Female	Male	Female
C2	Inf	16.5 (2.1)	14.7 (1.1)	20.2 (2.2)	18.5 (2.7)	262.7 (5.14)	214.6 (40.1)	0.939 (0.065)	0.903 (0.051)
C3	Sup	14.3 (1.6)	12.9 (1.8)	20.7 (2.9)	20.1 (3.6)	232.8 (44.5)	207.3 (57.3)	0.913 (0.053)	0.920 (0.056)
	Inf	17.5 (2.0)	15.7 (1.6)	21.9 (2.4)	20.0 (2.7)	302.1 (58.1)	249.2 (57.3)	0.960 (0.059)	0.926 (0.040)
C4	Sup	15.8 (3.1)	14.0 (1.9)	23.1 (4.0)	21.3 (3.1)	292.9 (103.8)	235.7 (57.3)	0.914 (0.045)	0.910 (0.042)
	Inf	18.3 (2.4)	16.3 (2.3)	22.4 (3.7)	21.5 (3.0)	324.3 (82.4)	279.7 (78.1)	0.921 (0.055)	0.932 (0.053)
C5	Sup	15.8 (2.9)	13.3 (2.1)	24.1 (3.5)	22.7 (3.6)	303.9 (95.8)	241.6 (72.1)	0.911 (0.043)	0.885 (0.049)
	Inf	19.5 (2.7)	17.2 (2.4)	25.1 (3.7)	23.4 (4.6)	386.8 (88.3)	321.5 (110.1)	0.949 (0.052)	0.932 (0.049)
C6	Sup	17.5 (2.7)	15.2 (2.5)	27.4 (4.5)	25.7 (4.2)	381.8 (110.7)	311.3 (95.1)	0.930 (0.048)	0.912 (0.049)
	Inf	19.3 (1.8)	16.5 (1.6)	26.4 (2.8)	23.6 (3.9)	401.5 (61.4)	308.8 (78.1)	0.958 (0.041)	0.935 (0.057)
C7	Sup	16.8 (2.2)	14.4 (1.5)	28.8 (3.1)	26.0 (3.4)	380.2 (71.3)	296.0 (66.5)	0.929 (0.036)	0.909 (0.047)
	Inf	18.2 (1.4)	15.7 (1.2)	27.6 (2.6)	24.9 (2.2)	395.6 (57.5)	308.2 (46.4)	0.948 (0.045)	0.934 (0.044)
T1	Sup	16.3 (1.7)	14.0 (1.8)	28.5 (3.1)	25.7 (3.7)	365.2 (61.7)	284.6 (68.3)	0.916 (0.055)	0.900 (0.036)
	Inf	18.8 (1.8)	16.6 (2.0)	31.3 (2.2)	28.7 (2.5)	462.2 (61.3)	375.3 (71.7)	0.929 (0.030)	0.907 (0.047)
T2	Sup	16.9 (1.6)	15.4 (2.1)	26.9 (2.7)	24.6 (2.2)	356.3 (46.3)	297.4 (59.0)	0.855 (0.045)	0.872 (0.074)
	Inf	19.7 (2.3)	17.7 (2.0)	31.8 (2.0)	28.3 (2.6)	492.4 (66.1)	394.0 (67.4)	0.947 (0.055)	0.926 (0.047)
T3	Sup	18.4 (1.8)	16.4 (2.0)	26.3 (2.5)	24.2 (2.2)	381.8 (54.8)	312.5 (56.0)	0.891 (0.047)	0.879 (0.038)
	Inf	21.7 (2.3)	19.3 (2.1)	30.7 (2.1)	26.9 (2.1)	523.1 (62.2)	409.7 (67.4)	0.974 (0.044)	0.928 (0.049)
T4	Sup	20.6 (2.2)	18.2 (2.2)	26.5 (2.2)	23.8 (1.9)	428.2 (55.2)	342.0 (58.6)	0.905 (0.050)	0.889 (0.040)
	Inf	23.0 (2.3)	20.3 (2.3)	29.5 (2.1)	27.3 (3.1)	533.7 (69.9)	438.5 (89.6)	0.956 (0.048)	0.926 (0.057)
T5	Sup	22.4 (2.0)	19.7 (2.2)	26.8 (2.0)	24.5 (2.0)	473.1 (62.9)	379.9 (65.1)	0.910 (0.046)	0.890 (0.041)
	Inf	24.3 (2.2)	22.0 (2.2)	30.5 (2.6)	27.3 (2.8)	583.6 (75.2)	474.6 (89.2)	0.963 (0.050)	0.913 (0.037)
T6	Sup	23.8 (2.2)	21.3 (1.9)	28.1 (2.5)	25.1 (2.2)	526.1 (75.0)	421.1 (65.9)	0.916 (0.048)	0.895 (0.042)
	Inf	25.8 (2.2)	23.4 (2.0)	31.4 (2.5)	28.1 (2.4)	637.3 (83.4)	517.9 (76.6)	0.945 (0.046)	0.906 (0.041)
T7	Sup	25.5 (2.0)	22.9 (2.0)	30.0 (2.6)	26.5 (2.0)	600.8 (79.9)	477.7 (70.7)	0.924 (0.042)	0.885 (0.031)
	Inf	27.2 (2.5)	24.1 (2.0)	33.2 (2.8)	29.6 (2.5)	710.6 (107.4)	561.9 (81.5)	0.943 (0.039)	0.905 (0.033)
T8	Sup	27.2 (2.3)	24.3 (1.8)	31.7 (2.8)	28.4 (2.4)	679.3 (105.9)	543.0 (74.9)	0.913 (0.054)	0.897 (0.034)
	Inf	28.6 (2.4)	25.3 (2.5)	34.8 (3.2)	30.8 (2.7)	782.9 (112.5)	615.8 (100.5)	0.941 (0.049)	0.929 (0.038)
T9	Sup	28.6 (2.6)	25.0 (2.0)	32.9 (2.9)	29.7 (2.5)	742.3 (118.1)	584.3 (84.9)	0.914 (0.049)	0.911 (0.046)
	Inf	29.6 (2.6)	25.7 (2.1)	37.1 (2.9)	33.0 (2.9)	862.9 (115.9)	668.2 (103.4)	0.955 (0.037)	0.928 (0.029)
T10	Sup	29.5 (2.2)	26.1 (1.7)	34.9 (3.1)	31.1 (2.8)	811.4 (116.7)	638.0 (84.5)	0.913 (0.045)	0.907 (0.033)
	Inf	29.9 (2.6)	26.3 (2.3)	40.1 (3.4)	35.7 (3.1)	946.1 (149.5)	741.1 (122.8)	0.932 (0.039)	0.893 (0.042)
T11	Sup	30.2 (2.5)	27.1 (2.6)	38.2 (2.5)	34.7 (3.0)	909.1 (119.6)	742.1 (126.4)	0.900 (0.034)	0.890 (0.035)
	Inf	30.0 (2.5)	26.8 (2.6)	43.7 (3.2)	37.8 (3.7)	1,034.4 (141.8)	800.3 (148.7)	0.922 (0.034)	0.901 (0.030)
T12	Sup	31.2 (2.5)	27.9 (2.7)	42.2 (3.2)	37.7 (3.2)	1,037.2 (143.9)	830.4 (148.4)	0.908 (0.041)	0.880 (0.037)
	Inf	30.1 (2.4)	27.8 (3.9)	45.3 (2.4)	40.0 (3.9)	1,073.0 (117.0)	881.6 (211.6)	0.914 (0.034)	0.908 (0.075)
L1	Sup	31.5 (2.5)	28.9 (3.0)	43.8 (3.2)	39.8 (3.7)	1,087.8 (147.7)	908.8 (176.0)	0.881 (0.031)	0.886 (0.033)
	Inf	32.3 (2.9)	29.8 (3.1)	47.0 (3.3)	42.3 (4.3)	1,195.6 (170.7)	996.4 (203.2)	0.911 (0.044)	0.899 (0.030)
L2	Sup	34.8 (3.2)	30.5 (3.4)	46.3 (3.4)	40.5 (3.7)	1,268.1 (195.9)	978.9 (196.8)	0.911 (0.038)	0.891 (0.036)
	Inf	33.8 (2.5)	30.8 (2.8)	50.5 (4.9)	43.8 (3.8)	1,344.4 (197.0)	1,064.3 (185.2)	0.937 (0.034)	0.916 (0.030)
L3	Sup	36.0 (4.2)	31.9 (3.2)	49.7 (4.5)	43.2 (4.3)	1,414.7 (265.0)	1,087.7 (216.1)	0.931 (0.037)	0.904 (0.034)
	Inf	34.7 (2.9)	32.2 (2.5)	52.2 (3.7)	46.5 (4.0)	1,427.8 (194.7)	1,179.1 (181.0)	0.935 (0.034)	0.942 (0.032)
L4	Sup	34.8 (3.5)	31.4 (3.3)	51.2 (3.5)	45.4 (4.9)	1,406.1 (210.5)	1,128.4 (233.6)	0.934 (0.035)	0.919 (0.035)
	Inf	36.2 (3.6)	33.1 (4.2)	54.9 (4.6)	49.6 (5.5)	1,566.8 (262.2)	1,304.9 (316.4)	0.969 (0.038)	0.960 (0.030)
L5	Sup	34.0 (3.0)	32.3 (4.2)	52.8 (3.8)	47.6 (7.0)	1,416.9 (211.0)	1,226.4 (363.5)	0.957 (0.032)	0.948 (0.031)
	Inf	34.6 (3.0)	31.5 (3.7)	53.4 (4.5)	48.0 (5.9)	1,461.7 (252.4)	1,201.2 (283.7)	1.007 (0.037)	0.997 (0.045)
S1	Sup	33.2 (4.1)	30.6 (3.5)	49.9 (6.3)	44.9 (8.0)	1,316.9 (327.3)	1,096.5 (312.6)	0.972 (0.048)	0.942 (0.032)

Mean (SD). Sup, superior endplate; Inf, inferior endplate; AP diameter, anterior-posterior diameter at mid-sagittal plane; Elliptical area = (AP diameter/2) × (transverse diameter/2) ×  $\pi$ .

## DISCUSSION

Although previous anthropological studies report linear dimensions for the vertebrae using cadaveric specimens,<sup>7–11,13,17</sup> the present study is the first to measure in vivo 3D surface area of the bony endplates

in humans along the entire spine. In this work, we formulated a linear relationship by introducing a new quantitative position parameter, which may be useful for quantitative studies in anthropology and comparative medicine. The present study measured 3D endplate

surface area, projected endplate surface area as the cross-sectional area, which may have different clinical relevance. The results of the present study showed gender differences in the endplate surface area, in both polygon and projected areas, at all levels but S1. The inferior endplate projected surface area was larger compared with the superior endplate of the same vertebra except for C6, C7, L3, and L5. When the superior and inferior endplates within the intervertebral disc were compared, the inferior endplate projected surface area of the cranial vertebra was larger than that in the superior endplate of the adjacent caudal vertebra excluding the C3/C4, C5/C6, C6/C7, T7/T8, T10/T11, L1/L2, L2/L3, and L3/4 disc levels. The endplate surface area increased linearly as a whole; however, there were regional specificities as described later.

The present study used two different methods to measure endplate surface area using subject-based 3D-CT whole-spine models. The polygon-mesh surface measurement determines the surface area of the endplates in spite of its complex 3D surface morphology. Since the 3D CT model is based on a polygon mesh, individual polygon surface measurement can be easily implemented (and extended to the entire surface model) once the proper segmentation of the endplate has been achieved. This method provides true surface area of the endplate which is relevant for studies involving the interface between the bony endplate and the intervertebral disc. However, when the cross-sectional area is of interest, the endplate area measured by summation of polygon-mesh surface may be overestimated due to concavity of the endplate and uncinat processes of the superior endplate at C3-T1. In fact, in the present study, the endplate area measured by polygon-mesh area measurement was always larger than the projected area especially in the cervical spine. The projected surface area represents the cross-sectional area and can be used for many purposes such as estimation of stress/pressure of the intervertebral disc and disc volume. Unlike projected area measurements using photographs of cadaveric specimens, the projected area measurement using the 3D model requires an additional procedure to define a reference plane in the model. In the present study, this procedure was done automatically by calculating the mean normal vector of the endplate to define orientation of the reference plane. It should be noted, however, that the polygon-based area measurement includes areas of small protrusions and dimples which may not be desirable for certain purposes. Especially, image-based polygon models potentially include rough surfaces due to image noise which causes overestimation of the surface area. Since we attempted to measure macroscopic surface area of the endplate in the present study, we eliminated surface structures that protruded or dipped less than 1.0 mm by surface smoothing considering voxel size used in this study. The endplate area estimated by elliptical approximation was about 92 % of the projected

area and could be used as a simple method to calculate the endplate area. It should be noted however, that the elliptical area calculated in the present study used diameters measured in the plane in 3D space considering 3D orientation of the endplate. Therefore, when the axial CT images are used for measurement of the diameter, especially AP diameter, reduction of the diameter due to obliquity of the endplate should be considered for evaluation of the area by elliptical approximation.

The superior and inferior endplate areas linearly increased five- to sixfold from C2 to L4 regardless of the measurement methods. Such large increases were achieved through 43 endplates between C2 and L4 levels; therefore, an increment in each spinal level was subtle; however, comparisons between the superior and inferior endplates within the same vertebra or same intervertebral disc in a paired fashion were able to show statistically-significant differences at each level. There are two possible mechanisms to increase the endplate area. One is to increase the endplate area within the same vertebral body; that is, to increase the endplate area between the superior endplate and the inferior endplate. Another is to increase the endplate area within an intervertebral disc; that is, to increase the endplate area between the inferior endplate of the cranial vertebral body and the superior endplate of the caudal vertebral body. As the results were summarized earlier, inferior endplate areas were larger than superior endplate areas in the same vertebral body in 17 disc levels for the polygon area and 18 disc levels for the projected area out of 23 disc levels. In comparison between the cranial and caudal endplates within an intervertebral disc, the areas of the cranial endplate (inferior endplate of the cranial vertebra) and the caudal endplate (superior endplate of the caudal vertebra), the cranial endplate of the disc was larger in 15 disc levels out of 23 disc levels studied in the present study. These findings indicate that an increase in endplate area is caused mainly by an increase in endplate area within each individual vertebral body. These results agree with a previous study which measured linear dimensions of cadaveric thoracic and lumbar spines in an attempt to characterize the so-called "vertebral wedging." In said study, Masharawi et al. described that the trapezoidal shape of the vertebral body and an inverted trapezoidal shape of the disc space lend a "Chinese pagoda" shape to the thoracolumbar vertebral column (T1-L5).<sup>15</sup>

Although the endplate areas and diameters increased with the each consecutive lower spinal level as a whole, regional specificity was noted at several spinal levels. Significant decrease in the inferior endplate AP diameter was shown between C5 and C7 in females. This finding may be explained by the existence of cervical enlargement of the spinal cord and larger vertebral body/spinal canal ratio in females.<sup>18</sup> Many of the parameters on endplate area and AP diameter lack statistical differences in the cervico-thoracic transitional

**Table 4.** Correlation Coefficient (r) Between Age Versus Endplate Polygon-Mesh Surface Area, Endplate Projected Area, Antero-Posterior (AP) Diameter, Transverse Diameter, and Endplate Area by Elliptical Approximation by Spinal Level, Site, and Gender

Level	Site	Polygon-Mesh Surface Area		Projected Area		AP Diameter		Transverse Diameter		Elliptical Area	
		Male	Female	Male	Female	Male	Female	Male	Female	Male	Female
C2	Inf	0.050	0.142	0.157	0.162	0.301 <sup>a</sup>	0.115	0.120	0.216 <sup>a</sup>	0.128	0.120
C3	Sup	0.018	0.271 <sup>a</sup>	0.082	0.299 <sup>a</sup>	0.500 <sup>b</sup>	0.218 <sup>a</sup>	0.130	0.156	0.231 <sup>a</sup>	0.203 <sup>a</sup>
	Inf	0.254 <sup>a</sup>	0.315 <sup>a</sup>	0.300 <sup>a</sup>	0.454 <sup>b</sup>	0.365 <sup>a</sup>	0.378 <sup>a</sup>	0.369 <sup>a</sup>	0.474 <sup>b</sup>	0.416 <sup>b</sup>	0.447 <sup>b</sup>
C4	Sup	0.156	0.349 <sup>a</sup>	0.236 <sup>a</sup>	0.379 <sup>a</sup>	0.286 <sup>a</sup>	0.191	0.203 <sup>a</sup>	0.364 <sup>a</sup>	0.303 <sup>a</sup>	0.316 <sup>a</sup>
	Inf	0.268 <sup>a</sup>	0.315 <sup>a</sup>	0.263 <sup>a</sup>	0.339 <sup>a</sup>	0.059	0.196	0.294 <sup>a</sup>	0.353 <sup>a</sup>	0.285 <sup>a</sup>	0.288 <sup>a</sup>
C5	Sup	0.048	0.367 <sup>a</sup>	0.014	0.353 <sup>a</sup>	0.065	0.384 <sup>a</sup>	0.084	0.291 <sup>a</sup>	0.034	0.358 <sup>a</sup>
	Inf	0.182	0.197 <sup>a</sup>	0.214 <sup>a</sup>	0.218 <sup>a</sup>	0.094	0.141	0.367 <sup>a</sup>	0.228 <sup>a</sup>	0.294 <sup>a</sup>	0.208 <sup>a</sup>
C6	Sup	0.108	0.186 <sup>a</sup>	0.148	0.204 <sup>a</sup>	0.055	0.176	0.211 <sup>a</sup>	0.283 <sup>a</sup>	0.065	0.227 <sup>a</sup>
	Inf	0.333 <sup>a</sup>	0.481 <sup>a</sup>	0.377 <sup>a</sup>	0.454 <sup>b</sup>	0.326 <sup>a</sup>	0.543 <sup>b</sup>	0.369 <sup>a</sup>	0.297 <sup>a</sup>	0.455 <sup>b</sup>	0.408 <sup>b</sup>
C7	Sup	0.084	0.398 <sup>a</sup>	0.138	0.423 <sup>b</sup>	0.038	0.440 <sup>b</sup>	0.272 <sup>a</sup>	0.342 <sup>a</sup>	0.158	0.411 <sup>b</sup>
	Inf	0.150	0.515 <sup>a</sup>	0.134	0.537 <sup>b</sup>	0.095	0.401 <sup>b</sup>	0.127	0.482 <sup>b</sup>	0.034	0.499 <sup>b</sup>
T1	Sup	-0.451 <sup>d</sup>	0.408 <sup>b</sup>	-0.466 <sup>d</sup>	0.437 <sup>b</sup>	0.018	0.369 <sup>a</sup>	-0.461 <sup>d</sup>	0.323 <sup>a</sup>	-0.354 <sup>c</sup>	0.393 <sup>a</sup>
	Inf	0.121	0.398 <sup>a</sup>	-0.134	0.421 <sup>b</sup>	0.066	0.284 <sup>a</sup>	-0.255 <sup>c</sup>	0.458 <sup>b</sup>	0.103	0.385 <sup>a</sup>
T2	Sup	-0.424 <sup>d</sup>	0.309 <sup>a</sup>	-0.482 <sup>d</sup>	0.347 <sup>a</sup>	-0.348 <sup>c</sup>	0.261 <sup>a</sup>	-0.365 <sup>c</sup>	0.400 <sup>b</sup>	-0.563 <sup>d</sup>	0.396 <sup>a</sup>
	Inf	0.075	0.430 <sup>b</sup>	-0.104	0.455 <sup>b</sup>	0.041	0.117	-0.316 <sup>c</sup>	0.516 <sup>b</sup>	0.187	0.299 <sup>a</sup>
T3	Sup	-0.302 <sup>c</sup>	0.324 <sup>a</sup>	-0.316 <sup>c</sup>	0.333 <sup>a</sup>	-0.179	0.171	-0.368 <sup>c</sup>	0.334 <sup>a</sup>	-0.371 <sup>c</sup>	0.449 <sup>b</sup>
	Inf	0.123	0.439 <sup>b</sup>	0.110	0.438 <sup>b</sup>	0.106	0.212 <sup>a</sup>	-0.124	0.588 <sup>b</sup>	0.026	0.370 <sup>a</sup>
T4	Sup	-0.151	0.368 <sup>a</sup>	-0.161	0.384 <sup>a</sup>	-0.039	0.262 <sup>a</sup>	0.035	0.366 <sup>a</sup>	-0.059	0.408 <sup>b</sup>
	Inf	0.263 <sup>a</sup>	0.408 <sup>b</sup>	0.237 <sup>a</sup>	0.419 <sup>b</sup>	0.325 <sup>a</sup>	0.222 <sup>a</sup>	0.046	0.469 <sup>b</sup>	0.297 <sup>a</sup>	0.289 <sup>a</sup>
T5	Sup	0.004	0.295 <sup>a</sup>	-0.023	0.306 <sup>a</sup>	0.083	0.099	-0.105	0.412 <sup>b</sup>	0.011	0.425 <sup>b</sup>
	Inf	0.277 <sup>a</sup>	0.397 <sup>a</sup>	0.261 <sup>a</sup>	0.424 <sup>b</sup>	0.370 <sup>a</sup>	0.287 <sup>a</sup>	0.005	0.497 <sup>b</sup>	0.314 <sup>a</sup>	0.259 <sup>a</sup>
T6	Sup	0.106	0.268 <sup>a</sup>	0.108	0.296 <sup>a</sup>	0.306 <sup>a</sup>	0.063	-0.102	0.349 <sup>a</sup>	0.203 <sup>a</sup>	0.399 <sup>a</sup>
	Inf	0.157	0.418 <sup>b</sup>	0.162	0.422 <sup>b</sup>	0.226 <sup>a</sup>	0.124	0.065	0.519 <sup>b</sup>	0.221 <sup>a</sup>	0.294 <sup>a</sup>
T7	Sup	0.066	0.304 <sup>a</sup>	0.065	0.310 <sup>a</sup>	0.091	0.200 <sup>a</sup>	0.255 <sup>a</sup>	0.313 <sup>a</sup>	0.117	0.398 <sup>a</sup>
	Inf	0.197	0.367 <sup>a</sup>	0.210 <sup>a</sup>	0.376 <sup>a</sup>	0.231 <sup>a</sup>	0.153	0.272 <sup>a</sup>	0.551 <sup>b</sup>	0.313 <sup>a</sup>	0.216 <sup>a</sup>
T8	Sup	0.060	0.363 <sup>a</sup>	0.056	0.344 <sup>a</sup>	0.021	0.077	0.211 <sup>a</sup>	0.437 <sup>b</sup>	0.138	0.322 <sup>a</sup>
	Inf	0.196	0.276 <sup>a</sup>	0.233 <sup>a</sup>	0.265 <sup>a</sup>	0.022	0.036	0.263 <sup>a</sup>	0.510 <sup>b</sup>	0.185	0.296 <sup>a</sup>
T9	Sup	0.130	0.236 <sup>a</sup>	0.146	0.250 <sup>a</sup>	0.065	0.078	0.296 <sup>a</sup>	0.487 <sup>b</sup>	0.191	0.251 <sup>a</sup>
	Inf	0.203 <sup>a</sup>	0.324 <sup>a</sup>	0.243 <sup>a</sup>	0.323 <sup>a</sup>	0.127	0.007	0.239 <sup>a</sup>	0.440 <sup>b</sup>	0.209 <sup>a</sup>	0.256 <sup>a</sup>
T10	Sup	0.213 <sup>a</sup>	0.218 <sup>a</sup>	0.236 <sup>a</sup>	0.387 <sup>a</sup>	0.118	0.191	0.312 <sup>a</sup>	0.432 <sup>b</sup>	0.266 <sup>a</sup>	0.374 <sup>a</sup>
	Inf	0.330 <sup>a</sup>	0.314 <sup>a</sup>	0.354 <sup>a</sup>	0.295 <sup>a</sup>	0.172	0.195	0.386 <sup>a</sup>	0.315 <sup>a</sup>	0.321 <sup>a</sup>	0.279 <sup>a</sup>
T11	Sup	0.256 <sup>a</sup>	0.396 <sup>a</sup>	0.295 <sup>a</sup>	0.396 <sup>a</sup>	0.180	0.194	0.362 <sup>a</sup>	0.483 <sup>b</sup>	0.308 <sup>a</sup>	0.359 <sup>a</sup>
	Inf	0.238 <sup>a</sup>	0.308 <sup>a</sup>	0.247 <sup>a</sup>	0.298 <sup>a</sup>	0.118	0.142	0.400 <sup>a</sup>	0.436 <sup>b</sup>	0.244 <sup>a</sup>	0.296 <sup>a</sup>
T12	Sup	0.252 <sup>a</sup>	0.361 <sup>a</sup>	0.268 <sup>a</sup>	0.355 <sup>a</sup>	0.083	0.056	0.289 <sup>a</sup>	0.539 <sup>b</sup>	0.220 <sup>a</sup>	0.289 <sup>a</sup>
	Inf	0.052	0.309 <sup>a</sup>	0.054	0.302 <sup>a</sup>	0.212 <sup>a</sup>	0.288 <sup>a</sup>	0.336 <sup>a</sup>	0.355 <sup>a</sup>	0.028	0.334 <sup>a</sup>
L1	Sup	0.209 <sup>a</sup>	0.331 <sup>a</sup>	0.246 <sup>a</sup>	0.355 <sup>a</sup>	0.087	0.142	0.341 <sup>a</sup>	0.430 <sup>b</sup>	0.237 <sup>a</sup>	0.277 <sup>a</sup>
	Inf	0.195	0.391 <sup>a</sup>	0.189	0.384 <sup>a</sup>	0.037	0.316 <sup>a</sup>	0.204 <sup>a</sup>	0.383 <sup>a</sup>	0.081	0.240 <sup>a</sup>
L2	Sup	0.332 <sup>a</sup>	0.277 <sup>a</sup>	0.379 <sup>a</sup>	0.280 <sup>a</sup>	0.284 <sup>a</sup>	0.236 <sup>a</sup>	0.349 <sup>a</sup>	0.234 <sup>a</sup>	0.341 <sup>a</sup>	0.381 <sup>a</sup>
	Inf	0.175	0.369 <sup>a</sup>	0.191	0.386 <sup>a</sup>	0.147	0.317 <sup>a</sup>	0.320 <sup>a</sup>	0.415 <sup>b</sup>	0.141	0.189
L3	Sup	0.391 <sup>a</sup>	0.368 <sup>a</sup>	0.414 <sup>b</sup>	0.395 <sup>a</sup>	0.307 <sup>a</sup>	0.338 <sup>a</sup>	0.381 <sup>a</sup>	0.404 <sup>b</sup>	0.399 <sup>a</sup>	0.372 <sup>a</sup>
	Inf	0.152	0.418 <sup>b</sup>	0.180	0.446 <sup>b</sup>	0.001	0.280 <sup>a</sup>	0.181	0.435 <sup>b</sup>	0.098	0.391 <sup>a</sup>
L4	Sup	0.241 <sup>a</sup>	0.264 <sup>a</sup>	0.260 <sup>a</sup>	0.285 <sup>a</sup>	0.134	0.353 <sup>a</sup>	0.144	0.282 <sup>a</sup>	0.164	0.333 <sup>a</sup>
	Inf	0.161	0.461 <sup>b</sup>	0.177	0.468 <sup>b</sup>	0.009	0.441 <sup>b</sup>	0.300 <sup>a</sup>	0.407 <sup>b</sup>	0.156	0.440 <sup>b</sup>
L5	Sup	0.028	0.421 <sup>b</sup>	0.001	0.426 <sup>b</sup>	-0.175	0.392 <sup>a</sup>	0.124	0.381 <sup>a</sup>	0.037	0.402 <sup>b</sup>
	Inf	0.124	0.358 <sup>a</sup>	0.039	0.363 <sup>a</sup>	0.043	0.363 <sup>a</sup>	0.008	0.261 <sup>a</sup>	0.010	0.341 <sup>a</sup>
S1	Sup	0.038	0.193	0.054	0.228 <sup>a</sup>	0.045	0.184	0.023	0.253 <sup>a</sup>	0.058	0.260 <sup>a</sup>

Sup, superior endplate; Inf, inferior endplate. <sup>a</sup>Weak positive correlation with  $0.2 < r < 0.4$ . <sup>b</sup>Moderate positive correlation with  $0.4 \leq r \leq 0.6$ . <sup>c</sup>Weak negative correlation with  $0.2 < r < 0.4$ . <sup>d</sup>Moderate negative correlation with  $0.4 \leq r \leq 0.6$ .

region; however, the reason for this remains unexplained. Significant decreases in the transverse diameters were found at T4 in both superior and inferior endplates in males and significant increases in superior

and inferior endplates in both genders were found below the T4 level. The decrease in the transverse diameter toward T4 and the increase from T4 was highlighted in the aforementioned study by Masharawi et al. and this



finding was discussed from evolutionary, kinematic and biomechanical aspects.<sup>19–24</sup> These sandglass-type changes in the transverse diameter may also be explained by influence of adjacent organs in the posterior mediastinum, especially arch of aorta and descending aorta. Interestingly, significant decreases in many parameters were also found at L5 and S1 levels in both genders, and this finding is consistent with previous cadaveric studies.<sup>6,8,9,12–15,21</sup> Higher stress is expected at the pelvic-lumbar junction as a base of the entire spinal column and therefore larger endplate area and dimensions are expected in this region from a biomechanical point of view. The reason of this finding is unclear; however, S1 consists of a pelvic inlet and adjacent pelvic organs and/or a fetus in the case of females, which may prevent increases in endplate area and dimensions at S1. Future studies will be required to clarify whether the endplate area in S1 satisfies the biomechanical demands or is sacrificed by anatomical constraints.

The results of the age effects on the geometrical parameters of the endplate showed remarkable differences between genders. In females, the transverse diameters increased with age at all endplates but one and appear to primarily contribute to the increase in endplate area. This systematic increase in the transverse diameter through the whole-spine may indicate continuous vertebral growth with age, similar to that of the transverse diameter of long bones with age by apposition of bone at the periosteum and resorption at the endosteum.<sup>25–27</sup> Our previous study showed an increase in inter-pedicle distance with age in the lumbar spine<sup>28</sup> and this finding may indicate the possibility of continuous increase of the transverse diameter and endplate area via this mechanism. Other possible explanations of such dimensional enlargement are vertebral body deformation associated with osteoporosis and osteophyte formation, although we strived to exclude osteophytes from the measurements. The osteophyte is often incorporated in the original bone structure, which makes it difficult to differentiate osteophytes from original bony structure.<sup>16,29</sup> We anticipated the increases in geometrical parameters of the endplate would be more prominent in males, especially due to the incorporated osteophytes; however, our results showed less consistent increases of the areas and diameters through the entire spine in males, even showed decreases of these parameters with age at the T1-T3 levels. As discussed earlier, the decrease in the transverse diameter with age in this region may be explained by enlargement and/or sclerosis of the adjacent cardio-vascular system associated with age, especially in males. Negative correlation of the AP diameter with age was also found at L5 in males ( $r = -0.175$ ) which may also be affected by the presence of adjacent anterior vessels in this region. Although the magnitude of the  $r$  value is small in the lumbar region, existence of regions with negative correlations with age in the spinal column may have

prevented to demonstrate clear age effects on the geometrical parameters of the endplate in males.

Strong linear correlations were found between the endplate area versus the distance from the C2 inferior endplate both in males and females in the present study. This finding, together with the results of higher endplate area in males, may be due to larger body mass and more muscle forces experienced at each consecutive lower spinal level. Busscher et al. compared anatomical dimensions of whole-spine obtained from human and porcine cadavers.<sup>7</sup> In this study, while the endplate width and depth (anteroposterior length) increased from C3 to L5 in human, less increase in width and consistent depth were found in the porcine spine. These findings suggest that increase in endplate area as a function of the distance from C2 is more influenced by increasing body mass in the lower levels in the upright position in humans. Future studies comparing endplate areas of whole-spine of the human and quadrupeds using the same method will be required to test this hypothesis.

One of the limitations of the present study was that the subjects were patients with spinal disorders. The patients who showed primarily lumbar symptoms underwent whole-spine myelography CT for diagnosis of multilevel spinal stenosis; therefore, about 88% of the patients had lumbar disorders. Although noticeable osteophytes were excluded from the endplate area measurements, degenerative change may have affected the quantification of endplate area. Larger variation of the endplate area in the lumbar spine as compared with cervical and thoracic spines in the present study (Fig. 5) may be caused by the presence of lumbar disorders.

Automatic measurement methods of the endplate area and diameter using the 3D endplate model were applied in this study to minimize operator bias and variability in addition to enabling effective measurements. However, there are several procedures in 3D modeling used in the present study which may affect the accuracy of the results. For example, the selection of threshold levels in binarization affects the dimensions of the vertebral body 3D models, and the resolution of CT images and smoothing affect the resulting polygon-mesh surface area. Given that the surface geometry of the endplate can be considered as a microscopic rough surface of a fractal nature, the endplate surface area increases as the resolution increases and smoothing procedures reduce the surface area depending on the smoothing algorithms and parameters employed. Validation of 3D modeling and image-based measurement methods used in this study needs to be accomplished by comparing model-based measurements and direct measurements on cadaveric specimens, which would be the gold-standard methods. Increases of the endplate dimensions along the whole-spine shown in the present study appear to be beneficial for humans in upright positions to sustain the loads applied to the spine effectively. However, the multiple

comparisons of the geometrical parameters within the whole-spine and their changes with age highlighted regional specificities in the whole-spine which does not follow the general rule of increasing size of the endplate in the lower spine. The reduction of the endplate dimensions at T4 and L5-S1 levels may be as a result of geometrical adaption of the adjacent organ. Reduction of the endplate area at L5/S1 may be one of the multifactorial causes of intervertebral disc degeneration. Future studies will be required to understand causes of this regional specificity and whether it is a deleterious or beneficial adaptation for humans.

## CLINICAL SIGNIFICANCE

Information on the endplate area is essential to design spine devices such as artificial discs, interbody devices and their corresponding pre-operative planning. The footprint of these devices on endplate area is important to estimate load transmission through the device. The present study provided endplate areas both from the real 3D surface and the projected area corresponding to the cross sectional area throughout entire spine in different sites (inferior or superior endplates) and both genders. Current imaging techniques have allowed measurements of endplate polygon-mesh surface area using patient-specific 3D models but not the endplate cross sectional area. The 3D polygon surface area to projected surface area ratio provided by the present study allows estimation of relevant cross-sectional area using patient-specific imaging techniques. The present study also provided the data on relative position of the centroid of individual endplate as a distance from C2 which allows for calculation of intervertebral disc height and vertebral body height at each spinal level. These parameters, combined with the projected endplate area can be used for simple estimation of volumes of the intervertebral disc and vertebral body at any spinal levels from C2/C3 through L5/S1 and C3 through L5, respectively. Localized decreases in endplate dimensions at T4 and L5-S1 and their reduction with age at T1-T3 in males were identified in the present study; therefore, caution is urged when selecting implants and surgical procedures. The decrease in endplate area from L5 to S1 may be considered as a risk factor for disc degeneration at this spinal level; however, further investigation is necessary to explain the decrease in endplate area at this level.

## AUTHORS' CONTRIBUTIONS

Research design; acquisition, analysis or interpretation of data: MK, KA, AS, NI. Drafting of manuscript/critical review: MK, KA, NI, AEO. Approval of final version: All authors have read and approved the final submitted manuscript.

## REFERENCES

- Hou Y, Luo Z. 2009. A study on the structural properties of the lumbar endplate: histological structure, the effect of bone density, and spinal level. *Spine* 34:E427–E433.
- Noshchenko A, Plaseied A, Patel VV, et al. 2013. Correlation of vertebral strength topography with 3-dimensional computed tomographic structure. *Spine* 38:339–349.
- Lotz JC, Fields AJ, Liebenberg EC. 2013. The role of the vertebral end plate in low back pain. *Global Spine J* 3:153–164.
- Grant JP, Oxland TR, Dvorak MF. 2001. Mapping the structural properties of the lumbosacral vertebral endplates. *Spine* 26:889–896.
- Moore RJ. 2006. The vertebral endplate: disc degeneration, disc regeneration. *Eur Spine J* 15:S333–S337.
- Wang Y, Battie MC, Videman T. 2012. A morphological study of lumbar vertebral endplates: radiographic, visual and digital measurements. *Eur Spine J* 21:2316–2323.
- Busscher I, Ploegmakers JJ, Verkerke GJ, et al. 2010. Comparative anatomical dimensions of the complete human and porcine spine. *Eur Spine J* 19:1104–1114.
- Chen H, Zhong J, Tan J, et al. 2013. Sagittal geometry of the middle and lower cervical endplates. *Eur Spine J* 22:1570–1575.
- Frobin W, Brinckmann P, Biggemann M, et al. 1997. Precision measurement of disc height, vertebral height and sagittal plane displacement from lateral radiographic views of the lumbar spine. *Clin Biomech (Bristol, Avon)* 12: S1–S63.
- Lakshmanan P, Purushothaman B, Dvorak V, et al. 2012. Sagittal endplate morphology of the lower lumbar spine. *Eur Spine J* 21:S160–S164.
- Mahato NK. 2011. Disc spaces, vertebral dimensions, and angle values at the lumbar region: a radioanatomical perspective in spines with L5-S1 transitions: clinical article. *J Neurosurg Spine* 15:371–379.
- Wang Y, Videman T, Battie MC. 2013. Morphometrics and lesions of vertebral end plates are associated with lumbar disc degeneration: evidence from cadaveric spines. *J Bone Joint Surg Am* 95:e26.
- Zhou SH, McCarthy ID, McGregor AH, et al. 2000. Geometrical dimensions of the lower lumbar vertebrae—analysis of data from digitised CT images. *Eur Spine J* 9:242–248.
- Chen H, Jiang D, Ou Y, et al. 2011. Geometry of thoracolumbar vertebral endplates of the human spine. *Eur Spine J* 20:1814–1820.
- Masharawi Y, Salame K, Mirovsky Y, et al. 2008. Vertebral body shape variation in the thoracic and lumbar spine: characterization of its asymmetry and wedging. *Clin Anat* 21:46–54.
- Otsuka Y, An HS, Ochia RS, et al. 2010. In vivo measurement of lumbar facet joint area in asymptomatic and chronic low back pain subjects. *Spine* 35:924–928.
- Tan SH, Teo EC, Chua HC. 2004. Quantitative three-dimensional anatomy of cervical, thoracic and lumbar vertebrae of Chinese Singaporeans. *Eur Spine J* 13:137–146.
- Hukuda S, Kojima Y. 2002. Sex discrepancy in the canal/body ratio of the cervical spine implicating the prevalence of cervical myelopathy in men. *Spine* 27:250–253.
- Bastir M, Garcia Martinez D, Recheis W, et al. 2013. Differential growth and development of the upper and lower human thorax. *PLoS ONE* 8:e75128.
- Garcia-Martinez D, Recheis W, Bastir M. 2016. Ontogeny of 3D rib curvature and its importance for the understanding of human thorax development. *Am J Phys Anthropol* 159:423–431.
- Kunkel ME, Herkommer A, Reinehr M, et al. 2011. Morphometric analysis of the relationships between intervertebral disc and vertebral body heights: an anatomical and radiographic study of the human thoracic spine. *J Anat* 219:375–387.
- Plomp KA, Vietharsdottir US, Weston DA, et al. 2015. The ancestral shape hypothesis: an evolutionary explanation for

- the occurrence of intervertebral disc herniation in humans. *BMC Evol Biol* 15:68.
23. Whitcome KK. 2012. Functional implications of variation in lumbar vertebral count among hominins. *J Hum Evol* 62:486–497.
  24. Wilke HJ, Geppert J, Kienle A. 2011. Biomechanical in vitro evaluation of the complete porcine spine in comparison with data of the human spine. *Eur Spine J* 20:1859–1868.
  25. Ahlborg HG, Johnell O, Turner CH, et al. 2003. Bone loss and bone size after menopause. *N Engl J Med* 349:327–334.
  26. Ruff CB, Hayes WC. 1988. Sex differences in age-related remodeling of the femur and tibia. *J Orthop Res* 6:886–896.
  27. Seeman E. 2003. Reduced bone formation and increased bone resorption: rational targets for the treatment of osteoporosis. *Osteoporos Int* 14:S2–S8.
  28. Ishihara Y, Espinoza Orias AA, An HS, et al. 2012. Age-related changes in pedicle morphology: correlation with lumbar canal diameter. *ORS Annual Meeting*. Long Beach, CA; p. 1123.
  29. Gilbertson EM. 1975. Development of periarticular osteophytes in experimentally induced osteoarthritis in the dog. A study using microradiographic, microangiographic, and fluorescent bone-labelling techniques. *Ann Rheum Dis* 34: 12–25.

# Safety of anterior chamber paracentesis using a 30-gauge needle integrated with a specially designed disposable pipette

Koji Kitazawa,<sup>1,2,3</sup> Chie Sotozono,<sup>2</sup> Noriko Koizumi,<sup>4</sup> Kenji Nagata,<sup>2</sup> Tsutomu Inatomi,<sup>2</sup> Hiroshi Sasaki,<sup>5</sup> Shigeru Kinoshita<sup>1,3</sup>

<sup>1</sup>Department of Frontier Medical Science and Technology for Ophthalmology, Kyoto Prefectural University of Medicine, Kyoto, Japan

<sup>2</sup>Department of Ophthalmology, Kyoto Prefectural University of Medicine, Kyoto, Japan

<sup>3</sup>Department of Ophthalmology, Baptist Eye Institute, Kyoto, Japan

<sup>4</sup>Faculty of Life and Medical Sciences, Department of Biomedical Engineering, Doshisha University, Kyotanabe, Japan

<sup>5</sup>Department of Ophthalmology, Kanazawa Medical University, Ishikawa, Japan

**Correspondence to** Professor Shigeru Kinoshita, Department of Frontier Medical Science and Technology for Ophthalmology, Kyoto Prefectural University of Medicine, 465 Kajii-cho, Hirokoji-agaru, Kawaramachi-dori, Kamigyo-ku, Kyoto 602-0841, Japan; shigeruk@koto.kpu-m.ac.jp

Received 11 September 2016  
Revised 8 December 2016  
Accepted 25 December 2016  
Published Online First  
18 January 2017

## ABSTRACT

**Aims** To investigate the safety of anterior chamber (AC) paracentesis using a 30-gauge needle integrated with a specially designed disposable pipette.

**Methods** In this retrospective observational case-series study, AC paracentesis was performed on 301 eyes of 301 patients between September 2009 and August 2016 at the Department of Ophthalmology, Kyoto Prefectural University of Medicine and the Baptist Eye Institute, Kyoto, Japan. AC paracentesis was performed with the patient placed in the supine position using a 30-gauge needle integrated with a disposable pipette with one hand, and the safety post procedure was then evaluated.

**Results** The indications for AC paracentesis were virus detection (ie, corneal endothelitis, anterior infectious uveitis, cytomegalovirus retinitis and acute retinal necrosis) in 264 eyes, bacterial detection (ie, endophthalmitis) in 8 eyes and malignancy (ie, primary intraocular lymphoma, leukaemia and retinoblastoma) in 29 eyes. No serious complications such as infection, hyphema, lens trauma or severe inflammation including hypopyon and AC fibrin formation were observed.

**Conclusions** Our findings show that AC paracentesis with a disposable pipette is safe with no severe complications.

## INTRODUCTION

Anterior chamber (AC) paracentesis is widely performed for the diagnosis of infectious uveitis<sup>1, 2</sup> and involves a comprehensive PCR being performed on an aqueous humour sample obtained to detect infectious antigen DNA and to assist with the diagnosis of infectious ocular diseases.<sup>3, 4</sup>

AC paracentesis using a 27 gauge (G) or 30 G needle on a tuberculin syringe is commonly performed. However, it requires that strict attention be paid to the length of the needle and the insertion angle in order to avoid touching the iris or lens. Various AC paracentesis-related complications have been reported, including trauma to the cornea, iris and lens, as well as hyphema,<sup>1</sup> corneal abscess<sup>5</sup> and endophthalmitis.<sup>6</sup>

In this study, we investigated the safety of AC paracentesis using a 30 G needle integrated with a specially designed disposable pipette.

## METHODS

### Subjects

This retrospective, observational case series was conducted at the Department of Ophthalmology, Kyoto Prefectural University of Medicine and the Baptist

Eye Institute, Kyoto, Japan, and was approved by the Institutional Review Board of Kyoto Prefectural University of Medicine. All study procedures were conducted in accordance with the tenets of the Declaration of Helsinki, and informed consent was obtained from all patients post detailed explanation of the study protocols. Clinical trial registration was obtained from UMIN (UMIN000021877; <http://www.umin.ac.jp/english/>).

This study involved patients who visited the Kyoto Prefectural University of Medicine or Baptist Eye Institute between September 2009 and August 2016. The recorded patient-related characteristics, including gender, age, pupil status, lens status and indications for AC paracentesis, were examined (table 1).

## AC paracentesis procedure

All procedures were performed under a microscope in an outpatient clinic and involved the use of a commercially available 30 G needle integrated with a specially designed disposable pipette (Nipro, Osaka, Japan) (figure 1A). The length of the exposed part of the needle is 4 mm. After topical anaesthesia, each patient was placed in a supine position on the bed in the outpatient clinic and the ocular surface was rinsed with povidone-iodine and sterile saline solution. All of the procedures were carefully undertaken using aseptic techniques to avoid any contamination. The paracentesis was inserted into the AC through the corneal limbus at a horizontal angle on the temporal side, paying attention to avoid contact with the patient's eyelashes, lens or iris when squeezing the bulb under a microscope. A 50–150 µL volume of aqueous humour was then spontaneously and slowly aspirated into the pipette when pressure was released from the bulb. The maximum of bulb volume to be aspirated was appropriately designed to be <300 µL to avoid the AC collapse (figure 1B). At the end of the procedure, the povidone-iodine was rinsed out with sterile saline solution. Complications secondary to paracentesis were evaluated within 3 months postoperative.

## RESULTS

A total of 301 eyes of 301 patients (169 males, 132 females; mean age: 61.4±16.7 years) were enrolled. At AC paracentesis, 173 of the 301 patients had dilated pupils. Indications for AC paracentesis were virus detection for anterior or posterior uveitis (264 eyes), bacteria detection for endophthalmitis (8 eyes) and malignancy (29 eyes)



CrossMark

**To cite:** Kitazawa K, Sotozono C, Koizumi N, et al. *Br J Ophthalmol* 2017;101:548–550.



**Table 1** Demographic characteristics of the patients

Gender, n (%)	
Male	169 (56.1)
Female	132 (43.9)
Mean age (SD)	61.4±16.7
Pupil status, n (%)	
Dilated pupil	173 (57.5)
Constricted pupil	128 (42.5)
Lens status, n (%)	
Phakia	188 (62.7)
Pseudophakia	113 (37.3)
Indication for paracentesis, n (%)	
Virus detection	264 (87.7)
Bacteria detection	8 (2.7)
Malignancy	29 (9.6)
Complication, n (%)	
Endophthalmitis	0 (0)
Corneal abscess	0 (0)
Lens trauma	0 (0)
Hyphema	0 (0)
AC fibrin formation	0 (0)
Hypopyon	0 (0)

AC, anterior chamber.

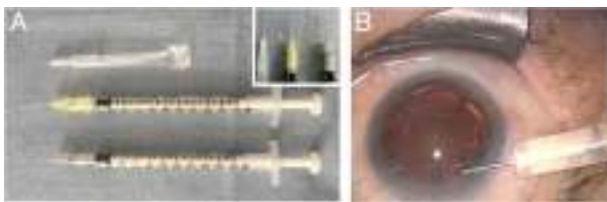


**Figure 1** Image showing the anterior chamber (AC) paracentesis procedure. (A) Comparison of needle length and pipette design. The length of 30-gauge (G) needle with the disposable pipette (4 mm) is shorter than that of the 27 G and 30 G needles (19 mm), and the total length of the disposable pipette is less than half of that of a tuberculin syringe (top). The 30 G needle integrated with the disposable pipette (middle). A 30 G needle attached to a tuberculin syringe (bottom). A 27 G needle attached to a tuberculin syringe. (B) The AC paracentesis was inserted into the AC through the corneal limbus at a horizontal angle, paying strict attention to avoid contact with the patient's eyelashes, lens and iris while squeezing the bulb at the head of the device.

(table 1). Anterior or posterior uveitis included corneal endotheliitis (122 eyes) and iridocyclitis (108 eyes) due to human simplex virus (HSV), varicella zoster virus (VZV), cytomegalovirus retinitis (25 eyes) and acute retinal necrosis (9 eyes). Malignancy included primary intraocular lymphoma (27 eyes), leukaemia (1 eye) and retinoblastoma (1 eye).

### Analysis of safety post AC paracentesis

No serious postoperative complications such as endophthalmitis, corneal abscess, hyphema, lens trauma and severe inflammation including AC fibrin formation and hypopyon were noted (table 1).

### DISCUSSION

In most AC paracentesis cases, a 27 G or 30 G needle on a tuberculin syringe is used, which requires to pull a plunger. However, we used a short 30 G needle combined with a disposable pipette with a squeeze bulb located at its head, thus

allowing the aqueous humour sample to be drawn from the patient using one hand. Potential risks after AC paracentesis include infection, hyphema, cataract formation and severe intraocular inflammation including AC fibrin formation and hypopyon; however, none of the 301 patients had serious post-operative complications. O'Rourke developed an aqueous pipette consisting of a short 30 G needle mounted inside plastic tubing,<sup>7</sup> and Wertheim also reported the 'minim' technique for diagnosing AC paracentesis.<sup>8</sup> Compared with a conventional syringe, the O'Rourke pipette and the minim technique, our pipette is designed with a shorter needle and is easier to control, and this modification decreases the risks of lens trauma and hyphema. Our pipette integrated with a needle offers the advantage of producing no dead space, which allows for the aqueous humour to be obtained efficiently, even in cases with a shallow AC. In fact, in the case of a tumour biopsy, although it could increase the risk of metastases due to the potential for tumour-cell transference to other tissues, AC paracentesis using this pipette was performed safely and was able to detect non-metastatic retinoblastoma tumour cells, thus leading to the judgement of enucleation.<sup>9</sup>

Recent developments in imaging technologies, such as optical coherence tomography, have enabled ophthalmologists to make more precise disease diagnoses.<sup>10–11</sup> However, the diagnosis of tumour and uveitis often require an AC paracentesis to be performed to detect the causative pathogen. For patients with uveitis of unknown origin, multiplex PCR is known to be useful for obtaining a correct diagnosis, as it can detect a small amount of virus and bacteria from the aqueous humour via DNA amplification.<sup>4–12–13</sup> Using PCR analysis of aqueous humour samples, we previously discovered that cytomegalovirus was the causative pathogen in patients with repeated corneal endotheliitis.<sup>14–15</sup> Thus, those findings indicate that AC paracentesis is a useful diagnostic tool.

In conclusion, our findings show that a short 30 G needle integrated with a disposable pipette is a safe device for obtaining aqueous humour without complications.

We hope that aqueous humour examinations will become widely performed in the future to improve the diagnosis and the understanding of pathophysiology in patients according to the detection virus/bacteria DNA or tumour cells and also the prognostic and predictive biomarkers of diseases.

**Acknowledgements** The authors wish to thank John Bush for editing the manuscript.

**Contributors** Conception and design of the study (KK, SK), collection of data (KK, NK, KN, TI, CS, SK), management of data (KK), analysis of data (KK), interpretation of data (KK), writing of the article (KK, SK), approval of the manuscript (KK, CS, NK, KN, TI, HS, SK) and searching the literature (KK).

**Funding** This research was partially supported in part by Research Funds from the Kyoto Foundation for the Promotion of Medical Science.

**Competing interests** None declared.

**Patient consent** Obtained.

**Ethics approval** Kyoto Prefectural University of Medicine.

**Provenance and peer review** Not commissioned; externally peer reviewed.

### REFERENCES

- 1 Van der Lelij A, Rothova A. Diagnostic anterior chamber paracentesis in uveitis: a safe procedure? *Br J Ophthalmol* 1997;81:976–9.
- 2 Trivedi D, Denniston AK, Murray PI. Safety profile of anterior chamber paracentesis performed at the slit lamp. *Clin Experiment Ophthalmol* 2011;39:725–8.
- 3 Shoughy SS, Alkatan HM, Al-Abdullah AA, et al. Polymerase chain reaction in unilateral cases of presumed viral anterior uveitis. *Clin Ophthalmol* 2015;9:2325–8.

- 4 Sugita S, Ogawa M, Shimizu N, *et al.* Use of a comprehensive polymerase chain reaction system for diagnosis of ocular infectious diseases. *Ophthalmology* 2013;120:1761–8.
- 5 Azuara-Blanco A, Katz LJ. Infectious keratitis in a paracentesis tract. *Ophthalmic Surg Lasers* 1997;28:332–3.
- 6 Helbig H, Noske W, Kleinedam M, *et al.* Bacterial endophthalmitis after anterior chamber paracentesis. *Br J Ophthalmol* 1995;79:866.
- 7 O'Rourke J, Taylor DM, Wang Y. Compact bulb pipette simplifies paracentesis. *Ophthalmic Surg Lasers Imaging* 2004;35:172–3.
- 8 Wertheim MS, Connell PP, Majid MA, *et al.* The minim technique for diagnostic anterior chamber paracentesis. *Eye (Lond)* 2009;23:1491.
- 9 Kitazawa K, Nagata K, Yamanaka Y, *et al.* Diffuse anterior retinoblastoma with sarcoidosis-like nodule. *Case Rep Ophthalmol* 2015;6:443–7.
- 10 Adhi M, Duker JS. Optical coherence tomography—current and future applications. *Curr Opin Ophthalmol* 2013;24:213–21.
- 11 Kitazawa K, Yokota I, Sotozono C, *et al.* Measurement of corneal endothelial surface area using anterior segment optical coherence tomography in normal subjects. *Cornea* 2016;35:1229–33.
- 12 Sugita S, Ogawa M, Inoue S, *et al.* Diagnosis of ocular toxoplasmosis by two polymerase chain reaction (PCR) examinations: qualitative multiplex and quantitative real-time. *Jpn J Ophthalmol* 2011;55:495–501.
- 13 Sugita S, Shimizu N, Watanabe K, *et al.* Use of multiplex PCR and real-time PCR to detect human herpes virus genome in ocular fluids of patients with uveitis. *Br J Ophthalmol* 2008;92:928–32.
- 14 Koizumi N, Yamasaki K, Kawasaki S, *et al.* Cytomegalovirus in aqueous humor from an eye with corneal endotheliitis. *Am J Ophthalmol* 2006;141:564–5.
- 15 Koizumi N, Inatomi T, Suzuki T, *et al.* Clinical features and management of cytomegalovirus corneal endotheliitis: analysis of 106 cases from the Japan corneal endotheliitis study. *Br J Ophthalmol* 2015;99:54–8.

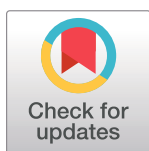
RESEARCH ARTICLE

# Chronological Profiling of Plasma Native Peptides after Hepatectomy in Pigs: Toward the Discovery of Human Biomarkers for Liver Regeneration

Kohta Iguchi<sup>1</sup>, Etsuro Hatano<sup>1\*</sup>, Takashi Nirasawa<sup>2</sup>, Noriyuki Iwasaki<sup>2</sup>, Motohiko Sato<sup>1</sup>, Gen Yamamoto<sup>1</sup>, Kenya Yamanaka<sup>1</sup>, Tatsuya Okamoto<sup>1</sup>, Yosuke Kasai<sup>1</sup>, Naohiko Nakamura<sup>1</sup>, Hiroaki Fuji<sup>1</sup>, Tomohito Sakai<sup>3</sup>, Nobuto Kakuda<sup>4</sup>, Satoru Seo<sup>1</sup>, Kojiro Taura<sup>1</sup>, Kei Tashiro<sup>3</sup>, Shinji Uemoto<sup>1</sup>, Masaya Ikegawa<sup>3,4\*</sup>

**1** Department of Surgery, Graduate School of Medicine, Kyoto University, Kyoto, Japan, **2** Bruker Daltonics K. K., Yokohama, Japan, **3** Department of Genomic Medical Sciences, Kyoto Prefectural University of Medicine, Graduate School of Medical Science, Kyoto, Japan, **4** Department of Life and Medical Systems, Faculty of Life and Medical Sciences, Doshisha University, Kyoto, Japan

\* [etsu@kuhp.kyoto-u.ac.jp](mailto:etsu@kuhp.kyoto-u.ac.jp) (EH); [mikegawa@mail.doshisha.ac.jp](mailto:mikegawa@mail.doshisha.ac.jp) (MI)



## OPEN ACCESS

**Citation:** Iguchi K, Hatano E, Nirasawa T, Iwasaki N, Sato M, Yamamoto G, et al. (2017) Chronological Profiling of Plasma Native Peptides after Hepatectomy in Pigs: Toward the Discovery of Human Biomarkers for Liver Regeneration. PLoS ONE 12(1): e0167647. doi:10.1371/journal.pone.0167647

**Editor:** Jyotshna Kanungo, National Center for Toxicological Research, UNITED STATES

**Received:** August 2, 2016

**Accepted:** November 17, 2016

**Published:** January 6, 2017

**Copyright:** © 2017 Iguchi et al. This is an open access article distributed under the terms of the [Creative Commons Attribution License](https://creativecommons.org/licenses/by/4.0/), which permits unrestricted use, distribution, and reproduction in any medium, provided the original author and source are credited.

**Data Availability Statement:** All relevant data are within the paper and its Supporting Information files.

**Funding:** This study was supported by Translational Research Grant from Translational Research Center, Kyoto University Hospital, <http://www.kuhp.kyoto-u.ac.jp/~trc/>, EH received the funding. The funder had a role in purchase of animals.

## Abstract

Liver regeneration after partial hepatectomy (PHx) is a time-dependent process, which is tightly regulated by multiple signaling cascades. Failure of this complex process leads to posthepatectomy liver failure (PHLF), which is associated with a high rate of mortality. Thus, it is extremely important to establish a useful biomarker of liver regeneration to help prevent PHLF. Here, we hypothesized that alterations in the plasma peptide profile may predict liver regeneration following PHx and hence we set up a diagnostic platform for monitoring posthepatectomy outcome. We chronologically analyzed plasma peptidomic profiles of 5 partially hepatectomized microminipigs using the ClinProt™ system, which consists of magnetic beads and MALDI-TOF/TOF MS. We identified endogenous circulating peptides specific to each phase of the postoperative course after PHx in pigs. Notably, peptide fragments of histones were detected immediately after PHx; the presence of these fragments may trigger liver regeneration in the very acute phase after PHx. An N-terminal fragment of hemoglobin subunit  $\alpha$  (3627  $m/z$ ) was detected as an acute-phase-specific peptide. In the recovery phase, the short N-terminal fragments of albumin (3028, 3042  $m/z$ ) were decreased, whereas the long N-terminal fragment of the protein (8926  $m/z$ ) was increased. To further validate and extract phase-specific biomarkers using plasma peptidome after PHx, plasma specimens of 4 patients who underwent PHx were analyzed using the same method as we applied to pigs. It revealed that there was also phase-specificity in peptide profiles, one of which was represented by a fragment of complement C4b (2378  $m/z$ ). The strategy described herein is highly efficient for the identification and characterization of peptide biomarkers of liver regeneration in a swine PHx model. This strategy is feasible for application to human biomarker studies and will yield clues for understanding liver regeneration in human clinical trials.

**Competing Interests:** We disclose that Bruker Daltonics K.K.'s contribution was purely scientific and technological. There is no financial nor material contribution toward this study. This does not alter our adherence to PLOS ONE policies on sharing data and materials.

## Introduction

Liver regeneration is a complex event and is tightly regulated by multiple signaling mechanisms that become activated in a time-dependent fashion [1]. To study the mechanisms underlying liver regeneration, partial hepatectomy (PHx), resulting in the removal of approximately 70% of the liver, has been widely utilized in experimental animals such as mice, rats, and pigs. In rats, the first peak of DNA synthesis in hepatocytes occurs at about 24 hours (h), with a smaller peak between 36–48 h. After that, the new vascular branches are formed, the extracellular matrix is synthesized, and finally, normal liver histology is reestablished 8–10 days after PHx [2]. During this time-dependently regulated process, posthepatectomy liver failure (PHLF), which results from a failure of liver regeneration, develops with high incidence in patients after PHx [3]. PHLF occurs when patients with poor liver function are exposed to excessive surgical stress including extensive blood loss or massive hepatectomy. The symptoms of PHLF include prolonged fluid retention and coagulation disorders within a week after PHx, and it is closely associated with postoperative mortality [4]. Thus, it is crucial to establish biomarkers of liver regeneration to improve the surgical outcomes of patients with liver diseases.

In recent years, mass-spectrometry (MS)-based protein identification has enabled us to map the liver-tissue specific proteome in combination with tissue-specific gene expression and antibody-based immunohistochemistry [5]. Because no less than 33% of the proteins expressed in the liver are classified as secreted proteins [5], serum or plasma is expected to become a promising source of biomarkers of liver diseases. Prior efforts in the search for serum and plasma protein biomarkers utilized gel-based separation technologies, which cannot readily separate and distinguish molecules of less than 10 kDa in size [6]. The application of MS to analyze such a low molecular weight range of molecules in blood has succeeded in providing disease-specific peptide signatures in patients with various cancers originating from ovary, prostate, breast, pancreas, and liver [7–11]. Precisely defining the chronological changes in the peptide profile of plasma following PHx using MS approach might also provide a sensitive biomarker of liver regeneration that cannot be detected using transcriptome-based or antibody-based approaches.

In the present study, we performed plasma peptidomic analyses after 70% PHx in pigs, which closely resemble man in anatomy, physiology, and genetics [12]. For detecting plasma peptides, we applied a magnetic bead separation and matrix-assisted laser desorption/ionization time-of-flight (MALDI-TOF) MS approach, which is a robust, precise, and rapid technique for the investigation of complex blood samples with a detection range of 12 orders of magnitude in protein abundance [13, 14]. The patterns of endogenous peptides circulating in plasma were chronologically analyzed and representative markers of each phase after PHx were identified. The postoperative course after PHx could be clearly delineated by the plasma peptidomic pattern. Finally, this strategy was successfully applied to clinical samples, and some native peptides that could be useful in monitoring the postoperative course were identified.

## Materials and Methods

### Animals

Five female specific pathogen-free microminipigs aged 1.5–2.0 years and weighing 20–22 kg were obtained from Fuji Micra (Shizuoka, Japan) [15]. Three pigs were used as a first cohort and the remaining 2 as a second cohort. After an overnight fast, pigs were sedated with xylazine HCl (0.3 mg/kg), midazolam (0.2 mg/kg), and atropine sulfate (0.025 mg/kg) intramuscularly, and intratracheal intubation was performed. Under general anesthesia with a mixture of oxygen/air (FiO<sub>2</sub> 0.4) and sevoflurane (1–1.5%), a 70% PHx procedure (removal of the left



lateral lobe and medial lobe of the liver) was successfully performed. The pigs were housed in cages under a 12:12-h light/dark cycle at 22°C. The physical conditions of the animals were checked every day until postoperative day 7 (168 h), when they underwent laparotomy under general anesthesia. After sampling of blood and liver, the animals were euthanized by cutting the inferior vena cava under deep anesthesia using sevoflurane. If abnormal symptoms such as general fatigue, decreased activity, frequent vomiting, or respiratory distress were observed, the pigs were euthanized before the predetermined day. As a result, all animals showed uneventful postoperative course until postoperative day 7. The remnant liver exhibited good regeneration with ~3-fold increase in its volume [16]. Blood samples were collected before (pre), at 0 minutes (min) and at 1, 3, 6, 24, 48, 72, 96, 120, 144, and 168 h after PHx through a central venous (CV) catheter cannulated in the right external jugular vein. Blood samples from portal vein (PV) were also collected before, at 0 min, and at 1, 3, and 168 h after PHx through a PV catheter cannulated from the jejunal branch of the superior mesenteric vein. The blood samples for plasma were collected into blood collection tubes containing 3.2% (w/v) sodium citrate. Serum and plasma were collected after centrifugation of blood samples at 2190 and 1720 × g for 10 min, respectively, and were stored at −80°C for later measurements. All animal experiments were conducted under a protocol approved by the animal research committee of Kyoto University (reference number: Med Kyo 14243), and all animals were cared for in accordance with Guide for the Care and Use of Laboratory Animals from the National Institutes of Health (USA).

## Human Samples

Plasma samples of 10 patients who underwent PHx at Kyoto University Hospital in 2014 were prospectively collected. To search for biomarkers of normal liver regeneration after major hepatectomy, 4 patients were analyzed; these patients underwent major hepatectomy without pathological liver fibrosis (F0 or F1) [17], and had an uneventful postoperative course with normal liver regeneration (S1 Table). Major hepatectomy refers to resection of more than 3 segments defined according to Couinaud's classification [18]. Blood samples were collected from peripheral veins at 0 min, 24, 48, and 168 h after PHx. Sample preparation and data measurement were performed using the same method as we applied to pigs, as described below. This study was approved by the Ethics Committee of Graduate School and Faculty of Medicine Kyoto University (C-512). Written informed consent was acquired from all patients.

## Peptide Purification with Magnetic Beads

A 3-μl aliquot of the serum or plasma was purified using magnetic beads based on hydrophobic interaction chromatography (C8-coated magnetic beads, MB-HIC, Bruker Daltonics GmbH, Bremen, Germany). The C8 magnetic beads are superparamagnetic, silica-based particles, and are surface-derivatized with common reversed-phase ligands of 8 carbon alkyl chains. In brief, 3 μl of the serum or plasma was diluted with 10 μl of binding buffer (MB-HIC kit, Bruker), followed by the addition of 5 μl of magnetic beads. The solution was then carefully mixed by pipetting in and out five times. After 1 min, the supernatant was separated from the magnetic beads in a magnetic separator. This was followed by 3 washing steps with 100 μl of wash buffer (MB-HIC kit, Bruker), and the supernatant was removed each time. After 1 min in 10 μl of elution buffer (stabilization buffer (MB-HIC kit, Bruker) in 50% acetonitrile), the magnetic beads were separated in the magnetic separator from the elution buffer. For MS analysis, 1 μl of the bead eluate was mixed with 10 μl of matrix solution (0.3 g/l α-cyano-4-hydroxycinnamic acid (Bruker) in 2:1 ethanol/acetone), and 1 μl of the mixture was then spotted in quadruplicate on an MTP AnchorChip 600/384 target (Bruker). All these processes were performed with the aid of ClinProt Robot (Bruker). Trypsin digestion was not performed.

## Mass Spectrometry

Samples applied to the AnchorChip were analyzed using an AutoFlex<sup>TM</sup> II MALDI-TOF MS operating in positive-ion linear mode (Bruker). To generate a mass spectrum, 1500 laser shots were acquired from random positions for each matrix spot. Four independent spectra were acquired for each spot. Acquisition was controlled by flexControl 3.0 software (Bruker) using the AutoXecute function and fuzzy control of laser intensity. The analysis was performed at mass to charge ratio ( $m/z$ ) of 2000–20000 and a signal-to-noise threshold of 5. Spectra were externally calibrated using a mixture of standardized protein/peptide calibrants (ClinProt Standard, Bruker).

## Statistical Analysis

The resulting spectra were analyzed using ClinProTools 2.2 bioinformatic software (Bruker) [19]. ClinProTools was used to carry out comparative analysis of peak intensities between postoperative days and to calculate corresponding statistics. When comparing 2 and more than 2 groups, we used the Wilcoxon–Mann–Whitney test or the Kruskal–Wallis test, respectively. In ClinProTools, a receiver operating characteristic (ROC) curve was generated for each peak within peak calculation for separating 2 groups. The area and the intensity of the peak represented the threshold that was used to reach the separation into 2 groups. Multivariate analysis techniques, including principal component analysis (PCA) and the support vector machine (SVM) algorithm were employed to extract, display, and rank the variance within each data set. PCA selects the principal components (PCs) that can separate the samples into homogeneous clusters and can be visualized in 3-dimensional plots in which calculated values for the top PCs serve as  $x$ ,  $y$ , and  $z$  axes [20]. The SVM algorithm, another machine-learning approach, was applied to the mass data to select clusters of signals able to discriminate between groups [19]. ClinProTools identified several features as useful for classifying 2 time points automatically by determining the best number of peaks (up to 25 peaks) to be integrated in the model by an internal iteration. Cross-validation accuracy is the percentage of data correctly classified. In pig experiments, peptidomic pattern analyses including PCA and SVM were performed and representative peaks were detected in the first cohort. In the second cohort, those peaks were validated. Multiple experiments were performed and representative data were shown in the figures. The mass numbers of proteins were described as average values with possible distribution of  $\pm 3$  Da.

## Reversed Phase-High Performance Liquid Chromatography (RP-HPLC)

Prior to RP-HPLC fractionation, the C8-purified eluate samples were mixed with 20  $\mu$ l of 0.1% (v/v) trifluoroacetic acid and centrifuged in a vacuum to remove organic solvent. A 10- $\mu$ l sample was injected in every run. RP-HPLC separations were performed using an easy-nLC II nanoHPLC system (Bruker) equipped with a PepSwift<sup>TM</sup> Monolithic PS-DVB column (0.2  $\times$  50 mm, Dionex, Osaka, Japan). Solvent A was 0.1% (v/v) trifluoroacetic acid in Milli-Q<sup>®</sup> purified water, and Solvent B was 100% acetonitrile. The flow rate was 900 nl/min. The following gradient was used for 0–60 min; 5–50% B, 60–61 min; 50–95% B, 61–64 min; 95% B constant. The HPLC eluent was mixed with LC-MALDI matrix ( $\alpha$ -cyano-4-hydroxycinnamic acid) at the flow rate of 1.67  $\mu$ l/min via MicroTee fittings (Upchurch Scientific, Oak Harbor, WA, USA), then deposited on an MTP AnchorChip 384 target with a spot pitch of 800  $\mu$ m (Chip 0) by a PROTEINEER fc II<sup>TM</sup> fraction collector (Bruker). Sample spots were deposited every 15 s, and a total of 248 spots were collected for each HPLC run. Calibration samples were manually spotted on calib. Anchor position (Chip 1) to use automatic calibration processing.

## MS/MS-based Sequencing and Identification

Automatic MS/MS experiments were performed using an ultrafleXtreme<sup>TM</sup> MALDI-TOF/TOF MS (Bruker). Spot selection, automatic MS/MS mass filtering, and Mascot database searching (ver. 2.4.1, Matrix Science, Boston, MA, USA) were commanded by WARP-LC 1.3 (Bruker). Data processing and assessment of MS/MS results were performed using ProteinScape<sup>TM</sup> 3.1 (Bruker). For measurement, MS spectra were automatically acquired on the ultrafleXtreme<sup>TM</sup> instrument in the positive reflector mode under the control of Compass 1.3 and WARP-LC 1.3 software (Bruker), and automatic MS calibration processing was controlled by the AutoXecute function. The detection range was 1000–4000 *m/z*. Detected peptide compounds with a signal-to-noise ratio higher than 10 were automatically subjected to LIFT<sup>TM</sup>-TOF/TOF experiments triggered with WARP-LC [21]. After each measurement, queries were automatically transferred to the ProteinScape 3.1 server. Database searches were also automatically achieved using an in-house Mascot server. Mascot search conditions were as follows; Database: SwissProt, Taxonomy: other Mammalia, Enzyme: none, Modifications: Acetyl (K), Delta: H (2) C (2), Methyl (K), Oxidation (M), Phospho (ST), tolerance: 50 ppm in MS, 0.8 Da in MS/MS.

## Results

### Discrimination of Plasma Peptide Profiles among Postoperative Time Points

PCA showed that each successive timing was clearly separated by 3 PCs (0 min vs. 24 h, 24 h vs. 48 h, 96 h vs. 120 h, 120 h vs. 168 h) except 48 h vs. 72 h, and 72 h vs. 96 h. (Fig 1) This suggests that the peptide profile in plasma dramatically changed during each perioperative period as defined above, reflecting the physiological process of liver regeneration after PHx.

### Classification of Postoperative Time Course by SVM

The lower left half of Fig 2 showed the results of cross-validation analyses in which generated SVM models were used to compare every 2 groups. For example, the spectra patterns at 1 and 3 h were not clearly separated, having a cross-validation accuracy of 57.5%. However, those at 6 and 24 h were quite different, with a cross-validation accuracy of 98.0%. Of note, studying the heat map diagonally from upper left to lower right revealed that the plasma peptidome changed in a biphasic manner after PHx. High cross-validation accuracy was detected at 2 phases, including around 24 h and 120 h. Based on these results, we defined the time points of around 24 h and 120 h as the acute and recovery phases, respectively.

Comparative analysis of spectra between groups revealed a number of peaks with significant differences in intensity. The right upper half of Fig 2 detailed the top 2 peaks enabling discrimination between every 2 groups. For example, when we compared the samples taken at 1 and 96 h after PHx, the peaks whose abundance was most different between these time points were at 8926 and 3852 *m/z*. Liquid chromatography-matrix-assisted laser desorption/ionization time-of-flight tandem mass spectrometry (LC-MALDI-TOF/TOF MS) analysis identified several peptides, including albumin (ALB; blue letters in Fig 2) and hemoglobin subunit  $\alpha$  (HBA; red letters in Fig 2). This result suggests that peptide fragments of HBA and ALB were the representative peaks in the acute and recovery phases, respectively.

### Marker Peak Extraction by ROC Curve Analysis

To clarify single peaks as representative markers of the acute and recovery phases, ROC curve analysis was performed to compare 0 min vs. 24 h, and 24 h vs. 120 h. (Table 1) This revealed

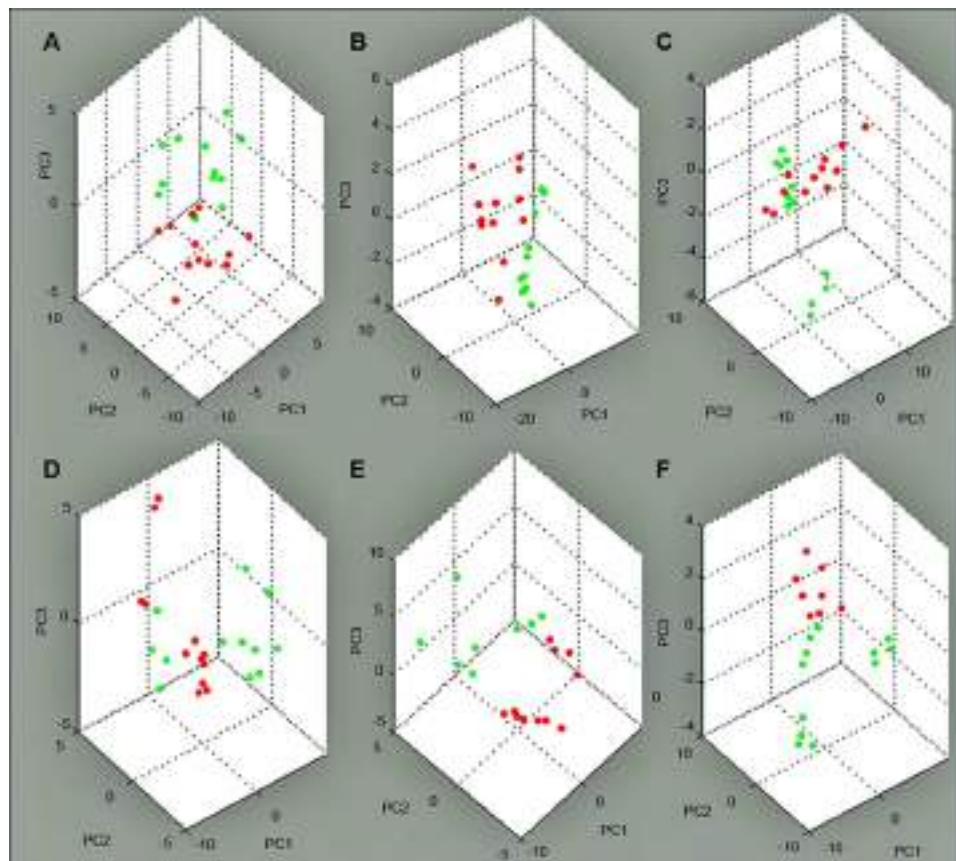


**Fig 1. Representation of the principal components generated from the data set of a first cohort.** (A) 0 min (red) vs. 24 h (green), (B) 24 h (red) vs. 48 h (green), (C) 48 h (red) vs. 72 h (green), (D) 72 h (red) vs. 96 h (green), (E) 96 h (red) vs. 120 h (green)\*, (F) 120 h (red)\* vs. 168 h (green). For each plasma sample, 4 measurements were automatically performed. The detailed data used for the analysis were provided as pseudogel and stack view of the spectra in [S1 Fig](#). \*Three pigs were analyzed, except at 120 h, at which time point data were missing for 1 pig. PC, principal component.

doi:10.1371/journal.pone.0167647.g001

that the peaks at 3627, 4160, 8327, and 9089  $m/z$  had the highest area under the curve (AUC) values during the acute phase, while the peaks at 3028, 3042, 3627, 6929, 8327, and 8926  $m/z$  had the highest AUC values during the recovery phase. This result was validated by the second cohort analysis. Among these discriminatory peaks, those at 3627 and 8926  $m/z$  showed the highest AUC values during the acute and recovery phases, respectively. LC-MALDI-TOF/TOF MS analysis identified the peaks at 3627 and 8926  $m/z$  as the N-terminal fragment of HBA (position: 1–36) and ALB (position: 25–103), respectively.

### Other Marker Peak Candidates with Characteristic Alterations

When 6 time points (pre, 0 min, and 24, 48, 120, and 168 h) were compared, several peaks were determined to become useful classifiers of the perioperative time points ([Fig 3](#)). In the first cohort analysis, the peaks at 3000 and 3028  $m/z$  were down-regulated in the recovery phase; the peaks at 8926, 4128, 4460, and 5539  $m/z$  were up-regulated in the recovery phase; and the peaks at 3627, 4160, and 8327  $m/z$  were down-regulated in the acute phase. These observations were fully replicated in the second cohort. Among the detected peaks, the peaks at 3000 and 3028  $m/z$  were identified as short N-terminal fragments of ALB (position: 25–49



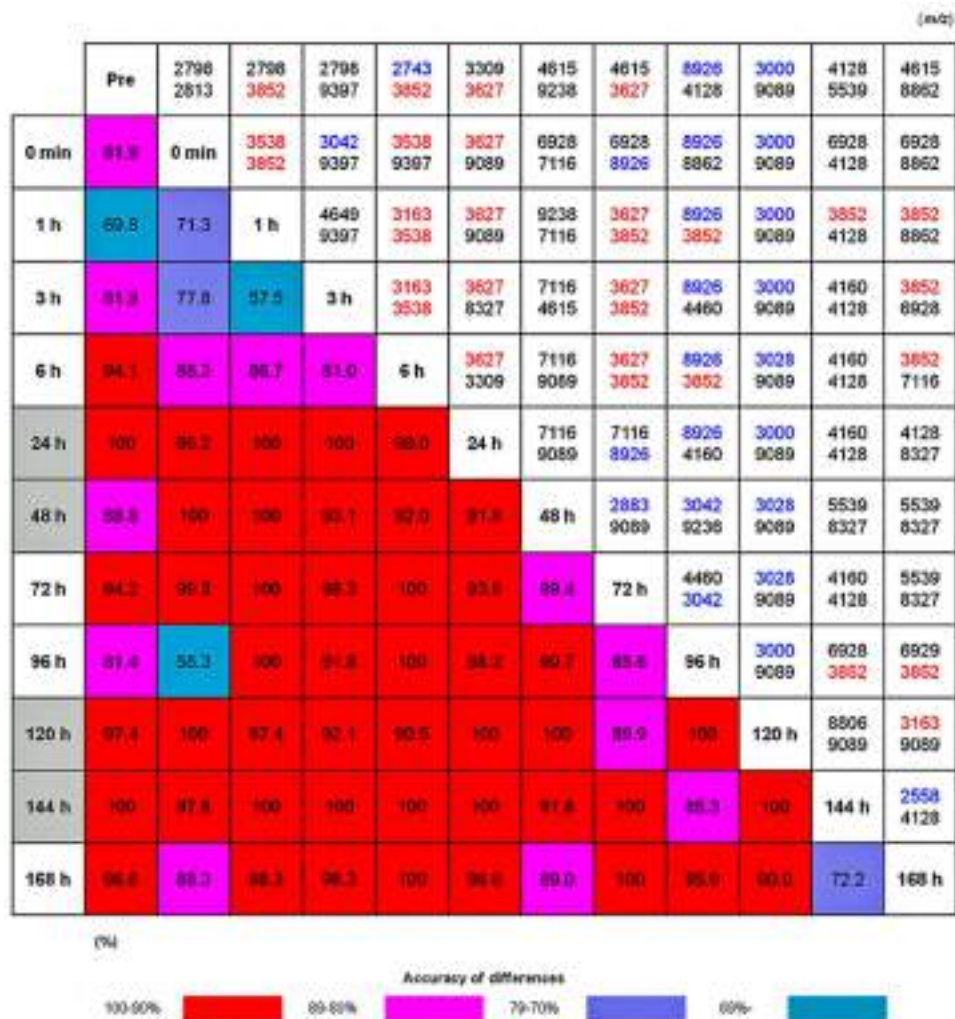


**Fig 2. Heat map of the SVM analysis to differentiate each time point after PHx.** The lower left half of the figure provides the results of cross-validation analyses to estimate the success rate of the SVM model in separating user-defined groups of spectra. The accuracy is denoted by color: 100–90% (red); 89–80% (pink); 79–70% (purple), and < 69% (blue). The upper right half of the figure describes the *m/z* of the top 2 peaks that most efficiently discriminated each time point with statistical significance. The detailed data used for the analysis were provided as pseudogel and stack view of the spectra in S1 Fig, and the statistical data were as S2 Table. The identified albumin peaks are shown in blue (2558: 25–45\*<sup>1</sup>; 2743: 26–48; 2883: 25–48\*<sup>2</sup>; 3000: 25–49\*<sup>3</sup>; 3028: 25–49\*<sup>4</sup>, 3042: 25–50, 8926: 25–103), and the hemoglobin subunit α is shown in red (3163: 1–32; 3538: 110–141; 3627: 1–36; 3852: 107–141). \*<sup>1</sup>: Ala->Pro: 4, \*<sup>2</sup>: Ala->Pro: 20, \*<sup>3</sup>: Gly -> Ser: 22, \*<sup>4</sup>: Q -> deamidated: 18, SVM, support vector machine; *m/z*, mass to charge ratio.

doi:10.1371/journal.pone.0167647.g002

amino acids), and the peak at 8926 *m/z* was a long N-terminal fragment of ALB (position: 25–103 amino acids). This result suggests that different peptide fragments, even those derived from the same protein, show different patterns of change after PHx.

## Comprehensive Identification of Swine Plasma Peptides after PHx by LC-MALDI-TOF/TOF MS

To further identify the circulating peptides at various time points following 70% PHx, we performed a comprehensive identification analysis using the C8-purified eluate of the plasma

**Table 1. AUC determined by ROC curve analysis for each peak used to compare 0 min vs. 24 h (acute phase), and 24 h vs.120 h (recovery phase).**

<i>m/z</i>	0 min vs. 24 h	24 h vs. 120 h
3028		1/0.80
3042		0.86/0.98
3627	1/1	0.96/0.98
4160	0.89/0.92	
6929		0.90/1
8327	0.96/1	0.99/1
8926		1/1
9089	0.90/0.94	

Peaks with AUC  $\geq 0.8$  were listed in the table. Values are given as first cohort/second cohort. The identified peaks were as follows; 3028 (ALB: 25–49, Q  $\rightarrow$  deamidated: 18), 3042 (ALB: 25–50), 3627 (HBA: 1–36), 8926 (ALB: 25–103). AUC, area under the curve; ROC, receiver operating characteristics; *m/z*, mass to charge ratio; ALB, albumin; HBA, hemoglobin subunit  $\alpha$ .

doi:10.1371/journal.pone.0167647.t001

samples at 0 min, and 24, 48, and 120 h. The results revealed that 75, 66, 24, and 20 peptides were identified with mascot scores of more than 50 at these time points, respectively ([S4 Table](#)), and these peptides were found to be fragments of 18, 7, 4, and 4 kinds of proteins, respectively ([Table 2](#)). Notably, more fragments were phase-specifically identified at 0 min (immediately after PHx, very acute phase) than other timings. Their parent proteins included histone family proteins (H1, H2A, H2B, H3, and H4). Representative MS/MS spectra were provided as [S2 Fig](#).

## Profiling Human Plasma Peptides after PHx

The SVM analyses revealed that the peptidomic patterns at 0 min, 24, 48, and 168 h were clearly separated, having a cross-validation accuracy of no less than 83.8%. The top 2 peaks that most efficiently discriminated among the time points at 0 min, 24, 48, and 168 h were those at 2378 and 9080 *m/z* (P-values  $< 0.00001$  and  $< 0.00001$ , respectively, ([Fig 4](#))). The peak at 2378 *m/z* was up-regulated until 168 h, whereas the peak at 9080 *m/z* was down-regulated. These observations were fully reproduced in the same experiments performed on consecutive 3 days ([S5 Table](#)). LC-MALDI-TOF/TOF MS analysis identified the peak at 2378 *m/z* as a fragment derived from complement C4b (position:1429–1449).

## Discussion

In this study, we provided a biomarker strategy based on peptide extraction using C8-coated magnetic beads and MALDI-TOF/TOF MS analysis for defining the peptide profiles in plasma during the postoperative course of PHx in a swine model. In order to construct stable peptide profile platform in this model, it is important to set a sampling point and method. After comparing the peptide profiles in PV and CV, or serum and plasma, it was confirmed that circulating peptide profiles could be influenced by the anatomical site from which samples were obtained as well as the clotting process ([S6 Table](#)). This provides a proof that the native plasma peptidome reflects proteolytic processes *in vivo*. Using plasma in CV, we successfully generated a plasma peptide profile that could be used for identification of the very acute (0 min), acute (24 h), and recovery phases (120 h) after surgery. To our knowledge, this is the first report indicating that endogenous plasma peptides after PHx can have a diagnostic value with phase-specific relevance. Several biomarker peaks were extracted that can potentially be used to

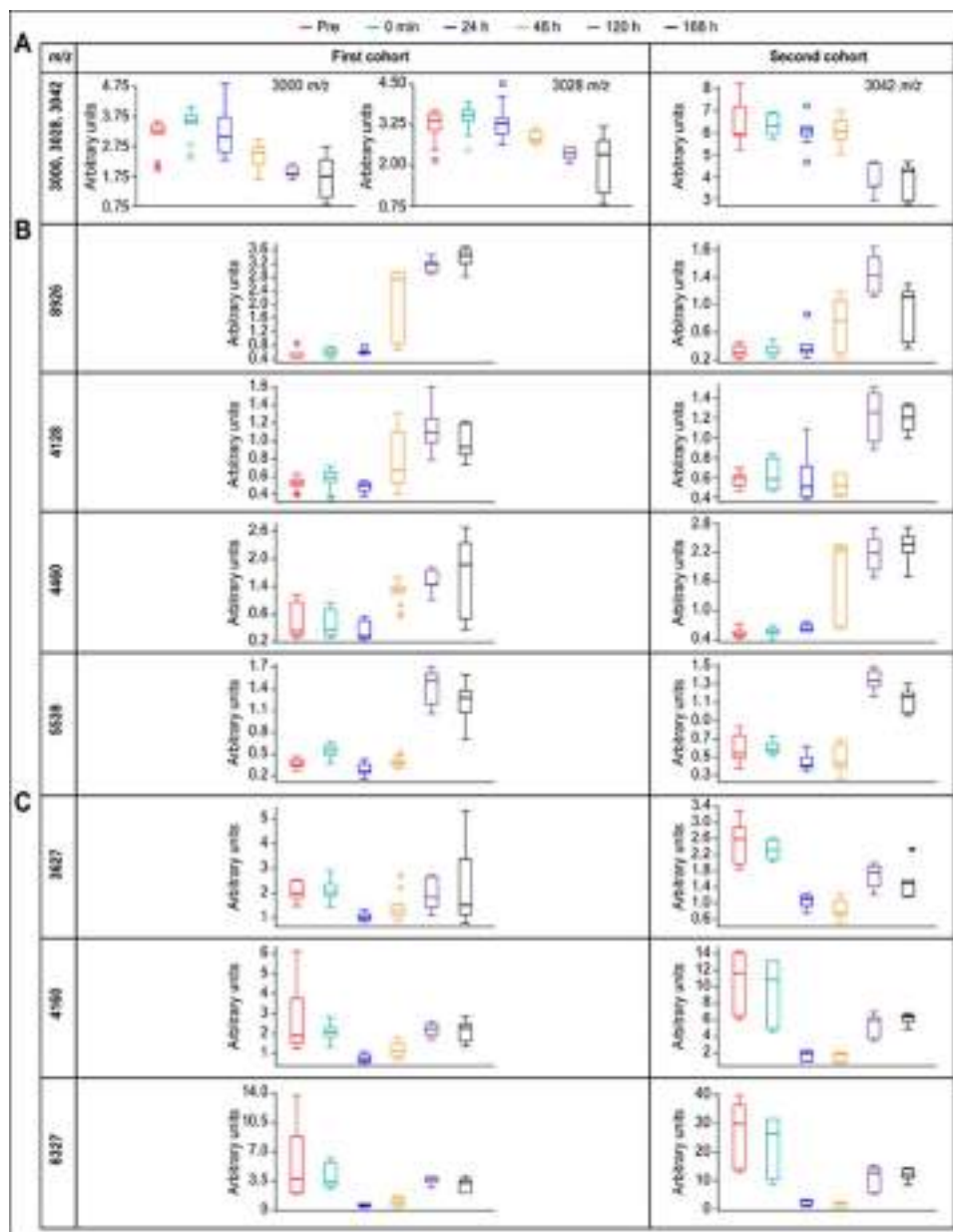


**Fig 3. Box-and-whisker plots of the representative markers for discriminating the phases after PHx.** The discriminatory peaks were classified into 3 groups according to the patterns of change; peptides (A) down-regulated at recovery phase; (B) up-regulated at recovery phase; (C) down-regulated at acute phase. Pre (red), 0 min (light green), 24 h (blue), 48 h (yellow), 120 h (purple), 168 h (black). The top and bottom end marks of the plot indicated the maximum and minimum peak area/intensity within a given class. The box indicated the 25%-quartile (bottom) and the 75%-quartile (top) and the horizontal intersection denotes the median. The statistical data were detailed in [S3 Table](#). The plot was drawn on a unique scale independent of the peak intensity scale. The identified peaks were as follows; 3000: ALB, 25–49\*<sup>1</sup>; 3028: ALB, 25–49\*<sup>2</sup>, 3042: ALB, 25–50, 8926: ALB, 25–103, 3627: HBA, 1–36. \*<sup>1</sup>: Gly → Ser; 22, \*<sup>2</sup>: Q → deamidated; 18. *m/z*, mass to charge ratio; ALB, albumin; HBA, hemoglobin subunit  $\alpha$ .

doi:10.1371/journal.pone.0167647.g003

reliably differentiate between each phase. Those phase-specific marker peptides were identified as fragments of histones in the very acute phase, fragments of HBA in the acute phase, and fragments of ALB in the recovery phase.

**Table 2. Swine Plasma peptides after PHx detected by magnetic bead-based LC-MALDI-TOF/TOF MS analyses.**

Time	Protein
0 min	Serum albumin
	Basic proline-rich protein
	Histone H1.2 <sup>b</sup>
	Histone H1.3 <sup>b</sup>
	Histone H1.3 <sup>o</sup>
	Histone H1.4 <sup>o</sup>
	Histone H2A type 1 <sup>b</sup>
	Histone H2B type 1 <sup>b</sup>
	Histone H3.1 <sup>b</sup>
	Histone H4
	Non-histone chromosomal protein HMG-17
	Hemoglobin subunit $\alpha$
	Vasodilator-stimulated phosphoprotein <sup>c</sup>
	Serotransferrin
	Apolipoprotein C-III
	Ryanodine receptor 1
	60S ribosomal protein L4
	Coatmer subunit beta
24 h	Basic proline-rich protein
	Serum albumin
	Hemoglobin subunit $\alpha$
	Vasodilator-stimulated phosphoprotein <sup>c</sup>
	Serotransferrin
	Radixin <sup>b</sup>
48 h	Ribosome-binding protein 1 <sup>c</sup>
	Basic proline-rich protein
	Serum albumin
	Ryanodine receptor 1
120 h	26S proteasome non-ATPase regulatory subunit 8 <sup>b</sup>
	Basic proline-rich protein
	Serum albumin
	Hemoglobin subunit $\alpha$
	Vasodilator-stimulated phosphoprotein <sup>b</sup>

Peptides with mass range of 1000–4000  $m/z$  were analyzed. Among them, those with mascot score of more than 50 were described in the table. Peptides were annotated using the protein sequence database of pigs. Those annotated using other species were indicated with superscripts b (*Bos Taurus*), c (*Canis familiaris*), or o (*Oryctolagus cuniculus*). PHx, partial hepatectomy; LC-MALDI-TOF/TOF MS, liquid chromatography-matrix-assisted laser desorption/ionization time-of-flight tandem mass spectrometry.

doi:10.1371/journal.pone.0167647.t002

Immediately after PHx, nucleosome components such as linker histone (H1), and core histones (H2A, H2B, H3, and H4) were detected. Through in-depth data analysis, a highly selective epitope was detected from each histone proteins; the C-tail of H2A, the N- and C-tails of H2B, and the N-tail of H4 were detected. The abundance of these particular fragments can probably be explained by the fact that the N-tails of all core histones protrude outside the nucleosome, and the C-tails of H2A and H2B also protrude outside the nucleosomal core; thus, these exposed tail regions are susceptible to proteolytic cleavage [22]. Acetylated lysine



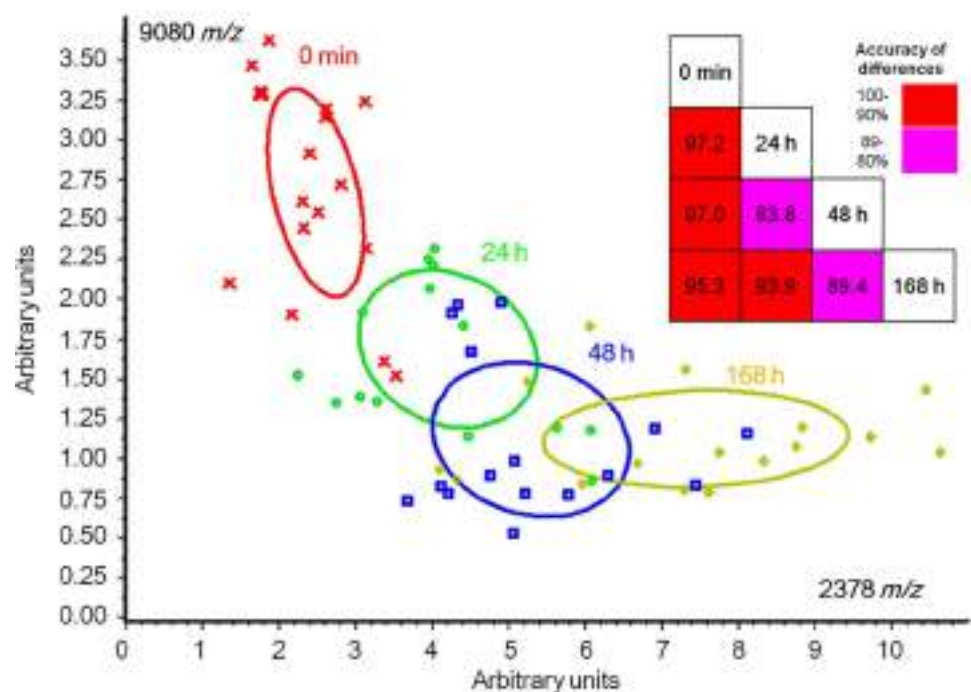


**Fig 4. Profiling of human plasma native peptides after PHx (n = 4).** The upper right part of the figure described the results of cross-validation analyses to estimate the success rate of the SVM model in separating user-defined groups of spectra. The accuracy is denoted by color: 100–90% (red); 89–80% (pink). The 2-dimensional distribution plot analysis revealed the top 2 representative peaks, which discriminated the peptidomic patterns at 0 min (red), 24 (light green), 48 (blue), and 168 h (yellow) (x axis: 2378 *m/z*, P-value: <0.000001, y axis: 9080 *m/z*, P-value: <0.00001). LC-MALDI-TOF/TOF MS analyses identified the peak at 2378 *m/z* as a fragment derived from complement C4b (position:1429–1449). PHx, partial hepatectomy; SVM, support vector machine; *m/z*, mass to charge ratio, LC-MALDI-TOF/TOF MS, liquid chromatography-matrix-assisted laser desorption/ionization time-of-flight tandem mass spectrometry.

doi:10.1371/journal.pone.0167647.g004

residues were found in the N-tail fragments of H4 which, as noted above, are more readily accessible than the nucleosomal core regions and therefore are also susceptible to post-translational modifications. Emerging studies indicate that besides having nuclear functions, histones can also be released into the extracellular space by both damaged and activated cells, exhibiting significant toxic or pro-inflammatory activity both *in vivo* and *in vitro* [23]. In a mice model of the hepatic ischemia/reperfusion injury, the extracellular histones released from liver parenchymal cells have been shown to exacerbate liver injuries through Toll-like receptor-9 activation [24]. The extracellular release of histone fragments might be an immediate/early signal for triggering liver regeneration after PHx.

The abundance of HBA fragments also changed in the acute phase. The abundance of the N-terminal part fragment (3627 *m/z*) decreased until 24 and 48 h after PHx. However, that of the C-terminal part fragments (3538 and 3852 *m/z*) increased until 6 h (S2 Table). HB is important not only as a component of red blood cells, but also as an extracellular substrate in plasma of various diseases [25]. In obese patients, serum HBA and HB subunit  $\beta$  were reported to be up-regulated according to the severity of liver disease from non-alcoholic fatty liver diseases to steatohepatitis [26]. At the transcriptomic level in liver, HBA has been reported to be repressed at 48–72 h after 70% PHx in rats [27]. In non-alcoholic steatohepatitis, high expression levels of HBA and HB subunit  $\beta$  have been observed in liver biopsy specimens due to

oxidative stress [28]. We consider that HB may be a prominent source of bioactive peptides playing an important role in maintaining homeostasis after PHx and in liver diseases.

During the recovery phase, ALB fragments were identified as the phase-determinant peptides and were mostly derived from the N-terminal part of ALB. (position: 25-X amino acids) Applied to the structure of human ALB, these fragments are considered to belong to the subdomain IA [29, 30]. This subdomain is structurally and functionally characterized as having a region of extended polypeptide chain and binding sites for metal ions such as copper and zinc. Among them, the short N-terminal fragments (3000, 3028 and 3042 *m/z*) were down-regulated, and the long N-terminal fragment (8926 *m/z*) was up-regulated. The short N-terminal fragments are estimated to reflect the turnover of ALB by the ubiquitin proteasome system and were continuously down-regulated until 168 h. The abundance of the long N-terminal fragment was increased, although its origin was unclear. At the transcriptomic level, ALB expression in liver was decreased until 36–48 h and gradually increased thereafter [31]. In clinical practice, the serum ALB level is a component of the Child–Pugh score, which is often used as a diagnostic tool of liver function [32]. Though the overall ALB concentration is important in this scoring system, it is reported to be easily influenced by the measurement method [33]. Many biomarker discovery efforts have searched for variations in the total abundance of particular proteins. In our data, different epitopes in the protein were specifically and significantly associated with phases of the postoperative course after PHx. Especially, the long N-terminal fragment (8926 *m/z*) was also seen in the recovery phase after carbon tetrachloride-induced liver injury in pigs (data not shown). Instead of the whole protein, the N-terminal fragments of ALB might have the potential to be used as biomarkers of liver recovery in various liver diseases.

However, there might be some arguments against sample preparation using only magnetic beads in light of the sensitivity of this method for detecting plasma native peptides. Because human plasma proteins range in abundance by 10–12 orders of magnitude, it is quite difficult to detect all of the proteins at the same time [13]. The detection of low-abundance proteins needs extensive sample preparation such as the immunodepletion of high-abundance proteins including albumin and immunoglobulin, and sample fractionation using 2-dimensional electrophoresis or chromatography [34]. In this study, we focused on moderate- to high-abundance plasma proteins and their fragments, resulting in novel findings regarding their phase-specific relevance and capacity to be used as biomarkers of liver regeneration after PHx. A growing body of evidence suggests that altered protease activities are involved in many diseases and could potentially generate a large number of peptides and small proteins [35]. They are thought to be released from their parent proteins by endoproteolytic cleavage, followed by the variable trimming of released peptides by aminopeptidases and carboxypeptidases [36]. While some researchers have dismissed the peptidome as biological trash, we can add an important diagnostic paradigm even by considering the fragments of major proteins, including histones, ALB, and HBA.

In this study, using a swine PHx model, we elucidated the phase-specificity of plasma peptide profiles and extracted peptide biomarkers of each phase after PHx. Because it is simple and needs no more than a few microliters of plasma specimens to analyze, the magnetic bead-based biomarker strategy is considered to be suitable for application in clinical trials. Our goal is to establish diagnostic markers of liver regeneration following human liver surgery using this approach. Clinical applications using a small number of subjects revealed that a fragment of complement C4b in plasma was increased by about 3–5 fold at 168 h of liver regeneration after PHx. Complement activation is a well-studied phenomenon in terms of ischemia/reperfusion liver injuries. This pathological condition is often a result of the Pringle maneuver during liver resection, which is routinely performed for reduction of blood loss. In all the 4 cases

in our study, major hepatectomies were performed using this maneuver. A previous study showed that the C4b fragment was deposited in the hepatocytes of ischemia/reperfusion injured liver after hepatectomy in humans [37]. Thus, our findings regarding C4b could be associated with ischemia/reperfusion injuries during liver surgery.

We have previously detected C4 fragments in a murine carbon tetrachloride-induced liver injury model and other groups have also reported the potential contribution of complement to regenerative process after PHx in mice [38, 39]. C4b has not been identified as a marker peptide in the pig experiments, and it could be in part because amino acid sequence of the swine C4b protein is not listed in the database. Approximately 80% of the pig proteome is still poorly annotated, and the existence of protein sequences is routinely inferred by sequence alignment with preexisting sequences [40].

It must be noted here that the study does not include data from sham-operated pigs. Considering the fact that sham operation is one way of extracting specific biomarkers in PHx model, certain limitations arising from the unavailability of such data in this study must be acknowledged. Instead, we carefully extracted phase-specific peptidomic profiles from 5 animals in a longitudinal time course. This is one of the advantages of using a pig model over a rodent model. The incorporation of proper sham-operated controls (0% PHx) and 30% or 90% PHx could further help validate the observations presented in this study, as well as enable extraction of more specific and sensitive biomarkers of liver regeneration, and therefore, must be considered in further studies. Furthermore, it would be interesting to compare these observations with those in other models such as carbon tetrachloride-induced liver injury model as we have done using mice [38]. The approach adopted in this study is considered to be applicable to the search for biomarkers of liver regeneration not only after PHx but also after preoperative portal vein embolization [41], and after associating liver partition and portal vein ligation for staged hepatectomy (ALPPS) surgery [42], and therefore, we cautiously plan to conduct clinical trials and elucidate biomarkers for clinical use in our subsequent work.

## Conclusions

We have proved that native plasma peptidomic profiling using MALDI-TOF MS can clearly delineate the postoperative course after PHx in a biphasic manner by distinguishing the acute phase and recovery phase. These phases could be clearly identified by the presence of HBA and ALB fragments, respectively. Further in-depth analysis using LC-MALDI-TOF/TOF MS revealed the presence of phase-specific peptides, such as histone fragments in the very acute phase. Finally, in a study of human plasma samples from hepatectomy cases, adopting the same strategy, we have extracted phase-specific peptidomic patterns by a machine learning method and further detected a fragment of complement C4b as a peptide biomarker of liver regeneration. We anticipate that the data presented in this study may help to understand the biological process of liver regeneration and improve the outcome of patients after PHx.

## Supporting Information

**S1 Fig. Pseudogel and stack view of the spectra obtained from plasma of 3 pigs.** (Page 2) 0 min vs. 24 h, 24 h vs. 48 h, (Page 3) 48 h vs. 72 h, 72 h vs. 96 h, (Page 4) 96 h vs. 120 h, 120 h vs. 168 h, (Page 5) Pre vs. 0 min, Pre vs. 1 h, (Page 6) Pre vs. 3 h, Pre vs. 6 h, (Page 7) Pre vs. 24 h, Pre vs. 48 h, (Page 8) Pre vs. 72 h, Pre vs. 96 h, (Page 9) Pre vs. 120 h, Pre vs. 144 h, (Page 10) Pre vs. 168 h, 0 min vs. 1 h, (Page 11) 0 min vs. 3 h, 0 min vs. 6 h, (Page 12) 0 min vs. 48 h, 0 min vs. 72 h, (Page 13) 0 min vs. 96 h, 0 min vs. 120 h, (Page 14) 0 min vs. 144 h, 0 min vs. 168 h, (Page 15) 1 h vs. 3 h, 1 h vs. 6 h, (Page 16) 1 h vs. 24 h, 1 h vs. 48 h, (Page 17) 1 h vs. 72 h, 1 h vs. 96 h, (Page 18) 1 h vs. 120 h, 1 h vs. 144 h, (Page 19) 1 h vs. 168 h, 3 h vs. 6 h, (Page 20) 3 h

vs. 24 h, 3 h vs. 48 h, (Page 21) 3 h vs. 72 h, 3 h vs. 96 h, (Page 22) 3 h vs. 120 h, 3 h vs. 144 h, (Page 23) 3 h vs. 168 h, 6 h vs. 24 h, (Page 24) 6 h vs. 48 h, 6 h vs. 72 h, (Page 25) 6 h vs. 96 h, 6 h vs. 120 h, (Page 26) 6 h vs. 144 h, 6 h vs. 168 h, (Page 27) 24 h vs. 72 h, 24 h vs. 96 h, (Page 28) 24 h vs. 120 h, 24 h vs. 144 h, (Page 29) 24 h vs. 168 h, 48 h vs. 96 h, (Page 30) 48 h vs. 120 h, 48 h vs. 144 h, (Page 31) 48 h vs. 168 h, 72 h vs. 120 h, (Page 32) 72 h vs. 144 h, 72 h vs. 168 h, (Page 33) 96 h vs. 144 h, 96 h vs. 168 h, (Page 34) 120 h vs. 144 h, 144 h vs. 168 h, (Page 35) all timings (pseudogel view), and (Page 36) all timings (stack view).  
(PDF)

**S2 Fig. Representative MS/MS spectra of swine plasma peptides.** (Page 2~9) serum albumin, (Page 10~14) hemoglobin subunit  $\alpha$ , (Page 15~17) basic proline-rich protein, (Page 18~19) histone H1.2, (Page 20) histone H2A1, (Page 21~22) histone H2B1, (Page 23~24) histone H3.1, (Page 25) histone H4, (Page 26~27) non-histone chromosomal protein HMG-17, (Page 28) serotransferrin, (Page 29) apolipoprotein C-III, (Page 30) ryanodine receptor I, and (Page 31) vasodilator-stimulated phosphoprotein.  
(PPTX)

**S1 Table. Characteristics of patients analyzed in this study.** Four patients who underwent major hepatectomy without pathological liver fibrosis (F0 or F1) [17], and had an uneventful postoperative course without PHLF, were included. <sup>\*1</sup>The primary tumor originated in stomach. <sup>\*2</sup>The definition of PHLF is an increase in the international normalized ratio of prothrombin time and concomitant hyperbilirubinemia (according to the normal limits of the local laboratory) on or after postoperative day 5 [4]. PHLF, posthepatectomy liver failure; nonB, nonC HCC, hepatocellular carcinoma without hepatitis B or C viral infection.  
(DOCX)

**S2 Table. Detailed results of comparative analyses between every 2 timings after PHx in pigs.** The top 2 peaks enabling discrimination between every 2 timings were shown in the table. AveN indicated peak area/intensity average of class N (1 or 2). StdDevN indicated standard deviation of the peak area/intensity average of class N. PHx, partial hepatectomy.  
(XLSX)

**S3 Table. Peak area/intensity of marker peptides in swine plasma after PHx.** (Page 1) first cohort and (Page 2) second cohort analyses. AveN indicated peak area/intensity average of class N (1 to 6). StdDevN indicated standard deviation of the peak area/intensity average of class N. Class 1, 2, 3, 4, 5, and 6 represented pre, 0 min, 24, 48, 120, and 168 h, respectively. PHx, partial hepatectomy.  
(XLSX)

**S4 Table. The endogenous swine plasma peptides after PHx identified by LC-MALDI-TOF/TOF MS.** (Page 1) 0 min, (Page 2) 24 h, (Page 3) 48 h, and (Page 4) 168 h after PHx. LC-MALDI-TOF/TOF MS, liquid chromatography-matrix-assisted laser desorption/ionization time-of-flight tandem mass spectrometry; PHx, partial hepatectomy.  
(XLSX)

**S5 Table. Three independent datasets for human plasma analyses.** The peaks at 2378 and 9080  $m/z$  clearly discriminated 0 min, 24, 48, and 168 h with P-values of no more than 0.0001 in every 3 experiments. AveN indicated peak area/intensity average of class N (1 to 4). StdDevN indicated standard deviation of the peak area/intensity average of class N. Class 1, 2, 3, and 4 represented 0 min, 24, 48, and 168 h, respectively. The  $x$  and  $y$  axes of the 2-dimensional distribution plots represented 2378 and 9080  $m/z$ , respectively.  
(XLSX)



**S6 Table. The peak list that had a significant difference\* in intensity regarding sampling points and methods.** (A) More peptide fragments were detected in PV than in CV. This result might reflect PV containing more humoral factors than CV that are capable of stimulating DNA synthesis after PHx. (B) More peptide fragments were observed in serum than in plasma. The lower stability of peptide fragments in serum is considered to result from ex vivo multi-protease activities due to clotting. The SVM analyses discriminated PV and CV, and serum and plasma with a cross-validation accuracy of more than 88 and 93% at all timings, respectively. In the present study, the plasma samples were analyzed to detect endogenous peptides. Considering the difficulty in repeated sampling from PV, which otherwise might be more informative, the CV specimens were used for further studies. \*Differences with AUC calculated by ROC curve analysis  $> 0.8$  were considered to be significant. Peaks were described with  $m/z$  values. Five and 4 pigs were used for analyses of (A) and (B), respectively. PV, portal vein; CV, central vein; AUC, area under the curve; ROC, receiver operating characteristics;  $m/z$ , mass to charge ratio. (DOCX)

## Author Contributions

**Conceptualization:** MI EH.

**Data curation:** KI TN NI MI.

**Formal analysis:** KI TN NI MI.

**Funding acquisition:** MI EH SU.

**Investigation:** KI TN NI NN TS NK MI.

**Methodology:** MI.

**Project administration:** SU.

**Resources:** KI EH TN NI MS GY KY TO YK HF NK SS K Taura K Tashiro MI.

**Software:** TN NI.

**Supervision:** SU.

**Validation:** KI TN NI NN TS MI.

**Visualization:** KI TN NI MI.

**Writing – original draft:** KI.

**Writing – review & editing:** EH TN NI MI.

## References

1. Fausto N. Liver regeneration. *J Hepatol.* 2000; 32:19–31.
2. Michalopoulos GK, DeFrances MC. Liver regeneration. *Science.* 1997; 276: 60–66. PMID: [9082986](#)
3. Clavien P, Petrowsky H, DeOliveira ML, Graf R. Medical progress: Strategies for safer liver surgery and partial liver transplantation. *New Engl J Med.* 2007; 356: 1545–1559. doi: [10.1056/NEJMra065156](#) PMID: [17429086](#)
4. Rahbari NN, Garden OJ, Padbury R, Brooke-Smith M, Crawford M, Adam R, et al. Posthepatectomy liver failure: A definition and grading by the International Study Group of Liver Surgery (ISGLS). *Surgery.* 2011; 149: 713–724. doi: [10.1016/j.surg.2010.10.001](#) PMID: [21236455](#)

5. Kampf C, Mardinoglu A, Fagerberg L, Hallstrom BM, Edlund K, Lundberg E, et al. The human liver-specific proteome defined by transcriptomics and antibody-based profiling. *Faseb J*. 2014; 28: 2901–2914. doi: [10.1096/fj.14-250555](https://doi.org/10.1096/fj.14-250555) PMID: [24648543](https://pubmed.ncbi.nlm.nih.gov/24648543/)
6. Liotta LA, Petricoin EF. Serum peptidome for cancer detection: spinning biologic trash into diagnostic gold. *J Clin Invest*. 2006; 116: 26–30. doi: [10.1172/JCI27467](https://doi.org/10.1172/JCI27467) PMID: [16395400](https://pubmed.ncbi.nlm.nih.gov/16395400/)
7. Petricoin EF, Ardekani AM, Hitt BA, Levine PJ, Fusaro VA, Steinberg SM, et al. Use of proteomic patterns in serum to identify ovarian cancer. *Lancet*. 2002; 359: 572–577. doi: [10.1016/S0140-6736\(02\)07746-2](https://doi.org/10.1016/S0140-6736(02)07746-2) PMID: [11867112](https://pubmed.ncbi.nlm.nih.gov/11867112/)
8. Adam BL, Qu YS, Davis JW, Ward MD, Clements MA, Cazares LH, et al. Serum protein fingerprinting coupled with a pattern-matching algorithm distinguishes prostate cancer from benign prostate hyperplasia and healthy men. *Cancer Res*. 2002; 62: 3609–3614. PMID: [12097261](https://pubmed.ncbi.nlm.nih.gov/12097261/)
9. Li JN, Zhang Z, Rosenzweig J, Wang YY, Chan DW. Proteomics and bioinformatics approaches for identification of serum biomarkers to detect breast cancer. *Clin Chem*. 2002; 48: 1296–1304. PMID: [12142387](https://pubmed.ncbi.nlm.nih.gov/12142387/)
10. Honda K, Hayashida Y, Umaki T, Okusaka T, Kosuge T, Kikuchi S, et al. Possible detection of pancreatic cancer by plasma protein profiling. *Cancer Res*. 2005; 65: 10613–10622. doi: [10.1158/0008-5472.CAN-05-1851](https://doi.org/10.1158/0008-5472.CAN-05-1851) PMID: [16288055](https://pubmed.ncbi.nlm.nih.gov/16288055/)
11. Poon TCW, Yip TT, Chan ATC, Yip C, Yip V, Mok TSK, et al. Comprehensive proteomic profiling identifies serum proteomic signatures for detection of hepatocellular carcinoma and its subtypes. *Clin Chem*. 2003; 49: 752–760. PMID: [12709366](https://pubmed.ncbi.nlm.nih.gov/12709366/)
12. Verma N, Rettenmeier AW, Schmitz-Spanke S. Recent advances in the use of *Sus scrofa* (pig) as a model system for proteomic studies. *Proteomics*. 2011; 11: 776–793. doi: [10.1002/pmic.201000320](https://doi.org/10.1002/pmic.201000320) PMID: [21229584](https://pubmed.ncbi.nlm.nih.gov/21229584/)
13. Anderson NL, Anderson NG. The human plasma proteome—History, character, and diagnostic prospects. *Mol Cell Proteomics*. 2002; 1: 845–867. PMID: [12488461](https://pubmed.ncbi.nlm.nih.gov/12488461/)
14. Baumann S, Ceglarek U, Fiedler GM, Lembcke J, Leichte A, Thierry J. Standardized approach to proteome profiling of human serum based on magnetic bead separation and matrix-assisted laser desorption/ionization time-of-flight mass spectrometry. *Clin Chem*. 2005; 51: 973–980. doi: [10.1373/clinchem.2004.047308](https://doi.org/10.1373/clinchem.2004.047308) PMID: [15845803](https://pubmed.ncbi.nlm.nih.gov/15845803/)
15. Kawaguchi H, Yamada T, Miura N, Ayaori M, Uto-Kondo H, Ikegawa M, et al. Rapid development of atherosclerosis in the world's smallest microminipig fed a high-fat/high-cholesterol diet a useful animal model due to its size and similarity to human pathophysiology. *J Atheroscler Thromb*. 2014; 21: 186–203. PMID: [24257467](https://pubmed.ncbi.nlm.nih.gov/24257467/)
16. Iguchi K, Hatano E, Yamanaka K, Sato M, Yamamoto G, Kasai Y, et al. Hepatoprotective effect by pre-treatment with olprinone in a swine partial hepatectomy model. *Liver Transplant*. 2014; 20: 838–849.
17. Bedossa P, Poynard T. An algorithm for the grading of activity in chronic hepatitis C. *Hepatology*. 1996; 24: 289–293. doi: [10.1002/hep.510240201](https://doi.org/10.1002/hep.510240201) PMID: [8690394](https://pubmed.ncbi.nlm.nih.gov/8690394/)
18. Couinaud C. Lobes et segments hépatiques—notes sur l'architecture anatomique et chirurgicale du foie. *Presse Medicale*. 1954; 62: 709–712. PMID: [13177441](https://pubmed.ncbi.nlm.nih.gov/13177441/)
19. Ketterlinus R, Hsieh S-Y, Teng S-H, Lee H, Pusch W. Fishing for biomarkers: analyzing mass spectrometry data with the new ClinProTools™ software. *BioTechniques*. 2005; 38: S37–S40.
20. Ivosev G, Burton L, Bonner R. Dimensionality reduction and visualization in principal component analysis. *Anal Chem*. 2008; 80: 4933–4944. doi: [10.1021/ac800110w](https://doi.org/10.1021/ac800110w) PMID: [18537272](https://pubmed.ncbi.nlm.nih.gov/18537272/)
21. Suckau D, Resemann A, Schuerenberg M, Hufnagel P, Franzen J, Holle A. A novel MALDI LIFT-TOF/TOF mass spectrometer for proteomics. *Anal Bioanal Chem*. 2003; 376: 952–965. doi: [10.1007/s00216-003-2057-0](https://doi.org/10.1007/s00216-003-2057-0) PMID: [12830354](https://pubmed.ncbi.nlm.nih.gov/12830354/)
22. Azad GK, Tomar RS. Proteolytic clipping of histone tails: the emerging role of histone proteases in regulation of various biological processes. *Mol Biol Rep*. 2014; 41: 2717–2730. doi: [10.1007/s11033-014-3181-y](https://doi.org/10.1007/s11033-014-3181-y) PMID: [24469733](https://pubmed.ncbi.nlm.nih.gov/24469733/)
23. Chen R, Kang R, Fan XG, Tang D. Release and activity of histone in diseases. *Cell Death Dis*. 2014; 5.
24. Huang H, Evankovich J, Yan W, Nace G, Zhang L, Ross M, et al. Endogenous histones function as alarmins in sterile inflammatory liver injury through Toll-like receptor 9 in mice. *Hepatology*. 2011; 54: 999–1008. doi: [10.1002/hep.24501](https://doi.org/10.1002/hep.24501) PMID: [21721026](https://pubmed.ncbi.nlm.nih.gov/21721026/)
25. Rother RP, Bell L, Hillmen P, Gladwin MT. The clinical sequelae of intravascular hemolysis and extracellular plasma hemoglobin—a novel mechanism of human disease. *Jama-J Am Med Assoc*. 2005; 293: 1653–1662.
26. Trak-Smayra V, Dargere D, Noun R, Albuquerque M, Yaghi C, Gannage-Yared MH, et al. Serum proteomic profiling of obese patients: correlation with liver pathology and evolution after bariatric surgery. *Gut*. 2009; 58: 825–832. doi: [10.1136/gut.2007.140087](https://doi.org/10.1136/gut.2007.140087) PMID: [18403495](https://pubmed.ncbi.nlm.nih.gov/18403495/)

27. Fukuhara Y, Hirasawa A, Li XK, Kawasaki M, Fujino M, Funeshima N, et al. Gene expression profile in the regenerating rat liver after partial hepatectomy. *J Hepatol*. 2003; 38: 784–792. PMID: [12763372](#)
28. Liu W, Baker SS, Baker RD, Nowak NJ, Zhu L. Upregulation of hemoglobin expression by oxidative stress in hepatocytes and its implication in nonalcoholic steatohepatitis. *Plos One*. 2011; 6(9).
29. Peters T. Serum-albumin—Recent progress in understanding of its structure and biosynthesis. *Clin Chem*. 1977; 23: 5–12. PMID: [318940](#)
30. He XM, Carter DC. Atomic-structure and chemistry of human serum-albumin. *Nature*. 1992; 358: 209–215. doi: [10.1038/358209a0](#) PMID: [1630489](#)
31. Kurumiya Y, Nozawa K, Sakaguchi K, Nagino M, Nimura Y, Yoshida S. Differential suppression of liver-specific genes in regenerating rat liver induced by extended hepatectomy. *J Hepatol*. 2000; 32: 636–644. PMID: [10782913](#)
32. Pugh RNH, Murrayly Im, Dawson JL, Pietroni MC, Williams R. Transection of esophagus for bleeding esophageal varices. *Brit J Surg*. 1973; 60: 646–649. PMID: [4541913](#)
33. Seimiya M, Ohno S, Yamamoto H, Fujiwara K, Yoshida T, Sawabe Y, et al. Child-Pugh score is altered by the albumin measurement method. *Hepatology*. 2013; 57: 2093–2094. doi: [10.1002/hep.25972](#) PMID: [22815135](#)
34. Polaskova V, Kapur A, Khan A, Molloy MP, Baker MS. High-abundance protein depletion: Comparison of methods for human plasma biomarker discovery. *Electrophoresis*. 2010; 31: 471–482. doi: [10.1002/elps.200900286](#) PMID: [20119956](#)
35. Fruitier I, Garreau I, Lacroix A, Cupo A, Piot JM. Proteolytic degradation of hemoglobin by endogenous lysosomal proteases gives rise to bioactive peptides: hemorphins. *Febs Lett*. 1999; 447: 81–86. PMID: [10218587](#)
36. Hortin GL. The MALDI-TOF mass spectrometric view of the plasma proteome and peptidome. *Clin Chem*. 2006; 52: 1223–1237. doi: [10.1373/clinchem.2006.069252](#) PMID: [16644871](#)
37. Straatsburg IH, Boermeester MA, Wolbink GJ, van Gulik TM, Gouma DJ, Frederiks WM, et al. Complement activation induced by ischemia-reperfusion in humans: a study in patients undergoing partial hepatectomy. *J Hepatol*. 2000; 32: 783–791. PMID: [10845665](#)
38. Shimada T, Nakanishi T, Toyama A, Yamauchi S, Kanzaki A, Fujiwake H, et al. Potential implications for monitoring serum bile acid profiles in circulation with serum proteome for carbon tetrachloride-induced liver injury/regeneration model in mice. *J Proteome Res*. 2010; 9: 4490–4500. doi: [10.1021/pr1002388](#) PMID: [20583827](#)
39. Mastellos DC, DeAngelis RA, Lambris JD. Complement-triggered pathways orchestrate regenerative responses throughout phylogenesis. *Semin Immunol*. 2013; 25: 29–38. doi: [10.1016/j.smim.2013.04.002](#) PMID: [23684626](#)
40. Piovesan D, Profiti G, Martelli PL, Fariselli P, Fontanesi L, Casadio R. SUS-BAR: a database of pig proteins with statistically validated structural and functional annotation. *Database*. 2013.
41. Kasai Y, Hatano E, Iguchi K, Seo S, Taura K, Yasuchika K, et al. Prediction of the remnant liver hypertrophy ratio after preoperative portal vein embolization. *Eur Surg Res*. 2013; 51: 129–137. doi: [10.1159/000356297](#) PMID: [24280661](#)
42. Schnitzbauer AA, Lang SA, Goessmann H, Nadalin S, Baumgart J, Farkas SA, et al. Right portal vein ligation combined with in situ splitting induces rapid left lateral liver lobe hypertrophy enabling 2-staged extended right hepatic resection in small-for-size settings. *Ann Surg*. 2012; 255: 405–414. doi: [10.1097/SLA.0b013e31824856f5](#) PMID: [22330038](#)

# Immune Cells on the Corneal Endothelium of an Allogeneic Corneal Transplantation Rabbit Model

Elena Koudouna,<sup>1</sup> Naoki Okumura,<sup>1,2</sup> Yugo Okazaki,<sup>1</sup> Shinichiro Nakano,<sup>1</sup> Ryota Inoue,<sup>1</sup> Nigel J. Fullwood,<sup>3</sup> Junko Hori,<sup>4</sup> Shigeru Kinoshita,<sup>2,5</sup> and Noriko Koizumi<sup>1</sup>

<sup>1</sup>Department of Biomedical Engineering, Faculty of Life and Medical Sciences, Doshisha University, Kyotanabe, Japan

<sup>2</sup>Department of Ophthalmology, Kyoto Prefectural University of Medicine, Kyoto, Japan

<sup>3</sup>Division of Biomedical and Life Sciences, Lancaster University, Lancaster, United Kingdom

<sup>4</sup>Department of Ophthalmology, Nippon Medical School, Tokyo, Japan

<sup>5</sup>Department of Frontier Medical Science and Technology for Ophthalmology, Kyoto Prefectural University of Medicine, Kyoto, Japan

Correspondence: Noriko Koizumi, Department of Biomedical Engineering, Faculty of Life and Medical Sciences, Doshisha University, Kyotanabe 610-0321, Japan; nkoizumi@mail.doshisha.ac.jp.

Submitted: May 27, 2016

Accepted: November 25, 2016

Citation: Koudouna E, Okumura N, Okazaki Y, et al. Immune cells on the corneal endothelium of an allogeneic corneal transplantation rabbit model. *Invest Ophthalmol Vis Sci*. 2017;58:242–251. DOI:10.1167/iovs.16-20019

**PURPOSE.** Corneal endothelial cell density undergoes a progressive decrease for many years after transplantation, eventually threatening patients with late endothelial failure. The purpose of this study was to investigate the possibility of an immunologic response in successfully grafted corneal endothelium.

**METHODS.** The corneal endothelium of patients who had undergone corneal transplantation was evaluated by specular microscopy. Rabbit models were subjected to penetrating keratoplasty (PK) with either syngeneic or allogeneic corneal transplants and Descemet's stripping endothelial keratoplasty (DSEK) with allogeneic corneal transplants. The presence of immune cells and expression of proinflammatory cytokines were determined by immunostaining. The corneal endothelium and immune cells were also evaluated by scanning electron microscopy.

**RESULTS.** Scanning slit contact specular microscopy of patients with no features of graft rejection revealed cell-like white dots on the grafted corneal endothelium. The corneal endothelium of the allogeneic PK and DSEK rabbit models displayed the presence of immune cells, including CD4<sup>+</sup> T-helper cells, CD8<sup>+</sup> cytotoxic T cells, CD20<sup>+</sup> B lymphocytes, CD68<sup>+</sup> macrophages, and neutrophils, but these immune cells were rarely observed in the syngeneic PK model. These immune cells also produced proinflammatory cytokines. Notably, some of the corneal endothelial cells situated near these immune cells exhibited features of apoptosis.

**CONCLUSIONS.** T lymphocytes, B lymphocytes, macrophages, and neutrophils are present on the grafted corneal endothelium in both PK and DSEK allogeneic rabbit models. The potential involvement of immune cells as an underlying pathophysiology for late endothelial failure deserves further examination.

**Keywords:** corneal endothelium, immune cells, inflammation

Corneal transplantation is one of the most common transplantations performed in the world.<sup>1</sup> The Eye Bank Association of America<sup>2</sup> reported that 47,530 donor corneas were provided for transplantation in the United States; similarly, 28,901 donor corneas were provided for transplantation in other countries in 2014. Corneal transplantation has been accepted as a successful procedure, but several large cohort studies have now shown that graft survival after 10 years following penetrating keratoplasty (PK) is only approximately 50%,<sup>3–5</sup> although this varies widely depending on the indications and the specific studies.<sup>6,7</sup> Endothelial dysfunction also accounts for 50% of the total graft failures, suggesting that corneal endothelial damage is the leading cause of graft failure.<sup>5,7</sup>

Endothelial graft failure can be divided into three types: primary graft failure (mainly iatrogenic), immunologic rejection, and late endothelial failure.<sup>6</sup> Graft rejection is clinically recognized by features that include the presence of endothelial rejection line, keratic precipitates, corneal edema, and conjunctival injection caused by immunologic responses against donor

cells.<sup>8–10</sup> One multicenter study revealed that 92 of 1090 patients (8.4%) experienced graft failure within 5 years of follow-up due to rejection after PK. On the other hand, late endothelial failure typically exhibits no clinical symptoms, but several studies, including a large cohort study based on graft registries, have demonstrated that corneal endothelial cell (CEC) density decreases continuously, even in clinically successful transplantation cases. For instance, the Cornea Donor Study Research Group reported that patients who underwent PK experienced a cell loss of 79%, resulting in a median 10-year corneal endothelial cell density (ECD) of 550 cells/mm<sup>2</sup>.<sup>7</sup>

The damage to the corneal endothelium associated with ECD drop is compensated by increased pump function and barrier function by remaining CECs, which maintains corneal transparency.<sup>11</sup> However, a decrease in the ECD to a critical level, typically 500 cells/mm<sup>2</sup>, overwhelms this ability to compensate, and the cornea begins to exhibit corneal edema with severe visual disturbance. This suggests that graft corneas, on average, come close to the threshold ability to maintain corneal transparency or exhibit haziness within a decade. Late





endothelial failure is accepted as a leading threat of graft failure, but the underlying mechanism remains unclear and no treatment is available. Hence, a better understanding of the source of this failure is urgently needed, not only for understanding the pathophysiology, but also for developing preventive treatments for late endothelial failure.

Birnbaum and colleagues<sup>12</sup> reported that the relative annual loss of endothelial cells was 1.1% after autologous rotational keratoplasty, whereas the relative annual loss was 16.7% in homologous PK.<sup>12</sup> Only six patients were analyzed as the autologous rotational keratoplasty group, but these authors hypothesized that immunologic influences might be the cause of the chronic endothelial cell loss observed after corneal transplantation.<sup>12</sup> We pursued this idea by investigating the potential involvement of an immunologic response in the CECs of corneal grafts that are clinically transparent without rejection symptoms after transplantation.

In this study, we explored the possibility of an immunologic response in the corneal endothelium in a rabbit corneal transplantation model. We showed that immune cells, such as CD4<sup>+</sup> T-helper cells, CD8<sup>+</sup> cytotoxic T cells, CD20<sup>+</sup> B lymphocytes, CD68<sup>+</sup> macrophages and neutrophils, were present on the corneal endothelium after allogeneic corneal transplantation, whereas these immune cells were rarely observed in syngeneic grafts. We also demonstrated that proinflammatory cytokines, such as TNF- $\alpha$  and IFN- $\gamma$ , were expressed by immune cells.

## METHODS

### Ethics Statement

All animals were housed and treated in strict accordance with the ARVO Statement for the Use of Animals in Ophthalmic and Vision Research. All experiments were carried out under a Doshisha University Animal Care and Use Committee approved protocol (approval no. A15012), and all efforts were made to ameliorate animal suffering.

### Clinical Data

The human clinical data were obtained in accordance with the tenets set forth in the Declaration of Helsinki and in accordance with a protocol approved by the Institutional Review Board of Kyoto Prefectural University of Medicine (approval no. RBMR-C-1073-1). Clinical trial registration was obtained from the University Hospital Medical Information Network (UMIN; ID: UMIN000021264) (<http://www.umin.ac.jp/english/>, provided in the public domain). The corneal endothelium was evaluated by contact specular microscopy (Konan scanning slit specular microscope; Konan Medical, Nishinomiya, Japan) at the follow-up clinical observations of patients who had undergone corneal transplantation at the Kyoto Prefectural University of Medicine.

### Rabbit Penetrating Corneal Transplantation Model

Twenty-one eyes of 15 rabbits were grafted with either syngeneic ( $n = 12$ ) or allogeneic ( $n = 15$ ) corneal transplants. For syngeneic corneal transplantation, 8-mm-diameter corneal buttons were trephined (Hessburg-Barron Vacuum Trephine; Barron Precision Instruments, LLC, Grand Blanc, MI, USA), stored in media (Optisol-GS; Bausch & Lomb, Inc., Rochester, NY, USA), and transplanted back into the original eye using 10-0 nylon ophthalmic sutures (MANI Ophthalmic Sutures; MANI, Inc., Utsunomiya, Japan). For allogeneic corneal transplantation, 8-mm-diameter corneal buttons were trephined with a trephine, stored in media (Optisol-GS; Bausch & Lomb, Inc.) and transplanted into a different rabbit eye. Following corneal

transplantation, 0.33-mg dexamethasone (Nichi-Iko Pharmaceutical Co., Ltd., Toyama, Japan) was injected into the subconjunctiva for 1 week. Anterior segments were assessed with a slit-lamp microscope. Corneal thickness and volume were evaluated with a camera system (Pentacam; OCULUS Optikgeräte GmbH, Wetzlar, Germany). The corneal endothelium was evaluated by contact specular microscopy (Konan scanning slit specular microscope; Konan Medical) ( $n = 6$ ). After observation for 2 weeks, corneal specimens were evaluated by immunofluorescence staining. To analyze rejected specimens, three rabbits with transplanted allogeneic grafts were observed for up to 2 months and subjected to histologic experiments when graft rejection was observed associated with clinical symptoms such as corneal haziness, corneal edema, and conjunctival injection.

### Rabbit Descemet's Stripping Endothelial Keratoplasty (DSEK) Model

For preparing DSEK graft, deep lamellar keratectomy was performed in eight rabbit corneas using microkeratome (Moria ALTK; MORIA, Inc., Doylestown, PA, USA), and the residual corneal bed was trephined with an 8-mm-diameter dermal punch (Dermapunch; Maruho Co., Ltd., Osaka, Japan). In recipient rabbits, lenses were removed using a series 20000 Legacy surgical system (Alcon, Inc., Fort Worth, TX, USA) under general anesthesia to deepen the anterior chamber 1 week prior to DSEK. Under general anesthesia, Descemet's membrane was stripped from eight eyes of eight rabbits, DSEK grafts were transplanted using the standard DSEK procedure applied in clinical settings.<sup>1</sup> One 0.33-mg dexamethasone dose was instilled by subconjunctival injection for 1 week. After observation for 2 weeks, corneal specimens were processed for immunofluorescence staining and scanning electron microscopy ( $n = 6$ ). Two samples were processed for semiquantitative RT-PCR.

### Immunofluorescence

Full-thickness corneal tissue was fixed in 4% paraformaldehyde for 10 minutes at room temperature, followed by perfusion in 0.5% Triton X-100 (Wako Pure Chemical Industries, Ltd., Osaka, Japan) for 5 minutes at room temperature to increase tissue permeability. Nonspecific binding was blocked using 2% BSA or 2% goat serum for 1 hour at room temperature. The corneal endothelium was stained with function-related markers: ZO-1 (1:200; Zymed Laboratories, South San Francisco, CA, USA) and Na<sup>+</sup>/K<sup>+</sup>-ATPase (1:200; Upstate Biotechnology, Lake Placid, NY, USA). The presence of immune cells was determined using primary antibodies against CD3 (pan T lymphocyte, 1:100; Abcam, Cambridge, UK), CD4 (T-helper cells, 1:100; R&D Biotechnology, Minneapolis, MN, USA), CD8 (cytotoxic T cells, 1:100; R&D Biotechnology), CD20 (B lymphocytes, 1:100; Santa Cruz Biotechnology, Inc., Santa Cruz, CA, USA), CD68 (macrophages, 1:100; Santa Cruz Biotechnology, Inc.), cathepsin G (neutrophils, 1:100; Abcam), TNF- $\alpha$  (1:100; Abcam), and IFN- $\gamma$  (1:100; Abcam). The secondary antibody was Alexa Fluor 488-conjugated goat anti-mouse (Life Technologies, Carlsbad, CA, USA) or Alexa Fluor 594-conjugated goat anti-rabbit IgG (Life Technologies), used at a 1:1000 dilution. Cell morphology was evaluated after actin staining with a 1:400 dilution of Alexa Fluor 635-conjugated phalloidin (Life Technologies). Nuclei were stained with 4',6-diamidino-2-phenylindole (DAPI; Vector Laboratories, Burlingame, CA, USA). The samples were observed by fluorescence microscopy (model TCS SP2 AOBS; Leica Microsystems, Wetzlar, Germany) or a confocal laser scanning electron microscopy (LEICA TCS SP8 Multiphoton; Leica Microsystems). Image J (<http://imagej.nih.gov/ij/>; provided in the public

TABLE. Oligonucleotide Sequences for RT-PCR

Gene	Sense Primer	Antisense Primer	Size, bp
<i>IL-1RA</i>	5'-GAAGTTGTGCTGTCTTGTGTG-3'	5'-CCTCCTGGAAGTAGAACTTGGT-3'	262
<i>IL-1b</i>	5'-TGTGTCTGGCACGTATGAGCTG-3'	5'-CTTCTTCTTTGGGTAACGGTTGGG-3'	227
<i>IL-6</i>	5'-CTGAAGAACATCCAACACCTGATC-3'	5'-CCTAACGCTCATCTTCTAGTTTC-3'	329
<i>IL-8</i>	5'-ACACTCCACACCTTCCATCC-3'	5'-CCTACGACAGATCCATGCAGT-3'	293
<i>IL-10</i>	5'-CCCGATCCTATTTATTTACCGAGC-3'	5'-GTTAGAAAGTGTGGTCAGGCACAG-3'	232
<i>IL-15</i>	5'-CTGTATCAGTGCAGGTCTTCC-3'	5'-CCTCCAGTTCCTCACATTCTTTC-3'	310
<i>TNF-<math>\alpha</math></i>	5'-CTCCAGGTTCTCTTCAGCGGTC-3'	5'-GTCCAGGTACTCAGGCTGGTTGA-3'	250
<i>TGF-<math>\beta</math>2</i>	5'-GATCTCCATCTACAACAGCACCAG-3'	5'-CTGAAGTAGGGTCTGTAGAAGGTG-3'	266
<i>CX3CR</i>	5'-TGGCCGCCAACTCCATTAAC-3'	5'-GATGGCTTTGGCTTTCTTGTGG-3'	292
<i>CCL2</i>	5'-CACCTGCTGTATACATTCACC-3'	5'-GTCGTGTGTTCTTGGGTTGTG-3'	236
<i>CCL4</i>	5'-CAGGAGTACGTGGATGACTTG-3'	5'-CAACAGCAGAGAAACAGTGGT-3'	263
<i>TLR4</i>	5'-CTAACCTGTCTAGCCTTGAGCAC-3'	5'-CCACTCAGCCCTTGAATACAG-3'	240
<i>TRAIL</i>	5'-CTGATCCTGATCTTCACAGTGCTCC-3'	5'-CTACTCTCTGAGGCCCTCTTCTC-3'	328
<i>GAPDH</i>	5'-GCGTGAACCACGAGAAGTATGACAAC-3'	5'-CAGTGGAGGCAGGGATGATGTTTC-3'	234

bp indicates base pairs.

domain by the National Institutes of Health, Bethesda, MD, USA) was used to create three-dimensional reconstructions.

### Semiquantitative RT-PCR

Descemet's membrane, with corneal endothelium that included immune cells, was stripped from corneas of the DSEK rabbit model. Descemet's membrane stripped from healthy corneas was used as control ( $n = 2$ ). Total RNA was isolated using a purification kit (RNeasy Mini Kit; Qiagen, Hilden, Germany). The quality of the RNA preparations was measured with a spectrophotometer (NanoDrop; Thermo Fisher Scientific, Inc., Waltham, MA, USA).

Ribonucleic acid was amplified using a transcriptome amplification kit (QuantiTect Whole Transcriptome Kit; Qiagen, Hilden, Germany). Specific primers, listed in the Table, were designed, and the cDNA was subjected to PCR. The internal control for gene analysis was glyceraldehyde 3-phosphate dehydrogenase (GAPDH). Polymerase chain reactions were carried out using DNA polymerase (Extaq; Takara Bio, Inc., Otsu, Japan). The PCR amplification program consisted of denaturation at 94°C for 30 seconds, 35 cycles of annealing at 54°C for 30 seconds, and elongation at 72°C for 30 seconds. The PCR products were separated by electrophoresis on 2% agarose gels and detected under ultraviolet illumination after ethidium bromide staining.

### Scanning Electron Microscopy

Corneal specimens were obtained from two syngeneic and two allogeneic PK rabbit models and two DSEK rabbit models. The

specimens were washed in 0.1 M Sörensen buffer, fixed with 2.5% glutaraldehyde and 2% paraformaldehyde in 0.1 M Sörensen buffer, and postfixed with 1% osmium tetroxide. This was followed by three washes in buffer before being dehydrated through an alcohol series and then transferred to hexamethyldilazane (HMDS) for two 30-minute changes (Agar Scientific, Stansted, Essex, UK). Samples were left overnight to allow the HMDS to undergo sublimation. Samples were mounted on cylinder stubs (Agar Scientific) sputter-coated with gold and examined in a JEOL 5600 scanning electron microscope (JEOL Ltd., Tokyo, Japan).

### Statistical Analysis

Data are reported as means  $\pm$  SEM. Differences between data sets were determined for statistical significance ( $P$  value) using Student's  $t$ -test.

## RESULTS

### Cell-like White Dots Were Observed on the Endothelium of Patients Following Corneal Transplantation

Representative images of a patient who underwent penetrating keratoplasty 24 years previously showed the presence of cell-like white dots on the corneal endothelium (Fig. 1A). Likewise, a patient who had undergone DSEK 5 years previously also showed the white dots (Fig. 1B). Similar white dots were

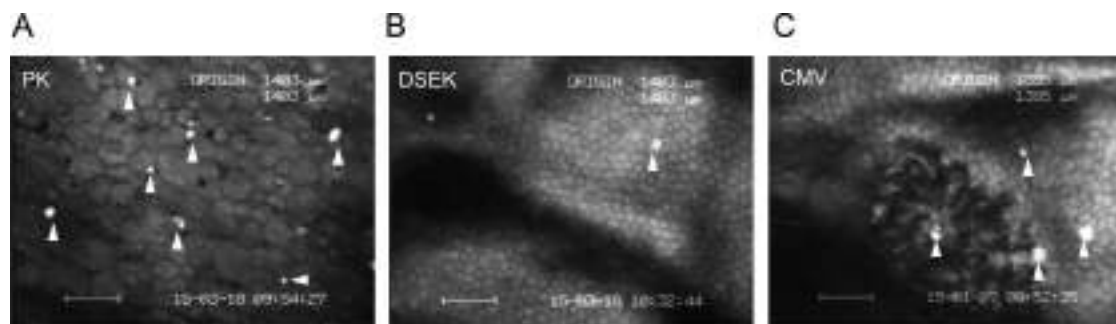
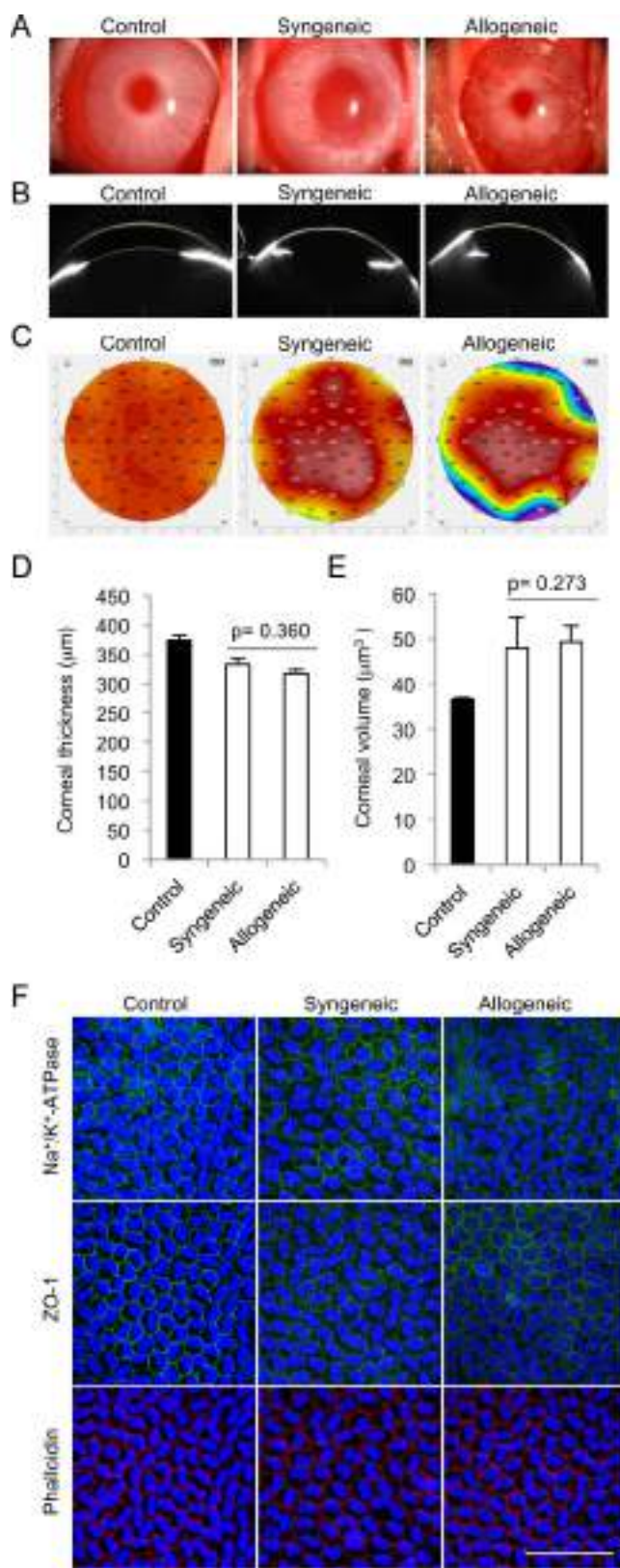


FIGURE 1. Cell-like white dots on the endothelium of patients following corneal transplantation. (A) Corneal endothelium was evaluated by contact specular microscopy in patients who had undergone corneal transplantation. Representative image of a 36-year-old male who underwent PK 24 years previously shows the presence of cell-like white dots on the corneal endothelium. (B) Image from a 67-year-old female who underwent DSEK 5 years previously, showing the cell-like white dots. (C) Image of a 70-year-old male who was diagnosed with CMV corneal endotheliitis infection, showing the cell-like white dots. Arrowheads indicate the cell-like white dots.





**FIGURE 2.** Syngeneic and allogeneic PK rabbit model. (A) Representative anterior segment images (*right*: control healthy eye; *middle*: syngeneic PK; and *left*: allogeneic PK) obtained by slit-lamp microscopy 14 days after transplantation are shown. (B, C) Anterior segment was also evaluated. Representative images and corneal thickness maps are shown. Values of the corneal thickness and corneal volume maps are indicated in micrometers. (D, E) Central corneal thickness and

observed on the corneal endothelium of a patient who was diagnosed with cytomegalovirus (CMV) corneal endotheliitis, which is an inflammatory disease due to CMV,<sup>13,14</sup> suggesting that the white dots were immune cells recruited due to an immune response (Fig. 1C).

### Allogeneic Corneal Transplantation Recruits Immune Cells in Rabbit Model

We used a rabbit PK model to determine whether the white dots observed on corneal endothelium were immune cells. Slit-lamp microscopy showed that a transparent corneal graft was maintained at 2 weeks postoperatively in both syngeneic and allogeneic groups (Fig. 2A). No clinical features of corneal allograft rejection, such as endothelial keratic precipitates, rejection lines, or severe conjunctival injection were observed in allogeneic or syngeneic grafts during the observation time of 2 weeks. Scheimpflug images and corneal thickness maps obtained with a Pentacam high-resolution camera also showed that an anatomically normal cornea had been restored by corneal transplantation (Figs. 2B, 2C). No significant difference was noted in the central corneal thickness and corneal volume between the syngeneic and allogeneic groups (Figs. 2D, 2E). The endothelial phenotype of the CECs in the syngeneic and allogeneic corneal grafts was retained, along with expression of function-related markers, such as ZO-1 (marker of barrier function) and Na<sup>+</sup>/K<sup>+</sup>-ATPase (marker of pump function), and the hexagonal monolayer morphology (Fig. 2F). Contact specular microscopy examination showed healthy morphology of corneal endothelium in both syngeneic and allogeneic groups 14 days after corneal transplantation. However, cell-like white dots that were similar to the dots observed in human subjects following corneal transplantation were observed on corneal endothelium in the allogeneic group (Fig. 3A). Scanning electron microscope analysis revealed the normal hexagonal morphology of the corneal endothelium in both the graft and peripheral recipient cornea in the syngeneic model as well as in control corneas. However, scanning electron microscope analysis revealed the presence of numerous cells that were well distinguished from the corneal endothelium on the surface of the allogeneic graft endothelium, and to a significantly lesser extent, on the recipient corneal endothelium. Notably, very few of these cells were observed in the syngeneic group, but massive numbers of cells were observed in the allogeneic group. Cell-cell junctions were partially disrupted, and membrane blebbing, presumably associated with the apoptotic process, was observed in nearby cells in the corneal endothelium (Fig. 3B). Taken together, these findings supported our hypothesis that the cell-like white dots were immune cells that might be exerting potentially deleterious effects on the corneal endothelium.

### T-Helper Cells, Cytotoxic T Cells, B Lymphocytes, Macrophages, and Neutrophils Infiltrate the Corneal Endothelium of Allogeneic Corneal Grafts

We conducted an immunohistochemical analysis to characterize the infiltrated cells present on the corneal endothelium

corneal volume were analyzed. No significant difference was noted in the central corneal thickness and corneal volume between the syngeneic and allogeneic transplantation groups. (F) Corneal endothelial structure and function of the syngeneic and allogeneic grafts were examined histologically 14 days after transplantation. Corneal endothelial morphology was assessed by actin staining, and endothelial function was assessed by immunostaining for ZO-1 and Na<sup>+</sup>/K<sup>+</sup>-ATPase. Cell nuclei were stained with DAPI. Representative images from at least two independent experiments are shown. Scale bar: 100 μm.

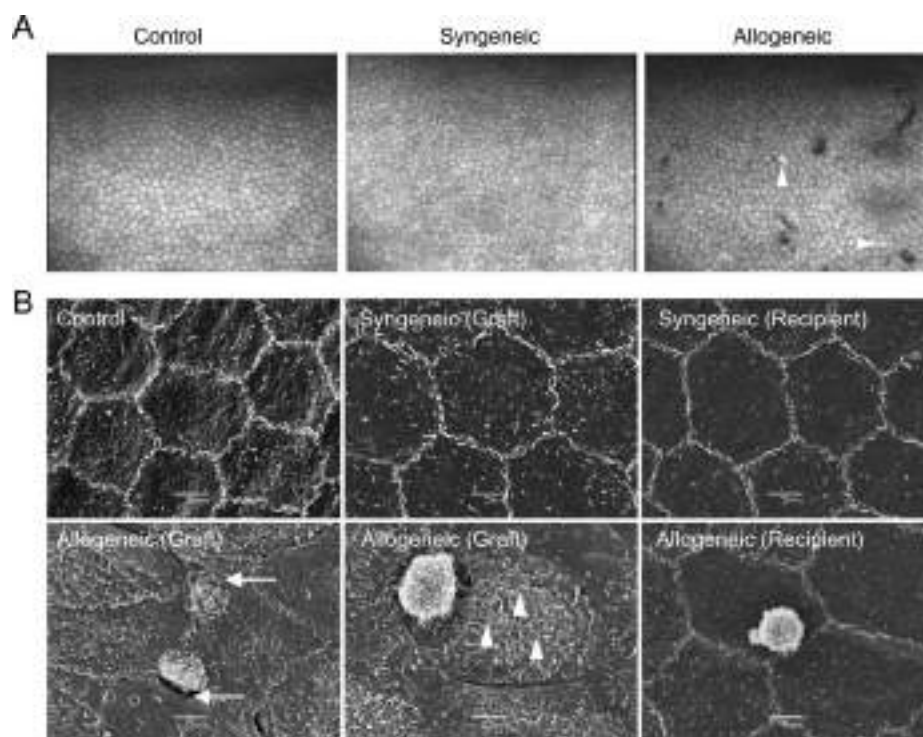


**FIGURE 3.** Contact specular and scanning electron microscopy analysis of the corneal endothelium in the syngeneic and allogeneic corneal grafts. (A) Corneal endothelial cell morphology was also assessed by contact specular microscopy, and representative images are shown for each experimental group. In the allogeneic PK group, the corneal graft endothelium shows cell-like white dots, indicated by white arrowheads. (B) Scanning electron microscope images of the corneal endothelium of a control healthy cornea, a syngeneic graft, and an allogeneic graft. Cell-cell junctions were partially disrupted (arrows), and membrane blebbing (arrowheads) was observed near the immune cell-like cells on the corneal endothelium of the allogeneic graft. All images are representative of two animals in each group. Scale bars: 5  $\mu$ m.

after allogeneic corneal transplantation in rabbits. None of the grafts (syngeneic or allogeneic) displayed any clinical signs of organ rejection, but immune cells, characterized by the presence of CD4<sup>+</sup> T-helper cells, CD8<sup>+</sup> cytotoxic T cells, CD20<sup>+</sup> B lymphocytes, CD68<sup>+</sup> macrophages, and neutrophils marked by cathepsin G, were observed on the endothelial layer in nine out of nine allogeneic graft specimens 2 weeks after transplantation. Similar to the scanning electron microscope findings, these immune cells were rarely observed in the syngeneic grafts (Fig. 4A). As a positive control, where infiltration of immune cells would be expected, we analyzed corneal grafts that had been rejected 2 months after allogeneic transplantation. All three rabbits that had been observed for 2 months exhibited signs associated with graft rejection, such as corneal haziness, corneal edema, and conjunctival injection at 1.5 to 2 months. The rejected corneal grafts exhibited distinct morphologic alterations as determined by the cellular distribution of F-actin, which suggested CEC transformation into fibroblast-like cells, as occurs in human corneal graft rejection. Higher numbers of infiltrating immune cells—CD4<sup>+</sup> T-helper cells, CD8<sup>+</sup> cytotoxic T cells, CD20<sup>+</sup> B lymphocytes, CD68<sup>+</sup> macrophages, and neutrophils—were observed on the rejected corneal endothelium than on the nonrejected allogeneic graft (Fig. 4A).

Immune cells secrete cytokines that are critical regulators of immune response; therefore, we investigated whether proinflammatory cytokines were secreted in corneal grafts. Tumor necrosis factor- $\alpha$  and IFN- $\gamma$  were detectable in the allogeneic graft endothelium, which showed no clinical features of rejection 2 weeks after corneal transplantation, but TNF- $\alpha$  and IFN- $\gamma$  were not detected in the syngeneic graft or the control (Fig. 4B). Co-staining showed that a certain population of CD4<sup>+</sup> T-helper cells expressed TNF- $\alpha$  and IFN- $\gamma$  and that a

certain population of CD8<sup>+</sup> cytotoxic T cells expressed TNF- $\alpha$  and IFN- $\gamma$  in the allogeneic grafts 2 weeks after surgery (Fig. 4C).

### Immune Cells Infiltrate on the Corneal Endothelium of Allogeneic DSEK Graft

We next determined the infiltration of immune cells onto the corneal endothelium of a DSEK graft, as the CEC declines seen after transplantation of DSEK grafts are at the same level (or even worse) as that seen in PK.<sup>6,15–17</sup> Corneal transplantation performed as a DSEK procedure in the rabbit gave a successful graft in all cases, with a transparent cornea and no serious complications such as graft rejection, graft failure, or graft dislocation. Representative slit-lamp microscopic images showed attachment of the graft to the back side of cornea, and corneal transparency was maintained in the rabbit model 2 weeks after surgery (Fig. 5A). Scanning electron microscope demonstrated the presence of numerous discrete nonendothelial cells, morphologically similar to immune cells in appearance, present near the graft-recipient interface (Fig. 5B). Notably, a high density of immune-like cells was observed on the corneal endothelium of the DSEK graft in contrast to the recipient corneal endothelium, where very few immune-like cells were found (Fig. 5C). The control eyes exhibited the normal hexagonal morphology of the corneal endothelium without any immune-like cells. Higher magnification scanning electron microscope images showed that immune-like cells were adjacent to a missing endothelial cell (Fig. 5D), suggesting that these cells may have the ability to damage the corneal endothelium.



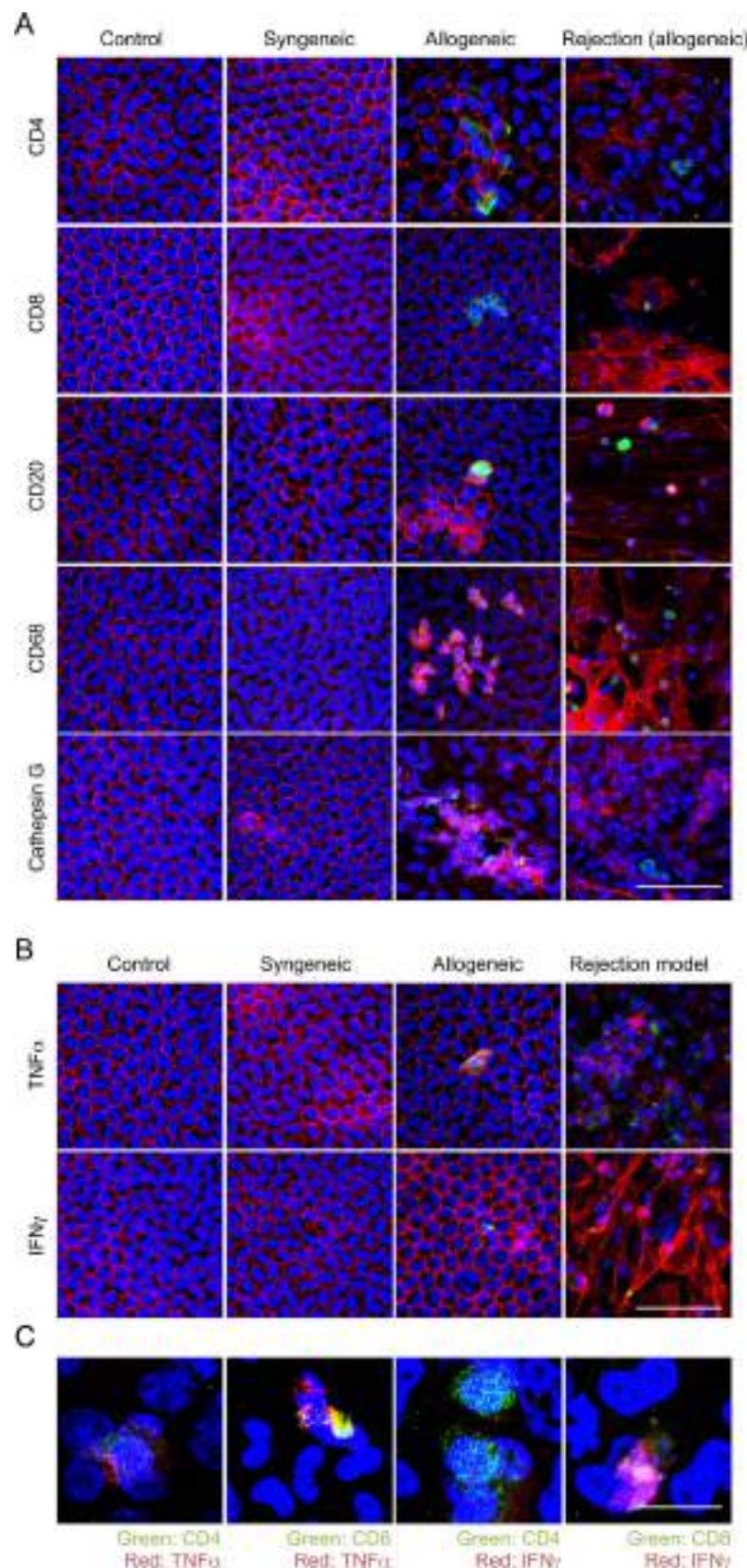


**FIGURE 4.** Immunofluorescence analysis of the corneal endothelium of the syngeneic and allogeneic PK model. (A) Control cornea, syngeneic corneal graft, allogeneic corneal graft, and rejected allogeneic corneal graft were immunostained with CD4 (T-helper cells), CD8 (cytotoxic T cells), CD20 (B cells), CD68 (macrophages), and cathepsin G (neutrophils) antibodies 14 days post transplantation. CD4<sup>+</sup> T lymphocytes, CD8<sup>+</sup> T lymphocytes, CD20<sup>+</sup> B lymphocytes, CD68<sup>+</sup> macrophages, and neutrophils characterized the allogeneic PK graft endothelium layer and the rejected graft cornea. DAPI was used to stain cell nuclei. Scale bar: 100  $\mu$ m. (B) Secretion of TNF- $\alpha$  and IFN- $\gamma$  was determined in the control corneal

syngeneic corneal graft, allogeneic corneal graft, and rejected allogeneic corneal graft. Actin and cell nuclei were stained with generic term and DAPI, respectively. All experiments were performed in duplicate. *Scale bar*: 100  $\mu$ m. (C) Co-staining of CD4/TNF- $\alpha$  and IFN- $\gamma$ , and CD8/TNF- $\alpha$  and IFN- $\gamma$  in allogeneic grafts 2 weeks after corneal transplantation. Nuclei were stained with DAPI. Experiments were performed on three independent animals. *Scale bar*: 50  $\mu$ m.

Similar to the PK model, immunofluorescence analysis demonstrated the presence of CD3<sup>+</sup> T lymphocytes, CD4<sup>+</sup> T-helper cells, CD8<sup>+</sup> cytotoxic T cells, CD20<sup>+</sup> B lymphocytes, and CD68<sup>+</sup> macrophages on the corneal endothelium (Fig. 5E). The recipient endothelium rarely showed the presence of these immune cells, suggesting that the allogeneic corneal endothelium has the ability to recruit immune cells. Consistent with the findings observed previously for the PK corneal grafts, TNF- $\alpha$ - and IFN- $\gamma$ -producing immune cells were also detected in the DSEK graft endothelium (Fig. 5E). Image stacks of specific depths and high resolution obtained by confocal laser scanning electron microscopy of the DSEK corneas revealed that these immune cells were attached onto the graft endothelium layer positioned at the anterior chamber site (Fig. 5F). The expression of cytokines related to inflammation was evaluated 2 weeks after DSEK in corneal endothelium that included immune cells. Semiquantitative RT-PCR showed higher expression of IL-1 receptor antagonist (IL-1RA), IL-1b, IL-6, IL-15, TNF- $\alpha$ , TGF- $\beta$ 2, CX3CR, and CCL2 in DSEK corneal endothelium than in healthy corneal endothelium, while IL-8, IL-10, TLR4, and TRAIL were detected at similar levels in both groups (Fig. 5G).

## DISCUSSION

The cornea is an immune-privileged tissue with properties that prevent alloimmune-mediated rejection responses, which then enables an advantageously high success rate of transplantation.<sup>18–24</sup> Numerous basic research studies have demonstrated that the immune privilege of the eye is not solely a phenomenon due to immunologic ignorance, but instead is a highly orchestrated immune system consisting of unique immune suppression mechanisms, widely known as anterior chamber-associated immune deviation.<sup>21–23,25</sup> This immune-privileged environment, as well as the underlying mechanisms involved in corneal graft rejection by host immune systems, has also been intensively investigated.<sup>22,26–29</sup>

By contrast, the mechanism of late endothelial failure is still unclear. The clinical data showing the much lower drop in cell density of CECs after autologous rotational corneal transplantation than after allogeneic transplantation suggested the possibility that immunologic influences are involved in the pathogenesis of chronic endothelial failure.<sup>12</sup> We showed that cell-like white dots can be observed on the corneal endothelium of a transplanted graft by scanning slit contact specular microscopy in the patients who show no clinical features of graft rejection. Similar cell-like white dots were also observed on the corneal endothelium of the CMV corneal endotheliitis patients, so we speculated that these dots might be immune cells. In agreement with our findings, *in vivo* confocal microscopy revealed the presence of indistinguishable small, rounded white cell bodies representing inflammatory cell structures on the corneal endothelium following corneal transplantation.<sup>30,31</sup> Our rabbit model experiments demonstrated that the cell-like white dots observed by scanning slit contact specular microscopy correspond to immune cells comprising at least T-helper cells, cytotoxic T cells, B cells, macrophages, and neutrophils. One limitation of our study is that these cell-like white dots, revealed to be immune cells, were observed 2 weeks after surgery in the rabbit model, but

they were observed in humans a longer time after the corneal transplantation. Further investigation, such as using postmortem corneal specimens in the patients, should determine whether immune cells exist on the corneal endothelium of patients who do not exhibit clinical features of graft rejection. Another important question to be answered is whether this immunologic response is induced owing to the surgical intervention or to the allogeneic graft, as leukocyte extravasation and migration to injury sites are important milestones of wound-healing process. Our histologic assessment demonstrated that immune cells were rarely observed on syngeneic grafts, whereas they were intensively observed on allogeneic grafts. This suggests that immune cells were recruited by allogeneic grafts, though the nature of the signal—whether immune cells recognized CECs or corneal stromal cells or did not recognize allogeneic cells—should be further investigated. In agreement with previous reports,<sup>26–29</sup> rejected allogeneic grafts were characterized by inflammatory cell aggregates composed of CD4<sup>+</sup> and CD8<sup>+</sup> T lymphocytes, B lymphocytes, macrophages, and neutrophils and by tissue destruction. Interestingly, unlike the case for the rejected grafts, the cells observed in transparent allogeneic grafts without clinical features of rejection were not associated with destruction of the surrounding CECs. One possible explanation for the presence of immune cells on a nonrejected graft is that they have a potency to precede typical graft rejection. Though this is speculative, if the grafted cornea successfully evaded rejection triggered by these immune cells, the graft would eventually exhibit CEC loss. Graft rejection is typically observed after 2 months; therefore, analysis of animal models for a longer time will help in understanding the role of these immune cells. Another possible explanation is that the corneal endothelium was damaged by an as yet unknown mechanism, and the immune cells were recruited for a wound-healing process. Further functional experiments to evaluate the cytotoxicity of the adhered immune cells to the graft corneal endothelium are needed to verify the role played by immune cells in corneal endothelial damage.

Penetrating keratoplasty was previously the only procedure for corneal transplantation, but new procedures, such as DSEK and DMEK (Descemet's membrane endothelial keratoplasty), have been developed for replacement of the corneal endothelium that do not involve full-thickness replacement.<sup>1</sup> Stripping endothelial keratoplasty and DMEK are less-invasive treatments and are now frequently performed.<sup>32,33</sup> Anshu et al.<sup>34</sup> reported rejection rates of 17% in PK, 9% in DSEK, and 0.7% in DMEK in a single center and suggested that DSEK and DMEK reduced the risk of rejection. This may be because DSEK and DMEK grafts do not include epithelium, as each layer of the cornea has different immunogenicity. Indeed, the use of reconstituted mouse corneal grafts confirmed that the corneal epithelium had a higher allosensitization potency when compared with endothelium.<sup>35–37</sup> By contrast, the incidence of graft rejection in DSEK, and even in DMEK, suggests that the corneal endothelium also has immunogenicity. Our current data for our rabbit DSEK model showed that immune cells migrated onto allogeneic graft corneal endothelium and expressed proinflammatory cytokines, as observed in PK. We also showed that the levels of cytokines related to inflammation are higher in the DSEK corneal endothelium. However, the source of these cytokines (i.e., the corneal endothelium or the



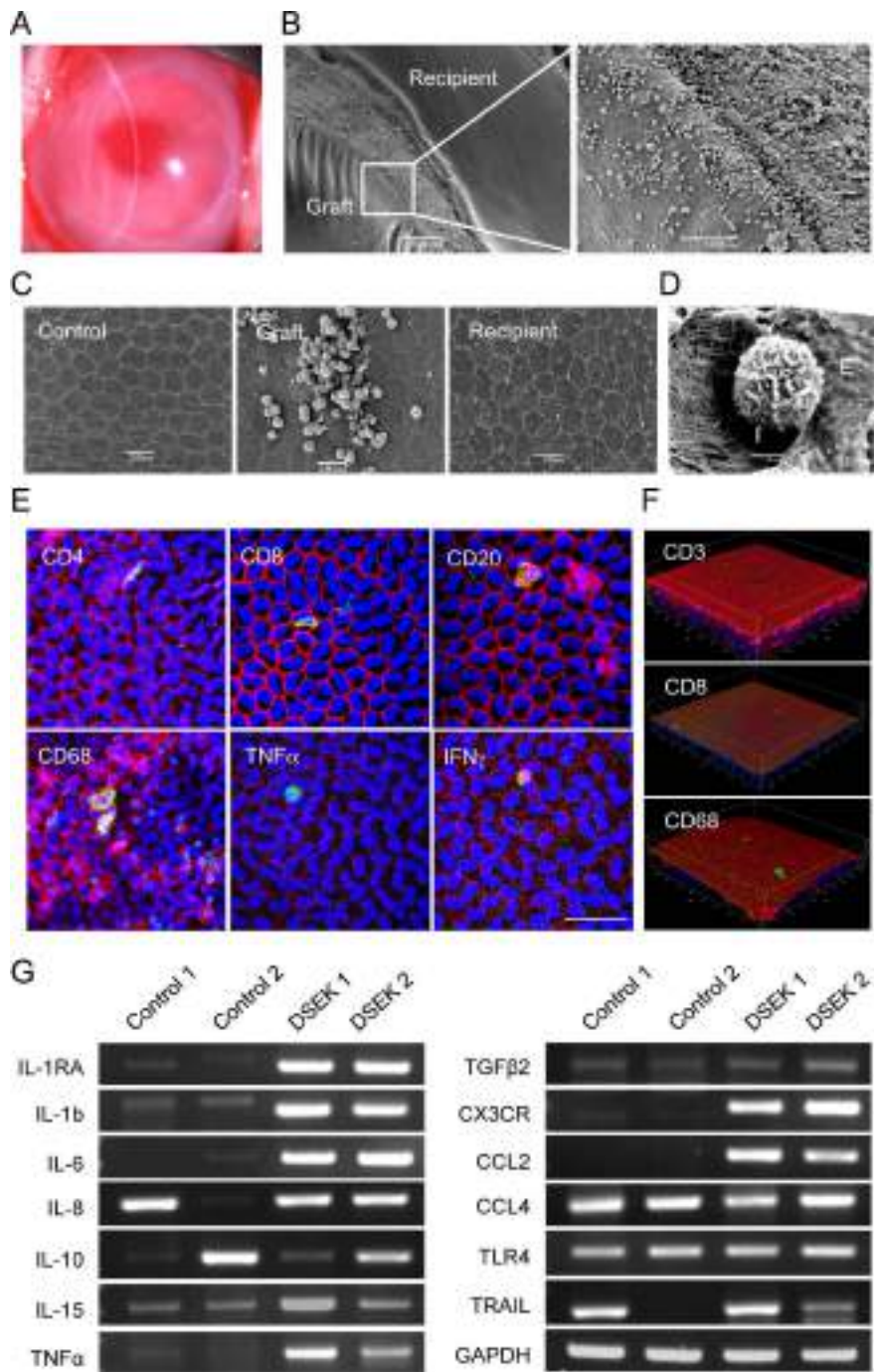


**FIGURE 5.** Involvement of immune cells in the corneal endothelium of a DSEK graft. (A) Corneal transplantation was performed as a DSEK procedure in six rabbits, and a representative slit-lamp microscopy image is shown. (B) Scanning electron microscopy evaluation of the donor-host junction of the DSEK rabbit model. Scale bar: 500  $\mu$ m. Higher magnification of the boxed area shown on the right-hand side. Scale bar: 100  $\mu$ m. (C) Scanning electron microscope demonstrated that numerous nonendothelial cells, morphologically with an immune cell-like appearance, were present near the graft-recipient interface. A high density of these immune-like cells was observed on the corneal endothelium of the DSEK graft, whereas the recipient corneal endothelium showed very few immune-like cells. The control eyes exhibited a hexagonal, normal morphologic corneal endothelium without any immune-like cells. All images are representative of two animals in each group. Scale bar: 2  $\mu$ m. (D) Higher magnification scanning electron microscope image showing immune-like cells adjacent to a missing endothelial cell. Scale bar: 2  $\mu$ m. (E) Corneal endothelium of the DSEK graft immunostained with immune cell-related markers: CD4<sup>+</sup> cell (T-helper cells), CD8<sup>+</sup> cell (cytotoxic T cells), CD20<sup>+</sup> cell (B cells), and CD68<sup>+</sup> cell (macrophages). Production of TNF- $\alpha$  and IFN- $\gamma$  was also evaluated by immunostaining. Actin and cell nuclei were stained with Alexa Fluor 594-conjugated phalloidin and DAPI, respectively. All experiments were performed in triplicate. Scale bar: 100  $\mu$ m. (F) Stripping endothelial keratoplasty corneas were analyzed by confocal laser scanning electron microscopy. Image stacks up to a depth of 150  $\mu$ m, at either 1- or 3- $\mu$ m intervals, were acquired, and three-dimensional reconstructions were created. Representative still images for CD3<sup>+</sup> T lymphocytes, CD8<sup>+</sup> T lymphocytes, and CD68<sup>+</sup> macrophages on the corneal endothelium are shown. Actin staining was performed to evaluate cell morphology. Nuclei were stained with DAPI. (G) The expression of cytokines related to inflammation was evaluated 2 weeks after DSEK in corneal endothelium that included immune cells by semiquantitative RT-PCR.

immune cells) was not established in the current study. Nevertheless, the elevated cytokine levels might suggest an involvement of immune cells as part of the underlying mechanism of CEC loss in corneal endothelial transplantation performed using procedures other than just conventional PK.

In conclusion, our data suggest that T lymphocytes, B lymphocytes, macrophages, and neutrophils are present on the grafted corneal endothelium following both PK and DSEK. The current findings should stimulate further research aimed at clearly elucidating the involvement of immune cells as an underlying pathophysiology to provide treatment for late endothelial failure.

### Acknowledgments

The authors thank Hiroko Nakagawa, MD, PhD, for valuable discussion and technical contribution for scanning slit specular microscopy and Shuichi Yano, PhD, for providing technical assistance with the multiphoton microscopy.

Supported by the Japanese Society for the Promotion of Science, Tokyo, Japan (EK) and by the Program for the Strategic Research Foundation at Private Universities from the Ministry of Education, Culture, Science, Sports and Technology, Tokyo, Japan (NK and NO).

Disclosure: E. Koudouna, None; N. Okumura, None; Y. Okazaki, None; S. Nakano, None; R. Inoue, None; N.J. Fullwood, None; J. Hori, None; S. Kinoshita, None; N. Koizumi, None

### References

1. Tan DT, Dart JK, Holland EJ, Kinoshita S. Corneal transplantation. *Lancet*. 2012;379:1749–1761.
2. Eye Bank Association of America. *Eye Banking Statistical Report*. Washington, DC: EBAA; 2013.
3. Williams KA, Roder D, Esterman A, Muehlberg SM, Coster DJ. Factors predictive of corneal graft survival. Report from the Australian Corneal Graft Registry. *Ophthalmology*. 1992;99:403–414.
4. Sit M, Weisbrod DJ, Naor J, Slomovic AR. Corneal graft outcome study. *Cornea*. 2001;20:129–133.
5. Tan DT, Janardhanan P, Zhou H, et al. Penetrating keratoplasty in Asian eyes: the Singapore Corneal Transplant Study. *Ophthalmology*. 2008;115:975–982 e971.
6. Patel SV. Graft survival and endothelial outcomes in the new era of endothelial keratoplasty. *Exp Eye Res*. 2012;95:40–47.
7. Sugar A, Gal RL, Kollman C, et al.; Writing Committee for the Cornea Donor Study Research Group. Factors associated with corneal graft survival in the cornea donor study. *JAMA Ophthalmol*. 2015;133:246–254.
8. Maumenee AE. Clinical aspects of the corneal homograft reaction. *Invest Ophthalmol Vis Sci*. 1962;1:244–252.
9. Khodadoust AA, Silverstein AM. Transplantation and rejection of individual cell layers of the cornea. *Invest Ophthalmol*. 1969;8:180–195.
10. Alldredge OC, Krachmer JH. Clinical types of corneal transplant rejection. Their manifestations, frequency, preoperative correlates, and treatment. *Arch Ophthalmol*. 1981;99:599–604.
11. Bourne WM. Clinical estimation of corneal endothelial pump function. *Trans Am Ophthalmol Soc*. 1998;96:229–239; discussion 239–242.
12. Birnbaum F, Reinhard T, Bohringer D, Sundmacher R. Endothelial cell loss after autologous rotational keratoplasty. *Graefes Arch Clin Exp Ophthalmol*. 2005;243:57–59.
13. Koizumi N, Suzuki T, Uno T, et al. Cytomegalovirus as an etiologic factor in corneal endotheliitis. *Ophthalmology*. 2008;115:292–297 e293.
14. Koizumi N, Inatomi T, Suzuki T, et al. Clinical features and management of cytomegalovirus corneal endotheliitis: analysis of 106 cases from the Japan corneal endotheliitis study. *Br J Ophthalmol*. 2015;99:54–58.
15. Guerra FP, Anshu A, Price MO, Giebel AW, Price FW. Descemet's membrane endothelial keratoplasty: prospective study of 1-year visual outcomes, graft survival, and endothelial cell loss. *Ophthalmology*. 2011;118:2368–2373.
16. Nanavaty MA, Wang X, Shortt AJ. Endothelial keratoplasty versus penetrating keratoplasty for Fuchs endothelial dystrophy. *Cochrane Database Syst Rev*. 2014;2:CD008420.
17. Hamzaoglu EC, Straiko MD, Mayko ZM, Sales CS, Terry MA. The first 100 eyes of standardized descemet stripping automated endothelial keratoplasty versus standardized descemet membrane endothelial keratoplasty. *Ophthalmology*. 2015;122:2193–2199.
18. Medawar PB. A second study of the behaviour and fate of skin homografts in rabbits: a report to the War Wounds Committee of the Medical Research Council. *J Anat*. 1945;79:157–176 154.
19. Billingham RE, Brent L, Medawar PB. Quantitative studies on tissue transplantation immunity. II. The origin, strength and duration of actively and adoptively acquired immunity. *Proc R Soc Lond B Biol Sci*. 1954;143:58–80.
20. Niederkorn J, Streilein JW, Shaddock JA. Deviant immune responses to allogeneic tumors injected intracamerally and subcutaneously in mice. *Invest Ophthalmol Vis Sci*. 1981;20:355–363.
21. Niederkorn JY, Streilein JW. Induction of anterior chamber-associated immune deviation (ACAID) by allogeneic intraocular tumors does not require splenic metastases. *J Immunol*. 1982;128:2470–2474.
22. Niederkorn JY. Mechanisms of immune privilege in the eye and hair follicle. *J Invest Dermatol Symp Proc*. 2003;8:168–172.
23. Streilein JW. Ocular immune privilege: therapeutic opportunities from an experiment of nature. *Nat Rev Immunol*. 2003;3:879–889.
24. Hori J, Joyce NC, Streilein JW. Immune privilege and immunogenicity reside among different layers of the mouse cornea. 2000. *Ocul Immunol Inflamm*. 2007;15:225–239.
25. Sonoda Y, Streilein JW. Orthotopic corneal transplantation in mice—evidence that the immunogenetic rules of rejection do not apply. *Transplantation*. 1992;54:694–704.
26. Cursiefen C, Chen L, Dana MR, Streilein JW. Corneal lymphangiogenesis: evidence, mechanisms, and implications for corneal transplant immunology. *Cornea*. 2003;22:273–281.
27. Streilein JW, Arancibia-Caracamo C, Osawa H. The role of minor histocompatibility alloantigens in penetrating keratoplasty. *Dev Ophthalmol*. 2003;36:74–88.
28. Niederkorn JY. Immune mechanisms of corneal allograft rejection. *Curr Eye Res*. 2007;32:1005–1016.
29. Niederkorn JY. High-risk corneal allografts and why they lose their immune privilege. *Curr Opin Allergy Clin Immunol*. 2010;10:493–497.
30. Imre L, Resch M, Nagymihaly A. [In vivo confocal corneal microscopy after keratoplasty]. *Ophthalmologe*. 2005;102:140–146.
31. Niederer RL, McGhee CN. Clinical in vivo confocal microscopy of the human cornea in health and disease. *Prog Retin Eye Res*. 2010;29:30–58.



32. Tourtas T, Laaser K, Bachmann BO, Cursiefen C, Kruse FE. Descemet membrane endothelial keratoplasty versus descemet stripping automated endothelial keratoplasty. *Am J Ophthalmol*. 2012;153:1082-1090.e1082.
33. Price MO, Price FW Jr. Descemet's membrane endothelial keratoplasty surgery: update on the evidence and hurdles to acceptance. *Curr Opin Ophthalmol*. 2013;24:329-335.
34. Anshu A, Price MO, Price FW Jr. Risk of corneal transplant rejection significantly reduced with Descemet's membrane endothelial keratoplasty. *Ophthalmology*. 2012;119:536-540.
35. Hori J, Joyce NC, Streilein JW. Immune privilege and immunogenicity reside among different layers of the mouse cornea. *Invest Ophthalmol Vis Sci*. 2000;41:3032-3042.
36. Hori J, Streilein JW. Survival in high-risk eyes of epithelium-deprived orthotopic corneal allografts reconstituted in vitro with syngeneic epithelium. *Invest Ophthalmol Vis Sci*. 2003;44:658-664.
37. Saban DR, Chauhan SK, Zhang X, El Annan J, Jin Y, Dana R. 'Chimeric' grafts assembled from multiple allodisparate donors enjoy enhanced transplant survival. *Am J Transplant*. 2009;9:473-482.